NEUROANATOMY FOR THE XXIst CENTURY

EDITED BY: Kathleen S. Rockland and Javier DeFelipe
PUBLISHED IN: Frontiers in Neuroanatomy

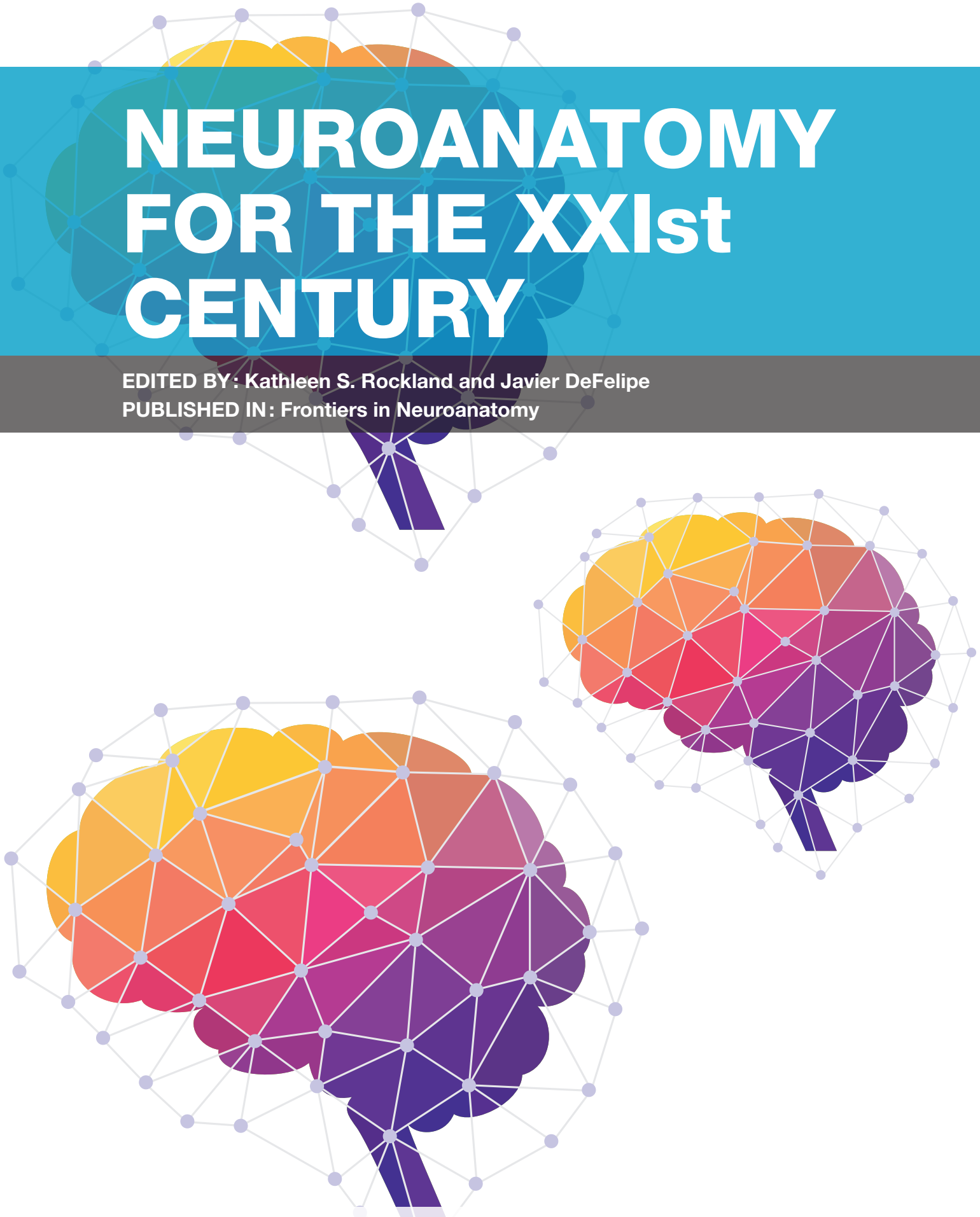

frontiers Research Topics

frontiers

ISSN 1664-8714
ISBN 978-2-88919-916-7
DOI 10.3389/978-2-88919-916-7

About Frontiers

Frontiers is more than just an open-access publisher of scholarly articles: it is a pioneering approach to the world of academia, radically improving the way scholarly research is managed. The grand vision of Frontiers is a world where all people have an equal opportunity to seek, share and generate knowledge. Frontiers provides immediate and permanent online open access to all its publications, but this alone is not enough to realize our grand goals.

Frontiers Journal Series

The Frontiers Journal Series is a multi-tier and interdisciplinary set of open-access, online journals, promising a paradigm shift from the current review, selection and dissemination processes in academic publishing. All Frontiers journals are driven by researchers for researchers; therefore, they constitute a service to the scholarly community. At the same time, the Frontiers Journal Series operates on a revolutionary invention, the tiered publishing system, initially addressing specific communities of scholars, and gradually climbing up to broader public understanding, thus serving the interests of the lay society, too.

Dedication to Quality

Each Frontiers article is a landmark of the highest quality, thanks to genuinely collaborative interactions between authors and review editors, who include some of the world's best academicians. Research must be certified by peers before entering a stream of knowledge that may eventually reach the public - and shape society; therefore, Frontiers only applies the most rigorous and unbiased reviews.
Frontiers revolutionizes research publishing by freely delivering the most outstanding research, evaluated with no bias from both the academic and social point of view.
By applying the most advanced information technologies, Frontiers is catapulting scholarly publishing into a new generation.

What are Frontiers Research Topics?

Frontiers Research Topics are very popular trademarks of the Frontiers Journals Series: they are collections of at least ten articles, all centered on a particular subject. With their unique mix of varied contributions from Original Research to Review Articles, Frontiers Research Topics unify the most influential researchers, the latest key findings and historical advances in a hot research area! Find out more on how to host your own Frontiers Research Topic or contribute to one as an author by contacting the Frontiers Editorial Office: **researchtopics@frontiersin.org**

NEUROANATOMY FOR THE XXIst CENTURY

Topic Editors:
Kathleen S. Rockland, Boston University School of Medicine, USA
Javier DeFelipe, Instituo Cajal (CSIC), Spain

An explosion of new techniques with vastly improved visualization and sensitivity is leading a veritable revolution in modern neuroanatomy. Basic questions related to cell types, input localization, and connectivity are being re-visited and tackled with significantly more accurate and higher resolution experimental approaches. A major goal of this e-Book is thus to highlight in one place the impressive range of available techniques, even as these are fast becoming routine. This is not meant as a technical review, however, but rather will project the technical explosion as indicative of a field now in a vibrant state of renewal. Thus, contributions will be mainly research articles using the newer techniques. A second goal is to showcase what has become the conspicuous interdisciplinary reach of the field: neuroanatomical standards and the close association of structure-function and underlying circuitry mechanisms are increasingly relevant to investigations in development, physiology, and disease. Another feature of this Research Topic is that it includes a breadth of cross-species contributions from investigators working with rodent, nonhuman primate, and human brains. This is important since most of our current knowledge of brain structure has been obtained from experimental animals. However, recent technical advances, coupled with researcher willingness to use the human tissue available, will undoubtedly lead to major advances in the near future regarding human brain mapping and connectomes. Thus, of particular interest will be the methods that can help to define general wiring principles in the brain, both structural and functional. Overall, the state of the field is: exciting.

Citation: Rockland, K. S., DeFelipe, J., eds. (2016). Neuroanatomy for the XXIst Century. Lausanne: Frontiers Media. doi: 10.3389/978-2-88919-916-7

Table of Contents

frontiers in Neuroanatomy

EDITORIAL
published: 22 June 2016
doi: 10.3389/fnana.2016.00070

Editorial: Neuroanatomy for the XXIst Century

Kathleen S. Rockland[1,2]* *and Javier DeFelipe*[3,4]

[1] Department of Anatomy and Neurobiology, Boston University School of Medicine, Boston, MA, USA, [2] Cold Spring Harbor Laboratory, New York, NY, USA, [3] Departamento de Neurobiología Funcional y de Sistemas, Instituto Cajal (CSIC), Madrid, Spain, [4] Laboratorio Cajal de Circuitos Corticales, Centro de Tecnología Biomédica, Universidad Politécnica de Madrid, Madrid, Spain

Keywords: light-sheet imaging, two-photon tomography, FIB/SEM, fMOST, polarized light microscopy, viral vectors, synaptic weights, human neuroanatomy

The Editorial on the Research Topic

Neuroanatomy for the XXIst Century

In this still young XXIst century, neuroanatomy returns to center stage, after decades of being criticized as too "descriptive," and consequent neglect at the end of the last century. This re-instatement is in part because "descriptive" has lost much of its pejorative connotation, and the recognition of the importance of functional, genetically- and molecularly-based categorization, and deeper understanding of cell types and network organization. Neuroanatomy as a discipline has an established commitment to structural-functional correlations and is thus well-positioned for progress in these fundamental areas. Indeed, the development of new neuroanatomical methods and segmentation tools to convert qualitative visual observations into quantitative data is fueling the return of neuroanatomy as a principal discipline for better understanding the structural and functional organization of the nervous system.

The 16 articles in this Research Topic represent some of the major techniques and issues giving a special mandate to the current resurgence of neuroanatomy. The technical advances are obvious and compelling. At the synaptic level, array tomography and automated transmission electron microscopy (Burette et al.) can effectively probe individual synapses and the dynamic patterns of synaptic weights; and FIB/SEM (Bosch et al.) has emerged as a reliable, efficient, and high-resolution technique for investigating identified synaptic contacts in a high-throughput manner.

A theme repeatedly emphasized in this Special Topic is the need for high-resolution and high-throughput investigations, able to cross over multiple scales of organization. Relatively new, promising approaches to this goal are mGRASP circuit mapping (Rah et al.) and light-sheet microscopy, applied by Silvestri et al. to the three-dimensional distribution of Purkinje cells in a B6C3Fe-L7-EGFP mouse. Alghamdi and Fern demonstrate how immuno-histochemistry combined with immuo-EM can provide novel criteria for distinguishing astroglia, oligodendroglia, and NG-2 cells. Sophisticated light microscopic techniques such as fMOST (Yuan et al.) and serial two photon tomography (Amato et al.) utilize to good advantage the expanding repertoire of fluorescent markers. These methods, however, are not routine and each article carefully sets forth the obstacles and challenges posed by large datasets. Computer vision techniques (Fua and Knott) are one approach to these data management problems.

Long-distance connectivity is central to the neuroanatomical portfolio. Here, technical progress has been conspicuous, with the arrival of a variegated assortment of anterograde, retrograde, transsynaptic, and cell-type specific tracers. These can elucidate not only "basic" connectivity, but also functionally relevant quantitative parameters, of how pre-and postsynaptic populations

OPEN ACCESS

Edited and reviewed by:
James A. Bourne, Australian Regenerative Medicine Institute, Australia

***Correspondence:**
Kathleen S. Rockland
krock@bu.edu

Received: *01 May 2016*
Accepted: *09 June 2016*
Published: *22 June 2016*

Citation:
Rockland KS and DeFelipe J (2016) Editorial: Neuroanatomy for the XXIst Century. Front. Neuroanat. 10:70. doi: 10.3389/fnana.2016.00070

intercommunicate. The technical toolbox, largely based on viral tracers, is briefly reviewed by Nassi et al.; and, as one specific application, Wang et al. chart a comprehensive mapping of the central melanocortin system by using cell-type specific viral vectors. Moving to neural assemblies, Roe et al. review how these can be mapped *in vivo* by focal electrical and optical stimulation methods combined with optical imaging and fMRI.

While much of neuroanatomy necessarily requires animal models to permit experimental intervention and high resolution visualization in brain tissue, the great need for human-specific results is widely recognized. In this area, also, there has been impressive progress, with new and faster methods of data analysis. Tellmann et al. demonstrate the strength of 3D probability maps in MNI-Colin27 space, as specifically applied to cytoarchitectonic mapping of the cerebellar nuclei and their connectivity-based co-activations. A second article (Reckfort et al.) discusses features of two complementary polarimetric setups for mapping fiber architecture at micro- and macroscopic resolution, along with methods for optimal multiscale analysis.

At the same time that technical advances and conceptual needs are propelling neuroanatomical investigations at multiple scales—from subcellular to neuronal assemblies, and connectional networks—the sheer amount of data and the inherent complexity of neuroanatomical space present significant problems. Issues of nomenclature, data integration, and whole brain analysis are discussed by the co-editors, here (Rockland) and in a separate issue (DeFelipe). Handling the massive and growing amount of neuroscientific literature is another challenge; and in the concluding article, Vasques et al. deal with text-mining models that might offer some aid in the process.

Finally, we note that these 16 contributions are clearly only a small subset of the huge amount of ongoing work and the large number of developments currently taking place. On the one hand, there is an explosion of new higher sensitivity and higher resolution brain imaging techniques, tools for 3D neuroanatomy, and advances in high-throughput technology and automation. On the other and concurrently, there are major challenges: for image processing and for the analysis and development of methods for accurate, large-scale quantification of the elements under study (e.g., see Budd et al.). It is important to keep in mind that most of our current knowledge of brain structure has been obtained from experimental animals and that our knowledge of human brain microorganization is very scant. Therefore, a major goal of the neuroanatomy for the XXIst century is to improve the current technologies for the microanatomical analysis of the human brain by adapting methodologies that are normally used to examine the brain of experimental animals.

AUTHOR CONTRIBUTIONS

JD and KR collaborated together in writing the Editorial and Introduction.

Conflict of Interest Statement: The authors declare that the research was conducted in the absence of any commercial or financial relationships that could be construed as a potential conflict of interest.

frontiers in Neuroanatomy

PERSPECTIVE
published: 28 July 2015
doi: 10.3389/fnana.2015.00100

Knowing a synapse when you see one

Alain Burette[1], *Forrest Collman*[2], *Kristina D. Micheva*[3], *Stephen J. Smith*[2]* *and Richard J. Weinberg*[1]

[1] *Department of Cell Biology and Physiology, University of North Carolina at Chapel Hill, Chapel Hill, NC, USA,* [2] *Allen Institute for Brain Science, Seattle, WA, USA,* [3] *Department of Molecular and Cellular Physiology, Stanford University, Stanford, CA, USA*

Recent years have seen a rapidly growing recognition of the complexity and diversity of the myriad individual synaptic connections that define brain synaptic networks. It has also become increasingly apparent that the synapses themselves are a major key to understanding the development, function and adaptability of those synaptic networks. In spite of this growing appreciation, the molecular, structural and functional characteristics of individual synapses and the patterning of their diverse characteristics across functional networks have largely eluded quantitative study with available imaging technologies. Here we offer an overview of new computational imaging methods that promise to bring single-synapse analysis of synaptic networks to the fore. We focus especially on the challenges and opportunities associated with quantitative detection of individual synapses and with measuring individual synapses across network scale populations in mammalian brain.

Keywords: synapse, network, cortex, microscopy, array tomography, electron microscopy, fluorescence

OPEN ACCESS

Edited by:
Kathleen S. Rockland, Boston University School Medicine, USA

Reviewed by:
Martha E. Bickford, University of Louisville, USA
Narayanan Kasthuri, Harvard University, USA

***Correspondence:**
Stephen J. Smith, Allen Institute for Brain Science, 551 N 34th St #200, Seattle, WA 98103, USA
stephens@alleninstitute.org

Received: *01 June 2015*
Accepted: *10 July 2015*
Published: *28 July 2015*

Citation:
Burette A, Collman F, Micheva KD, Smith SJ and Weinberg RJ (2015) Knowing a synapse when you see one. Front. Neuroanat. 9:100. doi: 10.3389/fnana.2015.00100

Introduction

What we see depends mainly on what we look for.

—John Lubbock (1892; Lord Avebury)

The individual synaptic contact is the fundamental element of all synaptic network signaling, including the human neocortical signaling that allows the reader to parse this sentence. We know that the myriad synapses of mammalian CNS are richly complex and diverse in structure, composition, and function, but so far our knowledge about the patterning of synapse diversity over the cubic millimeter scale of cortical local networks is very limited. With growing recognition that the processing, storage, and retrieval of information by CNS networks must be rooted fundamentally in dynamic patterns of individual synaptic weights, the shortage of information on synapse-level population diversity poses a major obstacle to understanding CNS synaptic network function. This shortage has resulted largely from technical barriers to identifying and measuring entities as small, complex, numerous and densely packed as the synapses in mammalian brain. Fortunately, methodology advances are now opening new avenues toward the analysis of large and diverse synapse populations with single-synapse resolution. Here we consider some of these new single-synapse analysis methods and how they are likely to advance our understanding of brain mechanisms and function.

What is a Synapse?

Sherrington's prescient term (Bennett, 1999; López-Muñoz and Alamo, 2009) did not become an anatomical reality until the 1950's, when electron microscopists demonstrated the characteristic structure of the synapse (Robertson, 1953; Peters et al., 1976). Notwithstanding differences between mammals and invertebrates, and between the neuromuscular junction and the CNS, the basic morphology of the synapse—a vesicle-rich axon terminal making a specialized electron-dense adhesive contact onto its postsynaptic target—is unmistakable and now represented in every neuroscience textbook. Ultrastructural study can distinguish two main types of synapses, generally corresponding to excitatory ("asymmetric," or Gray Type I), and inhibitory ("symmetric," or Gray Type II; Gray, 1959; Colonnier, 1968). This dichotomy between excitatory and inhibitory synapses has held up well, notwithstanding considerable heterogeneity among each of these types, as well as the presence of less common synapses that do not fit into a binary structure.

Electrophysiological study can also define synaptic connectivity, by measuring an evoked postsynaptic potential following the induction of a presynaptic spike. Electrophysiology can distinguish different functional types of synapses, characterizing their sign, time course, and patterns of short term and long-term plasticity. However, physiological detection of synapses faces an array of technical problems, including uncertainties as to dendritic loci of synaptic contact sites, and signal distortion consequent to electrical distance between the recording site and synaptic locus. Some synapses have been shown to be "silent," and some do not produce conductance change unless some modulatory condition is fulfilled (Millar et al., 1976; Kerchner and Nicoll, 2008; Crawford and Mennerick, 2012). Others produce no conductance changes at all, but act exclusively via "metabotropic" chemical signaling mechanisms.

More broadly, it is now clear that synapse populations of the mammalian cortex are extremely diverse in composition, structure and function (O'Rourke et al., 2012). This heterogeneity goes far beyond traditional excitatory/inhibitory or neurotransmitter categories and poses an experimental challenge best answered by single-synapse analysis. Unfortunately, the small size and dense packing of neocortical synapses pose formidable obstacles to single-synapse analysis. Electrophysiology and electron microscopy have provided the foundations of our modern understanding of synaptic mechanisms, but neither modality in its traditional form is suitable for the analysis of diverse individual synapses at the scale needed to build a mechanistic understanding of CNS network function. Even "simple" neocortical networks such as the well-studied rodent whisker column comprise hundreds of millions of densely-packed synapses, precluding the satisfactory application of traditional labor-intensive approaches to single-synapse analysis. Emerging methods of computational microscopy (Burns et al., 2013) are now poised to advance single-synapse imaging and measurement to the necessary scale, so careful thought is now due to questions about what we should be looking for, and what we need to measure once we see it.

Fluorescence Microscopy

Fluorescence microscopy is a core tool of synapse biology, invaluable for live cell, histochemical and multimodal applications including optical study of synapses in the awake behaving animal. Unfortunately, the limited resolution of conventional light microscopy poses problems for the study of synapses. This problem is manageable in cultures (which contain sparse neuropil confined to two dimensions; Craig et al., 1993) but can severely compromise use in the intact brain, unless sparse labeling methods are used. We have learned a lot about the function of individual synapses in culture, and now many new genetic approaches to both targeted and shotgun sparse labeling in brain tissue are now being put to excellent use.

Confocal microscopy has been used very effectively to measure individual synapses in cortical tissues (Dumitriu et al., 2011; Schoonover et al., 2014), but suffers resolution and depth limitations that have restricted quantitative application at the local network scale. New super-resolution optical microscopy approaches yield outstanding images of single-synapse molecular architecture (Ji et al., 2008; Eggeling et al., 2015), but again have so far not been extended to the scale of a cortical local network. A variety of new tissue clearing methods (Miyawaki, 2015) are raising hopes for network-scale imaging and single-synapse resolution, especially if appropriate 3D super-resolution microscopy modalities can be developed. These technologies have already provided exciting new data on synapse properties and offer great prospect for future rapid improvements in neural tissue imaging. Another promising new approach to effective super-resolution histology is based on isotropic expansion of tissue labels by an expanding gel matrix (Chen et al., 2015).

Optophysiology

Recent advances in fluorescence imaging methods and reagents have made possible the non-invasive measurement of function at the single-synapse level in intact cortical neuropil. Calcium-sensitive fluorescent molecules, both synthetic and protein based, allow the measurement of calcium influx at individual spines and boutons. Although originally applied for *in vitro* studies, recent progress has been made towards applying them *in vivo*, so that the functional properties of synapses can be mapped in the context of animal behavior (Rochefort and Konnerth, 2012). Voltage-sensitive molecules (both synthetic and protein-based) are the most direct probes of membrane potential at individual synapses, but have so far seen rather limited use (Palmer and Stuart, 2009; Canepari et al., 2010; Maclaurin et al., 2013; Hochbaum et al., 2014; St-Pierre et al., 2014). Fluorescence Lifetime Microscopy (FLIM) and Fluorescence Resonance Transfer (FRET) have also provided fascinating new glimpses of molecular signaling at individual cortical synapses (Yasuda, 2006).

Electron Microscopy

Notwithstanding remarkable recent progress in photon-based imaging, spatial resolution remains an obstacle for fluorescence-based study of synapses. Can electrons help? Using a technology already mature 30 years ago, the transmission electron microscope (TEM) routinely provides nm-level resolution in the X-Y axis, though technical constraints preclude its use on live tissue. While Z-axis resolution is more limited (∼50 nm), this is ample to allow crisp visualization of even the smallest synapses. However, several problems can make it difficult to identify a synapse even with TEM, including unfortunate plane of section (addressable by study of serial thin sections), the perhaps surprising abundance of tiny synapses (**Figure 1**), and synaptic immaturity (bearing in mind that synaptogenesis is present even in the adult brain).

Beyond the problem of synapse recognition, classical TEM technology is labor-intensive, especially as extended by serial-sectioning into 3D, and therefore poorly suited for large-scale study of synaptic neuropil. Stereological approaches to sampling can reduce the magnitude of the task (Vrensen and de Groot, 1973; DeFelipe et al., 1999; Witgen et al., 2006), but require careful experimental design and yield limited results. Several recent developments promise to make EM of bulk tissue more feasible (Knott and Genoud, 2013; Kubota, 2015), including "industrialization" of specimen preparation and image acquisition (Briggman and Bock, 2012), and the introduction of novel high-throughput scanning EM-based techniques, including the automatic tape-collecting ultramicrotome (Hayworth et al., 2014), serial block-face microscopy (Denk and Horstmann, 2004), and focused ion-beam methods (Knott et al., 2008). These methods were originally developed for connectomics, but Focused Ion Beam Scanning Electron Microscopes (FIBSEM) has now been adapted to provide exquisite visualization and precise measurement of synapses and on large synapse populations (**Figure 1**; Merchán-Pérez et al., 2009). Unfortunately, these tools are poorly suited for studies of synapse molecular heterogeneity.

Combining Optical and Electron Microscopy Methodologies

Because the strengths of optical and electron microscopy are complementary, putting these two methodologies together for large-scale studies of the brain has long been a coveted goal. While progress has been delayed by the often mutually-exclusive sample preparation requirements, recent advances are beginning to reveal the power of approaches that successfully incorporate large-scale optical and electron microscopy imaging, such as array tomography (AT) and automated TEM.

AT is an emerging technology well-suited to the challenges of assessing synaptic diversity quantitatively on cortical local network scale. The underlying technology is conceptually simple: thin (∼70 nm) serial sections cut from plastic-embedded pieces of fixed brain are collected onto coverslip arrays, yielding Z-axis resolution at least 10 times higher than provided by confocal microscopy. The arrays are immunostained using antibodies against three to four different substances of interest, and images are collected with immunofluorescence. Because the method relies on postembedding immunostaining, it minimizes an otherwise troublesome problem: using standard "pre-embedding" techniques, antibody access is problematic at protein-dense regions like synapses; this may require the use of proteolytic agents or very weak fixation, which in turn can cause problems with structural artifacts and disruption (Fukaya and Watanabe, 2000; Burette et al., 2002). The immunostains are then eluted under denaturing conditions, the arrays are restained with new antibodies, and imaged again, over multiple cycles. The resulting data are computationally assembled into Z-axis stacks.

Current techniques allow semi-automatic collection of high-dimensional proteometric data (>25 antibodies) on sizable (1000 × 200 × 50 μm^3) chunks of brain, at a resolution of 200 × 200 × 70 nm, which can be further improved to 100 × 100 × 70 nm using deconvolution (Wang and Smith, 2012; **Figure 2**). Much larger volumes (1 × 0.83 × 0.21 mm^3) have been successfully imaged after a single cycle of immunostaining with three different antibodies to identify thalamocortical synapses (Rah et al., 2013). AT arrays can then be imaged with scanning EM ("conjugate AT"), and the resulting images co-registered with single synapse precision (Oberti et al., 2011; Collman et al., 2015). Using conjugate AT, we recently confirmed that at least 90% of excitatory synapses are correctly identified over a wide range of sizes with fluorescence-based AT (**Figure 2**). Synapse identification could be further improved by combining AT with mGRASP (Kim et al., 2015), an approach likely to accelerate network analysis in the near future. The prospects look excellent for scaling up AT methods to acquire fluorescence images economically at the local network scale while retaining the opportunity to image selectively with Field emission scanning electron microscopy (FESEM) as needed for increased resolution and visualization of axonal, dendritic and synaptic membrane structures. Combinations of optophysiological fluorescence and AT imaging may prove an ideal match to the challenges of discovering the diverse molecular counterparts of diverse function at the level of individual synapses and doing so on the mm^3 volume scale of complete local networks.

Another new technology, called Automated TEM (ATEM), has already combined optical and electron microscopy to study of the retina at network scale. Like AT, ATEM uses serial ultrathin sections of plastic-embedded chemically fixed tissue, but performs immunohistochemistry on separate single sections intercalated within the long series of sections that are viewed by TEM. Registration of the optically imaged immunostained sections with the EM sections allows the molecular composition of cells to be established; their processes are then traced and synapses ultrastructurally identified on the TEM sections. Up to 11 different antibody labels have been used in this method, mostly against small molecules, such as GABA, glutamate and other neurotransmitters. Importantly, prior *in vivo* activity can be probed using the excitation marker 1-amino-4-guanidobutane (AGB), a channel-permeant organic cation whose presence can be subsequently detected in the fixed tissue using an antibody (Marc et al., 2005). Further advantages of this method are

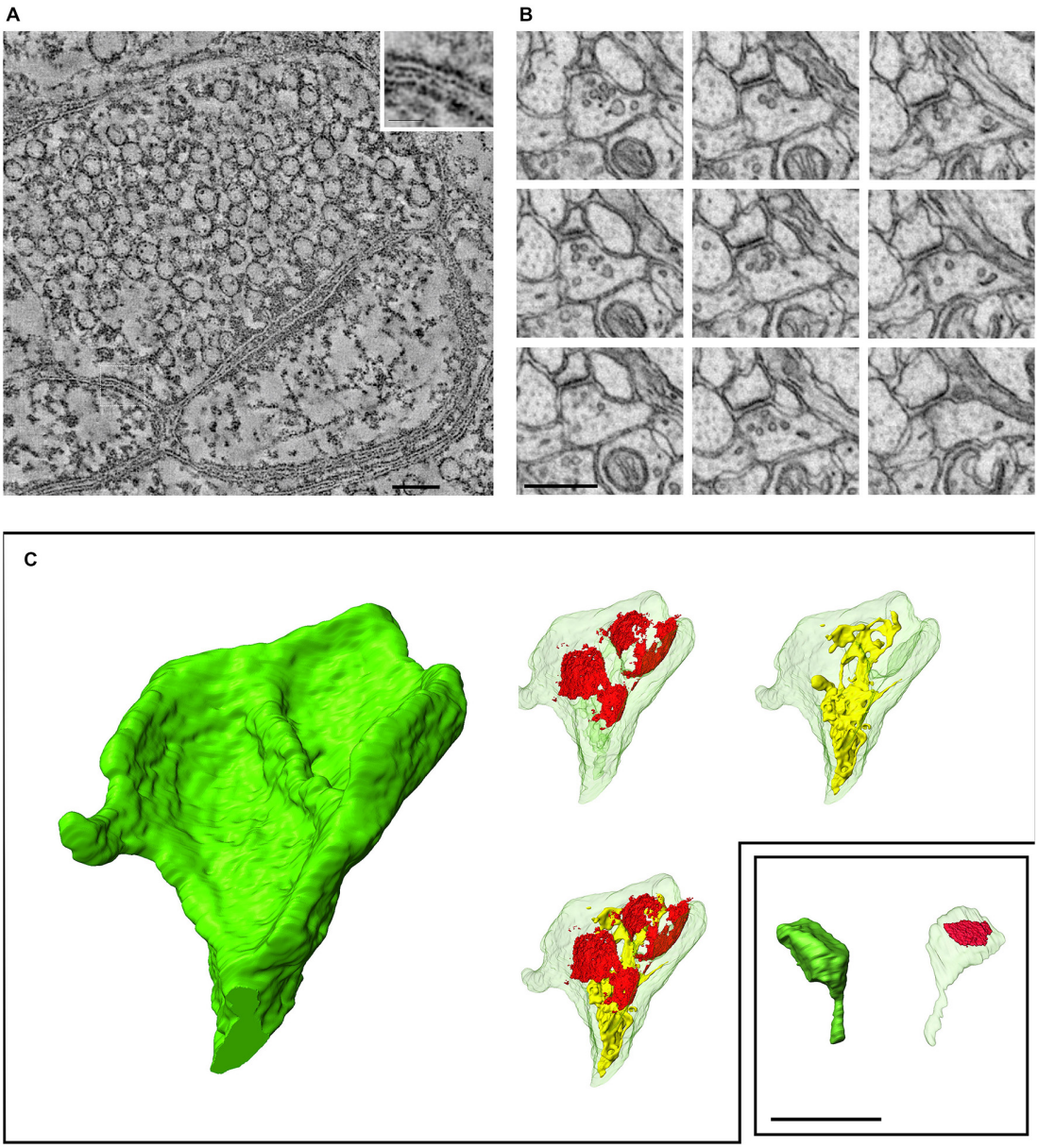

FIGURE 1 | Recent developments in electron microscopic imaging of synapses. (A) Electron tomography (cerebral cortex), a 2.2 nm-thick computed tomographic slice through the center of a synapse. The tomographic section was reconstructed from a dual-axis tilt series of images (from −65° to + 65°, with 2° increments) from cerebral cortex. Inset (enlargement of boxed region) shows the plasma membrane more clearly; the external surfaces of the lipid bilayer are lined with electron-dense particles (Burette et al., 2012). **(B)** Focused Ion Beam Scanning Electron Microscopes (FIBSEM) illustrates a series of ultrathin sections through a small synapse in nucleus accumbens (25 nm spacing between sections); such a small synapse would be likely to escape detection with standard serial-section TEM. **(C)** Three-dimensional reconstruction of two spines (ventral striatum) from a FIBSEM stack (red shows synaptic apposition; endomembranes shown in yellow); the two spines are shown to the same scale. Scale bars: **(A)**, 100 nm; **(B**,**C)**, 500 nm.

the very high resolution enabled by the use of TEM (down to 0.5 nm lateral resolution), and the automated nature of TEM image acquisition that has allowed the imaging and full reconstruction of a retinal circular segment with a diameter of 0.22 mm and approximate thickness of 0.03 mm. ATEM allows the collection of terabyte to petabyte image volumes which, similarly to AT, require new image processing, assembly, navigation and analysis algorithms, as well as new interpretive frameworks. Ongoing exploration of the acquired retinal volume has uncovered much greater complexity of the retinal synaptic network than previously acknowledged and recognized, and has demonstrated the existence of a number of new connection motifs and functions (Marc et al., 2013). Some of these newly-described contact architectures are now challenging the classical ultrastructural definition of a chemical synapse that is still used as the ultimate criterion for synapse identification.

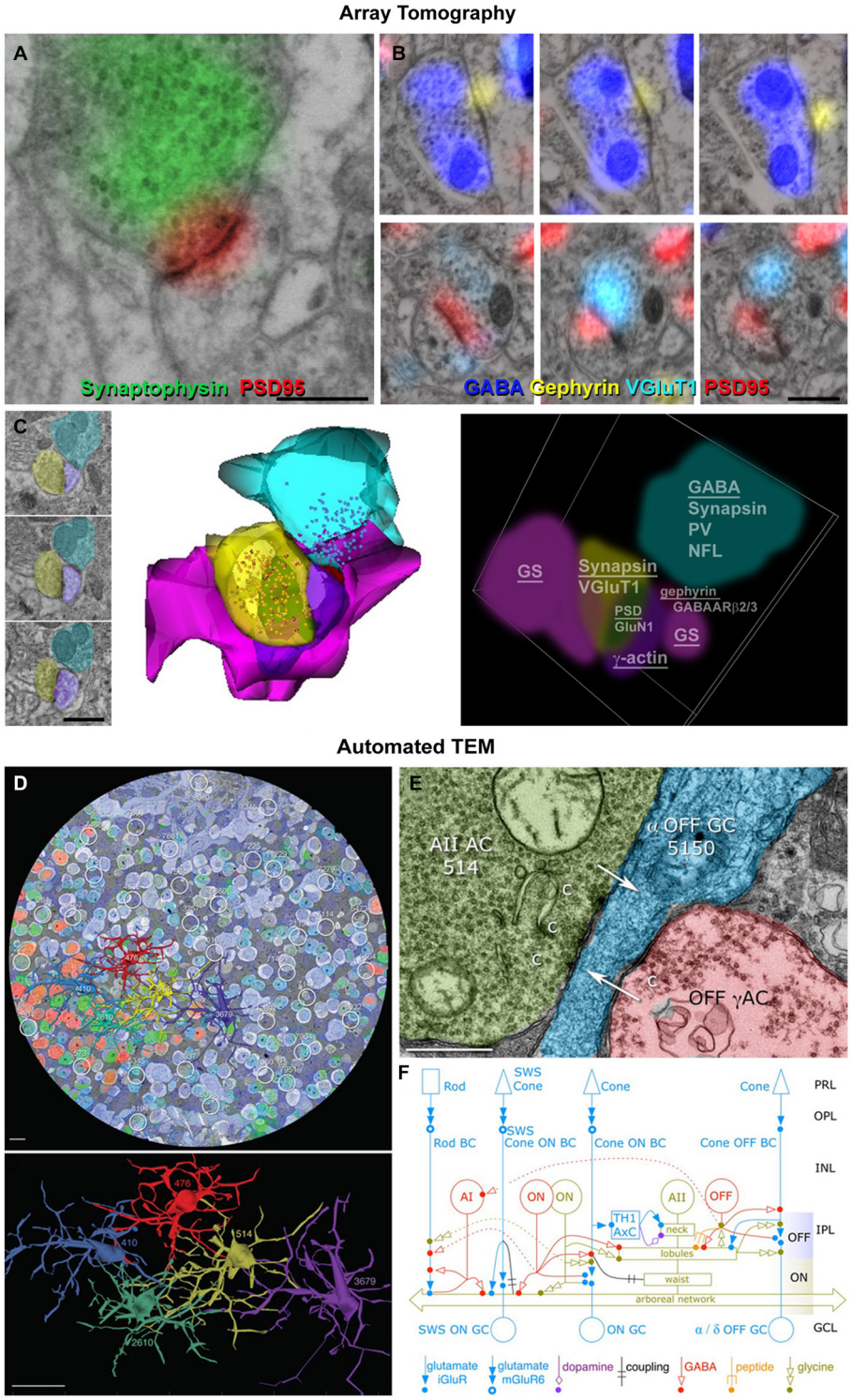

FIGURE 2 | Enhanced view of synapses using optical and electron microscopy. (A) Conjugate array tomography (AT) view of the ultrastructural features of a synapse (presynaptic vesicles, postsynaptic density, surrounding glia) and typical synaptic molecular markers (synaptophysin in the presynaptic compartment and postsynaptic density protein 95, PSD95 on the postsynaptic density). Scale bar, 500 nm. **(B)** Serial sections from an inhibitory (top) and excitatory (bottom) synapses. Scale bar, 500 nm. **(C)** Conjugate AT allows for detailed ultrastructural and molecular characterization of synaptic arrangements. A dually innervated spine from the mouse somatosensory cortex was imaged on serial sections (left), reconstructed from SEM images (middle) and from light microscopic images probing for 17 different synaptic and cytoskeletal markers (right). The underlined markers were used to reconstruct the different structures. Scale bar, 1 μm. **(D)** Automated transmission electron microscope (ATEM) view of the retinal connectome including synapse parent neurons,

(*Continued*)

FIGURE 2 | Continued
molecular markers and ultrastructure. A retinal slice overlaid with five different molecular markers and five reconstructed AII amacrine cells. Scale bars, 10 μm (up), 20 μm (bottom). **(E)** A synaptic contact made by cell 514 onto an OFF ganglion cell. Scale bar, 500 nm. **(F)** The new richer network description of AII amacrine cells obtained using ATEM. Reproduced with permission from Marc et al. (2014).

So, Really, Is this a Synapse?

Several decades ago, the ultrastructural definition of a chemical synapse was simple and precise. As emphasized by Alan Peters and Sanford Palay, "only the clear presence of all the principal features of the synaptic junction can verify the presence of a synapse: the presynaptic vesicles in characteristic clusters, the presynaptic densities, the synaptic cleft, and the postsynaptic densities" (Peters and Palay, 1996). Many EM studies further restricted this definition by requiring the presence of at least three presynaptic vesicles (Beaulieu and Colonnier, 1985). The goal at the time was to understand the synapse as a possibly invariant unit, and it only made good sense to focus on what one was certain to be a synapse.

Now, with goals of understanding network architectures in mind, the classical criterion for recognizing a synapse may be much too narrow. Synapses missed by standard electron microscopy because they are too small or immature to meet traditional criteria may nonetheless exist in such large number as to heavily impact network function (Buzsáki and Mizuseki, 2014). Small and immature synapses may also play critical roles in network plasticity and homeostasis that endow them with special importance. For instance, although small synapses may transmit only weakly or rarely, they may be the primary substrate of new memory formation (Fu et al., 2012). To truly understand the brain's synaptic networks, comprehensive new criteria may be needed to incorporate the abundant small but ill-defined synapses, as well as other somewhat atypical contact architectures. As a result of the technological advances outlined above, criteria for synapse identification may now include molecular, physiological, and ultrastructural characteristics. For these criteria to be useful in practice, they may need to overlap heavily, allowing the choice of different subsets of criteria to recognize a synapse. For example, a synapse sectioned *en face* will not show a clear postsynaptic density, but the presence of postsynaptic density protein 95 (PSD-95) or another synaptic scaffold protein might be sufficient as an affirmative criterion. While small, newly formed synapses may lack classical ultrastructural features and detectable concentrations of PSD proteins, evidence of synaptic signaling provided by optical physiology might confirm functional synaptic identity.

More Challenges and Opportunities Ahead

To understand the mechanisms of human neocortical information processing, we must grapple with intricacies of a machine that packs nearly a billion miraculous computing machines called "synapses" into each cubic millimeter of wet volume. Each synapse represents $\sim 10^5$ signaling proteins acting in some as yet unknown kind of concert. And each synapse is different. Indeed, a strong case can be made that our skills, memories, and emotional predilections are encoded primarily in our personal patterns of synaptic diversity, that is, in the differences amongst our synapses!

We need more powerful and economical means of measuring synaptic diversity patterns with single-synapse granularity, and to be able to relate those patterns, perhaps via modeling, to network function. These tools need to operate reliably and quantitatively over local network scale—volumes of approximately a cubic millimeter in mammalian cortex—and over a wide range of synapse types and sizes. We need to know how the synapse inherits its molecules and functional characteristics from its parent neurons, and how molecular and structural characteristics of the synapse predict and dictate synaptic function. Moreover, distinctive adhesion proteins concentrated at synapses likely encode much information about the identity, morphology and anatomic loci of the parent neurons. Tools like those we have mentioned here are likely soon to be reading such molecular codes.

Quantitative reliability of all the single-synapse analysis tools we have mentioned rely upon a person or (increasingly) an algorithm that *knows a synapse when it sees one*. The synapse recognition process must function predictably across a daunting range of anatomical scales and synapse sizes and forms, and deal with the many measurement complications discussed above. It still poses a great challenge to experimental neuroscience. The new technologies we have discussed here nonetheless inspire optimism that single-synapse analysis tools suitable for wide use in neuroscience will soon emerge.

Acknowledgments

The authors wish to thank JoAnn Buchanan (Allen Institute) for microscopy and many helpful discussions, Kristen Phend (UNC) for expert specimen preparation, and Harald Hess and Shan Xu (HHMI/Janelia) for the amazing FIBSEM imaging sessions. We are also grateful to the NIH (NINDS and NIMH) for supporting our work (Awards R01NS092474, R01NS075252, R21MH099797 to SJS; R01MH104227 to Yi Zuo, subcontract to SJS; R01NS039444 to RJW).

References

Beaulieu, C., and Colonnier, M. (1985). A laminar analysis of the number of round-asymmetrical and flat-symmetrical synapses on spines, dendritic trunks and cell bodies in area 17 of the cat. *J. Comp. Neurol.* 231, 180–189. doi: 10.1002/cne.902310206

Bennett, M. R. (1999). The early history of the synapse: from plato to sherrington. *Brain Res. Bull.* 50, 95–118. doi: 10.1016/s0361-9230(99)00094-5

Briggman, K. L., and Bock, D. D. (2012). Volume electron microscopy for neuronal circuit reconstruction. *Curr. Opin. Neurobiol.* 22, 154–161. doi: 10.1016/j.conb.2011.10.022

Burette, A. C., Lesperance, T., Crum, J., Martone, M., Volkmann, N., Ellisman, M. H., et al. (2012). Electron tomographic analysis of synaptic ultrastructure. *J. Comp. Neurol.* 520, 2697–2711. doi: 10.1002/cne.23067

Burette, A., Zabel, U., Weinberg, R. J., Schmidt, H. H., and Valtschanoff, J. G. (2002). Synaptic localization of nitric oxide synthase and soluble guanylyl cyclase in the hippocampus. *J. Neurosci.* 22, 8961–8970.

Burns, R., Roncal, W. G., Kleissas, D., Lillaney, K., Manavalan, P., Perlman, E., et al. (2013). The open connectome project data cluster: scalable analysis and vision for high-throughput neuroscience. *Sci. Stat. Database Manag.* doi: 10.1145/2484838.2484870

Buzsáki, G., and Mizuseki, K. (2014). The log-dynamic brain: how skewed distributions affect network operations. *Nat. Rev. Neurosci.* 15, 264–278. doi: 10.1038/nrn3687

Canepari, M., Willadt, S., Zecevic, D., and Vogt, K. E. (2010). Imaging inhibitory synaptic potentials using voltage sensitive dyes. *Biophys. J.* 98, 2032–2040. doi: 10.1016/j.bpj.2010.01.024

Chen, F., Tillberg, P. W., and Boyden, E. S. (2015). Optical imaging. Expansion microscopy. *Science* 347, 543–548. doi: 10.1126/science.1260088

Collman, F., Buchanan, J., Phend, K. D., Micheva, K. D., Weinberg, R. J., and Smith, S. J. (2015). Mapping synapses by conjugate light-electron array tomography. *J. Neurosci.* 35, 5792–5807. doi: 10.1523/JNEUROSCI.4274-14.2015

Colonnier, M. (1968). Synaptic patterns on different cell types in the different laminae of the cat visual cortex. An electron microscope study. *Brain Res.* 9, 268–287. doi: 10.1016/0006-8993(68)90234-5

Craig, A. M., Blackstone, C. D., Huganir, R. L., and Banker, G. (1993). The distribution of glutamate receptors in cultured rat hippocampal neurons: postsynaptic clustering of AMPA-selective subunits. *Neuron* 10, 1055–1068. doi: 10.1016/0896-6273(93)90054-u

Crawford, D. C., and Mennerick, S. (2012). Presynaptically silent synapses: dormancy and awakening of presynaptic vesicle release. *Neuroscientist* 18, 216–223. doi: 10.1177/1073858411418525

DeFelipe, J., Marco, P., Busturia, I., and Merchán-Pérez, A. (1999). Estimation of the number of synapses in the cerebral cortex: methodological considerations. *Cereb. Cortex* 9, 722–732. doi: 10.1093/cercor/9.7.722

Denk, W., and Horstmann, H. (2004). Serial block-face scanning electron microscopy to reconstruct three-dimensional tissue nanostructure. *PLoS Biol.* 2:e329. doi: 10.1371/journal.pbio.0020329

Dumitriu, D., Rodriguez, A., and Morrison, J. H. (2011). High-throughput, detailed, cell-specific neuroanatomy of dendritic spines using microinjection and confocal microscopy. *Nat. Protoc.* 6, 1391–1411. doi: 10.1038/nprot.2011.389

Eggeling, C., Willig, K. I., Sahl, S. J., and Hell, S. W. (2015). Lens-based fluorescence nanoscopy. *Q. Rev. Biophys.* 48, 178–243. doi: 10.1017/ss0033583514000146

Fu, M., Yu, X., Lu, J., and Zuo, Y. (2012). Repetitive motor learning induces coordinated formation of clustered dendritic spines in vivo. *Nature* 483, 92–95. doi: 10.1038/nature10844

Fukaya, M., and Watanabe, M. (2000). Improved immunohistochemical detection of postsynaptically located PSD-95/SAP90 protein family by protease section pretreatment: a study in the adult mouse brain. *J. Comp. Neurol.* 426, 572–586. doi: 10.1002/1096-9861(20001030)426:4<572::aid-cne6>3.3.co;2-0

Gray, E. G. (1959). Axo-somatic and axo-dendritic synapses of the cerebral cortex: an electron microscope study. *J. Anat.* 93, 420–433.

Hayworth, K. J., Morgan, J. L., Schalek, R., Berger, D. R., Hildebrand, D. G., and Lichtman, J. W. (2014). Imaging ATUM ultrathin section libraries with wafermapper: a multi-scale approach to EM reconstruction of neural circuits. *Front. Neural Circuits* 8:68. doi: 10.3389/fncir.2014.00068

Hochbaum, D. R., Zhao, Y., Farhi, S. L., Klapoetke, N., Werley, C. A., Kapoor, V., et al. (2014). All-optical electrophysiology in mammalian neurons using engineered microbial rhodopsins. *Nat. Methods* 11, 825–833. doi: 10.1038/nmeth.3000

Ji, N., Shroff, H., Zhong, H., and Betzig, E. (2008). Advances in the speed and resolution of light microscopy. *Curr. Opin. Neurobiol.* 18, 605–616. doi: 10.1016/j.conb.2009.03.009

Kerchner, G. A., and Nicoll, R. A. (2008). Silent synapses and the emergence of a postsynaptic mechanism for LTP. *Nat. Rev. Neurosci.* 9, 813–825. doi: 10.1038/nrn2501

Kim, J., Rah, J., Feng, L., Druckmann, S., and Lee, H. (2015). From a meso- to micro-scale connectome: array tomography and mGRASP. *Front. Neuroanat.* 9:78. doi: 10.3389/fnana.2015.00078

Knott, G., and Genoud, C. (2013). Is EM dead?. *J. Cell Sci.* 126, 4545–4552. doi: 10.1242/jcs.124123

Knott, G., Marchman, H., Wall, D., and Lich, B. (2008). Serial section scanning electron microscopy of adult brain tissue using focused ion beam milling. *J. Neurosci.* 28, 2959–2964. doi: 10.1523/JNEUROSCI.3189-07.2008

Kubota, Y. (2015). New developments in electron microscopy for serial image acquisition of neuronal profiles. *Microscopy (Oxf)* 64, 27–36. doi: 10.1093/jmicro/dfu111

López-Muñoz, F., and Alamo, C. (2009). Historical evolution of the neurotransmission concept. *J. Neural Transm.* 116, 515–533. doi: 10.1007/s00702-009-0213-1

Lubbock, J. (1892). *The Beauties of Nature and the Wonders of the World We Live In*. London: Macmillan and Co.

Maclaurin, D., Venkatachalam, V., Lee, H., and Cohen, A. E. (2013). Mechanism of voltage-sensitive fluorescence in a microbial rhodopsin. *Proc. Natl. Acad. Sci. U S A* 110, 5939–5944. doi: 10.1073/pnas.1215595110

Marc, R. E., Anderson, J. R., Jones, B. W., Sigulinsky, C. L., and Lauritzen, J. S. (2014). The AII amacrine cell connectome: a dense network hub. *Front. Neural Circuits* 8:104. doi: 10.3389/fncir.2014.00104

Marc, R. E., Jones, B. W., Watt, C. B., Anderson, J. R., Sigulinsky, C., and Lauritzen, S. (2013). Retinal connectomics: towards complete, accurate networks. *Prog. Retin. Eye Res.* 37, 141–162. doi: 10.1016/j.preteyeres.2013.08.002

Marc, R. E., Kalloniatis, M., and Jones, B. W. (2005). Excitation mapping with the organic cation AGB2+. *Vision Res.* 45, 3454–3468. doi: 10.1016/j.visres.2005.07.025

Merchán-Pérez, A., Rodriguez, J. R., Alonso-Nanclares, L., Schertel, A., and Defelipe, J. (2009). Counting synapses using FIB/SEM microscopy: a true revolution for ultrastructural volume reconstruction. *Front. Neuroanat.* 3:18. doi: 10.3389/neuro.05.018.2009

Millar, J., Basbaum, A. I., and Wall, P. D. (1976). Restructuring of the somatotopic map and appearance of abnormal neuronal activity in the gracile nucleus after partial deafferentation. *Exp. Neurol.* 50, 658–672. doi: 10.1016/0014-4886(76)90035-2

Miyawaki, A. (2015). Brain clearing for connectomics. *Microscopy (Oxf)* 64, 5–8. doi: 10.1093/jmicro/dfu108

Oberti, D., Kirschmann, M. A., and Hahnloser, R. H. (2011). Projection neuron circuits resolved using correlative array tomography. *Front. Neurosci.* 5:50. doi: 10.3389/fnins.2011.00050

O'Rourke, N. A., Weiler, N. C., Micheva, K. D., and Smith, S. J. (2012). Deep molecular diversity of mammalian synapses: why it matters and how to measure it. *Nat. Rev. Neurosci.* 13, 365–379. doi: 10.1038/nrn3170

Palmer, L. M., and Stuart, G. J. (2009). Membrane potential changes in dendritic spines during action potentials and synaptic input. *J. Neurosci.* 29, 6897–6903. doi: 10.1523/JNEUROSCI.5847-08.2009

Peters, A., and Palay, S. L. (1996). The morphology of synapses. *J. Neurocytol.* 25, 687–700. doi: 10.1007/bf02284835

Peters, A., Palay, S. L., and Webster, H. D. F. (1976). *The Fine Structure of the Nervous System*. New York: Harper and Row.

Rah, J. C., Bas, E., Colonell, J., Mishchenko, Y., Karsh, B., Fetter, R. D., et al. (2013). Thalamocortical input onto layer 5 pyramidal neurons measured using quantitative large-scale array tomography. *Front. Neural Circuits* 7:177. doi: 10.3389/fncir.2013.00177

Robertson, J. D. (1953). Ultrastructure of two invertebrate synapses. *Proc. Soc. Exp. Biol. Med.* 82, 219–223. doi: 10.3181/00379727-82-20071

Rochefort, N. L., and Konnerth, A. (2012). Dendritic spines: from structure to in vivo function. *EMBO Rep.* 13, 699–708. doi: 10.1038/embor.2012.102

Schoonover, C. E., Tapia, J. C., Schilling, V. C., Wimmer, V., Blazeski, R., Zhang, W., et al. (2014). Comparative strength and dendritic organization

of thalamocortical and corticocortical synapses onto excitatory layer 4 neurons. *J. Neurosci.* 34, 6746–6758. doi: 10.1523/JNEUROSCI.0305-14.2014

St-Pierre, F., Marshall, J. D., Yang, Y., Gong, Y., Schnitzer, M. J., and Lin, M. Z. (2014). High-fidelity optical reporting of neuronal electrical activity with an ultrafast fluorescent voltage sensor. *Nat. Neurosci.* 17, 884–889. doi: 10.1038/nn.3709

Vrensen, G., and de Groot, D. (1973). Quantitative stereology of synapses: a critical investigation. *Brain Res.* 58, 25–35. doi: 10.1016/0006-8993(73)90821-4

Wang, G., and Smith, S. J. (2012). Sub-diffraction limit localization of proteins in volumetric space using Bayesian restoration of fluorescence images from ultrathin specimens. *PLoS Comput. Biol.* 8:e1002671. doi: 10.1371/journal.pcbi.1002671

Witgen, B. M., Grady, M. S., Nyengaard, J. R., and Gundersen, H. J. (2006). A new fractionator principle with varying sampling fractions: exemplified by estimation of synapse number using electron microscopy. *J. Microsc.* 222, 251–255. doi: 10.1111/j.1365-2818.2006.01563.x

Yasuda, R. (2006). Imaging spatiotemporal dynamics of neuronal signaling using fluorescence resonance energy transfer and fluorescence lifetime imaging microscopy. *Curr. Opin. Neurobiol.* 16, 551–561. doi: 10.1016/j.conb.2006.08.012

Conflict of Interest Statement: SJS and KDM have founder's equity interests Aratome, LLC (Menlo Park, CA), an enterprise that produces array tomography materials and services. SJS and KDM are also listed as inventors on two US patents regarding array tomography methods that have been issued to Stanford University.

frontiers in Neuroanatomy

ORIGINAL RESEARCH
published: 21 May 2015
doi: 10.3389/fnana.2015.00060

FIB/SEM technology and high-throughput 3D reconstruction of dendritic spines and synapses in GFP-labeled adult-generated neurons

Carles Bosch[1,2,3], *Albert Martínez*[1], *Nuria Masachs*[1,2], *Cátia M. Teixeira*[1,2], *Isabel Fernaud*[2,4,5], *Fausto Ulloa*[1,2], *Esther Pérez-Martínez*[1,2], *Carlos Lois*[6], *Joan X. Comella*[2,3,7], *Javier DeFelipe*[2,4,5*†], *Angel Merchán-Pérez*[2,4,8*†] and *Eduardo Soriano*[1,2,3,9*†]

[1] Developmental Neurobiology and Regeneration Unit, Department of Cell Biology and Parc Cientific de Barcelona, University of Barcelona, Barcelona, Spain, [2] Centro de Investigación Biomédica en Red sobre Enfermedades Neurodegenerativas (CIBERNED), Insituto de Salul Carlos III, Madrid, Spain, [3] Institut de Recerca de l'Hospital Universitari de la Vall d'Hebron (VHIR), Barcelona, Spain, [4] Laboratorio Cajal de Circuitos Corticales, Centro de Tecnología Biomédica, Universidad Politécnica de Madrid, Campus de Montegancedo, Madrid, Spain, [5] Instituto Cajal (Consejo Superior de Investigaciones Científicas), Madrid, Spain, [6] Department of Neurobiology, University of Massachusetts Medical School, Worcester, MA, USA, [7] Institut de Neurociències, Departament de Bioquímica i Biologia Molecular, Facultat de Medicina, Universitat Autònoma de Barcelona, Bellaterra, Spain, [8] Departamento de Arquitectura y Tecnología de Sistemas Informáticos, Escuela Técnica Superior de Ingenieros Informáticos, Universidad Politécnica de Madrid, Madrid, Spain, [9] Institució Catalana de Recerca i Estudis Avançats Academia, Barcelona, Spain

The fine analysis of synaptic contacts is usually performed using transmission electron microscopy (TEM) and its combination with neuronal labeling techniques. However, the complex 3D architecture of neuronal samples calls for their reconstruction from serial sections. Here we show that focused ion beam/scanning electron microscopy (FIB/SEM) allows efficient, complete, and automatic 3D reconstruction of identified dendrites, including their spines and synapses, from GFP/DAB-labeled neurons, with a resolution comparable to that of TEM. We applied this technology to analyze the synaptogenesis of labeled adult-generated granule cells (GCs) in mice. 3D reconstruction of dendritic spines in GCs aged 3–4 and 8–9 weeks revealed two different stages of dendritic spine development and unexpected features of synapse formation, including vacant and branched dendritic spines and presynaptic terminals establishing synapses with up to 10 dendritic spines. Given the reliability, efficiency, and high resolution of FIB/SEM technology and the wide use of DAB in conventional EM, we consider FIB/SEM fundamental for the detailed characterization of identified synaptic contacts in neurons in a high-throughput manner.

Keywords: dendritic spines, synapses, 3D-reconstruction, electron microscopy, FIB/SEM, adult neurogenesis

OPEN ACCESS

Edited by:
Kathleen S. Rockland, Boston University School of Medicine, USA

Reviewed by:
Laszlo Acsady, Institute of Experimental Medicine, Hungary
Graham William Knott, University of Lausanne, Switzerland

***Correspondence:**
Javier DeFelipe, Instituto Cajal (CSIC), Ave. Dr. Arce, 37, 28002 Madrid, Spain
defelipe@cajal.csic.es;
Angel Merchán-Pérez, Laboratorio Cajal de Circuitos Corticales, Centro de Tecnología Biomédica, Universidad Politécnica de Madrid, Campus de Montegancedo, Pozuelo de Alarcón, 28223 Madrid, Spain
amerchan@fi.upm.es;
Eduardo Soriano, Developmental Neurobiology and Regeneration Unit, Department of Cell Biology and Parc Cientific de Barcelona, University of Barcelona, 08028 Barcelona, Spain
esoriano@ub.edu

†*Co-senior authors.*

Received: *18 December 2014*
Accepted: *29 April 2015*
Published: *21 May 2015*

Citation:
Bosch C, Martínez A, Masachs N, Teixeira CM, Fernaud I, Ulloa F, Pérez-Martínez E, Lois C, Comella JX, DeFelipe J, Merchán-Pérez A and Soriano E (2015) FIB/SEM technology and high-throughput 3D reconstruction of dendritic spines and synapses in GFP-labeled adult-generated neurons. Front. Neuroanat. 9:60. doi: 10.3389/fnana.2015.00060

Introduction

Adult neurogenesis has been described in most mammalian species (Lois and Alvarez-Buylla, 1994; Eriksson et al., 1998; Gage, 2000; Deng et al., 2010; Knoth et al., 2010; Sanai et al., 2011;

Spalding et al., 2013), in two brain regions: the subventricular zone (SVZ) of the lateral ventricles and the subgranular zone (SGZ) of the dentate gyrus (DG). The new neurons continuously generated in these areas later differentiate and become integrated into functional circuits of the olfactory bulb and hippocampus, respectively. Hippocampal adult neurogenesis in mice exhibits a highly accurate temporal development, which has been precisely studied with the help of retrovirally-labeled synchronous neurogenic populations (Zhao et al., 2006; Ge et al., 2007) among other techniques. In brief, new neurons born in the SGZ migrate to the inner granule cell layer during their first week of age. At 2 weeks they already have a neuron-like morphology and receive depolarizing GABAergic input from interneurons in the granular layer (Ge et al., 2006). It has been described that 3-week-old granule cells (GCs) then start becoming integrated into their local network: their dendrites reach the molecular layer, where they receive glutamatergic excitatory input from entorhinal cortex axons. At the same time, hyperpolarizing events are triggered by GABAergic input to their somata (Ge et al., 2006, 2008). At this stage, these cells also exhibit mossy fiber boutons that establish efferent synaptic contacts with CA3 pyramidal cells (Sun et al., 2013). From 4 to 6 weeks, newborn GCs undergo a critical period during which they show stronger plasticity than mature GCs, both in terms of increased amplitude of LTP and a lower threshold for LTP induction (Ge et al., 2007). Finally, 8-week-old newborn granule cells exhibit synaptic plasticity parameters identical to those of mature granule cells, even though some features related to structural plasticity take longer to display mature phenotypes (Toni et al., 2007; Toni and Sultan, 2011). Strikingly, the morphology of dendritic spines (for simplicity, spines) in these neurons has been shown to change in response to environmental enrichment (Zhao et al., 2014), thereby suggesting a direct relationship between structure and function of newborn GC spines.

The fine dissection of microcircuits is essential for understanding normal brain function and for identifying structural and physiological modifications associated with neural plasticity and neuropathological conditions. The development of transmission electron microscopy (TEM) allowed the first fine analysis of synapses and revealed the high structural synaptic complexity of the nervous system (Peters et al., 1991; Peters and Palay, 1996). A further breakthrough was the combination of TEM with single neuron tracing methods (Golgi method, intracellular filling, etc.), which allowed the study of synaptic connectivity of identified neurons (Fairen et al., 1977; Somogyi and Hodgson, 1985; Frotscher and Leranth, 1986; Fairen, 2005). Although these techniques have provided fundamental information, the requirement of performing observations in ∼60-nm ultrathin sections limits data analysis to a fragmented visualization as a result of the complex neuronal architecture. Efforts to successfully overcome this problem include analyzing serial ultrathin sections, which offers the possibility to reconstruct dendritic and axonal segments (Stevens et al., 1980; Harris et al., 2006; Arellano et al., 2007; Hoffpauir et al., 2007; Jain et al., 2010; Mishchenko et al., 2010; Bock et al., 2011). Obtaining series of such sections is extremely time-consuming and technically demanding, often making it impossible to reconstruct large volumes of tissue. Hence, the recent development of automated EM techniques is another crucial step for the study of synaptic contacts (Denk and Horstmann, 2004; Briggman and Denk, 2006; Knott et al., 2008; Merchan-Perez et al., 2009; Helmstaedter, 2013).

The combined use of focused ion beam milling (FIB) and scanning electron microscopy (SEM) has proven to be very useful for the study of brain ultrastructure (Knott et al., 2008; Merchan-Perez et al., 2009; Bushby et al., 2011; Peddie and Collinson, 2014). Furthermore, there is an increasing interest in using this technique to address correlative light and electron microscopy studies (Sonomura et al., 2013; Cane et al., 2014; Maco et al., 2014). Using FIB/SEM, synapses can be accurately identified, reconstructed and quantified (Merchan-Perez et al., 2009; Morales et al., 2011; Allegra Mascaro et al., 2013; Blazquez-Llorca et al., 2013; Maco et al., 2013; Sonomura et al., 2013). Here, we show that FIB/SEM technology reliably allows high-throughput 3D reconstruction of identified dendritic segments, spines, and input synapses from GFP-traced neurons, providing a resolution comparable to that of conventional TEM. We applied a correlative light microscope-FIB/SEM method to study developing synaptic inputs in retrovirally traced adult-generated granule cells (GCs). Adult neurogenesis and the recruitment of these neurons into the preexisting circuits are essential for learning and memory (Zhao et al., 2008; Deng et al., 2010; Southwell et al., 2014). FIB/SEM technology permitted the full 3D reconstruction of up to 248 spines and their synaptic inputs, thereby allowing us to perform a fine analysis of synaptogenesis in these neurons.

Materials and Methods

Retroviral Tracing

We used a CAG-GFP retrovirus (RV) stock encoding for GFP (Zhao et al., 2006) (a generous gift from Fred H. Gage, Salk Institute, CA, USA). To visualize PSD-95 clusters in newborn granule cells, we used the retroviral vector MRSVPSD95g (Kelsch et al., 2008). RVs were produced by transient transfection of 293 cells as described previously (Zhao et al., 2006). RV stocks were concentrated to working titers of 1×10^7-2×10^8 pfu/ml by means of ultracentrifugation. Adult mice of either sex (7–8 weeks old) were anesthetized and placed in a stereotaxic frame. The scalp was incised, and holes were drilled in the skull. Targets with coordinates (in mm) relative to bregma in the anteroposterior, mediolateral, and dorsoventral planes were as follows: [−2.0, 1.4, 2.2]. 1.5 µl of virus solution per DG was infused at 0.2 µl/min via a glass micropipette.

Tissue Preparation

After 3–4 ($N = 3$ mice) and 8–9 ($N = 2$) weeks, animals were anesthetized by isofluorane inhalation and intracardially perfused with 4% paraformaldehyde and 0.1% glutaraldehyde in 0.12M phosphate buffer (PB). The brain was then extracted from the skull and postfixed overnight in 4% paraformaldehyde. Vibratome slices (∼100 µm) were cryoprotected with 30% saccharose in 0.12M PB and permeabilized by three freeze-thawing cycles, immunostained with a rabbit polyclonal

anti-GFP antibody (Invitrogen #11122, 1:1000), a biotinylated goat anti-rabbit secondary antibody, and the ABC-peroxidase kit (both from Vector Labs) and developed with DAB and hydrogen peroxide. Slices were postfixed in 2% osmium tetroxide, incubated in 2% uranyl acetate, and flat-embedded in Araldite. All animals were handled in accordance with the guidelines for animal research set out in the European Community Directive 2010/63/EU, and all procedures were approved by the local ethics committee of the Spanish National Research Council (CSIC) and by the Ethics Committee for Animal Experimentation (CEEA), University of Barcelona (Barcelona, Spain).

Araldite-embedded slices containing DAB-labeled cells were glued on the top of araldite blocks and studied under light wide-field microscope (LM). The following three criteria were used to select the dendritic segments to be sampled later by FIB/SEM: (i) they were located in the mid-molecular layer of the dentate gyrus, 50 to 100 μm from the soma, where spines are numerous in adult GC dendrites (except for 3- to 4-week-old GCs, where 6 spines belong to the mid-molecular layer and 20 spines to the inner molecular layer); (ii) the dendritic tree was intensely and homogeneously labeled with DAB; and (iii) they were relatively straight segments that coursed parallel to the surface of the block. Although dendrites coursing in any direction can be sampled, this optimal orientation permits the acquisition of long series of images without the need to displace the field of view of the FIB/SEM microscope during the run.

Once the dendritic segment had been selected, the exposed surface of the block was removed using an ultramicrotome until the selected dendrite was 3 to 5 μm below the surface, so it was readily accessible for imaging by FIB/SEM. We finally acquired optical images of the surface of the final sample.

Three-Dimensional Electron Microscopy using FIB/SEM Technology

Afterwards, the blocks were treated as required to be imaged by the FIB/SEM microscope (Merchan-Perez et al., 2009). They were glued onto a sample stub using a conductive adhesive tab. To avoid charge artifacts, all surfaces of the block except the sample were painted with colloidal silver paint and dried in a vacuum chamber overnight. The blocks were then sputter-coated with gold/palladium for 15 s to facilitate charge dissipation.

3D brain tissue samples were obtained using an electron microscope that combines a focused ion beam (FIB) and a high-resolution field emission scanning electron microscope (SEM) (Crossbeam® Neon40 EsB, Carl Zeiss NTS GmbH, Oberkochen, Germany). This instrument uses a focused gallium ion beam that can mill the sample surface, removing thin layers of material on a nanometer scale. The samples were introduced in the SEM column, and low magnification images of the whole surface of the block were acquired with the secondary electron detector of the column (**Figure 1B**).

In order to accurately locate the selected dendritic segment for FIB/SEM image acquisition, we used the pair of OM and SEM microphotographs that were taken from the same tissue block. These two images were matched and overlaid using Photoshop (Adobe Systems). The block borders, surface impurities, and exposed DAB precipitates were visible in both microphotographs, so they were used as landmarks to correctly superpose the two images. As a result, we were able to trace the exact position of the selected dendritic segment (only visible in LM images) on the SEM microphotograph (**Figures 1A,B**).

The sample was then precisely oriented inside the column so as the viewing direction matched the preferred direction of the dendritic segment. A first coarse cross-section was milled with the FIB with a 10 nA gallium beam as a viewing channel for SEM observation at the appropriate location (**Figure 1C**). Exploration of the exposed surface helped to identify the target dendrite and to choose the final framing. Next, fine milling of the exposed surface was performed with the FIB, using a beam current of 750 pA, which removed a thin layer of material. After removing each slice, milling was paused, and the freshly exposed surface was imaged with a 1.7 kV acceleration potential using the in-column energy-selective backscattered electron detector. Imaging current was 1.2 nA; pixel dwell time was 100 ns and line averaging was set to four. Milling and imaging were sequentially repeated and long series of images were acquired through a fully automated procedure, thus obtaining a stack of images that represented a 3D sample of the tissue (Merchan-Perez et al., 2009). Image resolution on the XY plane was set to 3.7 nm/pixel. Resolution on the Z axis—equivalent to the thickness of the layer of material removed by the FIB in each cycle—was 25 nm. We found that 2048 × 1536 pixel serial micrographs (field of view of 7.6 × 5.7 μm, equivalent to 15000x magnification) allowed unambiguous identification of synaptic components and scanning cycles of about 3 min per microphotograph. For instance, in our study, the largest sample used—comprising 442 serial images—was obtained in a single overnight session of about 22 h, with little or no supervision. We therefore selected these values as the routine settings for obtaining image stacks for 3D reconstructions.

Automatic alignment (rigid registration without rotation) of the stacks of images and signal normalization across slices was performed with Fiji (Schindelin et al., 2012), and 3D reconstruction of the labeled dendritic segments and synaptic contacts was carried out using an improved version of the software packages Reconstruct (Fiala, 2005) and EspINA (Morales et al., 2011) (freely available at http://cajalbbp.cesvima.upm.es/espina/). Exploratory navigation through the stacks of images was performed either with Fiji or EspINA. Binary segmentations of dendrites and synapses were next used to generate surfaces using Imaris software.

A total of 7 mice were processed (1 for the 3-week-old group, 2 for the 4-week-old group, and 3 for the 8-9-week-old group), and 2 to 6 acquisitions were obtained from each group. Each acquisition comprised a tissue volume of between 67 and 481 μm^3 (mean 237 μm^3) that included at least one labeled dendritic segment.

Analysis of Afferent Bouton Connectivity

Various spine protrusions were identified and catalogued in a database, and information related to spine morphology, synapse presence and location, and innervating bouton connectivity were carefully annotated and reviewed by at least three independent specialized scientists. To assess spine morphology classification,

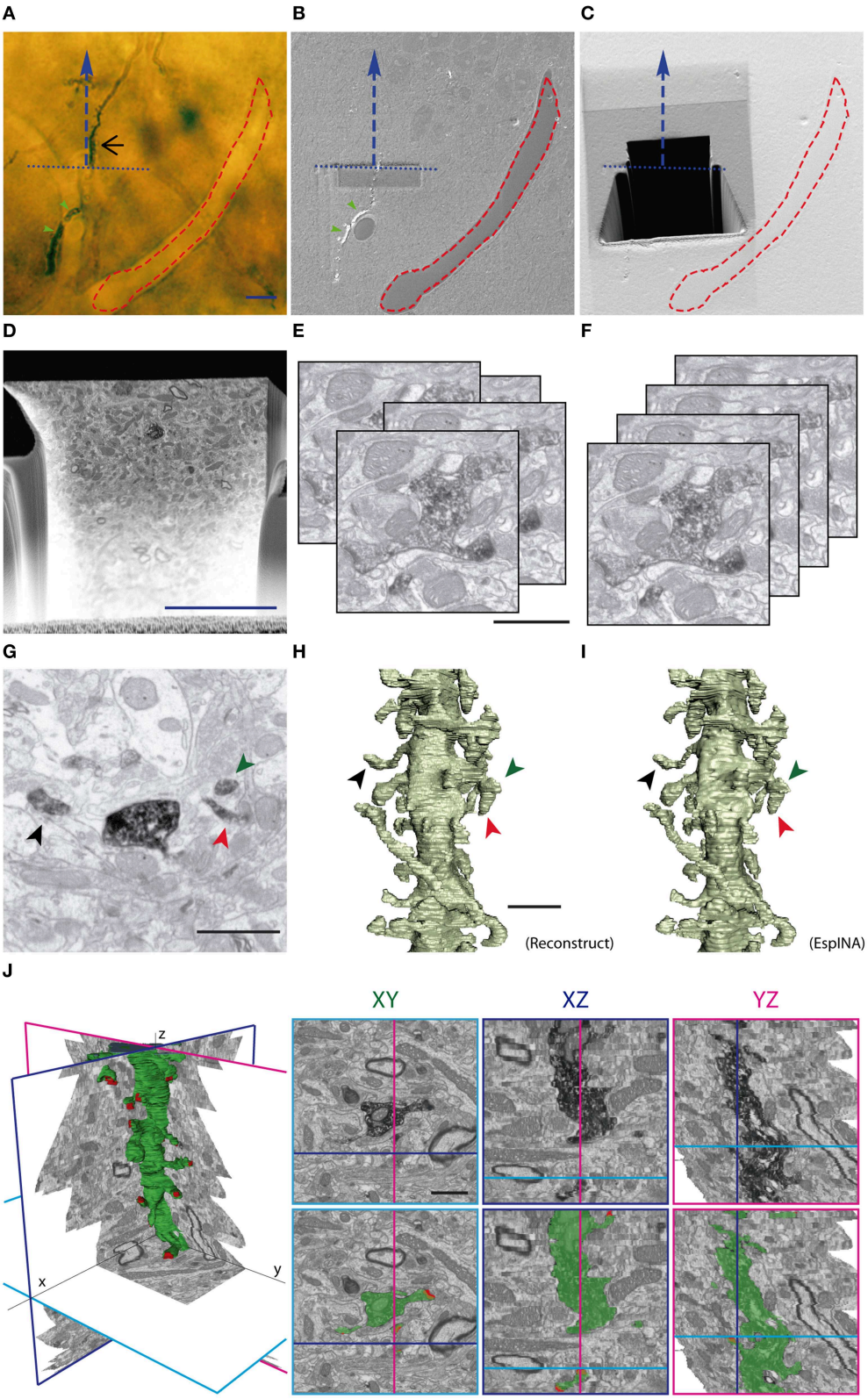

FIGURE 1 | Correlative light and FIB/SEM microscopy of DAB-stained GC dendrites allows high-resolution 3D reconstruction. (A) Light microscopy image of the araldite block surface (after trimming) allows the visualization and selection of the DAB-stained dendrite (black arrow) and the annotation of surface fiducial landmarks, such as blood vessels (red dashed line). The course line (blue dashed arrow) defines the trajectory of the dendrite of interest and the selected direction for serial milling and image acquisition.

(Continued)

FIGURE 1 | Continued
The blue dotted line indicates the desired acquisition starting plane. **(B)** SEM image of the block surface, revealing conserved traits (red dashed line, green arrowheads), allows the identification of the pre-selected starting plane for serial image acquisition. Note that dendritic segments that evolve at the block surface are visible in SEM (green arrowheads), but not dendritic segments evolving entirely below the surface (black arrow in **A**). **(C)** A trapezoidal trench has been milled behind the starting line (blue pointed line) to gain access to the region of interest. Afterwards, a smaller trench has been sequentially milled and imaged in the direction indicated by the blue dashed line. **(D)** Low magnification SEM backscattered electron image showing a freshly milled surface of the trench face during one of the milling-imaging cycles. The dendrite of interest is labeled by a red arrow. **(E,F)** Image acquisition provides up to several hundred serial images **(E)** that require alignment procedures **(F)** to obtain properly oriented stacks ready for 3D visualization and segmentation. **(G,H)** Spine identification in individual micrographs **(G)**; stacks serial images can be further traced to obtain 3D reconstructions performed with either manual segmentation with Reconstruct software **(H)** or with the EspINA software, which allows faster semi-automated reconstructions **(I)**. Note that the overall quality of 3D reconstructions using Reconstruct or EspINA are similar. **(J)** EspINA software allows the segmentation and visualization of labeled structures on the three orthogonal planes before and after segmentation (upper and lower rows, respectively). Scale bars are 10 μm in **(A,D)** 1 μm in **(E,J)**.

criteria was based on current classifications (Harris et al., 1992; Rochefort and Konnerth, 2012). We ended up with five spine types: thin (spines with small necks tipped by small round heads), filopodial (thin and long spines with a pointed PSD, with similar diameters in the neck and head), stubby (thick and short spines with no size differences between neck and head and spine length similar to neck width), mushroom (spines tipped by large heads typically displaying U-shapes), and branched (spines with more than 1 head arising from a single neck). Axon terminals presynaptic to the labeled spines were similarly reconstructed; the number and location of synapses and postsynaptic elements were recorded.

Image Segmentation and Quantitative Morphometric Analysis

3D reconstruction of the labeled dendritic segments and synaptic contacts was carried out with EspINA software (Morales et al., 2011). Briefly, aligned and normalized stacks were further processed with a Gaussian blur filter with a 10-pixel radius. The former "clean" stack was used for user-based segmentation, whereas the "blurred" stack served for automatic, seed-based segmentation in the same work environment. By combining both features, DAB-labeled dendrites and their spines were completely segmented along the stack. Furthermore, their synaptic specializations were segmented by manually tracing closed contours around both the PSD and the apposed presynaptic membrane in consecutive microphotographs. Each segmented synaptic junction was identified independently. We exported the image segmentation binary files into the Imaris platform (Bitplane). Using this software, we generated 3D objects that mimicked the segmentations by an absolute intensity and maximal thresholding approach, without any smoothing step. This allowed for a completely reproducible algorithm of 3D object generation, devoid of any user-biased subjective thresholding step. Next, all spines were cut from their parent dendritic shaft through the base of their neck in a 3D optimal orientation. Branched spines were duplicated and saved in different files to be analyzed separately, and further cut into individual spines at their shared neck isthmus. The volume and sphericity of the final 3D objects generated were annotated. Using Imaris, we calculated the following parameters: dendritic spine volume; synapse size (defined as the volume containing both the postsynaptic density and the presynaptic apposed membrane); and spine and synapse sphericities (defined as the ratio of the surface area of a sphere to the surface area of the structure analyzed, both having the same volume). The sphericity value provides a quantitative record of the morphological complexity of the 3D-reconstructed spines and synapses, since spherical objects would yield a sphericity value of 1, while more complex shapes with larger surface-to-volume ratios would yield progressively lower values (Wadell, 1935). In practice, the surface of reconstructed objects will not be smooth due to the faces and edges of voxels. However, this effect will equally affect all our reconstructions, since voxel size has been kept constant for all of them. Thus, the possible distortions of sphericity measurements will be similar in all reconstructions, and the comparison between them will still be valid. Next, all spines were cut from their parent dendritic shaft through the base of their neck in a 3D optimal orientation. Branched spines were duplicated and saved apart for separate analysis, and further cut into individual spines by their shared neck isthmus. The volume and sphericity of the final surfaces generated were annotated. We calculated the following parameters: dendritic spine volume, synapse size (defined as the volume containing both the postsynaptic density and the presynaptic apposed membrane), and spine and synapse sphericities (defined as the ratio of the surface area of a sphere to the surface area of the structure analyzed). For paired analysis of parameters of spine-synapse couples, a database was generated that included each spine and synapse-paired identifiers, as well as the morphometric values (volume and sphericity) associated with each item. Spines analyzed corresponded to fully 3D-reconstructed individualized spines from GCs aged 8–9 weeks. Correlation was statistically analyzed by non-parametric, two-tailed Spearman test. Binned analysis in the 8–9 week GCs was performed by further pooling and averaging of these data inside bins of constant width. We chose optimal bin widths of spine volume that allowed both the maximal number of values per bin while giving a maximal number of bins in the different analyses. Bins including a single data point were excluded. The bin width used was $5.0E+06\ nm^3$ for all analyses, including spine volume–synapse size ($n = 21$ bins; $n' = 16$ bins in the lower range), spine volume–spine sphericity ($n = 21$; $n' = 6$) and spine volume–synapse sphericity ($n = 21$; $n' = 12$). Linear regressions were performed by best-fit approaches and were statistically tested to be different from zero with the statistical software GraphPad Prism (GraphPad Software). Thresholds were determined by optimizing the goodness of fit (R^2) of these regressions in the data points inside the lower range. Comparisons of these parameters

between two experimental groups were assessed by the non-parametric Mann–Whitney test.

Results

FIB/SEM Allows the Analysis and High-Resolution 3D Reconstruction of Synaptic Interactions from Identified Neurons

To map the onset and development of synaptic inputs on adult-generated GCs in the DG, young adult mice were injected with a retroviral vector (MRSVPSD95g, (Kelsch et al., 2008)) expressing the postsynaptic protein PSD95 fused to GFP, a procedure that allows the visualization of postsynaptic densities (PSDs). While spines were rare in 2-week-old GCs, 3- to 4-week-old neurons displayed numerous spines, most of them tipped with PSD95-GFP-positive puncta (**Supplementary Figure 1**). Spines and PSD95-GFP-positive PSDs were more abundant at 8–9 weeks, when synaptogenesis is believed to be completed. These findings are consistent with previous studies on adult neurogenesis in the DG (Toni et al., 2007; Toni and Sultan, 2011) and prompted us to focus our FIB/SEM analysis on dendrites of adult-generated GCs aged 3–4 and 8–9 weeks.

To address the development of synaptic inputs with EM resolution, adult-generated neurons were labeled with retroviral vectors expressing GFP. Brain slices were processed for GFP-immunostaining, diaminobenzidine (DAB) development, and plastic embedding using conventional TEM procedures. Flat embedding of slices allowed the identification of labeled GCs and the subsequent trimming of tissue blocks. We next designed a correlation procedure that allowed us to apply FIB/SEM technology to identified dendrites previously selected under the light microscope (LM) (**Figure 1A**). In brief, labeled and straight dendritic segments evolving parallel to surface were identified and their precise position annotated with reference to fiducial landmarks present in both the LM and EM images (**Figures 1B,C**). Examination of these images revealed an overall quality of fine structure and resolution comparable to that of conventional TEM (**Figures 1**, **2**).

As a further step for the automation and analysis of 3D reconstructions, we implemented the EspINA program by

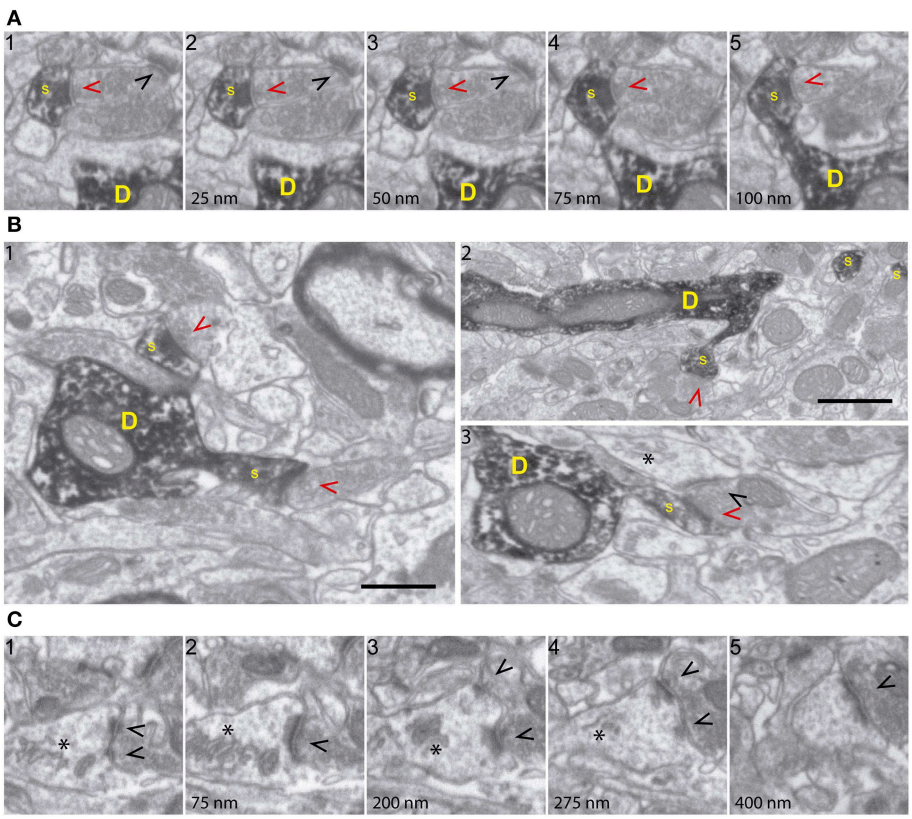

FIGURE 2 | FIB/SEM microscopy allows high-resolution ultrastructural analysis of identified synapses. (A) Five consecutive serial images (a1-5; spaced 25 nm each) demonstrating high fine structural resolution of GFP/DAB-stained dendrites, on both the XY and Z axes. The sequence shows a spine (s) emerging from the parent dendrite (D) and a presynaptic terminal forming a synapse with the labeled spine (red arrowhead) and with an unlabeled spine (black arrowhead). Note that 25 nm thick Z-axis image acquisitions allow efficient and repetitive visualization of structures of interest, such as synapses and spine necks. **(B)** Various FIB/SEM images (b1-3) demonstrating overall ultrastructural quality and the unambiguous identification of dendrites (D), spines (s), and axon terminals establishing synapses with either labeled (red arrowheads) or unlabeled (black arrowheads) profiles. **(C)** Selected serial/correlative images (c1-5; spaced 75–125 nm) showing distinct features, including spine apparatus (asterisk) and a perforated synapse (black arrowheads), on a single unlabeled spine. Scale bar in **(B1)** is 0.5 μm and applies to all panels, except for **(B2)**, which corresponds to 1 μm.

developing specific software for the reconstruction of labeled structures. Alignment of images, segmentation, and 3D reconstructions of tissue blocks of up to 10 μm in depth were efficiently obtained in a semi-automatic manner: alignment of FIB/SEM images was assessed by automatic registration with FIJI (Schindelin et al., 2012) and manually checked with Reconstruct software (Fiala, 2005). The resulting images were saved as stacks, and connectivity parameters were analyzed and annotated by visualizing them with FIJI (**Figures 1D–G**). Examples of 3D dendritic segments reconstructed using EspINA are shown in **Figure 1I** and were equivalent to segments reconstructed using the standard Reconstruct software (**Figure 1H**). Although EspINA-based reconstruction still requires frequent user intervention, in our experience it is at least 25% faster than fully manual reconstruction.

Moreover, EspINA-based 3D reconstructions allowed quality control by the researcher and the visualization of orthogonal sections on any of the XYZ axes (**Figure 1J**). Even when automatic or semiautomatic 3D reconstructions were not possible, manual reconstructions were facilitated by a good resolution in the z axis (25 nm in our study), and by the fact that images were virtually free of deformation artifacts, which allowed almost perfect alignment of serial images.

Qualitative analyses of 3D reconstructions allowed us to trace identified spines back to the parent dendrites and to study the 3D architecture of synaptic interactions and the fine structural features of synapses and presynaptic elements (**Supplementary Movies 1, 2**, **Figures 1–4** and **Supplementary Figure 2**). Thus, cell membranes, cytoskeletal components, and organelles were clearly identifiable. Hence, DAB-labeled dendrites and the spines arising from them were recognizable, as were the unlabeled presynaptic boutons filled with synaptic vesicles and establishing synaptic contacts with DAB-traced profiles (**Figures 2A,B**). PSDs and organelles present in axonal and postsynaptic (GFP-labeled) elements were clearly identifiable, including spine apparatus arranged in stacks, ER cisternae, and mitochondria (**Figure 2C**). We conclude that FIB/SEM technology is a reliable and straightforward procedure that allows high throughput, high resolution, semi-automated 3D analyses of identified neuron-to-neuron synaptic interactions at the ultrastructural level.

Three-Dimensional Analysis of Input Synapses onto Mature Adult-Generated Granule Cells

We first focused on neurons aged 8–9 weeks, when adult-generated GCs are considered to reach maturity (Zhao et al., 2006). Six dendritic segments were analyzed, allowing the 3D reconstruction of up to 271 spines, of which 226 were fully reconstructed (**Supplementary Movie 3**; **Supplementary Table 1**). A qualitative evaluation revealed that most spines were contacted by a single presynaptic bouton. A small percentage, however, were found to lack synaptic contacts (non-synaptic spines, ∼2%, $N = 5$) (**Supplementary Figure 2A**), with all the remaining spines bearing exclusively asymmetric synaptic contacts. Most synapses were established on the spine heads, while ∼3% ($N = 7$) received synaptic input on the spine neck (**Supplementary Figure 2B**). Three spines (∼1%) received both an excitatory contact on the spine head and a second synapse on the neck, established by different boutons (not shown).

The shapes and sizes of spines were highly variable. We observed extremely large spines (1.8E8 nm^3, around 0.60 μm in diameter) and spines with small heads (1.7E6 nm^3, around 0.25 μm in diameter). 3D reconstructions allowed us to classify spines into 5 main types: thin, filopodial, stubby, mushroom, and branched (**Figure 3**) (Peters and Kaiserman-Abramof, 1970; Harris et al., 1992; Bourne and Harris, 2008). The largest proportion of spines corresponded to the thin and mushroom categories (43 and 20%, respectively). Lower percentages were found for the filopodial and stubby categories (17 and 5%, respectively) (**Supplementary Table 1**). Furthermore, up to a 15% of the spines were branched. In general, such complex spines had two side branches (**Figures 4A–E**); however, we also found spines displaying up to three distinct tips. Virtually all the extensions that arose from these branched spines were tipped by synapses, which were established by various presynaptic terminals, thereby indicating that these spines were poly-innervated (**Supplementary Movies 4, 5**). We also classified the single spine heads present in branched spines. Interestingly, the percentage of spine types (filopodial, thin, mushroom, and stubby) in branched spines was similar to that of the whole population of spines (**Figure 6B**), indicating both individual heterogeneity in branched spines and robust conservation of spine categories. To our knowledge this is the first study reporting ramified, branched spines in adult-generated GCs. We compared the morphological parameters between both types of spine. Overall spine and synapse sizes were markedly larger in branched spines, which showed less sphericity, thus reflecting their complexity (**Figures 4F–H**).

We next took advantage of the complete 3D reconstructions to analyze the morphometric parameters of the spines (**Figure 5**). Spine and synapse sizes were distributed with a left-skewed curve, whereas sphericities distributed symmetrically around the means (**Figures 5A–D**). When spine volumes were correlated with other parameters, we found a positive correlation with synapse sizes (Spearman r 0.7414, $p < 0.001$) and a negative correlation with the spine and synapse sphericities (Spearman r of −0.3566 and -0.5016, $p < 0.001$, respectively; (**Supplementary Table 2**, **Figures 5E–G**). To further analyze such distributions, spine volumes were binned, and the pooled points inside each bin were averaged (**Figures 5H–J**). In all cases, the dependent variable evolved linearly with increasing spine volume until reaching a certain threshold, upon which it appeared to remain constant. These data suggest that above a given spine volume threshold, synapse size and sphericity remain unchanged (**Figures 5E–G**, **Supplementary Table 2**).

Taken together, the present FIB/SEM analyses highlight the complex synaptic architecture of spines in mature GCs and allowed us to describe vacant spines and branched spines, as well as to correlate spine and synaptic sizes and sphericity.

Developmental Analysis of Input Synapses onto Adult-Generated GCs

To study the development of dendritic spines in adult generated GCs, we performed 3D reconstructions of these structures in neurons aged 3–4 weeks. We found eight spines in two dendritic

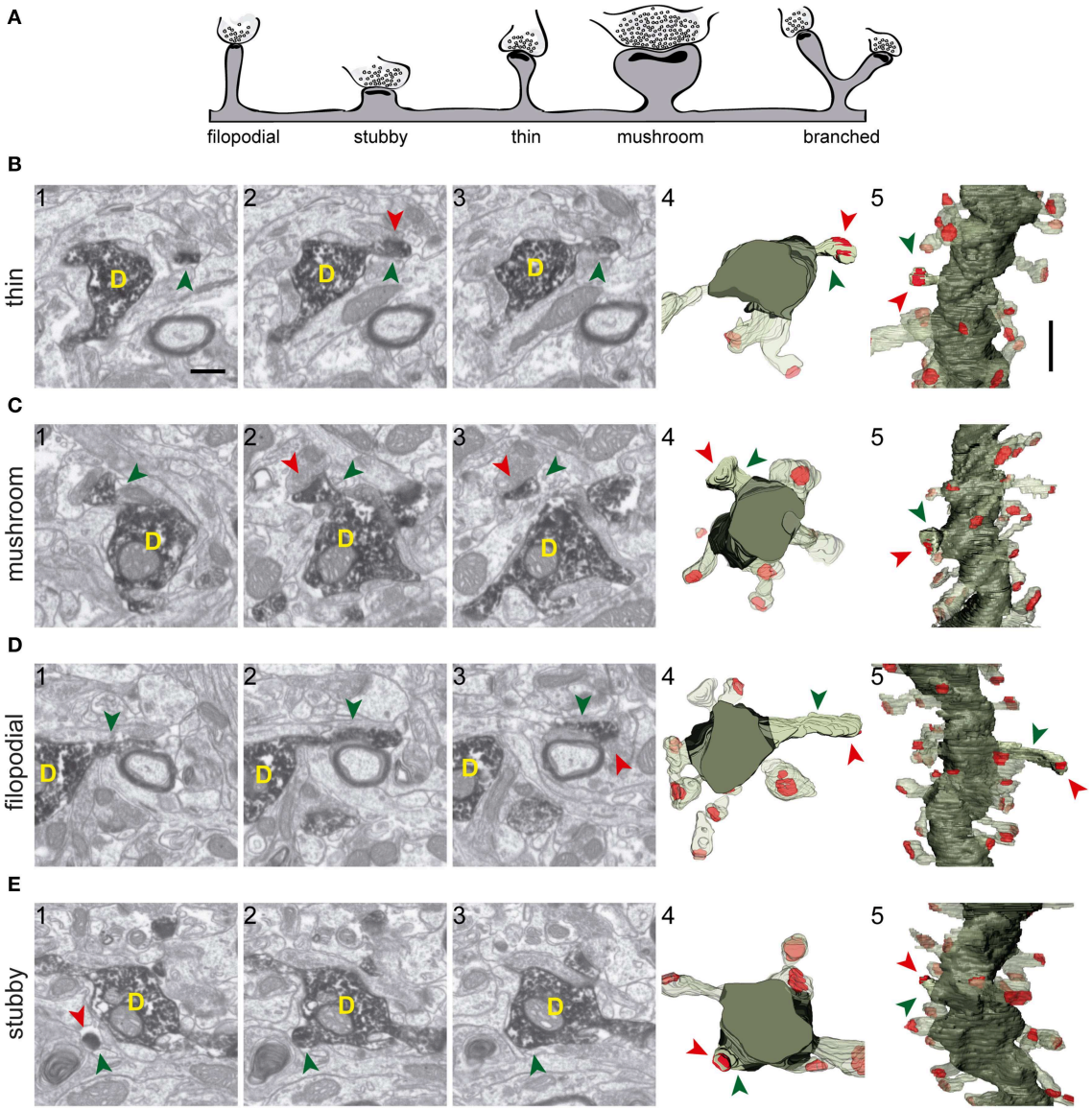

FIGURE 3 | Types of spines arising from 8-week-old GFP/DAB-labeled GCs as reconstructed with FIB/SEM microscopy. (A) Schematic representation of four e types of spines defined in the present study. Examples of thin **(B)**, mushroom **(C)**, filopodial **(D)**, and stubby **(E)** spines arising from their parent dendrite (D). The left images (1–3) show selected serial planes of the spines depicting the head (green arrowheads), neck, and synaptic contact (red arrowheads). The right 3D reconstructions (4–5) show the labeled spines in two orthogonal orientations. The dendritic shaft (D) is shown in solid dark green, the spine of interest in solid pale green, and its synapse in solid red. Neighboring spines and synapses are indicated in light pale green and red, respectively. Scale bar in (**B1**) is 0.5 μm and applies to **(B–E 1–4)**. Scale bar in **(B5)** is 1 μm and applies to **(B–E5)**.

segments of 3-week-old GCs, and 20 spines in six segments of 4-week-old GCs, of which 22 were fully reconstructed (**Figure 6**). As illustrated by our 3D reconstructions, the overall shapes of dendritic spines at 3–4 weeks were similar to those described for 8–9 week-old GCs (**Figures 6A–C**). To characterize developing GC spines, we pooled data from 3- and 4-week-old neurons (**Supplementary Table 1**). We did not find non-synaptic spines at these ages, and all synaptic contacts were on the spine heads. The vast majority of spines bore a single synapse, but we found two spines (∼7%) receiving more than one synaptic contact on their heads (from different boutons), a feature not found in mature GCs. Regarding the shapes of the spines, 48% were thin, 24% mushroom, and 24% filopodial. We also found one branched spine (4%) with three tips, but stubby spines were not found in GCs aged 3–4 weeks (**Figure 6B**, **Supplementary Table 1**).

A comparison of spine types at 3–4 and 8-9 weeks revealed similar percentages of asynaptic, thin, and mushroom categories at both ages, and slightly less filopodial spines at 3–4 weeks (**Figure 6B**). Moreover, in addition to the lack of stubby spines, branched spines were underrepresented at 3–4 weeks. These

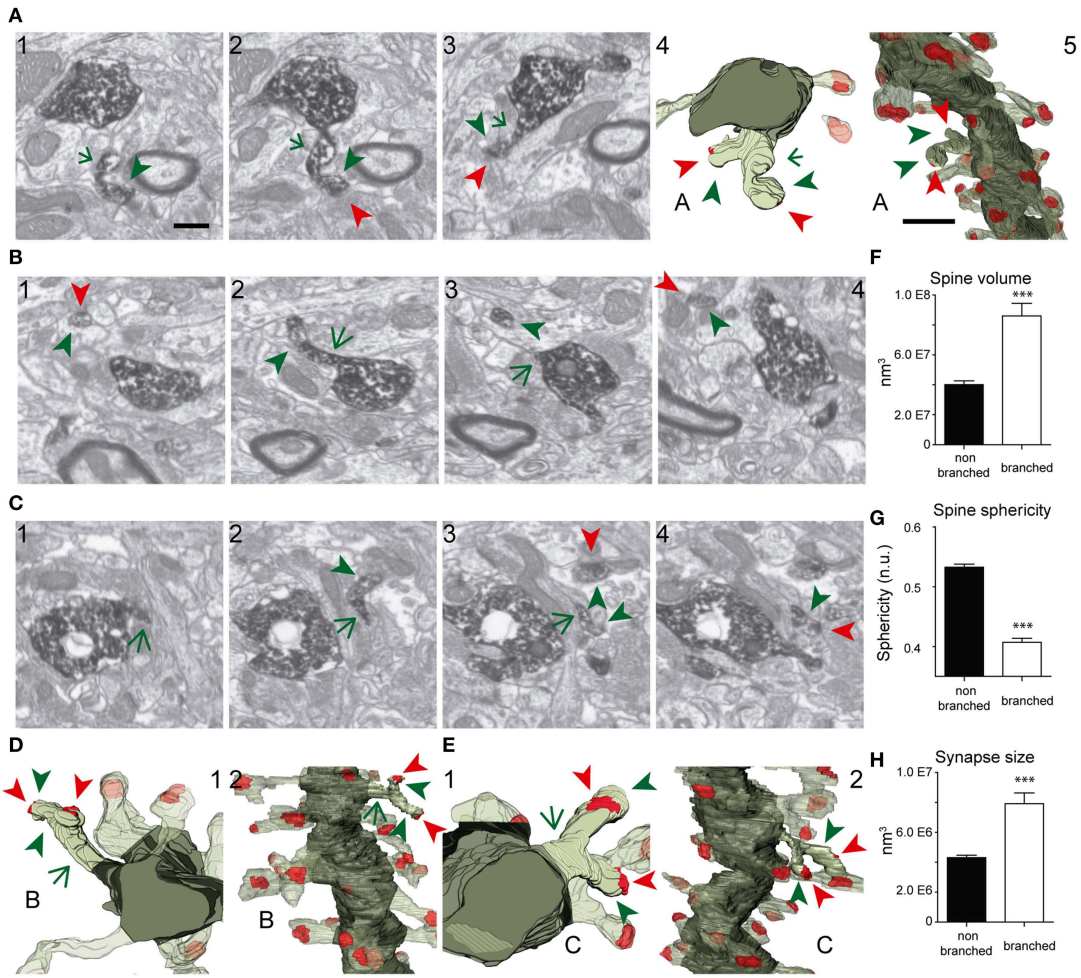

FIGURE 4 | FIB/SEM images and the corresponding 3D reconstructions illustrating branched spines in GCs aged 8–9 weeks. (A–C) Serial FIB/SEM images illustrating three examples of branched spines: **A1–3** (spine A), **B1–4** (spine B), and **C1–4** (spine C). The corresponding 3D reconstructions are shown in two orthogonal orientations in panels **A4,5** (spine A), **D1,2** (spine B), and **E1,2** (spine C). The labeling of synaptic contacts is as in **Figure 3**. The spine heads are shown by green arrowheads, the shared neck by a green arrow, and their synaptic contacts by red arrowheads. The colors in the 3D reconstructions are as follows: the dendritic shaft in solid dark green, the spine of interest in solid pale green, and its synapses in solid red. Neighboring spines and synapses are colored in light pale green and red, respectively. **(F–H)** Histograms showing average spine volume **(F)**, spine sphericity **(G)**, and synapse size **(H)** in non-branched and branched spines. Data represent mean ± SEM; $^{*}p < 0.05$; $^{**}p < 0.01$; $^{***}p < 0.001$; Mann–Whitney test. Scale bar in **(A1)** is 0.5 μm and is applicable to **(A–C 1–4, and D-E1)**. Scale bar in **(A5)** is 1 μm and is applicable to **(A5, D2, and E2)**. Abbreviations: *n.u.*, no units.

data show that while thin, mushroom, and filopodial types are constant, ramified and stubby types are a predominant feature of mature GCs.

We also observed that developing spine volumes correlated positively with synaptic sizes (Spearman r 0.8060, $p < 0.001$) and negatively with spine sphericity (Spearman r −0.6718, $p < 0.01$) (**Supplementary Figure 3**). When compared to 8–9 week-old GCs, spines at 3–4 weeks were less spherical and tended to be larger (**Figure 6D**). Taken together, our data show that although there is a remarkable robustness in most morphological and morphometric parameters at both ages, stubby and branched spines are clearly a characteristic feature of mature GCs, and spines decrease in size and complexity with age.

Spines from Adult-generated GCs are Preferentially Innervated by Multi-Synaptic Axon Terminals

We next examined axon terminals that were presynaptic to labeled GCs. We analyzed the connectivity of 271 terminals innervating identified spines (**Figure 7**). At 8–9 weeks, about one fourth (28%) of presynaptic boutons established synapses exclusively onto the GFP-labeled spine (Single Synaptic Boutons, SSBs; **Figures 7A–D**). The remaining axon terminals (72%) formed synapses with both the labeled spine and with one or more additional postsynaptic elements, the majority of these also being spines (Multiple Synaptic Boutons, MSBs). All the synapses were asymmetric. Most MSBs established a synapse

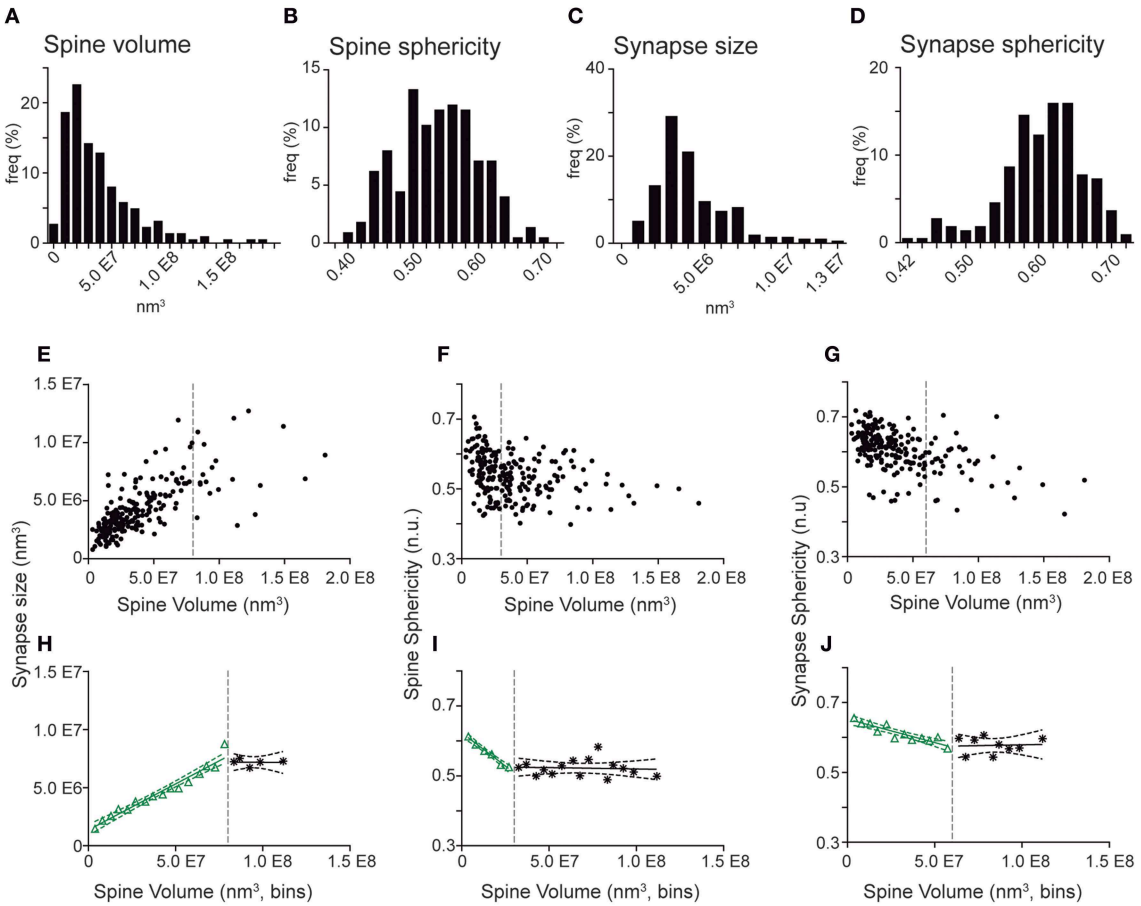

FIGURE 5 | Quantitative correlations of spine volumes and other morphometric parameters in spines and synapses from GC aged 8–9 weeks. (A–D) Frequency histograms show the distribution of spine volume **(A)**, spine sphericity **(B)**, synapse size **(C)**, and synapse sphericity **(D)**. Note that all distributions display a continuous range of values. **(E–G)** Plots showing correlation of individual spine volumes with synapse size **(E)**, spine sphericity **(F)**, and synapse sphericity **(G)**. **(H–J)**. Binned analysis of the data shown in **(E–G)** revealing linear regressions between spine volume and synaptic size **(H)**, spine sphericity **(I)**, and synapse sphericity **(J)** above (black) and below (green) defined volume thresholds (dashed gray lines). Dashed green and black lines represent the 95% confidence intervals for these fits. The data show that the three parameters evolve linearly with spine volumes until a certain threshold, after which the three parameters remain constant. Note in **(E–G)** that these parameters no longer correlate above these thresholds. Detailed correlation analyses are provided in **Supplementary Table 2.**

with one to three unlabeled spines, in addition to the GFP-positive spine (**Figures 7B,E**). Interestingly, up to 26% of axon terminals were involved in complex synaptic configurations, establishing simultaneous synapses with four or more spines, in addition to the identified spine (**Figure 7I**). Some MSBs (8%) exhibited highly complex configurations and established synapses with 7–10 postsynaptic elements (**Figures 7C,F**, **Supplementary Movies 6, 7**). Finally, the SSB/MSB ratio was similar for all spine types (**Figure 7J**), and spines postsynaptic to either SSBs or MSBs did not differ in their morphometric properties in neurons aged 8–9 weeks (spine volume: $0.036 \pm 0.027 \mu m^3$, $0.040 \pm 0.027 \mu m^3$, respectively; spine sphericity: 0.543 ± 0.008, 0.535 ± 0.005, respectively; synapse size: $4.07E+6 \pm 2.55E+5\,nm^3$, $4.24E+6 \pm 1.85E+6\,nm^3$, respectively; synapse sphericity: $0.60 \pm 7.66E\text{-}3$, $0.61 \pm 4.56E\text{-}3$, respectively. No significant differences were found; Mann–Whitney test).

At 3–4 weeks, six out of 25 axon terminals (24%) established a single synapse exclusively with the GFP-labeled spine, whereas 19 terminals (76%) established contacts with more than one postsynaptic element (11 of them with one additional element, and 8 boutons with 2–3 unlabeled spines, in addition to the GFP-traced spine) (**Figure 7G** and **Supplementary Table 1**). The mean number of contacts established by MSBs was higher at 8–9 weeks (**Figure 7H**), since terminals establishing synapses with five or more spines were not found at 3–4 weeks (**Figure 7I**). Thus, while the percentage of MSBs was similar at 3–4 and 8–9 weeks (76 and 72%, respectively), the average number of synapses established by these boutons increased at 8–9 weeks (**Figures 7G–I**). We conclude that although the innervation of GC spines by MSBs is a common feature of developing and adult spines, the complexity of synaptic multi-innervation increases in mature GCs.

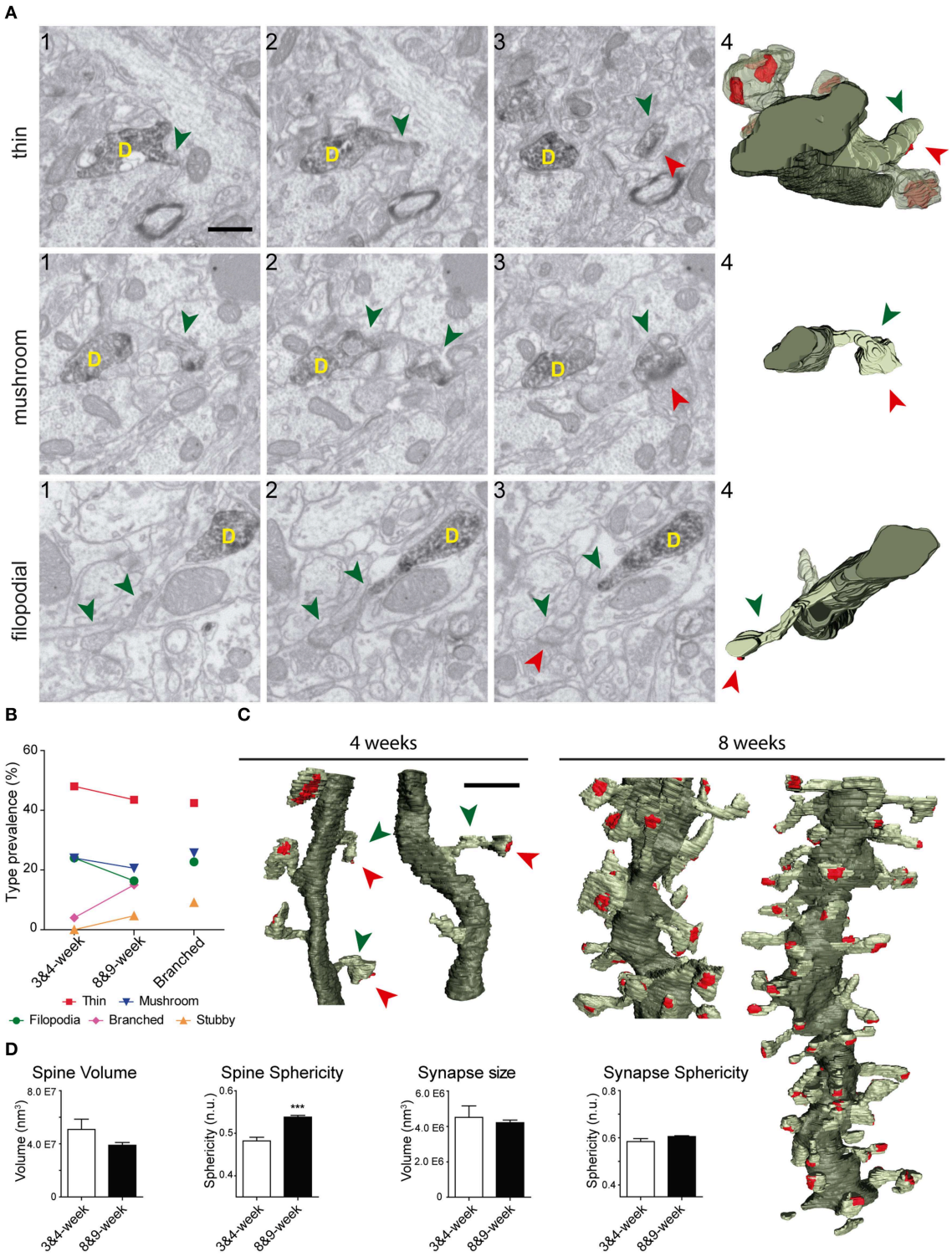

FIGURE 6 | Comparative analysis of spines in GC aged 3–4 and 8–9 weeks. (A) Examples of thin, filopodial, and mushroom spines arising from their parent dendrite (D) in 3- to 4-week-old GCs. The three left images (1–3) show selected serial planes of the spines, depicting the head (green arrowheads), neck, and synaptic contact (red arrowheads). The 3D reconstructions are shown to the right (4). **(B)** Plots showing the percentages of the different types of spines at 3–4 and 8–9 weeks; percentages of spine types are also shown for branched spines (right). **(C)** 3D reconstructions allowing comparison of dendritic segments and spines at 3–4 and 8–9 weeks. The color code is the same as described in **Figure 3**. **(D)** Histograms showing spine volumes and sphericity and synapse size and sphericity at both ages. Data represent mean ± SEM. ***$p < 0.001$; Mann–Whitney test. Scale bar in **(A)** is 0.5 μm. Scale bar in **(C)** is 1 μm.

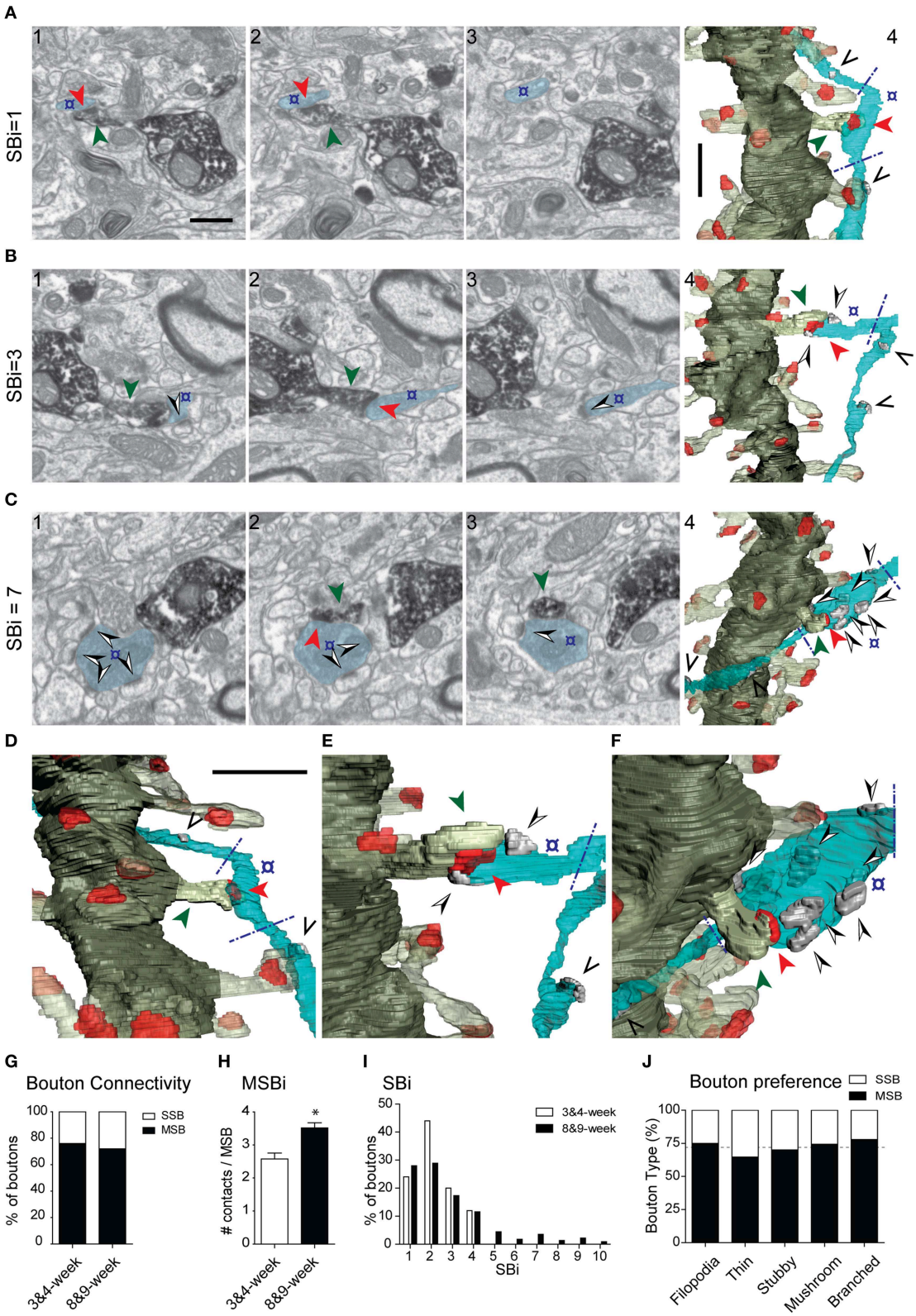

FIGURE 7 | Presynaptic innervation of GC spines at 3–4 and 8–9 weeks. (A–C) Three examples of synaptic configurations. The left FIB/SEM images (1–3) show selected serial planes of the dendritic spines and presynaptic boutons; **(A)** presynaptic bouton (o) contacting (red arrowhead) exclusively the DAB-labeled spine (green arrowhead); **(B,C)** axon terminals forming complex synaptic configurations contacting both the labeled spine and several unlabeled dendritic spines (black and white arrowheads) **(B,C)**.

(Continued)

FIGURE 7 | Continued
The corresponding 3D reconstructions are shown to the right (**A4**, **B4**, **C4**), as well as magnified tilted orientations in **D**–**F**, respectively. The number of postsynaptic spines innervated by the same bouton (SBi, Synaptic Bouton index) is shown to the left. Note that only the varicosities presynaptic to the labeled spine were analyzed (delimited by blue dashed lines in the 3D panels). The axons may establish other synapses elsewhere, not analyzed (black arrowheads in the 3D panels). The example shown in **(B)** illustrates a multisynaptic bouton establishing a total of three synapses and the example illustrated in **(C)** establishes seven synapses. The color code is as described in **Figure 3**; additionally, the axon is shown in light blue, and synapses established by the axon onto non-labeled spines in solid gray. **(G)** Percentage of single-synaptic (SSB) and multi-synaptic (MSB) boutons in dendritic spines aged 3–4 and 8–9 weeks. **(H)** Average number of synaptic contacts established by MSBs at 3–4 and 8–9 weeks. **(I)** Histogram showing the frequency of synaptic contacts established by axon terminals at 3–4 and 8–9 weeks. **(J)** Multisynaptic boutons innervate all spine types and morphologies equally. Percentage of single-synaptic (SSB) and multi-synaptic (MSB) boutons in various types of dendritic spines in 8- to 9-week-old neurons; the dashed line indicates the overall percentage of SSBs and MSBs. Data represent mean ± SEM. $^*p < 0.05$; Mann–Whitney test. Scale bar in (**A1**) is 0.5 μm and applies to **(A–C, 1–3)**. Scale bar in **(A4)** is 1 μm and applies to **(A–C4)**. Scale bar in **(D)** is 1 μm and applies to **(D–F)**.

Discussion

Here we show that the connectivity of newly generated neurons can be studied using FIB/SEM technology, which allows unambiguous identification and 3D analysis of synapses from identified neurons. Only recently, researchers have exploited the potential of FIB/SEM technology to study biological material, including neural tissue (Knott et al., 2008; Merchan-Perez et al., 2009, 2014; Briggman and Bock, 2012; Blazquez-Llorca et al., 2013; Helmstaedter, 2013). However, the complex 3D organization of nervous tissue requires pre-labeling of axons and dendrites from defined neurons. Here we have optimized a feasible and user-friendly procedure to capture FIB/SEM images from single GFP-immunostained (and DAB-processed) neurons.

An advantage of FIB/SEM microscopy is that serial images are obtained in a fully automated manner, with little user interaction once milling and imaging have been programmed, allowing the acquisition of long series of images from the regions of interest. This is a critical advantage of automated EM techniques. For example, in a previous study of the synaptic inputs of identified spines, we were able to reconstruct 144 spines using conventional TEM (Arellano et al., 2007). However, it took us over 2 years to complete. This is because serial-section TEM is susceptible to some important problems, including loss of sections, uneven section thickness, frequent presence of debris or artifacts in sections (e.g. folds) and geometrical distortions. Thus, many spines had to be discarded because they were incompletely reconstructed. All these problems are overcome by using current FIB/SEM technology.

Furthermore, the resulting resolution on the X-Y plane was comparable to that of TEM, since a resolution of around 4 nm/pixel was easily attained. The resolution on the Z axis, in our case 25 nm, proved even better than that of TEM, where uniform serial sections below 60 nm are difficult to obtain. FIB/SEM technology is also free of most of the main artifacts of TEM, such as the loss or folding of sections. Moreover, given that the images are taken from the block face, they are almost completely aligned, and the definitive alignment can also be automated (Merchan-Perez et al., 2009). Thus, the resolution and quality of the images obtained herein were comparable to those obtained with conventional TEM but without the need of manual serial sectioning and with none of the artifacts common to TEM sections.

Another advantage of FIB/SEM technology is the feasibility and accuracy of 3D EM reconstructions. The automated and sequential milling/image acquisition procedure greatly facilitates the harvesting of single images, and the feasibility of the method allows 3D reconstructions of samples up to 10 um thick. The generation and visualization of these 3D reconstructions can be performed in a user-friendly format by means of the EspINA software. For instance, our FIB/SEM approach allowed the identification of rare and unconventional dendritic spines, including extremely thin (filopodial) spines, non-synaptic and branched spines, and complex MSBs.

Finally, as the procedure described here uses standard protocols for TEM, and given the wide use of DAB for the characterization of neurons and their synaptic connections, the FIB/SEM technology developed would be of immediate use for the analysis of conventional TEM samples that have already been prepared. In conclusion, the high resolution, feasibility, and automation of the FIB/SEM technology described make this methodology a technological breakthrough not only for the imaging of identified neural microcircuits using neuron-specific markers, but also for the discovery of features that may have been overlooked.

Hippocampal adult neurogenesis is essential for cognitive processes (Zhao et al., 2008; Deng et al., 2010). Essential issues to tackle include how these new neurons become functionally integrated into pre-existing adult circuits and the identification of the factors that influence this process (Van Praag et al., 2002; Toni et al., 2007, 2008). Previous studies have described the developmental pattern of synapse formation and the establishment of efferent connections by these neurons (Zhao et al., 2006; Ge et al., 2007; Toni et al., 2007, 2008; Sun et al., 2013). Further, the functional integration of these neurons is modulated by a number of factors, including spatial memory training, stimulation of the entorhinal pathway, and the Reelin pathways (Kee et al., 2007; Garthe et al., 2009; Gu et al., 2012; Teixeira et al., 2012). However, how this integration takes place and the developmental modifications that occur during this process remain largely unknown. Here, we applied FIB/SEM technology to characterize mature synaptic inputs onto adult-born GCs. Although our observations largely support previous conventional TEM studies (Toni et al., 2007, 2008), several interesting features were revealed. Complex branched spines displaying up to four individual protrusions and receiving

independent synaptic inputs accounted for up to ∼15% of the spines. Although previous TEM studies pointed to the presence of branched spines in the DG (Geinisman et al., 1989; Trommald et al., 1996; Trommald and Hulleberg, 1997; Popov and Stewart, 2009), our study represents the first description of this type of spine in adult-generated GCs. Given current views on the relevance of the shape of spines for their physiological and integrative properties, it is likely that such complex ramified spines have a physiological impact on the dendritic physiology of adult-generated GCs (Rusakov et al., 1996; Yuste and Majewska, 2001; Harris and Weinberg, 2012; Rochefort and Konnerth, 2012).

The use of serial sections and the narrow spacing between consecutive EM images (25 nm) greatly facilitated the classification of spines into morphological types, since the structure of each spine could be easily compared across several planes and examined as a whole. It must be noted, however, that this classification is only descriptive and used for simplicity given that it is based on qualitative criteria and there is a continuum of spine morphological types (e.g., see Arellano et al., 2007). Nevertheless, this classification is a useful descriptive tool to compare our results with previous studies. For example, we found a considerable number of filopodial-like spines (17%) in mature GCs, while these spines have been traditionally associated with young neurons and immature spines, often lacking postsynaptic specializations (Ziv and Smith, 1996; Konur and Yuste, 2004; Knott et al., 2006; Yasumatsu et al., 2008). However, our data show that virtually all filopodial spines displayed synapses. Conversely, our 3D analyses revealed a low percentage of spines lacking synapses in these mature neurons. All together, our findings indicate that filopodial, branched, and vacant spines are constitutive of adult-generated GC dendrites, probably representing synaptic remodeling intermediate stages in these neurons (Toni et al., 2007; Ge et al., 2008; Toni and Sultan, 2011).

Our study also allowed a morphometric characterization of GC dendritic spines and synapses. This characterization was based on quantitative measurements of spine and synapse volume and sphericity. Furthermore, this quantitative analysis was performed independently of the qualitative classification of spine types. One striking finding is the increase in spine sphericity in mature spines, when compared to young spines (**Figure 6**). This process has already been described in other neurons and is likely to reflect spine maturation (Knott et al., 2006; Honkura et al., 2008; Racz and Weinberg, 2013). Another finding is that spine volumes correlated with synaptic sizes and with spine and synapse sphericities up to a given threshold (**Figure 5**), above which both the synaptic size and the spine and synapse sphericities remained constant. To our knowledge, such a two-regime distribution has not been reported previously. The boundaries detected may point to physiological thresholds relevant in the development of spine structural plasticity, and therefore they might be potentially related to calcium and cytoskeletal spine dynamics, among other mechanisms. Furthermore, our results offer a strong ground truth for the study and interpretation of how structural plasticity molds the synaptic elements during the integration of newborn GCs in the preexisting circuitry.

Our comparative 3D analyses on neurons aged 3–4 and 8–9 weeks allowed us to define the synaptogenesis in adult-generated GCs. The percentage of filopodial, thin, and mushroom spines was roughly similar at both ages (though with a tendency to decrease at 8–9 weeks), indicating that these spine types are constitutive of GC dendrites from the onset of synaptogenesis. In contrast, stubby spines were observed exclusively in mature GCs and branched spines were very rare at early stages. Therefore, while filopodial, thin, and mushroom spines appear to play a major role in the special electrophysiological properties of young adult-generated GCs, including hyperexcitability and low LTP threshold (Zhao et al., 2006; Ge et al., 2007), stubby and branched spines may contribute specifically to the physiological properties of mature GCs.

A previous study described that up to 40% of axon terminals that are presynaptic to newborn GCs are simultaneously enrolled in synapses with unlabeled spines (MSBs) (Toni et al., 2007). Our FIB/SEM study confirms this observation and adds two important findings. First, the percentage of MSBs establishing synapses with other targets is substantially higher (72%), and second, we describe the presence of highly complex synaptic configurations in which single boutons simultaneously contact four or more postsynaptic elements, in addition to the GFP-labeled spine (up to 9 additional spines). Although the function of such complex synaptic configurations in GC physiology remains to be elucidated, they have been associated with plasticity and LTP (Toni et al., 1999; Geinisman et al., 2001; Knott et al., 2006). We propose that the activation of a single axon terminal, driving coactive synaptic activity to several GCs, influences the generation of synchronous networks and rhythms in the DG, which are crucial for cognitive processes, including learning and memory (Deng et al., 2010; Aimone et al., 2011; Buzsaki and Moser, 2013). Finally, and although the identity of target spines of MSBs is not known, it is plausible that these complex axon terminals are specialized in driving coactive simultaneous activation to defined GC subpopulations, for instance to the dendrites of newborn GCs.

Our 3D reconstructions revealed that MSBs are equally present in young and mature GCs (about 76% in young GCs), and that the synaptic complexity of the axon terminals contacting GCs clearly increases with maturity (e.g., **Figure 7**); this finding indicates that such synaptic configurations are a robust feature of GC microcircuits, although the different age-dependent complexities suggest that they may differentially influence the physiological properties of young and adult GCs. Our analysis of two stages of spine development suggests that axons presynaptic to spines arising from immature newborn GCs are more prone to progressively establish additional synaptic contacts.

In summary, here we implemented FIB/SEM technology that allows the 3D analysis of identified, traced neurons, with high resolution and reliability. This technology would be implemental for the characterization of synaptic microcircuits in a high-throughput manner. This technology allowed us to reveal that

the synaptic architecture of adult-generated GCs is more complex than previously thought.

Acknowledgments

We thank Tanya Yates for editorial assistance, Jorge G Peña for the EspINA software development and Alfonso Pérez-Escudero for critical discussion. This work was supported by grants from Spanish MINECO (BFU2008-03980 and SAF2013-42445R to ES, SAF2013-2010-19930 and PIE13-00027to JC, and BFU2012-34963 to JD), CIBERNED (to ES, JC, and JD), the Cajal Blue Brain Project, Spanish partner of the Blue Brain Project initiative from EPFL (to JD) and the European Union Seventh Framework Programme (FP7/2007-2013) under grant agreement no. 604102 (Human Brain Project) (to JD).

Supplementary Material

The Supplementary Material for this article can be found online at: http://journal.frontiersin.org/article/10.3389/fnana.2015.00060/abstract

Supplementary Figure 1 | Dendritic spines and postsynaptic densities visualized in developing GCs. Newborn GCs were labeled with a retroviral vector expressing PSD95 and visualized at 3, 4 and 8 weeks post-injection. **(A)** Low magnification views of retrovirally labeled adult-born GCs. **(B)** Confocal reconstructions of GC dendritic segments showing spines (red) and postsynaptic densities (yellow). Note the increase in spines concomitant to post-injection times. Scale bars are 20 μm in **(A)** and 5 μm in **(B)**. Abbreviations: GCL, granule cell layer; ML, molecular layer; 3w, 3 weeks post-infection.

Supplementary Figure 2 | Types of dendritic spines in 8-week-old GFP/DAB-labeled GCs as reconstructed with FIB/SEM microscopy. Examples show a non-synaptic spine **(A)** and a spine receiving synaptic contact in the neck **(B)**. The images on the left show three selected serial planes (1-3) of the spines depicting the head (green arrowheads), neck, and synaptic contact (red arrowheads), while the images on the right show 3D reconstructions (4,5) of the labeled spines in two different orientations. The dendritic shaft (D) is shown in solid dark green, the spine of interest in solid pale green, and its synapse in solid red. Neighboring spines and synapses are shown in light pale green and red, respectively. Scale bar in **(A1)** is 0.5 μm and applies to **(A1-4, B1-4)**; scale bar in **(A5)** is 1 μm and applies to **(B5)**.

Supplementary Figure 3 | Correlation of 3- to 4-week-old GC spine volume with morphometric parameters. (A-c) Plots showing correlation of individual spine volumes with synapse size (Spearman r=0.8060, $p<0.001$) **(A)**, spine sphericity (Spearman r= −0.6718, $p<0.01$) **(B)**, and synapse sphericity (non-significant correlation, Spearman r= −0.29) **(c)**. Spine volume thresholds observed in the 8-9 week group are illustrated by gray dashed lines.

Supplementary Table 1 | Numbers of analyzed dendritic spines and presynaptic boutons and their classification.

Supplementary Table 2 | Statistical analysis of correlations between spine and synapse morphometric parameters in 8-9-week-old GCs.

Supplementary Movie Legends:

Entire fileset is available at: http://dx.doi.org/10.6084/m9.figshare.1266450

Supplementary Movies 1 and 2 | Complete 3D image stacks of labeled 8-week-old GC dendrites showing numerous spines, presynaptic boutons, and synapses. Slice depth respect to the first slice is shown at the lower right corner. Scale bar is 0.5 μm. **Supplementary Movie 1** is available at: http://dx.doi.org/10.6084/m9.figshare.1266442 **Supplementary Movie 2** is available at: http://dx.doi.org/10.6084/m9.figshare.1266443

Supplementary Movie 3 | 3D reconstruction of the dendritic segment displayed in Movie 1. The dendritic shaft is shown in dark green, the dendritic spines in pale green and their synapses in red. **Supplementary Movie 3** is available at: http://dx.doi.org/10.6084/m9.figshare.1266444

Supplementary Movies 4 and 5 | 3D image stack of an 8-week-old GC dendrite illustrating a branched spine (4). Green and red arrowheads show the individual heads and synapses, respectively, and a green arrow shows the shared neck that connects the branched spine with the dendritic shaft (D). Slice depth respect to the first slice is shown at the lower right corner. Scale bar is 0.5 μm. The 3D reconstruction is shown in (5). The dendritic shaft is shown in solid dark green and the branched spine in solid pale green, and its synapses in solid red. Neighboring spines and synapses are indicated in light pale green and red, respectively. **Supplementary Movie 4** is available at: http://dx.doi.org/10.6084/m9.figshare.1266445 **Supplementary Movie 5** is available at: http://dx.doi.org/10.6084/m9.figshare.1266446

Supplementary Movies 6 and 7 | 3D image stack of an 8-week-old GC dendrite illustrating a presynaptic bouton (MSB) forming up to eight synaptic contacts (6). A green arrowhead shows the spine head of a GFP-labeled spine receiving a synapse (red arrowhead) from a MSB. Yellow arrowheads show synaptic contacts established by the same MSB with neighboring non-labeled spines. Slice depth respect to the first slice is shown at the lower right corner. Scale bar is 0.5 μm. The 3D reconstruction is shown in (7). The dendritic shaft is shown in solid dark green, the labeled spine contacting the MSB in solid pale green, and its synapse in solid red. Neighboring spines and synapses are indicated in light pale green and red, respectively. The axon that contains the MSB is shown in light blue, and synapses established with non-labeled spines are shown in solid gray. Abbreviations: *MSB*, multisynaptic bouton; *D*, dendritic shaft of the GFP-labeled dendrite. **Supplementary Movie 6** is available at: http://dx.doi.org/10.6084/m9.figshare.1266447 **Supplementary Movie 7** is available at: http://dx.doi.org/10.6084/m9.figshare.1266448

References

Aimone, J. B., Deng, W., and Gage, F. H. (2011). Resolving new memories: a critical look at the dentate gyrus, adult neurogenesis, and pattern separation. *Neuron* 70, 589–596. doi: 10.1016/j.neuron.2011.05.010

Allegra Mascaro, A. L., Cesare, P., Sacconi, L., Grasselli, G., Mandolesi, G., Maco, B., et al. (2013). *In vivo* single branch axotomy induces GAP-43-dependent sprouting and synaptic remodeling in cerebellar cortex. *Proc. Natl. Acad. Sci. U.S.A.* 110, 10824–10829. doi: 10.1073/pnas.1219256110

Arellano, J. I., Benavides-Piccione, R., Defelipe, J., and Yuste, R. (2007). Ultrastructure of dendritic spines: correlation between synaptic and spine morphologies. *Front. Neurosci.* 1, 131–143. doi: 10.3389/neuro.01.1.1.010.2007

Blazquez-Llorca, L., Merchán-Pérez, A., Rodríguez, J.-R., Gascón, J., and Defelipe, J. (2013). FIB/SEM Technology and Alzheimer's disease: three-dimensional analysis of human cortical synapses. *J. Alzheimers Dis.* 34, 995–1013. doi: 10.3233/JAD-122038

Bock, D. D., Lee, W. C., Kerlin, A. M., Andermann, M. L., Hood, G., Wetzel, A. W., et al. (2011). Network anatomy and *in vivo* physiology of visual cortical neurons. *Nature* 471, 177–182. doi: 10.1038/nature09802

Bourne, J. N., and Harris, K. M. (2008). Balancing structure and function at hippocampal dendritic spines. *Annu. Rev. Neurosci.* 31, 47–67. doi: 10.1146/annurev.neuro.31.060407.125646

Briggman, K. L., and Bock, D. D. (2012). Volume electron microscopy for neuronal circuit reconstruction. *Curr. Opin. Neurobiol.* 22, 154–161. doi: 10.1016/j.conb.2011.10.022

Briggman, K. L., and Denk, W. (2006). Towards neural circuit reconstruction with volume electron microscopy techniques. *Curr. Opin. Neurobiol.* 16, 562–570. doi: 10.1016/j.conb.2006.08.010

Bushby, A. J., P'ng, K., M., Young, R. D., Pinali, C., Knupp, C., and Quantock, A. J. (2011). Imaging three-dimensional tissue architectures by focused ion beam scanning electron microscopy. *Nat. Protoc.* 6, 845–858. doi: 10.1038/nprot.2011.332

Buzsaki, G., and Moser, E. I. (2013). Memory, navigation and theta rhythm in the hippocampal-entorhinal system. *Nat. Neurosci.* 16, 130–138. doi: 10.1038/nn.3304

Cane, M., Maco, B., Knott, G., and Holtmaat, A. (2014). The relationship between PSD-95 clustering and spine stability *in vivo*. *J. Neurosci.* 34:2075–2086. doi: 10.1523/JNEUROSCI.3353-13.2014

Deng, W., Aimone, J. B., and Gage, F. H. (2010). New neurons and new memories: how does adult hippocampal neurogenesis affect learning and memory? *Nat. Rev. Neurosci.* 11, 339–350. doi: 10.1038/nrn2822

Denk, W., and Horstmann, H. (2004). Serial block-face scanning electron microscopy to reconstruct three-dimensional tissue nanostructure. *PLoS Biol.* 2:e329. doi: 10.1371/journal.pbio.0020329

Eriksson, P. S., Perfilieva, E., Bjork-Eriksson, T., Alborn, A. M., Nordborg, C., Peterson, D. A., et al. (1998). Neurogenesis in the adult human hippocampus. *Nat. Med.* 4, 1313–1317. doi: 10.1038/3305

Fairen, A., Peters, A., and Saldanha, J. (1977). A new procedure for examining Golgi impregnated neurons by light and electron microscopy. *J. Neurocytol.* 6, 311–337. doi: 10.1007/BF01175194

Fairen, A. (2005). Pioneering a golden age of cerebral microcircuits: the births of the combined Golgi-electron microscope methods. *Neuroscience* 136, 607–614. doi: 10.1016/j.neuroscience.2005.08.011

Fiala, J. C. (2005). Reconstruct: a free editor for serial section microscopy. *J. Microsc.* 218, 52–61. doi: 10.1111/j.1365-2818.2005.01466.x

Frotscher, M., and Leranth, C. (1986). The cholinergic innervation of the rat fascia dentata: identification of target structures on granule cells by combining choline acetyltransferase immunocytochemistry and Golgi impregnation. *J. Comp. Neurol.* 243, 58–70. doi: 10.1002/cne.902430106

Gage, F. H. (2000). Mammalian neural stem cells. *Science* 287, 1433–1438. doi: 10.1126/science.287.5457.1433

Garthe, A., Behr, J., and Kempermann, G. (2009). Adult-generated hippocampal neurons allow the flexible use of spatially precise learning strategies. *PLoS ONE* 4:e5464. doi: 10.1371/journal.pone.0005464

Ge, S., Goh, E. L., Sailor, K. A., Kitabatake, Y., Ming, G. L., and Song, H. (2006). GABA regulates synaptic integration of newly generated neurons in the adult brain. *Nature* 439, 589–593. doi: 10.1038/nature04404

Ge, S., Sailor, K. A., Ming, G. L., and Song, H. (2008). Synaptic integration and plasticity of new neurons in the adult hippocampus. *J. Physiol.* 586, 3759–3765. doi: 10.1113/jphysiol.2008.155655

Ge, S., Yang, C. H., Hsu, K. S., Ming, G. L., and Song, H. (2007). A critical period for enhanced synaptic plasticity in newly generated neurons of the adult brain. *Neuron* 54, 559–566. doi: 10.1016/j.neuron.2007.05.002

Geinisman, Y., Berry, R. W., Disterhoft, J. F., Power, J. M., and Van Der Zee, E. A. (2001). Associative learning elicits the formation of multiple-synapse boutons. *J. Neurosci.* 21, 5568–5573.

Geinisman, Y., Morrell, F., and Detoledo-Morrell, L. (1989). Perforated synapses on double-headed dendritic spines: a possible structural substrate of synaptic plasticity. *Brain Res.* 480, 326–329. doi: 10.1016/0006-8993(89)90201-1

Gu, Y., Arruda-Carvalho, M., Wang, J., Janoschka, S. R., Josselyn, S. A., Frankland, P. W., et al. (2012). Optical controlling reveals time-dependent roles for adult-born dentate granule cells. *Nat. Neurosci.* 15, 1700–1706. doi: 10.1038/nn.3260

Harris, K. M., Jensen, F. E., and Tsao, B. (1992). Three-dimensional structure of dendritic spines and synapses in rat hippocampus (CA1) at postnatal day 15 and adult ages: implications for the maturation of synaptic physiology and long-term potentiation. *J. Neurosci.* 12, 2685–2705.

Harris, K. M., Perry, E., Bourne, J., Feinberg, M., Ostroff, L., and Hurlburt, J. (2006). Uniform serial sectioning for transmission electron microscopy. *J. Neurosci.* 26, 12101–12103. doi: 10.1523/JNEUROSCI.3994-06.2006

Harris, K. M., and Weinberg, R. J. (2012). Ultrastructure of synapses in the mammalian brain. *Cold Spring Harb. Perspect. Biol.* 4:a005587. doi: 10.1101/cshperspect.a005587

Helmstaedter, M. (2013). Cellular-resolution connectomics: challenges of dense neural circuit reconstruction. *Nat. Methods* 10, 501–507. doi: 10.1038/nmeth.2476

Hoffpauir, B. K., Pope, B. A., and Spirou, G. A. (2007). Serial sectioning and electron microscopy of large tissue volumes for 3D analysis and reconstruction: a case study of the calyx of Held. *Nat. Protoc.* 2, 9–22. doi: 10.1038/nprot.2007.9

Honkura, N., Matsuzaki, M., Noguchi, J., Ellis-Davies, G. C., and Kasai, H. (2008). The subspine organization of actin fibers regulates the structure and plasticity of dendritic spines. *Neuron* 57, 719–729. doi: 10.1016/j.neuron.2008.01.013

Jain, V., Seung, H. S., and Turaga, S. C. (2010). Machines that learn to segment images: a crucial technology for connectomics. *Curr. Opin. Neurobiol.* 20, 653–666. doi: 10.1016/j.conb.2010.07.004

Kee, N., Teixeira, C. M., Wang, A. H., and Frankland, P. W. (2007). Preferential incorporation of adult-generated granule cells into spatial memory networks in the dentate gyrus. *Nat. Neurosci.* 10, 355–362. doi: 10.1038/nn1847

Kelsch, W., Lin, C. W., and Lois, C. (2008). Sequential development of synapses in dendritic domains during adult neurogenesis. *Proc. Natl. Acad. Sci. U.S.A.* 105, 16803–16808. doi: 10.1073/pnas.0807970105

Knoth, R., Singec, I., Ditter, M., Pantazis, G., Capetian, P., Meyer, R. P., et al. (2010). Murine features of neurogenesis in the human hippocampus across the lifespan from 0 to 100 years. *PLoS ONE* 5:e8809. doi: 10.1371/journal.pone.0008809

Knott, G., Marchman, H., Wall, D., and Lich, B. (2008). Serial section scanning electron microscopy of adult brain tissue using focused ion beam milling. *J. Neurosci.* 28, 2959–2964. doi: 10.1523/JNEUROSCI.3189-07.2008

Knott, G. W., Holtmaat, A., Wilbrecht, L., Welker, E., and Svoboda, K. (2006). Spine growth precedes synapse formation in the adult neocortex *in vivo*. *Nat. Neurosci.* 9, 1117–1124. doi: 10.1038/nn1747

Konur, S., and Yuste, R. (2004). Imaging the motility of dendritic protrusions and axon terminals: roles in axon sampling and synaptic competition. *Mol. Cell Neurosci.* 27, 427–440. doi: 10.1016/j.mcn.2004.07.005

Lois, C., and Alvarez-Buylla, A. (1994). Long-distance neuronal migration in the adult mammalian brain. *Science* 264, 1145–1148. doi: 10.1126/science.8178174

Maco, B., Cantoni, M., Holtmaat, A., Kreshuk, A., Hamprecht, F. A., and Knott, G. W. (2014). Semiautomated correlative 3D electron microscopy of *in vivo*-imaged axons and dendrites. *Nat. Protoc.* 9:1354–1366. doi: 10.1038/nprot.2014.101

Maco, B., Holtmaat, A., Cantoni, M., Kreshuk, A., Straehle, C. N., Hamprecht, F. A., et al. (2013). Correlative *in vivo* 2 photon and focused ion beam scanning electron microscopy of cortical neurons. *PLoS ONE* 8:e57405. doi: 10.1371/journal.pone.0057405

Merchan-Perez, A., Rodriguez, J. R., Alonso-Nanclares, L., Schertel, A., and Defelipe, J. (2009). Counting synapses using FIB/SEM microscopy: a true revolution for ultrastructural volume reconstruction. *Front. Neuroanat.* 3:18. doi: 10.3389/neuro.05.018.2009

Merchan-Perez, A., Rodriguez, J. R., Gonzalez, S., Robles, V., Defelipe, J., Larranaga, P., et al. (2014). Three-dimensional spatial distribution of synapses in the neocortex: a dual-beam electron microscopy study. *Cereb. Cortex* 24, 1579–1588. doi: 10.1093/cercor/bht018

Mishchenko, Y., Hu, T., Spacek, J., Mendenhall, J., Harris, K. M., and Chklovskii, D. B. (2010). Ultrastructural analysis of hippocampal neuropil from the connectomics perspective. *Neuron* 67, 1009–1020. doi: 10.1016/j.neuron.2010.08.014

Morales, J., Alonso-Nanclares, L., Rodriguez, J. R., Defelipe, J., Rodriguez, A., and Merchan-Perez, A. (2011). Espina: a tool for the automated segmentation and counting of synapses in large stacks of electron microscopy images. *Front. Neuroanat.* 5:18. doi: 10.3389/fnana.2011.00018

Peddie, C. J., and Collinson, L. M. (2014). Exploring the third dimension: volume electron microscopy comes of age. *Micron* 61, 9–19. doi: 10.1016/j.micron.2014.01.009

Peters, A., and Kaiserman-Abramof, I. R. (1970). The small pyramidal neuron of the rat cerebral cortex. The perikaryon, dendrites and spines. *Am. J. Anat.* 127, 321–355. doi: 10.1002/aja.1001270402

Peters, A., and Palay, S. L. (1996). The morphology of synapses. *J. Neurocytol.* 25, 687–700. doi: 10.1007/BF02284835

Peters, A., Palay, S. L., and Webster, H. (1991). *The Fine Structure of the Nervous System. Neurons and their Supporting Cells*, 3rd Edn. New York, NY: Oxford University Press.

Popov, V. I., and Stewart, M. G. (2009). Complexity of contacts between synaptic boutons and dendritic spines in adult rat hippocampus: three-dimensional reconstructions from serial ultrathin sections *in vivo*. *Synapse* 63, 369–377. doi: 10.1002/syn.20613

Racz, B., and Weinberg, R. J. (2013). Microdomains in forebrain spines: an ultrastructural perspective. *Mol. Neurobiol.* 47, 77–89. doi: 10.1007/s12035-012-8345-y

Rochefort, N. L., and Konnerth, A. (2012). Dendritic spines: from structure to *in vivo* function. *EMBO Rep.* 13, 699–708. doi: 10.1038/embor.2012.102

Rusakov, D. A., Stewart, M. G., and Korogod, S. M. (1996). Branching of active dendritic spines as a mechanism for controlling synaptic efficacy. *Neuroscience* 75, 315–323. doi: 10.1016/0306-4522(96)00253-9

Sanai, N., Nguyen, T., Ihrie, R. A., Mirzadeh, Z., Tsai, H. H., Wong, M., et al. (2011). Corridors of migrating neurons in the human brain and their decline during infancy. *Nature* 478, 382–386. doi: 10.1038/nature10487

Schindelin, J., Arganda-Carreras, I., Frise, E., Kaynig, V., Longair, M., Pietzsch, T., et al. (2012). Fiji: an open-source platform for biological-image analysis. *Nat. Methods* 9, 676–682. doi: 10.1038/nmeth.2019

Somogyi, P., and Hodgson, A. J. (1985). Antisera to gamma-aminobutyric acid. III. Demonstration of GABA in Golgi-impregnated neurons and in conventional electron microscopic sections of cat striate cortex. *J. Histochem. Cytochem.* 33, 249–257. doi: 10.1177/33.3.2579124

Sonomura, T., Furuta, T., Nakatani, I., Yamamoto, Y., Unzai, T., Matsuda, W., et al. (2013). Correlative analysis of immunoreactivity in confocal laser-scanning microscopy and scanning electron microscopy with focused ion beam milling. *Front. Neural Circuits* 7:26. doi: 10.3389/fncir.2013.00026

Southwell, D. G., Nicholas, C. R., Basbaum, A. I., Stryker, M. P., Kriegstein, A. R., Rubenstein, J. L., et al. (2014). Interneurons from embryonic development to cell-based therapy. *Science* 344:1240622. doi: 10.1126/science.1240622

Spalding, K. L., Bergmann, O., Alkass, K., Bernard, S., Salehpour, M., Huttner, H. B., et al. (2013). Dynamics of hippocampal neurogenesis in adult humans. *Cell* 153, 1219–1227. doi: 10.1016/j.cell.2013.05.002

Stevens, J. K., Davis, T. L., Friedman, N., and Sterling, P. (1980). A systematic approach to reconstructing microcircuitry by electron microscopy of serial sections. *Brain Res.* 2, 265–293. doi: 10.1016/0165-0173(80)90010-7

Sun, G. J., Sailor, K. A., Mahmood, Q. A., Chavali, N., Christian, K. M., Song, H., et al. (2013). Seamless reconstruction of intact adult-born neurons by serial end-block imaging reveals complex axonal guidance and development in the adult hippocampus. *J. Neurosci.* 33, 11400–11411. doi: 10.1523/JNEUROSCI.1374-13.2013

Teixeira, C. M., Kron, M. M., Masachs, N., Zhang, H., Lagace, D. C., Martinez, A., et al. (2012). Cell-autonomous inactivation of the reelin pathway impairs adult neurogenesis in the hippocampus. *J. Neurosci.* 32, 12051–12065. doi: 10.1523/JNEUROSCI.1857-12.2012

Toni, N., Buchs, P. A., Nikonenko, I., Bron, C. R., and Muller, D. (1999). LTP promotes formation of multiple spine synapses between a single axon terminal and a dendrite. *Nature* 402, 421–425. doi: 10.1038/46574

Toni, N., Laplagne, D. A., Zhao, C., Lombardi, G., Ribak, C. E., Gage, F. H., et al. (2008). Neurons born in the adult dentate gyrus form functional synapses with target cells. *Nat. Neurosci.* 11, 901–907. doi: 10.1038/nn.2156

Toni, N., and Sultan, S. (2011). Synapse formation on adult-born hippocampal neurons. *Eur. J. Neurosci.* 33, 1062–1068. doi: 10.1111/j.1460-9568.2011.07604.x

Toni, N., Teng, E. M., Bushong, E. A., Aimone, J. B., Zhao, C., Consiglio, A., et al. (2007). Synapse formation on neurons born in the adult hippocampus. *Nat. Neurosci.* 10, 727–734. doi: 10.1038/nn1908

Trommald, M., and Hulleberg, G. (1997). Dimensions and density of dendritic spines from rat dentate granule cells based on reconstructions from serial electron micrographs. *J. Comp. Neurol.* 377, 15–28.

Trommald, M., Hulleberg, G., and Andersen, P. (1996). Long-term potentiation is associated with new excitatory spine synapses on rat dentate granule cells. *Learn. Mem.* 3, 218–228. doi: 10.1101/lm.3.2-3.218

Van Praag, H., Schinder, A. F., Christie, B. R., Toni, N., Palmer, T. D., and Gage, F. H. (2002). Functional neurogenesis in the adult hippocampus. *Nature* 415, 1030–1034. doi: 10.1038/4151030a

Wadell, H. (1935). Volume, shape, and roundness of quartz particles. *J. Geol.* 43, 250–280. doi: 10.1086/624298

Yasumatsu, N., Matsuzaki, M., Miyazaki, T., Noguchi, J., and Kasai, H. (2008). Principles of long-term dynamics of dendritic spines. *J. Neurosci.* 28, 13592–13608. doi: 10.1523/JNEUROSCI.0603-08.2008

Yuste, R., and Majewska, A. (2001). On the function of dendritic spines. *Neuroscientist* 7, 387–395. doi: 10.1177/107385840100700508

Zhao, C., Deng, W., and Gage, F. H. (2008). Mechanisms and functional implications of adult neurogenesis. *Cell* 132, 645–660. doi: 10.1016/j.cell.2008.01.033

Zhao, C., Jou, J., Wolff, L. J., Sun, H., and Gage, F. H. (2014). Spine morphogenesis in newborn granule cells is differentially regulated in the outer and middle molecular layers. *J. Comp. Neurol.* 522, 2756–2766. doi: 10.1002/cne.23581

Zhao, C., Teng, E. M., Summers, R. G. Jr., Ming, G. L., and Gage, F. H. (2006). Distinct morphological stages of dentate granule neuron maturation in the adult mouse hippocampus. *J. Neurosci.* 26, 3–11. doi: 10.1523/JNEUROSCI.3648-05.2006

Ziv, N. E., and Smith, S. J. (1996). Evidence for a role of dendritic filopodia in synaptogenesis and spine formation. *Neuron* 17, 91–102. doi: 10.1016/S0896-6273(00)80283-4

Conflict of Interest Statement: The authors declare that the research was conducted in the absence of any commercial or financial relationships that could be construed as a potential conflict of interest.

frontiers in Neuroanatomy

REVIEW
published: 04 June 2015
doi: 10.3389/fnana.2015.00078

From a meso- to micro-scale connectome: array tomography and mGRASP

*Jong-Cheol Rah[1,2], Linqing Feng[3], Shaul Druckmann[4], Hojin Lee[3,5] and Jinhyun Kim[3,5]**

[1] Korea Brain Research Institute, Daegu, South Korea, [2] Department of Brain Science, Daegu Gyeongbuk Institute of Science and Technology (DGIST), Daegu, South Korea, [3] Center for Functional Connectomics, Korea Institute of Science and Technology (KIST), Seoul, South Korea, [4] Janelia Farm Research Campus, Howard Hugh Medical Institute, Ashburn, VA, USA, [5] Neuroscience Program, University of Science and Technology, Daejeon, South Korea

Mapping mammalian synaptic connectivity has long been an important goal of neuroscience because knowing how neurons and brain areas are connected underpins an understanding of brain function. Meeting this goal requires advanced techniques with single synapse resolution and large-scale capacity, especially at multiple scales tethering the meso- and micro-scale connectome. Among several advanced LM-based connectome technologies, Array Tomography (AT) and mammalian GFP-Reconstitution Across Synaptic Partners (mGRASP) can provide relatively high-throughput mapping synaptic connectivity at multiple scales. AT- and mGRASP-assisted circuit mapping (ATing and mGRASPing), combined with techniques such as retrograde virus, brain clearing techniques, and activity indicators will help unlock the secrets of complex neural circuits. Here, we discuss these useful new tools to enable mapping of brain circuits at multiple scales, some functional implications of spatial synaptic distribution, and future challenges and directions of these endeavors.

Keywords: connectome, mGRASP, array tomography, 3D atlasing, multiple scales

OPEN ACCESS

Edited by:
Kathleen S. Rockland, Boston University School of Medicine, USA

Reviewed by:
Ulrike Grünert, The University of Sydney, Australia
Lidia Alonso-Nanclares, Universidad Politécnica de Madrid, Spain

***Correspondence:**
Jinhyun Kim, Center for Functional Connectomics, Korea Institute of Science and Technology (KIST), 39-1 Hawolgokdong, Seoul 136-791, South Korea
kimj@kist.re.kr

Received: *15 March 2015*
Accepted: *21 May 2015*
Published: *04 June 2015*

Citation:
Rah J-C, Feng L, Druckmann S, Lee H and Kim J (2015) From a meso- to micro-scale connectome: array tomography and mGRASP. Front. Neuroanat. 9:78. doi: 10.3389/fnana.2015.00078

Introduction

It is no exaggeration to state that the beautiful drawings of the visionary Spanish neuroanatomist Santiago Ramon Cajal (1852–1934, Nobel Laureate 1906) illustrating neuronal structure and brain architecture, set the standard for neuroanatomy in the last century. Primary insights emerging from this and subsequent work are that the brain is a network of diverse types of neurons and glial cells communicating with one another mainly through synaptic connections, and

Abbreviations: 3D, three-dimensional; AT, array tomography; ATing, AT-assisted circuit mapping; ATLUM, automated tape collecting lathe ultra microtome; C. elegans, Caenorhabditis elegans; CaMPARI, calcium-modulated photoactivatable ratiometric integrator; E-I balance, excitatory-inhibitory balance; EM, electron microscopy; ENABLED, endogenous labeling via exon duplication; FIBSEM, focused ion bean scanning EM; GFP, green fluorescent protein; Kv, voltage-sensitive K+ channel; LM, light microscopy; mGRASP, mammalian GFP-Reconstitution Across Synaptic Partners; mGRASPing, mGRASP-assisted circuit mapping; MRI, magnetic resonance imaging; PALM, Photo-activated localization microscopy; PET, positron emission tomography; PSD, postsynaptic density; SBFSEM, serial block face scanning EM; SIM, Structured illumination microscopy; spGFP, split-GFP fragments; STED microscopy, Stimulated emission depletion microscopy; STORM, stochastic optical reconstruction microscopy; VGLUT, vesicular glutamate transporter.

that anatomical connections provide the structural framework for information processing in the brain. Comprehensive knowledge of the brain's wiring in complex neuronal circuits at both meso- (region-by-region) and micro-scales (synapse-by-synapse) is essential for understanding brain functions. In an era of advanced modern technologies including ever-increasing computer power, neuroanatomy for the XX1st century, aims to determine the complete connectomes (neural wiring diagrams) of several key species (i.e., human, mouse, fruit fly, worm, etc.; Chklovskii et al., 2004; Sporns et al., 2005; Behrens and Sporns, 2012; Oh et al., 2014). Recently, there has been much excitement about new techniques for establishing the brain-wide, cellular-level, meso-scale connectome for the mouse using injections of fluorescent protein-expressing virus and tracers (Hunnicutt et al., 2014; Oh et al., 2014; Pollak Dorocic et al., 2014; Zingg et al., 2014). These systematic and standardized approaches allow spatial registration of mesoscopic connectivity data from separate experiments into a collective 3D reference space, while computational analyses of connection strength in 3D topography provides a whole-brain connectivity matrix. These meso-scale connectome atlases of brain-wide tractography of defined cell-types in defined regions are freely available, providing a foundational resource for structural and functional investigations into neural circuits that underlie complex brain functions, such as behavioral and cognitive processes. To solve big puzzles of the brain, however, the meso-scale connectome is insufficient and micro-scale synaptic connectivity remains substantially unknown.

It is a challenging, ongoing task to map synaptic connectivity in the brain, a complex and compact tissue composed of thin ($<1\ \mu m$ in diameter) yet long (often >1 mm in length) neuronal processes from densely packed neurons, communicating with each other through synapses on the scale of nanometers ($\sim$20 nm). Mapping these structures requires advanced neuronal labeling, imaging, and reconstructing techniques that provide high-resolution in multiple scales (**Box 1**; Kleinfeld et al., 2011; Wickersham and Feinberg, 2012; Morgan and Lichtman, 2013; Yook et al., 2013). Traditional methods based on electron microscopy (EM) that offer high resolution on the nanometer scale have been used to find and characterize synapses, but these approaches lack the throughput capacity to reconstruct even a small portion of the connection matrix. Thus, despite recent advances, these approaches remain practical only for very small volumes (Knott et al., 2008; Bock et al., 2011; Briggman et al., 2011; Kreshuk et al., 2011). Recently, to circumvent time- and labor-intensive EM-based approaches and the low resolution of light microscopy (LM), researchers have developed fluorescence-based approaches combined with sophisticated genetic and optical methods (Livet et al., 2007; Micheva and Smith, 2007; Wickersham et al., 2007; Micheva et al., 2010; Cai et al., 2013; Yook et al., 2013). Of several advanced LM-based connectome technologies, array tomography (AT) and mammalian GFP-Reconstitution Across Synaptic Partners (mGRASP) can provide relatively high-throughput mapping synaptic connectivity at multiple scales. AT combines LM and EM approaches to resolve synapses by using multiple antibodies to label synaptic markers (Micheva and Smith, 2007; Micheva et al., 2010). It benefits from the high throughput of LM, high z-resolution of EM, and improved quantitative reliability of information obtained through multi-immunofluorescence. Furthermore, repeated cycles of antibody stripping and re-staining synaptic components provides a single-synapse analysis, or a synaptogram, that offers insights into synapse molecular diversity (Micheva et al., 2010). Meanwhile, mGRASP (Kim et al., 2011; Feng et al., 2012), synapse-specific labeling with two complementary GFP components, provides suitable tools for mapping mammalian synaptic connectivity at multiple scales: micro-scale for synapse-by-synapse or neuron-by-neuron measures, and meso-scale for local and long-range neuronal projections mappings. In addition, new online resources[1] (Oh et al., 2014; Zingg et al., 2014) provide useful references with brain-wide coverage and guidance for further detailed circuit mapping at the micro-scale, which can be accomplished by AT, and mGRASP-assisted circuit mapping (ATing and mGRASPing, respectively) which we review below. Most recently, using these two methods, we generated a comprehensive fine-scale circuit mapping of hippocampal and somatosensory cortical regions showing new spatially-structured synaptic connectivity patterns (Rah et al., 2013; Druckmann et al., 2014). Increasingly, studies reveal that nonrandom organization of interconnectivity exists to some degree within the nervous system at multiple scales, including individual neurons, groups of neurons, architectonic regions, and functional systems (DeBello et al., 2014).

The recent development of powerful tools for relatively high-throughput mapping of synaptic networks promises major advances in understanding brain functions. Yet, mapping neuroanatomical connectivity in most model organisms remains difficult owing to technical challenges and gaps between connectome mapping enterprises. Creating ties between meso- and micro-scale maps and turning anatomical connectivity maps to comprehensive knowledge remain difficult. Here we discuss useful new tools to enable mapping of brain circuits at multiple scales, some functional implications of spatial synaptic distribution, and future challenges.

Array Tomography-Assisted Circuit Mapping (ATing)

AT was developed to image synaptic architecture and neuronal circuits (Micheva and Smith, 2007; Micheva et al., 2010; Rah et al., 2013). It is achieved by repeated wide-field immunofluorescence imaging of arrays of ultrathin serial brain sections, followed by computational reconstruction into an isotropic three-dimensional (3D) volume (**Figure 1A**). Although optical sectioning by confocal or two-photon microscopy allows imaging of thick brain sections and reconstructing neuronal structures from the obtained images, its resolving power is inadequate to resolve nanometer-scale synapses, mainly because it provides poor z-resolution. As this technique uses pixel-thick or thinner brain sections (50$\sim$200 nm), the z-axial resolution is determined by not Abbe's rule but the thickness of the sections. Another significant advantage of ultrathin physical sectioning

[1] www.MouseConnectome.org and http://connectivity.brain-map.org

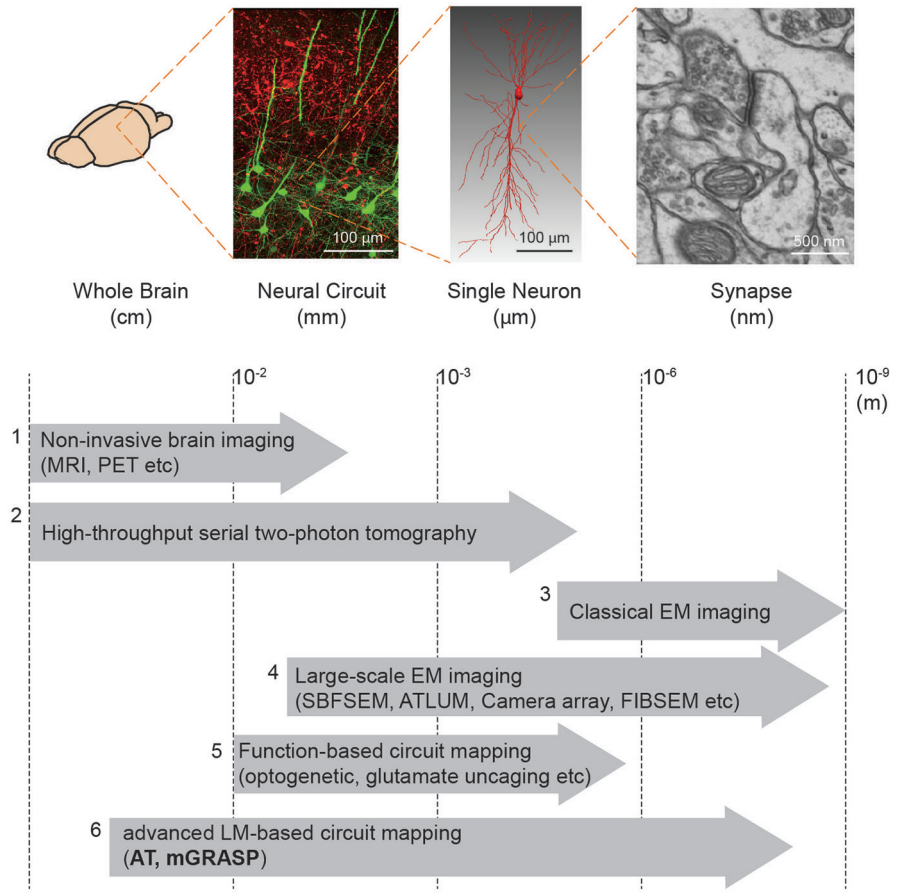

BOX 1 | Brain mapping methods.

We summarize the currently available methods to enable mapping of brain circuits at the scale levels (from macro- to micro-scale): (1) Non-invasive brain imaging methods, i.e., MRI and PET widely used for the whole human brain, provide information about region-to-region connectivity at millimeter-resolution (Catani and Thiebaut de Schotten, 2008). (2) High-throughput serial block face two-photon tomography (Ragan et al., 2012) has been used to achieve the meso-scale connectome of the whole mouse brain (Oh et al., 2014). (3) Conventional EM imaging has been considered as a gold-standard method to resolve the nanometer-scale synapses yet its low-throughput and reconstruction difficulty constrain achievable brain volume. (4) Therefore, much effort has been devoted to improving the EM-based imaging approach. Large-scale EM imaging techniques (e.g., Serial Block Face Scanning EM, Automated Tape-Collecting Lathe Ultra Microtome, Camera array, Focused Ion Beam Scanning EM) have been recently developed and demonstrated to enable dense reconstruction of local circuit (Merchán-Pérez et al., 2009, 2014; Bock et al., 2011; Briggman et al., 2011; Briggman and Bock, 2012; Blazquez-Llorca et al., 2013; Hayworth et al., 2014). Although these methods, at present, remain relatively time-consuming and volume limited, further advances in these techniques may allow for complete connectome in the large-scale (Hayworth et al., 2015). (5) For functional assessment along with connectivity, laser-scanning photostimulation (e.g., glutamate uncaging and optogenetic approach) combined with electrophysiological recordings have accelerated mapping region-to-cell and cell-to-cell connectivity together with measures of synaptic efficacy and strength (Shepherd and Svoboda, 2005; Shepherd et al., 2005; Yoshimura and Callaway, 2005; Yoshimura et al., 2005; Petreanu et al., 2007, 2009; Ashby and Isaac, 2011; Fino and Yuste, 2011; Hooks et al., 2011; Mao et al., 2011). A potential concern, though, is that these methods can yield ambiguous results owing to the low precision of uncaging and the low resolution of photostimulation. (6) Advanced LM-based circuit mapping tools such as AT and mGRASP can provide relatively high-throughput mapping synaptic connectivity at multiple scales. Details of these two methods are described in this review.

is that it circumvents some technical hurdles including the laser and antibody penetration problems that often limit the usefulness of immunofluorescence staining and imaging in thick brains sections. AT enables detailed and reliable investigations of the proteomic diversity of individual synapses by using repeated cycles of antibody stripping and re-staining with a large number of multiplex of synaptic makers, resulting in a comprehensive description called a synaptogram (Micheva et al., 2010).

AT reveals not only anatomical circuits but also the synaptic proteome, thus offering insights into synaptic physiology. It has been suggested that synapse-level physiology can be inferred from molecular information of individual synapses (Yasuda et al., 2006). A good example of this approach is the physiological relevance of the expression patterns of vesicular glutamate transporter isoforms, i.e., VGLUT1 and 2 (Wojcik et al., 2004; Moechars et al., 2006; Fioravante and Regehr, 2011). Intensive anatomical analysis with LM and EM showed that the expression

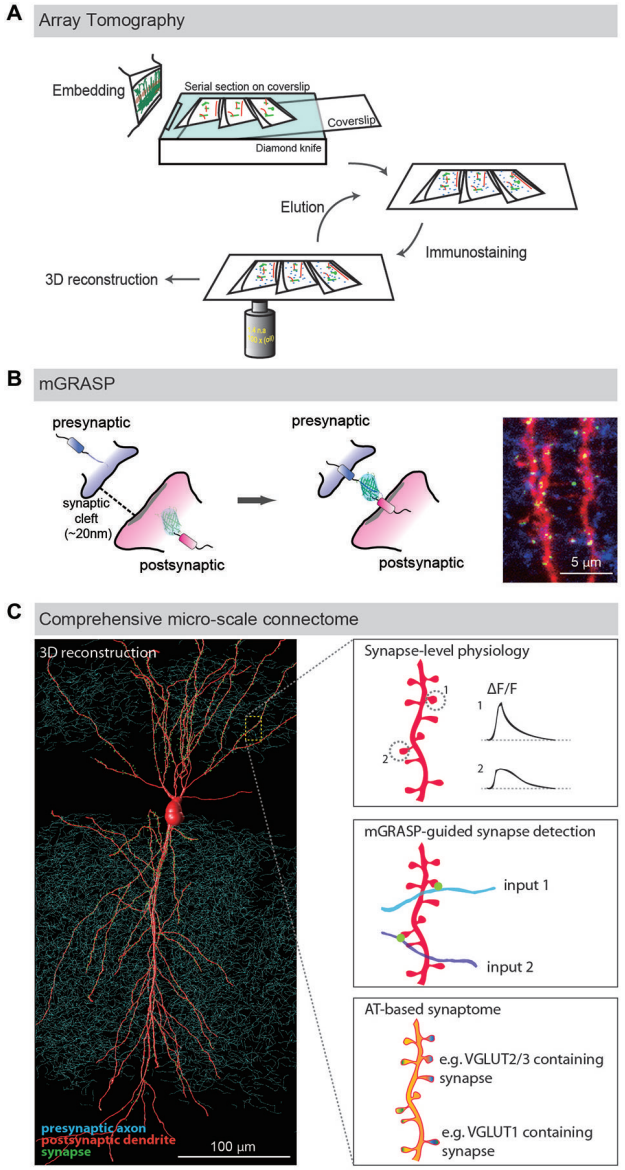

FIGURE 1 | LM-based circuit mapping. (A) Schematic illustration of Array tomography. Embedded brain tissue is serially sectioned into nanometer ultrathin slice array and repeatedly immunostained with multiplex synaptic makers. Then the stained serial sections are imaged and computationally reconstructed into isotropic three-dimensional structure. **(B)** Schematic illustration of mGRASP. Two complementary split-GFP fragments, non-fluorescent are tethered to each side of synaptic membranes. When the two neurons form synapses, thus closely opposed across a synaptic cleft, fluorescent GFP is reconstituted. Example image shows mGRASP signals (Green) in hippocampal CA3 (blue) -to-CA1 (red) synapses. **(C)** Schematic illustration of comprehensive micro-scale connectome with functional assessments. Physiological characteristics of individual synapses accessed by two-photon microscopy and electrophysiology, presynaptic input sources by mGRASP or anterograde labeling in combination with AT-based synaptogram will reveal relationships of the proteomic diversity, function and input sources at the level of individual synapses. Eventually one will be able to estimate functions and input sources of synapses based on AT images. (Panels **A,B** are modifications of the figures from Kim et al., 2011; Rah et al., 2013, respectively).

of these two major isoforms of VGLUT is spatially and temporally distinctive (Boulland et al., 2004; Graziano et al., 2008; Lei et al., 2013). Interestingly, the expression levels of VGLUT1 and VGLUT2 affect specific forms of signal processing like short-term plasticity by controlling quantal size and neurotransmitter release probability (Wojcik et al., 2004; Moechars et al., 2006; Fioravante and Regehr, 2011). These findings raised perplexing questions since other studies demonstrated that these isoforms are equally effective in transporting glutamate into vesicles (Fremeau et al., 2004). This puzzle was solved by identifying an additional synaptic molecule, endophilin A1, and determining its distinct interplay with VGLUTs (Weston et al., 2011). Endophilin A1, a positive regulator of glutamate release, is inhibited by VGLUT1 but not VGLUT2 or 3 so that synapses with VGLUT2/3 have higher vesicular release probabilities. Thus, the quantitative synapse proteome together with circuit maps using AT will help provide synapse-level physiological information including type of inputs, synaptic strength, and plasticity.

A potential drawback of AT, though, is its limited accuracy of synapse detection (Micheva et al., 2010; Rah et al., 2013). This occurs because the lateral resolution of AT is still agonized by the light diffraction limit while the *z*-axial resolution of AT is determined solely by the section thickness, which is as good as that of conventional TEM. The accuracy AT reaches for synapse detection has been estimated and validated in thalamocortical tissue by a synapse-by-synapse comparison with results obtained by EM, taking advantage of the ready comparability of AT to EM: Up to ~80% of thalamocortical synapses detected by AT were validated by TEM and 86% of total TEM-identified synapses were detected by AT (Rah et al., 2013). Although the current level of accuracy of synapse detection by AT is considerably greater than that of traditional LM-based approaches (approximately 20–50%), we expect that AT accuracy can be improved by combining it with advanced optical methods or/and supplementary synapse labeling methods. Given the success of recent advanced super-resolution LM techniques such as PALM (Betzig et al., 2006), STORM (Rust et al., 2006), SIM (Gustafsson, 2005), and STED microscopy (Willig et al., 2006) allowing multi-fluorescence imaging with nanometer resolution, there are now increasing efforts to combine super-resolution microscopy with AT. In fact, it has been demonstrated that STORM and STED are compatible with AT to enhance lateral resolution up to the single molecular level (Punge et al., 2008; Nanguneri et al., 2012). Another way to improve the accuracy of synapse detection by AT, possibly together with high-resolution imaging too, is to make use of additional and improved synapse labeling strategies instead of using only immunostaining with synaptic markers. The main reasons AT achieves relatively low accuracy in detecting synapses are the high density of synapses in the brain (~$1/\mu m^3$; Schüz and Palm, 1989; DeFelipe et al., 1999) and the relatively low antibody specificity for synaptic vesicle proteins. A theoretical study predicted that the labeling of synapse specific proteins (e.g., PSD-95, piccolo, bassoon), instead of synaptic vesicle proteins could detect 95–99% of all synapses (Mishchenko, 2010). Recently developed stoichiometric endogenous labeling of synaptic proteins, called endogenous

labeling via exon duplication (ENABLED), may provide a promising way to solve these problems (Fortin et al., 2014). Thus, when combined with other advanced optical and supplementary synapse labeling methods, ATing offers unique fundamental synaptic molecule profiles that may be used to describe neuronal networks. We will further discuss the marriage of AT and mGRASP in the following sections.

mGRASP-Assisted Circuit Mapping (mGRASPing)

mGRASP is a genetically-controlled, molecular engineering method to detect mammalian synapses using LM (Kim et al., 2011; Feng et al., 2012, 2014; Druckmann et al., 2014). It is based on two complementary split-GFP fragments (called spGFP1-10 and spGFP11), separately non-fluorescent, each tethered to synaptic membranes in each of two neuronal populations. When two neurons, each expressing one of the fragments, are closely opposed across a synaptic cleft, the split fragments unite and fluorescent GFP is reconstituted in that location (**Figure 1B**). This molecular engineering approach allows the resolution, at nanometer-scale, of synapses viewable by LM.

The GRASP technique was initially implemented in *C. elegans* (Feinberg et al., 2008). Recently, we successfully adapted mGRASP for the more complex synapses of mammals by optimizing the synaptic transmembrane carriers (Kim et al., 2011). We achieved this by engineering spGFP carriers that are specifically targeted to synaptic membranes, and that accommodate the physical spacing of the synaptic cleft to precisely label actual synapses, not non-synaptic membrane contacts. The manifest benefit of mGRASP technology is that it can rapidly and accurately detect nanometer-scale (∼20 nm) synapses despite the diffraction limitations of LM: using this technique, fluorescence indicates the locations of mammalian synapses quickly, confidently, and with high spatial resolution. When tested with known synaptic and non-synaptic connections in samples full of axonal contacts, mGRASP was shown to specifically detect actual synapses with very few false positives. When combined with specialized analysis software (Feng et al., 2012, 2014, 2015), mGRASP can relatively quickly reveal the precise locations and numbers of synapses along postsynaptic dendrites, sites responsible for determining many important characteristics of signal processing.

More recently, using our mGRASP technology, we performed a comprehensive fine-scale circuit mapping of hippocampal regions and identified new patterns of spatially-structured synaptic connectivity (Druckmann et al., 2014). An advantage of mGRASP technology is that, when used with an improved computational analysis, it can map mammalian synaptic connectivity at multiple scales: micro-scale for synapse-by-synapse or neuron-by-neuron measures, and meso-scale for local and long-range neuronal projection measures. A potential concern, though, is that this technique sometimes registers false negatives, making it difficult to determine absolute numbers of synapses. The problem of false negatives is common to all LM approaches and varies with instrumental parameters (e.g., laser power, emission spectra, etc.). Further optimizing of mGRASP technology and applying it in combination with other technologies will lead to useful new tools for mapping mammalian synaptic connectivity. We recently offered a step-by-step protocol for mGRASP to map synaptic connectivity in the mouse brain (Feng et al., 2014). Although our technique uses combinations of well-established experimental methods (e.g., virus production, *in utero* electroporation, stereotaxic injection, brain slice preparation, and confocal imaging), in practice, each experimental step needs to be adjusted specifically to make mGRASPing effective. Our well-optimized protocol allows the rapid and precise characterization of synaptic connectivity in neuronal circuits of both healthy and pathological tissues, potentially aiding in the diagnosis of abnormal synaptic connectivity.

Furthermore, creative combinations of mGRASP with currently available techniques for imaging mammalian synaptic connectivity will contribute substantially to brain mapping, since thus far, none of these currently available techniques for imaging mammalian synaptic connectivity is in itself perfect (Yook et al., 2013). The stochastic multicolor labeling of Brainbow combined with mGRASP, for instance, could identify the presynaptic partners of a given neuron; it would require labeling each neuron and preparing dense-reconstructions of synaptic connectivity under LM (Cai et al., 2013). Together with new optical clearing methods (Chung and Deisseroth, 2013; Ke et al., 2013; Renier et al., 2014; Susaki et al., 2014) or the very recently developed expansion imaging method which uses the physical expansion (∼4.5-fold) of tissue, resulting in physical magnification (Chen et al., 2015), mGRASPing with multicolored axonal labeling allows mapping connectivity from multiple inputs. Also, mGRASP combined with a new retrograde label virus system (Kato et al., 2011a,b) could help unlock the secrets of disynaptic circuits as well as monosynaptic pairs of cells. Further, a common drawback of all methods for anatomical synaptic mapping, the lack of information about synaptic activity and strength, can be overcome through combinations of techniques including existing activity indicators and optogenetic tools.

Comprehensive Micro-Scale Connectome with Triple Combination of AT, mGRASP, and Activity Sensors

Given the distinctive advantages and pitfalls of both AT and mGRASP, we propose the combination of these two technologies into a powerful tool for determining the micro-scale connective synaptome. As described above, ATing is beneficial for revealing detailed synapse proteomes but is hampered by limited accuracy of synapse detection compared to those achievable through more laborious procedures. Meanwhile, mGRASPing provides high-throughput and accurate synapse detection but provides no information about synaptic molecular diversity. A marriage of these two complementary technologies would provide powerful descriptions of neuronal circuits. In principle, advanced mGRASP can accurately and rapidly detect specific synapses in a particular connection and AT can subsequently denote molecular profiles of the synapses. This approach will not only enhance the accuracy of ATing but also provide fundamental information of complex neuronal networks for understanding brain functions.

It is widely believed that the number, morphology, and molecular compositions of synapses intimately related to synaptic functions. And, abnormalities in synaptic number, shape, and compositions have been demonstrated to be accompanied by synaptic dysfunctions in many neurological disorders such as Alzheimer's disease (Selkoe, 2002), Parkinson's disease (Calabresi et al., 2006), Schizophrenia (Stephan et al., 2006), Fragile X syndrome (Pfeiffer and Huber, 2009), and Rett syndrome (Chao et al., 2007). Also, growing lines of evidence show that a functional balance of excitatory and inhibitory systems is fundamental for the healthy function of brains by providing for the fine tuning of neuronal circuits (Wehr and Zador, 2003; Xue et al., 2014); disruption of excitatory-inhibitory (E-I) balance engenders neurological disorders such as autism spectrum disorder, schizophrenia, and epilepsy (Chao et al., 2007; Kehrer et al., 2008; Dudek, 2009). Therefore, it is important to precisely map the number, distribution, and molecular profiles of excitatory and inhibitory (and possibly modulatory as well) synapses in healthy and pathological brains. A combination of AT and mGRASP is suitable for this task.

All of the currently available techniques for imaging mammalian synaptic connectivity provide fundamental structural descriptions but none provide direct assessments of function, such as synaptic strength and efficacy (Yook et al., 2013). A long-term goal in neuroscience is to understand how neuronal activities convey information through network connections. To understand the relationship between the structure and function of neuronal networks, recent studies have attempted to combine EM-based reconstruction with calcium imaging or simultaneous multiple whole cell recordings that can detect active synapses (Bock et al., 2011; Briggman et al., 2011; Ko et al., 2014). However, the issue of relatively low throughput including reconstruction and difficulty in finding cell-to-cell or branch-to-branch correspondence between functional images and reconstructed structural images hinders functional connectivity mapping in large volumes. High-accuracy ATing guided by mGRASPing could serve this purpose and help generate the functional connectome along with synaptome. We propose, for example, high-accuracy ATing guided by mGRASPing in barrel cortex. Barrel cortex is a well-studied multisensory integration system conveying information from whisker movements and object touches into an organized laminar architecture. These features will allow us to study relationships between the structure and function of a network associated with known behaviors (Larkum et al., 2004; Hill et al., 2011) by use of multi-colored calcium sensors (Akerboom et al., 2013; Oheim et al., 2014), followed by high accuracy AT-based circuit reconstruction (i.e., mGRASP aided AT). Recently, it has been shown that accurate subcellular synaptic distributions can be reconstructed on a similar scale using AT and mGRASP in vS1 and hippocampus, respectively (Rah et al., 2013; Druckmann et al., 2014).

Comprehensive 3D Whole-Brain Atlas at Multiple Scales

Thus far, we have described imaging methods useful for mapping synaptic connectivity and their applications for deciphering functional features of the structural map. The connectome project at multiple scales will necessitate further development of algorithms to reliably extract wiring information from digitized images, and to bring data from different sections and animals into register with one another. Furthermore, creating ties between meso-scale and micro-scale datasets is essential. To achieve this, three main steps are required: (1) Photomicrographs from an individual animal must be registered in 3D while accounting for tissue distortions. (2) Labeled axonal segments must be detected to determine the meso-scale connectome. This step is somewhat challenging, and typically relies on manual or software-assisted tracing, although progress has been made toward providing automated, quantitative estimates of axonal length and density. (3) Individual neurons and their full distributions of synapses must be represented in a common framework to determine the micro-scale connectome. At present, the largest gap between meso- and micro-scale connectome datasets is the difference in data representation used for each. Micro-scale connectome data consist of individual reconstructed neurons and their synapses, while meso-scale connectome data usually consist of the densities of axonal projections from one injection site to another, typically summarized by connectivity matrix as a list of projection tables. The rows and columns of these tables are grouped brain regions, and the table's data represent the strength of connections between segmented brain regions which can be quantified by the intensity of labeled axons either subjectively by manual rating (Hunnicutt et al., 2014; Zingg et al., 2014), or objectively by image segmentation (Oh et al., 2014; Pollak Dorocic et al., 2014). To reconcile meso- and micro-scale data into a hierarchical structure, all processed data must be mapped to a common 3D reference space (such as the Allen Institute mouse reference atlas).

Integrating connectivity information into a reference space requires registration or co-registration of raw brain slice images to the reference brain images, which in turn provide anatomical annotations of raw brain images. In practice, manual annotation seems to provide the most accurate anatomical information (Zingg et al., 2014), yet better automatic algorithms will be required as data sets grow. The purpose of registration is to find the one-to-one mapping or transformation between pixels of brain slice images and pixels of the reference brain images. Main components of the registration framework are referred to as transform, metric and optimizer: transform defines the parameterization of pixel mapping; metric measures the quality of transformations; and optimizer drives the parameters of transformation to reach the best possible alignment by seeking optimal metric values. As the deformations of brain structures between animals are highly variable, non-rigid transformations are required to model the pixel mapping (**Figure 2**).

B-spline transformation has emerged as a popular choice for modeling non-rigid transformation. A uniform grid of control points forms the local support of the B-spline pixel transformation, and the transformation of each pixel can be calculated from only a few of its neighboring control points. These advantages make B-spline transformation suitable for modeling the local deformations of brain structures. In fact, B-spline based non-rigid registration with mutual information and

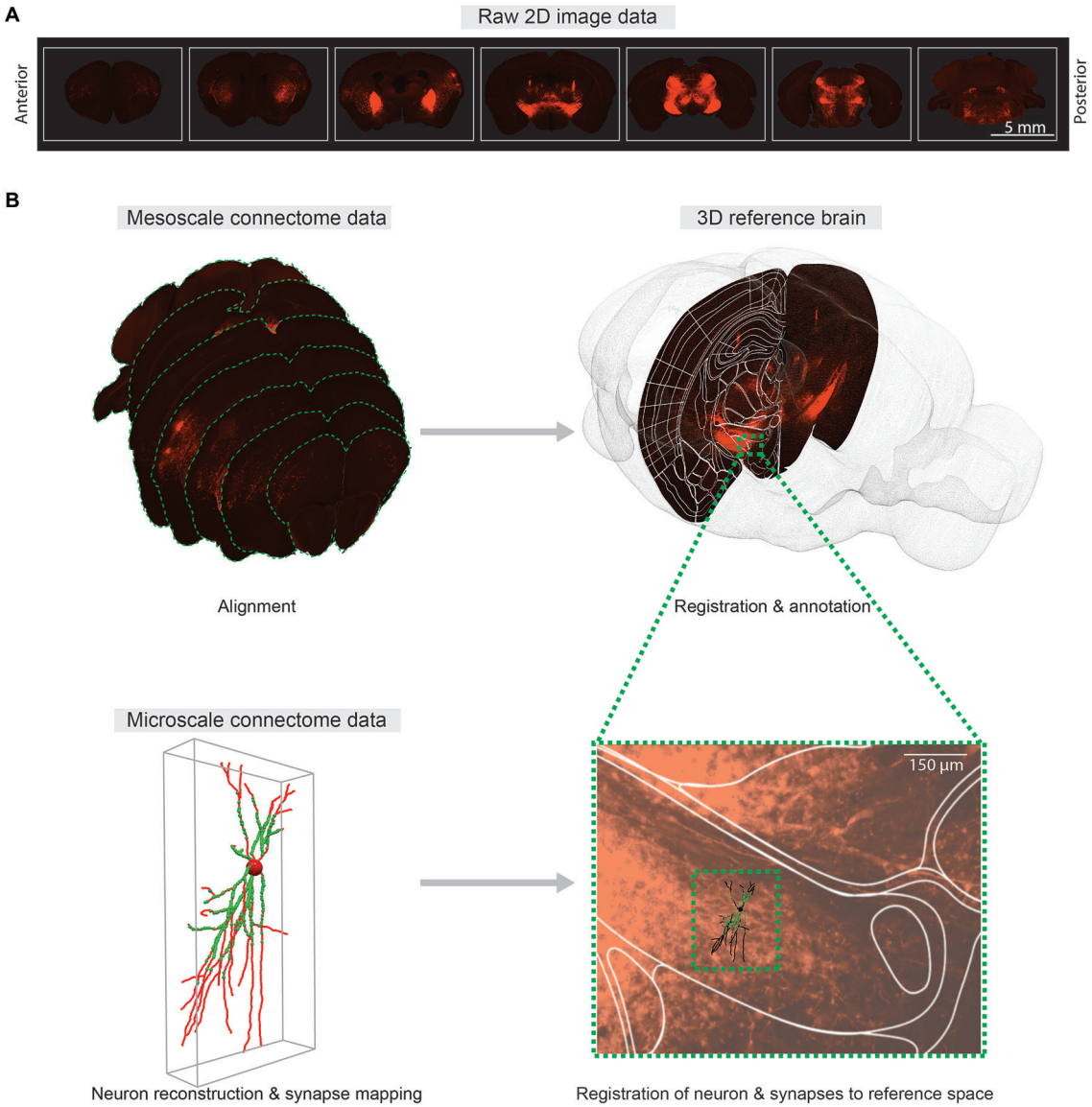

FIGURE 2 | Comprehensive 3D whole-brain atlas at multiple scales. (A) Representative coronal sections of the mouse brain with 400 µm intervals showing fluorescent axonal projections for meso-scale connectome. **(B)** Mapping meso- (*top*) and micro-scale (*bottom*) data into a common 3D reference atlas pace. Meso-scale sections are aligned and registered to the Allen Institute Mouse Reference Atlas Space (P56). At micro-scale level, neuTube-reconstructed individual neuron and synapses (Feng et al., 2015) are mapped to the same reference atlas space.

smooth constraints as metric has been applied in several previous studies of mesoscopic connectivity mapping (Oh et al., 2014; Pollak Dorocic et al., 2014).

Because brain slice images and reference brain images are usually acquired using different methods and protocols, mutual information that can measure the similarity between images of different modalities is useful as a metric. Smooth constraints are used to avoid irregular transformations on homogenous parts of images. Many factors can influence the registration result, including spacing between grid points, intensity levels for mutual information, balance between mutual information and smooth constraints, choice of optimization algorithm, etc. A carefully designed registration strategy may include parameter tuning, coarse-to-fine, global-to-local or intermediate registration targets. This registration framework works well with large brain structures that have distinct intensity levels and that have been validated by checking the location deviation of several brain landmarks such as Area Postrema, Medial Mammillary Nucleus, and Arbor Vitae (Oh et al., 2014). However, it must be evaluated on a case-by-case basis whether the registration framework accurately delineates small neighboring brain regions with similar intensity levels. As there is no other information to guide the registration in such regions, the registration results must be guided mostly by manually tuned smooth constraints

rather than the image signals. Quantitative evaluation like Klein et al. (2009) and Ou et al. (2014) is essential for choosing an appropriate registration method and setting optimal parameters.

To merge micro-scale connectome data using mGRASP or AT with meso-scale data, reconstructed neurons and their synapses should also be mapped to a reference space (**Figure 2B**). Intermediate meso-scale images can be utilized as guidance to locate neurons in the reference 3D space. Once correctly mapped, these micro-scale data can be indexed and efficiently queried by space-partitioning data structures. This pipeline may allow us to merge connectome data on different scales from different research groups into unified hierarchical anatomical structures. We believe that comprehensive cross-referencing of connectivity data from different scales into the same reference space will allow us to explore intermingled neuronal networks at multiple scales and will facilitate understanding of circuit functions.

From Neuroanatomical Connectivity Maps to Neuro-Knowledge

Understanding the dynamics of neuronal circuits is crucial for studying information processing by these circuits. Knowledge of neuroanatomical connectivity in a comprehensive 3D brain atlas (i.e., topographic axonal projections on the meso-scale and spatial synaptic distributions on the micro-scale) will help in the extraction of dynamics of neuronal circuits. Parceling out brain regions according to their connectivity can serve to define neural circuits, situated between the level of the single neuron and that of the entire circuit.

Meso-scale descriptions have been previously offered in terms of an inventory of cell-types (Bohland et al., 2009; Seung and Sümbül, 2014) and by approaches that smooth over fine anatomical details (coarse-graining) arising from microscopic fluctuations, thus allowing for effective mesoscopic descriptions, and the classification of neuronal populations into functional groups (Bohland et al., 2009; Mitra, 2014). Determining the axonal projections from a given set of neurons to target brain areas can assist in defining cell-types (Mitra, 2014). Recently, examples of such efforts have been published (Hunnicutt et al., 2014; Oh et al., 2014; Zingg et al., 2014) and even cell-type-specific connectivity has been reported in a whole brain atlas (Pollak Dorocic et al., 2014). In this work, image alignment, registration, and annotation, connectivity patterns were summarized, as described above, in a large matrix tabulating the projection density between the different injection sites and a list of predefined target areas (**Figure 3A**). The information found in this series of papers could be used to generate a meso-scale description by a clustering analysis that groups together regions revealed by separate experiments according to the similarity of their input and output projections (**Figures 3A–E**). Thus, information about anatomical projections can be used to define meso-areas that serve as a mid-level layer of description between the single neuron and the full brain area. This should assist in assigning a more interpretable level of functional roles to neural circuits as well as guiding development of a micro-scale connectome.

Beyond coarse-scale anatomical projection paths, micro-scale descriptions, for instance using AT or mGRASP, can be used to

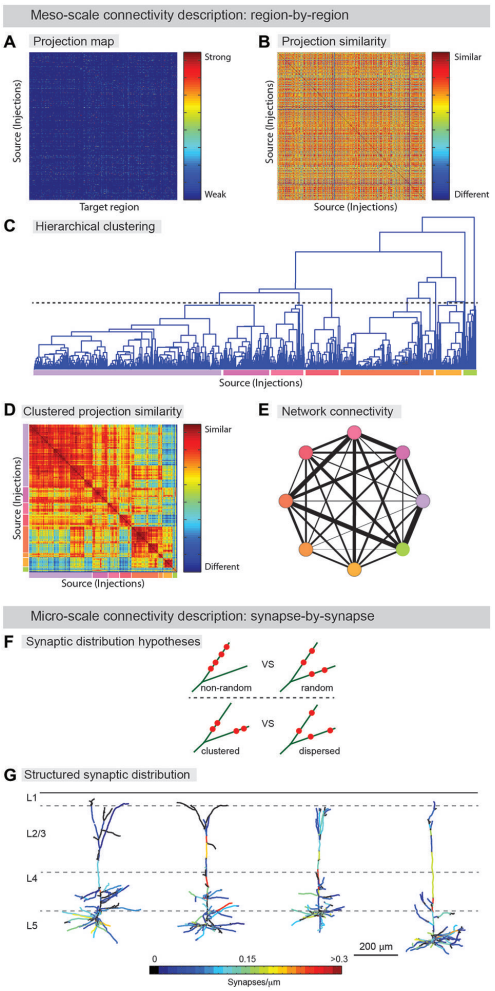

FIGURE 3 | From neuroanatomical connectivity maps to neuro-knowledge. (A–E) Computational analysis of meso-scale data yields coarse grain network description. (A) Data from registered meso-scale image data (see **Figure 2**) is expressed as a map of projection intensity from source to target regions. Each row shows the projection signals from each injected brain to target brain regions based on an atlas. Projection strength is indicated by colors. **(B)** Projection map transformed to show similarity between injection sites. **(C)** Hierarchical clustering is used to agglomerate individual projection sites into larger zones. A threshold (dashed line) is chosen to indicate the output division for clustering. Colored lines below indicate the different clusters. **(D)** Similarity matrix sorted by clustering identity shows that clustering indeed finds groups of similar injection sites. Colors from **(D)** indicate clusters. Note additional structure can be found on scales other than the one chosen for clustering **(E)** Clusters are aggregated into zones and the averaged connectivity between these zones is shown as a schematic network representation. Colors indicate cluster identity as in **(C,D)**. Width of lines indicates strength of averaged projection. **(F,G)** Micro-scale descriptions. **(F)** Synaptic distribution on the dendrites is one of the most important determinants for input-output functions of the neuron. Do different branches within a neuron have different synapse density (*upper*) and are synapses on a branch clustered (*lower*)? Significant tropism over subset of dendritic branches and spatial clustering of synapses were demonstrated by ATing and mGRASPing, supporting active dendritic integration. **(G)** Structured synaptic distribution of the reconstructed pyramidal neurons in somatosensory cortex (L5) from thalamus inputs. The density of thalamocortical synapses on dendrites is indicated in color-spectrum. (Panel **G** is a modification of the figure from Rah et al., 2013).

provide a detailed understanding of neuronal signal processing. By identifying the number of synapses in a projection between two groups of neurons, and the specific spatial distribution of individual synapses along the dendritic arbor of the postsynaptic cells, the transfer of signals from one population to another can be studied in far greater detail. Recently, such micro-scale synaptic connectivity mapping with AT and mGRASP provided direct evidence for significant spatial synapse clustering and for a substantial level of structured synaptic distribution over subsets of dendritic branches (**Figures 3F,G**; Rah et al., 2013; Druckmann et al., 2014).

For many years a number of electrophysiological and theoretical studies have demonstrated the presence of biophysical substrates for local processing on dendritic branches. These studies led to a hypothesis that a structured organization of synapses at the cellular and dendritic levels may also exist to utilize this specialized biophysics (Poirazi et al., 2003). Such an organization may provide advantages for computation. On the biophysical level, spatially clustered, temporally synchronized synaptic inputs tend to be amplified by triggering local dendritic spikes through the opening of voltage-dependent cation channels (such as voltage-dependent sodium channels, voltage-sensitive calcium channels, NMDA receptor channels), which enhance local voltage deflection supra-linearly, thereby increasing the chance of generating action potentials (Magee et al., 1998; London and Häusser, 2005; Magee and Johnston, 2005; Johnston and Narayanan, 2008; Sjöström et al., 2008). However, the technical challenge of determining electrophysiologically whether the distribution of synaptic inputs follows the local structure has made it difficult to test the hypothesis, particularly across neuronal populations.

To extend the hypothesis, one would want to know whether synapses convey *related information (origin, subtype, response specificity etc.)*, in a spatially clustered manner. Multiple functional studies supported this idea that spatially clustered synapses receive related information (Larkum et al., 1999; Poirazi and Mel, 2001; Harnett et al., 2013). Furthermore, it has been shown that dendritic branches have collective response properties to stimuli as shown by the coupling between local dendritic spikes and the somatic voltage change being dependent upon the specific branch rather than individual synapses in the branch (Losonczy and Magee, 2006). The coupling can be modified in a branch-specific manner by plasticity driven by NMDA dependent regulation of local $Kv_{4.2}$ potassium channels (Kim et al., 2007; Losonczy et al., 2008) and dependent upon the excitation history of neighboring dendrites (Remy et al., 2009). Additional studies, performed *in vivo*, that demonstrated distinct functions of dendritic branches support the notion of input clustering (Lavzin et al., 2012; Xu et al., 2012). Using AT and mGRASP, we have directly observed the structured nature of synaptic inputs, by describing both between-branch structure, and within-branch clustering, in terms of micro-scale descriptions in thalamocortical and hippocampal connections (Rah et al., 2013; Druckmann et al., 2014). To achieve micro-scale descriptions of connectivity, functional characteristics of synapses, such as their efficacy and response specificity, need to be pursued with a high-throughput process. We propose that advanced optogenetic and sensory stimulation paradigms paired with activity sensors, such as the recently developed activity history marker, CaMPARI (Fosque et al., 2015), followed by large-scale AT or mGRASP, will provide complete pictures of micro-scale descriptions of input-specific synaptic connectivity. Combining such meso- and micro-scale descriptions will greatly facilitate our understanding of the operations of complex neuronal networks.

Conclusion and Perspective

Here we reviewed two techniques, AT and mGRASP, which are useful for imaging mammalian synaptic connectivity at multiple scales. Combining the advantage of mGRASP to accurately detect synapses and AT to profile synapses on the molecular level will enable functional assessments that allow building up from network wiregrams to synaptograms, thus revealing the secrets of complex neural circuits. We suggest that, in addition, future endeavors need to focus on linking meso- and micro-scale connectivity maps. The best way to fill the gaps between maps on different scales would involve creating "standardized linkers" such as common 3D reference space. The increasing pace of technology developments for neuroanatomy in the XX1st century make us feel that it is indeed exciting time to be a neuroscientist witnessing our steps towards keys to unlock the mystery of the brain.

Acknowledgments

J-CR is supported by KBRI Program (2231-415), Basic Science Research Program (NRF-2014R1A1A2057804), and Korea Health Technology R&D Project (HI14C1135). LF, HL, and JK are supported by the KIST Institutional Program (2E25540 and 2E25600).

References

Akerboom, J., Carreras Calderón, N., Tian, L., Wabnig, S., Prigge, M., Tolö, J., et al. (2013). Genetically encoded calcium indicators for multi-color neural activity imaging and combination with optogenetics. *Front. Mol. Neurosci.* 6:2. doi: 10.3389/fnmol.2013.00002

Ashby, M. C., and Isaac, J. T. (2011). Maturation of a recurrent excitatory neocortical circuit by experience-dependent unsilencing of newly formed dendritic spines. *Neuron* 70, 510–521. doi: 10.1016/j.neuron.2011.02.057

Behrens, T. E. J., and Sporns, O. (2012). Human connectomics. *Curr. Opin. Neurobiol.* 22, 144–153. doi: 10.1016/j.conb.2011.08.005

Betzig, E., Patterson, G. H., Sougrat, R., Lindwasser, O. W., Olenych, S., Bonifacino, J. S., et al. (2006). Imaging intracellular fluorescent proteins at nanometer resolution. *Science* 313, 1642–1645. doi: 10.1126/science.1127344

Blazquez-Llorca, L., Merchán-Pérez, A., Rodriguez, J. R., Gascón, J., and DeFelipe, J. (2013). FIB/SEM technology and Alzheimer's disease: three-deimensional analysis of human cortical synapses. *J. Alzheimers Dis.* 34, 995–1013. doi: 10.3233/JAD-122038

Bock, D. D., Lee, W.-C. A., Kerlin, A. M., Andermann, M. L., Hood, G., Wetzel, A. W., et al. (2011). Network anatomy and *in vivo* physiology of visual cortical neurons. *Nature* 471, 177–182. doi: 10.1038/nature09802

Bohland, J. W., Wu, C., Barbas, H., Bokil, H., Bota, M., Breiter, H. C., et al. (2009). A proposal for a coordinated effort for the determination of brainwide neuroanatomical connectivity in model organisms at a mesoscopic scale. *PLoS Comput. Biol.* 5:e1000334. doi: 10.1371/journal.pcbi.1000334

Boulland, J.-L., Qureshi, T., Seal, R. P., Rafiki, A., Gundersen, V., Bergersen, L. H., et al. (2004). Expression of the vesicular glutamate transporters during development indicates the widespread corelease of multiple neurotransmitters. *J. Comp. Neurol.* 480, 264–280. doi: 10.1002/cne.20354

Briggman, K. L., and Bock, D. D. (2012). Volume electron microscopy for neuronal circuit reconstruction. *Curr. Opin. Neurobiol.* 22, 154–161. doi: 10.1016/j.conb.2011.10.022

Briggman, K. L., Helmstaedter, M., and Denk, W. (2011). Wiring specificity in the direction-selectivity circuit of the retina. *Nature* 471, 183–188. doi: 10.1038/nature09818

Cai, D., Cohen, K. B., Luo, T., Lichtman, J. W., and Sanes, J. R. (2013). Improved tools for the Brainbow toolbox. *Nat. Methods* 10, 540–547. doi: 10.1038/nmeth.2450

Calabresi, P., Picconi, B., Parnetti, L., and Di Filippo, M. (2006). A convergent model for cognitive dysfunctions in Parkinson's disease: the critical dopamine-acetylcholine synaptic balance. *Lancet. Neurol.* 5, 974–983. doi: 10.1016/s1474-4422(06)70600-7

Catani, M., and Thiebaut de Schotten, M. (2008). A diffusion tensor imaging tractography atlas for virtual *in vivo* dissections. *Cortex* 44, 1105–1132. doi: 10.1016/j.cortex.2008.05.004

Chao, H.-T., Zoghbi, H. Y., and Rosenmund, C. (2007). MeCP2 controls excitatory synaptic strength by regulating glutamatergic synapse number. *Neuron* 56, 58–65. doi: 10.1016/j.neuron.2007.08.018

Chen, F., Tillberg, P. W., and Boyden, E. S. (2015). Optical imaging. Expansion microscopy. *Science* 347, 543–548. doi: 10.1126/science.1260088

Chklovskii, D. B., Mel, B. W., and Svoboda, K. (2004). Cortical rewiring and information storage. *Nature* 431, 782–788. doi: 10.1038/nature03012

Chung, K., and Deisseroth, K. (2013). CLARITY for mapping the nervous system. *Nat. Methods* 10, 508–513. doi: 10.1038/nmeth.2481

DeBello, W. M., McBride, T. J., Nichols, G. S., Pannoni, K. E., Sanculi, D., and Totten, D. J. (2014). Input clustering and the microscale structure of local circuits. *Front. Neural Circuits* 8:112. doi: 10.3389/fncir.2014.00112

DeFelipe, J., Marco, P., Busturia, I., and Merchán-Pérez, A. (1999). Estimation of the number of synapses in the cerebral cortex: methodological considerations. *Cereb. Cortex* 9, 722–732. doi: 10.1093/cercor/9.7.722

Druckmann, S., Feng, L., Lee, B., Yook, C., Zhao, T., Magee, J. C., et al. (2014). Structured synaptic connectivity between hippocampal regions. *Neuron* 81, 629–640. doi: 10.1016/j.neuron.2013.11.026

Dudek, F. E. (2009). Epileptogenesis: a new twist on the balance of excitation and inhibition. *Epilepsy Curr.* 9, 174–176. doi: 10.1111/j.1535-7511.2009.01334.x

Feinberg, E. H., Vanhoven, M. K., Bendesky, A., Wang, G., Fetter, R. D., Shen, K., et al. (2008). GFP Reconstitution Across Synaptic Partners (GRASP) defines cell contacts and synapses in living nervous systems. *Neuron* 57, 353–363. doi: 10.1016/j.neuron.2007.11.030

Feng, L., Kwon, O., Lee, B., Oh, W. C., and Kim, J. (2014). Using mammalian GFP reconstitution across synaptic partners (mGRASP) to map synaptic connectivity in the mouse brain. *Nat. Protoc.* 9, 2425–2437. doi: 10.1038/nprot.2014.166

Feng, L., Zhao, T., and Kim, J. (2012). Improved synapse detection for mGRASP-assisted brain connectivity mapping. *Bioinformatics* 28, i25–i31. doi: 10.1093/bioinformatics/bts221

Feng, L., Zhao, T., and Kim, J. (2015). neuTube 1.0: a new design for efficient neuron reconstruction software based on the SWC format. *eNeuro* 2, e0049-14.2014 1-0. doi: 10.1523/ENEURO.0049-14.2014

Fino, E., and Yuste, R. (2011). Dense inhibitory connectivity in neocortex. *Neuron* 69, 1188–1203. doi: 10.1016/j.neuron.2011.02.025

Fioravante, D., and Regehr, W. G. (2011). Short-term forms of presynaptic plasticity. *Curr. Opin. Neurobiol.* 21, 269–274. doi: 10.1016/j.conb.2011.02.003

Fortin, D. A., Tillo, S. E., Yang, G., Rah, J.-C., Melander, J. B., Bai, S., et al. (2014). Live imaging of endogenous PSD-95 using ENABLED: a conditional strategy to fluorescently label endogenous proteins. *J. Neurosci.* 34, 16698–16712. doi: 10.1523/JNEUROSCI.3888-14.2014

Fosque, B. F., Sun, Y., Dana, H., Yang, C.-T., Ohyama, T., Tadross, M. R., et al. (2015). Neural circuits. Labeling of active neural circuits *in vivo* with designed calcium integrators. *Science* 347, 755–760. doi: 10.1126/science.1260922

Fremeau, R. T., Kam, K., Qureshi, T., Johnson, J., Copenhagen, D. R., Storm-Mathisen, J., et al. (2004). Vesicular glutamate transporters 1 and 2 target to functionally distinct synaptic release sites. *Science* 304, 1815–1819. doi: 10.1126/science.1097468

Graziano, A., Liu, X.-B., Murray, K. D., and Jones, E. G. (2008). Vesicular glutamate transporters define two sets of glutamatergic afferents to the somatosensory thalamus and two thalamocortical projections in the mouse. *J. Comp. Neurol.* 507, 1258–1276. doi: 10.1002/cne.21592

Gustafsson, M. G. L. (2005). Nonlinear structured-illumination microscopy: wide-field fluorescence imaging with theoretically unlimited resolution. *Proc. Natl. Acad. Sci. U S A* 102, 13081–13086. doi: 10.1073/pnas.0406877102

Harnett, M. T., Xu, N.-L., Magee, J. C., and Williams, S. R. (2013). Potassium channels control the interaction between active dendritic integration compartments in layer 5 cortical pyramidal neurons. *Neuron* 79, 516–529. doi: 10.1016/j.neuron.2013.06.005

Hayworth, K. J., Morgan, J. L., Schalek, R., Berger, D. R., Hildebrand, D. G., and Lichtman, J. W. (2014). Imaging ATUM ultrathin section libraries with WaferMapper: a multi-scale approach to EM reconstruction of neural circuits. *Front. Neural Circuits* 8:68. doi: 10.3389/fncir.2014.00068

Hayworth, K. J., Xu, C. S., Lu, Z., Knott, G. W., Fetter, R. D., Tapia, J. C., et al. (2015). Ultrastructurally smooth thick partitioning and volume stitching for large-scale connectomics. *Nat. Methods* 12, 319–322. doi: 10.1038/nmeth.3292

Hill, D. N., Curtis, J. C., Moore, J. D., and Kleinfeld, D. (2011). Primary motor cortex reports efferent control of vibrissa motion on multiple timescales. *Neuron* 72, 344–356. doi: 10.1016/j.neuron.2011.09.020

Hooks, B. M., Hires, S. A., Zhang, Y.-X. X., Huber, D., Petreanu, L., Svoboda, K., et al. (2011). Laminar analysis of excitatory local circuits in vibrissal motor and sensory cortical areas. *PLoS Biol.* 9:e1000572. doi: 10.1371/journal.pbio.1000572

Hunnicutt, B. J., Long, B. R., Kusefoglu, D., Gertz, K. J., Zhong, H., and Mao, T. (2014). A comprehensive thalamocortical projection map at the mesoscopic level. *Nat. Neurosci.* 17, 1276–1285. doi: 10.1038/nn.3780

Johnston, D., and Narayanan, R. (2008). Active dendrites: colorful wings of the mysterious butterflies. *Trends Neurosci.* 31, 309–316. doi: 10.1016/j.tins.2008.03.004

Kato, S., Kobayashi, K., Inoue, K.-I., Kuramochi, M., Okada, T., Yaginuma, H., et al. (2011a). A lentiviral strategy for highly efficient retrograde gene transfer by pseudotyping with fusion envelope glycoprotein. *Hum. Gene. Ther.* 22, 197–206. doi: 10.1089/hum.2009.179

Kato, S., Kuramochi, M., Takasumi, K., Kobayashi, K., Inoue, K.-I., Takahara, D., et al. (2011b). Neuron-specific gene transfer through retrograde transport of lentiviral vector pseudotyped with a novel type of fusion envelope glycoprotein. *Hum. Gene. Ther.* 22, 1511–1523. doi: 10.1089/hum.2011.111

Ke, M.-T., Fujimoto, S., and Imai, T. (2013). SeeDB: a simple and morphology-preserving optical clearing agent for neuronal circuit reconstruction. *Nat. Neurosci.* 16, 1154–1161. doi: 10.1038/nn.3447

Kehrer, C., Maziashvili, N., Dugladze, T., and Gloveli, T. (2008). Altered excitatory-inhibitory balance in the NMDA-hypofunction model of schizophrenia. *Front. Mol. Neurosci.* 1:6. doi: 10.3389/neuro.02.006.2008

Kim, J., Jung, S.-C., Clemens, A. M., Petralia, R. S., and Hoffman, D. A. (2007). Regulation of dendritic excitability by activity-dependent trafficking of the A-type K+ channel subunit Kv4.2 in hippocampal neurons. *Neuron* 54, 933–947. doi: 10.1016/j.neuron.2007.05.026

Kim, J., Zhao, T., Petralia, R. S., Yu, Y., Peng, H., Myers, E., et al. (2011). mGRASP enables mapping mammalian synaptic connectivity with light microscopy. *Nat. Methods* 9, 96–102. doi: 10.1038/nmeth.1784

Klein, A., Andersson, J., Ardekani, B. A., Ashburner, J., Avants, B., Chiang, M.-C., et al. (2009). Evaluation of 14 nonlinear deformation algorithms applied to human brain MRI registration. *Neuroimage* 46, 786–802. doi: 10.1016/j.neuroimage.2008.12.037

Kleinfeld, D., Bharioke, A., Blinder, P., Bock, D. D., Briggman, K. L., Chklovskii, D. B., et al. (2011). Large-scale automated histology in the pursuit of connectomes. *J. Neurosci.* 31, 16125–16138. doi: 10.1523/JNEUROSCI.4077-11.2011

Knott, G., Marchman, H., Wall, D., and Lich, B. (2008). Serial section scanning electron microscopy of adult brain tissue using focused ion beam milling. *J. Neurosci.* 28, 2959–2964. doi: 10.1523/JNEUROSCI.3189-07.2008

Ko, H., Mrsic-Flogel, T. D., and Hofer, S. B. (2014). Emergence of feature-specific connectivity in cortical microcircuits in the absence of visual experience. *J. Neurosci.* 34, 9812–9816. doi: 10.1523/JNEUROSCI.0875-14.2014

Kreshuk, A., Straehle, C. N., Sommer, C., Koethe, U., Cantoni, M., Knott, G., et al. (2011). Automated detection and segmentation of synaptic contacts in nearly isotropic serial electron microscopy images. *PLoS One* 6:e24899. doi: 10.1371/journal.pone.0024899

Larkum, M. E., Senn, W., and Lüscher, H.-R. (2004). Top-down dendritic input increases the gain of layer 5 pyramidal neurons. *Cereb. Cortex* 14, 1059–1070. doi: 10.1093/cercor/bhh065

Larkum, M. E., Zhu, J. J., and Sakmann, B. (1999). A new cellular mechanism for coupling inputs arriving at different cortical layers. *Nature* 398, 338–341. doi: 10.1038/18686

Lavzin, M., Rapoport, S., Polsky, A., Garion, L., and Schiller, J. (2012). Nonlinear dendritic processing determines angular tuning of barrel cortex neurons *in vivo*. *Nature* 490, 397–401. doi: 10.1038/nature11451

Lei, W., Deng, Y., Liu, B., Mu, S., Guley, N. M., Wong, T., et al. (2013). Confocal laser scanning microscopy and ultrastructural study of VGLUT2 thalamic input to striatal projection neurons in rats. *J. Comp. Neurol.* 521, 1354–1377. doi: 10.1002/cne.23235

Livet, J., Weissman, T. A., Kang, H., Draft, R. W., Lu, J., Bennis, R. A., et al. (2007). Transgenic strategies for combinatorial expression of fluorescent proteins in the nervous system. *Nature* 450, 56–62. doi: 10.1038/nature06293

London, M., and Häusser, M. (2005). Dendritic computation. *Annu. Rev. Neurosci.* 28, 503–532. doi: 10.1146/annurev.neuro.28.061604.135703

Losonczy, A., and Magee, J. C. (2006). Integrative properties of radial oblique dendrites in hippocampal CA1 pyramidal neurons. *Neuron* 50, 291–307. doi: 10.1016/j.neuron.2006.03.016

Losonczy, A., Makara, J. K., and Magee, J. C. (2008). Compartmentalized dendritic plasticity and input feature storage in neurons. *Nature* 452, 436–441. doi: 10.1038/nature06725

Magee, J., Hoffman, D., Colbert, C., and Johnston, D. (1998). Electrical and calcium signaling in dendrites of hippocampal pyramidal neurons. *Annu. Rev. Physiol.* 60, 327–346. doi: 10.1146/annurev.physiol.60.1.327

Magee, J. C., and Johnston, D. (2005). Plasticity of dendritic function. *Curr. Opin. Neurobiol.* 15, 334–342. doi: 10.1016/j.conb.2005.05.013

Mao, T., Kusefoglu, D., Hooks, B., Huber, D., Petreanu, L., and Svoboda, K. (2011). Long-range neuronal circuits underlying the interaction between sensory and motor cortex. *Neuron* 72, 111–123. doi: 10.1016/j.neuron.2011.07.029

Merchán-Pérez, A., Rodriguez, J.-R., Alonso-Nanclares, L., Schertel, A., and DeFelipe, J. (2009). Counting synapses using FIB/SEM microscopy: a true revolution for ultrastructural volume reconstruction. *Front. Neuroanat.* 3:18. doi: 10.3389/neuro.05.018.2009

Merchán-Pérez, A., Rodriguez, J.-R., Gonzalez, A., Robles, V., DeFelipe, J., Larrañaga, P., et al. (2014). Three-dimensional spatial distribution of synapses in the neocortex: a dual-beam electron microscopy study. *Cereb. Cortex* 24, 1579–1588. doi: 10.1093/cercor/bht018

Micheva, K. D., Busse, B., Weiler, N. C., O'Rourke, N., and Smith, S. J. (2010). Single-synapse analysis of a diverse synapse population: proteomic imaging methods and markers. *Neuron* 68, 639–653. doi: 10.1016/j.neuron.2010.09.024

Micheva, K. D., and Smith, S. J. (2007). Array tomography: a new tool for imaging the molecular architecture and ultrastructure of neural circuits. *Neuron* 55, 25–36. doi: 10.1016/j.neuron.2007.06.014

Mishchenko, Y. (2010). On optical detection of densely labeled synapses in neuropil and mapping connectivity with combinatorially multiplexed fluorescent synaptic markers. *PLoS One* 5:e8853. doi: 10.1371/journal.pone.0008853

Mitra, P. P. (2014). The circuit architecture of whole brains at the mesoscopic scale. *Neuron* 83, 1273–1283. doi: 10.1016/j.neuron.2014.08.055

Moechars, D., Weston, M. C., Leo, S., Callaerts-Vegh, Z., Goris, I., Daneels, G., et al. (2006). Vesicular glutamate transporter VGLUT2 expression levels control quantal size and neuropathic pain. *J. Neurosci.* 26, 12055–12066. doi: 10.1523/jneurosci.2556-06.2006

Morgan, J. L., and Lichtman, J. W. (2013). Why not connectomics? *Nat. Methods* 10, 494–500. doi: 10.1038/nmeth.2480

Nanguneri, S., Flottmann, B., Horstmann, H., Heilemann, M., and Kuner, T. (2012). Three-dimensional, tomographic super-resolution fluorescence imaging of serially sectioned thick samples. *PLoS One* 7:e38098. doi: 10.1371/journal.pone.0038098

Oh, S. W., Harris, J. A., Ng, L., Winslow, B., Cain, N., Mihalas, S., et al. (2014). A mesoscale connectome of the mouse brain. *Nature* 508, 207–214. doi: 10.1038/nature13186

Oheim, M., van't Hoff, M., Feltz, A., Zamaleeva, A., Mallet, J.-M., and Collot, M. (2014). New red-fluorescent calcium indicators for optogenetics, photoactivation and multi-color imaging. *Biochim. Biophys. Acta* 1843, 2284–2306. doi: 10.1016/j.bbamcr.2014.03.010

Ou, Y., Akbari, H., Bilello, M., Da, X., and Davatzikos, C. (2014). Comparative evaluation of registration algorithms in different brain databases with varying difficulty: results and insights. *IEEE Trans. Med. Imaging* 33, 2039–2065. doi: 10.1109/TMI.2014.2330355

Petreanu, L., Huber, D., Sobczyk, A., and Svoboda, K. (2007). Channelrhodopsin-2-assisted circuit mapping of long-range callosal projections. *Nat. Neurosci.* 10, 663–668. doi: 10.1038/nn1891

Petreanu, L., Mao, T., Sternson, S., and Svoboda, K. (2009). The subcellular organization of neocortical excitatory connections. *Nature* 457, 1142–1145. doi: 10.1038/nature07709

Pfeiffer, B. E., and Huber, K. M. (2009). The state of synapses in fragile X syndrome. *Neuroscientist* 15, 549–567. doi: 10.1177/1073858409333075

Poirazi, P., Brannon, T., and Mel, B. W. (2003). Pyramidal neuron as two-layer neural network. *Neuron* 37, 989–999. doi: 10.1016/s0896-6273(03)00149-1

Poirazi, P., and Mel, B. W. (2001). Impact of active dendrites and structural plasticity on the memory capacity of neural tissue. *Neuron* 29, 779–796. doi: 10.1016/s0896-6273(01)00252-5

Pollak Dorocic, I., Fürth, D., Xuan, Y., Johansson, Y., Pozzi, L., Silberberg, G., et al. (2014). A whole-brain atlas of inputsto serotonergic neuronsof the dorsal and median raphe nuclei. *Neuron* 83, 663–678. doi: 10.1016/j.neuron.2014.07.002

Punge, A., Rizzoli, S. O., Jahn, R., Wildanger, J. D., Meyer, L., Schönle, A., et al. (2008). 3D reconstruction of high-resolution STED microscope images. *Microsc. Res. Tech.* 71, 644–650. doi: 10.1002/jemt.20602

Ragan, T., Kadiri, L. R., Venkataraju, K. U., Bahlmann, K., Sutin, J., Taranda, J., et al. (2012). Serial two-photon tomography for automated ex vivo mouse brain imaging. *Nat. Methods* 9, 255–258. doi: 10.1038/nmeth.1854

Rah, J.-C., Bas, E., Colonell, J., Mishchenko, Y., Karsh, B., Fetter, R. D., et al. (2013). Thalamocortical input onto layer 5 pyramidal neurons measured using quantitative large-scale array tomography. *Front. Neural Circuits* 7:177. doi: 10.3389/fncir.2013.00177

Remy, S., Csicsvari, J., and Beck, H. (2009). Activity-dependent control of neuronal output by local and global dendritic spike attenuation. *Neuron* 61, 906–916. doi: 10.1016/j.neuron.2009.01.032

Renier, N., Wu, Z., Simon, D. J., Yang, J., Ariel, P., and Tessier-Lavigne, M. (2014). iDISCO: a simple, rapid methodto immunolabel large tissue samples for volume imaging. *Cell* 159, 896–910. doi: 10.1016/j.cell.2014.10.010

Rust, M. J., Bates, M., and Zhuang, X. (2006). Sub-diffraction-limit imaging by stochastic optical reconstruction microscopy (STORM). *Nat. Methods* 3, 793–795. doi: 10.1038/nmeth929

Schüz, A., and Palm, G. (1989). Density of neurons and synapses in the cerebral cortex of the mouse. *J. Comp. Neurol.* 286, 442–455. doi: 10.1002/cne.902860404

Selkoe, D. J. (2002). Alzheimer's disease is a synaptic failure. *Science* 298, 789–791. doi: 10.1126/science.1074069

Seung, H. S., and Sümbül, U. (2014). Neuronal cell types and connectivity: lessons from the retina. *Neuron* 83, 1262–1272. doi: 10.1016/j.neuron.2014.08.054

Shepherd, G. M., Stepanyants, A., Bureau, I., Chklovskii, D., and Svoboda, K. (2005). Geometric and functional organization of cortical circuits. *Nat. Neurosci.* 8, 782–790. doi: 10.1038/nn1447

Shepherd, G. M., and Svoboda, K. (2005). Laminar and columnar organization of ascending excitatory projections to layer 2/3 pyramidal neurons in rat barrel cortex. *J. Neurosci.* 25, 5670–5679. doi: 10.1523/jneurosci.1173-05.2005

Sjöström, P. J., Rancz, E. A., Roth, A., and Häusser, M. (2008). Dendritic excitability and synaptic plasticity. *Physiol. Rev.* 88, 769–840. doi: 10.1152/physrev.00016.2007

Sporns, O., Tononi, G., and Kötter, R. (2005). The human connectome: a structural description of the human brain. *PLoS Comput. Biol.* 1:e42. doi: 10.1371/journal.pcbi.0010042

Stephan, K. E., Baldeweg, T., and Friston, K. J. (2006). Synaptic plasticity and dysconnection in schizophrenia. *Biol. Psychiatry* 59, 929–939. doi: 10.1016/j.biopsych.2005.10.005

Susaki, E. A., Tainaka, K., Perrin, D., Kishino, F., Tawara, T., Watanabe, T. M., et al. (2014). Whole-brain imaging with single-cell resolution using chemical cocktails and computational analysis. *Cell* 157, 726–739. doi: 10.1016/j.cell.2014.03.042

Wehr, M., and Zador, A. M. (2003). Balanced inhibition underlies tuning and sharpens spike timing in auditory cortex. *Nature* 426, 442–446. doi: 10.1038/nature02116

Weston, M. C., Nehring, R. B., Wojcik, S. M., and Rosenmund, C. (2011). Interplay between VGLUT isoforms and endophilin A1 regulates neurotransmitter release and short-term plasticity. *Neuron* 69, 1147–1159. doi: 10.1016/j.neuron.2011.02.002

Wickersham, I. R., and Feinberg, E. H. (2012). New technologies for imaging synaptic partners. *Curr. Opin. Neurobiol.* 22, 121–127. doi: 10.1016/j.conb.2011.12.001

Wickersham, I. R., Lyon, D. C., Barnard, R. J. O., Mori, T., Finke, S., Conzelmann, K.-K., et al. (2007). Monosynaptic restriction of transsynaptic tracing from single, genetically targeted neurons. *Neuron* 53, 639–647. doi: 10.1016/j.neuron.2007.01.033

Willig, K. I., Rizzoli, S. O., Westphal, V., Jahn, R., and Hell, S. W. (2006). STED microscopy reveals that synaptotagmin remains clustered after synaptic vesicle exocytosis. *Nature* 440, 935–939. doi: 10.1038/nature04592

Wojcik, S. M., Rhee, J. S., Herzog, E., Sigler, A., Jahn, R., Takamori, S., et al. (2004). An essential role for vesicular glutamate transporter 1 (VGLUT1) in postnatal development and control of quantal size. *Proc. Natl. Acad. Sci. U S A* 101, 7158–7163. doi: 10.1073/pnas.0401764101

Xu, N.-L., Harnett, M. T., Williams, S. R., Huber, D., O'Connor, D. H., Svoboda, K., et al. (2012). Nonlinear dendritic integration of sensory and motor input during an active sensing task. *Nature* 492, 247–251. doi: 10.1038/nature11601

Xue, M., Atallah, B. V., and Scanziani, M. (2014). Equalizing excitation-inhibition ratios across visual cortical neurons. *Nature* 511, 596–600. doi: 10.1038/nature13321

Yasuda, R., Harvey, C. D., Zhong, H., Sobczyk, A., van Aelst, L., and Svoboda, K. (2006). Supersensitive Ras activation in dendrites and spines revealed by two-photon fluorescence lifetime imaging. *Nat. Neurosci.* 9, 283–291. doi: 10.1038/nn1635

Yook, C., Druckmann, S., and Kim, J. (2013). Mapping mammalian synaptic connectivity. *Cell. Mol. Life Sci.* 70, 4747–4757. doi: 10.1007/s00018-013-1417-y

Yoshimura, Y., and Callaway, E. (2005). Fine-scale specificity of cortical networks depends on inhibitory cell type and connectivity. *Nat. Neurosci.* 8, 1552–1559. doi: 10.1038/nn1565

Yoshimura, Y., Dantzker, J. L., and Callaway, E. M. (2005). Excitatory cortical neurons form fine-scale functional networks. *Nature* 433, 868–873. doi: 10.1038/nature03252

Zingg, B., Hintiryan, H., Gou, L., Song, M. Y., Bay, M., Bienkowski, M. S., et al. (2014). Neural networks of the mouse neocortex. *Cell* 156, 1096–1111. doi: 10.1016/j.cell.2014.02.023

Conflict of Interest Statement: The authors declare that the research was conducted in the absence of any commercial or financial relationships that could be construed as a potential conflict of interest.

frontiers in Neuroanatomy

ORIGINAL RESEARCH
published: 27 May 2015
doi: 10.3389/fnana.2015.00068

Quantitative neuroanatomy of all Purkinje cells with light sheet microscopy and high-throughput image analysis

Ludovico Silvestri[1,2†], Marco Paciscopi[3†], Paolo Soda[4], Filippo Biamonte[5], Giulio Iannello[4], Paolo Frasconi[2] and Francesco S. Pavone[1,2,6,7]*

[1] National Institute of Optics, National Research Council, Sesto Fiorentino, Italy, [2] European Laboratory for Non-Linear Spectroscopy, Sesto Fiorentino, Italy, [3] Department of Information Engineering, University of Florence, Florence, Italy, [4] Department of Engineering, University Campus Bio-Medico of Rome, Rome, Italy, [5] Institute of Histology and Embryology, Catholic University of the Sacred Heart "A. Gemelli", Rome, Italy, [6] Department of Physics and Astronomy, University of Florence, Sesto Fiorentino, Italy, [7] International Center for Computational Neurophotonics, Sesto Fiorentino, Italy

Characterizing the cytoarchitecture of mammalian central nervous system on a brain-wide scale is becoming a compelling need in neuroscience. For example, realistic modeling of brain activity requires the definition of quantitative features of large neuronal populations in the whole brain. Quantitative anatomical maps will also be crucial to classify the cytoarchtitectonic abnormalities associated with neuronal pathologies in a high reproducible and reliable manner. In this paper, we apply recent advances in optical microscopy and image analysis to characterize the spatial distribution of Purkinje cells (PCs) across the whole cerebellum. Light sheet microscopy was used to image with micron-scale resolution a fixed and cleared cerebellum of an L7-GFP transgenic mouse, in which all PCs are fluorescently labeled. A fast and scalable algorithm for fully automated cell identification was applied on the image to extract the position of all the fluorescent PCs. This vectorized representation of the cell population allows a thorough characterization of the complex three-dimensional distribution of the neurons, highlighting the presence of gaps inside the lamellar organization of PCs, whose density is believed to play a significant role in autism spectrum disorders. Furthermore, clustering analysis of the localized somata permits dividing the whole cerebellum in groups of PCs with high spatial correlation, suggesting new possibilities of anatomical partition. The quantitative approach presented here can be extended to study the distribution of different types of cell in many brain regions and across the whole encephalon, providing a robust base for building realistic computational models of the brain, and for unbiased morphological tissue screening in presence of pathologies and/or drug treatments.

Keywords: quantitative neuroanatomy, Purkinje cells, cerebellum, light sheet microscopy, image analysis, brain imaging

OPEN ACCESS

Edited by:
Kathleen S. Rockland, Boston University School of Medicine, USA

Reviewed by:
José A. Armengol, Universidad Pablo de Olavide, Spain
Yugo Fukazawa, University of Fukui, Japan

***Correspondence:**
Ludovico Silvestri, European Laboratory for Non-Linear Spectroscopy, National Institute of Optics, National Research Council, Via Nello Carrara 1, Sesto Fiorentino 50019, Italy
silvestri@lens.unifi.it

† These authors have contributed equally to this work.

Received: *09 March 2015*
Accepted: *11 May 2015*
Published: *27 May 2015*

Citation:
Silvestri L, Paciscopi M, Soda P, Biamonte F, Iannello G, Frasconi P and Pavone FS (2015) Quantitative neuroanatomy of all Purkinje cells with light sheet microscopy and high-throughput image analysis. Front. Neuroanat. 9:68. doi: 10.3389/fnana.2015.00068

Introduction

Since the times of Golgi and Ramòn y Cajal, technological advances always played a crucial role in helping neuroanatomists to disentangle the complex architecture of the mammalian brain. Indeed,

methodological innovations always brought, sooner or later, to deep biological insights, and to novel paradigms of neuroanatomical investigation. The development and refinement of imaging techniques, like electron microscopy (Gray, 1969), fluorescence optical microscopy (Lichtman and Conchello, 2005) and magnetic resonance imaging (Duyn and Koretsky, 2008), allowed studying brain organization on different scales and resolutions, leading to the definition and the study of different anatomical structures, ranging from single synapses (Palay, 1956) to entire neurons (Meinertzhagen et al., 2009), from cortical columns (Rockland, 2010) to long-range fiber tracts (Tench et al., 2002).

Imaging technology has thus played a crucial role in the development of contemporary neuroscience; anyway, its limitations can somehow distort the great picture of the brain we are painting, providing us with partly biased representations of the central nervous system. One traditional limitation in neuroanatomical reconstructions is the relatively small throughput: the imaged volume decreases as the resolution increases. Thus, for instance, dendritic morphology is usually investigated on the level of few neurons, while cell spatial distribution is analyzed within single cortical columns (or structures of similar size). The loss of resolution when zooming out to large volumes hides to the researcher any possible long-range correlation in the fine details of neuronal organization. Furthermore, since high-resolution studies are limited to small areas, one has usually to select the region of interest in advance, usually based on previous literature, at the risk of neglecting unexpected neuroanatomical features in other parts of the brain. This exposes the analysis and thus the conclusions drawn upon it to potential bias.

Recent advances in imaging technology can help contemporary neuroanatomists to afford a more comprehensive view of the brain cytoarchitecture. Indeed, nowadays there is a clear trend toward high-throughput microscopy methodologies (both optical and electronic), as larger and larger portion of tissue can be imaged with higher and higher resolution (Briggman and Denk, 2006; Osten and Margrie, 2013). On the one hand, focused-ion-beam milling serial electron microscopy (Knott et al., 2008) and multiple-beam scanning electron microscopy (Keller et al., 2014) allows reconstructing small brain regions with nanometric resolution, providing useful data for the reconstruction of local connections. On the other hand, light sheet microscopy (LSM; Dodt et al., 2007; Silvestri et al., 2012), coupled with chemical clearing of the tissue (Becker et al., 2012; Chung et al., 2013; Tomer et al., 2014) can be used to image entire murine brains with micrometric resolution without the need for physical sectioning. Optical methods based on serial sectioning (Li et al., 2010; Ragan et al., 2012; Gong et al., 2013) can as well-provide whole-brain μm-resolution images, although at the cost of destroying the sample.

Anyhow, the impact of all these technical improvements on XXIst century neuroanatomy has been very limited hitherto. In fact, the amount of data produced by novel, high-throughput imaging methods easily falls in the TeraByte range or beyond, moving the throughput bottleneck from data production to data analysis. Large-scale projects have benefit from the massive contribution of human supervision in manual or semi-manual data segmentation tool, either hiring dozens of students (Briggman et al., 2011) or leaning on crowd contributions via an interactive videogame (Kim et al., 2014). Nevertheless, such brute-force approaches are out of the reach for most laboratories worldwide, which have to cope with limited human and financial resources. Automatic methods for management of large images, for their visualization and annotation, and for cell soma localization, have been recently described (Peng et al., 2010, 2014; Bria and Iannello, 2012; Frasconi et al., 2014). Since these automatic methods are conceived to minimize the computational resources needed (most of them can run even on high-end workstations), they offer the possibility for neuroanatomists to finally solve the data bottleneck and reach a real output from high-throughput imaging methodologies.

Here, we present a complete experimental pipeline, integrating recent innovations in the fields of imaging technology and computer science, to extract quantitative information about the three-dimensional distribution of a selected neuronal population. The approach we describe, summarized in **Figure 1**, encompasses specimen clearing with organic solvents, imaging with confocal LSM, image stitching and automatic soma detection, and eventually allows localizing each individual fluorescent neuronal soma across a large brain region. We demonstrate this pipeline by reconstructing the full neuroanatomy of the Purkinje cells (PCs) layer which are known to be the most important inhibitory neurons that carry the only output of the cerebellar cortex. To this aim, we imaged the whole cerebellum of a B6C3Fe-L7-EGFP (L7-GFP) mouse (Oberdick et al., 1990). Starting from the point cloud representing the position of single PCs, we are able to clusterize the PCs in groups based on their representation in the 3D space, which might delineate some significant neuroanatomical parcellation and reveal isolated neurons. Finally, by locally unwrapping the two-dimensional lamellar structure of the Purkinje layer, we can locate empty spaces within the layer, known as gaps. Such gaps are thought to play a significant role in autism spectrum disorders (McKimm

FIGURE 1 | Experimental pipeline for large-volumes quantitative neuroanatomy. After animal fixation, the brain is render transparent and imaged with high-throughput light sheet microscopy. Raw image stacks are then stitched together, and a software for automatic cell localization applied. The resulting cloud of points representing the position of labeled cells can be the starting point for many different quantitative neuroanatomical analysis.

et al., 2014). With the high-output comprehensive approach described here, we are able to draw a map of Purkinje gaps in the whole cerebellum and highlight their spatial organization, which would be hardly accessible with conventional techniques.

Materials and Methods

Sample Preparation

The whole cerebellum from a young male L7-GFP mouse was cleared following a protocol based on the one reported by Dodt et al. (2007). A post-natal day (PND) 10 mouse was deeply anesthetized by hypothermia and intraperitoneal injection of tribromoethanol (220 mg/kg), and transcardially perfused with 0.1 M PBS (pH 7.4) followed by 4% paraformaldehyde (PFA) in 0.1 M PBS for fixation. The brain was then removed from the skull, post-fixed in 4% PFA overnight at 4°C and stored in PBS at 4°C. Afterward, the cerebellum was dissected out and embedded in a 0.5% (w/w) low melting point agarose gel, prepared in 10 mM sodium borate buffer (pH 8). The embedded sample was dehydrated in a graded ethanol series (30, 50, 80, 96% 2 h each, 100% overnight). The ethanol was diluted in sodium borate buffer to avoid considerable pH variations that would possibly decrease EGFP fluorescence. After dehydration, we incubated the specimens in freshly prepared clearing solution (Benzyl Alcohol/Benzyl Benzoate 1:2, BABB) for ∼36 h. All dehydration/clearing steps were performed at room temperature (18–22°C). The dehydration and clearing procedure led to a linear shrinkage of the tissue of about 25% (Silvestri et al., 2014), so the volume is reduced to about 42% of its original size.

All experimental protocols involving animals were designed in accordance with the regulations of the Italian Ministry of Health.

Confocal Light Sheet Microscopy

In LSM, the sample is illuminated with a thin sheet of light, confining fluorescence excitation in the focal plane of detection optics (Keller and Dodt, 2012). In this way, optical sectioning (i.e., 3-dimensional resolution) is afforded in a wide-field detection scheme, where millions of pixels are collected simultaneously by a camera instead of sequentially as in point-scanning techniques (as standard confocal or two-photon microscopy). This high imaging throughput with high 3-dimensional resolution makes LSM an ideal technique to reconstruct the anatomy of large specimens, as murine brains.

The custom made confocal LSM used here has been described in detail in Silvestri et al. (2012). Briefly, planar illumination is achieved by fast scanning of a line inside the specimen (Keller et al., 2008), and a de-scanning system in the detection path is used to create a fixed image of the scanning excitation line. At the position of this fixed image a linear spatial filter (slit) is used to block out-of-focus and scattered light. This confocal line detection affords a contrast enhancement of 100% in cleared specimens (Silvestri et al., 2012). A third scanning system re-creates a 2-dimensional image onto the chip of an electron-multiplying charge-coupled device (EM-CCD), which collects the photons producing a digital image. The objective used to collect the data analyzed here was a Nikon Plan SLWD 20× (NA 0.35), with long working distance (24 mm) and designed to work in air; slit width was set to 1 μm (in object space). During imaging, the specimen was kept immersed in clearing solution inside a custom chamber. The chamber was mounted on a XYZθ stage, assembled using three linear stages and a rotation one (M-122.2DD and M-116.DG, Physik Instrumente, Germany).

To collect a full optical tomography of the cerebellum, many parallel adjacent image stacks were acquired to cover the entire volume. A partial overlap of about 10% of the field of view was introduced to allow subsequent stitching of image tiles (see below). A custom-made software written in LabVIEW (National Instruments, Austin, TX, USA) orchestrated all the hardware components of the microscope to perform automated imaging of the volume.

Image Stitching

To stitch the tiled raw image, the TeraStitcher tool (Bria and Iannello, 2012) has been used. TeraStitcher is a free and fully automated 3D stitching tool specifically designed to match the special requirements coming out of teravoxel-sized tiled microscopy images. It is able to stitch such images in a reasonable time even on machines with limited resources. It can be freely downloaded from https://github.com/abria/TeraStitcher.

TeraStitcher consists of a pipeline of six stages. After the import stage, in which the raw data are scanned to reconstruct the nominal position of every tile in the instrument space, the alignment between every pair of adjacent tile is computed. The alignment stage is based on the MIP-NCC algorithm, i.e., an alignment strategy based on using 2D Normalized Cross-Correlation on Maximum Intensity Projections in each direction of the two volumes to be aligned. MIP-NCC is applied to multiple homologous sub-stacks of any pair of adjacent tiles, so as multiple alignments for each tiles pair are computed. An index measuring the reliability of each alignment is also computed and used in the third stage to select the most reliable alignment for each tiles pair. In the fourth stage, alignments between tiles pairs with reliability below a given threshold are discarded. Indeed, these alignments should not affect final image stitching, since they correspond with high probability to adjacent tiles that share only empty sub-volumes. In the fifth stage, the remaining reliable and possible redundant alignments are given as an input to an optimization algorithm that uses alignment reliabilities to find the tile positions that minimizes the global alignment error. Finally, in the last stage, according to the output alignments of the fifth stage, overlapping tiles are merged, and the final stitched image generated.

It is worth noting that the above strategy is computationally cheap, greatly limits memory occupancy, and requires only two reads and one write of the whole image data. The size of the raw data corresponding to the whole mouse cerebellum was 198,78 Gbytes. On a workstation with 96 GB of RAM, 9 TB of disk space, 2 quad-core CPUs at 2.26 GHz, TeraStitcher took 771 min to stitch the whole volume, 539 of which spent in I/O operations. The peak memory occupancy was only 1.13 Gbyte.

Automatic Cell Localization

We proceed in separate stages to identify the 3D coordinates all Purkinje somata in the cerebellum image. The method is detailed in Frasconi et al. (2014) and briefly summarized here. Since the image is large (1.2×10^{11} voxels), it is not practical to process it as a whole. We therefore split it into 9000 overlapping substacks of size $280 \times 282 \times 246$. This approach has other advantages, including the ability to exploit data parallelism in a computer cluster.

The first stage of the identification pipeline is called *semantic deconvolution* and aims at addressing the high variability in quality and contrast found in confocal LSM images. Semantic deconvolution is performed by training a deep neural network to clean-up small ($13 \times 13 \times 13$ voxels) image patches so that cell somata ideally appear as small white spheres in a black background. The neural network has an input layer of 2197 units, two hidden layers of 500 and 200 sigmoidal units, respectively, and a linear output layer of 2197 units that are supervised with a clean version of the input image patch. The network is run in a convolutional fashion throughout whole substacks, using a stride of 4 voxels.

Such an approach allows us to obtain a significant speedup over the naive approach where a network with a single output was trained to predict the conditional probability that the central voxel of the patch belongs to a cell soma. Processing the whole cerebellum image takes about 2 days on a small cluster with 32 Xeon cores (compared to an estimated 2 months running time for the naive approach). The effect of semantic deconvolution is illustrated in **Figure 2**.

The second stage identifies somata coordinates using a variant of the mean shift algorithm (Comaniciu and Meer, 2002) a non-parametric clustering algorithm that takes as input a data set of points L (described in our case by their 3D coordinates x, y, z, and the corresponding gray-level intensity), and a set of seed points S. It partitions L into k subsets, each representing the voxels in a given soma. More precisely, L contains all foreground voxels in a given substack, where the foreground threshold t is determined by a two-levels maximum entropy algorithm (Sahoo et al., 1988). A voxel is included in the seed set S if the following two conditions hold true simultaneously: (1) the voxel is a local maximum in the 3D image, and (2) the average intensity in a sphere of radius r around the voxels is above the foreground threshold t. Subsequently, for each seed s in S, the mean shift algorithm iterates the following two steps until convergence: (1) place a spherical kernel or radius R around s and compute the center of mass of the points falling within the kernel (using voxel intensities as the "masses"); (2) replace s by the center of mass. Overall, the two parameters controlling the algorithm behavior are the radius r of the seed ball and the radius R of the mean shift kernel. Both are interpretable in terms of geometrical properties of the image contents and, in facts, best results tend to be obtained when r and R are set to values close to the expected Purkinje radius (6 voxels at the micron image resolution used in this study). Note, however, that smaller values of r favor higher recall[1] (at the expense of precision).

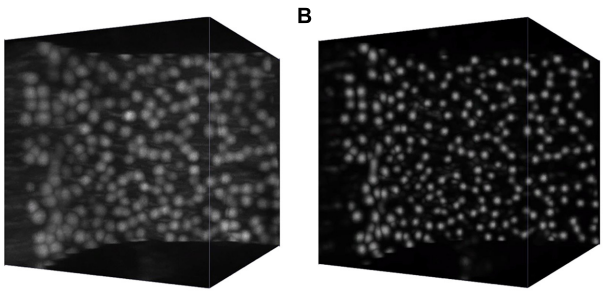

FIGURE 2 | Semantic deconvolution. A small volume from the cerebellum of an L7-GFP mouse before **(A)** and after **(B)** semantic deconvolution. On the final image is much easier to run a reliable automatic localization algorithm.

The third stage aims at further reducing the false positive rate by exploiting domain knowledge about the cerebellum cytoarchitecture. In particular, the cerebellum cortex folds into folia that can be modeled as two-dimensional manifolds. As it turns out, most of the false positives detected by mean shift actually correspond to fragments of axon bundles or various other fragments of neurites where GFP was expressed. Since these false detections are very often found far away from the Purkinje layer the precision can be significantly improved by estimating the distance between any predicted soma center and the manifold formed by the nearby predicted centers. For this purpose, we used a combination of manifold learning (via the Isomap algorithm Tenenbaum et al., 2000) and locally weighted regression (Cleveland and Devlin, 1988). Significant improvements can be obtained by discarding all predictions whose estimated manifold distance exceed a certain threshold.

The software for automatic cell localization, and the results shown in this paper, can be downloaded from http://bcfind.dinfo.unifi.it/. Developers can found extensive documentation on the same website.

Cell Clustering

The algorithm used to compute the clusters of connected somas from the cell cloud uses the notion of k-nearest neighbors (kNNs; Cover and Hart, 1967) and it works as follows. Given two cells c_i and c_j we introduce the relation:

$$c_i \overset{k}{\longleftrightarrow} c_j$$

If $c_i \in kNN(c_j) \wedge c_j \in kNN(c_i)$, the connected clusters are the equivalence classes of the transitive closure of relation $\overset{k}{\longleftrightarrow}$.

In practice, for each cell c_i (with $i = 1, 2, \ldots, m$) of the cloud, the algorithm searches its kNNs somas that are collected in the set $s_i = \{c_j^{(i)}\}$, with $j = 0, 1, \ldots, p$ and $p \leq k$. Next, the algorithm runs again a kNNs search for each element of s_i in order to determine if $c_j^{(i)}$ is a neighbor of c_i. If this is the case, the somas c_i and $c_j^{(i)}$ are correlated and assigned to the same cluster n_n. Now, the

[1]Recall, precision and F_1 measure are standard performance measures in information retrieval. Recall (R) is defined as $\frac{TP}{TP+FN}$, Precision (P) is defined as $\frac{TP}{TP+FP}$, and $F_1 = \frac{2PR}{P+R}$. TP means True Positives, FP False Positives, FN False Negatives.

aforementioned operations are repeated for all cells assigned to n_n, i.e., the algorithm tries to expand the net n_n looking for new connections. The growing phase of the cluster n_n ends when the kNNs search return an empty set or a set which members are all already in n_n, and the algorithm picks a new cell c_i (which does not belong to any n_n estimated so far) from the cloud and executes again all the previous computations. Note that, when a cell c_i does not belong to any cluster, i.e., it is not in the set s_i of any of its kNNs, c_i is said to be an *isolated* cell.

The result of this algorithm is a list of clusters composed of somas that are mutually kNN-connected in the space and a list of isolated cells. In general, k is chosen to be a small integer. Indeed, small values of k fragment the cloud of somas in relatively small clusters. Conversely, due to the observed spatial distribution of PCs, the higher the value of k, the larger the number of cells assigned to the same cluster. Note also that clustering with higher k values is less sensitive to possible errors in cell localization. Multiple analysis with different values of k may highlight the presence of clearly defined and stable neuronal clusters, which might have a direct neuroanatomical significance.

The software used for cell clustering can be downloaded from https://bitbucket.org/paolosoda/manifold-cluster-cell. Developers can found extensive documentation on the same website.

Gap Localization

We employed a semi-automatic approach to identify regions in the Purkinje layer where the spatial distribution of cell somata shows rarefactions. We started from the set of automatically detected soma centers as described above, but omitting the last processing stage to avoid as many false negatives as possible. Furthermore, we set the r parameter in the above procedure to 3 in order to achieve a recall as high as 0.98 measured on the 56 ground truth substacks. The point cloud was split into 15 overlapping slices with cuts perpendicular to the sagittal plane (each slice was about 2000 voxels high, with an overlap of 120 voxels). Each slice was manually cleaned up using the CloudCompare software[2]. In particular we removed obvious false positives (i.e., somata excessively delaminated with respect to the Purkinje layer), resulting in a set of 221107 soma centers for the whole cerebellum. Finally, from all the slices, we manually cut a total of 89 charts containing between 292 and 6023 soma centers each. We cut each slice along regions of minimal curvature and keeping a reasonable overlap between adjacent charts to prevent border effects in the subsequent analysis. **Figure 3** shows some examples of the extracted charts, each corresponding to a portion of the PC layer.

Each chart was then automatically analyzed to identify the presence of gaps in the cell layout. We define gaps as large convex areas in the layer containing no cells. Finding holes or void regions in point clouds has been investigated in various forms in the literature. For example (Boyce et al., 1985) studied the problems of finding maximum perimeter and maximum area convex k-gons for given k. Unlike those previous studies, here we formally define the problem as follows: given a point in the surface described by the cell layer, we want to determine the largest surface portion containing that point and no cells. As a first step, our algorithm uses Isomap to embed 3D coordinates *(x, y, z)* of soma centers into the 2D space, with coordinates *(u, v)*, corresponding to the manifold describing a Purkinje layer folium. We subsequently seek convex polygons of maximal area in the 2D space. For this purpose, we first compute a Delaunay triangulation of the set of soma centers in the 2D space. Since the triangulation can produce artifacts, i.e., very large triangles connecting distant points, we delete them with an iterative approach, discarding at each iteration boundary triangles with perimeter above a threshold. For every triangle in the triangulation, we finally grow a region by adding adjacent triangles if the polygon resulting from an addition remains convex. Clearly, the convex regions created in this way do not contain any cell in their interiors. At the end, the algorithm returns, for every triangle, the area of the convex region grown around it. The steps described in this paragraph are illustrated in **Figure 4**.

The software used for gap localization can be downloaded from https://bitbucket.org/marco_paciscopi/manifold-find-holes. Developers can found extensive documentation on the same website.

Image Visualization and Further Analysis

3D volume renderings of the original microscopy images were obtained with VAA3D[3]; meshes representing the layer folia were visualized with MeshLab[4], while point clouds representing PCs were visualized using CloudCompare. Statistical analysis of the distribution of inter-cellular areas was performed using Matlab R2014b (MathWorks Inc., USA).

Results

All the results shown below, as well as the raw image data, are available for download at https://dataverse.harvard.edu/dataverse/mouse_cerebellum.

Clustering of Purkinje Cells

The refined version of the point cloud obtained with additional manual removal of false positives was processed according to the clustering algorithm discussed above (**Figure 5**). Setting the number k of nearest neighbors equal to 3, we found that most identified PCs (207190 out of 221107, almost 94%) cluster in a big class spanning the whole cerebellum, with the exclusion of the two side lobes (**Figure 5B**). The rest of the neurons, with the exception of two bigger clusters located in the lobes, is divided in small groups (**Figures 5C,D**). 1131 clusters are made by less than 100 cells, and 1389 isolated neurons are found. Smaller clusters and isolated cells seem to be distributed almost uniformly across the whole sample, although preferentially on the external regions of the cerebellum. If bigger values of k are used, the

[2]http://www.danielgm.net/cc/, Open Source Project managed by Daniel Girardeau-Monteaut.

[3]http://home.penglab.com/proj/vaa3d/Vaa3D/About_Vaa3D.html

[4]http://meshlab.sourceforge.net/

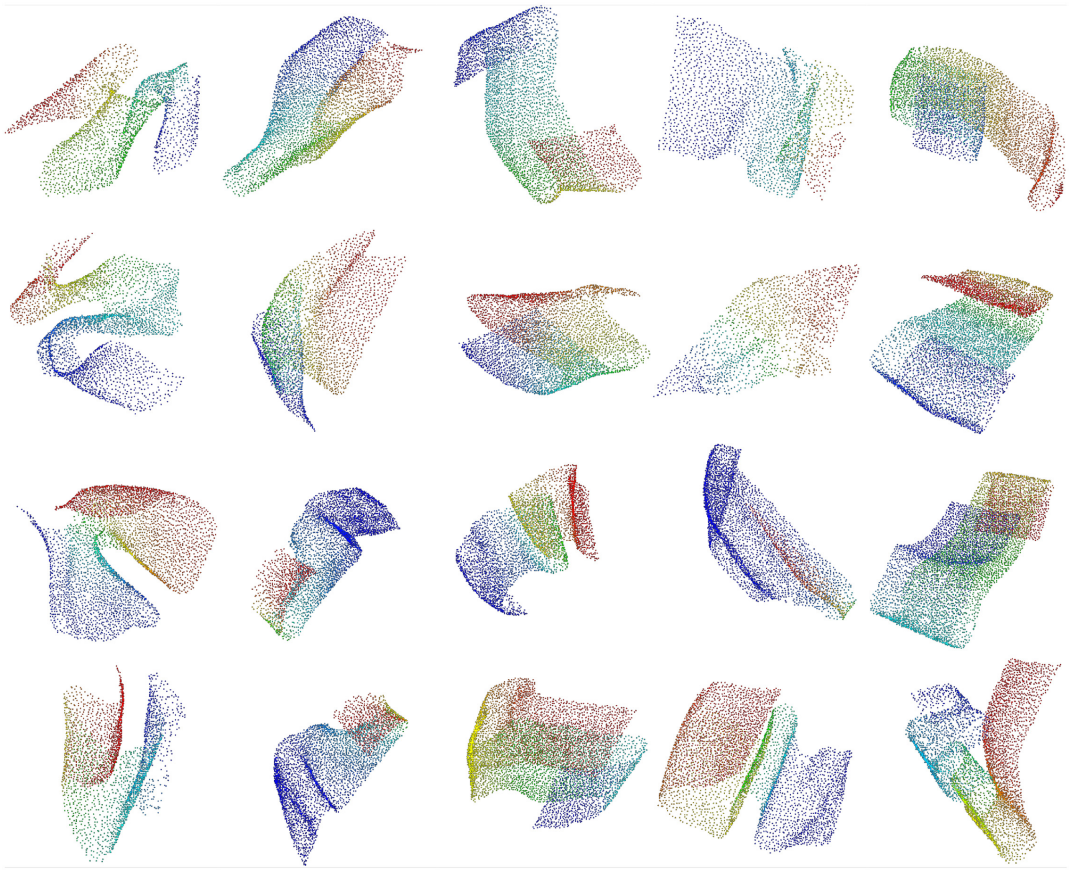

FIGURE 3 | Extracted charts from the Purkinje layer. Examples of manually cleaned charts. Pseudo-colors (based on Fiedler vectors) are associated with points representing Purkinje somata in order to suggest their 3D arrangement.

biggest component becomes the only significant one: for $k = 5$, almost 99.9% of PCs belong to this component, and the number of smaller clusters and of isolated neurons are reduced to 41 and 204, respectively. For $k = 8$, no isolated cells are found, and more than 99.9% of cells belong the biggest component.

The kNN clustering of the cerebellum seems thus to be more effective when the number of nearest neighbors considered is small. In this regime, clustering is more selective and smaller classes are preserved. For bigger k almost all PCs are clustered in a single component, highlighting their compact spatial organization. The parcellation of the sample we obtained using kNN clustering with $k = 3$ does not have a straightforward interpretation in terms of traditional neuroanatomy or physiology (i.e., being in the same cluster is unrelated to structural and functional connectivity). However, it could be a fine anatomical signature useful to compare subjects of different ages or in presence of a disease.

Distributions of Gaps in the Purkinje Cells Layer

The distribution of gaps in the PC layer can be inferred by the presence of large convex polygons in the 2D manifolds locally describing the layer folia. In **Figure 6A**, a complete view of the cerebellum is shown where all these polygons are remapped to the 3D space and colored according to their area. If the whole dataset is sliced along the medio-lateral axis, the distribution of gaps in the complete lamellar structure becomes more evident (**Figure 6B**). In the Figure, three areas can be identified where inter-cellular distances are particularly large (in red): one in the middle and two close to the side lobes. However, from visual inspection of the original data, it turns out that in these regions the sample was partially cracked during clearing (**Figure 7A**). The large intercellular distance in these areas is therefore due to some artifact during tissue preparation, and not to the real distribution of gaps in the layer (**Figures 7B,C**).

On the other hand, from closer analysis of single slices it appears that (real) larger inter-cellular gaps are mostly localized in correspondence to the internal curvatures of the lamellar structure (**Figure 6B**). This is confirmed by visual inspection of the original data (**Figures 7D,E**). Considering the young age of the mouse (PND 10), this could be due to the incomplete migration or topographically localized apoptotic death of the PCs (Dusart et al., 2006; Castagna et al., 2014).

The area of the largest convex polygon tangent to each cell show a mono-modal distribution, with mean value 2950 μm^2 and standard deviation 2583 μm^2 (**Figure 8**). This distribution can

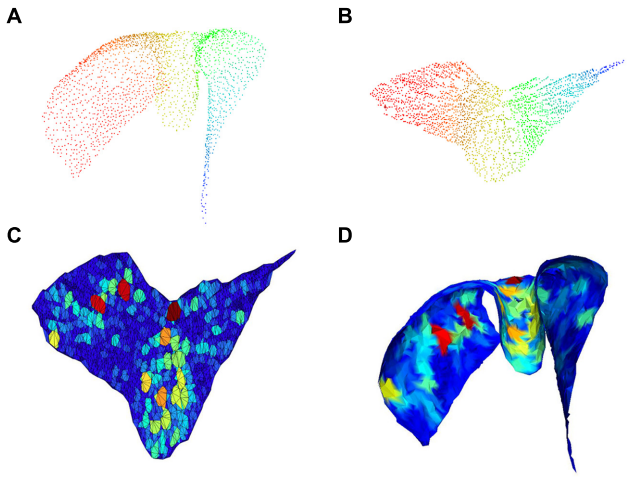

FIGURE 4 | Gap size estimation. 3D cloud point of a single chart **(A)** and associated 2D embedding **(B)**; pseudo-colors (from Fiedler vector) are only used to identify points. Triangulation with colors proportional to void area (red highest) in the 2D embedding space is shown in **(C)** and corresponding mesh back in the 3D space in **(D)**.

be well-fitted by a log-normal curve, with $\mu = 7.779 \pm 0.003$ and $\sigma = 0.488 \pm 0.002$ (99% confidence intervals). This kind of probability distributions is quite common in neuroscience (Buzsaki and Mizuseki, 2014). Thus, although many different measurements from different animals would be needed to validate it, the findings that inter-cellular areas between PCs are distributed in a log-normal fashion seems at least plausible. In perspective, the distribution parameters can also be used as global fingerprints to compare different mice.

Discussion

Contemporary neuroscience is in urgent need of a new generation of neuroanatomical techniques allowing scalable, reliable, specific, and quantitative analysis of macroscopic portions of brain tissue with cellular or sub-cellular resolution. Such a technical advance requires the integration of recent efforts in terms of transgenic animal development, sample clearing and staining, high-throughput imaging, and image analysis. Here, we presented a proof-of-principles of such combined approach on the cerebellum of an L7-GFP mouse. The sample was cleared with organic solvents and imaged with a confocal LSM; raw images produced by the apparatus were stitched together and subsequently analyzed to localize all PCs. Starting from the cloud of points representing all the Purkinje neurons in the cerebellum, further analysis was performed, highlighting both the clusterization properties of the point cloud and the distribution of gaps in the layer. Although we showed this experimental pipeline on a single sample, all the methods used (with the exception of cell clustering and gap localization) have been already demonstrated elsewhere (Becker et al., 2012; Silvestri et al., 2012; Frasconi et al., 2014), and a further validation of their capabilities is out of the scope of this work. The growing amount of papers exploiting sample clearing, LSM and the software tools described here, e.g. (Jahrling et al., 2010; Mertz and Kim, 2010; Erturk et al., 2012; Silvestri et al., 2014; Tomer et al., 2014), demonstrates the reliability of each single component of our workflow, paving the way to its application on a larger number of samples.

When repeated on a significantly cohort of mice, the measurements shown here can provide robust and bias-free insights into the distribution of PCs under different physiological or pathological conditions. For instance PCs loss can be quantified in heterozygous reeler (rl/+) mice, an animal model that has been used for studying the interplay of reelin deficiency with environmental factors during early development (Biamonte et al., 2014). Indeed, it has been reported that adult male rl/+ mice have reduced numbers of PCs, in comparison to female rl/+ mice and wild-type mice of either sex (Biamonte et al., 2009). The pipeline described in this paper can shine a new light in previous findings, allowing a more comprehensive characterization of the effect of reelin deficiency not only on the average number of PCs, but also on their spatial arrangement. The non-biased global

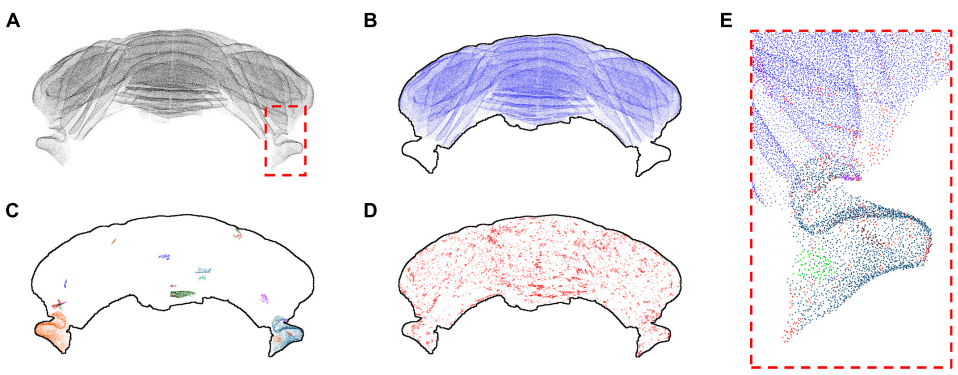

FIGURE 5 | k-Nearest neighbor clustering of Purkinje cells ($k = 3$). The whole Purkinje cells point cloud **(A)** and the largest cluster of kNN-connected cells **(B)**. The 20 biggest clusters after the first are shown with different colors in **(C)**, while in **(D)** all the remaining clusters and isolated cells are shown in red. The dashed red square depicted in **(A)** is shown at higher magnification in **(E)**, using a similar color scheme as the one used in **(B–D)**. All results for $k = 3$. In **(B–D)** a profile of the cerebellum is added to help the reader.

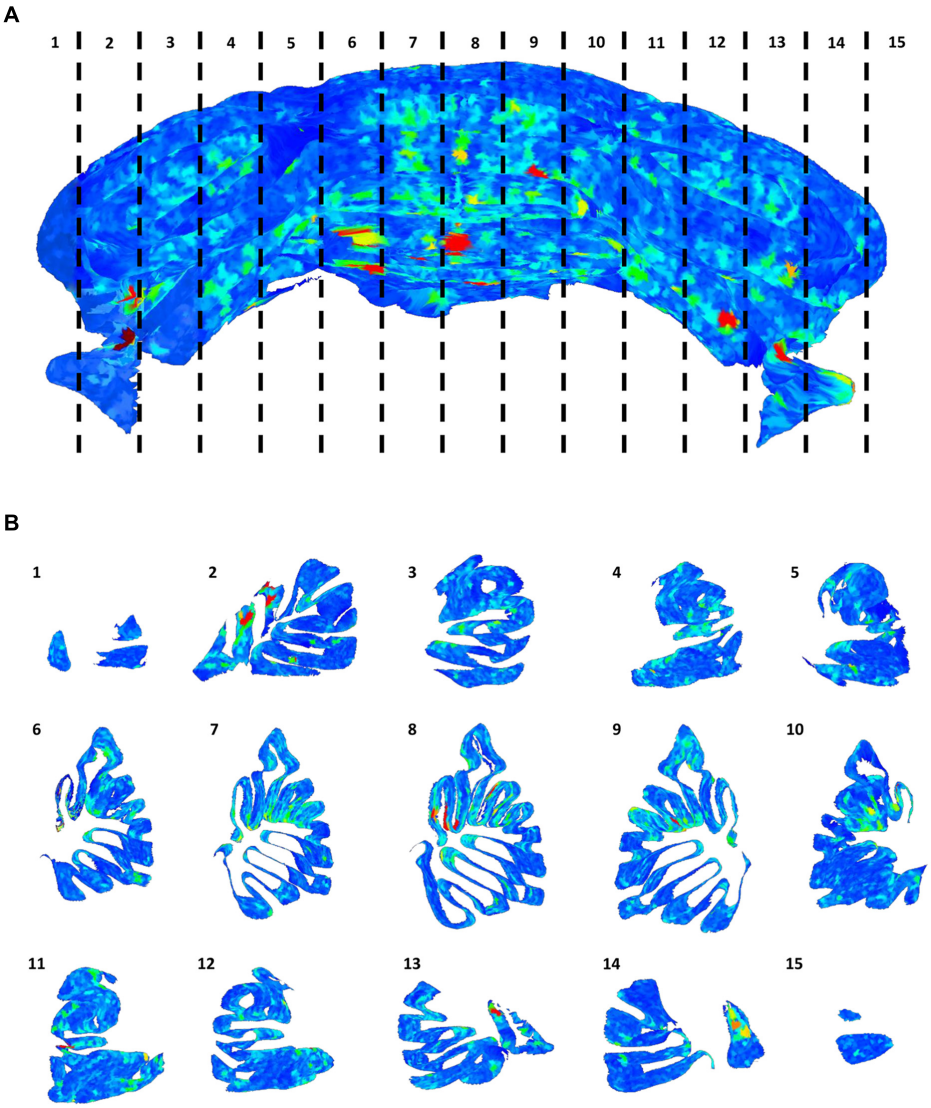

FIGURE 6 | Distribution of gaps in the Purkinje cells layer. The full 3D mesh representing the Purkinje layer **(A)**, colored according to the size of empty areas between the cells (blue smallest, red largest). To help visualize the internal structure of the mesh, single slices (according to the numeration in **A**) are reported **(B)**.

analysis presented here can easily reveal if the reduction in the number of PCs reported previously is due to cell death or rather to ectopic cell migration.

Although our proof-of-principle was on a single specific cell population (Purkinje neurons) and in a portion of the mouse brain (the cerebellum), the integrative approach we describe can be extended to different animal models (highlighting other cell types) and to larger specimens (as whole murine brains). In fact, recent advances in tissue clearing, as CLARITY (Chung et al., 2013) or CUBIC (Susaki et al., 2014), and in LSM (Tomer et al., 2014) are leading to a next generation of imaging protocols capable of producing high-resolution and high-contrast reconstructions of cm-wide samples. Furthermore, the ability of CLARITY of immunostaining macroscopic tissue portions can pave the way for quantitative large-volume neuroanatomy in humans as well as in non-human primates.

High-throughput imaging methods with improved contrast and resolution would both benefit and challenge computational tools. On the one hand, better images will increase the robustness and reliability of software: image stitching will be more precise since the cross-correlation will have a sharper peak, and cell localization will be more accurate because of the improved signal-to-noise ratio. On the other hand, the size of data is going to go well-beyond the TeraByte threshold, as soon as one is able to collect high-quality data from larger samples. Therefore, existing software tools should be adapted to cope with larger datasets, exploiting parallel architectures for both data processing and storage.

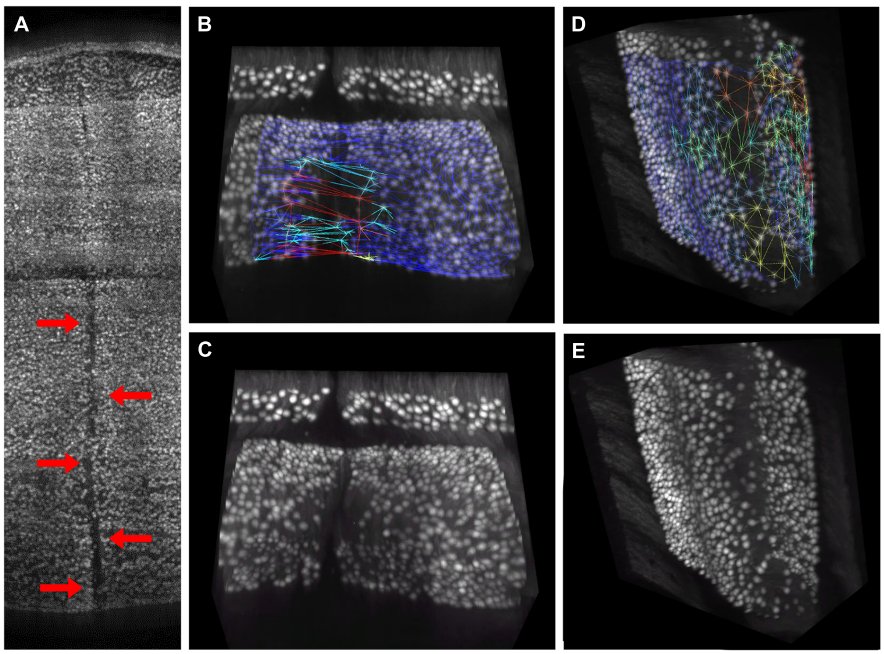

FIGURE 7 | Visual confirmation of gaps distribution map. 3D rendering of the central region of the cerebellum, where a crack caused by tissue clearing (indicated by red arrows) is clearly visible **(A)**. This crack gives rise to large "pseudo-gaps" in the 3D mesh: a 3D rendering of a smaller volume with the mesh superimposed is reported in **(B)**. The same volume without mesh is in **(C)**. In absence of macroscopic cracks, the triangular mesh correctly highlights regions with smaller planar density of Purkinje cells, which are commonly found at the folium curvature: a representative volume with and without mesh is reported in **(D,E)**, respectively. Mesh triangles are colored according to their areas (blue smallest, red largest).

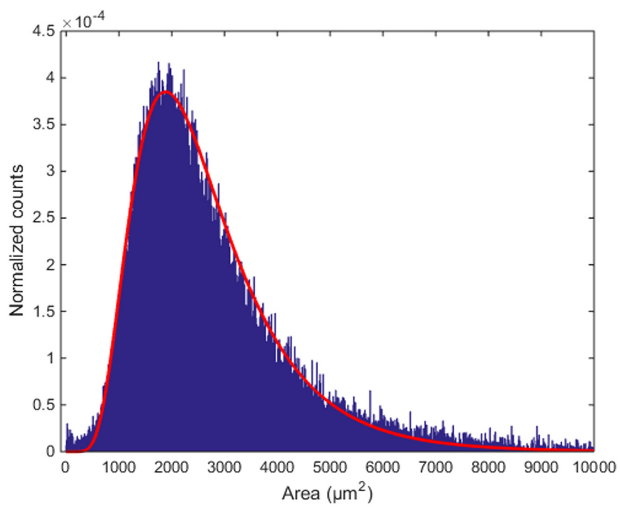

FIGURE 8 | Distribution of inter-cellular areas. The histogram of empty areas in the Purkinje layer (in blue) and its fit with a log-normal distribution (in red).

Beyond improving single technical aspects, as microscopy or image analysis, special efforts should be devoted to the integration of all those methodologies in a common and well-coordinated experimental pipeline. In this respect, it is crucial to have visualization and annotation tools designed for large images (Peng et al., 2014) that can be used to tune the protocols and for quality check. For instance, the comparison with original data was crucial to interpret the results found here, in particular to identify artifacts due to specimen cracking. Furthermore, since large-scale quantitative neuroanatomy is still in its infancy, a lot of trial and error will be needed to find out the best analysis methods and to properly use and interpret them. As an example, removal of localized points too far from the Purkinje layer significantly improves the quality of results (Frasconi et al., 2014), but may lead to biased analysis when cells are located quite out of the specimen – for instance in very early development stages (Larouche et al., 2008; Miyata et al., 2010). Manual inspection of images is also recommended to check the consistency of image stitching, which might fail when image quality is very low (Bria and Iannello, 2012).

Conclusion

We demonstrated that when state-of-the-art methodologies from various fields are properly combined they can produce data that would have been out of the neuroanatomists' reach only a few years ago. If this integrated approach will be kept updated with the most recent advances in each field, in the next decades researchers can gain further and further insight into the complexity of brain anatomy, chasing the ultimate dreams of Golgi and Ramòn y Cajal.

Acknowledgments

The research leading to these results has received funding from the European Union Seventh Framework Program (FP7/2007-2013) under grant agreements no. 604102 (Human Brain Project) and no. 284464 (LASERLAB-EUROPE). The research has also been supported by the Italian Ministry for Education, University and Research in the framework of the Flagship Project NanoMAX, by "Ente Cassa di Risparmio di Firenze" (private foundation).

References

Becker, K., Jahrling, N., Saghafi, S., Weiler, R., and Dodt, H. U. (2012). Chemical clearing and dehydration of GFP expressing mouse brains. *PLoS ONE* 7:e33916. doi: 10.1371/journal.pone.0033916

Biamonte, F., Assenza, G., Marino, R., D'Amelio, M., Panteri, R., Caruso, D., et al. (2009). Interactions between neuroactive steroids and reelin haploinsufficiency in Purkinje cell survival. *Neurobiol. Dis.* 36, 103–115. doi: 10.1016/j.nbd.2009.07.001

Biamonte, F., Latini, L., Giorgi, F. S., Zingariello, M., Marino, R., De Luca, R., et al. (2014). Associations among exposure to methylmercury, reduced Reelin expression, and gender in the cerebellum of developing mice. *Neurotoxicology* 45, 67–80. doi: 10.1016/j.neuro.2014.09.006

Boyce, J. E., Dobkin, D. P., Drysdale, R. L., and Guibas, L. J. (1985). Finding extremal polygons. *SIAM J. Comput.* 14, 134–147. doi: 10.1137/0214011

Bria, A., and Iannello, G. (2012). TeraStitcher – a tool for fast automatic 3D-stitching of teravoxel-sized microscopy images. *BMC Bioinformatics* 13:316. doi: 10.1186/1471-2105-13-316

Briggman, K. L., and Denk, W. (2006). Towards neural circuit reconstruction with volume electron microscopy techniques. *Curr. Opin. Neurobiol.* 16, 562–570. doi: 10.1016/j.conb.2006.08.010

Briggman, K. L., Helmstaedter, M., and Denk, W. (2011). Wiring specificity in the direction-selectivity circuit of the retina. *Nature* 471, 183–188. doi: 10.1038/nature09818

Buzsaki, G., and Mizuseki, K. (2014). The log-dynamic brain: how skewed distributions affect network operations. *Nat. Rev. Neurosci.* 15, 264–278. doi: 10.1038/nrn3687

Castagna, C., Aimar, P., Alasia, S., and Lossi, L. (2014). Post-natal development of the Reeler mouse cerebellum: an ultrastructural study. *Ann. Anat.* 196, 224–235. doi: 10.1016/j.aanat.2013.11.004

Chung, K., Wallace, J., Kim, S. Y., Kalyanasundaram, S., Andalman, A. S., Davidson, T. J., et al. (2013). Structural and molecular interrogation of intact biological systems. *Nature* 497, 332–337. doi: 10.1038/nature12107

Cleveland, W. S., and Devlin, S. J. (1988). Locally weighted regression – an approach to regression-analysis by local fitting. *J. Am. Stat. Assoc.* 83, 596–610. doi: 10.1080/01621459.1988.10478639

Comaniciu, D., and Meer, P. (2002). Mean shift: a robust approach toward feature space analysis. *IEEE Trans. Pattern Anal. Mach. Intell.* 24, 603–619. doi: 10.1109/34.1000236

Cover, T., and Hart, P. (1967). Nearest neighbor pattern classification. *IEEE Trans. Inf. Theory* 13, 21–27. doi: 10.1109/TIT.1967.1053964

Dodt, H. U., Leischner, U., Schierloh, A., Jahrling, N., Mauch, C. P., Deininger, K., et al. (2007). Ultramicroscopy: three-dimensional visualization of neuronal networks in the whole mouse brain. *Nat. Methods* 4, 331–336. doi: 10.1038/nmeth1036

Dusart, I., Guenet, J. L., and Sotelo, C. (2006). Purkinje cell death: differences between developmental cell death and neurodegenerative death in mutant mice. *Cerebellum* 5, 163–173. doi: 10.1080/14734220600699373

Duyn, J., and Koretsky, A. P. (2008). Magnetic resonance imaging of neural circuits. *Nat. Clin. Pract. Cardiovasc. Med.* (5 Suppl. 2), S71–S78. doi: 10.1038/ncpcardio1248

Erturk, A., Mauch, C. P., Hellal, F., Forstner, F., Keck, T., Becker, K., et al. (2012). Three-dimensional imaging of the unsectioned adult spinal cord to assess axon regeneration and glial responses after injury. *Nat. Med.* 18, 166–171. doi: 10.1038/nm.2600

Frasconi, P., Silvestri, L., Soda, P., Cortini, R., Pavone, F. S., and Iannello, G. (2014). Large-scale automated identification of mouse brain cells in confocal light sheet microscopy images. *Bioinformatics* 30, i587–i593. doi: 10.1093/bioinformatics/btu469

Gong, H., Zeng, S., Yan, C., Lv, X., Yang, Z., Xu, T., et al. (2013). Continuously tracing brain-wide long-distance axonal projections in mice at a one-micron voxel resolution. *Neuroimage* 74, 87–98. doi: 10.1016/j.neuroimage.2013.02.005

Gray, E. G. (1969). Electron microscopy of excitatory and inhibitory synapses: a brief review. *Prog. Brain Res.* 31, 141–155. doi: 10.1016/S0079-6123(08)63235-5

Jahrling, N., Becker, K., Schonbauer, C., Schnorrer, F., and Dodt, H. U. (2010). Three-dimensional reconstruction and segmentation of intact *Drosophila* by ultramicroscopy. *Front. Syst. Neurosci.* 4:1. doi: 10.3389/neuro.06.001.2010

Keller, A. L., Zeidler, D., and Kemen, T. (2014). High throughput data acquisition with a multi-beam SEM. *Scanning Microsc.* 2014:9236.

Keller, P. J., and Dodt, H. U. (2012). Light sheet microscopy of living or cleared specimens. *Curr. Opin. Neurobiol.* 22, 138–143. doi: 10.1016/j.conb.2011.08.003

Keller, P. J., Schmidt, A. D., Wittbrodt, J., and Stelzer, E. H. (2008). Reconstruction of zebrafish early embryonic development by scanned light sheet microscopy. *Science* 322, 1065–1069. doi: 10.1126/science.1162493

Kim, J. S., Greene, M. J., Zlateski, A., Lee, K., Richardson, M., Turaga, S. C., et al. (2014). Space-time wiring specificity supports direction selectivity in the retina. *Nature* 509, 331–336. doi: 10.1038/nature13240

Knott, G., Marchman, H., Wall, D., and Lich, B. (2008). Serial section scanning electron microscopy of adult brain tissue using focused ion beam milling. *J. Neurosci.* 28, 2959–2964. doi: 10.1523/JNEUROSCI.3189-07.2008

Larouche, M., Beffert, U., Herz, J., and Hawkes, R. (2008). The Reelin receptors Apoer2 and Vldlr coordinate the patterning of Purkinje cell topography in the developing mouse cerebellum. *PLoS ONE* 3:e1653. doi: 10.1371/journal.pone.0001653

Li, A., Gong, H., Zhang, B., Wang, Q., Yan, C., Wu, J., et al. (2010). Micro-optical sectioning tomography to obtain a high-resolution atlas of the mouse brain. *Science* 330, 1404–1408. doi: 10.1126/science.1191776

Lichtman, J. W., and Conchello, J. A. (2005). Fluorescence microscopy. *Nat. Methods* 2, 910–919. doi: 10.1038/nmeth817

McKimm, E., Corkill, B., Goldowitz, D., Albritton, L. M., Homayouni, R., Blaha, C. D., et al. (2014). Glutamate dysfunction associated with developmental cerebellar damage: relevance to autism spectrum disorders. *Cerebellum* 13, 346–353. doi: 10.1007/s12311-013-0541-4

Meinertzhagen, I. A., Takemura, S. Y., Lu, Z., Huang, S., Gao, S., Ting, C. Y., et al. (2009). From form to function: the ways to know a neuron. *J. Neurogenet.* 23, 68–77. doi: 10.1080/01677060802610604

Mertz, J., and Kim, J. (2010). Scanning light-sheet microscopy in the whole mouse brain with HiLo background rejection. *J. Biomed. Opt.* 15:016027. doi: 10.1117/1.3324890

Miyata, T., Ono, Y., Okamoto, M., Masaoka, M., Sakakibara, A., Kawaguchi, A., et al. (2010). Migration, early axonogenesis, and Reelin-dependent layer-forming behavior of early/posterior-born Purkinje cells in the developing mouse lateral cerebellum. *Neural Dev.* 5:23. doi: 10.1186/1749-8104-5-23

Oberdick, J., Smeyne, R. J., Mann, J. R., Zackson, S., and Morgan, J. I. (1990). A promoter that drives transgene expression in cerebellar Purkinje and retinal bipolar neurons. *Science* 248, 223–226. doi: 10.1126/science.2109351

Osten, P., and Margrie, T. W. (2013). Mapping brain circuitry with a light microscope. *Nat. Methods* 10, 515–523. doi: 10.1038/nmeth.2477

Palay, S. L. (1956). Synapses in the central nervous system. *J. Biophys. Biochem. Cytol.* 2, 193–202. doi: 10.1083/jcb.2.4.193

Peng, H., Ruan, Z., Long, F., Simpson, J. H., and Myers, E. W. (2010). V3D enables real-time 3D visualization and quantitative analysis of large-scale biological image data sets. *Nat. Biotechnol.* 28, 348–353. doi: 10.1038/nbt.1612

Peng, H., Tang, J., Xiao, H., Bria, A., Zhou, J., Butler, V., et al. (2014). Virtual finger boosts three-dimensional imaging and microsurgery as well as terabyte volume image visualization and analysis. *Nat. Commun.* 5:4342. doi: 10.1038/ncomms5342

Ragan, T., Kadiri, L. R., Venkataraju, K. U., Bahlmann, K., Sutin, J., Taranda, J., et al. (2012). Serial two-photon tomography for automated ex vivo mouse brain imaging. *Nat. Methods* 9, 255–258. doi: 10.1038/nmeth.1854

Rockland, K. S. (2010). Five points on columns. *Front. Neuroanat.* 4:22. doi: 10.3389/fnana.2010.00022

Sahoo, P. K., Soltani, S., Wong, A. K. C., and Chen, Y. C. (1988). A survey of thresholding techniques. *Comput. Vis. Graph. Image Process.* 41, 233–260. doi: 10.1016/0734-189X(88)90022-9

Silvestri, L., Allegra Mascaro, A. L., Costantini, I., Sacconi, L., and Pavone, F. S. (2014). Correlative two-photon and light sheet microscopy. *Methods* 66, 268–272. doi: 10.1016/j.ymeth.2013.06.013

Silvestri, L., Bria, A., Sacconi, L., Iannello, G., and Pavone, F. S. (2012). Confocal light sheet microscopy: micron-scale neuroanatomy of the entire mouse brain. *Opt. Express* 20, 20582–20598. doi: 10.1364/OE.20.020582

Susaki, E. A., Tainaka, K., Perrin, D., Kishino, F., Tawara, T., Watanabe, T. M., et al. (2014). Whole-brain imaging with single-cell resolution using chemical cocktails and computational analysis. *Cell* 157, 726–739. doi: 10.1016/j.cell.2014.03.042

Tench, C. R., Morgan, P. S., Wilson, M., and Blumhardt, L. D. (2002). White matter mapping using diffusion tensor MRI. *Magn. Reson. Med.* 47, 967–972. doi: 10.1002/mrm.10144

Tenenbaum, J. B., De Silva, V., and Langford, J. C. (2000). A global geometric framework for nonlinear dimensionality reduction. *Science* 290, 2319–2323. doi: 10.1126/science.290.5500.2319

Tomer, R., Ye, L., Hsueh, B., and Deisseroth, K. (2014). Advanced CLARITY for rapid and high-resolution imaging of intact tissues. *Nat. Protoc.* 9, 1682–1697. doi: 10.1038/nprot.2014.123

Conflict of Interest Statement: The authors declare that the research was conducted in the absence of any commercial or financial relationships that could be construed as a potential conflict of interest.

frontiers in Neuroanatomy

ORIGINAL RESEARCH
published: 12 May 2015
doi: 10.3389/fnana.2015.00049

Phenotype overlap in glial cell populations: astroglia, oligodendroglia and NG-2(+) cells

Badrah Alghamdi[1] *and Robert Fern*[2]*

[1] Department of Cell Physiology and Pharmacology, University of Leicester, Leicester, UK, [2] Peninsula School of Medicine and Dentistry, University of Plymouth, Plymouth, UK

The extent to which NG-2(+) cells form a distinct population separate from astrocytes is central to understanding whether this important cell class is wholly an oligodendrocyte precursor cell (OPC) or has additional functions akin to those classically ascribed to astrocytes. Early immuno-staining studies indicate that NG-2(+) cells do not express the astrocyte marker GFAP, but orthogonal reconstructions of double-labeled confocal image stacks here reveal a significant degree of co-expression in individual cells within post-natal day 10 (P10) and adult rat optic nerve (RON) and rat cortex. Extensive scanning of various antibody/fixation/embedding approaches identified a protocol for selective post-embedded immuno-gold labeling. This first ultrastructural characterization of identified NG-2(+) cells revealed populations of both OPCs and astrocytes in P10 RON. NG-2(+) astrocytes had classic features including the presence of glial filaments but low levels of glial filament expression were also found in OPCs and myelinating oligodendrocytes. P0 RONs contained few OPCs but positively identified astrocytes were observed to ensheath pre-myelinated axons in a fashion previously described as a definitive marker of the oligodendrocyte lineage. Astrocyte ensheathment was also apparent in P10 RONs, was absent from developing nodes of Ranvier and was never associated with compact myelin. Astrocyte processes were also shown to encapsulate some oligodendrocyte somata. The data indicate that common criteria for delineating astrocytes and oligodendroglia are insufficiently robust and that astrocyte features ascribed to OPCs may arise from misidentification.

Keywords: astrocyte, development, glia, oligodendrocyte, NG-2

OPEN ACCESS

Edited by:
Javier DeFelipe, Cajal Institute, Spain

Reviewed by:
Fernando De Castro, Hospital Nacional de Parapléjicos-Servicio de Salud de Castilla-La Mancha, Spain
Fiorenzo Conti, Università Politecnica delle Marche, Italy

***Correspondence:**
Robert Fern, Peninsula School of Medicine and Dentistry, University of Plymouth, John Bull Building, Research Way, Plymouth, PL6 8BU, UK
robert.fern@plymouth.ac.uk

Received: *02 February 2015*
Accepted: *02 April 2015*
Published: *12 May 2015*

Citation:
Alghamdi B and Fern R (2015) Phenotype overlap in glial cell populations: astroglia, oligodendroglia and NG-2(+) cells. Front. Neuroanat. 9:49. doi: 10.3389/fnana.2015.00049

Introduction

Glial cells expressing the NG-2 proteoglycan act as oligodendrocyte precursor cells (OPCs) and are retained in the mature CNS where they form a reservoir of progenitors that may be significant for the development of effective treatment strategies for common neurological diseases (Nishiyama et al., 2009). NG-2(+) cells can receive synaptic input and therefore they challenge the dogmatic separation of neural cells into either neuronal/excitable or glial/support roles. Historically, cells with features of NG-2(+) cells have been variously described as "small glioblasts" (Vaughn, 1969), "3rd glial element" cells (Vaughn and Peters, 1968), "β-astrocytes" (Reyners et al., 1982),"oligodendrocyte/type 2 astrocytes" (O2A) (Raff et al., 1983), "smooth protoplasmic astrocytes" (Levine and Card, 1987), "OPCs" (Ong and Levine, 1999), "astons"

(Matthias et al., 2003), "polydendrocytes" (Nishiyama et al., 2009) and "synantocytes" (Leoni et al., 2009). This diversity of nomenclature reflects the degree of uncertainty regarding the cells' ontogeny and their physiological functions. In particular, early studies noted the morphological similarity between NG-2(+) cells and astrocytes, while subsequent reports have documented astrocyte-type features such as process extension into the node of Ranvier, synapses encapsulation (Levine and Card, 1987; Ong and Levine, 1999; Wigley and Butt, 2009), and reactive gliosis with features of astrocytosis (Greenwood and Butt, 2003; Lytle et al., 2009). The degree to which these cells may exhibit astrocyte-type behavior remains controversial, as does the extent to which astrocytes and NG-2(+) cells share a common cell fate.

Materials and Methods

UK home office regulations were followed for all experimental work which was conducted in accordance with the Council Directive 2010/63EU of the European Parliament and the Council of 22 September 2010 on the protection of animals used for scientific purposes. The animal welfare and ethics committee of University of Leicester approved all the experimental protocols. Rat optic nerves (RONs) were dissected from Lister-hooded rats on post-natal day 0 (referred to as "P0"), P8-12 ("P10"), or >P80 (adult).

Immuno-Histochemistry

RONs were lightly fixed in 2% paraformaldehyde/0.1M PBS for 30 min prior to incubation in 0.1M PBS plus 20% sucrose w/v for 5 min and freeze-sectioning. Twenty micro meter sections were subsequently blocked for 60 min in 0.1M PBS +10% normal goat serum +0.5% Triton-X 100 (PBST). Sections were then incubated in this solution (plus primary antibody) overnight at 4°C. Antibodies were raised against NG-2 (1:100 Millipore MAB5384 and GFAP 1:200 Sigma G4546). Staining was detected using appropriate Alexa-conjugated secondary antibodies (1:1000 Molecular probes). Primary antibody omission controls were blank. Images were collected using an Olympus confocal microscope and image stacks were analyzed using NIH Image-J.

Immuno-Electron Microscopy (I-EM)

After extensive testing using a variety of fixation protocols (3% glutaraldehyde in Sorensen's +1% osmium / 3% glutaraldehyde +2% paraformaldehyde in Sorensen's +1% osmium), embedding (propylene oxide + Spurr's resin / propylene oxide + Agar low viscosity resin / ethanol + LR White resin), etching and staining protocols, the following technique produced acceptable results: RONs were dissected in Sorenson's buffer, washed in 0.1 M sodium cacodylate buffer (2 mM $CaCl_2$/pH 7.4) and post-fixed in 2% formaldehyde +3% glutaraldehyde in cacodylate buffer overnight. Nerves were then washed prior to secondary fixation (1% osmium tetroxide / 1.5% potassium ferricyanide) and washed again prior to tertiary fixation (2% uranyl acetate). RONs were sequentially dehydrated, washed in propylene oxide, and embedded using the following steps: (a) 2:1 propylene oxide + modified Spurr's low viscosity resin for 90 min; (b) 1:1 propylene oxide + modified Spurr's resin for 60 min; (c) 1:2 propylene oxide + modified Spurr's resin for 60 min; (d) 100% Spurr's low viscosity resin (30 min, then overnight, then 180 min); and (e) polymerization for 16 h at 60°C.

Post-embedded I-EM for NG-2 has not previously been achieved. We tested five different antibodies and antibody cocktails (4 h primary staining followed by washing and secondary staining for 60 min) in sections that had been either etched (saturated sodium metaperiodate 30 min), blocked (PBST 30 min), etched and blocked, or left untreated. The primary antibodies tested were: (a) Rabbit polyclonal AB62341 from Abcam; (b) Rabbit polyclonal generously gifted from William Stallcup; (c) Mouse monoclonal MAB5384 from Millipore; (d) Mouse monoclonal cocktail generously gifted from William Stallcup; and (e) Mouse monoclonal cocktail (D120.43/D4.11/N143.8/N109.6 clones) 37-2700 from Zymed. Staining using all five antibodies/cocktails was tested on ultrathin sections at 1:200, 1:100, 1:50 and 1:20 and reactivity detected using a goat anti-mouse or goat anti-rabbit 30 nm gold conjugate, as appropriate (1:50; Sigma). Ultrathin sections were counter-stained with uranyl acetate and lead citrate and examined with a Jeol 100CX electron microscope.

Results

Double immuno-labeled P10 RON 10 μm projections indicate apparent regions of single and co-expression for GFAP/NG-2 (**Figures 1A–C**). Ortho-projections revealed non-overlapping regions of expression in individual cells (e.g., the dark blue arrow in **Figure 1C1** shows an NG-2(+)/GFAP(−) soma) and regions of co-expression in both cell somata and processes (e.g., **Figures 1C1,C2**, light blue arrows). The analysis indicates a large population of cells express both proteins, but often in separate structures. Cell counting of stack projections in P 10 RON showed 38.5 +/− 2.7% of cells were GFAP(+)/NG-2(−), 28.5 +/− 2.6% were GFAP(−)/NG-2(+) and 33.0 +/− 5.3% were GFAP(+)/NG-2(+) (544 cells analyzed from 5 sections). Control staining with omission of one or both primary antibodies showed no cross-labeling of secondary antibodies, bleed through of channels, significant background fluorescence, or non-specific staining (**Figures 1D1–D6**). All comparable images were collected using identical image and acquisition settings to allow direct comparison of test and controls.

Projections of GFAP and NG-2 immuno-staining in adult RON (**Figures 2A–D**) show a mixture of single and double labeling of cells and processes. Ortho-projections of the boxed areas (**Figures 2C1,C2**) again revealed examples of single (e.g., dark blue arrows) and double (e.g., light blue arrows) staining. Cell counting of stack projections showed 19.5 +/− 1.4% of cells were GFAP(+)/NG-2(−), 20.6 +/− 2.6% were GFAP(−)/NG-2(+) and 59.9 +/−1.6% were GFAP(+)/NG-2(+) (369 cells analyzed from 5 sections). This was a higher apparent proportion of co-expressing cells than found in the P10 nerves.

A similar approach in adult cortical gray matter produces comparable co-stained cells (**Figure 3**), with a population of NG-2(+) cells having no apparent regions of GFAP expression

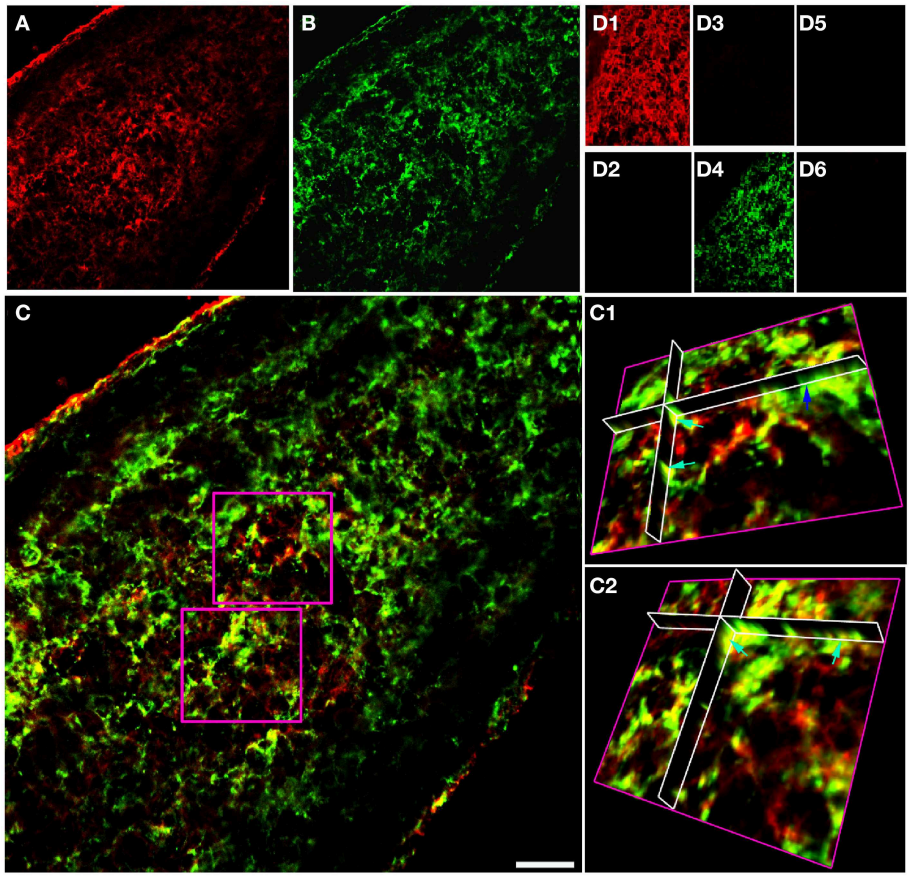

FIGURE 1 | GFAP and NG-2 co-localization in P10 RON glial cells. **(A)** GFAP immuno-reactivity (red). **(B)** NG-2 immuno-reactivity (green). **(C)** Overlay with boxed areas shown at higher gain as 3-D projections in **(C1)** and **(C2)**. Note the NG-2 co-localization (red or orange regions e.g., light blue arrows) in parts of cells that may also have regions that are only GFAP(+) (green regions e.g., dark blue arrow). **(D)** Controls showing GFAP staining **(D1)** and absence of NG-2 staining **(D2)** when the NG-2 antibody was omitted from the otherwise identical protocol; NG-2 staining **(D3)** and no GFAP staining **(D4)** when the GFAP antibody was omitted, and the absence of any staining when both primary antibodies were omitted (**D5,D6**). All images were collected and displayed using identical settings. Bar = 10 μm.

(**Figure 3A1**, dark blue arrow) and a population that co-expresses both proteins (**Figure 3A2**, single blue arrows). Similar data were observed in the adjacent sub-cortical white matter structures. Cell counting of stack projections showed 68.9 +/− 3.8% of cells were GFAP(+)/NG-2(−), 10.8 +/−2.8% were GFAP(−)/NG-2(+) and 20.3 +/−1.4% were GFAP(+)/NG-2(+) (384 cells analyzed from 5 sections) in the gray matter. As in the examples shown, it was often the case in cortical sections that GFAP reactivity was localized individually to the processes of cells that expressed NG-2 on the soma.

NG-2(+) cells and GFAP(+) cells may form close morphological arrangements that are problematic to sufficiently resolved using the immuno-fluorescent approach described above. We therefore developed an immuno-gold post-embedded methodology for the ultrastructural analysis of NG-2(+) cells in P10 RON. Retaining antigenicity for NG-2 in tissue prepared for I-EM proved difficult. A variety of polyclonal and monoclonal antibodies (and cocktails) were tested over a range of concentrations on P10 RONs collected under a number of fixation and embedding protocols (see Materials and Methods). Cell-specific staining was achieved with a polyclonal antibody on nerves using an overnight primary fixation (3% glutaraldehyde/2% formaldehyde) in cacodylate buffer followed by two further fixation steps, gradual embedding in modified Spurr's resin, and sodium metaperiodate etching. Using this protocol, staining levels were low but selective. Blinded counting of gold particles in 10 grid sections each from three independent nerves found 7.4% in axons ($n = 11/1239$ axons), 59.4% in glia somata ($n = 35/101$ somata), 27.9% in glial processes and 6.1% in glial nuclei ($n = 9/101$ nuclei; total $n = 148$ particles). 87.3% of staining was therefore in the glial cell membrane or cytoplasm, with the remaining gold particles showing a background level of non-specific staining in axons and nuclei. This level of background staining is consistent with a number of other studies using I-EM in RON (e.g., Alix et al., 2008; Arranz et al., 2008; Alix and Fern, 2009). In total, six fixation and embedding protocols were attempted for all 5 antibody/cocktail mixtures over 4 concentration ranges; only the one successful protocol was

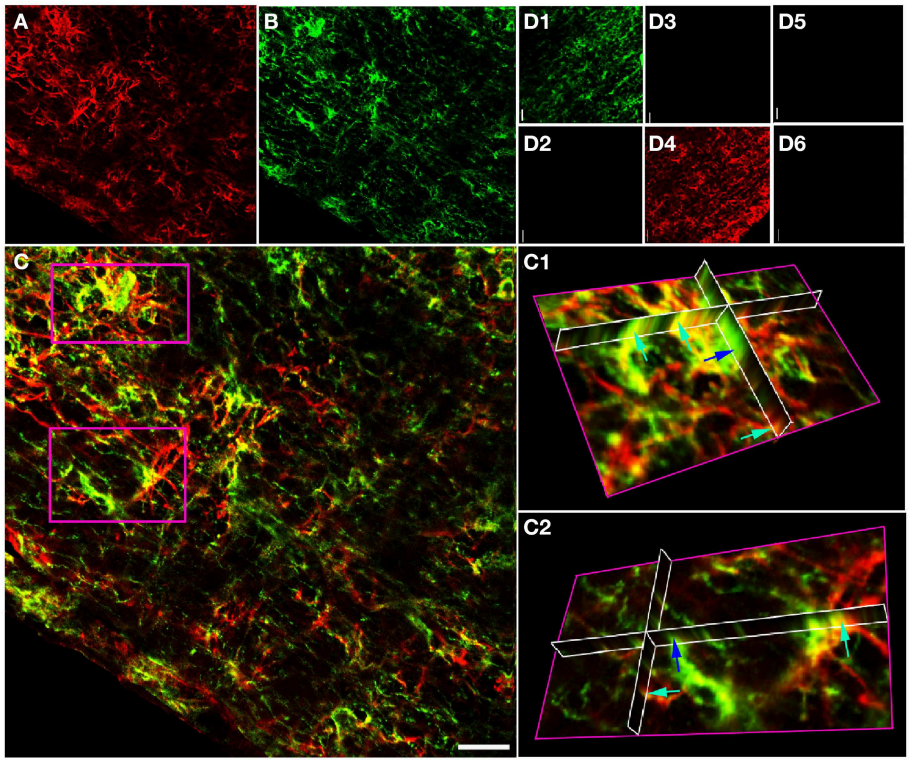

FIGURE 2 | GFAP and NG-2 co-localization in the adult RON. (A) GFAP immuno-reactivity (red). **(B)** NG-2 immuno-reactivity (green). **(C)** Overlay with boxed areas shown at higher gain as 3-D projections in **(C1)** and **(C2)**. Note the NG-2 co-localization (red or orange, e.g., light blue arrows) in parts of cells that may express GFAP alone in other regions, and in cells that are only GFAP(+) (e.g., dark blue arrow). **(D)** Controls showing NG-2 staining **(D1)** and absence of GFAP staining **(D2)** when the GFAP antibody was omitted from the otherwise identical protocol; GFAP staining **(D4)** and no NG-2 staining **(D3)** when the NG-2 antibody was omitted, and the absence of any staining when both primary antibodies were omitted (**D5,D6**). All images were collected and displayed using identical settings. Bar = 10 μm.

identified, with non-selective staining and null-staining proving to be the major shortfalls of the other fixation/embedding staining combinations.

In P10 RON, gold particles were frequently detected in the cell membrane or cytoplasm of glial somata (**Figures 4A–D**, single arrows). Labeled cells most frequently had a wide-bore endoplasmic reticulum (ER; **Figures 4A–C**, arrow heads) and a granular chromatin that was often clustered under the nuclear envelope. These cells occasionally exhibited stacked glial filaments in the cytoplasm (**Figures 4A–C**, double arrows) and have the classic features of astrocytes, which are the predominant type of cell present in the nerve at this age (Vaughn and Peters, 1967; Vaughn, 1969). NG-2 reactivity (gold particles) was also present in glial processes that did not contain obvious glial filaments and in some that did (**Figure 4E**), as well as in oligodendrocyte processes that had initiated axon wrapping and myelination (**Figure 4F**). Staining was rarely observed in undifferentiated glioblasts which will include OPCs, but such cells make up <10% of the glial population at this age (Vaughn, 1969; Barres et al., 1992). The ultrastructural analysis therefore aligns with the confocal immuno-fluorescent data showing NG-2(+) GFAP(+) astrocytes in the neonatal optic nerve.

Co-expression of the early oligodendroglial lineage marker NG-2 and astrocyte marker GFAP in glial cells of the optic nerve raises questions about how these two cell fates are distinguished. We examined P0 RON, a developmental point before the wide-spread arrival of OPC (Vaughn, 1969; Small et al., 1987; Barres et al., 1992) and a point when astrocyte production has peaked (Vaughn and Peters, 1967; Vaughn, 1969; Skoff et al., 1976; Skoff, 1990). A population of astrocytes can be unambiguously identified at this age, for example by the radiating processes found in cross-sections that contribute to the glial limitans, a wholly astrocytic structure (**Figure 5A**, arrows). Such cells often expressed small bundles of glial filaments in the somata and processes (**Figure 5B**, arrow head) and have a wide-bore ER typical of astrocytes, see (Vaughn and Peters, 1967; Vaughn, 1969; Federoff and Vernadakis, 1986) (**Figures 5B,D,F**). Thick astrocytes processes separate axons into fascicles (**Figure 5A**) and run parallel to axons along the nerve (**Figure 5F**). "Finger processes" have previously been described in these cells (**Figure 5B**) and had been thought to represent process extension prior to fasciculation but these structures exist in cells that appear to have completed fasciculation (**Figures 5A,B**) and often wrap around pre-myelinated axons of various diameters (**Figure 5D**).

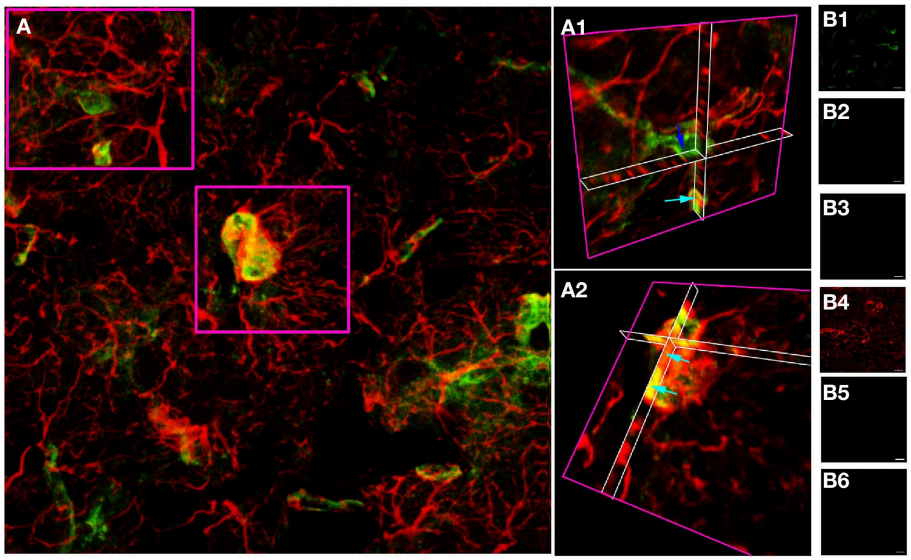

FIGURE 3 | GFAP and NG-2 co-localization in adult cortical gray matter. (A) GFAP immuno-reactivity (red) and NG-2 immuno-reactivity (green), with the two boxed areas shown at higher gain as 3-D projections in **(A1)** and **(A2)**. Note the NG-2 co-localization (e.g., light blue arrows) in parts of cells that may also have regions that are only GFAP(+), while other NG-2(+) cells are GFAP(–) (e.g., dark blue arrow). **(B)** Controls showing GFAP staining **(B1)** and absence of NG-2 staining **(B2)** when the NG-2 antibody was omitted from the otherwise identical protocol; NG-2 staining **(B4)** and no GFAP staining **(B3)** when the GFAP antibody was omitted, and the absence of any staining when both primary antibodies were omitted (**B5,B6**). All images were collected and displayed using identical settings. Bar = 10 μm.

Transverse sections confirm the presence of ensheathing processes (**Figure 5C**), which sometimes contain glial filaments (**Figure 5C**, black arrows). Unlike ensheathing oligodendrocyte processes, NG-2 reactivity was not observed on the ensheathing astrocyte processes.

Numerous finger processes are also found in P10 RON and are more likely to contain glial filaments than other regions of the astrocyte (**Figure 6A**). Examples are present that bifurcate to initiate ensheathment of small axons (**Figures 6A,B**) and double finger processes erupting from large processes to flank axons from either side (**Figures 6A,D,E**), while single finger processes occasionally wrap the entire axon circumference (**Figure 6C**). Multiple layers of ensheathment can be seen (**Figures 6D,E**) but compact myelin cannot be unambiguously associated with these processes (**Figure 6F**) and myelinating oligodendrocyte processes never contain any of the features of astrocytes (e.g., stacked glial filaments, wide-bore ER), although single glial filaments are apparent on occasion (**Figure 6H**). Fine processes that lack classical astrocyte features are present and make close connections with larger pre-myelinated axons (**Figure 6G**) and may be oligodendroglial. Small axons are also sometimes embedded in the surface of astrocyte somata that have prominent glial filament expression and wide-bore ER (**Figures 6I,J**). In long section, glial filament-containing processes are frequently found in early nodes of Ranvier (**Figure 6K**) and at hemi-nodes sites where one myelinating process has yet to arrive (**Figure 6L**), but were not observed to wrap around the larger myelinating axon at these points. If axons wrapping by astrocytes is a feature of early node of Ranvier sites, it must, therefore, reverse as myelination progresses.

Oligodendrocytes can sometimes be unambiguously identified in P10 RON by the presence of myelinated sheaths contiguous with the cell membrane (**Figure 7**). The general form and distribution of organelles such as mitochondria and Golgi apparatus were not distinguishing features of these cells but nuclear morphology was generally spheroid and often contained a nucleolus. The chromatin was less likely to be clustered under the nuclear envelope than that found in astrocytes and a narrow-bore ER was a clear distinguishing feature (**Figure 7**). Oligodendrocytes in P10 nerves were a mixture of larger, more differentiated cells (**Figures 7A–C**) and smaller, less mature cells, which tended to have a more clustered chromatin and often lacked large processes (**Figures 7D–F,K,L**). This distinction has been made previously e.g., by (Vaughn and Peters, 1967; Vaughn, 1969; Skoff et al., 1976; Skoff, 1990) but it should be noted that these "immature" cells of the oligodendrocyte lineage sometimes had ensheathed neighboring axons (**Figures 7E,L**, double arrows) and may in fact be sections through cells at a level close to the nuclear envelope. Positively identified oligodendrocytes frequently expressed microtubules apparently randomly arrayed throughout the cytoplasm (**Figures 7B,C,E**, arrows) and in some cases contained loose bundles of glial filaments (**Figures 7E,F**) and regions of stacked glial filaments (**Figures 7H,J,L**).

Oligodendrocytes are readily identifiable in adult RON due to their ensheathment of axons (e.g., **Figure 8A**, arrow) and have features previously described for this cell type. Glial filaments were not observed. A previously unremarked close morphological relationship between oligodendrocyte somata and astrocytes was often present, with oligodendrocytes

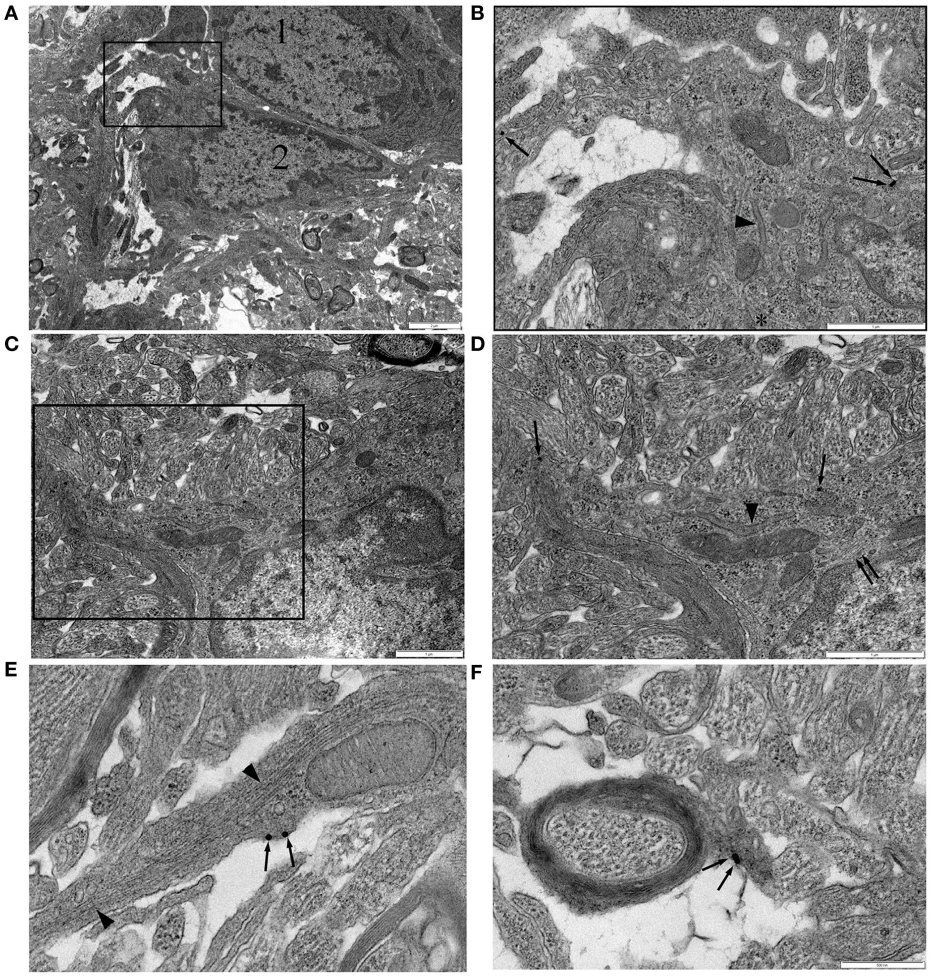

FIGURE 4 | NG-2 immuno-gold labeling in P10 RON. (A,B) Two closely apposed glial soma ("1" and "2"). Cell "1" has features typical of an early cell of the oligodendroglial lineage including an ovoid nucleus and narrow bore ER. Cell "2" has features that are typical of astrocytes in this preparation. The boxed area is shown at higher gain in (**B**). Note the gold particles (some indicated by arrows) which identify this cell as NG-2(+). A lobular nuclear morphology with clustered chromatin under the nuclear envelope and a wide bore ER (arrow heads) are astrocyte features. The cytoplasm also contains microtubules (e.g., asterisk). Glial filaments cannot be positively identified in this cell. **(C,D)** Another NG-2(+) cell with astrocyte features which does express glial filaments (double arrows). Boxed area shown at higher gain in **(D)**. **(E)** High-gain micrograph of NG-2 staining in glial processes (arrows) which contains glia filaments (arrowhead). **(F)** An example of NG-2(+) (arrows) oligodendrocyte processes ensheathing an axon.

completely encased in glial filament expressing astrocyte processes (**Figures 8A–C**, arrow heads). Astrocyte processes also made very close contact with the outer layer of the myelin sheath (**Figure 8D**) and with rare non-myelinated axon (**Figure 8D**).

Discussion

NG-2(+) cells are OPCs capable of receiving synaptic input which may regulate their cell fate (Bergles et al., 2000, 2010; Kukley et al., 2007; Ziskin et al., 2007). These cells may also extend processes into the node of Ranvier and can transform into reactive astrocytes under pathological and cell culture conditions (Levine and Stallcup, 1987; Hirsch and Bahr, 1999; Leoni et al., 2009; Honsa et al., 2012). There have been several prior attempts to immuno-label NG2 protein for ultrastructural analysis of these cells, utilizing peroxides DAB pre-embedded approaches that do not preserve fine cellular characteristics (Levine and Card, 1987; Levine and Stallcup, 1987; Ong and Levine, 1999; Peters and Sethares, 2004; Leoni et al., 2009). Prior studies have noted that preservation of NG-2 reactivity requires light fixation and that NG-2(+) cells are particularly poorly preserved compared to other cell types (Peters and Sethares, 2004). This is consistent with our observation that staining is highly sensitive to fixation and embedding conditions. The current study is the first to describe the cellular features of these NG-2(+) cells, which constitute two distinct populations of cells in the P10 RON: astrocytes and OPCs.

P10 RON Astrocytes can Express NG-2 and Transiently Ensheath Axons

The results show that astrocytes in the developing RON identified by unambiguous ultrastructural features or by the commonly

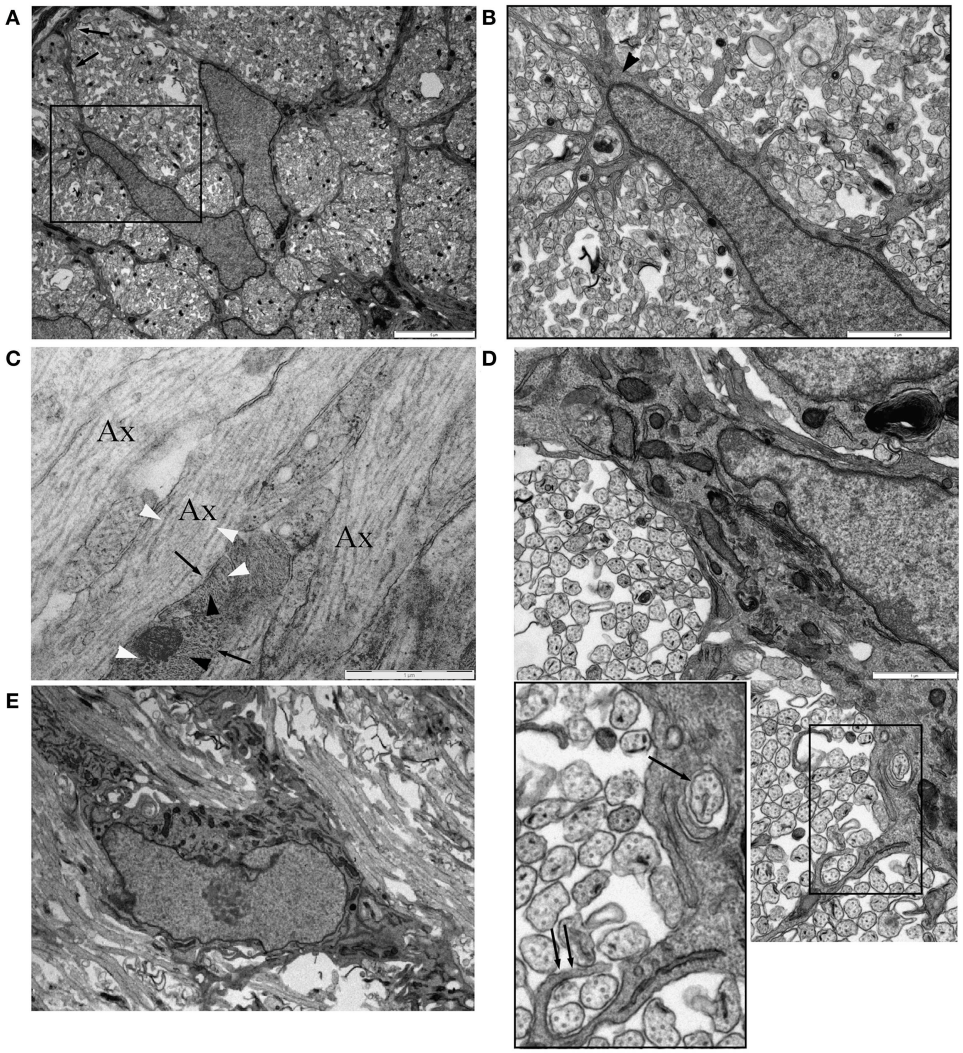

FIGURE 5 | Astrocytes in P0 RON ensheath axons. (A) Low magnification micrograph showing two neighboring astrocytes in cross-section RON. The boxed area is shown at higher power in **(B)**, revealing the highly ramified nature of the many fine processes that extend from the soma and main branches of the cell, which can be identified as an astrocyte due to occasional glial filaments (arrow head) and the contribution the cell makes to the glial limitans (**A**: arrows). **(C)** Long-section of P0 RON at high gain, showing the close apposition of pre-myelinated axons ("Ax") and astrocyte processes (arrows). Microtubules (white arrow heads) and neurofilaments are arranged longitudinally in axons while glial filaments (black arrow heads) are arranged generally transversely in astrocyte processes. **(D)** Montage showing an astrocyte ensheathing a single axon (arrow) and extending a finger process around two axons (double arrow). Boxed area shown at higher gain in the inset. **(E)** An astrocyte shown in long-section extending thick processes parallel to pre-myelinated axons.

used GFAP(+) criterion widely express the NG-2 proteoglycan. We also observed co-expression in adult RON and in gray matter, with orthogonal immuno-fluorescent confocal image stacks indicating populations of GFAP/NG-2(+) cells in both regions. This observation is consistent with studies using GFP expression driven from the GFAP promoter, which reveal duel populations of GFP bright/NG-2(−) and GFP dim/NG-2(+) cells in several brain locations (Matthias et al., 2003; Grass et al., 2004; Leoni et al., 2009). Common recombination systems employing the GFAP promoter are inefficient and drive expression in only a small proportion of astrocytes, suggesting under reporting of NG-2 expression of cells with a GFAP(+) phenotype in these animals (Casper and McCarthy, 2006). There is also convincing evidence for NG-2/GFAP co-expression in astrocytes raised in culture conditions (e.g., Levine and Stallcup, 1987; Hirsch and Bahr, 1999), and for transformation of NG-2 expressing into GFAP expressing cells in organotypic slices (Leoni et al., 2009). Recent evidence implicates the Olig2 transcription factor in regulating NG-2 cell fate switching between the astrocyte and oligodendrocyte lineages (Zhu et al., 2012). NG-2 cells have been documented as GFAP(+) in a variety of forms of injury and disease models including in the area surrounding demyelination in multiple sclerosis (Nair et al., 2008) while viral demyelination evokes proliferation of O4(+)/GFAP(+) cells in the spinal

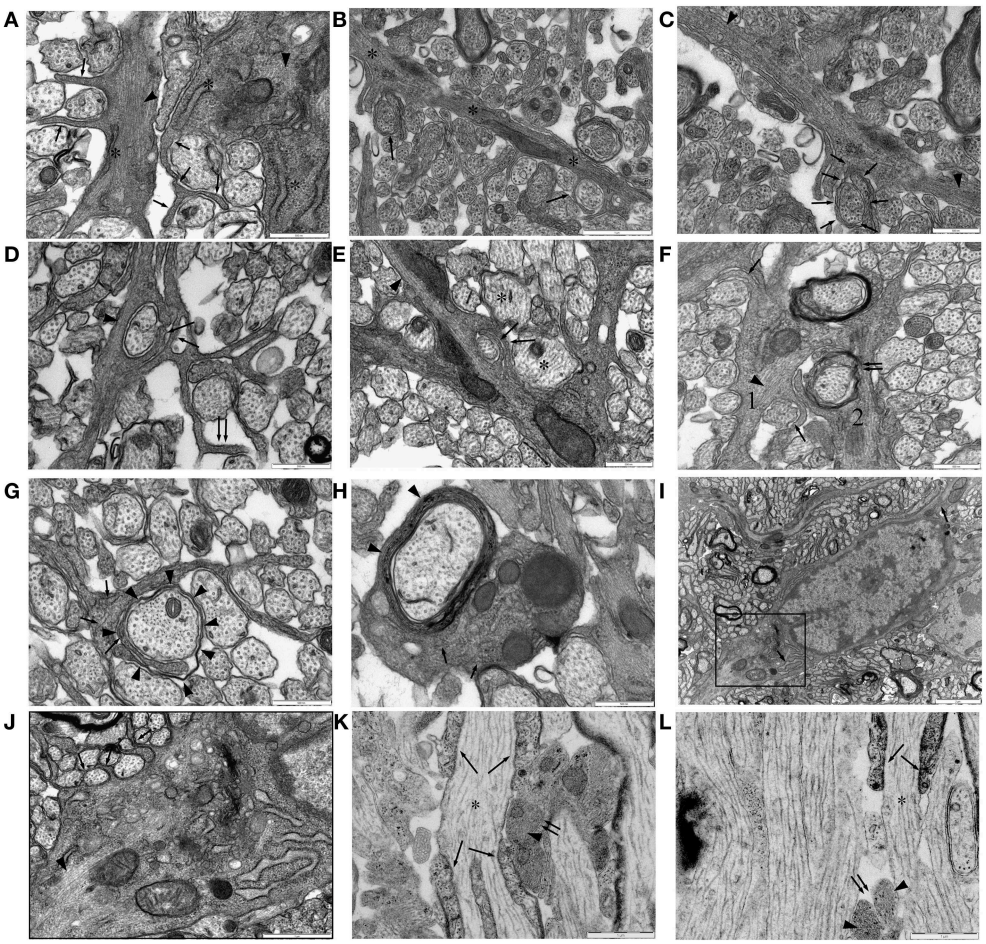

FIGURE 6 | Ensheathing astrocytes in P10 RON. (A–I) Micrographs of nerve cross-sections. (A) Two astrocyte processes identified by the presence of glial filaments (dark arrow heads, typically oriented transversely) also containing wide-bore ER ("*") and extending finger-processes between small diameter pre-myelinated axons (arrows). **(B)** An astrocyte processes oriented radially ("*") navigates between pre-myelinated axons. Ensheathing processes either partially or completely surround several neighboring small-diameter axons (arrows). **(C)** The top left section of **(B)** shown at higher gain, reveals extensive glial filaments within the main astrocyte processes (arrow heads) and cytoplasmic continuity with an ensheathing processes (arrows). **(D,E)** Examples of double-wrapping of small diameter pre-myelinated axons (dark arrows) by glial filament-containing (arrow heads) processes. Note the presence of neighboring larger-diameter pre-myelinating axons that are not ensheathed (e.g., "*"), and the "en-passent" nature of the ensheathment, with processes continuing on to navigate between neighboring axons (e.g., double-arrows). **(F)** Two glial processes. Process "1" contains glial filaments (dark arrow head) and has partially ensheathed several small axons (e.g., dark arrows). Process "2" appears to have wrapped several layers around a larger axon (double arrows) and looks similar to "1" except that it contains no obvious filaments. **(G)** A glial processes containing neurofilaments, some oriented transversely (arrows) but no glial filaments, navigates between small diameter axons and has initiated wrapping of a large axon (arrow heads). **(H)** Oligodendrocyte processes showing multiple layers of myelin (arrow head) contain neurofilaments (arrows) but no glial filaments. Note the presence of glial filaments in neighboring glial processes. **(I)** Astrocyte somata, note the wide-bore ER (arrows) and the characteristic hetero-chromatin. The boxed area is shown at higher gain in **(J)**. **(J)** Note the glial filaments (arrow head) and the finger processes originating directly from the soma ensheathing small diameter axons (e.g., arrows). **(K,L)** Examples of long-section micrographs showing early myelination of a node of Ranvier in **(K)** and a hemi-node in **(L)** ("*"). Oligodendroglial processes navigate along the axon (arrows), and glial filament-filled (arrow heads) astrocyte processes cluster adjacent to the putative nodal membrane but do not wrap around it (double arrows).

cord (Godfraind et al., 1989), and anti-galactocerebroside (GC) induced demyelination resulted in proliferation of GFAP(+) GC(+) cells (Carroll et al., 1987). Numerous GFAP(+)/MBP(+) cells are reported in a mouse model of phenylketonuria, which is associated with central hypo-mylination (Dyer et al., 1996), and there is strong evidence for astrocyte production from NG-2 cells following traumatic injury (Carmen et al., 2007), ischemia (Honsa et al., 2012) and spinal cord injury (Wu et al., 2005). The picture is not straightforward however, since NG-2 transformation into GFAP(+) astrocytes does not appear to occur after neocortical stab injury (Komitova et al., 2011), while NG-2 expressing cells derived from optic nerve explants do not express GFAP (Merchan et al., 1965; Spassky et al., 2002).

While it is often stated that immuno-labeling studies show no NG2/GFAP co-expression in the CNS, examples where partial co-expression is apparent from published data include:

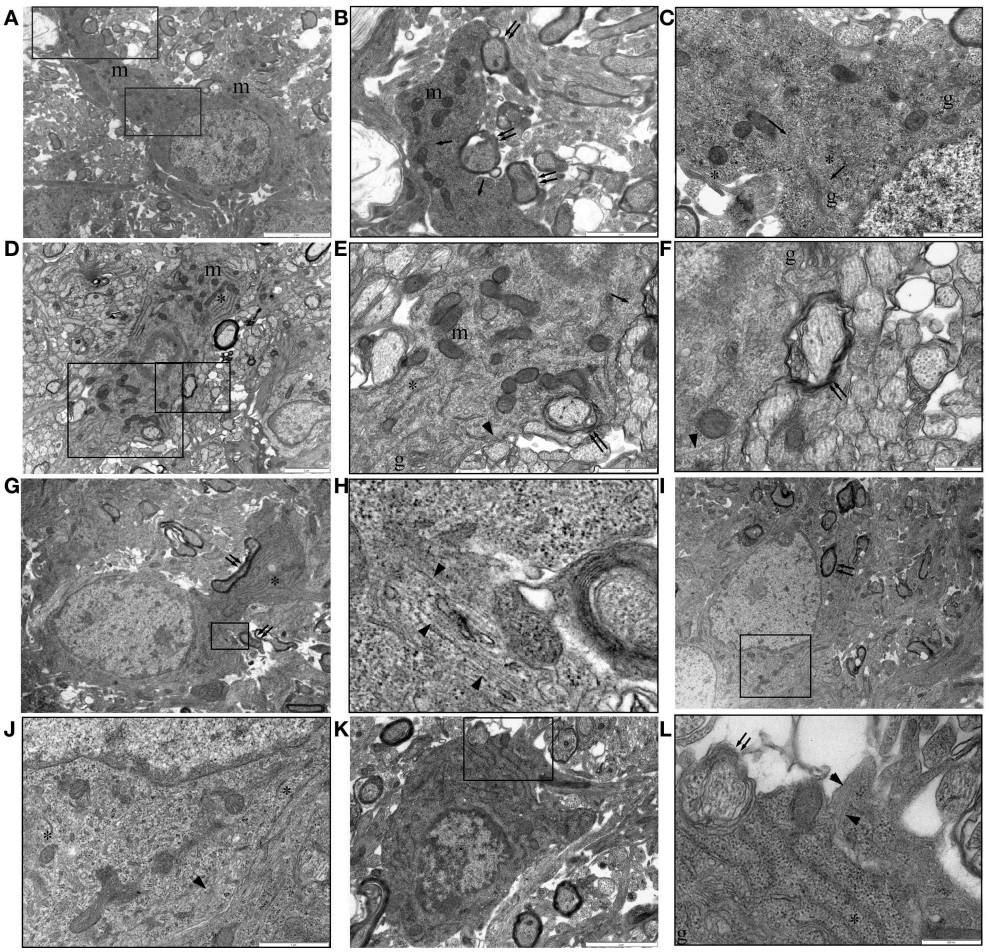

FIGURE 7 | P10 RON: Oligodendrocytes. (A–C) Typical oligodendrocyte (boxed areas in "**A**" shown at higher gain in "**B**" and "**C**"). This cell contains numerous mitochondria ("m"), golgi-apparatus ("g"), narrow-bore ER ("*"), and microtubules (arrows). A large process is actively myelinating several large-diameter axons (double arrows). **(D–F)** An oligodendrocyte with an immature phenotype (boxed areas in "**C**" shown at higher gain in "**D**" and "**E**"). Mitochondria ("m"), golgi-apparatus ("g"), and narrow-bore ER ("*") are present throughout the cytoplasm and several large diameter axons are in the early stages of myelination (double arrows). Microtubules (arrows) and glial filaments (arrow heads) are present in the cytoplasm. A large process is actively myelinating several large-diameter axons (double arrows). **(G,H)** An otherwise typical oligodendrocyte that is actively myelinated several axons (double arrows) contains a small area of glial filaments (arrow head). **(I,J)** Further example of a myelinating (double arrow) oligodendrocyte (boxed area shown at higher gain in "**J**") containing glial filaments (arrow head). In both cases, note the typical narrow-bore ER ("*") and nuclear morphology. **(K,L)** A less mature oligodendrocyte (note size and nuclear morphology) is starting to ensheath an axon (double arrows) and contains a glial filament bundle (arrow heads).

(Redwine et al., 1997, Figure 2; Hamilton et al., 2009 Figure 4C; and Nishiyama et al., 1996 Figure 7C). Examples where NG2 and GFAP co-staining appears too complex to meaningfully distinguish include (Butt et al., 1999, Figure 2 and Polito and Reynolds, 2005, Figure 1A). The current data provide strong evidence that astrocyte-type functions ascribed to NG-2(+) cells are in fact examples of NG-2(+) astrocytes. For example, the extension of NG-2(+) glial processes into the node of Ranvier is based on pre-embedded DAB I-EM that fails to preserve sufficient ultrastructural detail to reveal the presence or absence of glial filaments (Leoni et al., 2009). The presence of GFAP(+) / NG-2(+) astrocytes in the nerve and the well-documented extension of astrocyte processes into the node of Ranvier suggest that these NG-2(+) processes are astrocytic in nature.

In P0 and P10 RON, astrocyte finger processes were observed to extend around axons, on occasion depositing several layers of membrane. These processes differed from those extended by oligodendroglia, in that they frequently contained glial filaments, did not appear to discriminate in terms of axon diameter, and never produced compact myelin. Axon encirclement by astrocyte processes was not observed in adult RON or at nodes of Ranvier and must therefore be a transient phenomenon. Astrocyte finger processes have been described before (Vaughn and Peters, 1967; Lord and Duncan, 1987; Wolff, 2007), but axon wrapping of several membrane layers has not been recognized. The functional significance is not clear and there were no specific cellular inclusions within either axons or glial processes at these specializations.

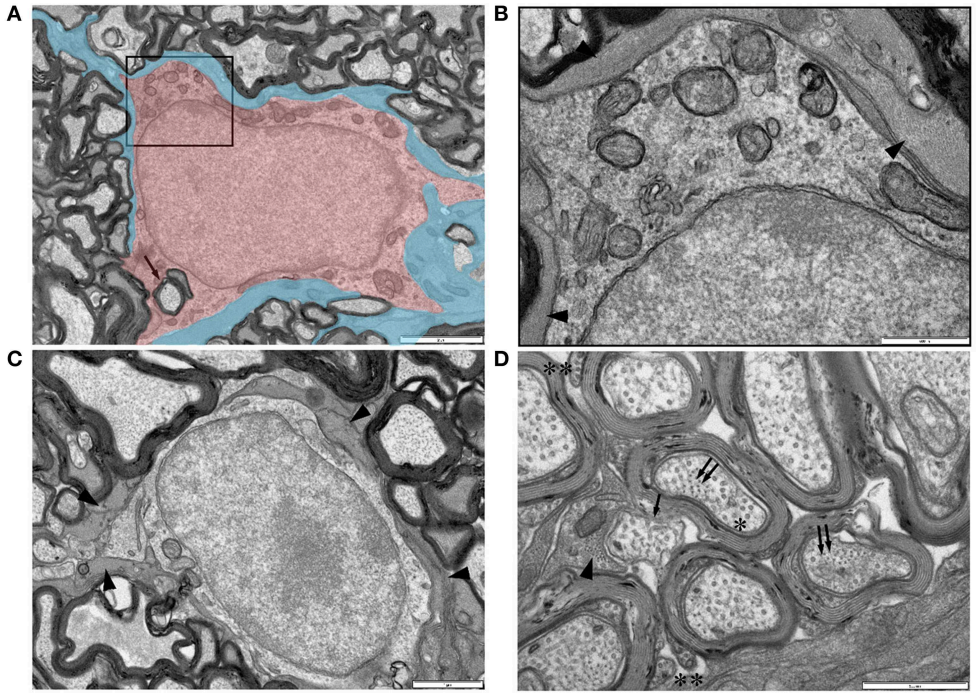

FIGURE 8 | Ultrastructural features of glia in adult RON. (A,B) An oligodendrocyte (shaded red), identified on the basis that it completely encircles a myelinated axon in which the outer membrane is contiguous with the cell (arrow) (boxed area in "**A**" is shown at higher gain in "**B**"). Note the relatively uniform chromatin throughout the large nucleus and the numerous mitochondria in the soma. The cell is completely ensheathed by astrocyte processes, identified by the presence of glial filaments (**A**: shaded blue; **B**: arrow heads). **(C)** A further example of an astrocyte ensheathed oligodendrocyte, astrocyte processes indicated by arrow heads. **(D)** High-gain cross-section micrograph showing a non-myelinated section of an axon that may be a node of Ranvier (arrow). Note the close apposition of an astrocyte process which contains glial filaments in cross-section (arrow head) that are somewhat smaller than neuro-filaments in neighboring axons (double arrows). Axon microtubules (e.g., "*") are indistinguishable from those in oligodendrocyte outer tongue processes on the outer spiral of myelin sheaths ("**").

Immature Oligodendroglia can Retain Glial Filaments

In addition to NG-2 expression in astrocytes in neonatal white matter, a number of immature oligodendrocytes were found to contain glial filaments. Considering the GFAP(+) stem cell origin of many oligodendrocytes (Malatesta et al., 2003; Casper and McCarthy, 2006), and the exceptional stability of filamentous GFAP [half-life ∼8 days (Chiu and Goldman, 1984)], the presence of a low number of glial filaments is predicted in immature oligodendroglia. There are prior reports of GFAP expression in cells of the early oligodendroglial lineage. For example, GFAP(+)/MBP(+) cells have been described in fetal human and mouse spinal white matter (Choi and Kim, 1984, 1985; Choi, 1986) and GFAP(+)/myelin oligodendrocyte-specific protein (MOSP)(+) cells in central white matter tracts (Dyer et al., 2000). Clonal analysis indicates a shared cell fate for some astrocytes and oligodendrocytes in the brain (Levison and Goldman, 1993; Zerlin et al., 2004), while OPCs transplanted into glial depleted CNS generate both oligodendrocytes and astrocytes (Franklin et al., 1995; Windrem et al., 2004). However, the current observation of glial filament-rich astrocyte encapsulation of mature oligodendrocytes will make the spatial resolution of these two glial elements difficult. Indeed, the coexistence of GFAP(+) / NG-2(+) and GFAP(+) / NG-2(−)astrocytes, the presence of glial filaments in immature oligodendroglia, the multiple layer wrapping of immature axons by astrocytes, and the encapsulation of mature oligodendrocytes by astrocytes are all phenomena that make the identification and differentiation of the two cell types problematic.

Transgenic Studies of Oligodendroglial Origins

Studies using transgenic reporter targeting to glial specific promoters paint a confused picture, with several lines of evidence suggesting that some astrocytes share a lineage with oligodendrocytes. NG-2 (Zhu et al., 2008; Komitova et al., 2009), PLP (Guo et al., 2010; Michalski et al., 2011), and PLP/Olig2 (Chung et al., 2013) promoters report GFAP immuno-reactive progeny variously in ventral brain, olfactory bulb, spinal cord, optic nerve, and cerebellum. The Olig2 promoter shows reporter expression in GFAP(+) cells throughout the brain (Dimou et al., 2008), and MBP-lacZ mice show a similar pattern of reporter/GFAP co-expression (Dyer et al., 2000). In addition to these reports of GFAP(+) progeny in oligodendroglial-specific promoter lineage cells, NG-2(+) cells have been reported in the developing spinal cord that are negative for reporter in oligodendrocyte lineage promoters such as CNP-GFP (Yuan

et al., 2002; Lytle et al., 2009). (Lytle et al., 2009) suggest that these cells are immature astrocytes because some express the astrocyte marker S-100β. Similar results are reported in reporter expressing cells throughout the brain at all post-natal points by Karram et al. (2008) using an NG2 knock in.

Contradicting these reports suggesting a shared origin for some populations of astrocytes and oligodendrocytes, PDGFαR-CreER mice show no astrocyte progeny (Rivers et al., 2008; Kang et al., 2010). PDGFαR(+) cells are also consistently found to be NG-2(+) (Nishiyama et al., 1996; Rivers et al., 2008; He et al., 2009). However, the reverse is not the case and the ratio of NG-2(+) cells that express reporter in PDGFαR-GFP mice varies between ∼30–90%, depending on location and post-natal age (Clarke et al., 2012). There are also reports of NG-2(+) cells that are PDGFαR(−) at particular points in development (Diers-Fenger et al., 2001; Liu et al., 2002; Wilson et al., 2006; He et al., 2009), although these data contrast with the work of (Rivers et al., 2008) and (Kang et al., 2010), who found 100% co-expression of both markers in the adult mouse.

The current findings of NG-2 expression in astrocytes identified by ultrastructural and immuno-label approaches confirm the non-selective nature of NG-2 expression with, as a minimum, some populations of astrocytes expressing the antigen (see Richardson et al., 2011). This observation and the data showing the presence of glial filaments in immature oligodendroglia, which may contribute to the prior reports of GFAP(+) cells in transgenic mice with oligodendroglia-specific reporter expression, emphasize the difficulty of positively identifying either astrocytes or oligodendrocytes via transgenic or immuno-labeling approaches alone.

Acknowledgments

We wish to thank William Stallcup for his generosity in sharing antibodies and Natalie Allcock for her technical assistance. This study was funded in part by the BBSRC (BB/J016969/1 to RF) and the government of Saudi Arabia (BA).

References

Alix, J. J., Dolphin, A. C., and Fern, R. (2008). Vesicular apparatus, including functional calcium channels, are present in developing rodent optic nerve axons and are required for normal node of Ranvier formation. *J. Physiol.* 586(Pt 17), 4069–4089. doi: 10.1113/jphysiol.2008.155077

Alix, J. J., and Fern, R. (2009). Glutamate receptor-mediated ischemic injury of premyelinated central axons. *Ann. Neurol.* 66, 682–693. doi: 10.1002/ana.21767

Arranz, A. M., Hussein, A., Alix, J. J., Perez-Cerda, F., Allcock, N., Matute, C., et al. (2008). Functional glutamate transport in rodent optic nerve axons and glia. *Glia* 56, 1353–1367. doi: 10.1002/glia.20703

Barres, B. A., Hart, I. K., Coles, H. S., Burne, J. F., Voyvodic, J. T., Richardson, W. D., et al. (1992). Cell death and control of cell survival in the oligodendrocyte lineage. *Cell* 70, 31–46. doi: 10.1016/0092-8674(92)90531-G

Bergles, D. E., Jabs, R., and Steinhauser, C. (2010). Neuron-glia synapses in the brain. *Brain Res. Rev.* 63, 130–137. doi: 10.1016/j.brainresrev.2009.12.003

Bergles, D. E., Roberts, J. D., Somogyi, P., and Jahr, C. E. (2000). Glutamatergic synapses on oligodendrocyte precursor cells in the hippocampus. *Nature* 405, 187–191. doi: 10.1038/35012083

Butt, A. M., Duncan, A., Hornby, M. F., Kirvell, S. L., Hunter, A., Levine, J. M., et al. (1999). Cells expressing the NG2 antigen contact nodes of Ranvier in adult CNS white matter. *Glia* 26, 84–91.

Carmen, J., Magnus, T., Cassiani-Ingoni, R., Sherman, L., Rao, M. S., and Mattson, M. P. (2007). Revisiting the astrocyte-oligodendrocyte relationship in the adult CNS. *Prog. Neurobiol.* 82, 151–162. doi: 10.1016/j.pneurobio.2007.03.001

Carroll, W. M., Jennings, A. R., and Mastaglia, F. L. (1987). Reactive glial cells in CNS demyelination contain both GC and GFAP. *Brain Res.* 411, 364–369.

Casper, K. B., and McCarthy, K. D. (2006). GFAP-positive progenitor cells produce neurons and oligodendrocytes throughout the CNS. *Mol. Cell. Neurosci.* 31, 676–684. doi: 10.1016/j.mcn.2005.12.006

Chiu, F. C., and Goldman, J. E. (1984). Synthesis and turnover of cytoskeletal proteins in cultured astrocytes. *J. Neurochem.* 42, 166–174. doi: 10.1111/j.1471-4159.1984.tb09713.x

Choi, B. H. (1986). Glial fibrillary acidic protein in radial glia of early human-fetal cerebrum—a light and electron-microscopic immunoperoxidase study. *J. Neuropathol. Exp. Neurol.* 45, 408–418. doi: 10.1097/00005072-198607000-00003

Choi, B. H., and Kim, R. C. (1984). Expression of glial fibrillary acidic protein in immature oligodendroglia. *Science* 223, 407–409. doi: 10.1126/science.6197755

Choi, B. H., and Kim, R. C. (1985). Expression of glial fibrillary acidic protein by immature oligodendroglia and its implications. *J. Neuroimmunol.* 8, 215–235. doi: 10.1016/S0165-5728(85)80064-3

Chung, S. H., Guo, F., Jiang, P., Pleasure, D. E., and Deng, W. (2013). Olig2/Plp-positive progenitor cells give rise to Bergmann glia in the cerebellum. *Cell Death Dis.* 4:e546. doi: 10.1038/cddis.2013.74

Clarke, L. E., Young, K. M., Hamilton, N. B., Li, H., Richardson, W. D., and Attwell, D. (2012). Properties and fate of oligodendrocyte progenitor cells in the corpus callosum, motor cortex, and piriform cortex of the mouse. *J. Neurosci.* 32, 8173–8185. doi: 10.1523/JNEUROSCI.0928-12.2012

Diers-Fenger, M., Kirchhoff, F., Kettenmann, H., Levine, J. M., and Trotter, J. (2001). AN2/NG2 protein-expressing glial progenitor cells in the murine CNS: isolation, differentiation, and association with radial glia. *Glia* 34, 213–228. doi: 10.1002/glia.1055

Dimou, L., Simon, C., Kirchhoff, F., Takebayashi, H., and Gotz, M. (2008). Progeny of Olig2-expressing progenitors in the gray and white matter of the adult mouse cerebral cortex. *J. Neurosci.* 28, 10434–10442. doi: 10.1523/JNEUROSCI.2831-08.2008

Dyer, C. A., Kendler, A., Jean-Guillaume, D., Awatramani, R., Lee, A., Mason, L. M., et al. (2000). GFAP-positive and myelin marker-positive glia in normal and pathologic environments. *J. Neurosci. Res.* 60, 412–426. doi: 10.1002/(SICI)1097-4547(20000501)60:3<412::AID-JNR16>3.3.CO;2-5

Dyer, C. A., Kendler, A., Philibotte, T., Gardiner, P., Cruz, J., and Levy, H. L. (1996). Evidence for central nervous system glial cell plasticity in phenylketonuria. *J. Neuropathol. Exp. Neurol.* 55, 795–814. doi: 10.1097/00005072-199607000-00005

Federoff, S., and Vernadakis, A. (1986). *Astrocytes Pt 1: Development, Morphology, and Regional Specialization of Astrocytes*. London: Academicd Press Inc.

Franklin, R. J., Bayley, S. A., Milner, R., Ffrench-Constant, C., and Blakemore, W. F. (1995). Differentiation of the O-2A progenitor cell line CG-4 into oligodendrocytes and astrocytes following transplantation into glia-deficient areas of CNS white matter. *Glia* 13, 39–44. doi: 10.1002/glia.440130105

Godfraind, C., Friedrich, V. L., Holmes, K. V., and Dubois-Dalcq, M. (1989). Dubois-Dalcq: *in vivo* analysis of glial cell phenotypes during a viral demyelinating disease in mice. *J. Cell Biol.* 109, 2405–2416. doi: 10.1083/jcb.109.5.2405

Grass, D., Pawlowski, P. G., Hirrlinger, J., Papadopoulos, N., Richter, D. W., Kirchhoff, F., et al. (2004). Diversity of functional astroglial properties in the respiratory network. *J. Neurosci.* 24, 1358–1365. doi: 10.1523/JNEUROSCI.4022-03.2004

Greenwood, K., and Butt, A. M. (2003). Evidence that perinatal and adult NG2-glia are not conventional oligodendrocyte progenitors and do not depend on axons for their survival. *Mol. Cell. Neurosci.* 23, 544–558. doi: 10.1016/S1044-7431(03)00176-3

Guo, F., Maeda, Y., Ma, J., Xu, J., Horiuchi, M., Miers, L., et al. (2010). Pyramidal neurons are generated from oligodendroglial progenitor cells in adult piriform cortex. *J. Neurosci.* 30, 12036–12049. doi: 10.1523/JNEUROSCI.1360-10.2010

Hamilton, N., Hubbard P. S., and Butt, A. M. (2009). Effects of glutamate receptor activation on NG2-glia in the rat optic nerve. *J. Anat.* 214, 208–218. doi: 10.1111/j.1469-7580.2008.01017.x

He, Y., Cai, W., Wang, L., and Chen, P. (2009). A developmental study on the expression of PDGFalphaR immunoreactive cells in the brain of postnatal rats. *Neurosci. Res.* 65, 272–279. doi: 10.1016/j.neures.2009.07.011

Hirsch, S., and Bahr, M. (1999). Immunocytochemical characterization of reactive optic nerve astrocytes and meningeal cells. *Glia* 26, 36–46.

Honsa, P., Pivonkova, H., Dzamba, D., Filipova, M., and Anderova, M. (2012). Polydendrocytes display large lineage plasticity following focal cerebral ischemia. *PLoS ONE* 7:e36816. doi: 10.1371/journal.pone.0036816

Kang, S. H., Fukaya, M., Yang, J. K., Rothstein, J. D., and Bergles, D. E. (2010). NG2+ CNS glial progenitors remain committed to the oligodendrocyte lineage in postnatal life and following neurodegeneration. *Neuron* 68, 668–681. doi: 10.1016/j.neuron.2010.09.009

Karram, K., Goebbels, S., Schwab, M., Jennissen, K., Seifert, G., Steinhauser, C., et al. (2008). NG2-expressing cells in the nervous system revealed by the NG2-EYFP-knockin mouse. *Genesis* 46, 743–757. doi: 10.1002/dvg.20440

Komitova, M., Serwanski, D. R., Lu, Q. R., and Nishiyama, A. (2011). NG2 cells are not a major source of reactive astrocytes after neocortical stab wound injury. *Glia* 59, 800–809. doi: 10.1002/glia.21152

Komitova, M., Zhu, X., Serwanski, D. R., and Nishiyama, A. (2009). NG2 cells are distinct from neurogenic cells in the postnatal mouse subventricular zone. *J. Comp. Neurol.* 512, 702–716. doi: 10.1002/cne.21917

Kukley, M., Capetillo-Zarate, E., and Dietrich, D. (2007). Vesicular glutamate release from axons in white matter. *Nat. Neurosci.* 10, 311–320. doi: 10.1038/nn1850

Leoni, G., Rattray, M., and Butt, A. M. (2009). NG2 cells differentiate into astrocytes in cerebellar slices. *Mol. Cell. Neurosci.* 42, 208–218. doi: 10.1016/j.mcn.2009.07.007

Levine, J. M., and Card, J. P. (1987). Light and electron microscopic localization of a cell surface antigen (NG2) in the rat cerebellum: association with smooth protoplasmic astrocytes. *J. Neurosci.* 7, 2711–2720.

Levine, J. M., and Stallcup, W. B. (1987). Plasticity of developing cerebellar cells *in vitro* studied with antibodies against the NG2 antigen. *J. Neurosci.* 7, 2721–2731.

Levison, S. W., and Goldman, J. E. (1993). Both oligodendrocytes and astrocytes develop from progenitors in the subventricular zone of postnatal rat forebrain. *Neuron* 10, 201–212. doi: 10.1016/0896-6273(93)90311-E

Liu, L., Korzh, V., Balasubramaniyan, N. V., Ekker, M., and Ge, R. (2002). Platelet-derived growth factor A (pdgf-a) expression during zebrafish embryonic development. *Dev. Genes Evol.* 212, 298–301. doi: 10.1007/s00427-002-0234-3

Lord, K. E., and Duncan, I. D. (1987). Early postnatal development of glial cells in the canine cervical spinal cord. *J. Comp. Neurol.* 265, 34–46. doi: 10.1002/cne.902650104

Lytle, J. M., Chittajallu, R., Wrathall, J. R., and Gallo, V. (2009). NG2 cell response in the CNP-EGFP mouse after contusive spinal cord injury. *Glia* 57, 270–285. doi: 10.1002/glia.20755

Malatesta, P., Hack, M. A., Hartfuss, E., Kettenmann, H., Klinkert, W., Kirchhoff, F., et al. (2003). Neuronal or glial progeny: regional differences in radial glia fate. *Neuron* 37, 751–764. doi: 10.1016/S0896-6273(03)00116-8

Matthias, K., Kirchhoff, F., Seifert, G., Huttmann, K., Matyash, M., Kettenmann, H., et al. (2003). Segregated expression of AMPA-type glutamate receptors and glutamate transporters defines distinct astrocyte populations in the mouse hippocampus. *J. Neurosci.* 23, 1750–1758.

Merchan, P., Bribian, A., Sanchez-Camacho, C., Lezameta, M., Bovolenta, P., and de Castro, F. (1965). Sonic hedgehog promotes the migration and proliferation of optic nerve oligodendrocyte precursors. *Mol. Cell. Neurosci.* 36, 355–368. doi: 10.1016/j.mcn.2007.07.012

Michalski, J. P., Anderson, C., Beauvais, A., De Repentigny, Y., and Kothary, R. (2011). The proteolipid protein promoter drives expression outside of the oligodendrocyte lineage during embryonic and early postnatal development. *PLoS ONE* 6:e19772 doi: 10.1371/journal.pone.0019772

Nair, A., Frederick, T. J., and Miller, S. D. (2008). Astrocytes in multiple sclerosis: a product of their environment. *Cell. Mol. Life Sci.* 65, 2702–2720. doi: 10.1007/s00018-008-8059-5

Nishiyama, A., Komitova, M., Suzuki, R., and Zhu, X. (2009). Polydendrocytes (NG2 cells): multifunctional cells with lineage plasticity. *Nat. Rev. Neurosci.* 10, 9–22. doi: 10.1038/nrn2495

Nishiyama, A., Lin, X. H., Giese, N., Heldin, C. H., and Stallcup, W. B. (1996). Co-localization of NG2 proteoglycan and PDGF alpha-receptor on O2A progenitor cells in the developing rat brain. *J. Neurosci. Res.* 43, 299–314.

Ong, W. Y., and Levine, J. M. (1999). A light and electron microscopic study of NG2 chondroitin sulfate proteoglycan-positive oligodendrocyte precursor cells in the normal and kainate-lesioned rat hippocampus. *Neuroscience* 92, 83–95. doi: 10.1016/S0306-4522(98)00751-9

Peters, A., and Sethares, C. (2004). Oligodendrocytes, their progenitors and other neuroglial cells in the aging primate cerebral cortex. *Cereb. Cortex* 14, 995–1007. doi: 10.1093/cercor/bhh060

Polito, A., and Reynolds, R. (2005). NG2-expressing cells as oligodendrocyte progenitors in the normal and demyelinated adult central nervous system. *J. Anat.* 207, 707–716. doi: 10.1111/j.1469-7580.2005.00454.x

Raff, M. C., Abney, E. R., Cohen, J., Lindsay, R., and Noble, M. (1983). Two types of astrocytes in cultures of developing rat white matter: differences in morphology, surface gangliosides, and growth characteristics. *J. Neurosci.* 3, 1289–1300.

Redwine, J. M., Blinder, K. L., and Armstrong, R. C. (1997). *In situ* expression of fibroblast growth factor receptors by oligodendrocyte progenitors and oligodendrocytes in adult mouse central nervous system. *J. Neurosci. Res.* 50, 229–237.

Reyners, H., Gianfelici de Reyners, E., and Maisin, J. R. (1982). The beta astrocyte: a newly recognized radiosensitive glial cell type in the cerebral cortex. *J. Neurocytol.* 11, 967–983. doi: 10.1007/BF01148311

Richardson, W. D., Young, K. M., Tripathi, R. B., and McKenzie, I. (2011). NG2-glia as multipotent neural stem cells: fact or fantasy? *Neuron* 70, 661–673. doi: 10.1016/j.neuron.2011.05.013

Rivers, L. E., Young, K. M., Rizzi, M., Jamen, F., Psachoulia, K., Wade, A., et al. (2008). PDGFRA/NG2 glia generate myelinating oligodendrocytes and piriform projection neurons in adult mice. *Nat. Neurosci.* 11, 1392–1401. doi: 10.1038/nn.2220

Skoff, R. P. (1990). Gliogenesis in rat optic nerve: astrocytes are generated in a single wave before oligodendrocytes. *Dev. Biol.* 139, 149–168. doi: 10.1016/0012-1606(90)90285-Q

Skoff, R. P., Price, D. L., and Stocks, A. (1976). Electron microscopic autoradiographic studies of gliogenesis in rat optic nerve. I. Cell proliferation. *J. Comp. Neurol.* 169, 291–312. doi: 10.1002/cne.901690303

Small, R. K., Riddle, P., and Noble, M. (1987). Evidence for migration of oligodendrocyte—type-2 astrocyte progenitor cells into the developing rat optic nerve. *Nature* 328, 155–157. doi: 10.1038/328155a0

Spassky, N., de Castro, F., Le Bras, B., Heydon, K., Queraud-LeSaux, F., Bloch-Gallego, E., et al. (2002). Directional guidance of oligodendroglial migration by class 3 semaphorins and netrin-1. *J. Neurosci.* 22, 5992–6004. doi: 20026573

Vaughn, J. E. (1969). An electron microscopic analysis of gliogenesis in rat optic nerves. *Z. Zellforsch. Mikrosk. Anat.* 94, 293–324. doi: 10.1007/BF00319179

Vaughn, J. E., and Peters, A. (1967). Electron microscopy of the early postnatal development of fibrous astrocytes. *Am. J. Anat.* 121, 131–152. doi: 10.1002/aja.1001210109

Vaughn, J. E., and Peters, A. (1968). A third neuroglial cell type. An electron microscopic study. *J. Comp. Neurol.* 133, 269–288. doi: 10.1002/cne.901330207

Wigley, R., and Butt, A. M. (2009). Integration of NG2-glia (synantocytes) into the neuroglial network. *Neuron Glia Biol.* 5, 21–28. doi: 10.1017/S1740925X09990329

Wilson, H. C., Scolding, N. J., and Raine, C. S. (2006). Co-expression of PDGF alpha receptor and NG2 by oligodendrocyte precursors in human CNS and multiple sclerosis lesions. *J. Neuroimmunol.* 176, 162–173. doi: 10.1016/j.jneuroim.2006.04.014

Windrem, M. S., Nunes, M. C., Rashbaum, W. K., Schwartz, T. H., Goodman, R. A., McKhann, G. II, et al. (2004). Fetal and adult human oligodendrocyte progenitor cell isolates myelinate the congenitally dysmyelinated brain. *Nat. Med.* 10, 93–97. doi: 10.1038/nm974

Wolff, J. (2007). [Electron microscopic investigations of the structure and form of astrocyte porcesses] (Ger)processes]. *Z. Zellforsch. Mikrosk. Anat.* 66, 811–828. doi: 10.1007/BF00342958

Wu, D., Shibuya, S., Miyamoto, O., Itano, T., and Yamamoto, T. (2005). Increase of NG2-positive cells associated with radial glia following traumatic spinal cord injury in adult rats. *J. Neurocytol.* 34, 459–469. doi: 10.1007/s11068-006-8998-4

Yuan, X., Chittajallu, R., Belachew, S., Anderson, S., McBain, C. J., and Gallo, V. (2002). Expression of the green fluorescent protein in the oligodendrocyte lineage: a transgenic mouse for developmental and physiological studies. *J. Neurosci. Res.* 70, 529–545. doi: 10.1002/jnr.10368

Zerlin, M., Milosevic, A., and Goldman, J. E. (2004). Glial progenitors of the neonatal subventricular zone differentiate asynchronously, leading to spatial dispersion of glial clones and to the persistence of immature glia in the adult mammalian CNS. *Dev. Biol.* 270, 200–213. doi: 10.1016/j.ydbio.2004.02.024

Zhu, M., Chen, M., Lichtler, A. C., O'Keefe, R. J., and Chen, D. (2008). Tamoxifen-inducible Cre-recombination in articular chondrocytes of adult Col2a1-CreER(T2) transgenic mice. *Osteoarthritis Cartilage* 16, 129–130. doi: 10.1016/j.joca.2007.08.001

Zhu, X., Zuo, H., Maher, B. J., Serwanski, D. R., LoTurco, J. J., Lu, Q. R., et al. (2012). Olig2-dependent developmental fate switch of NG2 cells. *Development* 139, 2299–2307. doi: 10.1242/dev.078873

Ziskin, J. L., Nishiyama, A., Rubio, M., Fukaya, M., and Bergles, D. E. (2007). Vesicular release of glutamate from unmyelinated axons in white matter. *Nat. Neurosci.* 10, 321–330. doi: 10.1038/nn1854

Conflict of Interest Statement: The authors declare that the research was conducted in the absence of any commercial or financial relationships that could be construed as a potential conflict of interest.

frontiers in Neuroanatomy

REVIEW
published: 28 May 2015
doi: 10.3389/fnana.2015.00070

Visible rodent brain-wide networks at single-neuron resolution

*Jing Yuan[1,2], Hui Gong[1,2], Anan Li[1,2], Xiangning Li[1,2], Shangbin Chen[1,2], Shaoqun Zeng[1,2] and Qingming Luo[1,2]**

[1] Britton Chance Center for Biomedical Photonics, Wuhan National Laboratory for Optoelectronics-Huazhong University of Science and Technology, Wuhan, China, [2] Key Laboratory of Biomedical Photonics of Ministry of Education, College of Life Science and Technology, Huazhong University of Science and Technology, Wuhan, China

There are some unsolvable fundamental questions, such as cell type classification, neural circuit tracing and neurovascular coupling, though great progresses are being made in neuroscience. Because of the structural features of neurons and neural circuits, the solution of these questions needs us to break through the current technology of neuroanatomy for acquiring the exactly fine morphology of neuron and vessels and tracing long-distant circuit at axonal resolution in the whole brain of mammals. Combined with fast-developing labeling techniques, efficient whole-brain optical imaging technology emerging at the right moment presents a huge potential in the structure and function research of specific-function neuron and neural circuit. In this review, we summarize brain-wide optical tomography techniques, review the progress on visible brain neuronal/vascular networks benefit from these novel techniques, and prospect the future technical development.

Keywords: neural circuit, cell type, vasculature, labeling, brain-wide optical imaging, single axon

OPEN ACCESS

Edited by:
Javier DeFelipe, Cajal Institute, Spain

Reviewed by:
Jose L. Lanciego, University of Navarra, Spain
Francesco S. Pavone, University of Florence, Italy

****Correspondence:***
Qingming Luo, Britton Chance Center for Biomedical Photonics, Wuhan National Laboratory for Optoelectronics-Huazhong University of Science and Technology, 1037 Luoyu Rd., Wuhan 430074, China
qluo@mail.hust.edu.cn

Received: *08 March 2015*
Accepted: *13 May 2015*
Published: *28 May 2015*

Citation:
Yuan J, Gong H, Li A, Li X, Chen S, Zeng S and Luo Q (2015) Visible rodent brain-wide networks at single-neuron resolution. Front. Neuroanat. 9:70. doi: 10.3389/fnana.2015.00070

Introduction

The brain is the most sophisticated, complex and significant organ in the bodies of humans and other higher organisms. The brain is the seat of action and cognition; however, its function is hindered by various neurological and mental diseases. Thus far, the structure and functions of the mammalian brain remain largely unknown. Elucidating the structure and functions of the brain is one of the most challenging research subjects since the Human Genome Project (Petreanu et al., 2009). Characterizing the structure of the brain at high resolution is crucial for understanding its functions and dysfunction (Koch and Reid, 2012).

The brain consists of multiple fine components. The human brain generally contains approximately one hundred billion neurons and a greater number of glial cells, as well as blood vessels that travel through the densely packed cells to form extremely complex neurovascular networks. These blood vessels provide neurons and glia with energy and nutrition and clear away waste. For example, once their blood supply is blocked, neurons cease to produce action potentials within seconds and die of irreversible damage within minutes. The sizes of these brain components vary greatly: the diameter of a typical neuron is approximately 10–30 μm, and the diameters of small cells and capillaries range from 2 to 5 μm (Petersen et al., 2003; Tsai et al., 2009), whereas the diameter of a common neurite projected from soma reaches the submicron level, approximately 1 μm or less (Sun et al., 2014). Therefore, to reconstruct neural and neurovascular networks at single-neuron resolution, the imaging voxel size of the detection system should not exceed one cubic micron, which guarantees the true representation of the brain-wide neuronal and vascular systems.

The brain's functions, including the generation of thoughts, emotions, perceptions, actions and memories, rely primarily on interconnected groups of neurons, called neuronal networks rather than on individual neurons. The brain has two types of neural circuits: local circuits, which neurites inhabit in the same brain area, and distant circuits, which neurites projecting cross long-range distance within different brain areas. Distant neural circuits possibly project from the cerebral cortex to neurons as far away as the spinal cord, whose input and output may travel throughout the whole brain (Jbabdi and Behrens, 2013). Similar to the integrated circuits of a microchip, local neural circuits are connected by the wire-like projections of long-distance neural circuits. Cooperation between local and distant circuits is vital to advanced neural functions (Miyamichi et al., 2011). Due to the interconnected, long-range nature of many neuronal networks, visualization of the brain's structure and function must be conducted over a large volume, preferably brain-wide (Osten and Margrie, 2013).

Because of the differences between individual brains, the ideal of visualizing neural pathways and the neurovascular networks is to simultaneously detail the fine morphology of cells and blood vessels in regions of interest in high resolution. However, in higher mammals, complicated neural circuits are composed of tens of billions of neurons, rendering traditional imaging methods inadequate (Bassett and Gazzaniga, 2011; Amunts et al., 2013). Even the fine cellular-vascular architecture of the comparatively less complicated mouse brain and the interconnections within its regions remain unclear (Silvestri et al., 2013).

Using multiple labeling and imaging techniques, several brain research projects have sought to reconstruct at high resolution the fine cellular-vascular morphology of regions of interest in mammals, particularly rodents, and to provide a visualization of neural pathways and the neurovascular networks. Optical microscopy techniques, combined with advanced labeling methods, provide the best access for exploring the brain-wide neuronal/vascular networks at single-neuron resolution. Here, we review the recent advances with a focus on two aspects: (1) techniques for the brain-wide optical tomography and the matchable labeling for neuronal/vascular networks; and (2) application of brain-wide labeling and optical imaging, which include neuronal morphology, long-distance projection of the specific labeled neurons, and cytoarchitecture and vascular networks. Challenges are also discussed in the final part of prospectives.

Brain-Wide Labeling and Optical Imaging

Labeling the Brain for Optical Imaging

Owing to a lack of optical contrast, nervous tissue must be labeled before imaging by optical microscopy. Golgi silver staining, which was invented by Golgi and improved by Ramon y Cajal one hundred years ago, has been recognized as one of the most elegant and effective methods for distinguishing the morphology of neurons (Sotelo, 2003). Since then, many methods have been developed for staining the cytoarchitecture of the brain such as Nissl staining, in which neuronal somas are visualized by staining the rough endoplasmic reticulum (or "Nissl bodies") (Windhorst and Johansson, 1999). To study the structure and organization of neural circuits and neurovascular networks, neuronal tracers were developed to ascertain the cell population and to analyze the neuronal anatomical connections (Garey, 1999). Standard neuronal tracers can label the entire structure of the neuron and circuit but fail to identify the interconnected cell types (Miyamichi et al., 2011). Histochemical techniques such as immunolabeling can label specific cell types but are unable to label deep structures in the intact brain (Shi et al., 2011). Therefore, histochemistry is typically performed on cultured neurons, tissue slices or superficial layers of *in vivo* tissue. To study neural circuits spanning vast volumes, these conventional methods have to be improved to label the whole brain or tissue uniformly. Luo's group modified the Golgi-Cox (Zhang et al., 2011) and Nissl (Wu et al., 2014) staining methods and first achieved uniform whole-brain staining of rodents. Recently, whole brain immunohistochemistry has been developed to immunolabel deep tissue for volume imaging and applied to embryonic and adult brains (Chung et al., 2013; Renier et al., 2014). Golgi-Cox or Nissl staining are usually simpler and cheaper, but nonspecific for different neuronal types. Since Golgi staining is known that axons of the randomly stained neurons (less than 5%) are not always completely labeled (Binzegger et al., 2010), it is better suitable to study dendritic arbor morphologies than axonal projections. On the other hand, immunolabeling and transgenetic labeling allow specifically targeting selected neuronal populations, although with a payback of higher costs and complexity.

Transgenic and fluorescent probe labeling techniques make it possible to visualize neurons of a specific subtype and to trace neurite projections and transsynaptic circuits (Markram et al., 2004; Luo et al., 2008; Madisen et al., 2010; Huang and Zeng, 2013). To label diverse neurons in different regions simultaneously, the use of multiple fluorescent probes has been introduced to neural labeling and imaging (Shaner et al., 2005; Livet et al., 2007; Dumas et al., 2015). Neuroanatomy has been revolutionized by genetic dissection (Luo et al., 2008), which enables the systematic mapping and classification of both long-distance and local connections. However, due to the complexity of whole-brain imaging procedures, fluorescent signals are likely to be quenched, thereby compromising the detection of weak connections (Chung et al., 2013; Gong et al., 2013; Renier et al., 2014; Susaki et al., 2014; Yang et al., 2014). Efforts are being made to find a way of preserving this fluorescence based on the fact that GFP and YFP fluorescence can be recovered in an alkaline environment (Heim et al., 1995; Robey et al., 1998). Xiong et al. found that the loss of GFP or YFP fluorescence during resin embedding results from the protonation of the chromophore (Xiong et al., 2014). This result provides theoretical guidance for conserving and recovering weak fluorescence used to reveal neural circuits.

Brain-Wide Optical Tomography

The imaging depth of traditional optical microscopy is restricted by the absorption and scattering of light in tissue. Normally, an imaging depth of only a few hundred microns can be reached

by optical microscopes. The application of traditional optical microscopy is thus limited to the imaging of brain slices or of the superficial layer of the cortex. To achieve both high voxel resolution and a large detection range in three dimensions, optical microscopy and histology have to be combined to acquire serial images, from which 3D reconstructions of the brain structure can be generated. To obtain an optical tomograph of a whole rodent brain that spans several centimeters, many parameters have to be considered and balanced, such as isotropic resolution, imaging range, imaging time, robustness of the imaging system, auto-registration of the images, and expenses, et al. Several approaches have been developed, such as light-sheet illumination microscopy (LSM), serial two-photon tomography (STP) and micro-optical sectioning tomography (MOST).

Optical Tomography by Light-Sheet Illumination with Chemical Clearing

Dodt et al. combined LSIM (Siedentopf and Zsigmondy, 1902) and chemical clearing (Spalteholz, 1914), two 100-year-old techniques, to achieve fast imaging of transparent intact mouse brain (Dodt et al., 2007). They named it Ultramicroscopy. Side illumination is employed in parallel, and only a thin layer of brain tissue perpendicular to the optical imaging light path is illuminated. Thus, the interference from out-of-focus background light is eliminated. With this illumination scheme, wide-field imaging can be used to acquire section images at a high rate. Three-dimensional imaging of the whole brain sample can be achieved by moving the sample or by translating the illumination beam.

In recent years, many optical clearing techniques have been invented to generate transparent brain tissue so that the illumination light can pass through the entire sample. Methods including Scale (Hama et al., 2011), CUBIC (Susaki et al., 2014), SeeDB (Ke et al., 2013), 3DISCO (Ertürk et al., 2012a,b, 2014), iDISCO (Renier et al., 2014), and ClearT (Kuwajima et al., 2013) make the brain transparent by immersion in a clearing reagent. The scatters in fixed tissues are exchanged with optical clearing reagents, and then the refractive indexes of tissues become uniform to reduce the amount of light scattering. While techniques such as CLARITY (Chung and Deisseroth, 2013; Chung et al., 2013; Tomer et al., 2014) and other similar solutions (Yang et al., 2014) employ electrophoresis to remove lipids from the tissue, making the tissue transparent.

Imaging intact transparent mouse brain enables to avoid mechanical process during imaging (Kim et al., 2013). The imaging speed of wide-field LSM is much faster than those of point-scanning brain-wide optical imaging techniques. With LSM, the brain can be imaged multiple times. However, even with chemical clearing, it is still a big challenge to obtain a brain-wide tomograph with a consistent voxel resolution since the brain cannot be completely transparent, which may lead to a dramatic drop of imaging contrast and resolution somewhere deep in the brain. Structural illumination (Kalchmair et al., 2010), confocal slit detection (Silvestri et al., 2012) and a virtual-slit effect of sCMOS camera (Tomer et al., 2014) had been introduced to significantly increase image contrast also deep inside the sample. But these attempts fail to improve the axial resolution of LSM, which still limited to 10 μm. Therefore, LSM hasn't been suitable for distinguishing and tracing axons currently and more efforts should be focused on the improvement of axial resolution.

Optical Tomography by Optical Sectioning with Sequential Tissue Removal

Another way to achieve deep brain optical imaging is to remove imaged brain tissue before imaging at each step. Only the superficial layer of tissue needs to be imaged, thus avoiding the limitation posed by light penetration depth. An optical sectioning scheme is used to restrain the interference from an out-of-focus background.

Tsai et al. proposed an all-optical histology (AOH) method, combining laser tissue ablation by amplified ultrashort laser pulses with two-photon excitation imaging by unamplified pulses (Tsai et al., 2003). Iterative ablation and imaging of samples lasted until the data acquisition ended. However, this method has not been demonstrated to visualize whole brain.

Ragan et al. developed the STP method, which utilizes a microtome and a two-photon excitation microscope based on mechnical scannings (Ragan et al., 2007, 2012). In the latest version, mouse brain samples were embedded in agarose and fixed to a motorized three-dimensional translation stage. At each step, two-photon imaging of the superficial layers of the tissue was performed in mosaic splicing mode. After imaging, the sample was translated to the vibratome, and the imaged layers of tissue were removed. This process was serially repeating. Simple agarose-embedded sample preparation and short data acquisition due to sparse axial sampling make STP become a useful tool for mesoscale anatomy. STP has demonstrated to obtain the specific cell-type distribution in the olfactory bulbs of transgenic mouse by imaging *z*-stack of 800 optical sections (2.5 μm *z* spacing) (Ragan et al., 2012). The image datasets covering the entire mouse brains (over 1000 samples) were acquired by STP by imaging single optical sections at a coarse axial sampling manner (50 or 100 μm *z* spacing) (Ragan et al., 2012; Oh et al., 2014).

Zheng et al. adopted another imaging strategy to increase the imaging speed of brain-wide optical tomography (Zheng et al., 2013). Acoustic-optic deflector (AOD) and sample stage had been used for fast line scanning and continuous sample motion of high-speed automated two-photon excitation microscope, respectively, which resulted in about 2.5-fold faster than the conventional mosaic imaging one (Ragan et al., 2012) using similar optical parameters. AOD enables to improve the prolonged system stability due to it is a kind of inertia-free and non-mechanical scanning device.

All of these three mentioned methods employed two-photon excitation microscopy to acquire optical sections and determine axial resolution. Two-photon excitation imaging can penetrate relatively deep into the tissue; thus, some influence of surface roughness caused by slicing on image quality can be avoided by imaging at a certain depth beneath the surface. Current point-scan serial imaging mode of two-photon excitation determines the imaging speed. Continuous running of several days for each full-volumetric whole-brain dataset acquisition asks a high demand of the prolonged system stability. Brain-wide optical

tomography based on optical section has a great potential to be improved.

Optical Tomography by Imaging with Simultaneously Ultrathin Physical Sectioning

An alternative methodology of axial resolution improvement is to employ physical rather than optical sectioning approaches. Array tomography has been demonstrated to obtain ordered ultrathin resin-embedded sections and corresponding images. However, this approach needs manual image registration. The optimal idea is to section and image simultaneously and automatically to avoid extra registration.

McCormick et al. invented a knife-edge scanning microscopy (KESM), which features a knife-collimator assembly of providing illumination as well as the means to cut individual sections of tissue (McCormick et al., 2004; Mayerich et al., 2008). Although KESM has been tried to perform large-scale imaging of the mouse brain with a stair-step cutting, several obstacles have to be overcome before obtaining high-quality and high-resolution brain-wide image data, such as the non-uniform deformation of the fine structure, unpredictable chatter during the physical sectioning, the matched sample preparation, and so on.

Luo's group developed a novel combination of the microscopic optical imaging and sectioning to obtain tomography (MOST) of a whole mouse brain with micrometer resolution (Li et al., 2010). MOST decouples the illumination and cutting and makes the physical sectioning more easily free of chatter. The tomographic sectioning mode in MOST is carried out column-by-column in the same layer to provide a short and constant immersion time for each layer, which avoids non-uniform deformation of the brain structure. Both KESM and MOST use the ultrathin physical sectioning to achieve uniform and high axial resolution. The specific design of MOST ultimately simplifies the optical imaging system and makes it possible to establish a prolonged stable and robust equipment since each part can be easily optimized. Combining with various traditional histological staining methods, such as Golgi (Li et al., 2010) and Nissl staining (Wu et al., 2014), MOST enabled to explore the detailed 3D map of different components in the brain at 1-micron voxel resolution. Coupled with a confocal laser scanning fluorescence imaging, a fluorescence MOST (fMOST) system has been reported. Combining a novel resin-embedding method for maintaining fluorescence, the fMOST has shown the ability to image a fluorescent protein transgenic whole mouse brain at a one-micron voxel resolution, and the long-distance pathways were traced minutely and without interruption for the first time (Gong et al., 2013). The MOST and its series have shown the robustness of consistent high-resolution imaging over a large range (Parekh and Ascoli, 2013), and provided a means to traversal each voxel in the entire brain, rather than sample limited numbers of sections.

These techniques enable brain-wide imaging at unprecedented resolution and have created opportunities for exploring and understanding the structure and functions of neuronal networks across the whole brain; these opportunities are of great interest to neuroscientists. The requirements of neuroscientists for new technologies have expedited the development of whole-brain optical imaging methods quickly from the laboratory to the user. Products employing the above-mentioned techniques have been commercialized [e.g., LSM (by Zeiss or Lavision Biotech), STP (by TissueVision) and MOST (by OeBio)]. Developments in whole-brain optical imaging will open a new chapter in neuroscience research.

Progress in Characterizing Visible Brain-Wide Networks

Cell Type

The brain's complexity is exemplified by its variety of neuronal cell types (Huang, 2014; Mitra, 2014). Different types of neurons can be considered analogous to the various components of integrated electrical circuits. To understand the path of information flow in a neural circuit, the first questions we must address are as follows: How many "components" are in the brain? Despite its importance, a reasonable classification scheme for neuronal subtypes has not emerged, even after more than 100 years of debate. What is the distribution of axonal arborizations in different brain sub-regions? How many ascending and descending axons do individual neurons have? What are the relative locations of the axonal and dendritic arbors? These remain basic questions of neuroscience. Therefore, a fundamental goal of neuroscience is to acquire fine structural and positional descriptions of different neurons and to define their cell type and distribution.

Morphology

The diversity of neuronal subtypes is first reflected in their morphology. Whether in different brain areas or in the same brain area, the vast variation in neuronal morphologies provides an abundance of natural distinctions that facilitate neuron classification. Criteria for the classification of neuron subtypes remain in dispute (DeFelipe et al., 2013); however, morphology is widely considered one of primary criteria of cell type (Svoboda, 2011). The intact morphology of a neuron enables a dissection of its information input and output, and its spatial range and location can suggest its role in neural circuits, which determines specific function of a neuron in different brain functions (Lichtman and Denk, 2011; Parekh and Ascoli, 2013).

The imaging of neuronal morphology still currently uses traditional sectioning methods. Digital methods for the reconstruction of neuronal morphology have shifted scientists away from manually drawing to either interactively or automatically tracing (Parekh and Ascoli, 2013). Sakmann's group systematically described excitatory neurons in the barrel cortex and interneurons in L2/3 in adult rats using the traditional method (Helmstaedter et al., 2009; Oberlaender et al., 2011, 2012). In addition, Markram's group studied the diversity of somatosensory cortical interneurons and neurons in L1 based on neuronal morphology (Markram et al., 2004; Parekh and Ascoli, 2013; Muralidhar et al., 2014). NeuroMorpho.Org has collected published reconstructions of neuronal morphology contributed

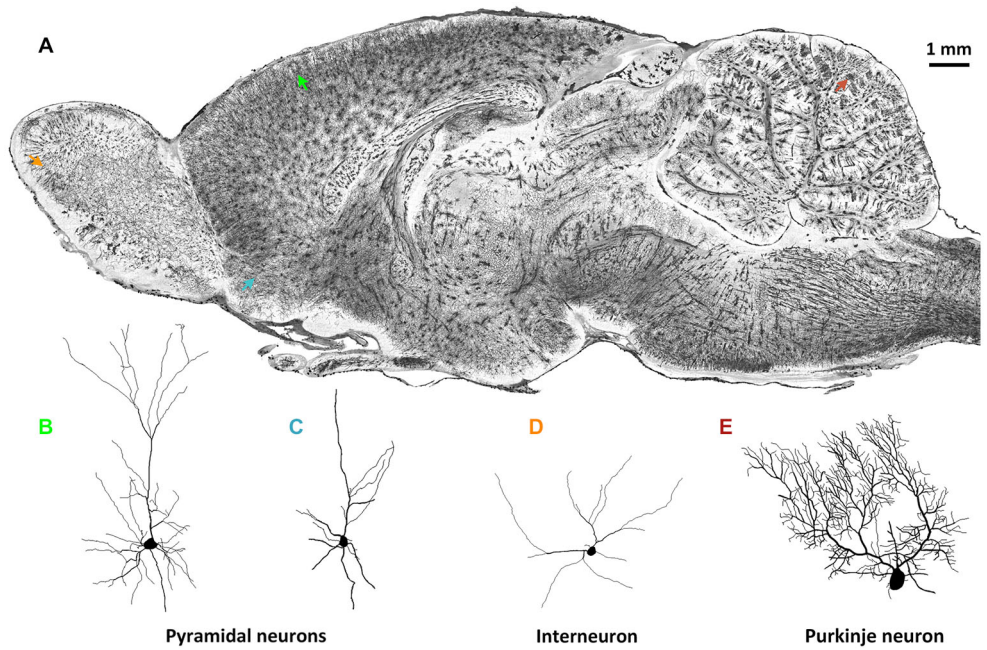

FIGURE 1 | Whole-brain imaging of rat neuronal morphology with Golgi staining (Vbn, 2015). **(A)** A sagittal image of a 200 μm thickness projection from a whole-brain imaging dataset acquired by MOST method (Li et al., 2010). Arrowheads in different colors in **(A)** indicate individual neurons. **(B)** Pyramidal neuron in somato motor cortex (green in **(A)**); **(C)** Pyramidal neuron in anterior olfactory nucleus of olfactory bulb (blue); **(D)** Interneuron in glomerular layer of olfactory bulb (orange); **(E)** Purkinje cell in cerebellum (brown).

by more than 100 labs and has set up the largest open-access neuronal three-dimensional reconstruction database thus far. However, the manual acquisition approach only suits a small number of studies involving important neuronal subtypes. Acquiring the morphology of all cell types in the brain by a manual approach is an impossible task.

Brain-wide optical tomography capable of acquiring data on the fine morphological characteristics of neurons in the intact rodent brain would be helpful for the expansion of the current neuron morphology database. Because brain-wide optical tomography avoids the irreversible physical damage to neuronal morphology caused by the limited thickness of traditional histology sections, high-resolution brain-wide optical imaging would enable the acquisition of the 3D morphology of single intact neurons. MOST (Li et al., 2010) allowed the reconstruction of detailed cell morphology in the whole brain not only of mouse but also of rat using Golgi staining. **Figure 1** shows the detailed morphology of multiple types of neurons in different brain regions in the same rat brain by the MOST method (Li et al., 2010). 3D imaging and reconstruction of neurons of various shapes in the whole brain would be helpful for codifying new morphology standards, which would permit a more systematic classification of neurons.

Cell Type-Specific Distributions

To analyze the organization and signal processing mechanisms of the nervous system, knowledge of the spatial distributions of specific cell types is fundamental. The distributions of specific neuronal population, such as acetyl cholinergic (Armstrong et al., 1983), dopaminergic (Björklund and Dunnett, 2007) and serotonergic neurons (Fu et al., 2010; Russo and Nestler, 2013), have been analyzed using traditional methods; however, these studies were limited primarily to local areas. Recently, the projection, location and distribution of specific subtypes of interneurons (Weissbourd et al., 2014) and of serotonergic neurons (Pollak Dorocic et al., 2014) have been characterized in the mouse brain with manually sectioning and imaging. To facilitate mapping of whole brain distribution patterns, automatic imaging techniques have been combined with cell type-specific markers. Using these approaches, we can investigate the distribution and specific connections of neurons at the bulk volume level. For example, STP (Ragan et al., 2012), fMOST (Gong et al., 2013) and LSIM techniques (Chung et al., 2013) have revealed the distribution of Thy-1 neurons (expressed GFP or YFP) and the projection patterns of their neuritis (**Figure 2**). In addition, the whole-brain distribution of somatostatin-positive interneurons (Taniguchi et al., 2011) was revealed. These methods have provided an unprecedented level of information on the spatial distribution of specific neuronal types and of circuits, which is necessary to further understand the functions of the central nervous system.

Mesoscale Brain-Wide Neuroanatomical Connectivity

Complex brain functions are constrained and defined by neural circuits formed by numerous interconnected neural cells.

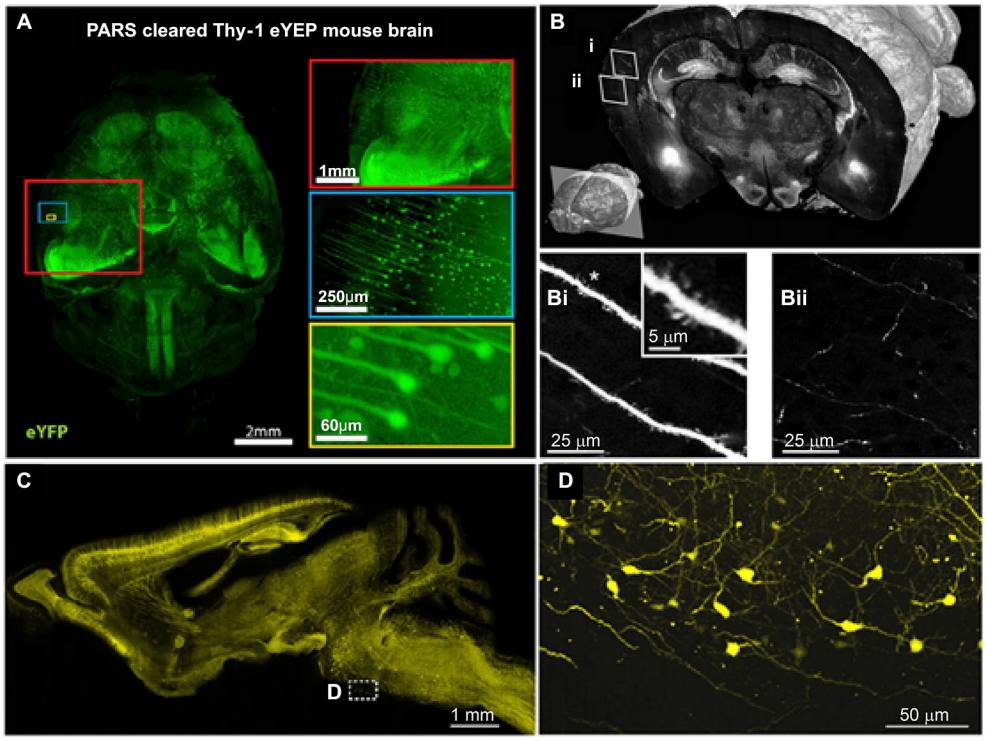

FIGURE 2 | Brain-wide distribution of Thy-1 neurons imaged by LSM, STP and fMOST. **(A)** Whole-brain image (z = 6 mm) of adult Thy1-eYFP mouse after PARS clearing for 10 days. The boxes on the right show high-magnification images of indicated areas. PARS, perfusion-assisted agent release *in situ*. Taken from Yang et al. (2014). **(B)** 3D view of a coronal section of the GFP brain. Lower left: position of the coronal plane in the imaged mouse brain (approximately 2.5 mm from Bregma). Enlarged views demonstrating visualization of dendritic spines **(Bi)** and fine axon fibers **(Bii)**. Adapted from Ragan et al. (2012). **(C)** Sagittal image reconstructed from a stack of virtual sagittal sections (thickness: 50 μm) of an adult Thy1-eYFP mouse brain. **(D)** Higher magnification views of some soma and fine neurites in the white box of **(C)**. **(C)** and **(D)** redrawn from the imaging dataset published in Gong et al. (2013).

Thus far, knowledge of intricate neuroanatomical circuitry has remained extremely sparse. To this end, a project dubbed the "mesoscale brainwide neuroanatomical connectivity of the mouse" has been undertaken by the neuroscience community (Bohland et al., 2009).

Brain Region-Level Connectivity

In recent decades, both fMRI and diffusion tensor imaging have promoted our understanding of the structure and functions of the nervous system at the macroscale. The BOLD signal defined functional connectivity and diffusion tensor determined that white matter tracts represent an indirect description or gross representation of neural circuits, missing finer-scale information such as the locations of axons, dendrites and synapses (Silasi and Murphy, 2014). In the 21st century, a combination of advanced anatomical tract tracing and optical microscopy has provided powerful tools for dissecting neural circuits (Osten and Margrie, 2013). Initially, the study of neural circuits in rodents primarily focused on local circuits or on specific functional systems in small regions (Petersen et al., 2003). Zingg et al. applied anterograde and retrograde tracers and section imaging to a systemic study of intracortical connections. They revealed that the whole mouse cortex consists of 8 subnetworks with unique topologies (Zingg et al., 2014). However, the manual sectioning and reconstruction of the brain is time consuming and labor intensive, making it unsuitable for the study of brain-wide neural circuits.

The invention of automatic whole brain imaging has allowed large-scale and systematic studies of detailed neuronal connections between different brain regions. For example, Ragan et al. exploited the STP technique to acquire high-throughput fluorescence imaging (Ragan et al., 2012). This method supplies an efficient tool for routine neuroanatomy studies in mouse models. Oh et al. made advantage of automation and the high-throughput nature of STP to trace axonal projections throughout the brain from defined regions, generated a whole-brain connectivity matrix and demonstrated the network properties to be small-world and scale-free (Oh et al., 2014). All the 469 injected brains and 295 non-overlapping target regions were investigated to make quantitative analysis on connections. This study presents an unprecedented region-level connectivity in different regions across whole brain (Oh et al., 2014).

Neurite-Level Connectivity

Neuroscientists have been attempting to map detailed neural circuits to better understand the relationship between the

structure and functions of the brain (Lichtman and Denk, 2011). For example, researchers have found that many olfactory sensory neurons in the mouse are characterized by the expression of one of approximately 1,400 odorant receptors defined by genes (Ghosh et al., 2011). A genetically defined class of olfactory sensory neurons has convergent axonal projections to two glomeruli at mirror symmetric locations in the olfactory bulb, forming an odor map (Miyamichi et al., 2011). However, axons from individual glomeruli project diffusely to the olfactory cortex without an apparent spatial order (Sosulski et al., 2011). The long-range connections from the olfactory bulb to the olfactory cortex remain unclear and are an impediment in the study of olfaction (Miyamichi et al., 2011).

Similar to integrated electrical circuits, which are composed of different components, neural circuits consist of extensively interconnected neuronal cells. To study the information flow within neural circuits, the complete structure of neurons, together with axons and dendrites, in the whole brain must be resolved at high resolution. This study requires single-neuron resolution imaging of the whole brain. The STP method is capable of good resolution in the transverse x-y plane but has a large interval between axial sections, leading to incomplete 3D datasets, which cannot be used to decipher real pathways and connections within neural circuits. Even with the advancement of optical clearing, LSM cannot image clear and complete long-range neural circuits deep in the mouse brain.

In 2013, the fMOST method had demonstrated the first long-range tracing of individual axons in the mouse brain (Gong et al., 2013; Osten and Margrie, 2013). These findings not only confirmed previously discovered pathways but also confirmed several unreported, putative projection pathways. Thus far, this has been a valuable technique to provide sufficiently intricate data describing the neural circuits in an arbitrary region of the mouse brain. A representative projection pattern of homotopic axons originating from the primary motor cortex is shown in **Figure 3**. Hopefully, the combination of fMOST and newly developed trans-synaptic tracing methods will provide new insight into acquiring long-range and trans-synaptic tracking of specific-labeled neural circuits. Without doubt, these methods will accelerate the characterization of information flow in brain circuits.

Based on the automation of advanced optical microscopy, the current study of mesoscale brain-wide neuroanatomical connectivity of the mouse provides greater benefits than conventional manual neuroanatomy. A more complete knowledge of the local and long-range connections exhibited by neural circuits will help us to understand fundamental brain functions and neural diseases.

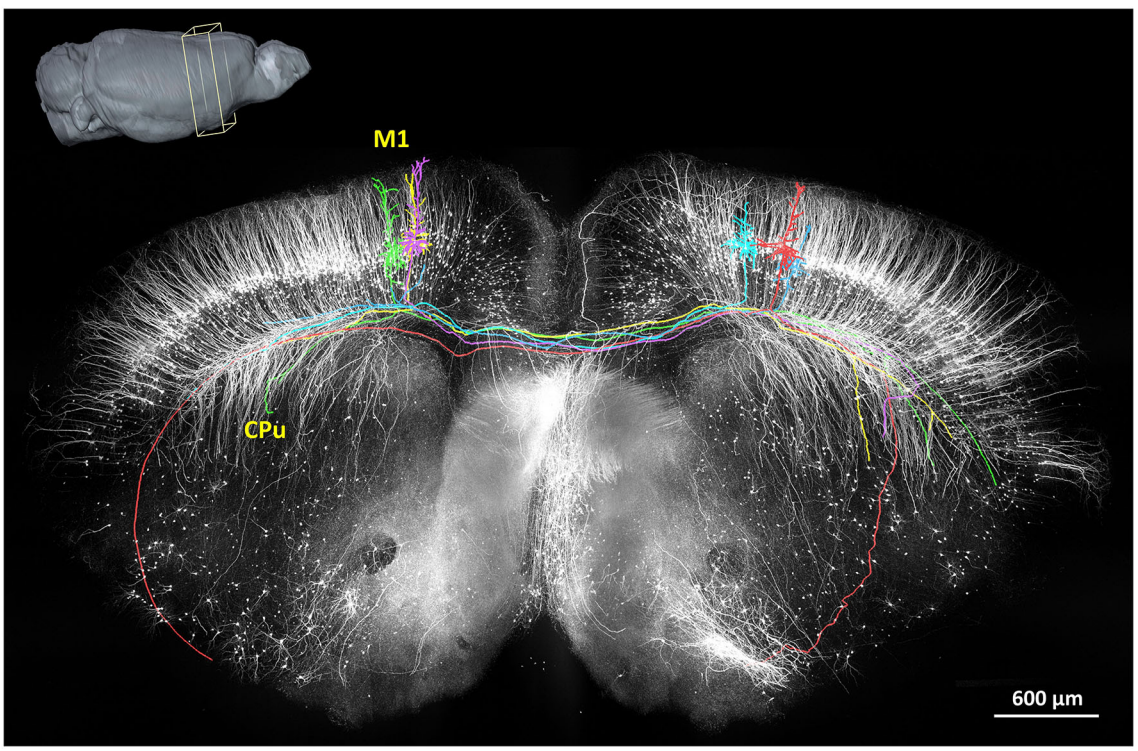

FIGURE 3 | The reconstruction of the coronal plane imaging (300 μm thick) of GFP-M line mouse brain using fMOST. A 3D reconstruction of the mouse brain is in the top left corner; the cube at the coronal plane presents the spatial location of the data at the center. Six individual pyramidal neurons were segmented and traced, indicated in different colors. Axon arbors extend in the ipsilateral hemisphere and to the caudate putamen in the contralateral hemisphere via the corpus callosum. Redrawn from the imaging dataset published in Gong et al. (2013).

Simultaneous Acquisition of Multiple Types of Information from the Brain

Simultaneous Visualization of the Structure and Location of Neurons

Simultaneously acquiring the structural and locational information describing neural circuits is a key issue in understanding how neural systems organize and process information. Nissl staining is the gold standard for the anatomical location of neurons in the brain. Many reference atlases based on Nissl staining have been established and widely used in anatomical studies (Dong, 2008; George Paxinos, 2012). However, due to differences between various mouse lines and different developmental stages, precisely matching every brain slice to a reference atlas is impossible. Accurately identifying structures and referencing anatomical locations remain challenging (Toga, 1999; Simmons and Swanson, 2009). Locating the projections of neurites and subnets of neural circuits in 3D space is even more difficult. Researchers have been attempting to acquire specific cell type distributions, neural connections and location information in a single intact brain using a combination of whole brain imaging and nuclear staining (Oh et al., 2014; Susaki et al., 2014), although a reference providing simultaneously collected neural circuit and anatomical data in one animal at high resolution needs to be established.

Acquiring Cell-Vascular Information Simultaneously

Acquiring data on detailed neurovascular networks simultaneously with other types of neural data is essential to understanding the mechanisms of energy metabolism in the central nervous system. Based on computed tomography (CT) technology and magnetic resonance imaging (MRI), the brain-wide live imaging and localization of large vessels have been achieved at 20 μm isotropic resolution (Dorr et al., 2007, 2008). A combination of optical imaging and perfusion is common for visualizing the vessels. Kleinfeld et al. conducted vascular network imaging with 1 μm resolution in multiple small brain regions but were limited by the imaging field and depth of traditional two-photon imaging (Blinder et al., 2013). Images of large vessels in the whole mouse brain were acquired at a resolution of 3–5 μm with LSM (Hashimoto et al., 2008; Ertürk et al., 2012a). Nissl staining also provides contrast images of vessels in the neural tissue. The cytoarchitecture and vascular network data can be acquired simultaneously with unprecedented details of both individual cells and blood vessels, including capillaries (Wu et al., 2014) from the mouse brain by combining the MOST technique and a modified whole-brain Nissl staining method (**Figure 4**). It raises the possibility of imaging vascular networks and neural circuits as well as corresponding landmarks of brain regions/nuclei in the whole brain simultaneously.

Perspectives

In recent years, brain-wide optical tomography has been well developed, promoting the acquisition of neural anatomical information at single-neuron resolution. However, much remains to be explored in the complicated brain. Additionally, rodent models have obvious limitations in terms of understanding the advanced functions and dysfunctions of the human brain and the corresponding drug research. We are sure that non-human primates are better models to deal with the question, and even humans. Therefore, future studies must be conducted in a systematic and multi-disciplinary way and must include sample labeling and imaging techniques, as well as methods for processing big image data.

Optical labeling and imaging techniques that enable the fine structural characterization of neuronal networks from a large volume of brain tissue with high accuracy and efficiency still present a challenge. During the imaging process, the somas of marked neurons emit much more light than their axons and dendrites. To reduce the influence of the high intensity of light coming from the soma, the neuron must be marked sparsely, while the axons and the dendrites must contain stable, high-intensity fluorescence. Then the precious signal must remain strong until all digitized intensity distribution is recorded. Meanwhile, developing sectioning and imaging techniques with better SNR and spatial resolution is urgently needed. The resolution of whole-brain optical imaging technology should be improved from one μm to several hundred nms and may even break the optical diffraction limit. Moreover, to study the decimeter-sized primate brain, available effective specific labeling techniques, such as CLARITY (Chung et al., 2013), iDISCO (Renier et al., 2014) and CUBIC (Susaki et al., 2014), need to be optimized, and more effective novel labeling techniques need to be developed. On the other hand, imaging techniques currently used for rodents must be improved to get the faster speed, the larger detection range and the more robust performance.

With the increasing imaging resolution and sample volume, massive amounts of data are being obtained at an unprecedented rate, exceeding the processing capability of current hardware and software technologies, which have contributed to the increasing problem of "big data". The 3D mouse brain data set in Li et al. (2010) is 8 TB (1 TB = 1024 GB), equaling the total storage capacity of ten thousands of DVD disks. Once the 3D reconstruction of whole human brain is completed in the future, the resulting data will total 8 PB (1 PB = 1024 TB). As the primary bottleneck limiting of neuroscience studies, "big data" have been widely noted for the challenge these data pose to all current methods of data storage, image processing and analysis, and data management and sharing (Akil et al., 2011). Recently, more efforts have been attempted to fully automatize image processing and information extraction (Latorre et al., 2013; Quan et al., 2013, 2014; Frasconi et al., 2014). At the end of 2014, Nature Neuroscience, with the theme "Focus on Big Data", indicated that, neuroscientists have to learn to manage and take advantage of the big waves of data that are being generated. Fully automated methods will facilitate neuroscientists to handle the big data.

Establishing more effective research strategies is a necessity, in addition to considering the scientists, research facilities, and methods and techniques devoted to this area. Referring to the Human Genome Project, international cooperation under the guidance of the roadmap presents an important alternative to independent project teams. The Allen Institute for Brain Science in the USA has already made many beneficial attempts, starting

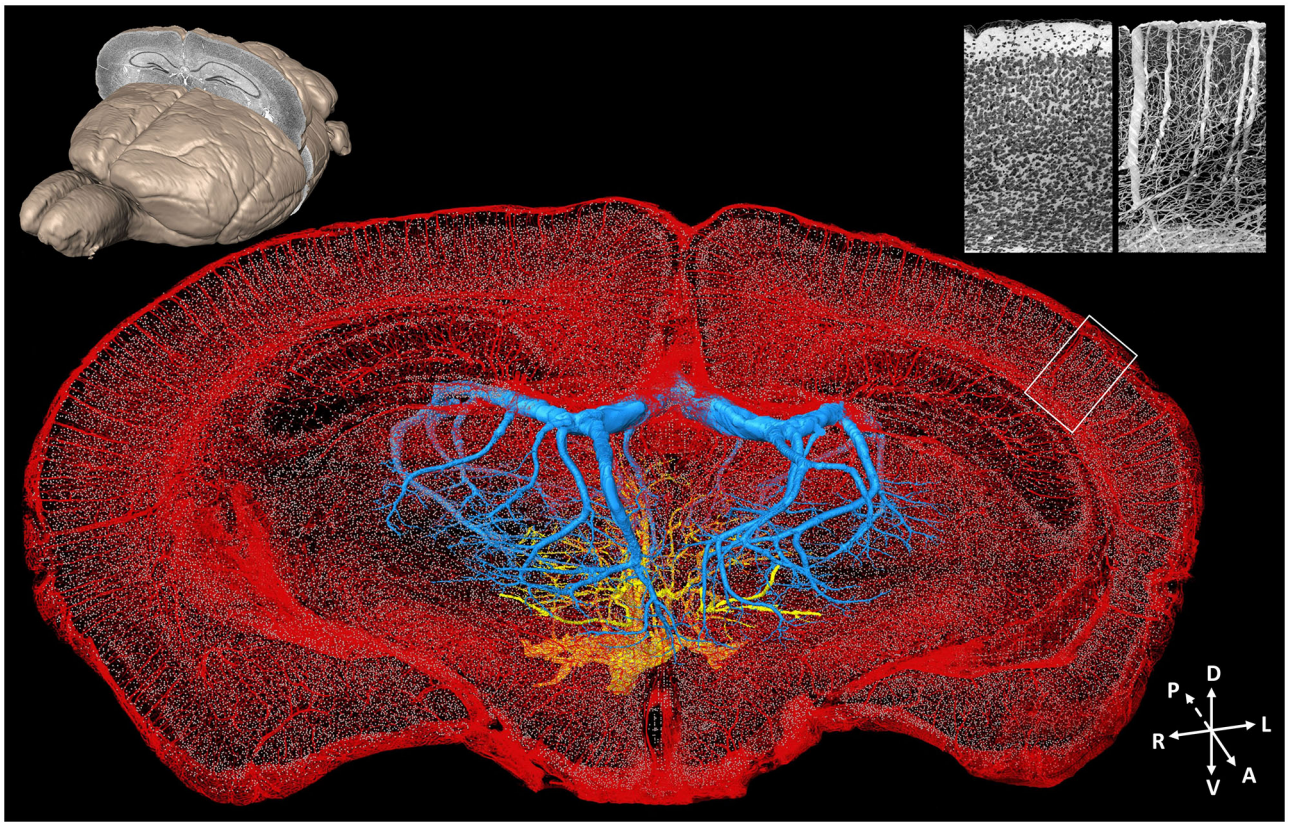

FIGURE 4 | Whole-brain cytoarchitecture and vascular networks acquired by the MOST method. A 3D reconstruction of the mouse brain is in the top left corner; the selected 300 μm slab at the coronal plane presents the spatial location of the data at the center. The center shows the cytoarchitecture and vascular network, simultaneously acquired in the brain. Blue and yellow represents the branches of the longitudinal hippocampal vein and some thalamo-perforating arteries in thalamus, respectively, red represents all else vessels in this data set, and gray dots represent the center of somas. The enlarged views of the cytoarchitecture and vascular architecture of the white rectangle in cortical region in the data at the center are in the top right corner. Redrawn from the imaging dataset published in Wu et al. (2014).

in 2003. In addition, the integration and application of current knowledge is another area that should be a focus (Akil et al., 2011). In recent years, the 3D brain atlas database and search engines opened to the public via the internet have sprung up.

The neuroscience boom is well underway. How are neural circuits organized? How are they interconnected? How many types of neurons exist in the brain? These questions can be addressed by the interdisciplinary cooperation between researchers in the fields of neuroscience, optics, engineering, chemistry, computer science and statistics.

Acknowledgments

We appreciate Jie Peng, Congdi Guo, Benyi Xiong and Hang Lu for image processing, Prof. Tonghui Xu for valuable discussion, and the financial supports from the Science Fund for Creative Research Group of China (Grant No. 61421064), National Natural Science Foundation of China (Grant Nos. 91432105, 91432116 and 91232000) and National Key Scientific Instrument and Equipment Development Program of China (Grant No. 2012YQ030260).

References

Akil, H., Martone, M. E., and Van Essen, D. C. (2011). Challenges and opportunities in mining neuroscience data. *Science* 331, 708–712. doi: 10.1126/science.1199305

Amunts, K., Lepage, C., Borgeat, L., Mohlberg, H., Dickscheid, T., Rousseau, M. É., et al. (2013). Bigbrain: an ultrahigh-resolution 3D human brain model. *Science* 340, 1472–1475. doi: 10.1126/science.1235381

Armstrong, D. M., Saper, C. B., Levey, A. I., Wainer, B. H., and Terry, R. D. (1983). Distribution of cholinergic neurons in rat brain: demonstrated by the immunocytochemical localization of choline acetyltransferase. *J. Comp. Neurol.* 216, 53–68. doi: 10.1002/cne.902160106

Bassett, D. S., and Gazzaniga, M. S. (2011). Understanding complexity in the human brain. *Trends Cogn. Sci.* 15, 200–209. doi: 10.1016/j.tics.2011.03.006

Binzegger, T., Douglas, R. J., and Martin, K. A. C. (2010). "An axonal perspective on cortical circuits," in *New Aspects of Axonal Structure and Function*, eds D. Feldmeyer and J. H. R. Lübke (New York: Springer Science+Business Media), 117.

Björklund, A., and Dunnett, S. B. (2007). Dopamine neuron systems in the brain: an update. *Trends Neurosci.* 30, 194–202. doi: 10.1016/j.tins.2007.03.006

Blinder, P., Tsai, P. S., Kaufhold, J. P., Knutsen, P. M., Suhl, H., and Kleinfeld, D. (2013). The cortical angiome: an interconnected vascular network with noncolumnar patterns of blood flow. *Nat. Neurosci.* 16, 889–897. doi: 10.1038/nn.3426

Bohland, J. W., Wu, C., Barbas, H., Bokil, H., Bota, M., Breiter, H. C., et al. (2009). A proposal for a coordinated effort for the doneterminati of brainwide neuroanatomical connectivity in model organisms at a mesoscopic scale. *PLoS Comput. Biol.* 5:e1000334. doi: 10.1371/journal.pcbi.1000334

Chung, K., and Deisseroth, K. (2013). CLARITY for mapping the nervous system. *Nat. Methods* 10, 508–513. doi: 10.1038/nmeth.2481

Chung, K., Wallace, J., Kim, S. Y., Kalyanasundaram, S., Andalman, A. S., Davidson, T. J., et al. (2013). Structural and molecular interrogation of intact biological systems. *Nature* 497, 332–337. doi: 10.1038/nature12107

DeFelipe, J., López-Cruz, P. L., Benavides-Piccione, R., Bielza, C., Larrañaga, P., Anderson, S., et al. (2013). New insights into the classification and nomenclature of cortical GABAergic interneurons. *Nat. Rev. Neurosci.* 14, 202–216. doi: 10.1038/nrn3444

Dodt, H. U., Leischner, U., Schierloh, A., Jährling, N., Mauch, C. P., Deininger, K., et al. (2007). Ultramicroscopy: three-dimensional visualization of neuronal networks in the whole mouse brain. *Nat. Methods* 4, 331–336. doi: 10.1038/nmeth1036

Dong, H. W. (2008). *The Allen Reference Atlas: A Digital Color Brain Atlas of the C57Bl/6J Male Mouse.* Hoboken: John Wiley and Sons.

Dorr, A. E., Lerch, J. P., Spring, S., Kabani, N., and Henkelman, R. M. (2008). High resolution three-dimensional brain atlas using an average magnetic resonance image of 40 adult C57Bl/6J mice. *Neuroimage* 42, 60–69. doi: 10.1016/j.neuroimage.2008.03.037

Dorr, A., Sled, J. G., and Kabani, N. (2007). Three-dimensional cerebral vasculature of the CBA mouse brain: a magnetic resonance imaging and micro computed tomography study. *Neuroimage* 35, 1409–1423. doi: 10.1016/j.neuroimage.2006.12.040

Dumas, L., Heitz-Marchaland, C., Fouquet, S., Suter, U., Livet, J., Moreau-Fauvarque, C., et al. (2015). Multicolor analysis of oligodendrocyte morphology, interactions and development with Brainbow. *Glia* 63, 699–717. doi: 10.1002/glia.22779

Ertürk, A., Becker, K., Jährling, N., Mauch, C. P., Hojer, C. D., Egen, J. G., et al. (2012a). Three-dimensional imaging of solvent-cleared organs using 3DISCO. *Nat. Protoc.* 7, 1983–1995. doi: 10.1038/nprot.2012.119

Ertürk, A., Lafkas, D., and Chalouni, C. (2014). Imaging cleared intact biological systems at a cellular level by 3DISCO. *J. Vis. Exp.* 89:e51382. doi: 10.3791/51382

Ertürk, A., Mauch, C. P., Hellal, F., Förstner, F., Keck, T., Becker, K., et al. (2012b). Three-dimensional imaging of the unsectioned adult spinal cord to assess axon regeneration and glial responses after injury. *Nat. Med.* 18, 166–171. doi: 10.1038/nm.2600

Frasconi, P., Silvestri, L., Soda, P., Cortini, R., Pavone, F. S., and Iannello, G. (2014). Large-scale automated identification of mouse brain cells in confocal light sheet microscopy images. *Bioinformatics* 30, i587–i593. doi: 10.1093/bioinformatics/btu469

Fu, W., Le Maître, E., Fabre, V., Bernard, J. F., David Xu, Z. Q., and Hökfelt, T. (2010). Chemical neuroanatomy of the dorsal raphe nucleus and adjacent structures of the mouse brain. *J. Comp. Neurol.* 518, 3464–3494. doi: 10.1002/cne.22407

Garey, L. (1999). Cortex: statistics and geometry of neuronal connectivity, 2nd edn. by V. BRAITENBERG and A. SCHüZ. (Pp. xiii+249; 90 figures; ISBN 3 540 63816 4). Berlin: Springer. 1998. *J. Anat.* 194, 153–157. doi: 10.1046/j.1469-7580.1999.194101535.x

George Paxinos, A. K. B. J. F. (2012). *The Mouse Brain in Stereotaxic Coordinate.* 4th Edn. San Diego: Academic Press.

Ghosh, S., Larson, S. D., Hefzi, H., Marnoy, Z., Cutforth, T., Dokka, K., et al. (2011). Sensory maps in the olfactory cortex defined by long-range viral tracing of single neurons. *Nature* 472, 217–220. doi: 10.1038/nature09945

Gong, H., Zeng, S., Yan, C., Lv, X., Yang, Z., Xu, T., et al. (2013). Continuously tracing brain-wide long-distance axonal projections in mice at a one-micron voxel resolution. *Neuroimage* 74, 87–98. doi: 10.1016/j.neuroimage.2013.02.005

Hama, H., Kurokawa, H., Kawano, H., Ando, R., Shimogori, T., Noda, H., et al. (2011). Scale: a chemical approach for fluorescence imaging and reconstruction of transparent mouse brain. *Nat. Neurosci.* 14, 1481–1488. doi: 10.1038/nn.2928

Hashimoto, H., Kusakabe, M., and Ishikawa, H. (2008). A novel method for three-dimensional observation of the vascular networks in the whole mouse brain. *Microsc. Res. Tech.* 71, 51–59. doi: 10.1002/jemt.20522

Heim, R., Cubitt, A. B., and Tsien, R. Y. (1995). Improved green fluorescence. *Nature* 373, 663–664. doi: 10.1038/373663b0

Helmstaedter, M., Sakmann, B., and Feldmeyer, D. (2009). L2/3 interneuron groups defined by multiparameter analysis of axonal projection, dendritic geometry and electrical excitability. *Cereb. Cortex* 19, 951–962. doi: 10.1093/cercor/bhn130

Huang, Z. J. (2014). Toward a genetic dissection of cortical circuits in the mouse. *Neuron* 83, 1284–1302. doi: 10.1016/j.neuron.2014.08.041

Huang, Z. J., and Zeng, H. (2013). Genetic approaches to neural circuits in the mouse. *Annu. Rev. Neurosci.* 36, 183–215. doi: 10.1146/annurev-neuro-062012-170307

Jbabdi, S., and Behrens, T. E. (2013). Long-range connectomics. *Ann. N Y Acad. Sci.* 1305, 83–93. doi: 10.1111/nyas.12271

Kalchmair, S., Jährling, N., Becker, K., and Dodt, H.-U. (2010). Image contrast enhancement in confocal ultramicroscopy. *Opt. Lett.* 35, 79–81. doi: 10.1364/ol.35.000079

Ke, M.-T., Fujimoto, S., and Imai, T. (2013). SeeDB: a simple and morphology-preserving optical clearing agent for neuronal circuit reconstruction. *Nat. Neurosci.* 16, 1154–1161. doi: 10.1038/nn.3447

Kim, S.-Y., Chung, K., and Deisseroth, K. (2013). Light microscopy mapping of connections in the intact brain. *Trends Cogn. Sci.* 17, 596–599. doi: 10.1016/j.tics.2013.10.005

Koch, C., and Reid, R. C. (2012). Neuroscience: observatories of the mind. *Nature* 483, 397–398. doi: 10.1038/483397a

Kuwajima, T., Sitko, A. A., Bhansali, P., Jurgens, C., Guido, W., and Mason, C. (2013). ClearT: a detergent- and solvent-free clearing method for neuronal and non-neuronal tissue. *Development* 140, 1364–1368. doi: 10.1242/dev.091844

Latorre, A., Alonso-Nanclares, L., Muelas, S., Peña, J.-M., and Defelipe, J. (2013). 3D segmentations of neuronal nuclei from confocal microscope image stacks. *Front. Neuroanat.* 7:49. doi: 10.3389/fnana.2013.00049

Li, A., Gong, H., Zhang, B., Wang, Q., Yan, C., Wu, J., et al. (2010). Micro-optical sectioning tomography to obtain a high-resolution atlas of the mouse brain. *Science* 330, 1404–1408. doi: 10.1126/science.1191776

Lichtman, J. W., and Denk, W. (2011). The big and the small: challenges of imaging the brain's circuits. *Science* 334, 618–623. doi: 10.1126/science.1209168

Livet, J., Weissman, T. A., Kang, H., Draft, R. W., Lu, J., Bennis, R. A., et al. (2007). Transgenic strategies for combinatorial expression of fluorescent proteins in the nervous system. *Nature* 450, 56–62. doi: 10.1038/nature06293

Luo, L., Callaway, E. M., and Svoboda, K. (2008). Genetic dissection of neural circuits. *Neuron* 57, 634–660. doi: 10.1016/j.neuron.2008.01.002

Madisen, L., Zwingman, T. A., Sunkin, S. M., Oh, S. W., Zariwala, H. A., Gu, H., et al. (2010). A robust and high-throughput Cre reporting and characterization system for the whole mouse brain. *Nat. Neurosci.* 13, 133–140. doi: 10.1038/nn.2467

Markram, H., Toledo-Rodriguez, M., Wang, Y., Gupta, A., Silberberg, G., and Wu, C. (2004). Interneurons of the neocortical inhibitory system. *Nat. Rev. Neurosci.* 5, 793–807. doi: 10.1038/nrn1519

Mayerich, D., Abbott, L., and McCormick, B. (2008). Knife-edge scanning microscopy for imaging and reconstruction of three-dimensional anatomical structures of the mouse brain. *J. Microsc.* 231, 134–143. doi: 10.1111/j.1365-2818.2008.02024.x

McCormick, B. H., Koh, W., Choe, Y., Abbott, L. C., Keyser, J., Mayerich, D., et al. (2004). Construction of anatomically correct models of mouse brain networks. *Neurocomputing* 58–60, 379–386. doi: 10.1016/s0925-2312(04)00075-x

Mitra, P. P. (2014). The circuit architecture of whole brains at the mesoscopic scale. *Neuron* 83, 1273–1283. doi: 10.1016/j.neuron.2014.08.055

Miyamichi, K., Amat, F., Moussavi, F., Wang, C., Wickersham, I., Wall, N. R., et al. (2011). Cortical representations of olfactory input by trans-synaptic tracing. *Nature* 472, 191–196. doi: 10.1038/nature09714

Muralidhar, S., Wang, Y., and Markram, H. (2014). Synaptic and cellular organization of layer 1 of the developing rat somatosensory cortex. *Front. Neuroanat.* 7:52. doi: 10.3389/fnana.2013.00052

Oberlaender, M., Boudewijns, Z. S. R. M., Kleele, T., Mansvelder, H. D., Sakmann, B., and de Kock, C. P. J. (2011). Three-dimensional axon morphologies of individual layer 5 neurons indicate cell type-specific intracortical pathways for

whisker motion and touch. *Proc. Natl. Acad. Sci. U S A* 108, 4188–4193. doi: 10.1073/pnas.1100647108

Oberlaender, M., de Kock, C. P. J., Bruno, R. M., Ramirez, A., Meyer, H. S., Dercksen, V. J., et al. (2012). Cell type-specific three-dimensional structure of thalamocortical circuits in a column of rat vibrissal cortex. *Cereb. Cortex* 22, 2375–2391. doi: 10.1093/cercor/bhr317

Oh, S. W., Harris, J. A., Ng, L., Winslow, B., Cain, N., Mihalas, S., et al. (2014). A mesoscale connectome of the mouse brain. *Nature* 508, 207–214. doi: 10.1038/nature13186

Osten, P., and Margrie, T. W. (2013). Mapping brain circuitry with a light microscope. *Nat. Methods* 10, 515–523. doi: 10.1038/nmeth.2477

Parekh, R., and Ascoli, G. A. (2013). Neuronal morphology goes digital: a research hub for cellular and system neuroscience. *Neuron* 77, 1017–1038. doi: 10.1016/j.neuron.2013.03.008

Petersen, C. C., Grinvald, A., and Sakmann, B. (2003). Spatiotemporal dynamics of sensory responses in layer 2/3 of rat barrel cortex measured *in vivo* by voltage-sensitive dye imaging combined with whole-cell voltage recordings and neuron reconstructions. *J. Neurosci.* 23, 1298–1309.

Petreanu, L., Mao, T., Sternson, S. M., and Svoboda, K. (2009). The subcellular organization of neocortical excitatory connections. *Nature* 457, 1142–1145. doi: 10.1038/nature07709

Pollak Dorocic, I., Fürth, D., Xuan, Y., Johansson, Y., Pozzi, L., Silberberg, G., et al. (2014). A whole-brain atlas of inputs to serotonergic neurons of the dorsal and median raphe nuclei. *Neuron* 83, 663–678. doi: 10.1016/j.neuron.2014.07.002

Quan, T., Li, J., Zhou, H., Li, S., Zheng, T., Yang, Z., et al. (2014). Digital reconstruction of the cell body in dense neural circuits using a spherical-coordinated variational model. *Sci. Rep.* 4:4970. doi: 10.1038/srep04970

Quan, T., Zheng, T., Yang, Z., Ding, W., Li, S., Li, J., et al. (2013). NeuroGPS: automated localization of neurons for brain circuits using L1 minimization model. *Sci. Rep.* 3:1414. doi: 10.1038/srep01414

Ragan, T., Kadiri, L. R., Venkataraju, K. U., Bahlmann, K., Sutin, J., Taranda, J., et al. (2012). Serial two-photon tomography for automated ex vivo mouse brain imaging. *Nat. Methods* 9, 255–258. doi: 10.1038/nmeth.1854

Ragan, T., Sylvan, J. D., Kim, K. H., Huang, H., Bahlmann, K., Lee, R. T., et al. (2007). High-resolution whole organ imaging using two-photon tissue cytometry. *J. Biomed. Opt.* 12:014015. doi: 10.1117/1.2435626

Renier, N., Wu, Z., Simon, D. J., Yang, J., Ariel, P., and Tessier-Lavigne, M. (2014). iDISCO: a simple, rapid method to immunolabel large tissue samples for volume imaging. *Cell* 159, 896–910. doi: 10.1016/j.cell.2014.10.010

Robey, R. B., Ruiz, O., Santos, A. V., Ma, J., Kear, F., Wang, L. J., et al. (1998). pH-dependent fluorescence of a heterologously expressed Aequorea green fluorescent protein mutant: in situ spectral characteristics and applicability to intracellular pH estimation. *Biochemistry* 37, 9894–9901. doi: 10.1021/bi980857x

Russo, S. J., and Nestler, E. J. (2013). The brain reward circuitry in mood disorders. *Nat. Rev. Neurosci.* 14, 609–625. doi: 10.1038/nrn3381

Shaner, N. C., Steinbach, P. A., and Tsien, R. Y. (2005). A guide to choosing fluorescent proteins. *Nat. Methods* 2, 905–909. doi: 10.1038/nmeth819

Shi, S. R., Shi, Y., and Taylor, C. R. (2011). Antigen retrieval immunohistochemistry: review and future prospects in research and diagnosis over two decades. *J. Histochem. Cytochem.* 59, 13–32. doi: 10.1369/jhc.2010.957191

Siedentopf, H., and Zsigmondy, R. (1902). Uber sichtbarmachung und größenbestimmung ultramikoskopischer teilchen, mit besonderer anwendung auf goldrubingläser. *Ann. Phys.* 315, 1–39. doi: 10.1002/andp.19023150102

Silasi, G., and Murphy, T. H. (2014). Stroke and the connectome: how connectivity guides therapeutic intervention. *Neuron* 83, 1354–1368. doi: 10.1016/j.neuron.2014.08.052

Silvestri, L., Bria, A., Sacconi, L., Iannello, G., and Pavone, F. S. (2012). Confocal light sheet microscopy: micron-scale neuroanatomy of the entire mouse brain. *Opt. Express* 20, 20582–20598. doi: 10.1364/OE.20.020582

Silvestri, L., Sacconi, L., and Pavone, F. S. (2013). The connectomics challenge. *Funct. Neurol.* 28, 167–173. doi: 10.11138/FNeur/2013.28.3.167

Simmons, D. M., and Swanson, L. W. (2009). Comparing histological data from different brains: sources of error and strategies for minimizing them. *Brain Res. Rev.* 60, 349–367. doi: 10.1016/j.brainresrev.2009.02.002

Sosulski, D. L., Bloom, M. L., Cutforth, T., Axel, R., and Datta, S. R. (2011). Distinct representations of olfactory information in different cortical centres. *Nature* 472, 213–216. doi: 10.1038/nature09868

Sotelo, C. (2003). Viewing the brain through the master hand of Ramon y Cajal. *Nat. Rev. Neurosci.* 4, 71–77. doi: 10.1038/nrn1010

Spalteholz, W. (1914). Über das durchsichtigmachen von menschlichen und tierischen präparaten. *S. Hierzel Leipzig* 2, 91.

Sun, Y., Nguyen, A. Q., Nguyen, J. P., Le, L., Saur, D., Choi, J., et al. (2014). Cell-type-specific circuit connectivity of hippocampal CA1 revealed through Cre-dependent rabies tracing. *Cell Rep.* 7, 269–280. doi: 10.1016/j.celrep.2014.02.030

Susaki, E. A., Tainaka, K., Perrin, D., Kishino, F., Tawara, T., Watanabe, T. M., et al. (2014). Whole-brain imaging with single-cell resolution using chemical cocktails and computational analysis. *Cell* 157, 726–739. doi: 10.1016/j.cell.2014.03.042

Svoboda, K. (2011). The past, present and future of single neuron reconstruction. *Neuroinformatics* 9, 97–98. doi: 10.1007/s12021-011-9097-y

Taniguchi, H., He, M., Wu, P., Kim, S., Paik, R., Sugino, K., et al. (2011). A resource of Cre driver lines for genetic targeting of GABAergic neurons in cerebral cortex. *Neuron* 71, 995–1013. doi: 10.1016/j.neuron.2011.07.026

Toga, A. W. (1999). *Brain Warping.* San Diego: Academic Press.

Tomer, R., Ye, L., Hsueh, B., and Deisseroth, K. (2014). Advanced CLARITY for rapid and high-resolution imaging of intact tissues. *Nat. Protoc.* 9, 1682–1697. doi: 10.1038/nprot.2014.123

Tsai, P. S., Friedman, B., Ifarraguerri, A. I., Thompson, B. D., Lev-Ram, V., Schaffer, C. B., et al. (2003). All-optical histology using ultrashort laser pulses. *Neuron* 39, 27–41. doi: 10.1016/s0896-6273(03)00370-2

Tsai, P. S., Kaufhold, J. P., Blinder, P., Friedman, B., Drew, P. J., Karten, H. J., et al. (2009). Correlations of neuronal and microvascular densities in murine cortex revealed by direct counting and colocalization of nuclei and vessels. *J. Neurosci.* 29, 14553–14570. doi: 10.1523/JNEUROSCI.3287-09.2009

Vbn (2015). *Visible Brainwide Network at Single-Neuron Resolution.* Available online at: http://vbn.org.cn/showGallery?directory=Fig1%20Morphology_600dpi. Accessed on April 23, 2015.

Weissbourd, B., Ren, J., DeLoach, K. E., Guenthner, C. J., Miyamichi, K., and Luo, L. (2014). Presynaptic partners of dorsal raphe serotonergic and GABAergic neurons. *Neuron* 83, 645–662. doi: 10.1016/j.neuron.2014.06.024

Windhorst, U., and Johansson, H. (1999). *Modern Techniques in Neuroscience Research.* New York: Springer Verlag.

Wu, J., He, Y., Yang, Z., Guo, C., Luo, Q., Zhou, W., et al. (2014). 3D BrainCV: simultaneous visualization and analysis of cells and capillaries in a whole mouse brain with one-micron voxel resolution. *Neuroimage* 87, 199–208. doi: 10.1016/j.neuroimage.2013.10.036

Xiong, H., Zhou, Z., Zhu, M., Lv, X., Li, A., Li, S., et al. (2014). Chemical reactivation of quenched fluorescent protein molecules enables resin-embedded fluorescence microimaging. *Nat. Commun.* 5:3992. doi: 10.1038/ncomms4992

Yang, B., Treweek, J. B., Kulkarni, R. P., Deverman, B. E., Chen, C. K., Lubeck, E., et al. (2014). Single-cell phenotyping within transparent intact tissue through whole-body clearing. *Cell* 158, 945–958. doi: 10.1016/j.cell.2014.07.017

Zhang, B., Li, A., Yang, Z., Wu, J., Luo, Q., and Gong, H. (2011). Modified Golgi-Cox method for micrometer scale sectioning of the whole mouse brain. *J. Neurosci. Methods* 197, 1–5. doi: 10.1016/j.jneumeth.2010.10.001

Zheng, T., Yang, Z., Li, A., Lv, X., Zhou, Z., Wang, X., et al. (2013). Visualization of brain circuits using two-photon fluorescence micro-optical sectioning tomography. *Opt. Express* 21, 9839–9850. doi: 10.1364/OE.21.009839

Zingg, B., Hintiryan, H., Gou, L., Song, M. Y., Bay, M., Bienkowski, M. S., et al. (2014). Neural networks of the mouse neocortex. *Cell* 156, 1096–1111. doi: 10.1016/j.cell.2014.02.023

Conflict of Interest Statement: The authors declare that the research was conducted in the absence of any commercial or financial relationships that could be construed as a potential conflict of interest.

frontiers in Neuroanatomy

TECHNOLOGY REPORT
published: 22 March 2016
doi: 10.3389/fnana.2016.00031

Whole Brain Imaging with Serial Two-Photon Tomography

*Stephen P. Amato[1], Feng Pan[2], Joel Schwartz[1] and Timothy M. Ragan[1]**

[1] TissueVision, Inc., Cambridge, MA, USA, [2] Pfizer, Inc., Cambridge, MA, USA

Imaging entire mouse brains at submicron resolution has historically been a challenging undertaking and largely confined to the province of dedicated atlasing initiatives. This has limited systematic investigations into important areas of neuroscience, such as neural circuits, brain mapping and neurodegeneration. In this article, we describe in detail Serial Two-Photon (STP) tomography, a robust, reliable method for imaging entire brains with histological detail. We provide examples of how the basic methodology can be extended to other imaging modalities, such as Optical Coherence Tomography (OCT), in order to provide unique contrast mechanisms. Furthermore, we provide a survey of the research that STP tomography has enabled in the field of neuroscience, provide examples of how this technology enables quantitative whole brain studies, and discuss the current limitations of STP tomography-based approaches.

Keywords: serial two-photon tomography, serial section tomography, brain mapping, neural circuits, Alzheimer's disease

INTRODUCTION

Over the last two decades there have been dramatic improvements in the fields of microscopy, tissue labeling, and computational image analysis. Each of these fields address an important aspect of quantitative biological imaging: optical microscopy methods visualize tissues and map the spatial-temporal relationship between components too small to be seen by the naked eye; tissue labeling techniques establish contrast and biochemical specificity of tissue components; computer-aided image analyses quantitatively explore relationships between the various components and makes it possible to handle the vast amounts of data that is generated (Klunk et al., 2002; Dean and Palmer, 2014; Piccinini and Shagrir, 2014; Jordan and Mitchell, 2015; Feng et al., 2015). The combination of advances in these three disciplines have a sum greater than the individual parts and particularly benefit the field of neuroscience, where researchers studying the central nervous system (CNS) are attempting to decipher a complex and enormous 3D network of interconnected neural circuits and cell types.

The three dimensional (3D) structure of the CNS (Bourdenx et al., 2014) is critical for proper network formation and function and therefore has been intensely studied. Traditionally, these studies have relied upon serial section analysis to investigate 3D cytoarchitecture of the CNS. In this technique, a tissue is manually sectioned into thin slices on a cryostat before the tissue section is mounted onto a microscope slide, stained and imaged using a microscope. For studies attempting to construct a 3D representation of the original tissue, the individually imaged sections must be aligned and digitally reassembled. However, as this method requires that tissue samples be sectioned prior to imaging, irreducible distortions are introduced into the tissue sections that preclude accurate full 3D reconstructions of the tissue. Furthermore, as this process is performed manually, the large datasets, required to generate robust and conclusive data, pose challenges both in terms of the labor and cost involved.

OPEN ACCESS

Edited by:
Javier DeFelipe, Cajal Institute, Spain

Reviewed by:
Francisco Clasca, Autonoma University, Spain
Pavel Osten, Cold Spring Harbor Laboratory, USA

***Correspondence:**
Timothy M. Ragan
tragan@tissuevision.com

Received: *15 July 2015*
Accepted: *07 March 2016*
Published: *22 March 2016*

Citation:
Amato SP, Pan F, Schwartz J and Ragan TM (2016) Whole Brain Imaging with Serial Two-Photon Tomography. Front. Neuroanat. 10:31. doi: 10.3389/fnana.2016.00031

To circumvent some of the limitations imposed by serial section analysis, block-face approaches have been developed. In block-face imaging, the surface of the tissue block is removed using a microtome and the newly exposed tissue surface is imaged (Ewald et al., 2002; Denk and Horstmann, 2004). This process is then repeated throughout the tissue volume at fixed increments to achieve whole organ imaging. While less labor intensive than serial section analysis there are several limitations. First, sectioning the surface of the block introduces unavoidable distortions onto the surface. Since the newly exposed tissue has yet to be imaged, these distortions can corrupt the data. Second, since the axial resolution of the dataset is determined by the thickness of the slice, high resolution datasets will require numerous physical sections to be made which is time consuming and technically challenging. Finally, scattered or fluorescent light from layers below the block surface will distort the surface image, thereby reducing effective axial resolution and contrast (Krishnamurthi et al., 2010).

To address these limitations, we have developed a robust alternative that allows for a high degree of automation while maintaining sub-micron resolution and compatibility with current histological preparations, fluorescent proteins and dyes. While our approach, referred to as Serial Two-Photon Tomography (STP tomography; Ragan et al., 2007, 2012), is based on two photon microscopy (TPM), the methodology is applicable to a variety of 3D microscopy techniques. Here, we describe the key features of STP tomography and provide examples of research currently utilizing the method.

SERIAL SECTION TOMOGRAPHY

STP tomography is based upon the basic methodology of alternating 3D imaging and physical sectioning and while our approach utilizes TPM, this technique is compatible with a variety of 3D imaging modalities. Examples include optical coherence microscopy, second harmonic generation (SHG), third harmonic generation (THG), coherent anti-stokes Raman scattering, and stimulated Raman scattering (SRS). Therefore, to distinguish between STP Tomography and the more general case, we will use the term Serial Section Tomography (SST) for the remainder of this technical report.

SST has two key technical features that distinguish it from serial section analysis and block-face imaging. First, unlike serial section analysis, the tissue section of interest is always imaged before it has been removed from the tissue block. Second, as opposed to traditional block-face imaging, the imaged portion of the tissue is tens to hundreds of microns below the surface of the block and not at the block surface (**Figure 1**). Taken together, these two features offer significant advantages. First, by imaging the section before it has been cut from the tissue block, SST can achieve near perfect registration between successive tissue sections. As shown later, this is of particular importance when constructing brain atlases. Further, since tissue images are acquired below the block surface, the tissue remains in a pristine state, free from the deformations resulting from mechanical sectioning. Moreover, by automating the alternating steps of 3D optical sectioning and mechanical sectioning, it is possible to rapidly image through large volumes of tissue with no user intervention (**Figure 2**). This procedure effectively transforms 3D histology from an error-prone, low-throughput undertaking to a high-throughput, high-fidelity discipline.

Below we provide a brief description of the main features of SST.

Straightforward Specimen Preparation

Specimen preparation consists of a standard formaldehyde perfusion fixation that introduces the fixative transcardially, harnessing the endogenous vasculature to distribute the fixative evenly throughout the entire brain. In addition to preserving the brain, fixation acts to stiffen the tissue, thus ensuring even and consistent sectioning throughout the tissue volume. To prepare the tissue for imaging and sectioning, the brain is embedded in an agarose block to provide mechanical stability, which is then glued to a glass slide and placed in a water bath. The sample preparation procedure is thus straightforward, robust, and does not require specialized equipment or chemicals. Furthermore, the tissue samples can be imaged 24 h after perfusion fixation or stored indefinitely in phosphate buffered saline.

Minimal Tissue Processing

Tissue processing is a critical step for histological preparations as the experiment is of little value if tissue processing distorts the very biology in question. Given that chromophores, particularly fluorescent proteins, are sensitive to harsh preparation protocols (Giepmans et al., 2006) and that tissue preparation methods may display dramatic effects on tissue morphology (Howat and Wilson, 2014) the proper choice of the fixative and downstream processing steps are crucial. Importantly, tissue imaging using SST does not necessitate optical clearing, and only requires that brains be fixed prior to imaging, thereby avoiding the use of additional chemicals and tissue processing procedures. While a variety of tissue fixatives are available, formaldehyde fixation remains the gold standard for maintaining tissue morphology and antigen preservation (Roberts et al., 1990).

Automation and Robustness

Straightforward sample preparation, in combination with the automated, and robust nature of the acquisition, results in a minimal failure rate for SST data production. When problems do occur, they can usually be attributed to improper fixation or embedding of samples and subsequent poor sectioning of the relatively soft paraformaldehyde fixed tissue. This failure rate is significantly reduced when a perfusion fixation is performed vs. an immersion fixation. To further ensure a high success rate, a 24 h post fix in 4% paraformaldehyde will also improve results. In the end, the high reliability opens the door for large-scale studies involving tens to even thousands of unique

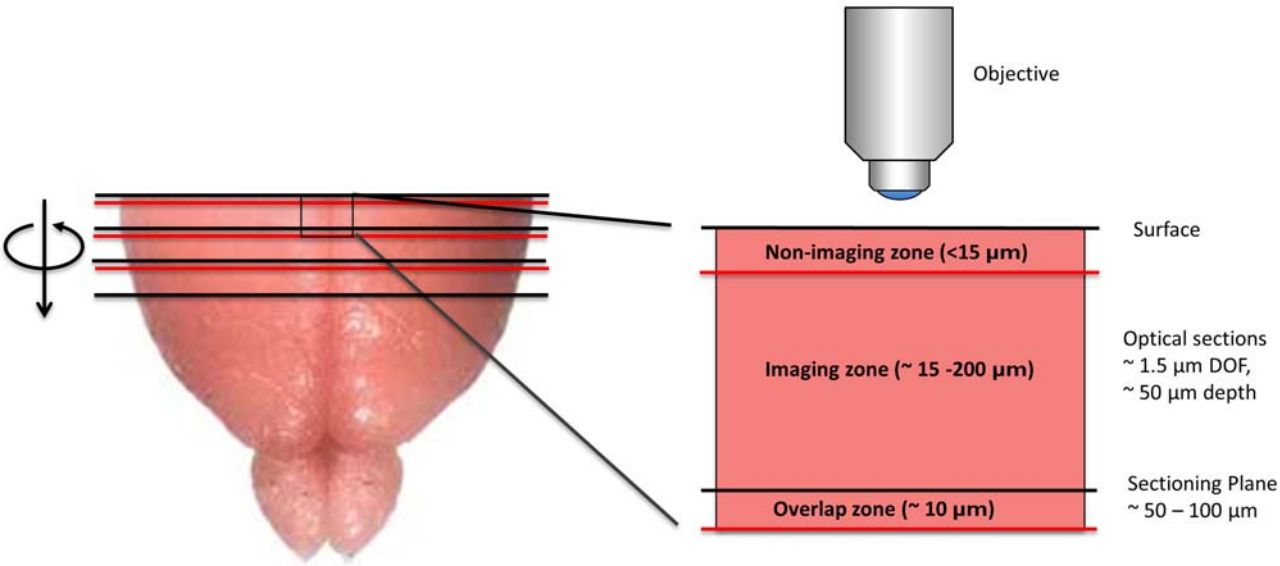

FIGURE 1 | Diagram depicting the imaging methodology employed by serial section tomography (SST). The uppermost portion of the brain is sectioned using a vibratome and removed from the tissue block. The newly exposed tissue surface is imaged anywhere from 15 to 200 μm below the surface, thereby avoiding sectioning artifacts. Two-photon applications allow single layers or *z*-stacks to be acquired within the imaging zone of the tissue. While the imaging depth is usually restricted to 200 μm below the tissue surface to maintain sufficient contrast and resolution, deeper sections can be imaged in cleared or transparent tissues. Section thickness typically ranges from 50 to 100 μm, as this allows captured tissue slices to be used in additional investigations, including immunohistochemical analysis. If full 3D tissue reconstruction is desired, volumetric stacks extending past the sectioning depth can be acquired, stitching successive volumes together axially to form full 3D images.

samples, including behavioral conditioning paradigms or systematic investigations like the Allen Mouse Brain Connectivity Atlas, which involved over 1200 C57BL/6J mice individually injected with distinct viral tracers (Oh et al., 2014).

Full 3D Reconstructions

As noted, full 3D reconstructions can be achieved by scanning overlapping volumes between successive sections. Volumes are constructed by adjusting the focus of the objective lens to image multiple layers within the tissue. After scanning the volume, the uppermost portion of the tissue is mechanically removed but at a depth that is less than the extent of the volume scan, thus leaving an overlap region (**Figure 1**). The next successive volume scan can then be overlaid with the previous to form a contiguous volume. Hence, the axial resolution is not determined by the thickness of the physical section, but by the axial resolution of the imaging modality. In the case of TPM, an axial resolution of approximately 0.8 microns can be obtained. A challenge associated with obtaining seamless 3D reconstructions with SST however is the fall-off in intensity with increasing imaging depth. Increasing the laser power as imaging depth increases helps offset this issue; however, very dense tissue can still pose a challenge. Two ways to address this is to combine very mild clearing techniques that increase the imaging depth to approximately a few hundred microns (Economo et al., 2016) or to simply reduce the thickness of the physical sections.

High Resolution

High resolution is critical for CNS studies as many key components of the brain are less than a micron in size, such as dendritic spines which require sub-micron resolution in order to be resolved (Adrian et al., 2014). SST is well suited for such applications as the methodology is capable of providing highly resolved images throughout the tissue. This is in part due to SST's advantageous imaging geometry and the close

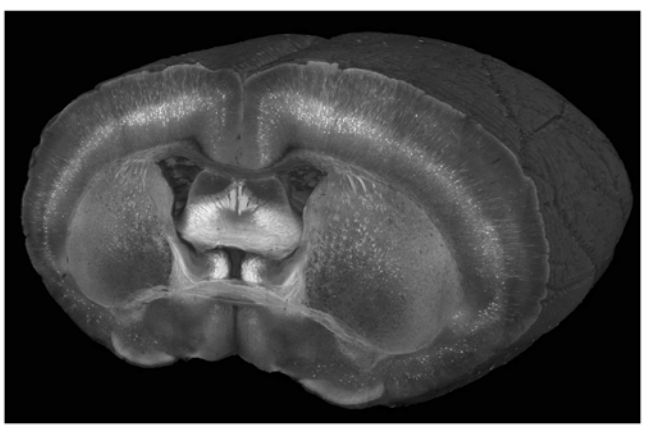

FIGURE 2 | A cutaway view of a Thy1-YFP-3204 mouse brain imaged at a wavelength of 900 nm with a coronal spacing of 100 μm and an *xy* resolution of 1.2 μm.

proximity of a high numerical aperture objective lens to the brain surface. Furthermore, as the imaging depth commonly ranges from 25 to 100 microns below the tissue surface, there is little intervening tissue to produce light scattering effects. For these reasons, it is possible to achieve sub-micron resolution across the entire mouse brain with no degradation in resolution in the interior portions of the sample (**Figure 3**; Ragan et al., 2012; Economo et al., 2016). We note that even when imaging optically cleared tissues with TPM and long working distance objectives, significant degradation of image quality can be expected when imaging beyond approximately 2 mm into the tissue, due to the out-of-focus fluorescence that is generated. Thus, mechanically sectioning the tissue remains the best option to maintain sufficient resolution and contrast throughout the tissue volume (Richardson and Lichtman, 2015; Albanese and Chung, 2016; Economo et al., 2016).

Specimen Size and Photobleaching

There is no fundamental limit to the size of the sample that can be imaged using SST. This feature is due to the fact that the imaging geometry employed by SST remains constant as tissue sections are sequentially removed. In comparison, light sheet microscopy relies upon lateral sample illumination and therefore must pass through the entirety of the tissue, ranging from millimeters to centimeters, in order to visualize interior compartments (Huisken and Stainier, 2009). Even with the best clearing techniques, the required tissue penetration depth broadens the light sheet, effectively reducing the optical sectioning capabilities of the approach and results in light scattering and aberration artifacts which reduce imaging resolution. To date, light sheet approaches have not been able to demonstrate consistent one micron resolution across samples more than a few millimeters in extent. In contrast, SST has displayed the ability to maintain near diffraction limited resolution across tissue samples centimeters wide. The main limitation to specimen size is dataset size and acquisition times, both of which we discuss in the limitations sections.

Non-linear imaging techniques such as multiphoton microscopy confer the advantage of limiting photobleaching outside the focal plane. The large tissue samples referenced above, extending centimeters in depth, can be imagined with no decrease in signal at deeper depths even after hours or days of extended imaging. Moreover, the individual image tiles used to assemble large high resolution images, can be constructed in a manner that discard photobleached overlapping regions in the final mosaic, effectively removing them from the dataset altogether.

Specimen Preservation

While SST relies upon tissue sectioning, all of the sections are available for tissue collection and subsequent analysis. In contrast, other techniques such as 2p-fMOST require that the tissue be embedded into a hard resin and sectioned into thin strips which are difficult to recover, and susceptible to tears along the edges of the ribbon sections (Zheng et al., 2013). The tissue sections in SST are most often acquired at a thickness 25–50 microns, and are ideal for either free floating IHC labeling or a multitude of different analytical strategies, providing a significant advantage for many applications. For instance, researchers interested in performing genomic or proteomic investigations on SST processed tissue have the ability to analyze whole or partial tissue slices via RT-PCR,

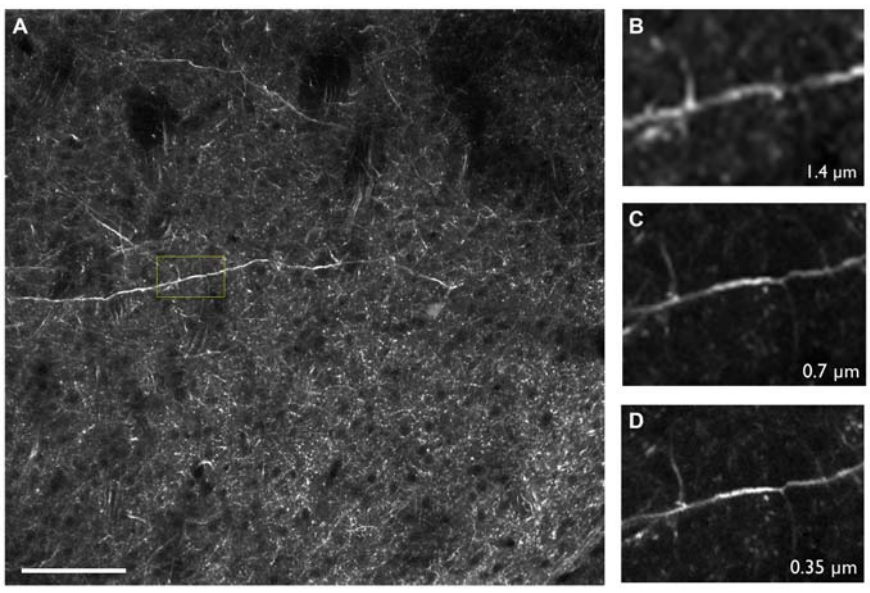

FIGURE 3 | (A) Thy1-YFP-3204 transgenic mouse brain expressing YFP-positive neurons imaged using two-photon tomography. **(B–D)** Inset depicted in **(A)** enlarged and displayed with pixel sizes of 1.4, 0.7 and 0.35 µm respectively. Images were acquired using a 16× Nikon, 0.8 NA objective. Scale bar = 100 µm.

microarray analysis, imaging mass spectrometry or other biochemical means. In this way imaging investigations can provide information that is either difficult or impossible to obtain using current imaging-based approaches. Importantly, the resulting sections can be reimaged by employing additional imaging modalities such as confocal microscopy or wide field fluorescence. Information obtained from these modalities can easily be overlaid onto the original 3D data set to create rich, multimodal datasets (Van de Plas et al., 2015). Moreover, the flexibility afforded by having tissue sections indexed back to the 3D dataset allows investigators to later re-label and re-image tissue sections to address follow-on questions.

SST IMAGING MODALITIES

While fluorescence is an extremely valuable imaging modality, it does come with some practical limitations. First, given the wide emission spectrum of fluorescent dyes and proteins and the typical signal levels achieved by these labels, it is difficult to separate more than four components at once. This presents a problem when attempting to image multiple targets within a single sample. Second, it is often necessary to exogenously label the structure of interest with a fluorescent dye, which can be particularly difficult when dealing with thick tissue preparations. As such, label free imaging modalities based on endogenous signatures can provide extremely valuable complementary information that extend the reach of SST. By combining additional imaging modalities with SST's standard imaging geometry and use of nonlinear excitation it is possible to produce feature rich datasets. Below we describe compatible imaging modalities.

Two Photon Microscopy

TPM is a high resolution 3D fluorescent imaging technique (Denk et al., 1990; So et al., 2000) and while the advantages of TPM are well documented for *in vivo* imaging, the technique also brings significant advantages to *ex vivo* imaging as well. First, due to the nonlinear nature of the excitation process, TPM provides inherent 3D sectioning, an excellent imaging depth of several hundred microns, minimal photobleaching outside the focal plane and works well with both opaque and cleared samples. The typical two photon excitation point spread function has a full width half maximum of 0.35 μm in the radial direction and 0.9 μm in the axial direction for tissue imaging at 920 nm with a 1.0 NA objective (Zipfel et al., 2003), a feature that becomes increasingly important when imaging axially extended samples such as whole brains. In addition, TPM has superior background rejection arising from the wide separation of excitation and emission wavelengths, and possesses the ability to excite multiple chromophores with a single excitation wavelength. Further, large field of views can be achieved with small depths of focus that are limited only by the objective optics. For instance, by perfusing FITC-conjugated gelatin throughout a C57BL/6 mouse brain after paraformaldehyde fixation (Tsai et al., 2009), we were able to utilize STP tomography to generate a three dimensional reconstruction of a portion of the cerebral vasculature (**Figure 4**). In contrast, the confocal parameter of the light sheet limits the field of view to often less than a few hundred microns, thus necessitating extensive tiling.

Optical Coherence Microscopy

Optical Coherence Tomography (OCT) is a 3D optical imaging technique capable of imaging several hundreds of microns into biological tissues while producing high resolution images. OCT, originally introduced in 1991 (Huang et al., 1991), is an interferometric technique that combines low coherence interferometry and a broad spectral bandwidth light source to capture backscattered light of tissue samples. This methodology makes OCT sensitive to differences in the index of refraction within tissues and intrinsic contrast can be observed in cell bodies and myelinated fibers (Saxena and Jain, 2011).

While OCT has traditionally been employed for *in vivo* imaging studies, multiple groups over the last several years have begun to demonstrate its utility for histopathology of the CNS (Goergen et al., 2012; Srinivasan et al., 2012; Magnain et al., 2014, 2015). Srinivasan et al. (2012) used high resolution OCT to image the cerebral cortex of the rat and successfully identified neuronal bodies and myelin sheaths surrounding axons. Magnain et al. (2014, 2015) imaged the human entorhinal cortex and compared the OCT images with traditional Nissl stained images of the same regions (**Figure 5**; Magnain et al., 2014, 2015). More recently, Wang et al. (2014) integrated a vibratome into a polarization sensitive OCT system and generated extended volumetric datasets of rat brains across several physical sections.

Additional Modalities

Additional imaging modalities include, SHG, THG, coherent anti-stokes Raman scattering (Heneka et al., 2015), confocal reflected, and SRS. While it is beyond the scope of this article to describe each technique in detail, we point out that each of these is a label free method that is compatible with SST and does not require the introduction of exogenous dyes. For example, CARS microscopy can detect a wide array of brain structures, including myelin and fiber bundles (Evans et al., 2007), SRS has shown the ability to differentiate between healthy mouse brain tissue vs. tumor infiltrated tissue (Ji et al., 2013) and THG possesses the ability to visualize neurons, vasculature and white matter (WM) structures within the brain, showing particular sensitivity to lipid structures (Witte et al., 2011).

APPLICATIONS

The brain is unique in that it is composed of interconnected, yet functionally distinct, neuronal circuits that occupy spatially distinct sub-regions across the entire organ. For these reasons, systematic investigations attempting to elucidate the finer details of both intra- and inter-network communication have benefitted heavily from imaging techniques that provide spatial information containing all three dimensions (Guzowski et al., 2005). An SST approach provides the opportunity to examine multiple circuits in their entirety

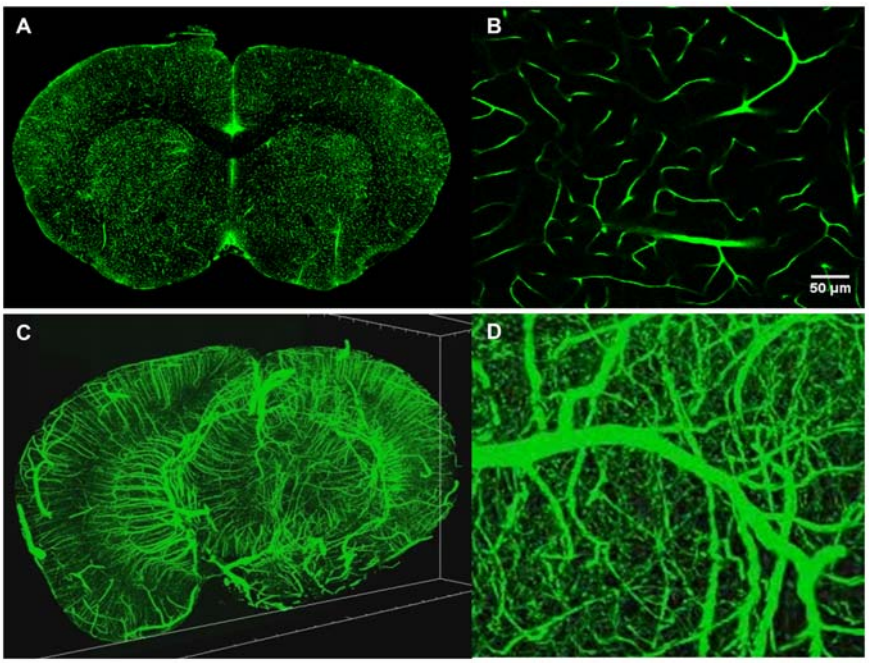

FIGURE 4 | Intravital vascular labeling of a whole mouse brain. Following transcardial perfusion fixation, the mouse is perfused with FITC-conjugated gelatin, effectively filling the vasculature before cooling and solidifying. The FITC-signal provides a strong signal which can easily be isolated from the background using a global threshold approach. **(A)** Representative 2D coronal section of a C57/BL6 mouse labeled with FITC-conjugated gelatin. **(B)** Representative enlarged region of 2D coronal section similar to the one depicted in **(A)**. **(C)** 3D visualization of FITC-labeled mouse brain vasculature. 4 mm portion is shown. Resolution is 1 µm radial by 2 µm axial. **(D)** Representative enlarged region of 3D coronal section similar to the one depicted in **(C)**.

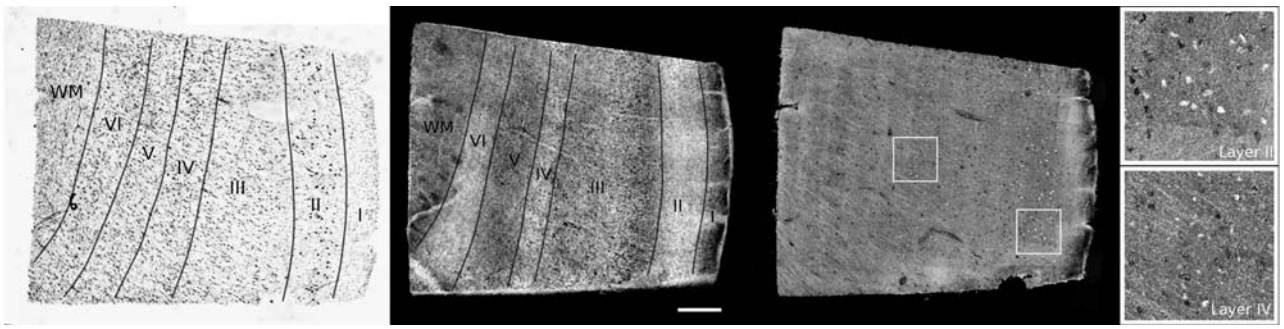

FIGURE 5 | Cortical layers of entorhinal cortex observed using Nissl staining (left) and maximum intensity projection of lower resolution optical coherence tomography (OCT; center). Layers I to IV have been labeled, as well as the white matter (WM). The neurons are observed by OCT using a higher magnification (right). The insets show the neurons of layer II (top) and IV (bottom). Scale bar = 500 µm. Figure Credited from Magnain et al. (2015).

and simultaneously allows for the visualization of spatially defined cellular and morphological data. Here, we briefly touch upon a variety of applications where SST has been utilized to address fundamental questions in the field of neuroscience, as well as propose theoretical applications of the approach.

Mapping Neuronal Activation

While SST can be characterized as a static methodology, relying upon fixed tissue for imaging, experimental techniques have been developed that allow SST to measure dynamic biological processes, including neuronal circuit activity. Specifically, through the utilization of fluorescently tagged immediate early gene (IEG) proteins, researchers are able to effectively monitor neuronal activation. IEG proteins, such as *c-fos* and *Arc*, undergo rapid and transient expression in response to neuronal activation and when expressed in transgenic animals as fluorescently conjugated proteins, can serve as reliable reporters for neuronal circuit activation in response to stimuli (Kovács, 2008; Eguchi and Yamaguchi, 2009). To-date, the majority of studies evaluating neuronal activity have relied exclusively upon fMRI and while this imaging modality provides both

spatial and temporal resolution, it offers only gross macroscale resolution devoid of cellular or morphological information (Heeger and Ress, 2002; Logothetis, 2008). Conversely, whereas electrophysiology and *in vivo* imaging enable enhanced spatial resolution, these methods only allow for coverage over a small region of interest. The use of SST for *ex vivo* imaging, albeit lacking temporal resolution, overcomes the highlighted shortcomings of both fMRI and *in vivo* imaging by providing the ability to image entire brains at cellular resolution.

Underscoring this point, a study by Vousden et al. (2015) illustrated the ability of SST to perform *ex vivo* whole brain mapping of circuit activation in response to fear memory retrieval in transgenic mice expressing the IEG reporter, arc-venus. Specifically, SST was utilized to visualize arc-venus expression across the whole brain and the resulting high-resolution datasets were subsequently registered and annotated using the Allen Institute brain atlas. In combining whole-brain imaging with image registration and cell segmentation, researchers were able to determine the number of activated neurons per brain region in response to distinct behavioral stimuli. Importantly, this study identified specific neuronal networks in the amygdala, hippocampus and neocortex that are activated in response to fear memory retrieval, thereby demonstrating the utility of a SST approach.

The ability to map neuronal network activation using SST methodology, like the experimental paradigm highlighted by Vousden et al. (2015) is applicable to additional IEG transgenic animals. To this point, Kim et al. (2015) used a similar workflow to study behavioral-induced brain activation in a c-fos-GFP expressing transgenic mouse. Using the SST methodology in conjunction with computational image analysis, researchers performed a side-by-side comparison of female and male interaction-evoked whole-brain activation. Their results highlight distinct sex-dependent differences in the spatial organization of the circuits downstream of the medial olfactory bulb, leading to activation of distinct populations of neurons in the piriform and entorhinal cortex. The cellular data acquired on a whole-brain level, enabled researchers to quantitatively estimate neuron activation per brain region and ultimately correlate spatial activation patterns with specific features of social behavior. The results from this study again highlight the advantages that high-resolution whole-brain imaging affords systematic investigations attempting to dissect the relationship between specific behavioral stimuli and neuronal circuit activation.

Mapping Neuronal Networks

A comprehensive understanding of the neuronal connections within the brain will provide us with invaluable insights as to how complex information is processed by the human brain and ultimately advance our understanding of both physiological and pathological brain function (Feng et al., 2015). However, our ability to map neuronal connections is dependent upon the ability to visualize and track neuronal cell bodies and their projections across multiple, anatomically distinct brain regions. To this point, SST is particularly well suited to satisfy the whole brain sub-cellular imaging required by such network mapping endeavors, providing whole-organ, high resolution imaging. Moreover, the high throughput capability of SST, combined with exceptional image registration, provides a significant advantage over alternative technologies.

In support of this notion, a recent study by Zapiec and Mombaerts (2015) has illustrated the ability of SST to successfully map axonal tracts in the mouse olfactory system. The mouse olfactory system consists of sub-populations of olfactory sensory neurons (OSNs) expressing the same odorant receptor type. These distinct groupings of OSNs project their axons to the olfactory bulb, where they converge onto a small number of glomeruli (Bozza et al., 2002). In order to precisely map the anatomical position of the glomeruli and their corresponding sub-populations of OSNs, researchers utilized genetically modified mice expressing multiple odorant receptor type specific axonal markers. Using a multiplexed approach, images acquired through SST were used to generate an anatomical 3D reconstruction of the mouse olfactory bulb, in which axonal tracts of fluorescently labeled OSNs were traced to their respective glomeruli. Using this approach, researchers quantitatively determined the degree of positional variability for a total of 352 glomeruli within the olfactory system of the mouse and determined that positional variability effectively correlates with odorant receptor subtype. This study elegantly illustrates the ability SST methodology to successfully map neuronal projections within the brain.

As previously mentioned, the highly automated, high resolution nature of SST methodology provides investigators with a unique avenue for investigating whole-brain connectomics. In fact, the Allen Institute, one of several worldwide groups focusing on brain organization, utilized SST to acquire high resolution whole-brain images and successfully map the mouse connectome on a mesoscopic scale (Oh et al., 2014). By utilizing a series of stereotaxic injections of GFP-expressing adeno-associated viruses (AAVs) into different brain regions, in combination with whole brain imaging, image registration, image processing and analysis, researchers were able to map the neuronal networks of the mouse brain at single-cell resolution (Kuan et al., 2015). The acquired high-resolution datasets with 0.35 μm x, y sampling and 100 μm z intervals totaling at 750 gigabytes per brain, were used to identify transfected neurons and trace their projections across whole mouse brains.

The automated and the high throughput capabilities of SST were key for reproducibly processing the 3000 animals used in the study, while the distortion-free images enabled the successful registration and annotation of the identified neuronal connection. The framework developed by the Allen Institute has been adopted by Japan's Brain/MINDS project, where SST is currently being used to map neuronal networks within the marmoset brain on a macroscopic, mesoscopic and microscopic level (Okano et al., 2015).

Gene Therapy

The promise afforded by advances in gene therapy has again placed AAVs at the forefront of drug discovery for neurological diseases (Foust et al., 2009; Bourdenx et al., 2014). For instance, in Parkinson's disease, several gene therapy clinical trials have been tested using local injections of AAV2 into the striatum and subthalamic nucleus of PD patients, in hopes of maintaining or restoring dopaminergic neuron function (Eberling et al., 2008; Christine et al., 2009). Importantly, the discovery of BBB penetrant AAV serotypes presents a unique opportunity for CNS applications, where efficient and specific AAV distribution circumvents the need for highly invasive intracranial injections. However, while the repertoire of AAV serotypes demonstrating BBB penetrance has significantly expanded (Bourdenx et al., 2014), most clinical applications have been limited to the AAV2 (Mingozzi and High, 2011).

In order to take advantage of systemic administration of AAVs newly identified BBB penetrant AAV serotypes must be extensively profiled to protect against unwanted side effects resulting from nonspecific tissue distribution. Current biochemical practices, such as qPCR and ELISA, while capable of quantitatively analyzing genomic copy number or protein expression to determine AAV distribution, require manual dissection of individual brain regions to achieve modest spatial resolution. Additionally, data derived via biochemical analysis alone are devoid of any morphological and cellular information, thereby excluding critical information that may aid in the evaluation of potential therapeutics. Lastly, whereas traditional optical methods relying upon serial section analysis do in fact offer higher resolution and morphological data, the process of manually sectioning and imaging individual brain slices generally restricts these investigations to a fewer number of representative images across the brain.

For applications such as this, the automated and comprehensive imaging employed by SST could have a profound impact on the screening and characterization of brain-wide AAV distribution. For instance, utilizing an SST approach to perform systematic whole-brain imaging of mice injected with various serotypes of GFP-expressing AAVs will provide investigators with spatial and morphological rich information that can be used to accurately determine the distribution of AAV serotypes across the brain, allowing visualization of both individual cells and their projections. Based on a comprehensive whole brain distribution of uncharacterized and novel AAV serotypes, researchers will be able to effectively correlate specific AAV serotypes with their targeted brain regions, ensuring specific delivery of their gene of interest. This information will be of the utmost value as researchers evaluate the potential therapeutic and safety profiles of innovative AAV-based therapies.

Alzheimer's Disease and Amyloid Plaque Imaging

Accumulating evidence suggests that abnormal protein aggregation is central to Alzheimer's disease (AD) pathology, affecting multiple neuronal cell types in functionally distinct networks throughout the brain (Dickerson and Sperling, 2008; Liu et al., 2010). Accordingly, these aggregates, composed of either beta amyloid (Aβ) or hyper-phosphorylated Tau proteins form plaques or neurofibrillary tangles, respectively, and commonly serve as a readout for determining the efficacy of novel therapeutics for AD. The importance of monitoring both the spatial and temporal dynamics of protein aggregation as they appear within specific brain regions is critical not only to understanding the molecular and physiological underpinnings of AD progression but also for calculating an individual patient's response to potential therapies.

Researchers frequently rely upon biochemical methods, such as ELISA, for determining total brain Aβ concentration. While this approach provides quantitative data concerning the total concentration of Aβ across the brain, it is devoid of information pertaining to plaque size, shape or spatial patterning per brain region. Moreover, these methods fail to report on morphological changes that may occur as a result of treatment, including such parameters as the parenchymal vs. vascular plaque ratio as they lack the requisite resolution and contrast.

For this reason, we performed a proof-of-principle experiment involving STP whole-brain imaging of a transgenic mouse model of AD harboring the amyloid precursor protein (APP) S1 mutation. The APP mouse possess a genetic mutation that results in enhanced Aβ plaque formation, exhibiting both parenchymal and vascular plaques, and is currently being used in AD drug discovery (Howlett, 2011). To evaluate both parenchymal and vascular plaques, we injected 3 month old APP mice with methoxy-X04, a systemically administered plaque-labeling compound, along with a fluorescently conjugated gelatin to effectively highlight the vasculature (**Figures 6A–C**). We then segmented all plaques across the brain with an adaptive threshold and classified each plaque as either parenchymal or vascular using an trained classifier (Shamir et al., 2008). The location of each plaque was then mapped against a standard atlas (Ma et al., 2008).

Using the described methodology we were able to successfully quantify both parenchymal and vascular plaques on a per region basis across the brain (**Figures 6D,E**). Our results illustrate a heavy plaque burden in the neo-cortex, consistent with previous studies investigating the APP mouse (Yan et al., 2009). However, by classifying plaque type, we effectively identified distinct trends of parenchymal and vascular plaque deposition across the brain. Specifically, while the neocortex of the APP mouse showed the greatest number of parenchymal plaques among the regions analyzed, the hindbrain contained the highest counts of vascular plaques. Findings of this nature may significantly impact treatments that target individual pathologies of complex neurological diseases and simultaneously reveal spatial differences in treatment efficacy.

LIMITATIONS

While this review has discussed a number of applications that have benefitted from SST based approaches, the full potential of the described methodology remains limited by a

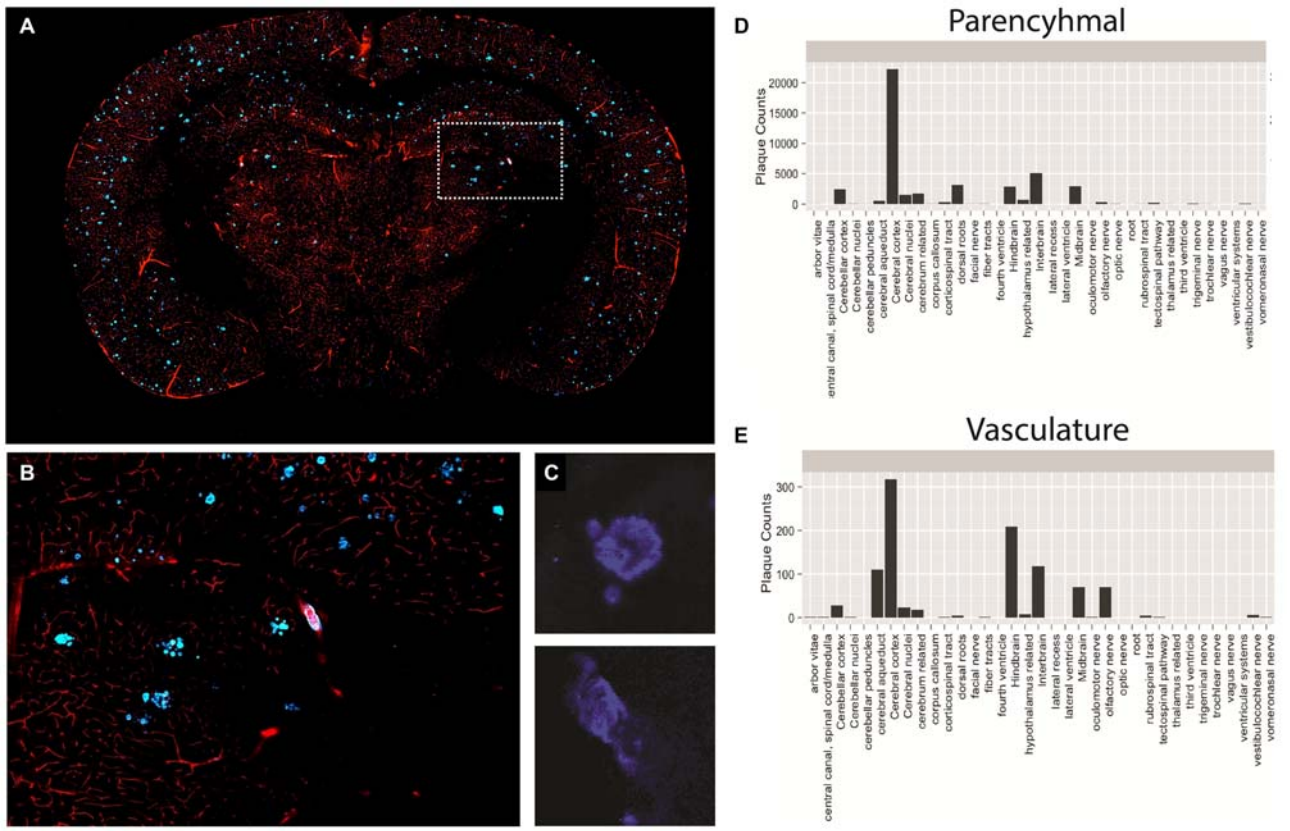

FIGURE 6 | Plaque and vasculature labeling in 3 month old amyloid precursor protein (APP)/PS1 mice. (A) Representative coronal section of APP/PS1 mouse, exhibiting rhodamine positive vasculature and methoxy-X04 labeled plaques. **(B)** Inset depicted in **(A)**, enlarged to show a region of the methoxy-X04, rhodamine labeled brain slice in greater detail. **(C)** Methoxy-X04 signal for representative parenchymal and vascular plaques. **(D,E)** Classification and quantification of parenchymal and vascular plaques segmented by brain region. As described in the text, plaque type was determined by morphological shape and the spatial location of each plaque was determined by atlasing the whole brain image against the Ma 2008 atlas. The resulting information was used to classify plaque type and plot total plaque number against the individual brain regions.

number of factors. Firstly, many of the SST-based imaging approaches, including STP, rely upon a single focal point for sample scanning. While this limitation does not result in egregious imaging durations for atlas level imaging (1.2 μm *x-y* resolution and 100 μm sampling in the *z*-direction), processing an entire mouse brain in under 4 h, studies employing significantly higher sampling or much larger tissue specimens can quickly add hours to processing times. For instance, at current imaging speeds, an entire mouse brain at 1 μm × 1 μm × 2 μm sampling would take nearly a week of continuous imaging. However, there are several strategies that can be used to reduce this time. First, the imaging speed can be increased by integrating resonant scanners or scanning multiple foci in parallel (Bahlmann et al., 2007; Kim et al., 2007). These improvements can lead to an increase in the frame rate by at least a factor of 10. Additionally, selective imaging strategies can ameliorate long imaging times by focusing on specific regions of interest within a larger volume. While faster image times are feasible to achieve, a major hurdle faced by all whole brain imaging studies is processing the large amount of data generated. For instance, imaging a mouse brain with 15 μm spacing throughout the tissue volume using an SST-based approach can easily produce 1 terabyte worth of imaging data. With this in mind, researchers must establish a capable data transfer and storage infrastructure to accommodate large data volumes. Even with substantial IT infrastructure for data storage, the segmentation, registration and analysis of whole brain datasets will remain a significant challenge for the foreseeable future. Finally, while whole mount labeling strategies are currently being developed and improved (Renier et al., 2014; Kim et al., 2015), SST-based methods are currently most efficient when imaging samples that contain inherent fluorescence, achieved by either genetic modification or intracranial injection of fluorescently tagged components. While the SST approach does enable the option of performing IHC on post-SST processed tissue slices, additional work is required to produce a fully automated workflow from sample labeling to imaging. Once achieved, this approach will allow a multitude of biological readouts to be investigated across the brain as part of a fully

automated and comprehensive image acquisition and analysis pipeline.

CONCLUSION

In conclusion, STP tomography is a robust imaging technique that lends itself well to whole brain studies. The basic methodology can be expanded to include additional imaging and biochemical modalities leading to rich multi-component datasets. With a high success rate and minimal sample preparation, it is well suited for quantitative, large scale studies consisting of tens to hundreds of samples. In this review, we have highlighted a number of applications where the high optical and spatial resolution provided by SST has allowed researchers to assess global changes in numerous biological readouts. Furthermore, we provide a proof-of-concept experiment illustrating how an SST-based approach can be used to classify and quantitate Aβ plaques across multiple brain regions in a relevant mouse model of AD. Studies of this nature will help to provide a comprehensive understanding of clinical pathologies and pave the way for novel therapeutics.

ETHICAL STATEMENT

The animal work was done under TGA Sciences, Incorporated Instiutional Animal Care and Use Committee Vertebrate Animal Use. TGA Sciences, Inc. is located in Medford, MA, USA. The IACUC approval date was 5/21/2014 and the animal assurance number was A4497-01.

AUTHOR CONTRIBUTIONS

All authors listed, have made substantial, direct and intellectual contribution to the work, and approved it for publication.

REFERENCES

Adrian, M., Kusters, R., Wierenga, C. J., Storm, C., Hoogenraad, C. C., and Kapitein, L. C. (2014). Barriers in the brain: resolving dendritic spine morphology and compartmentalization. *Front. Neuroanat.* 8:142. doi: 10.3389/fnana.2014.00142

Albanese, A., and Chung, K. (2016). Whole-brain imaging reaches new heights (and lengths). *Elife* 5:e13367. doi: 10.7554/eLife.13367

Bahlmann, K., So, P. T., Kirber, M., Reich, R., Kosicki, B., McGonagle, W., et al. (2007). Multifocal multiphoton microscopy (MMM) at a frame rate beyond 600 Hz. *Opt. Express* 15, 10991–10998. doi: 10.1364/oe.15.010991

Bourdenx, M., Dutheil, N., Bezard, E., and Dehay, B. (2014). Systemic gene delivery to the central nervous system using Adeno-associated virus. *Front. Mol. Neurosci.* 7:50. doi: 10.3389/fnmol.2014.00050

Bozza, T., Feinstein, P., Zheng, C., and Mombaerts, P. (2002). Odorant receptor expression defines functional units in the mouse olfactory system. *J. Neurosci.* 22, 3033–3043.

Christine, C. W., Starr, P. A., Larson, P. S., Eberling, J. L., Jagust, W. J., Hawkins, R. A., et al. (2009). Safety and tolerability of putaminal AADC gene therapy for Parkinson disease. *Neurology* 73, 1662–1669. doi: 10.1212/WNL.0b013e3181c29356

Dean, K. M., and Palmer, A. E. (2014). Advances in fluorescence labeling strategies for dynamic cellular imaging. *Nat. Chem. Biol.* 10, 512–523. doi: 10.1038/nchembio.1556

Denk, W., and Horstmann, H. (2004). Serial block-face scanning electron microscopy to reconstruct three-dimensional tissue nanostructure. *PLoS Biol.* 2:e329. doi: 10.1371/journal.pbio.0020329

Denk, W., Strickler, J. H., and Webb, W. W. (1990). Two-photon laser scanning fluorescence microscopy. *Science* 248, 73–76. doi: 10.1126/science.2321027

Dickerson, B. C., and Sperling, R. A. (2008). Functional abnormalities of the medial temporal lobe memory system in mild cognitive impairment and Alzheimer's disease: insights from functional MRI studies. *Neuropsychologia* 46, 1624–1635. doi: 10.1016/j.neuropsychologia.2007.11.030

Eberling, J. L., Jagust, W. J., Christine, C. W., Starr, P., Larson, P., Bankiewicz, K. S., et al. (2008). Results from a phase I safety trial of hAADC gene therapy for Parkinson disease. *Neurology* 70, 1980–1983. doi: 10.1212/01.wnl.0000312381.29287.ff

Economo, M. N., Clack, N. G., Lavis, L. D., Gerfen, C. R., Svoboda, K., Myers, E. W., et al. (2016). A platform for brain-wide imaging and reconstruction of individual neurons. *Elife* 5:e10566. doi: 10.7554/elife.10566

Eguchi, M., and Yamaguchi, S. (2009). *In vivo* and *in vitro* visualization of gene expression dynamics over extensive areas of the brain. *Neuroimage* 44, 1274–1283. doi: 10.1016/j.neuroimage.2008.10.046

Evans, C. L., Xu, X., Kesari, S., Xie, X. S., Wong, S. T., and Young, G. S. (2007). Chemically-selective imaging of brains structures with CARS microscopy. *Opt. Express* 15, 12076–12087. doi: 10.1364/oe.15.012076

Ewald, A. J., McBride, H., Reddington, M., Fraser, S. E., and Kerschmann, R. (2002). Surface imaging microscopy, an automated method for visualizing whole embryo samples in three dimensions at high resolution. *Dev. Dyn.* 225, 369–375. doi: 10.1002/dvdy.10169

Feng, D., Lau, C., Ng, L., Li, Y., Kuan, L., Sunkin, S. M., et al. (2015). Exploration and visualization of connectivity in the adult mouse brain. *Methods* 73, 90–97. doi: 10.1016/j.ymeth.2015.01.009

Foust, K. D., Nurre, E., Montgomery, C. L., Hernandez, A., Chan, C. M., and Kaspar, B. K. (2009). Intravascular AAV9 preferentially targets neonatal neurons and adult astrocytes. *Nat. Biotechnol.* 27, 59–65. doi: 10.1038/nbt.1515

Giepmans, B. N., Adams, S. R., Ellisman, M. H., and Tsien, R. Y. (2006). The fluorescent toolbox for assessing protein location and function. *Science* 312, 217–224. doi: 10.1126/science.1124618

Goergen, C. J., Radhakrishnan, H., Sakadžić, S., Mandeville, E. T., Lo, E. H., Sosnovik, D. E., et al. (2012). Optical coherence tractography using intrinsic contrast. *Opt. Lett.* 37, 3882–3884. doi: 10.1364/ol.37.003882

Guzowski, J. F., Timlin, J. A., Roysam, B., McNaughton, B. L., Worley, P. F., and Barnes, C. A. (2005). Mapping behaviorally relevant neural circuits with immediate-early gene expression. *Curr. Opin. Neurobiol.* 15, 599–606. doi: 10.1016/j.conb.2005.08.018

Heeger, D. J., and Ress, D. (2002). What does fMRI tell us about neuronal activity? *Nat. Rev. Neurosci.* 3, 142–151. doi: 10.1038/nrn730

Heneka, M. T., Carson, M. J., El Khoury, J., Landreth, G. E., Brosseron, F., Feinstein, D. L., et al. (2015). Neuroinflammation in Alzheimer's disease. *Lancet Neurol.* 14, 388–405. doi: 10.1016/S1474-4422(15)70016-5

Howat, W. J., and Wilson, B. A. (2014). Tissue fixation and the effect of molecular fixatives on downstream staining procedures. *Methods* 70, 12–19. doi: 10.1016/j.ymeth.2014.01.022

Howlett, D. R. (2011). APP transgenic mice and their application to drug discovery. *Histol. Histopathol.* 26, 1611–1632.

Huang, D., Swanson, E. A., Lin, C. P., Schuman, J. S., Stinson, W. G., Chang, W., et al. (1991). Optical coherence tomography. *Science* 254, 1178–1181. doi: 10.1126/science.1957169

Huisken, J., and Stainier, D. Y. R. (2009). Selective plane illumination microscopy techniques in developmental biology. *Development* 136, 1963–1975. doi: 10.1242/dev.022426

Ji, M., Orringer, D. A., Freudiger, C. W., Ramkissoon, S., Xiaohhi, L., Lau, D., et al. (2013). Rapid, label-free detection of brain tumors with stimulated Raman scattering microscopy. *Sci. Transl. Med.* 5:201ra119. doi: 10.1126/scitranslmed.3005954

Jordan, M. I., and Mitchell, T. M. (2015). Machine learning: trends, perspectives and prospects. *Science* 349, 255–260. doi: 10.1126/science.aaa8415

Kim, K. H., Buehler, C., Bahlmann, K., Ragan, T., Lee, W. C., Nedivi, E., et al. (2007). Multifocal multiphoton microscopy based on multianode photomultiplier tubes. *Opt. Express* 15, 11658–11678. doi: 10.1364/oe.15.011658

Kim, S. Y., Cho, J. H., Murray, E., Bakh, N., Choi, H., Ohn, K., et al. (2015). Stochastic electrotransport selectively enhances the transport of highly electromobile molecules. *Proc. Natl. Acad. Sci. U S A* 112, E6274–E6283. doi: 10.1073/pnas.1510133112

Kim, Y., Venkataraju, K. U., Pradhan, K., Mende, C., Taranda, J., Turaga, S. C., et al. (2015). Mapping social behavior-induced brain activation at cellular resolution in the mouse. *Cell Rep.* 10, 292–305. doi: 10.1016/j.celrep.2014.12.014

Klunk, W. E., Bacskai, B. J., Mathis, C. A., Kajdasz, S. T., McLellan, M. E., Frosch, M. P., et al. (2002). Imaging β plaques in living transgenic mice with multiphoton microscopy and methoxy-X04, a systemically administered Congo red derivative. *J. Neuropathol. Exp. Neurol.* 61, 797–805. doi: 10.1093/jnen/61.9.797

Kovács, K. J. (2008). Measurement of immediate-early gene activation- c-fos and beyond. *J. Neuroendocrinol.* 20, 665–672. doi: 10.1111/j.1365-2826.2008.01734.x

Krishnamurthi, G., Wang, C. Y., Steyer, G., and Wilson, D. L. (2010). Removal of subsurface fluorescence in cryo-imaging using deconvolution. *Opt. Express* 18, 22324–22338. doi: 10.1364/OE.18.022324

Kuan, L., Li, Y., Lau, C., Feng, D., Bernard, A., Sunkin, S. M., et al. (2015). Neuroinformatics of the allen mouse brain connectivity atlas. *Methods* 73, 4–17. doi: 10.1016/j.ymeth.2014.12.013

Liu, Z. P., Wang, Y., Zhang, X. S., and Chen, L. (2010). Identifying dysfunctional crosstalk of pathways in various regions of Alzheimer's disease brains. *BMC Syst. Biol.* 4:S11. doi: 10.1186/1752-0509-4-S2-S11

Logothetis, N. K. (2008). What we can do and what we cannot do with fMRI. *Nature* 453, 869–878. doi: 10.1038/nature06976

Ma, Y., Smith, D., Hof, P. R., Foerster, B., Hamilton, S., Blackband, S. J., et al. (2008). *In vivo* 3D digital atlas database of the adult C57BL/6J mouse brain by magnetic resonance microscopy. *Front. Neuroanat.* 2:1. doi: 10.3389/neuro.05.001.2008

Magnain, C., Augustinack, J. C., Konukoglu, E., Frosch, M. P., Sakadzic, S., Varjabedian, A., et al. (2015). Optical coherence tomography visualizes neurons in human entorhinal cortex. *Neurophotonics* 2:015004. doi: 10.1117/1.nph.2.1.015004

Magnain, C., Augustinack, J. C., Reuter, M., Wachinger, C., Frosch, M. P., Ragan, T., et al. (2014). Blockface histology with optical coherence tomography: a comparison with Nissl staining. *Neuroimage* 84, 524–533. doi: 10.1016/j.neuroimage.2013.08.072

Mingozzi, F., and High, K. A. (2011). Therapeutic *in vivo* gene transfer for genetic disease using AAV: progress and challenges. *Nat. Rev. Genet.* 12, 341–355. doi: 10.1038/nrg2988

Oh, S. W., Harris, J. A., Ng, L., Winslow, B., Cain, N., Mihalas, S., et al. (2014). A mesoscale connectome of the mouse brain. *Nature* 508, 207–214. doi: 10.1038/nature13186

Okano, H., Miyawaki, A., and Kasai, K. (2015). Brain/MINDS: brain-mapping project in Japan. *Philos. Trans. R. Soc. Lond. B Biol. Sci.* 370:20140310. doi: 10.1098/rstb.2014.0310

Piccinini, G., and Shagrir, O. (2014). Foundations of computational neuroscience. *Curr. Opin. Neurobiol.* 25, 25–30. doi: 10.1016/j.conb.2013.10.005

Ragan, T., Kadiri, L. R., Venkataraju, K. U., Bahlmann, K., Sutin, J., Taranda, J., et al. (2012). Serial two-photon tomography for automated ex vivo mouse brain imaging. *Nat. Methods* 9, 255–258. doi: 10.1038/nmeth.1854

Ragan, T., Sylvan, J. D., Kim, K. H., Huang, H., Bahlmann, K., Lee, R. T., et al. (2007). High-resolution whole organ imaging using two-photon tissue cytometry. *J. Biomed. Opt.* 12:014015. doi: 10.1117/1.2435626

Renier, N., Wu, Z., Simon, D. J., Yang, J., Ariel, P., and Tessier-Lavigne, M. (2014). iDISCO: a simple, rapid method to immunolabel large tissue samples for volume imaging. *Cell* 159, 896–910. doi: 10.1016/j.cell.2014.10.010

Richardson, D. S., and Lichtman, J. W. (2015). Clarifying tissue clearing. *Cell* 162, 246–257. doi: 10.1016/j.cell.2015.06.067

Roberts, J. C., McCrossan, M. V., and Jones, H. B. (1990). The case for perfusion fixation of large tissues for ultrastructural pathology. *Ultrastruct. Pathol.* 14, 177–191. doi: 10.1080/01913129009025130

Saxena, S., and Jain, A. (2011). Three-dimensional optical coherence tomography of the optic nerve head with myelinated nerve fibers. *J. Ocul. Biol. Dis. Infor.* 4, 145–148. doi: 10.1007/s12177-012-9082-1

Shamir, L., Orlov, N., Eckley, D. M., Macura, T., Johnston, J., and Goldberg, I. G. (2008). Wndchrm–an open source utility for biological image analysis. *Source Code Biol. Med.* 3:13. doi: 10.1186/1751-0473-3-13

So, P. T., Dong, C. Y., Masters, B. R., and Berland, K. M. (2000). Two-photon excitation fluorescence microscopy. *Annu. Rev. Biomed. Eng.* 2, 399–429. doi: 10.1146/annurev.bioeng.2.1.399

Srinivasan, V. J., Radhakrishnan, H., Lo, E. H., Mandeville, E. T., Jiang, J. Y., Barry, S., et al. (2012). OCT methods for capillary velocimetry. *Biomed. Opt. Express* 3, 612–629. doi: 10.1364/BOE.3.000612

Tsai, P. S., Kaufhold, J. P., Blinder, P., Friedman, B., Drew, P. J., Karten, H. J., et al. (2009). Correlations of neuronal and microvascular densities in murine cortex revealed by direct counting and colocalization of nuclei and vessels. *J. Neurosci.* 29, 14553–14570. doi: 10.1523/JNEUROSCI.3287-09.2009

Van de Plas, R., Yang, J., Spraggins, J., and Caprioli, R. M. (2015). Image fusion of mass spectrometry and microscopy: a multimodality paradigm for molecular tissue mapping. *Nat. Methods* 12, 366–372. doi: 10.1038/nmeth.3296

Vousden, D., Epp, J., Okuno, H., Nieman, B., van Eede, M., Dazai, J., et al. (2015). Whole-brain mapping of behaviourally induced neural activation in mice.*Brain Struct. Funct.* 220, 2043–2057. doi: 10.1007/s00429-014-0774-0

Wang, H., Zhu, J., Reuter, M., Vinke, L. N., Yendki, A., Boas, D. A., et al. (2014). Cross-validation of serial optical coherence scanning and diffusion tensor imaging: a study on neural fiber maps in the human medulla oblongata. *Neuroimage* 100, 395–404. doi: 10.1016/j.neuroimage.2014.06.032

Witte, S., Negrean, A., Lodder, J. C., de Kock, C. P., Testa Silva, G., Mansvelder, H. D., et al. (2011). Label-free live brain imaging and targeted patching with third-harmonic generation microscopy. *Proc. Natl. Acad. Sci. U S A* 108, 5970–5975. doi: 10.1073/pnas.1018743108

Yan, P., Bero, A. W., Cirrito, J. R., Xiao, Q., Hu, X., Wang, Y., et al. (2009). Characterizing the appearance and growth of amyloid plaques in APP/PS1 mice. *J. Neurosci.* 29, 10706–10714. doi: 10.1523/JNEUROSCI.2637-09.2009

Zapiec, B., and Mombaerts, P. (2015). Multiplex assessment of the positions of odorant receptor-specific glomeruli in the mouse olfactory bulb by serial two-photon tomography. *Proc. Natl. Acad. Sci. U S A* 112, E5873–E5882. doi: 10.1073/pnas.1512135112

Zheng, T., Yang, Z., Li, A., Lv, X., Zhou, Z., Wang, X., et al. (2013). Visualization of brain circuits using two-photon fluorescence micro-optical sectioning tomography. *Opt. Express* 21, 9839–9850. doi: 10.1364/OE.21.009839

Zipfel, W. R., Williams, R. M., and Webb, W. W. (2003). Nonlinear magic: multiphoton microscopy in the biosciences. *Nat. Biotechnol.* 21, 1369–1377. doi: 10.1038/nbt899

Conflict of Interest Statement: TMR and SPA are employees of TissueVision, Inc., which own the patents for serial section tomography and serial two-photon tomography and has commercialized the technology. The other authors declare that the research was conducted in the absence of any commercial or financial relationships that could be construed as a potential conflict of interest.

frontiers in Neuroanatomy

REVIEW
published: 07 April 2015
doi: 10.3389/fnana.2015.00042

Modeling brain circuitry over a wide range of scales

Pascal Fua[1]* *and Graham W. Knott*[2]

[1] *Computer Vision Lab, I&C School, École Polytechnique Fédérale de Lausanne, Lausanne, Switzerland,* [2] *Bioelectron Microscopy Core Facility, École Polytechnique Fédérale de Lausanne, Lausanne, Switzerland*

If we are ever to unravel the mysteries of brain function at its most fundamental level, we will need a precise understanding of how its component neurons connect to each other. Electron Microscopes (EM) can now provide the nanometer resolution that is needed to image synapses, and therefore connections, while Light Microscopes (LM) see at the micrometer resolution required to model the 3D structure of the dendritic network. Since both the topology and the connection strength are integral parts of the brain's wiring diagram, being able to combine these two modalities is critically important. In fact, these microscopes now routinely produce high-resolution imagery in such large quantities that the bottleneck becomes automated processing and interpretation, which is needed for such data to be exploited to its full potential. In this paper, we briefly review the Computer Vision techniques we have developed at EPFL to address this need. They include delineating dendritic arbors from LM imagery, segmenting organelles from EM, and combining the two into a consistent representation.

Keywords: delineation, segmentation, connectomics, mitochondria, synapses, dendritic arbors

OPEN ACCESS

Edited by:
Kathleen S. Rockland, Boston University School Medicine, USA

Reviewed by:
Lidia Alonso-Nanclares, Universidad Politécnica de Madrid, Spain
Juan Morales, Universidad Politécnica de Madrid, Spain

***Correspondence:**
Pascal Fua, Computer Vision Lab, I&C School, École Polytechnique Fédérale de Lausanne, Station 14, Lausanne 1015, Switzerland
pascal.fua@epfl.ch

Received: *13 February 2015*
Paper pending published: *03 March 2015*
Accepted: *17 March 2015*
Published: *07 April 2015*

Citation:
Fua P and Knott GW (2015) Modeling brain circuitry over a wide range of scales. Front. Neuroanat. 9:42. doi: 10.3389/fnana.2015.00042

1. Introduction

As our ability to image neurons with light and electron microscopes improves, so does our understanding of their form and function. Today we can image large volumes of both live and fixed brain tissue across a wide range of resolutions. At the micrometer scale, light microscopy (LM) of fluorescently labeled structures reveals dendrites and axons of a subset of neurons that can potentially be reconstructed revealing their complex 3D network, as shown in **Figure 1B**. However, their internal structures and all their surrounding elements remain invisible when using this technique. To see them, one must turn to electron microscopes (EM). These provide images at the nanometer scale making it possible to visualize all the structural elements and especially those that are important for understanding the basic connectivity and activity of different cells. These include synapses, dendritic spines, vesicles, and mitochondria, as depicted by **Figure 1C**.

These recent technologies will therefore provide crucial information about the structural, functional, and plasticity principles that govern neural circuits. And since most neurological and psychiatric disorders involve deviations from these principles, such an understanding is key to treating them. Furthermore, neural circuits exhibit a computational power that no known technology can match. A more thorough understanding of their complexities could therefore spur development of new paradigms and bio-inspired devices that would far outperform existing ones.

However, a major bottleneck stands in the way of this promise: These new microscopes can produce terabytes upon terabytes of image data that is so rich and so complex that humans cannot analyze them effectively in their entirety. In this paper, we will briefly present the algorithms we have developed at EPFL to automatically recover the dendritic and axonal trees, segment intra-neuronal

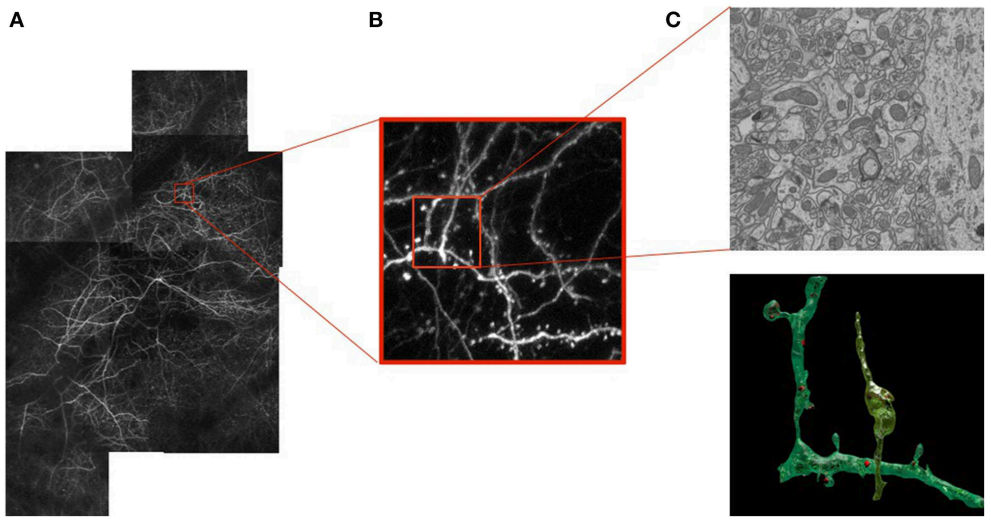

FIGURE 1 | Correlative Microscopy. (A) Fluorescent neurons *in vivo* in the adult mouse brain imaged through a cranial window. **(B)** Image stack at the 1 μm resolution acquired using a 2-photon microscope. **(C)** Image slice of a sub-volume at the 5 nm resolution above a reconstruction of a neuron, dendrite, and associated organelles.

structures from EM images, and register the resulting models. For further details, we refer the interested reader to the original publications.

2. Delineation

The automated delineation of curvilinear structures has been investigated since the inception of the field of Computer Vision in the 1960s and 1970s. Nevertheless, despite decades of sustained effort, full automation remains elusive when the image data is as noisy and the structures exhibit as complex a morphology as they do in microscopy data. As a result, practical systems still require extensive manual intervention that is both time-consuming and tedious. For example, in the DIADEM challenge to map nerve cells, the results of all the finalists still required substantial time and effort to proofread and correct Ascoli et al. (2010); Peng et al. (2011).

Part of the problem comes from the fact that many existing techniques rely mostly on weak local image evidence, and employ greedy heuristics that can easily get trapped in local minima. As a result, they lack robustness to imaging noise and artifacts. Another common issue is that curvilinear networks are usually treated as tree-like structures without any loops. In practice, however, many interesting networks are not trees since they contain cycles. Furthermore, even among those that really are trees, such as neurites, the imaging resolution is often so low that the branches appear to cross, thus introducing several spurious cycles that can only be recognized once the whole structure has been recovered. In fact, this is reported as one of the major sources of error in Bas and Erdogmus (2011); Chothani et al. (2011); Turetken et al. (2011); Wang et al. (2011); Zhao et al. (2011); Choromanska et al. (2012) and a number of heuristics have been proposed to avoid spurious connections in Chothani et al. (2011); Turetken et al. (2011); Zhao et al. (2011).

2.1. Approach

In our work, we attempt to overcome these limitations by formulating the reconstruction problem as one of solving an Integer Program (IP) on a graph of potential tubular paths. As shown in **Figure 2**, the resulting algorithm goes through the following steps:

- We first compute a *tubularity* value at each image location and radius value. It quantifies the likelihood that there exists a tubular structure of this radius at that location. Given an 3D stack, this creates an 4D scale-space tubularity volume.
- We select regularly spaced high-tubularity points as seed points and connect pairs of them that are within a given distance from each other. This results in a directed tubular graph, such as those shown in **Figure 2B**, which serves as an overcomplete representation for the underlying curvilinear networks.
- Having trained a path classifier using such graphs and ground-truth delineations, we assign probabilistic weights to pairs of consecutive edges of a given graph at detection time.
- We use these weights and solve an integer program to compute the maximum-likelihood directed subgraph of this graph to produce a final result such as the one of **Figure 2C**.

These four steps come in roughly the same sequence as those used in most algorithms that build trees from seed points, as in Fischler et al. (1981); Turetken et al. (2011); Wang et al. (2011); Zhao et al. (2011), but with three key differences. First, whereas heuristic optimization algorithms such as MST followed by pruning or the k-MST algorithm of Turetken et al. (2011) offer no guarantee of optimality, our approach guarantees that the solution is within

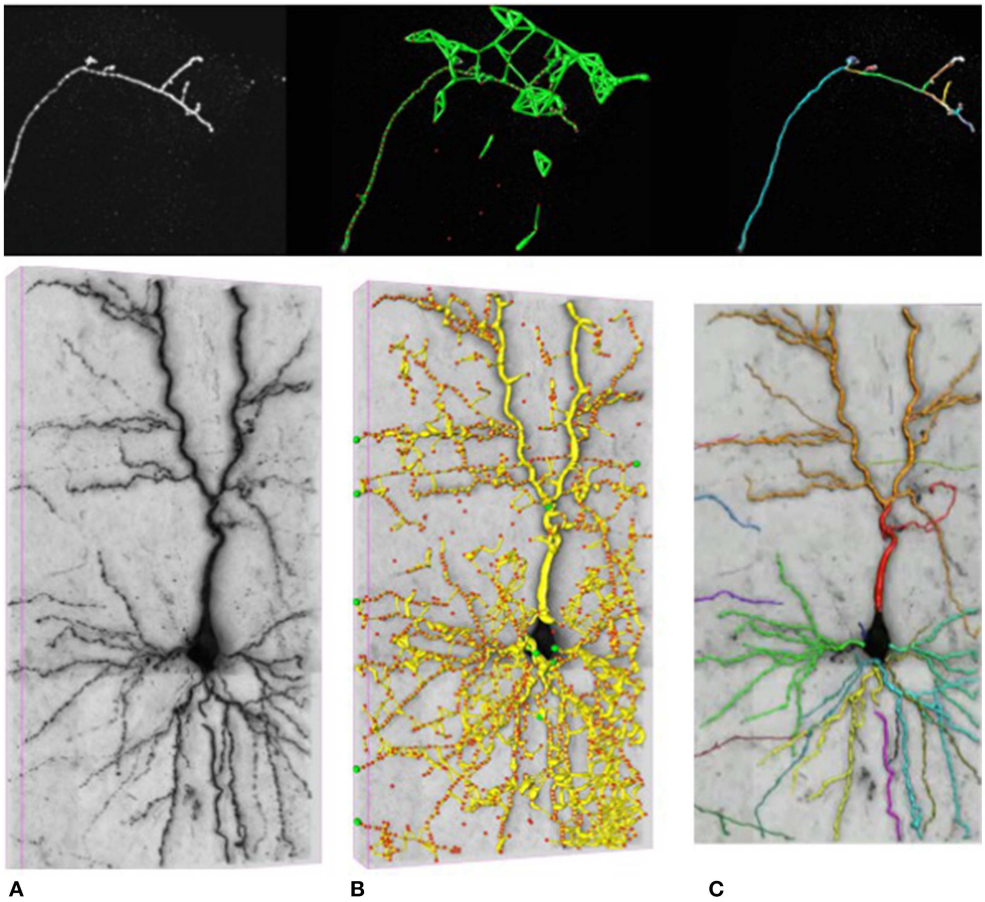

FIGURE 2 | Delineation in confocal (top) and brightfield (bottom) imagery. (A) The original 3D stacks. **(B)** The nodes appear as red circles with the tubular paths connecting them overlaid in green and yellow. **(C)** The final 3D delineations.

a small tolerance of the global optimum. Second, our approach to scoring individual paths using a classifier instead of integrating pixel values as usually done gives us more robustness to image noise and provides peaky probability distributions, which helps ensure that the global optimum is close to the ground truth. Finally, instead of constraining the subgraph to be a tree as many state-of-the-art approaches, we allow it to contain cycles and instead penalize spurious junctions and early branch terminations as described in more details in Turetken et al. (2012, 2013a).

2.2. Results

Here, we demonstrate the effectiveness of our approach on the two datasets depicted in **Figure 2**:

- *Confocal-Axons*, 8 image stacks of Olfactory Projection Fibers (OPF) of the Drosophila fly acquired using a 3D confocal microscope and taken from the DIADEM competition.
- *Brightfield*: 6 image stacks were acquired by brightfield microscopy from biocytin-stained rat brains.

In both datasets, the neurites form tree structures without cycles. However, in the latter, disjoint branches appear to cross, introducing false loops, due to the low z-resolution. In both cases, we used half the stacks for training and half for testing. We used a semi-automated delineation tool Turetken et al. (2013b) to extract ground truth tracings from the training stacks and train our path-classifiers.

In **Table 1**, we compare our approach (OURS) to several state-of-the-art algorithms on the confocal-axons. They are the pruning-based approach (APP2) of Xiao et al. (2013), the active contour algorithm (OSnake) of Wang et al. (2011), the NeuronStudio (NS) software of Wearne et al. (2005), the focus-based depth estimation method (Focus) of Narayanaswamy et al. (2011), and finally the k-MST technique of Turetken et al. (2011), the last two of which were finalists in the DIADEM competition. For all these algorithms, we used the implementations provided by their respective authors with default parameters. We report DIADEM scores as described in Ascoli et al. (2010), which were designed to compare topological accuracy of a reconstructed tree against a ground truth tree.

TABLE 1 | DIADEM Ascoli et al. (2010) scores on four test stacks from the Confocal-Axons dataset.

	OURS	k-MST Turetken et al. (2011)	NS Wearne et al. (2005)	OSnake Wang et al. (2011)	APP2 Xiao et al. (2013)
OPF4	**0.91**	0.87	0.58	0.00	0.67
OPF6	**0.91**	0.90	0.65	0.80	0.82
OPF7	**0.94**	0.91	0.42	0.68	0.76
OPF8	**0.90**	0.74	0.58	0.69	0.63

Each row corresponds to an image stack denoted by OPi. Higher scores are better.

We also evaluated the APP2 Xiao et al. (2013), OSnake Wang et al. (2011), and Focus Narayanaswamy et al. (2011) algorithms on the Brightfield dataset. Since they do not allow the user to provide multiple root vertices, the DIADEM score of their output cannot be computed. To compare their algorithms to ours, we therefore used the NetMets measure of Mayerich et al. (2012) instead because it does not rely heavily on roots. As the DIADEM metric, this measure takes as input the reconstruction and the corresponding ground truth tracings. However, it is more local because it does not account for network topology.

Table 2 shows the NetMets scores on the test images of the *Brightfield* dataset. Note that the Focus algorithm of Narayanaswamy et al. (2011) is specifically designed for brightfield image stacks distorted by a point spread function. Our approach nevertheless brings about a systematic improvement except in one case (BRF3—connectivity FPR). However, the algorithm does that best in this category does significantly worse in the other three.

3. Segmentation

To observe the connectivity between neurons electron microscopy is required. In our work, we have used Focus Ion Beam Scanning Electron Microscopy (FIBSEM) at a 5 nm nearly isotropic sampling. The resulting image stacks reveal the fine neuronal structures, including the synaptic contacts. However, segmenting EM data poses unique challenges in part because the volumes are heavily cluttered with structures that exhibit similar textures and are therefore difficult to distinguish based solely on local image statistics. In this section, we outline our approach to segmenting both synapses and mitochondria. They are described in more details in Becker et al. (2013); Lucchi et al. (2014).

3.1. Synapses

3.1.1. Approach

Synapses are difficult to distinguish from other structures based solely on local texture, as shown in **Figure 4**. Human experts confirm their presence by looking for nearby for post-synaptic densities and vesicles. This protocol cannot be emulated simply by measuring filter responses at the target voxel as in Kreshuk et al. (2011), pooling features into a global histogram as in Narasimha et al. (2009); Lucchi et al. (2012) or relying on hand-determined locations for feature extraction as in Venkataraju et al. (2009); Jurrus et al. (2010).

To emulate this human ability, we designed features we call *context features*, which can be extracted in any cube contained within a large volume centered on the voxel to be classified at 3D location $\boldsymbol{\ell}_i$ with local orientation $\mathbf{n}_i$, as depicted in **Figure 3**. They are computed in several image channels using a number of Gaussian kernels. This yields more than 100, 000 potential features and we rely on AdaBoost to select the most discriminative ones.

3.1.2. Results

We evaluated our method on three different EM stacks acquired from different regions of the adult rat brain, the Somatosensory Cortex, the Hippocampus, and the Cerebellum. Example slices from each dataset are shown in **Figure 4** along with our results.

To evaluate the performance of our approach and compare it to that of Kreshuk et al. (2011), we performed a voxel-wise evaluation against manually acquired ground-truth data. To discount the influence of boundary voxels whose classification may be ambiguous, we defined a testing exclusion zone around the labeled border of the synapse within a distance of d. The voxels within that exclusion zone are ignored and, in **Figure 5**, we plot the Jaccard index between the ground-truth labeling and the one the two algorithms produce as a function of d. To highlight the importance of using context, we plot a third curve that correspond to our approach using only boxes centered on the voxel to be classified, which is much worse than the other two.

3.2. Mitochondria

Mitochondria participate in a wide range of cellular functions and their morphology and localization play a key role in cellular physiology Campello and Scorrano (2010). Furthermore, localization and morphology of mitochondria have been tightly linked to neural functionality. For example, pre- and post-synaptic presence of mitochondria is known to have an important role in synaptic function, as shown in Lee et al. (2007), and mounting evidence also indicates a close link between mitochondrial function and many neuro-degenerative diseases Knott et al. (2008); Poole et al. (2008).

New approaches to detecting mitochondria in EM images have therefore begun to appear. For example, in Vitaladevuni et al. (2008) a Gentle-Boost classifier was trained to detect them based on textural features. In Narasimha et al. (2009), texton-based mitochondria classification in melanoma cells was performed using a variety of classifiers including k-NN, SVM, and Adaboost. While these techniques achieve reasonable results,

TABLE 2 | NetMets Mayerich et al. (2012) scores on the Brightfield dataset.

OURS	BRF1				BRF2				BRF3			
	0.05	**0.29**	**0.71**	**0.65**	**0.11**	**0.29**	**0.81**	**0.78**	**0.07**	**0.28**	0.77	**0.70**
k-MST Turetken et al. (2011)	0.10	0.44	0.79	0.88	**0.11**	0.53	0.84	0.91	0.13	0.35	0.81	0.92
Focus Narayanaswamy et al. (2011)	0.39	0.54	0.75	1.00	0.49	0.53	0.90	1.00	0.38	0.46	**0.74**	1.00
OSnake Wang et al. (2011)	0.66	0.63	0.98	0.99	0.66	0.59	0.99	1.00	0.69	0.38	0.95	0.99
APP2 Xiao et al. (2013)	0.68	0.64	1.00	1.00	0.63	0.54	1.00	1.00	0.65	0.49	1.00	1.00

The NetMets software outputs four values for each trial, which are geometric False Positive Rate (FPR), geometric False Negative Rate (FNR), connectivity FPR, and connectivity FNR, respectively from left to right. Lower scores are better. The best scores are shown in bold face.

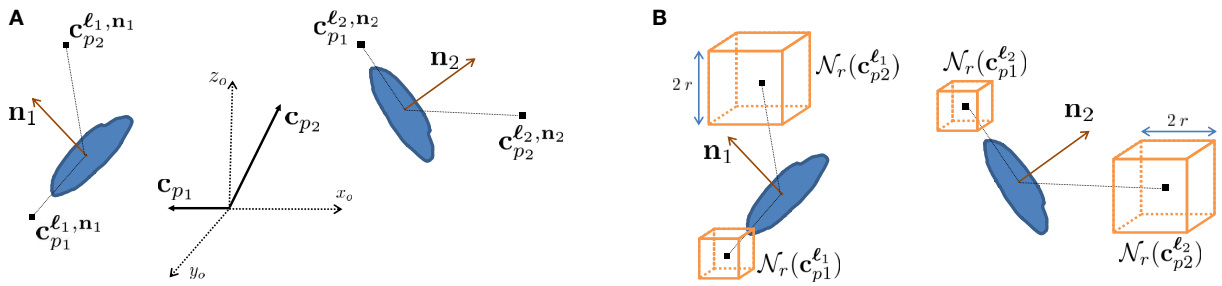

FIGURE 3 | Context features. (A) Relative context cue locations $\mathbf{c}_p$ in the global coordinate system x_o, y_o, z_o are rotated according to the orientation estimate of the voxel of interest $\mathbf{n}_i$ to yield locations $\mathbf{c}_p^{\ell_i}$ that are consistent. **(B)** At each of these locations, image channels are summed over cubes of radius r around their center. Our approach employs AdaBoost to select the most discriminative features for synapse segmentation.

they incorporate only textural cues while ignoring shape information. More recently, more sophisticated features have been successfully used in Kumar et al. (2010); Sommer et al. (2010); Lucchi et al. (2012) in conjunction with either a Random Forest classifier as in Kreshuk et al. (2011). The algorithm of Marquez-Neila et al. (2014) could be used to impose higher-order shape constraints but would be very difficult to extend to 3D volume segmentation because its computational requirements are prohibitive. Our approach overcomes this limitation and extends these earlier techniques by explicitly modeling membranes and exploiting the power of our context features in a Structured SVM framework Lucchi et al. (2014).

3.2.1. Approach

To reduce the computational complexity, our first step of our approach is to over-segment the image stack into *supervoxels*, that is, small voxel clusters with similar intensities. We use the algorithm of Achanta et al. (2012) to compute them. It lets us choose their approximate diameter, which we take to be on the order of the known thickness of the outer mitochondrial membranes. This means that membranes are typically one supervoxel thick. All subsequent computations are performed on supervoxels instead of individual voxels, which speeds them up by several orders of magnitude. Our task is now to classify these supervoxels as being inside the mitochondria, part of the membrane, or outside, as shown in **Figure 6B**.

To this end, we introduce a three-class Conditional Random Field (CRF) Lafferty et al. (2001). It is defined over a graph $\mathcal{G} = (\mathcal{V}, \mathcal{E})$ whose nodes $i \in \mathcal{V}$ correspond to supervoxels and whose edges $(i, j) \in \mathcal{E}$ connect nodes i and j if they are adjacent in the 3D volume. Each node is associated to a feature vector x_i computed from the image data and a label y_i denoting one of the three classes to which a supervoxel can belong. Let Y be the vector of all y_i, which we will refer to as a *labeling*. The most likely labeling of a volume is then found by minimizing an objective function of the form

$$E^{\mathbf{w}}(Y) = \sum_{i \in \mathcal{V}} D_i^{\mathbf{w}}(y_i) + \sum_{(i,j) \in \mathcal{E}} V_{ij}^{\mathbf{w}}(y_i, y_j), \qquad (1)$$

where D_i is referred to as the unary data term and V_{ij} as the pairwise term. The superscript denotes the dependency of these two terms to a parameter vector $\mathbf{w}$.

The unary data term D_i is taken to be a kernelized function of the context features of Section 3.1.1. The pairwise term is a linear combination of a spatial regularization term and a containment term. The spatial term is learned from data and reflects the transition cost between nodes i and j from label y_i to label y_j. The containment term constrains the membrane class to completely enclose the inside class and to be at least one supervoxel thick, as originally proposed in Delong and Boykov (2009). This containment term is hand-defined and does not depend on any parameters. The set of parameters $\mathbf{w}$ to be learned are therefore the weights given to individual features in the unary term and the spatial regularization term. These parameters are learned within the Structured SVM framework discussed above, which requires solving an inference problem on the supervoxel graph $\mathcal{G}$.

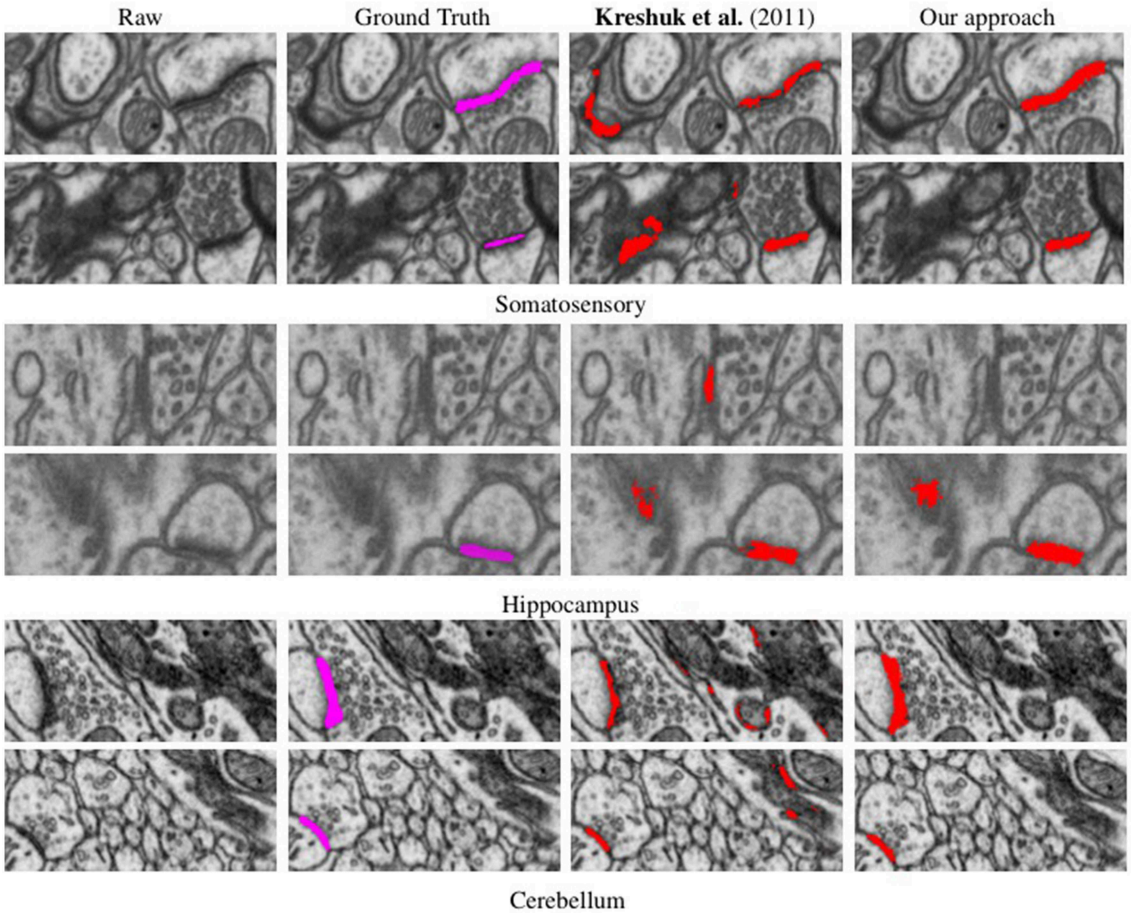

FIGURE 4 | Synapse segmentations overlaid on individual slices from three different datasets after thresholding. Note that our approach yields more accurate results than the method of Kreshuk et al. (2011) with almost no false positives.

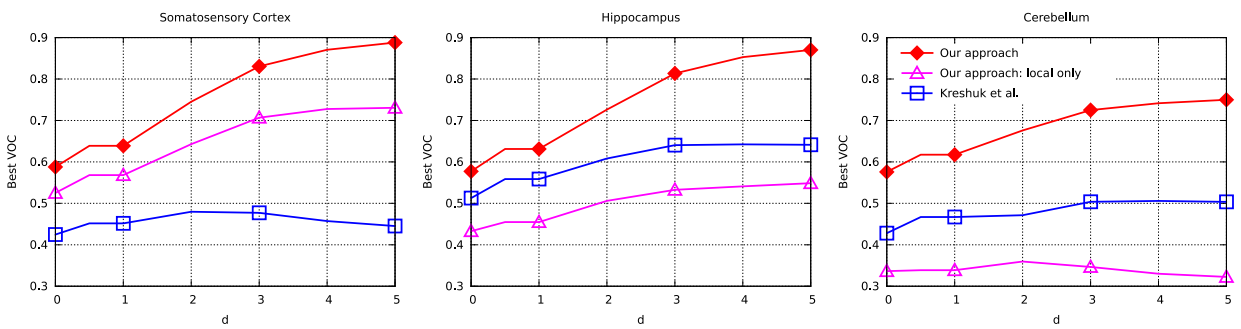

FIGURE 5 | Jaccard index (VOC score) as a function of exclusion zone size *d* for the different datasets. Our approach outperforms Kreshuk et al. (2011) for all values of *d*.

3.2.2. Results

Figure 6C depicts the 3D reconstructions we obtained from a $3.21 \times m \times 3.21 \mu m \times 1.08 \mu m$ volume. In **Figure 6D**, we show the same results after having been proof-read and hand-corrected by a trained neuroscientist. The whole process, including generating the training data, took a little under 2 h. For comparison purposes, the neuroscientist re-generated these results entirely manually and that took him about 6 h for a similar level of precision in terms of the mitochondria volumes and surface areas, which are the relevant biological quantities. In other words, automation

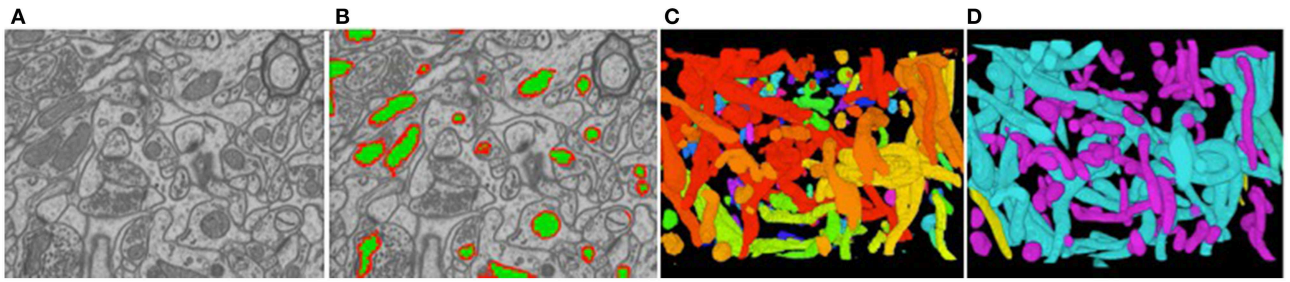

FIGURE 6 | Reconstructed mitochondria. (A) Slice from a 3D image stack. **(B)** The inside of the mitochondria are overlaid in green and the membranes in red. **(C)** Raw results. **(D)** Edited results. The dendritic mitochondria are shown in cyan and axonal ones in purple.

reduced the required amount of manual intervention by a factor 3. Going further will require deploying tools based on deformable models such as those of Neuenschwander et al. (1994, 1997); Jorstad and Fua (2014) to automatically refine mitochondria boundaries and break apart incorrectly merged ones.

To further quantify the performance of our approach, we compared it against other recent automatic methods on image stacks from the Hippocampus and Striatum, which are similar to those we used to detect synapses. In **Table 3**, we report the Jaccard index for the foreground and membrane class jointly, which is representative for this task since whole mitochondria are the object of interest being segmented. The first one is a very recent mitochondria segmentation method Seyedhosseini et al. (2013) that does *not* rely on structured learning. Instead, it trains a cascade of classifiers at different scales and has been shown to outperform earlier algorithms based on Neural Networks, SVMs, and Random Forests on EM imagery. The others correspond to different approaches to performing structured learning. As can be seen, we consistently outperform the competing methods.

4. Registration

Registering LM and EM stacks such as those of **Figures 1B,C** is required to identify the same region in both images and to combine the specific information each modality provides, as discussed earlier. However, this is challenging because the scale-discrepancy between the two modalities—1000 nm for EM vs. 5 nm for LM—produces drastic appearance changes. It makes it impractical to use standard registration techniques that rely on maximizing image similarity, such as those described in Pluim et al. (2003).

Instead, we have proposed in Serradell et al. (2015) a new approach for matching graph structures embedded in 3D volumes, which can deal with the scale-change while being robust to topological differences between the two graphs and even changes in the distances between vertices, unlike earlier graph-matching techniques such as those of Deng et al. (2010); Smeets et al. (2010). It requires no initial position estimate, can handle non-linear deformations, and does not rely on local appearance or global distance matrices. Instead, given graphs extracted from the two images or image-stacks to be registered, we treat graph nodes as the features to be matched. We model the geometric mapping from one data set to the other as a Gaussian Process whose predictions are progressively refined as more correspondences are added. These predictions are in turn used to explore the set of all possible correspondences starting with the most likely ones, which allows convergence at an acceptable computational cost even though no appearance information is available.

4.1. Approach

Given graphs $\mathcal{G}^A = (\mathbf{X}^A, \mathbf{E}^A)$ and $\mathcal{G}^B = (\mathbf{X}^B, \mathbf{E}^B)$ extracted from image-stacks A and B, let the $\mathbf{E}$s denote edges and the $\mathbf{X}$s nodes. The edges, in turn, are represented by dense sets of points forming 3D paths connecting the nodes. Our goal is to use these two graphs to find a geometrical mapping m from A to B such that $m(\mathbf{x}_i^A)$ is as close as possible to $\mathbf{x}_j^B$ in the least-squares sense assuming that $\mathbf{x}_i^A$ and $\mathbf{x}_j^B$ are corresponding voxels.

If correspondences between points belonging to the two graphs were given, we could directly use the Gaussian Process Regression (GPR) as in Rasmussen and Williams (2006) to estimate a non-linear mapping that would yield a prediction of m and its associated variance. In our case, however, the correspondences are initially unavailable and cannot be established on the basis of local image information because the A and B are too different in appearance. In short, this means that we must rely only on geometrical properties to simultaneously establish the correspondences and estimate the underlying non-linear transform. Since attempting to do this directly for all edge points would be computationally intractable, our algorithm goes through the following two steps:

1. **Coarse alignment:** We begin by only matching graph nodes so that the resulting mapping is a combination of an affine deformation and a smooth non-linear deformation. We initialize the search by randomly picking D correspondences, which roughly fixes relative scale and orientation, and using them to instantiate a Gaussian Process (GP). We then recursively refine it as follows: Given some matches between $\mathcal{G}^A$ and $\mathcal{G}^B$ nodes, the GP serves to predict where other $\mathcal{G}^A$ nodes should map and restricts the set of potential correspondences. Among these possibilities, we select the most promising one and use it to refine the GP. Repeating this procedure recursively until enough mutually consistent correspondences have been established and backtracking when necessary lets us quickly

TABLE 3 | Comparing segmentation performance as measured by the Jaccard index of the foreground class for the Striatum and Hippocampus datasets against that of a number of baselines.

	Seyedhosseini et al. (2013) (%)	Tsochantaridis et al. (2004) (%)	Wick et al. (2011) (%)	Lacoste-Julien et al. (2013) (%)	Ratliff et al. (2007) (%)	OURS (%)
Hippocampus	83.8	92.7	83.3	92.7	89.2	**94.8**
Striatum	83.5	90.6	89.6	90.5	88.1	**92.1**

The best scores are shown in bold face.

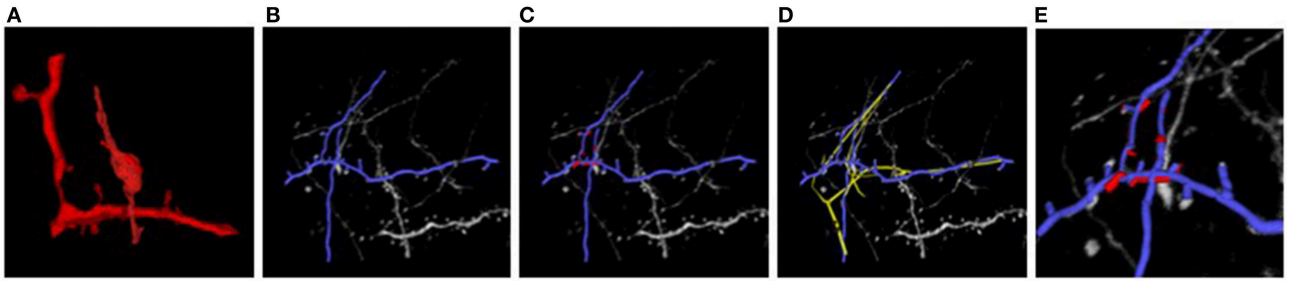

FIGURE 7 | Light and electron microscopy neuronal trees. (A) Graph structure extracted from the electron microscopy image stack, in red. **(B)** Segmented light microscope neurons in blue. **(C)** After the non-linear registration process using ATS-RGM, the EM segmented neuron is deformed and aligned over the LM extracted neuron. **(D)** Registration using CPD, in yellow, which falls into a local minimum. **(E)** A zoom over the region where the EM stack has been extracted. The two neurons have been completely aligned. Best viewed in color.

explore the set of potential correspondences and recover an approximate geometric mapping.

2. **Fine alignment:** Having been learned only from potentially distant graph nodes, the above-mapping is coarse. To refine it, we also establish correspondences between points that form the edges connecting the nodes in such a way that distances along these edges, which we will refer to as *geodesic* distances, are changed as little as possible between the two graphs. Because there are many more such points than nodes, this would be extremely expensive to do from scratch. Therefore, we constrain the correspondence candidates to edges between already matched nodes and rely on the Hungarian algorithm of Munkres (1957) to perform the optimal assignment quickly.

4.2. Results

Figure 7 illustrates the two stages of our approach applied to the EM and LM stacks of **Figure 1**. Even though the two images look extremely different, our algorithm returns a non-rigid deformation that lets us correctly superpose the two stacks. The technique is generic and allows us to correctly align other biological structures, such as blood-vessels networks, that are non-linearly transformed and extracted with different techniques, without having to pre-aligning them and in a manageable amount of time.

5. Conclusion

If we are ever to unravel the mysteries of brain function at its most fundamental level, we will need a precise understanding of how neurons connect to each other. With the advent of new high-resolution light and electron microscopes, fast computers, and high-capacity storage media, the data required to perform this task is now becoming available. Electron microscopes (EM) can now provide the nanometer resolution that is needed to image synapses, and therefore connections, while Light Microscopes (LM) see at the micrometer resolution required to model the 3D structure of the dendritic network. Since both the arborescence and the connections are integral parts of the wiring diagram, combining these two modalities is critically important to answer a growing need for automated quantitative assessment of neuron morphology and connectivity.

Here, we have reviewed our approach to addressing this daunting task. Our algorithms are effective at delineating linear structures in LM, segmenting mitochondria and synapses in EM, and putting the results into a unified coordinate systems to produce a joint representation[1]. However, we have so far only modeled small fractions of cells, which only represent minute parts of simple neural circuit. Our challenge therefore is now to scale up our methods so that they can handle much larger volumes, which will involve parallelizing them and using GPUs, instead of CPUs, to massively increase the processing speed.

Acknowledgments

This work was supported in part by the EU MicroNano ERC project.

[1]Some of the corresponding software can be downloaded from our lab's website http://cvlab.epfl.ch/software.

References

Achanta, R., Shaji, A., Smith, K., Lucchi, A., Fua, P., and Susstrunk, S. (2012). SLIC superpixels compared to state-of-the-art superpixel methods. *IEEE Trans. Pattern Anal. Mach. Intell.* 34, 2274–2282. doi: 10.1109/TPAMI.2012.120

Ascoli, G. A., Svoboda, K., and Liu, Y. (2010). *Digital Reconstruction of Axonal and Dendritic Morphology Diadem Challenge.* Available online at: http://diademchallenge.org/

Bas, E., and Erdogmus, D. (2011). Principal curves as skeletons of tubular objects - locally characterizing the structures of axons. *Neuroinformatics* 9, 181–191. doi: 10.1007/s12021-011-9105-2

Becker, C., Ali, K., Knott, G., and Fua, P. (2013). Learning context cues for synapse segmentation. *IEEE Trans. Med. Imaging* 32, 1864–1877. doi: 10.1109/TMI.2013.2267747

Campello, S., and Scorrano, L. (2010). Mitochondrial shape changes: orchestrating cell pathophysiology. *EMBO Rep.* 11, 678–684. doi: 10.1038/embor.2010.115

Choromanska, A., Chang, S., and Yuste, R. (2012). Automatic reconstruction of neural morphologies with multi-scale graph-based tracking. *Front. Neural Circ.* 6:25. doi: 10.3389/fncir.2012.00025

Chothani, P., Mehta, V., and Stepanyants, A. (2011). Automated tracing of neurites from light microscopy stacks of images. *Neuroinformatics* 9, 263–278. doi: 10.1007/s12021-011-9121-2

Delong, A., and Boykov, Y. (2009). "Globally optimal segmentation of multi-region objects," in *International Conference on Computer Vision* (Anchorage, AK), 285–292. doi: 10.1109/ICCV.2009.5459263

Deng, K., Tian, J., Zheng, J., Zhang, X., Dai, X., and Xu, M. (2010). Retinal fundus image registration via vascular structure graph matching. *Int. J. Biomed. Imaging*. 2010:906067. doi: 10.1155/2010/906067

Fischler, M., Tenenbaum, J., and Wolf, H. (1981). Detection of roads and linear structures in low-resolution aerial imagery using a multisource knowledge integration technique. *Comput. Vis. Graph. Image Process.* 15, 201–223. doi: 10.1016/0146-664X(81)90056-3

Jorstad, A., and Fua, P. (2014). "Refining mitochondria segmentation in electron microscopy imagery with active surfaces," in *ECCV Workshop on Non-Rigid Shape Analysis and Deformable Image Alignment* (Zurich)

Jurrus, E., Paiva, A., Watanabe, S., Anderson, J., Whitaker, R., Jones, B., et al. (2010). Detection of neuron membranes in electron microscopy images using a serial neural network architecture. *Med. Image Anal.* 14, 770–783. doi: 10.1016/j.media.2010.06.002

Knott, A., Perkins, G., Schwarzenbacher, R., and Bossy-Wetzel, E. (2008). Mitochondrial fragmentation in neurodegeneration. *Nat. Rev. Neurosci.* 9, 505–518. doi: 10.1016/j.media.2010.06.002

Kreshuk, A., Straehle, C. N., Sommer, C., Koethe, U., Knott, G., and Hamprecht, F. (2011). "Automated segmentation of synapses in 3D EM data," in *International Symposium on Biomedical Imaging* (Chicago, IL)

Kumar, R., Vazquez-Reina, A., and Pfister, H. (2010). "Radon-like features and their application to connectomics," in *Workshop on MMBIA* (San Francisco, CA)

Lacoste-Julien, S., Jaggi, M., Schmidt, M., and Pletscher, P. (2013). "Block-coordinate frank-wolfe optimization for structural SVMs," in *International Conference on Machine Learning* (Atlanta, GA), 53–61.

Lafferty, J., McCallum, A., and Pereira, F. (2001). "Conditional random fields: probabilistic models for segmenting and labeling sequence Data," in *International Conference on Machine Learning* (Bellevue, WA), 282–289.

Lee, D., Lee, K., Ho, W., and Lee, S. (2007). Target cell-specific involvement of presynaptic mitochondria in post-tetanic potentiation at hippocampal mossy fiber synapses. *J. Neurosci.* 27, 13603–13613. doi: 10.1523/JNEUROSCI.3985-07.2007

Lucchi, A., Smith, K., Achanta, R., Knott, G., and Fua, P. (2012). Supervoxel-based segmentation of mitochondria in EM image stacks with learned shape features. *IEEE Trans. Med. Imaging* 31, 474–486. doi: 10.1109/TMI.2011.2171705

Lucchi, A., Li, Y., Becker, C., Marquez-Neila, P., Smith, K., Knott, G., et al. (2014). Learning structured models for segmentation of 2D and 3D imagery. *IEEE Trans. Med. Imaging*. doi: 10.1109/TMI.2014.2376274. [Epub ahead of print].

Marquez-Neila, P., Kohli, P., Rother, C., and Baumela, L. (2014). "Non-parametric higher-order random fields for image segmentation," in *European Conference on Computer Vision* (Zurich), 269–284.

Mayerich, D., Bjornsson, C., Taylor, J., and Roysam, B. (2012). Netmets: software for quantifying and visualizing errors in biological network segmentation. *BMC Bioinformatics* 13:S7. doi: 10.1186/1471-2105-13-S8-S7

Munkres, J. (1957). Algorithms for the assignment and transportation problems. *J. Soc. Ind. Appl. Math.* 5, 32–38. doi: 10.1137/0105003

Narasimha, R., Ouyang, H., Gray, A., McLaughlin, S., and Subramaniam, S. (2009). Automatic joint classification and segmentation of whole cell 3D images. *Pattern Recognit.* 42, 1067–1079. doi: 10.1137/0105003

Narayanaswamy, A., Wang, Y., and Roysam, B. (2011). 3D image pre-processing algorithms for improved automated tracing of neuronal arbors. *Neuroinformatics* 9, 219–231. doi: 10.1007/s12021-011-9116-z

Neuenschwander, W., Fua, P., Székely, G., and Kubler, O. (1994). "Initializing snakes," in *Conference on Computer Vision and Pattern Recognition* (Seattle, WA), 613–615.

Neuenschwander, W., Fua, P., Székely, G., and Kubler, O. (1997). Velcro surfaces: fast initialization of deformable models. *Comput. Vis. Image Underst.* 2, 237–245. doi: 10.1006/cviu.1996.0578

Peng, H., Long, F., Zhao, T., and Myers, E. (2011). Proof-editing is the bottleneck of 3D neuron reconstruction: the problem and solutions. *Neuroinformatics* 9, 103–105. doi: 10.1007/s12021-010-9090-x

Pluim, J. P. W., Maintz, J. B. A., and Viergever, M. A. (2003). Mutual information based registration of medical images: a survey. *IEEE Trans. Med. Imaging* 22, 986–1004. doi: 10.1109/TMI.2003.815867

Poole, A., Thomas, R., Andrews, L., McBride, H., Whitworth, A., and Pallanck, L. (2008). The pink1/parkin pathway regulates mitochondrial morphology. *Proc. Natl. Acad. Sci. U.S.A.* 105, 1638–1643. doi: 10.1073/pnas.0709336105

Rasmussen, C. E., and Williams, C. K. (2006). *Gaussian Process for Machine Learning*. MIT Press.

Ratliff, N., Bagnell, J. A., and Zinkevich, M. (2007). "(Online) subgradient methods for structured prediction," in *International Conference on Artificial Intelligence and Statistics* (San Juan), 380–387.

Serradell, E., Pinheiro, M., Sznitman, R., Kybic, J., Moreno-Noguer, F., and Fua, P. (2015). Non-rigid graph registration using active testing search. *IEEE Trans. Pattern Anal. Mach. Intell.* 37, 625–638. doi: 10.1109/TPAMI.2014.2343235

Seyedhosseini, M., Sajjadi, M., and Tasdizen, T. (2013). "Image segmentation with cascaded hierarchical models and logistic disjunctive normal networks," in *International Conference on Computer Vision* (Sydney, NSW), 2168–2175. doi: 10.1109/ICCV.2013.269

Smeets, D., Bruyninckx, P., Keustermans, J., Vandermeulen, D., and Suetens, P. (2010). "Robust matching of 3D lung vessel trees," in *MICCAI Workshop on Pulmonary Image Analysis* (Beijing)

Sommer, C., Straehle, C., Koethe, U., and Hamprecht, F. (2010). "Interactive learning and segmentation tool kit," in *Systems Biology of Human Disease* (Boston, MA), 230–233.

Tsochantaridis, I., Hofmann, T., Joachims, T., and Altun, Y. (2004). "Support vector machine learning for interdependent and structured output spaces," in *International Conference on Machine Learning* (New York, NY), 104.

Turetken, E., Benmansour, F., Andres, B., Pfister, H., and Fua, P. (2013a). "Reconstructing loopy curvilinear structures using integer programming," in *Conference on Computer Vision and Pattern Recognition* (Portland, OR)

Turetken, E., Benmansour, F., and Fua, P. (2012). "Automated reconstruction of tree structures using path classifiers and mixed integer programming," in *Conference on Computer Vision and Pattern Recognition* (Providence, RI)

Turetken, E., Benmansour, F., and Fua, P. (2013b). *Semi-Automated Reconstruction of Curvilinear Structures in Noisy 2D Images and 3D Image Stacks*, Technical report, EPFL.

Turetken, E., Gonzalez, G., Blum, C., and Fua, P. (2011). Automated reconstruction of dendritic and axonal trees by global optimization with geometric priors. *Neuroinformatics* 9, 279–302. doi: 10.1007/s12021-011-9122-1

Venkataraju, K., Paiva, A., Jurrus, E., and Tasdizen, T. (2009). "Automatic markup of neural cell membranes using boosted decision stumps," in *IEEE Symposium on Biomedical Imaging: From Nano to Macro* (Boston, MA), 1039–1042.

Vitaladevuni, S., Mishchenko, Y., Genkin, A., Chklovskii, D., and Harris, K. (2008). "Mitochondria detection in electron microscopy images," in *Workshop on Microscopic Image Analysis with Applications in Biology* (New York, NY).

Wang, Y., Narayanaswamy, A., and Roysam, B. (2011). "Novel 4D open-curve active contour and curve completion approach for automated tree structure

extraction," in *Conference on Computer Vision and Pattern Recognition*. (Colorado Springs, CO), 1105–1112.

Wearne, S., Rodriguez, A., Ehlenberger, D., Rocher, A., Henderson, S., and Hof, P. (2005). New techniques for imaging, digitization and analysis of three-dimensional neural morphology on multiple scales. *Neuroscience* 136, 661–680. doi: 10.1016/j.neuroscience.2005.05.053

Wick, M., Rohanimanesh, K., Bellare, K., Culotta, A., and McCallum, A. (2011). "Samplerank: training factor graphs with atomic gradients," in *International Conference on Machine Learning* (Bellevue, WA), 777–784.

Xiao, C., Staring, M., Wang, Y., Shamonin, D., and Stoel, B. (2013). Multi-scale bi-gaussian filter for adjacent curvilinear structures detection with application to vasculature images. *IEEE Trans. Image Process.* 22, 174–188. doi: 10.1109/TIP.2012.2216277

Zhao, T., Xie, J., Amat, F., Clack, N., Ahammad, P., Peng, H., et al. (2011). Automated reconstruction of neuronal morphology based on local geometrical and global structural models. *Neuroinformatics* 9, 247–261. doi: 10.1007/s12021-011-9120-3

Conflict of Interest Statement: The authors declare that the research was conducted in the absence of any commercial or financial relationships that could be construed as a potential conflict of interest.

frontiers in Neuroanatomy

REVIEW
published: 01 July 2015
doi: 10.3389/fnana.2015.00080

Neuroanatomy goes viral!

Jonathan J. Nassi[1], *Constance L. Cepko*[2,3], *Richard T. Born*[4,5]* *and Kevin T. Beier*[6]

[1] Systems Neurobiology Laboratories, Salk Institute for Biological Studies, La Jolla, CA, USA, [2] Department of Genetics, Harvard Medical School, Boston, MA, USA, [3] Department of Ophthalmology, Howard Hughes Medical Institute, Harvard Medical School, Boston, MA, USA, [4] Department of Neurobiology, Harvard Medical School, Boston, MA, USA, [5] Center for Brain Science, Harvard University, Cambridge, MA, USA, [6] Department of Psychiatry and Behavioral Sciences and Department of Biology, Stanford University, Stanford, CA, USA

The nervous system is complex not simply because of the enormous number of neurons it contains but by virtue of the specificity with which they are connected. Unraveling this specificity is the task of neuroanatomy. In this endeavor, neuroanatomists have traditionally exploited an impressive array of tools ranging from the Golgi method to electron microscopy. An ideal method for studying anatomy would label neurons that are interconnected, and, in addition, allow expression of foreign genes in these neurons. Fortuitously, nature has already partially developed such a method in the form of neurotropic viruses, which have evolved to deliver their genetic material between synaptically connected neurons while largely eluding glia and the immune system. While these characteristics make some of these viruses a threat to human health, simple modifications allow them to be used in controlled experimental settings, thus enabling neuroanatomists to trace multi-synaptic connections within and across brain regions. Wild-type neurotropic viruses, such as rabies and alpha-herpes virus, have already contributed greatly to our understanding of brain connectivity, and modern molecular techniques have enabled the construction of recombinant forms of these and other viruses. These newly engineered reagents are particularly useful, as they can target genetically defined populations of neurons, spread only one synapse to either inputs or outputs, and carry instructions by which the targeted neurons can be made to express exogenous proteins, such as calcium sensors or light-sensitive ion channels, that can be used to study neuronal function. In this review, we address these uniquely powerful features of the viruses already in the neuroanatomist's toolbox, as well as the aspects of their biology that currently limit their utility. Based on the latter, we consider strategies for improving viral tracing methods by reducing toxicity, improving control of transsynaptic spread, and extending the range of species that can be studied.

Keywords: neurotropic virus, neuroanatomy, review, transsynaptic tracing, expression vectors

OPEN ACCESS

Edited by:
Kathleen S. Rockland, Boston University School Medicine, USA

Reviewed by:
Antonio Pereira, Federal University of Rio Grande do Norte, Brazil
Mitsuko Watabe-Uchida, Harvard University, USA

***Correspondence:**
Richard T. Born, Department of Neurobiology, Harvard Medical School, 220 Longwood Ave., Boston, MA 02115, USA
rborn@hms.harvard.edu

Received: *15 March 2015*
Accepted: *25 May 2015*
Published: *01 July 2015*

Citation:
Nassi JJ, Cepko CL, Born RT and Beier KT (2015) Neuroanatomy goes viral! Front. Neuroanat. 9:80. doi: 10.3389/fnana.2015.00080

Introduction

The Brain: a Problem of "Organized Complexity"

In 1958, Warren Weaver (Weaver, 1958), a mathematician and former Director for the Natural Sciences of The Rockefeller Foundation, introduced an important distinction between what he called "problems of disorganized complexity" and those of "organized complexity." The former consist of situations in which a very large number of individual entities might be involved, such as the individual molecules within a container of nitrogen gas, but where the interactions between

the entities were helter-skelter; that is, there was no special relationship between any one molecule and any other. The aggregate behavior of such systems could be remarkably well described using statistical methods, one important example being the development of statistical mechanics in the late 19th century by Gibbs, Boltzmann and others. The second class of problems—those of *organized* complexity—were different in the key respect that the particular ways in which the individuals interacted was a critical part of the problem. This may consist of individual humans participating in a market economy, of honeybees within a hive, or of neurons within a brain.

In this last case, it is the connections that define the emergent behavior of the system. Knowing these is arguably as or more important than knowing the precise location of the individual neurons—a possibility that was imaginatively explored in Arnold Zuboff's "The Story of a Brain," (Zuboff, 1981) in which his mad-scientist characters create a "spread-brain" where the brain's individual hemispheres (and, ultimately, individual neurons) could be kept alive in separate nutrient baths, preserving the brain's owner's consciousness so long as they were appropriately wired together. Practical (and ethical) issues aside, this idea that if one understood all of the brain's connections—the so-called "connectome"—one would be a long way towards understanding how it works, continues to drive modern neuroanatomy.

A Brief, Focused History of Connection Mapping with Non-viral Tracers

In this section, we briefly describe the historical development of non-viral tracers, mainly as it pertains to issues relevant to the viral tracers we discuss below. For readers desiring a more thorough and technical treatment of this topic, we have provided relevant references in **Table 1** and further recommend several excellent reviews: for early, transport-based methods, see Cowan and Cuenod (1975) and for more recent methods Lanciego and Wouterlood (2011) and Wouterlood et al. (2014).

With Augustus Waller's (1850) histological description of degenerating axons following section of the glossopharyngeal and hypoglossal nerves of frogs, it became possible to use "Wallerian degeneration" to trace the course of nerve fibers within the brain. This lesion-based method was greatly augmented by the discovery that the degenerating nerve terminals could be labeled with metallic silver (Hoff, 1932; Glees, 1946; Nauta and Gygax, 1951; Fink and Heimer, 1967). In a separate development, the silver-based Golgi method, most famously exploited by Ramón y Cajal (1909), allowed one to visualize entire neurons, including their dendrites and unmyelinated axons, thus permitting a scientist with a superb visual imagination, such as Cajal possessed, to map out the first "circuits" with surprising perspicuity. While the Golgi method produced beautifully labeled neurons whose morphology could thus be studied in detail, it did not permit the reliable demonstration of long-distance anatomical connections; this required the discovery of molecules that would be taken up and actively transported by neurons.

The very fact of Wallerian degeneration made it clear that the distal part of the axon was somehow dependent for its viability on substances supplied by the cell body, and, consequently, that there must exist mechanisms to transport these substances. This deduction was experimentally confirmed by Paul Weiss and colleagues at the University of Chicago (Weiss and Hiscoe, 1948) and not long thereafter exploited to trace connections with the use of radioactively tagged amino acids that were taken up by cell bodies, incorporated into proteins and transported *anterogradely* to axon terminals where they could be rendered visible with autoradiography (Taylor and Weiss, 1965; Lasek et al., 1968). This method, while subject to many limitations (see Cowan and Cuenod, 1975 for details), represented a revolution in neuroanatomy, as it was the first time that connections could be directly demonstrated without having to first inflict damage on the structures of interest. This opened the door to experiments combining connectivity mapping with measurements of neuronal function and development.

The first method that exploited the *retrograde* transport of substances by axons was that demonstrated by the intramuscular injection of proteins, such as, initially, fluorescently labeled albumin (Kristensson, 1970), and then, with greater success, horseradish peroxidase (HRP; Kristensson and Olsson, 1971) which labeled the appropriate pool of motor neurons. HRP was subsequently shown to work in the central nervous system as well (LaVail and LaVail, 1972). It is interesting to note that the early pioneers of these methods were well aware of the powerful cell biological phenomena into which they had tapped. The final sentence of the paper by Kristensson and Olsson (1971) is particularly prescient: "The finding that axons are capable of taking up exogenous proteins and transporting them in a retrograde direction to the nerve cell body may have important implications for the understanding of certain puzzling neurobiological phenomena such as trophic influences of end-organs on the nerve cell body, the signal for chromatolysis after axonal lesions, and how certain toxins and neurovirulent viruses spread from the periphery to the central nervous system."

The use of HRP provided an important benefit over albumin, because its enzymatic activity could be exploited to produce a visible reaction product when post-mortem sections were incubated in a mixture of hydrogen peroxide and diaminobenzidine (Graham and Karnovsky, 1965), a feature that was further improved upon by the use of other substrates, most notably tetramethyl benzidine (Mesulam, 1982). The latter method could produce a reaction product consisting of birefringent crystals that, when viewed under darkfield illumination, revealed brightly labeled neuronal cell bodies on a black background. Even so, these methods did not completely fill neurons and their dendritic arbors, so while retrogradely labeled cell bodies could be identified, their morphology remained poorly defined (though, see Keefer et al., 1976). It was only later, with the discovery of tracers such as biocytin (King et al., 1989), *Phaseolus vulgaris*-leucoagglutinin (PHA-L; Gerfen and Sawchenko, 1984) and biotinylated dextran amine (BDA; Veenman et al., 1992), that "Golgi-like" fills of projection neurons became possible.

While HRP continued to be a workhorse for neuroanatomists, it lacked the desired degree of sensitivity, because its uptake

TABLE 1 | Overview of non-viral neuroanatomical tracers.

Family	Examples	Dir	Spd	Fill?	Reference
Small proteins	Horseradish peroxidase (HRP)	**R**/A	F	N	Kristensson and Olsson (1971)
	albumin				LaVail and LaVail (1972)
Inorganic fluorescent molecules	Fast Blue (FB)	R	M	N	Kuypers et al. (1979)
	Diamidino yellow (DY)				Bentivoglio et al. (1980)
	Fluoro-gold (FG)				Schmued and Fallon (1986)
Dextrans	Fluoro-Ruby (FR)	**A**/R	M	N	Glover et al. (1986)
	Biotinylated dextran amine (BDA)	**A**/R		Y	Nance and Burns (1990)
					Veenman et al. (1992)
Lectins	Wheat germ agglutinin (WGA; WGA-HRP)	**R**/A	F	N	Schwab et al. (1978)
	Phaseolus				Gonatas et al. (1979)
	vulgaris-leucoagglutinin (PHA-L)	A		Y	Gerfen and Sawchenko (1984)
Beads	Latex microspheres	R	F	N	Katz et al. (1984)
					Katz and Iarovici (1990)
Bacterial toxins	Tetanus	R	F	N	Stoeckel et al. (1977)
	cholera (B fragment)	**R**/A			Schwab and Agid (1979)
					Trojanowski et al. (1981)
Trophins	Nerve growth factor (NGF) brain-derived	R	F	N	Hendry et al. (1974)
	neurotrophic factor (BDNF)				Stoeckel and Thoenen (1975)
Amino acids	^{3}H-leucine	A	F/S	N	Cowan et al. (1972)
	^{3}H-proline			Y	Hendrickson (1982)
	biocytin				King et al. (1989)
Carbocyanine dyes	DiI	A/R	S	N	Honig and Hume (1986)
	DiO				Honig and Hume (1989)

Abbreviations: "Dir", direction; "A", anterograde; "R", retrograde (for bi-directionally transported substances, bold-face indicates predominant direction or most common usage); "Spd", speed; "F", fast; "S", slow; "M", moderate; "Fill?", Does the tracer produce Golgi-like fills of neuronal cell bodies?; "Y", yes; "N", no.

by neurons at the injection site was relatively inefficient. This was improved dramatically by conjugating HRP to certain plant lectins, especially wheat germ agglutinin (WGA; Gonatas et al., 1979), a breakthrough that took tracing connections from something of a dark art to a reliable technique that even physiologists could use (M. S. Livingstone, personal communication). Motivated by the notion that the improved sensitivity was due to interactions of the lectins with specific cell-surface molecules on neurons, investigators also explored other conjugates, including cholera toxin (Trojanowski et al., 1981, 1982) and tetanus toxin (Stoeckel et al., 1975; Schwab and Agid, 1979), which were known to be retrogradely transported by neurons and which were subsequently shown to selectively interact with specific gangliosides that were enriched on the surfaces of neurons (Stoeckel et al., 1977).

While this brief history omits a number of important tracers, such as the inorganic fluorescent dyes discovered by Kuypers and colleagues (Kuypers et al., 1979; Bentivoglio et al., 1980), we can already begin to see many of the key properties that would make for an ideal tracer. First, it would be selectively and efficiently taken up by neurons, preferably by intact cell bodies or axon terminals and not damaged fibers (i.e., "axons of passage"); second, it could be targeted to a specific class of intracellular motor proteins that would selectively transport it in either the anterograde or the retrograde direction (Dodding and Way, 2011; Maday et al., 2014); third, upon arriving at its destination, it could be readily amplified and rendered visible, providing a Golgi-like fill with minimal need for histological processing; and fourth, it would be available in a variety of different, distinguishable colors so that experiments with multiple tracers could be performed. A fifth property, not directly addressed above, but a property of some classical tracers, e.g., (Schwab et al., 1979), is that it could potentially cross synapses to label second- and, possibly, higher-order neurons in a given pathway.

Tracers exhibiting some of these properties have been discovered over the past several decades by a combination of trial-and-error, educated guesses and luck. However, given the vast time and superior tinkering skills available to Mother Nature, one is not surprised to learn that she has already produced devices with all of these properties, in the form of neurotropic viruses. What's more, because they carry information encoded by nucleic acids, they can be genetically engineered for specific desired properties (e.g., to travel in anterograde vs. retrograde directions; or to cross or not cross synapses—see "Engineering Viruses to Control Transport" Section) and also be used to introduce foreign genes that can be used to easily detect their presence [e.g., green fluorescent protein, (GFP)] or, more powerfully, to directly monitor or manipulate neuronal function (see "Viruses Engineered to Carry Functional Genes" Section). After a primer on viruses, we will describe some of the modern neuroanatomical strategies permitted by viruses and their

genetically altered cousins, ending with a discussion of possible directions for further development of these powerful biological tools.

A Primer on Viruses for Neuroanatomists

Each gene transfer application calls for a particular set of features in a *vector*, which is defined here as a derivative of a virus used for the delivery of genes. They include: target cell type(s), vector genome size, expression level and duration, vector concentration (titer), DNA or RNA genome, speed of expression after infection, ease of altering the genome and capsid, and safety. One other property of note is whether the virus has an envelope, a lipid bilayer surrounding the capsid, derived from the host plasma membrane. Enveloped viruses have glycoproteins inserted into their envelope, and one can substitute the glycoprotein of one virus for another, to create "pseudotypes," which can alter the host range of the virus (Hirst and Gotlieb, 1953). Viral vectors commonly in use by neuroscientists, summarized in **Table 2**, will be discussed in the next section, with a focus on the features that underlie the choices of each vector for application by neuroscientists. However, prior to the discussion of specific properties, it is worth considering the overarching replication potential of a vector, and how this relates to its use by neuroanatomists.

To use a vector as a transsynaptic tracer, it must replicate, that is, produce more infectious virion particles in the initially infected (or "starter") cell, so that a connected cell can be infected by transmission. A virus that can replicate is referred to as "replication-competent," and examples include the original forms of pseudorabies virus (PRV; Card and Enquist, 2014) and rabies virus (RABV; Kelly and Strick, 2000). Another type of vector is crippled by deletion of an essential gene, but replication can occur when the missing gene is supplied, *in trans*. These "replication-conditional" vectors have an advantage in that replication can be controlled through the delivery of the missing component. Examples of replication-conditional vectors are the Cre-dependent PRV (DeFalco et al., 2001) and glycoprotein (G)-deleted RABV (Wickersham et al., 2007a). A third category consists of vectors that are unable to replicate at all, or "replication-incompetent" vectors. Some replication-incompetent vectors are useful to neuroanatomists in that they can be used as retrograde tracers; that is, they can be taken up by axonal terminals, whereupon they travel to the cell body and initiate vector gene expression [e.g., herpesvirus (HSV) amplicon vectors, Spaete and Frenkel, 1982]. Replication-incompetent vectors do not spread and thus are not transsynaptic tracers. Some of them have been used for an additional role for neuroanatomy, however, in that they can express genes that aid in the transsynaptic tracing carried out by replication-conditional vectors. For example, a viral G gene can be supplied by a replication-incompetent adeno-associated vector (AAV) to complement a replication-conditional RABV (G-deleted) virus. For some viruses, such as HSV vectors, all of these types of replication styles can be created by different types of genome manipulation (Spaete and Frenkel, 1982; Ugolini et al., 1989; Krisky et al., 1998; Lilley et al., 2001).

Viruses that do not Cross Synapses

Retroviridae

A retrovirus is an enveloped, single-stranded RNA virus. Its most salient feature is that it provides for stable, long-term gene expression by virtue of its ability to stably integrate its DNA genome (created from its RNA genome upon entry into a host cell) into a host cell's genome, and express virally-encoded genes from a wide range of integration sites (Knipe and Howley, 2013). This ability to integrate distinguishes it from other commonly used vectors, such as AAV. Target cells that are dividing gradually lose viral genomes that are not integrated, due to dilution, and thus any application that requires retention of expression over a number of cell cycles must use a virus that integrates. An example of such an application for neuroscientists might be the introduction of a retrovirus encoding a viral receptor, e.g., avian tumor virus receptor A (TVA), into a progenitor zone early in development. Integration would allow expansion of the number of cells with the integrated TVA gene, so that there would be a large number of TVA-expressing cells at some later point, to facilitate targeted infection using tracing viruses that contain the cognate glycoprotein, EnvA (as discussed in "Use of Monosynaptic and Transsynaptic Tracing *in vivo*" Section).

The two types of retroviruses commonly used as viral vectors are the gamma-retroviruses and lentiviruses. The critical distinction between these two types of retroviruses concerns their ability to enter a host cell's nucleus in order to integrate the viral DNA. Viral gene expression requires that the genome be integrated, so this step is essential to the use of these viruses as vectors. Gamma-retroviruses are unable to gain entry to the nucleus through an intact nuclear envelope, and thus need a cell to undergo a nuclear envelope breakdown during M phase in order to access a host cell's genome. In contrast, lentiviral DNA can enter the nucleus without nuclear envelope breakdown, and thus can integrate in a postmitotic cell. This feature makes lentiviruses particularly useful for gene transfer into neurons (Naldini et al., 1996). Both types of retroviruses have been modified to render them unable to replicate after infection, i.e., they are replication-incompetent. Lack of replication makes these vectors safe for use in the laboratory (Schambach et al., 2013), and similarly does not lead to disease in animals, with some rare exceptions due to alterations in the host genome due to viral integration (Hacein-Bey-Abina et al., 2003).

Genome size is an important consideration when choosing a vector for a particular application. Lentiviruses and gamma-retroviruses can package a genome of approximately 10 Kb (Kumar et al., 2001), which allows for expression of more than one gene, as well as use of more than one promoter or regulatory element. In contrast, AAV can only package approximately 4.8 Kb. Retroviruses can express cDNAs from the viral long terminal repeat (LTR) promoter, or they can be engineered to use an internal, non-retroviral promoter, e.g., for tissue specificity (Montiel-Equihua et al., 2012). In the latter case, use of a viral genome rigged to lose the activity of the viral LTR appears to give a greater probability of correct regulation of an internal promoter

(Miyoshi et al., 1998; Ginn et al., 2003). However, even with such crippled LTRs, internal promoters are not always properly regulated, and the rules that govern regulation are not known.

Retroviral vectors can be engineered to express small-hairpin RNAs (shRNAs) from Pol III promoters (Paddison et al., 2004; Harpavat and Cepko, 2006), and can use multiple promoters in

TABLE 2 | Summary of viruses of interest to neuroanatomists.

Family	Genome	Size	Titer*	Comments/Applications	Dir	Cyto-toxic?	Bio-safety level
Retroviridae Gamma-retrovirus, e.g., Moloney Murine Leukemia virus (MMLV), lentivirus, (e.g., HIV)	Positive-strand, single strand RNA that is made into cDNA	9–12 Kb	10^7–10^9 cfu/ml	Viral genome integrates into host genome. Use gamma-retrovirus when target cells are dividing and want stable expression; use lentivirus when target cells are not dividing; expression level is typically relatively low	–	N	BSL1–2
Parvoviridae Adeno-associated virus (AAV)	Single strand DNA	4.8 Kb	10^{12}–10^{13} gc/ml	Do not integrate; work well with neurons for stable expression, small genome can limit use of cell-type-specific enhancer/promoter, or large cDNAs; high titer allows for co-infection with >1 genome to enable combinations of genes	–	N	BSL1
Adenoviridae Human adenovirus 5 (Ad5)	Double strand DNA	36 Kb	10^{10}–10^{12} vg/ml	Do not integrate; replication-incompetent forms used for rapid and transient expression in neurons; capsids can elicit inflammatory response. CAV is used as a replication-incompetent retrograde tracer	–	N	BSL2
Canine adenovirus (CAV)	Double strand DNA	36 Kb	10^{10}–10^{12} vg/ml	As above for Ad5	–	N	BSL2
Herpesviridae Alpha-herpesviruses, HSV-1 and Pseudorabies virus (PRV)	Double strand DNA	153 Kb (HSV-1); 144 Kb (PRV)	10^7– 10^9 cfu/ml	Large and complex genomes, making for more difficult genome engineering; replication-competent and conditional versions are used for transsynaptic tracing	**R**/A	Y	BSL2
				Two versions of replication-incompetent forms, short-term (ST) and long term (LT), are used for gene transfer into neurons; large genome capacity and rapid onset of expression; can achieve co-infection with >1 genome; can go retrograde from injection site	**R**	N	BSL2
Rhabdoviridae Rabies virus (RABV), Vesicular stomatitis virus (VSV)	Negative-strand, single strand RNA	12 Kb	10^8–10^9 cfu/ml (**Δ**G) 10^{10}– 10^{12} cfu/ml (wt)	Simple genome makes engineering straightforward; offer good strategy for selection of gene expression level; genome can NOT be recombined with DNA recombinases (Cre and Flp)	**R**/A	Y	BSL1–2
Alphaviridae Sindbis virus (SIN) Semliki forest virus (SFV)	Positive-strand, single strand RNA	12 Kb	10^8– 10^9 cfu/ml	Rapid expression makes it well suited for delivery of transgenes on a short time scale	–	Y	BSL2

Abbreviations: wt, wild type, i.e., replication-competent, meaning virus can spread, ΔG, G gene is deleted rendering virus unable to spread unless the G gene is supplied in trans*, (i.e., by another genetic element such as AAV), Dir, direction of transsynaptic transmission; "A", anterograde; "R", retrograde (for bi-directional transsynaptic transmission, bold-face indicates predominant direction or most common usage).*Titer: The concentration of virion particles and/or infectious units are measured differently for different viruses. While the concentration of infectious units is the most useful for applications, such as cfu/ml (colony forming units/ml) or pfu/ml (plaque forming units/ml), these are not always measured for technical reasons. Alternative methods typically assay viral genome concentration, and different descriptions are used in different publications, e.g., gc/ml (genome copies/ml) or vg/ml (vector genomes/ml). This is important to note as the ratio of particles to infectious particles (p/pfu) can be very high, from 10–10,000. The titers for a virus preparation vary widely due to effects of the genome alterations on virus replication and the preparation method; a range is listed in the Table but there are stocks outside of this range. References: An overview of all of the viruses listed in* ***Table 2*** *can be found in the following virology textbooks: (Flint, 2009; Knipe and Howley, 2013).*

the same genome. For example, a lentivirus was designed to use the Pol III promoters, H1 and U6, to express multiple shRNAs targeting complexin-1 and complexin-2. The same virus used the Pol II promoter, derived from the human ubiquitin-C gene, to express an shRNA-resistant form of complexin-1 (Ahmad et al., 2012).

The choice of the type of retrovirus to use is typically driven by whether the target cell type is mitotic or postmitotic. Gamma-retroviruses have been used to trace lineages in the nervous system, as they will only integrate (and thus express) in mitotic cells, which is exactly what one needs for lineage tracing (Turner and Cepko, 1987). As mentioned previously, lentiviruses are used when one wants to deliver genes to neurons. Both types of retroviruses have been used for gene therapy in humans, due to their stable integration, which provides for long-term gene expression, and again, the choice of which type to use takes into consideration whether the target cell is actively dividing (Wiznerowicz and Trono, 2005; Hacein-Bey-Abina et al., 2014).

Another issue to consider in choosing a viral vector is the percentage of cells at an injection site that need to be infected for the experimental outcome. A limitation of retroviruses is that they do not grow to as high a titer (typically in the range of 10^8–10^9 colony forming units per mL, cfu/mL) as AAVs or adenovirus vectors, which can be several $\log_{10}$ units higher. The expression level should also be taken into consideration. In part, due to the fact that there is usually only a single viral genome in an infected cell, the level of expression from retroviruses tends to be modest (Wickersham et al., 2007a), though a recently developed lentiviral vector with a tetracycline regulatory element and activator may overcome this problem for some applications (Cetin and Callaway, 2014). Relatively low expression is a disadvantage of using these vectors, as not all neuronal processes are well labeled.

The genome structure of retroviruses is fairly flexible, allowing for the design of vectors using different types of promoters and cargoes. In addition, retroviruses, which have an RNA genome packaged in their capsids, create a DNA copy of themselves after infection, which is integrated into the host genome. This means that the integrated viral genome can be modified by Cre- or Flp-mediated recombination (Gonçalves et al., 2010; Sommer et al., 2010), and allows the use of cellular promoters, neither of which is possible when using RNA viruses. The virion particles also can be modified to suit certain applications. Retrovirus particles have a lipid envelope, and can accept the envelope glycoprotein from other viruses, or pseudotyped with, for example, the avian EnvA glycoprotein that targets the infection to cells that express the avian TVA receptor (Bates et al., 1993; Holland et al., 1998). This approach has been used to target infection for lineage studies (Beier et al., 2011a; Hafler et al., 2012) as well as transsynaptic tracing studies using RABV (Wickersham et al., 2007b) and vesicular stomatitis virus (VSV; Beier et al., 2011b).

Parvoviridae—Adeno-Associated Virus (AAV)

AAV is a non-enveloped, single-stranded, small DNA virus of the Parvovirus family (Knipe and Howley, 2013) that has proven effective for gene transfer in the CNS (for a recent review of AAV in the CNS, see Murlidharan et al., 2014). AAV can be used for long-term, stable gene expression in neurons, with little or no toxicity (Kaspar et al., 2002). Its other notable feature is that it grows to very high titers, which can allow the simultaneous infection of cells with more than one AAV vector. There are hundreds of naturally occurring "species" of AAV (Gao et al., 2004), referred to as serotypes, which can be exploited for infection of different cell types. In addition to differences in capsid proteins, the different serotypes have different sequences in their inverted terminal repeats (ITRs), sequences required for replication of the viral genome, as well as differences in the viral replicases that recognize these sequences. The ITRs from serotype 2 have been the most extensively employed in AAV vectors. The ITR serotype is the number that is listed first in the name of an AAV vector, while the capsid type is the second number, e.g., AAV2/8 has the ITRs from AAV 2 and the capsid proteins from AAV 8 (Gao et al., 2005). Serotypes vary in terms of the speed of onset of viral gene expression, with some of the serotypes being particularly slow, needing up to several weeks for the maximum number of cells to show evidence of infection (Vandenberghe et al., 2013). Some of the reasons for this remain unknown, but uncoating and the need to replicate a second strand of DNA (as the virus only packages a single DNA strand) contribute to the lag time. AAV vectors with a genome that is self-complementary, and thus are double-stranded in the capsid, are much faster in terms of onset of expression as they do not need to produce a second DNA strand before initiating gene expression (McCarty et al., 2001; Gray et al., 2011). However, the packaging size of these vectors is very small, about half that of conventional vectors.

Another feature of a serotype to consider is the target cell specificity (e.g., Burger et al., 2004; Cearley and Wolfe, 2006; Taymans et al., 2007; Zincarelli et al., 2008; Aschauer et al., 2013), whether the capsid is transported away from the inoculation site and, if transported, whether in the retrograde (Taymans et al., 2007; Hollis et al., 2008; McFarland et al., 2009; Towne et al., 2010; Masamizu et al., 2011; Aschauer et al., 2013; Castle et al., 2014) or/and anterograde (Castle et al., 2014) directions. AAVs can also access the CNS and PNS from intravascular perfusion, with different efficacies and tropisms depending upon the capsid (Zhang et al., 2011). Toxicity also can vary with the serotype (Howard et al., 2008), or even with a given virus preparation. Toxicity can be due to a high level of expression of the encoded gene, and/or acute inflammation, though this is typically quite low for AAV (McPhee et al., 2006; Zhang et al., 2011; Sondhi et al., 2012), especially relative to adenovirus (Seiler et al., 2007). T-cell mediated toxicity for AAV-infected cells has been seen in humans due to memory T cells (Mingozzi and High, 2013), but has not been reported for rodents. In addition, there may be toxic elements in a virus preparation that do not elicit toxicity through immune system interactions. For example, we have found that different preparations of the same genome in the same capsid type can vary in toxicity, and others have reported differences in toxicity among serotypes for cells cultured from different areas of the CNS (Howard et al.,

2008). Acute toxicity in certain preparations may be due to the capsid itself, or to something that is tightly complexed with the capsid, as we have been unable to eliminate toxicity through multiple purification methods. However, dilution of a stock has proven an effective approach to minimizing toxicity.

In general, AAVs have proven to be very useful for long-term, relatively high-level gene expression in the mammalian CNS. In addition, as with retroviruses, their genome is double-stranded DNA after they infect and convert their single stranded packaged genome into a double strand. Their genomes can thus be modified by recombinase technology, with the tightest Cre-dependent vectors using two pairs of loxP sites, called Flip-excision (FLEx) vectors (Schnütgen et al., 2003). Multiple Cre-dependent vectors can be used to simultaneously infect the same cells, but there are some interesting caveats that must be considered when designing such vectors, due to presumed interactions between AAV-encoded loxP sites on two or more vectors. For similar reasons, there appear to be interactions between AAV-encoded loxP sites and genomic loxP sites (Saunders et al., 2012). Cre-dependent AAV vectors have been exploited for transsynaptic tracing protocols and for targeting optogenetic protein expression to specific types of neurons that express Cre (Atasoy et al., 2008; see also "Viruses Engineered to Carry Functional Genes" Section). The popularity of AAV vectors with neuroscientists also derives from the fact that they are straightforward to engineer, and there are multiple companies and core facilities that make virus constructs as well as virus preparations.

AAVs can be produced as high titer stocks [10^{12}–10^{13} genome copies per mL (gc/mL) for AAV]. Note that AAV titers are usually given in gc/mL, and retroviral titers in infectious units (e.g., cfu/mL). AAV stocks using different capsid types, and different preparations of a given capsid type (Auricchio et al., 2001), can vary in their ratio of capsids to infectious capsids, also referred to as the particle to infectious particle ratio (p/pfu), or infectivity. These ratios range from 10–1000:1 (Auricchio et al., 2001; Vandenberghe, personal communication) and will affect the percentage of cells infected at an injection site. Due to the fact that it is not always trivial to measure infectious particle activity for AAVs, the p/pfu ratio is usually not measured but is one reason why stocks vary in their infectivity. The variables of toxicity and infectivity argue for pilot experiments with each new stock before investing a great deal of time in its use.

Although the naturally occurring AAVs integrate their genome into the host chromosome, at a specific locus on human chromosome 19, the deletion of the rep genes from the vector form of AAV has led to the loss of such targeted integration (McCarty et al., 2004). Some random integration occurs at a low level, but it is not clear if such integrated genomes express viral genes. Most AAV genomes exist as non-integrated episomes, either as single viral genomes or as concatamers (Yang et al., 1999; Nakai et al., 2000). The reason(s) that these genomes remain stably associated with the host cell and persist in expression has not been determined. The lack of consistent integration makes AAV vectors a poor choice if the target cells are dividing and retention of viral gene expression through several cell cycles is required. As noted above, in such cases, retroviruses are a better choice.

The natural promoters of AAV have been replaced with promoters from other viruses, e.g., cytomegalovirus (CMV; Boshart et al., 1985), or host cells, e.g., EF1α (Fitzsimons et al., 2002). Other regulatory elements that can be included are introns, to provide for splicing, polyA sites, and a regulatory element known as the woodchuck post-transcriptional regulatory element (WPRE), which increases the cytoplasmic level of virus-encoded mRNAs (Donello et al., 1998; Zufferey et al., 1999). As with all viral vectors, the exact sequences and their arrangement in the vector can have effects on the level of expression as well as the specificity of expression. As an example, we have found that different intron sequences can have a major effect on the level of expression in the retinal pigmented epithelium (Xiong et al., Unpublished observations). Due to these variables, one should assay for expression of an easily scored gene, such as GFP, using a vector that has all of the regulatory elements and the capsid serotype that one wishes to use in future experiments. In addition, such tests should be performed on animals that are of the age that will be used for future experiments, as we have found that the age of the tissue at the time of inoculation can affect the types of cells infected (Xiong and Cepko, 2014). One can obtain a series of relatively inexpensive, small aliquots of different serotypes from companies to test for the optimum vector characteristics.

The major drawback of AAV vectors is their limited packaging capacity. AAVs can only incorporate about 4.8 Kb of DNA (Dong et al., 2010), which limits the expression to one or two small genes, and also limits the use of different promoter/enhancer elements. There have been several approaches to overcome this limitation. For example, there are trans-splicing vectors where two genomes with different exons of a large gene are co-injected, and result is expression of a large protein, but only if there is a high rate of co-infection (Wu et al., 2010). However, generally if a larger genome is desired, another vector, such as an adenovirus or lentivirus, should be considered.

Adenoviridae—Adenovirus

An adenovirus is a non-enveloped, double-stranded DNA virus, with a larger genome and capsid than AAV, but not as large as those of the HSVs (Knipe and Howley, 2013). Human adenovirus type 5 (Ad5) has been developed for use for gene therapy and most commonly used adenovirus vectors are derived from Ad5 (Gonçalves and de Vries, 2006). The newest generation of adenoviruses (helper-dependent adenovirus or HDV) have had all of their genes removed, both to make the virus less susceptible to immune system modulation and to create space for transcriptional regulatory elements and large or multiple genes (Parks et al., 1996; Ehrhardt and Kay, 2005). These HDVs have a capacity of 35–36 Kb. Adenovirus vectors are not quite as straightforward to genetically engineer or produce (Palmer and Ng, 2003) relative to retroviruses and AAVs. In addition, they remain more pro-inflammatory than retroviruses or AAV (Seiler et al., 2007). As with AAVs, they do not integrate and thus are not used for applications where the target cells are mitotic. Also, as with AAVs, they can be grown to high titer, but unlike AAVs,

they express at a high level within a few days of infection (Akli et al., 1993). Adenovirus vectors have been directly compared to AAVs and lentiviruses for gene transfer in the CNS, and have not fared well in these comparisons when the time course has gone beyond a few days (e.g., Doherty et al., 2011). Still, transient and immediate expression of a gene, such as Cre, using adenovirus vectors can be useful and high titer stocks that express Cre can be purchased from several vendors.

The canine adenoviruses (CAV) are employed for their potent retrograde transport capabilities (Kremer et al., 2000; Soudais et al., 2001; Kissa et al., 2002; Peltékian et al., 2002; Hnasko et al., 2006). In addition, these vectors have been used to express Cre, and a few other genes, e.g., GFP (Kremer et al., 2000). Cre has been used to turn on the expression of floxed endogenous genes (Hnasko et al., 2006), including floxed genes used to enable monosynaptic tracing by RABV (Pivetta et al., 2014). These vectors may become increasingly useful when a DNA virus is required, as the packaging limit of AAVs often limits the experiments that one can do with them. As adenoviruses have double-stranded DNA genomes, they are amenable to Cre or Flp-mediated recombination.

Alphaviridae—Semliki Forest Virus (SFV) and Sindbis Virus (SIN)

The alphaviruses, semliki forest virus (SFV) and sindbis virus (SIN), are enveloped, plus-strand single-stranded RNA viruses. They can be engineered to be replication-incompetent, and typically grow to as high a titer as retroviruses (in the range of 10^8–10^9 cfu/mL). However, unlike retroviruses, multiple viral genes are still expressed from these vectors, resulting in rapid gene expression, but also rapid toxicity.

They have been used in cases where this rapid, high expression is desirable (Bredenbeek et al., 1993; de Hoop et al., 1994; Gwag et al., 1998; Ehrengruber et al., 1999). For example, they have been used for robust labeling of a small number of axons of neurons near the injection site in the brain (Ghosh et al., 2011; Kuramoto et al., 2015), as well as for delivering genes to neurons (including a fluorescent tag for visualization) for single-cell electrophysiological experiments (Kopec et al., 2007; Malinow et al., 2010), among others. However, rapid toxicity limits the use of these vectors. The fast expression and toxicity of these alphaviruses make them similar to VSV, though the transgene expression from VSV is even quicker, occurring within hours (van den Pol et al., 2009; Beier et al., 2011b, 2013b), as discussed further below.

Viruses that Cross Synapses

Herpesviridae—HSV and PRV

HSVs are large, enveloped, double-stranded DNA viruses which are classified into three subfamilies (Davison, 2010). PRV and HSV-1 are members of the subfamily, alphaherpesviruses, and are those used for circuitry tracing. Another subfamily is the betaherpesviruses, which includes CMV, one strain of which is the source of the popular human CMV immediate early enhancer/promoter used extensively in expression vectors (Boshart et al., 1985). The herpesviruses were the first to be extensively employed to trace neuronal circuitry. Though some of the early reports of herpesviruses traveling along nerves were made in the 1920s (Goodpasture and Teague, 1923), the first applications of this type of virus for tracing did not begin until the late 1980s (Ugolini et al., 1989). In these early studies, the virus was injected into peripheral locations, and transmission to specific areas in the brain known to project to the spinal cord was observed. This permitted the mapping of brain projections onto these peripheral sites. Later studies also examined the transmission patterns of different strains of HSVs, such as PRV, in the brain (Card et al., 1990; Strack and Loewy, 1990). All of these initial studies used viruses that were replication-competent and thus could spread across many synapses. The fact that HSV's can spread raises a question of safety for laboratory workers. As PRV does not infect primates from peripheral sites of infection, this is not a major concern, though the virus can replicate, and kill neurons, when cells of the CNS are exposed to the virus, by direct injection (Hurst, 1933) or nasal instillation (Baskerville and Lloyd, 1977). HSV-1, in contrast, is a natural pathogen of humans, giving rise to genital and oral lesions (Lafferty et al., 2000). In addition, these viruses are toxic to cells, as is true with the other viral transsynaptic tracers.

Specific strains of the virus are able to transmit only in the retrograde direction, as in the case of the PRV Bartha strain (Card et al., 1992; Levine et al., 1994; Moore et al., 1995). Other strains, such as the HSV-1 strain H129 (Zemanick et al., 1991; Sun et al., 1996), appear to transmit transsynaptically only in the anterograde direction. The retrograde specificity of the Bartha strain is likely due to a large deletion in the viral genome, which eliminates the expression of three viral genes (Lomniczi et al., 1987), while the anterograde specificity of the HSV H129 is not understood (Szpara et al., 2010). The mechanisms of axonal transport, both retrograde and anterograde, have been studied, and while there is still much to be learned, the process is better understood than for the rhabdoviruses, RABV and VSV. However, for a good review of how difficult it is to clearly define these mechanisms, see Kratchmarov et al. (2012).

HSVs are DNA viruses, and thus their genomes can be engineered using standard recombinant DNA methods. However, as these viral genomes are very large, about 150 Kb, and have many regulatory elements and genes, even minor genome alterations can cripple the virus's ability to replicate. Since at least one cycle of replication is required for a virus to transmit across a synapse, any modification that affects viral fitness can greatly reduce the utility of a construct. Some modifications have been made to enable the use of these viruses as tracers. Fluorescent protein genes have been successfully inserted, and there are versions which include the Brainbow or rainbow cassettes of fluorescent proteins (Boldogkoi et al., 2009; Kobiler et al., 2010). In addition, there is a version that can be used as a calcium sensor, and through the use of both GFP and DsRed, there is a version which can be used to indicate the timing of arrival of the virus in a circuit, as well as the health of infected cells (Boldogkoi et al., 2009). PRV and H129 also have been rendered dependent upon Cre expression for replication, allowing one to use Cre expression patterns in transgenic mice to dictate tracing of a particular circuit (DeFalco et al., 2001; Lo and Anderson,

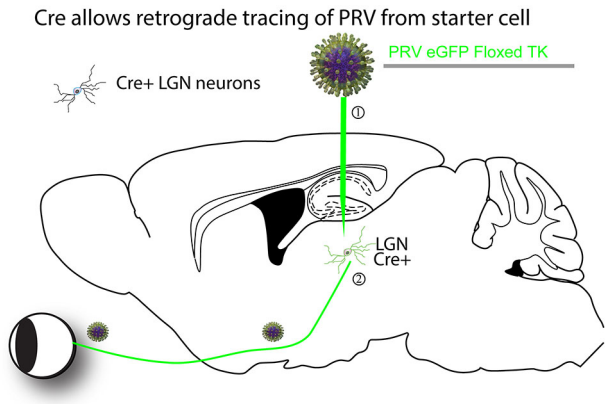

FIGURE 1 | An example of a Cre-dependent tracing strategy. The first Cre-dependent tracing virus was a PRV that expressed a gene essential for virus replication in neurons, thymidine kinase (TK), in a Cre-dependent manner (DeFalco et al., 2001). A theoretical example is as follows. (1) The virus is first injected into a region of interest with cells expressing Cre. (2) Cre recombines the PRV genome so that it can express GFP and TK. The virus can then transsynaptically move from the starter cells to input neurons, such as retinal ganglion cells (RGCs) in the retina in this theoretical example. The virus can continue to transmit polysynaptically, as once Cre recombined the viral genome, it is permanently activated for transmission.

2011; **Figure 1**), or to express a variety of transgenes which can aid in circuit mapping (Boldogkoi et al., 2009; Kobiler et al., 2010). As mentioned above, PRV and HSV-1 are toxic to cells, and have been suggested to have the ability to alter neuronal connectivity (McCarthy et al., 2009). However, a variant of PRV was recently generated that lacks the master transcriptional regulator of endogenous PRV genes, and can therefore express transgenes without replicating or apparent toxicity (Oyibo et al., 2014), auguring an expanded use of these vectors. In terms of speed, PRV has been seen to label infected tissue culture cells in 6 h (Kobiler et al., 2010), and initially infected neurons *in vivo* in just over 1 day post-infection, while the first instances of spread *in vivo* were seen at around 2 days post-infection (e.g., Card et al., 1990). As with all transsynaptic tracer viruses, the kinetics of expression are slower in variants that reduce the fitness of the virus. In addition, the kinetics of labeling of circuits are determined by such variables as the distance of the injection site to the cell bodies of the initial target cells, and the distances from the initial sites of replication to the cell bodies of the secondarily infected cells. Titers of these HSV vectors are typically 10^7–10^9 cfu/ml, and the p/pfu is variable and can be up to 40,000 (Flint, 2000) perhaps due to the fact that the virion particle is large and complex, leading to failures in assembly and/or uncoating.

In addition to its utility as a transsynaptic tracing vector, HSV-1 has been engineered to be a replication-incompetent retrograde tracer, and to be an effective vector for other types of gene transfer into neurons (Spaete and Frenkel, 1982; Krisky et al., 1998; Samaniego et al., 1998; Lilley et al., 2001). These replication-incompetent vectors are not toxic to cells, and can be made into forms that express for different lengths of time, including several months. Given their large size, and certain aspects of vector design, they can be engineered to express at high levels, to express multiple genes, and to use large and/or multiple regulatory elements. They are somewhat more difficult to produce than some of the other vectors discussed here, but there are core facilities that can produce them.

Rhabdoviridae—RABV and VSV

Rhabdoviruses are enveloped, single-stranded RNA viruses, with two members, RABV and VSV, serving as transsynaptic tracers. RABV and VSV each encode five genes, with a genome of approximately 12 Kb. Their capsids are flexible enough to allow packaging of genomes both significantly smaller (Epstein et al., 1980; Timm et al., 2014), or larger (McGettigan et al., 2003), than the native genome. The genes of RABV and VSV are expressed at high levels, permitting robust gene expression and visualization shortly after infection. RABV and VSV have a simple genome organization optimized for the levels of expression of each gene, with a gradient of expression from the 3′-most gene (highest) to the 5′-most (lowest). RABV is typically engineered to encode non-viral genes at the G locus, which is in the fourth position. This means that the expression level of such a gene (Osakada et al., 2011) is less rapid and robust than that of a gene in the first (most 3′) position (van den Pol et al., 2009; Beier et al., 2011b, 2013b; Osakada et al., 2011). However, vectors can be made in which the fluorophore is placed at the 3′-most end, which results in more robust expression (Wickersham et al., 2013).

Due to fact that the genome is RNA, and rhabdoviruses do not have a DNA phase in their lifecycle, it has been challenging to produce infectious virus from engineered plasmids that represent the genomes (Whelan et al., 1995; Mebatsion et al., 1996). Nonetheless, methods have been worked out, and after a virus preparation is made from engineered plasmids, they are then straightforward to propagate by simply infecting host cells *in vitro* (Osakada et al., 2011). It is worth noting that the lack of a DNA phase in their replication also means that one cannot use DNA recombinases, such as Cre, to recombine their genomes. A summary of the unique features of RABV and VSV as transsynaptic tracers is given below.

RABV

RABV, like HSV, can infect neurons from the axon terminals and be retrogradely trafficked to the cell body, as well as transmit among neurons transsynaptically in the retrograde direction (Astic et al., 1993; Ugolini, 1995; Kelly and Strick, 2000). Its use has been more limited than that of HSV, however, due to the biosafety concerns of using RABV, as it is often lethal upon human infection. However, it has been very useful for retrograde transsynaptic tracing in non-human primates (Nassi and Callaway, 2006; Nassi et al., 2006; Rathelot and Strick, 2006, 2009).

The first studies linking RABV to transmission from synaptic junctions occurred in the 1970s and 1980s (Iwasaki et al., 1975; Charlton and Casey, 1979; Tsiang et al., 1983). This was followed by studies in which the time-course of RABV infection was monitored in order to construct circuit diagrams. In one such early study, the tongue muscle was injected with RABV followed by survival times of 1–4 days in different animals (Ugolini,

1995). As expected, after a single day, only first-order hypoglossal motor neurons were labeled. Between 2 and 3 days post-injection, second-order neurons in various brainstem nuclei were identified, while 4-day survival times resulted in the labeling of putatively third-order neurons, including forebrain nuclei. This approach permitted the identification of a chain of connections based on the timing of transsynaptic transmission of RABV. Similar studies using transsynaptic transport of RABV (CVS-11 strain) have revealed connectivity in the monkey visual system (Kelly and Strick, 2000; Nassi and Callaway, 2006; Nassi et al., 2006).

However, the biosafety concerns inherent in using a replication-competent RABV made the use of this virus restricted to a small number of labs that were proficient in its handling and use. A major advance occurred in 2000, when RABV was engineered to become replication-conditional by removal of the G gene from the genome (Etessami et al., 2000). This virus could be used in the laboratory to robustly label neurons projecting to a defined site (Nassi and Callaway, 2007; Wickersham et al., 2007a). In addition, because the virus could not spread, it became more accessible to neurobiology labs who were less familiar with viruses.

The next major advance was the use of this replication-conditional virus for *monosynaptic* retrograde transmission (Wickersham et al., 2007b). This technology permitted, for the first time, unambiguous identification of synaptic inputs onto defined neuronal types. It was also the first virus whose transsynaptic specificity was physiologically verified (Wickersham et al., 2007b). This has led to the widespread use of these vectors to trace circuits in the rodent (discussed further in "Engineering Viruses to Control Transport" Section).

As with HSVs, RABV is toxic to cells. While less rapidly cytotoxic than other transsynaptic vectors such as VSV (van den Pol et al., 2009; Beier et al., 2011b), and HSV-1 and PRV (McCarthy et al., 2009), physiological analyses on RABV-infected neurons should be performed with caution. Also, while many studies have reported the neuronal specificity of RABV transsynaptic tracing, others have reported that glial cells are occasionally observed from viral infection, just as with PRV (Viney et al., 2007; Marshel et al., 2010) and VSV (Beier et al., 2011b). Therefore, viral transmission is not always exclusively limited to traditional synapses.

VSV

The activity of VSV in the CNS was not studied as early as the other transsynaptic tracers, though a few studies reported replication in the CNS (Lundh, 1990; Plakhov et al., 1995; van den Pol et al., 2002, 2009). The first study to modify the VSV genome and examine its transmission patterns showed that the virus could indeed cross synapses and label neurons (Beier et al., 2011b). Importantly, the direction of transmission was shown to be dictated by the nature of the glycoprotein. VSV with its own G showed an *anterograde* transsynaptic transmission pattern, while VSV encoding the RABV G showed a *retrograde* transsynaptic pattern (Beier et al., 2011b).

As VSV is non-pathogenic in nature, one can safely use VSV as a polysynaptic tracer, that is, in its replication-competent form. Infection of a peripheral tissue leads to a rapid shut-down of VSV replication, via the innate immune system (Junt et al., 2007). The lack of escape from this immune response renders VSV safe for laboratory use, which is one of the reasons why VSV has been well studied by virologists and cell biologists. However, direct injection of wild type VSV into the CNS can lead to rapid spread in the brain, which can kill mice very quickly, particularly young mice (Sabin and Olitsky, 1937). The recombinant forms of VSV that encode fluorescent proteins and other viral glycoproteins, such as RABV-G, are attenuated and spread in the CNS more slowly than the wild type (Roberts et al., 1998; Beier et al., 2011b). Other genome modifications have been made to create a monosynaptic tracer (Beier et al., 2011b), following the strategy used for monosynaptic RABV (Wickersham et al., 2007b). When the glycoprotein from the lymphocytic choriomeningitis virus (LCMV-G) was supplied *in trans* in hippocampal organotypic slices, VSV was observed to transmit between neurons in an anterograde direction. This was confirmed electrophysiologically, by optically stimulating the starter cell and recording from the post-synaptic neuron (Beier et al., 2011b). VSV is currently being developed for use *in vivo*, for monosynaptic and either anterograde or retrograde transmission.

Engineering Viruses to Control Transport

Monosynaptic and Restricted Transsynaptic Tracing Systems Offer Advantages in Interpretation

Viruses that can cross multiple synapses have proven highly valuable in constructing connectivity maps in various systems. The general strategy has been to use progressively longer survival times after injection to label progressively higher order neurons, as discussed for RABV in the previous section (e.g., Ugolini, 1995).

While such studies have been very informative, they suffer from two major limitations. One is that the virus infects neurons indiscriminately at the injection site, making it impossible to distinguish differences in inputs to different cell types that are intermingled at one location. A second limitation is using survival time to establish the order of connectivity. Variability in viral replication, intracellular transport and neuronal geometry may create timing differences in labeling that do not strictly reflect synaptic order in a chain of connected neurons. For example, a weak, distal input to a large pyramidal neuron may be transsynaptically labeled considerably later than a strong, proximal input, thus leading to confusion between distal, or weak, n^{th} order connections and proximal $n + 1^{th}$ order connections.

The first report of a cell-type specific virus was published in 2001 (DeFalco et al., 2001). PRV was modified to make the expression of a gene necessary for viral replication, thymidine kinase (TK), Cre-dependent so that tracing was only initiated from cell types expressing Cre (**Figure 1**). However, as the virus could spread across multiple synapses after activation by Cre, it was uncertain whether the novel connections identified represented direct monosynaptic inputs to starter neurons.

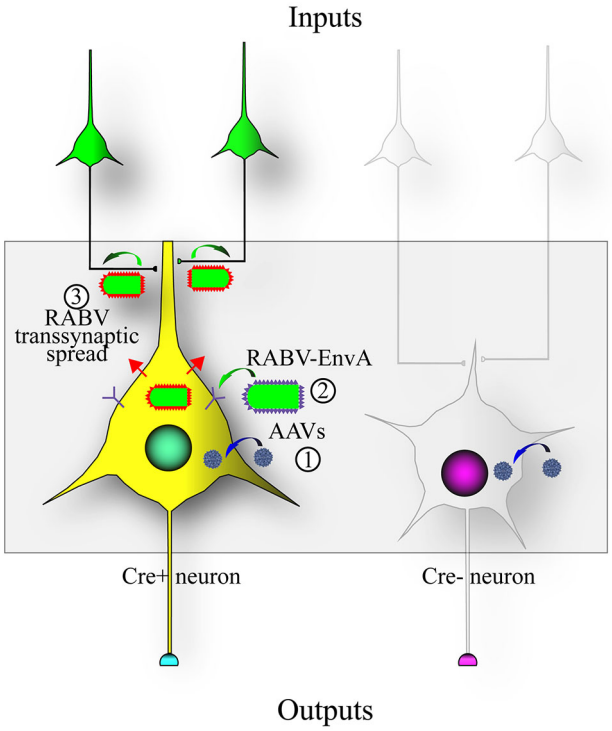

FIGURE 2 | Design of the RABV monosynaptic technique. Expression of the avian tumor virus receptor A (TVA) dictates the types of cells that can be infected by a transsynaptic tracing virus that has a glycoprotein with the extracellular domain of a type A avian retrovirus (EnvA). A chimeric protein with the RABV-G intracellular domain fused to the EnvA extracellular domain (aka ASLV-A/RABV-G fusion, or A/G) is often used in place of the native EnvA. (1) The TVA and RABV-G genes are encoded as Cre-dependent genes in adeno-associated virus (AAV) vectors (blue virions) that are injected into an area with Cre-expressing neurons; (2) After Cre-recombination of the AAV encoded genes, a RABV pseudotyped with EnvA (EnvA shown as purple spikes on the virion surface) can infect the TVA-expressing cells; and (3) transsynaptic transmission of the RABV to synaptically-connected input neurons can occur due to the expression of the RABV-G gene (RABV-G shown as red spikes on the virion surface) in the Cre-expressing cells. This method enables RABV to transmit from an initially infected ("starter") cell to a directly connected presynaptic cell, but no further.

To address this issue, RABV was genetically modified to allow it to specifically infect desired cell types, as well as to spread only to monosynaptically connected inputs (Wickersham et al., 2007b). A schematic of this process is shown in **Figure 2**. Cell type specificity was obtained by expressing the viral receptor in cell types of choice, and monosynaptic restriction of transsynaptic spread was obtained by deleting the G gene from the viral genome, and resupplying it *in trans* specifically in cells also expressing the viral receptor. The investigators initially delivered these genes to cortical slice cultures by biolistic transfection, and subsequently applied the cell-type specific RABV to these cultures. They observed that: (1) RABV infection was specific to defined cell types; (2) the RABV G was necessary and sufficient for transsynaptic spread; and (3) they verified electrophysiologically that these neurons were, in 9 of 11 cases, synaptic partners.

Use of Monosynaptic and Transsynaptic Tracing *In Vivo*

Since the initial demonstration in organotypic slices, the monosynaptic tracing technique has been applied *in vivo* in numerous studies (**Figure 3**). In the first experiments, investigators used mice expressing Cre in specific cell populations and injected Cre-conditional (FLEx) viruses into the target region (**Figure 3A**; Wall et al., 2010). In this case, the Cre mice were crossed to a mouse line conditionally expressing TVA, making only the RABV-G necessary to be delivered virally. Other groups have delivered both TVA and RABV-G virally into Cre populations, using either a single virus (Haubensak et al., 2010; Wall et al., 2013) or multiple viruses (Watabe-Uchida et al., 2012; Miyamichi et al., 2013). Another strategy used the tet system, making the expression of tTA2 Cre-dependent, and the AAV expressing TVA and RABV-G used the TRE promoter (Miyamichi et al., 2011). A recent innovation will allow the use of GFP to direct expression of Cre-dependent genes. This system uses AAV encoding Cre-DOG (Cre-*D*ependent *O*n *G*FP), and AAV FLEx vectors, e.g., for TVA and RABV-G (Tang et al., in press; **Figure 3B**). This is similar to the GFP-dependent transcription system of Tang et al. (2013). It expands the use of transgenic GFP lines for viral tracing through, for example, the selection of GFP+ cells as starter cells. In all of these cases, at least one component is delivered virally (or through the use of Cre and floxed TVA in transgenic mice) in order to spatially restrict the neurons to be infected by RABV.

One additional method that uses TVA and RABV-G for tracing specificity employed a strategy that is the opposite of that outlined above. Rather than use TVA to direct the infection of the starter cells, TVA was used to direct infection of cells presynaptic to the starter cells (**Figure 3D**; Beier et al., 2013a). A VSV vector with the EnvA fusion protein, ASLV-A/RABV-G (A/G), in the genome was grown *in vitro* with the RABV-G protein supplied *in trans*. This created virions with both the A/G and RABV-G glycoproteins on the virion surface. Infection with this preparation allowed retrograde labeling of cells that projected to the injection site by virtue of the RABV-G on the virion surface. Replication of the virus in the starter cells then led to production of virions with the A/G glycoprotein on the surface, as this was the G encoded by the viral genome. Such virions could only infect presynaptic TVA-expressing cells. In this way, one can interrogate the postsynaptic partners of the TVA-expressing cells, as was done to identify retinal ganglion cells postsynaptic to starburst amacrine cells in the retina (Beier et al., 2013a).

While most studies have used the EnvA-TVA strategy to direct viral infection to specific cell types, other possibilities exist. For example, one method employed a viral receptor-ligand bridge protein. In this strategy, TVB was conjugated to neuregulin, which, when injected *in vivo*, binds to the neuregulin receptor, Erb4 (Choi et al., 2010). This was done in order to make cells with Erb4 on the surface also have TVB on the surface, without requiring these cells to carry the gene expressing TVB. RABV pseudotyped with EnvB, a viral glycoprotein that infects cells with TVB, could then specifically infect Erb4-expressing cells.

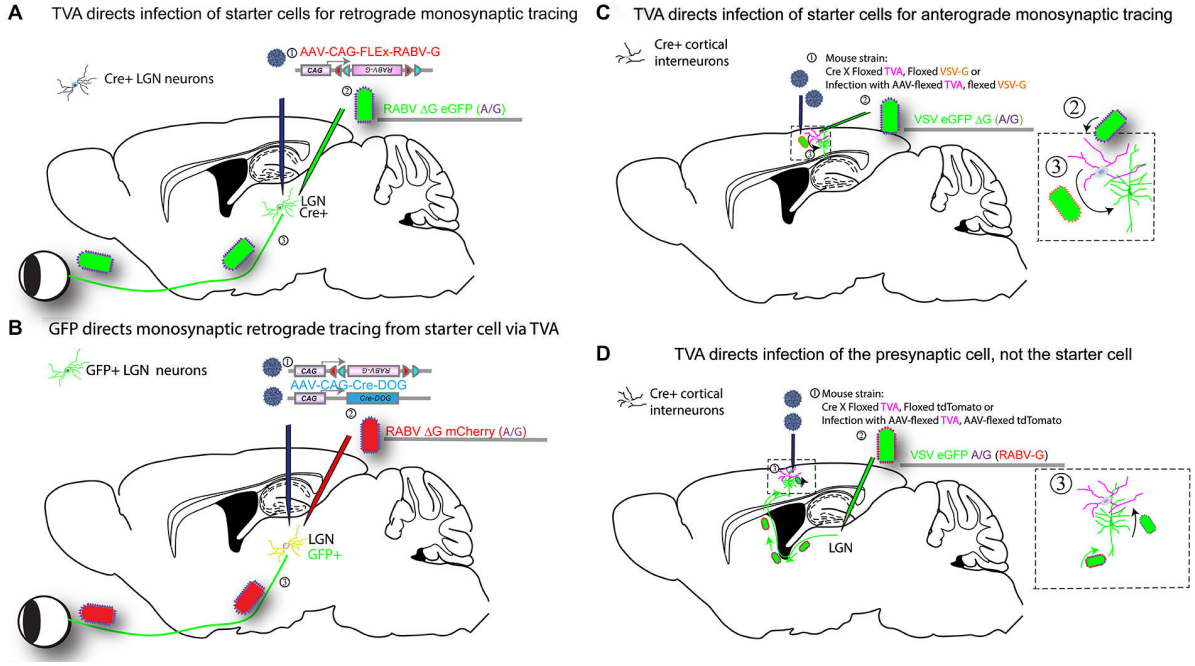

FIGURE 3 | Infection of TVA-expressing cells determines specificity of tracing. Expression of TVA can be arranged using transgenic mouse strains, by crossing a strain expressing Cre in a neuronal cell type of interest to a strain with a Cre-dependent TVA. In addition, one can include in this cross a Cre-dependent G protein (e.g., RABV-G) to enable the tracing virus to transmit, and/or a Cre-dependent fluorescent protein to label the cells with Cre history, i.e., the TVA-expressing cells. AAV vectors encoding such Cre-dependent genes can be used as an alternative to transgenic mouse strains (as shown in **Figure 2**). Four versions of tracing experiments using TVA are shown. **(A)** A transgenic mouse strain that expresses Cre, in e.g., in LGN neurons, will enable identification of the presynaptic partners of the Cre-expression neurons. In this example, the Cre strain is crossed to a strain with a Cre-dependent TVA gene (Beier et al., 2011a), (or, alternatively, an AAV is delivered in step 2 with the Cre-dependent TVA): (1) AAV encoding a Cre-dependent (FLEx) RABV-G is injected into the LGN of mice crossed to have TVA in LGN neurons that are postsynaptic to RGCs, approximately 2 weeks prior to the initiation of tracing. The AAV will uncoat, make a second DNA strand, then initiate expression of the RABV-G protein only in cells that have Cre. Depending upon the serotype of AAV, this process can take over 1 week; (2) A second injection is then made into the same area of the LGN with a tracer virus, RABV ΔG GFP (EnvA or A/G). RABV ΔG GFP will only infect cells with TVA, i.e., those with Cre; (3) When RABV ΔG GFP infects a cell that was previously infected with AAV, and which expresses Cre, RABV ΔG GFP will be transmitted to presynaptic RGCs. Infected RGCs will become GFP+, but will not be able to transmit the virus any further due to the lack of the G gene in the virus and in the RGCs. **(B)** GFP expression determines tracing specificity. The same strategy outlined in **(A)** can be used with a transgenic mouse line that expresses GFP in the LGN: (1) Infection of the LGN with two AAVs encoding Cre-DOG (Cre-dependent upon GFP) enables the GFP-expressing cells to become Cre-expressing cells (Tang et al., in press). Co-infection with an AAV with a Cre-dependent RABV-G and TVA allows the GFP-expressing cells to express RABV-G and TVA; (2) Infection with RABV ΔG mCherry (EnvA or A/G); and (3) transmission from the starter cells to presynaptic cells then proceeds as in scheme shown in **(A)**. **(C)** TVA determines the starter cell type for anterograde monosynaptic tracing. The strategy outlined in A is carried out for anterograde tracing: (1) A mouse cross or AAV are used to determine the TVA-expressing starter cell type. The direction of transsynaptic transmission is set by the choice of G gene, in this case, VSV-G for anterograde tracing. If AAV is used, infection into the cortex is done 2 weeks prior to the initiation of a tracing experiment; (2) Infection of TVA-expressing cells by injection of VSV ΔG GFP (A/G) into the cortex; (3) VSV will replicate in the TVA-expressing cells and if VSV-G is present, will allow transmission to postsynaptic cells. VSV ΔG GFP will not spread from these postsynaptic cells due to the absence of a G gene in the virus and the postsynaptic cells. **(D)** TVA determines the specificity of retrograde infection from starter cells defined by projection site: (1) TVA expression is initiated in cells as shown in **(A)**, but the Cre-dependent RABV-G gene is not used. Instead, one may use a Cre-dependent tdTomato allele to enable the identification of cells with a history of Cre expression (but this is optional). If AAV is used, infection into the LGN is done 2 weeks prior to the initiation of a tracing experiment; (2) A VSV encoding the A/G fusion protein in the genome, and RABV-G protein on the virion surface, is injected, here into the LGN. The RABV-G on the virion surface allows the VSV to travel retrogradely from the LGN injection site to neurons that project into the LGN, e.g., layer 6 pyramidal neurons in V1; and (3) VSV will replicate in the pyramidal neurons and transsynaptically transmit specifically to presynaptic TVA-expressing cells in the cortex. Transmission out of these TVA-expressing cells will only occur to other presynaptic cells that express TVA.

In addition to delivery of TVA and RABV-G by AAVs, other studies have provided these genes by single cell electroporation *in vivo* (Marshel et al., 2010; Nguyen et al., 2012). This technique has the advantage of allowing for the physiological characterization of the neurons that are later used for input tracing *before* they are infected with RABV and potentially physiologically compromised by the virus. It also has the advantage of allowing the investigator to conclude that all virally labeled inputs make direct synaptic connections onto a single, identified cell.

The monosynaptic restriction of transsynaptic tracing does not appear to be limited to tracing only in the retrograde direction. Monosynaptic anterograde tracing was first achieved in slice cultures using VSV that expressed the glycoprotein of either LCMV or of VSV itself (Beier et al., 2011b). *In vivo* applications using VSV and VSV-G are currently being

developed (**Figure 3C**). A recent report also suggested that RABV itself may display anterograde transsynaptic transmission in certain systems (Zampieri et al., 2014). Further studies into the mechanisms of viral transsynaptic transmission should shed light on the mechanisms of directional viral transsynaptic transmission, allowing for more precise direction-specific investigation of connectivity.

Use of RABV as an Unbiased Screening Method for Identifying Direct, Monosynaptic Inputs

One of the major advantages of the monosynaptic RABV technique is the ability to examine direct synaptic inputs to the targeted neuronal populations without a presupposition about their identity or strength. The advantages of using the monosynaptic virus for this purpose are that it does not label axons of passage, which can be problematic when using some classical tracers, and that its high level of amplification at the cell body allows it to strongly label even weakly connected inputs. For example, this approach was used to determine the inputs to AgRP-Cre expressing neurons in the ventral hypothalamus that are critical for the control of hunger (Krashes et al., 2014). The major inputs were the dorsal medial hypothalamus (DMH, 26% of inputs), and the paraventricular hypothalamus (PVH, 18% of inputs). As the monosynaptic method suggested that these are direct inputs, the investigators then used channelrhodopsin-assisted circuit mapping techniques to show that the strength of these glutamatergic afferents to the AgRP neurons was stronger from the PVH than the DMH, and that these connections subsequently were important for the control of feeding behavior. Another study used the virus to suggest a potential feedforward circuit in the PVH (Betley et al., 2013).

Monosynaptic Input Tracing used to Map Circuit Organization

In addition to identifying the presence or absence of connections, RABV can be used to elucidate the topology of neuronal circuits. For example, in the olfactory circuitry in the mouse, it was known that each glomerulus in the olfactory bulb receives projections from one type of olfactory receptor neuron, but it was unknown how the olfactory map was represented in downstream regions, such as in the anterior olfactory nucleus (AON), or in the piriform cortex. RABV was injected into downstream targets of the olfactory bulb projection neurons, the mitral and tufted cells. It was found that the olfactory bulb-AON projection maintained the dorsal-ventral topography present in the olfactory bulb, that the projection to the amygdala was dorsally biased, and that the olfactory cortex appeared to get input from a random assortment of mitral/tufted cells. Thus RABV tracing was able to identify that each of the three different efferent projection sites appeared to have a different representation of the olfactory map than the one present in the olfactory bulb, a finding supported by other studies (Stettler and Axel, 2009; Choi et al., 2011; Sosulski et al., 2011).

These represent only a few examples of the many studies that have used RABV to map connectivity in different circuits throughout the central nervous system (Yonehara et al., 2011; Sun et al., 2014) as well as the spinal cord (Stepien et al., 2010; Tripodi et al., 2011; Esposito et al., 2014).

Use of Monosynaptic Input Tracing to Identify Input Specificity of Different Cell Populations

The monosynaptic RABV technique has also been used to quantitatively compare inputs to two or more different cell populations. One study used the virus to compare the inputs to the two major dopaminergic cell populations in the ventral midbrain, the ventral tegmental area (VTA) and substantia nigra pars compacta (SNc; Watabe-Uchida et al., 2012). The authors restricted infection to dopamine neurons using a Cre mouse line (DAT-Cre) and used injections of viruses to target the two anatomical locations. They then counted all of the monosynaptic inputs to each of these regions throughout the entire brain. The first observation was that each of these regions received direct inputs from a much wider array of brain regions than previously appreciated. Many of these inputs were not detected by previous studies, as they may have escaped detection using less sensitive methods, or their relatively low abundance may have been ascribed to an error in injection targeting. It was also surprising that the VTA and SNc largely shared the same inputs, in largely the same proportions, with a few unique exceptions that include the motor cortices and subthalamic nucleus for the SNc and the lateral hypothalamus for the VTA. A similar approach has been used to examine the inputs to different groups of serotonergic neurons (Ogawa et al., 2014; Pollak Dorocic et al., 2014; Weissbourd et al., 2014), as well as the dorsal striatum (Wall et al., 2013) and hippocampus (Sun et al., 2014).

RABV Tracing During Development can Reveal the Timing of Synapse Formation

Viral tracing methods have also been used to investigate the timing of wiring and synapse formation during development. One such study investigated neurons potentially involved in rodent whisking behavior (Takatoh et al., 2013). The monosynaptic technique is particularly useful for this application, as it is able to identify *when* synaptic connections between neurons are formed, which would not be possible using classical tracers. In order to find such neurons, the investigators used the fact that whisking is initiated postnatally, and therefore examined inputs to the vibrissal motor neurons at different postnatal days, with the goal of finding populations of inputs that were specifically labeled *after* the onset of whisking. By comparing the label produced by injections at P1 and P8, the authors discovered new inputs from the rostral part of the lateral paragigantocellularis in the hindbrain that were identified during the later time window. As these neurons appear to get direct input from the motor cortex, the authors suggest that the formation of inputs from these hindbrain neurons is critical for active whisking. Another study used RABV to examine the formation of inputs onto newly generated neurons in the dentate gyrus in the hippocampus, and adult-born neurons in the olfactory bulb (Deshpande et al., 2013). In both cases, they found that at early time points post-maturation, the majority of the transsynaptically-labeled inputs were located nearby the cells from which tracing was initiated. If the researchers initiated tracing a few weeks after maturation, they observed the presence of an increasing number of inputs located at greater

distances from the targeted neurons, suggesting that newly born neurons first integrate into local circuitry before they receive inputs from distant sites. The similar pattern of observations in both the hippocampus and the olfactory bulb may indicate a common mechanism for integrating newborn neurons into already-established neural networks.

Viruses Engineered to Carry Functional Genes

In addition to the rapid development of transsynaptic viral technologies, in the past decade there has been a veritable explosion of genetically-encoded functional tools for measuring and manipulating neuronal activity (Fenno et al., 2011; Looger and Griesbeck, 2012; Farrell and Roth, 2013). These include, but are not limited to, genetically-encoded calcium and voltage indicators for imaging neuronal activity (Looger and Griesbeck, 2012) and optogenetic and pharmacogenetic effectors for manipulating neuronal activity (Fenno et al., 2011; Farrell and Roth, 2013). These new functional tools have already led to a plethora of circuit-level discoveries, primarily aided by transgenic strategies that target expression to specific cell-types in localized regions of the brain (Ting and Feng, 2013). In some cases, as in the Thy1 lines of transgenic mice, expression of these genes can be restricted to specific subsets of projection neurons, offering the possibility of pathway-specific functional analysis and behavioral readout (Arenkiel et al., 2007; Dana et al., 2014).

Ultimately, though, transgenic strategies alone are insufficient to target the many different cell-types in the brain that are currently defined not by their genetic profile, but by their unique pattern of connections with other neurons within and between different brain areas (Jones, 1984; Douglas and Martin, 2004). Recently, there has been a concerted effort to exploit the power of viral tracers in order to deliver these functional tools to neuronal populations defined by their connectivity. This has led to a revolution in efforts to directly relate structure to function, with enormous promise for model species such as the primate for which transgenic technology is not currently available (but see Kishi et al., 2014).

The viral tracing tools outlined in the previous section enable researchers to study anatomical circuits with unprecedented precision. However, the rapid gene expression from these vectors, which may be critical for their high efficiency of transsynaptic transfer, makes them disadvantageous for studying circuit function, as the speed of gene expression comes at the expense of neuronal health. This is usually not an issue for anatomical studies with relatively short survival times, but it poses a major challenge for functional studies, especially those that require chronic experimentation in behaviorally trained animals. Therefore, in order to deliver genes to defined neuronal classes in which long-term monitoring or manipulation is necessary, a different methodology and set of reagents is required.

To be useful for functional and behavioral experiments, it is essential that the virus of choice be able to deliver a high payload without harming the infected cells. This has motivated a variety of viral targeting strategies, the most successful of which have so far involved AAV, either alone or in combination with other viruses, due to its ability to express high levels of protein with relatively low levels of toxicity. In most cases, regardless of the specific functional tool or application, the relevant viral targeting strategies are similar. Some specific examples using these strategies have already been described in previous sections, so here we provide a broad overview of three main types of viral approaches that have been pursued to target the expression of genes to specific cell types for long-term analyses, highlighting previous and ongoing efforts to obtain a functional or behavioral readout of a specific pathway or circuit in the brain.

Axon Terminals

The most successful integration of viruses and functional tools thus far has relied on a viral strategy that does not explicitly employ viruses as tracers, but, instead, simply depends on robust expression of a virus's genetic payload throughout the soma, dendrites and, in particular, axons of neurons local to the injection site (**Figure 4A**). AAVs and lentiviruses have been the most commonly used viruses for purposes of local infection and robust expression throughout the axonal tree, with the important advantage of being chronically well-tolerated and minimally toxic (Osten et al., 2006; Büning et al., 2008). In this way, these viruses serve as a sort of anterograde tracer, enabling functional analysis of specific efferent pathways originating from neurons at the injection site (**Figure 4A**).

For example, in the case of optogenetics, light can be delivered specifically to a particular target area and activate only the axon terminals of the infected neuronal population, thus allowing the physiological and behavioral consequences of a particular set of inputs to be measured (Petreanu et al., 2007; Gradinaru et al., 2009; Cruikshank et al., 2010; Stuber et al., 2011). Such axonal stimulation can be used to map out how long-range connections in the brain interact with a local microcircuit (Petreanu et al., 2007) or, with the aid of functional magnetic resonance imaging (fMRI), across the entire brain (Lee et al., 2010; Desai et al., 2011).

For imaging applications, calcium levels within axons in a particular target area of the infected neuronal population can be measured (Reiff et al., 2010; Petreanu et al., 2012; Glickfeld et al., 2013). Note that in all of these cases, pathway specificity is not obtained by the virus alone, which will often infect a heterogeneous population of neurons projecting to many different brain regions. Rather, pathway specificity is achieved by combining the viral infection of the soma with spatial restriction of either the light beam used for stimulation or the field of view of the microscope to a brain region where only one particular projection pathway terminates (**Figure 4A**). In some circuits, however, spatially intermixed parallel pathways exist, requiring additional tricks to disentangle the functional influence of one pathway from another. Cell-type specific expression can sometimes aid in such efforts, either by using AAVs and lentiviruses encoding cell-type specific promoter sequences or by using transgenic lines with cell-type specific expression of Cre-recombinase and viruses with Cre-

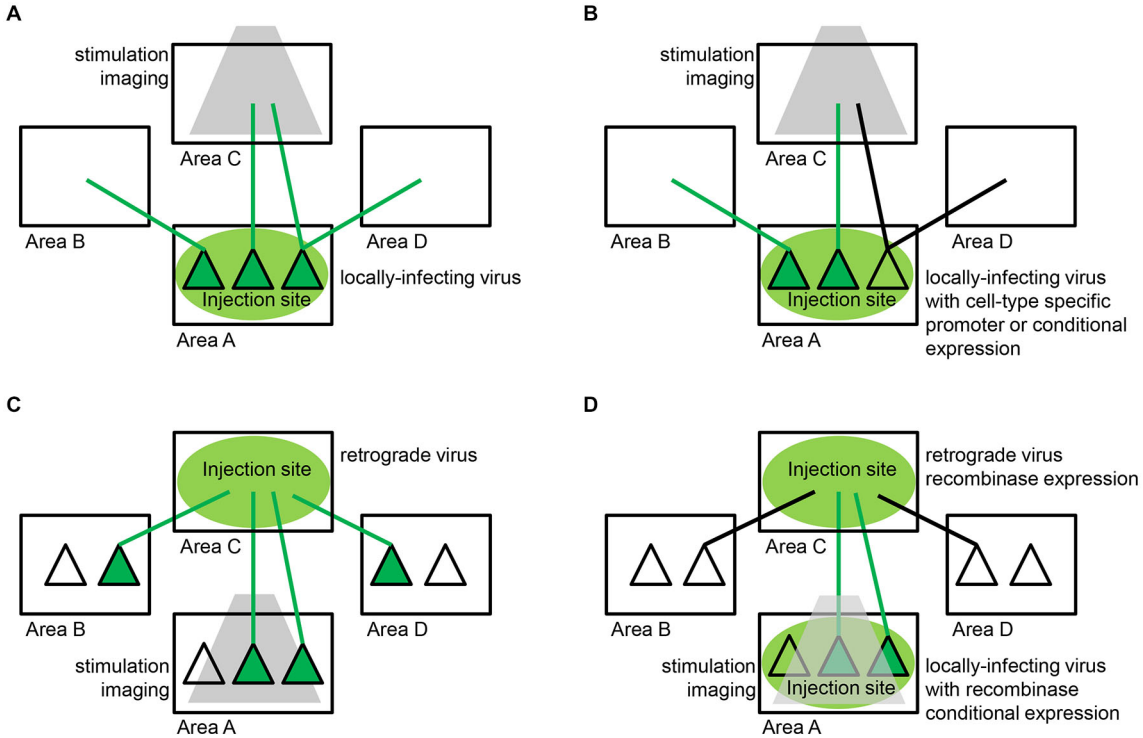

FIGURE 4 | Viral strategies for delivering functional tools to neuronal populations defined by their connectivity. (A) Axon terminal targeting. The most successful approach to date relies on locally-infecting viruses, such as lentivirus and adeno-associated virus (AAV), which enable expression of a functional tool within neuronal cell bodies (dark green triangles) and dendrites local to the injection site (area A) and throughout their axons (green lines) that terminate both locally and in remote areas of the brain (areas B,C,D). Specific efferent pathways originating from the injection site are targeted by restricting stimulation or imaging (gray) to one particular target area (area C). **(B)** Cell-type specific axon terminal targeting. In some circuits, spatially-intermixed parallel pathways converge on the same target area of interest. In order to disentangle these pathways, the same locally-infecting viruses described in **(A)** can be engineered to target specific cell-types local to the injection site (area A). This can be accomplished with cell-type specific promoter sequences or recombinase-dependent expression sequences that restrict expression of a functional tool to a genetically-defined subpopulation (dark green triangles in area A). Specific efferent pathways originating from that particular subpopulation (green lines) and not other parallel pathways (black lines) are targeted as in **(A)** by restricting stimulation or imaging (gray) to one particular target area (area C). **(C)** Projection neuron targeting. Retrograde viruses, such as rabies, enable expression of a functional tool in specific projection neuron populations. Retrograde virus is taken up by axonal terminations (green lines) local to the injection site (area C) and travels back to cell bodies (dark green triangles) throughout the brain (areas A,B,D). Specific afferent pathways projecting to the injection site are targeted by restricting stimulation or imaging (gray) to one particular input area (area A). Retrograde viruses alone are often unable to achieve the high levels of expression needed for long-term functional studies. **(D)** Intersectional approaches. A combination of the strategies described in **(A,C)** above have enabled high levels of expression with low levels of toxicity in specific projection-neuron populations. The most successful strategy to date involves delivering small amounts of Cre-recombinase via a retrograde virus and also injecting a locally-infecting virus encoding Cre-dependent expression of a functional tool at the location where the targeted projection neurons originate. Specifically, retrograde virus is taken up by axonal terminations (green and black lines) local to the injection site (area C) and travels back to cell bodies throughout the brain (areas A,B,D). The retrograde virus expresses Cre-recombinase within these infected projection neurons. Specific afferent pathways (dark green triangles) projecting to the injection site are targeted by injecting a locally-infecting virus, such as AAV, encoding Cre-dependent expression of a functional tool in the target area of interest (area A). This strategy can functionally isolate neurons that reside in area A and project to area C, obviating the need for site-specific stimulation or imaging (gray).

dependent expression sequences (Betley and Sternson, 2011; **Figure 4B**).

Cell Bodies of Projection Neurons

While stimulation and imaging of axons has already led to great progress in the field, there are many instances in which it would be preferable to modulate or image the activity of specific projection neuron populations at their site of origin (**Figure 4C**). This is especially true when the axons of a particular pathway are difficult to access or when they are defined not simply by the brain area in which they terminate, but by the specific cell-type within that area onto which they synapse. In such cases, researchers have turned toward several of the retrograde viruses described previously, which travel back from axonal termination to the cell body. Similarly to the axonal stimulation strategy described above in the "Axon Terminals" Section, pathway specificity is obtained not by the retrograde virus alone, which will infect neurons projecting from many

different brain regions, but by restricting the stimulation area of the light or the field of view of the microscope to a brain region where only one particular projection pathway originates (**Figure 4C**).

One of the most powerful viral tracers for these purposes is RABV, due to its exclusively retrograde spread, fast expression dynamics and high amplification of its genes (Ugolini, 1995; Kelly and Strick, 2000). Though not useful for chronic, longitudinal experiments because of its relatively fast-onset toxicity (cell death as early as 14 days post-infection), the SAD-B19-ΔG strain of rabies can be used in an acute setting to express high levels of light-sensitive channel or calcium indicator in specific projection neuron populations based on the target region injected with virus (Wickersham et al., 2007a; Osakada et al., 2011). It can also be complemented *in trans* to enable monosynaptic spread restricted to the inputs of an initially infected population of neurons (Wickersham et al., 2007b).

For chronic experiments, however, retrograde viruses with lower toxicity profiles are required. While potentially somewhat cytotoxic, genetically-modified retrograde viruses could potentially be used for these purposes, including Herpes Simplex Virus Type 1 (HSV-1), the Bartha strain of pseudorabies (PRV) or CAV (Kremer et al., 2000; Frampton et al., 2005; Tomioka and Rockland, 2006; Card and Enquist, 2014). Another possibility is to pseudotype viruses of low toxicity that do not normally move retrogradely, such as lentivirus, with RABV or RABV-VSV-G chimeric glycoproteins, so that they do in fact move retrogradely from the site of injection (Mazarakis et al., 2001; Kato et al., 2011). Ultimately, though, the expression levels produced by most of these retrograde viruses on their own are typically insufficient for functional efficacy. While certain genetic modifications might enable higher expression levels (Cetin and Callaway, 2014), it remains to be seen whether any low-toxicity, retrograde virus on its own can produce the high levels of expression needed for long-term chronic functional and behavioral studies.

Intersectional Approaches

A combination of different viral approaches has recently shown promise as a way to achieve high levels of expression with low levels of toxicity in specific projection-neuron populations. The most successful strategy to date involves delivering small amounts of Cre-recombinase via a retrograde virus after injecting a locally-infecting AAV encoding Cre-dependent expression of a functional tool at the location where the targeted projection neurons originate (**Figure 4D**). This has already been successful with several retrograde viruses including HSV-1 (Lima et al., 2009; Senn et al., 2014), PRV (Granstedt et al., 2010; Chaudhury et al., 2013) and CAV-2 (Hnasko et al., 2006; Senn et al., 2014). The approach requires careful matching of the two injection sites in order to target the same projection population with both viruses. Non-viral retrograde delivery of Cre-recombinase, such as with the plant lectin WGA, is also an option (Gradinaru et al., 2010; Xu and Südhof, 2013), though bi-directional and diluted multi-synaptic spread of WGA may limit its utility (Köbbert et al., 2000).

These intersectional approaches have the important added advantage of specific expression in the particular projection neuron population of interest, rather than all populations that project to the injection site (**Figure 4D**). This, then, opens up the possibility of using systemic rather than local effectors such as in the case of tetracycline-controlled transcriptional activation (tet-ON and tet-OFF) or designer receptors exclusively activated by designer drugs (DREADDs; Mansuy and Bujard, 2000; Farrell and Roth, 2013). Anterograde viral strategies currently under development would likely benefit from a similar intersectional approach and would vastly expand the pathways and circuitry accessible to functional and behavioral analysis in future studies (Beier et al., 2011b; Lo and Anderson, 2011). Intersectional approaches for either anterograde or retrograde tracing also can be employed that use the overlap of expression patterns of Cre and Flp. These two recombinases can be expressed from transgenic configurations (Dymecki et al., 2010) and/or via viral delivery (Fenno et al., 2014). Use of an effector gene, such as TVA, that is dependent upon expression of both Cre and Flp creates greater specificity in the cell types being targeted for infection or viral spread. This type of intersectional approach will also benefit from a new method of manipulating GFP-expressing cells, referred to as "Cre-dependent upon GFP" (Cre-DOG) where GFP+ cells in a transgenic GFP line are induced to express Cre (Tang et al., in press). These GFP+/Cre+ cells can be intersectionally selected by expressing Flp from either a transgenic locus or a virally delivered Flp.

Future Directions

The use of neurotropic viruses has vastly expanded the scope of neuroanatomy, and the genetic engineering of these viruses has permitted exciting new experiments in which functional studies are coupled to anatomy in a direct way that has revealed new insights into neural circuits. As the preceding sections have made clear, however, there remains room for improvement along several dimensions. In this section, we briefly consider several major obstacles and possible strategies for overcoming them.

Reducing Toxicity

One of the major limiting factors for merging transsynaptic viral vectors with functional approaches is their rapid toxicity. Efforts are ongoing to reduce the toxicity of these transsynaptic vectors, largely by mutating viral proteins. For example, a point mutant in the VSV M protein (M51R) was used to permit slice recordings in VSV-infected neurons where VSV encoding the wild-type M protein was too toxic to permit physiological investigation of post-synaptic cells (Beier et al., 2011b). The M protein has been implicated in the persistence of infection (Ahmed and Lyles, 1997; Desforges et al., 2001) as well as other deleterious processes. There are several mutations in M that can be tested for their effects on toxicity and efficacy on transsynaptic tracing. As RABV has a similar set of genes as VSV, similar mutations might be profitably applied to these vectors as well. In addition, while RABV, VSV, and PRV/HSV have been used for controlled studies of transsynaptic transmission, synapse-restricted transmission may not be an

exclusive property of these viruses. For example, the Borna virus (BDV) has been reported to have patterns of neuron-to-neuron spread consistent with transsynaptic transmission (Carbone et al., 1987; Morales et al., 1988; Gosztonyi et al., 1993). It may therefore be possible to engineer viruses that are inherently less toxic than those currently used to trace synaptic connections.

Improving Control of Transsynaptic Spread

One of the major limitations of manipulating viruses for monosynaptic tracing is that the only two viruses thus far used for this purpose (RABV and VSV) are RNA viruses, and are therefore inaccessible to recombinase technology. Therefore, no methods currently exist to modify the virus once it is injected into the animal. However, it may be possible to directly modify viral RNA. For example, one could take advantage of the differential effects of three-dimensional structure on RNA function. Riboswitches are short sequences in messenger RNAs that bind small molecules, changing the RNA conformation and the levels of proteins translated from those RNAs (Vitreschak et al., 2004; Roth and Breaker, 2009). These can be screened or selected from a pool of synthetic libraries for binding to specific small molecules. Such RNA aptamers could be expressed from the viral genome, and could bind to a small molecule administered to the animal after the virus was injected. It may also be possible to express shRNAs or antisense transcripts within certain cell types that could either eliminate or slow viral replication and/or transcription within those cells. Also, we may be able to take advantage of the clues that Mother Nature has provided. The innate immune response, which limits the spread of VSV, but not RABV, from the periphery may provide a mechanism to limit spread once a virus enters the CNS. We will need to better understand the immune response to different transsynaptic viruses to exploit this system.

Improving the Efficiency of Transsynaptic Spread

We currently have only a limited understanding of how transsynaptic spread occurs. It is not always appreciated that these viruses spread among non-neuronal cells *in vitro*. That is, synapses are not needed for infection or for transmission, and many different cell types can host virus replication. Studies of the mechanism(s) that limit spread to synaptically connected neurons *in vivo*, as well as govern the direction of spread, are needed to allow an improvement in efficiency, which is currently only 2–5% for retrograde labeling of presynaptic partners of VSV and RABV (Marshel et al., 2010; Beier et al., 2013a). In addition, the mechanisms that limit transmission in some species, such as Drosophila, require investigation.

Extending the Range of Species that can be Studied

The vast majority of anatomical studies cited in this review were performed in mice. Mouse genetics have allowed for a great deal of flexibility in the design and execution of experiments that rely on the introduction of genes that direct infection and spread of the virus. However, it is clearly necessary to extend viral tracing methods to other organisms—ranging from flies to monkeys—both because such animals represent important model systems in their own right and because comparative studies are essential to investigate the evolution of circuits. One virus with the potential to infect a wide range of species is VSV, which was recently shown to infect neurons in animals ranging from invertebrates to nonhuman primates and to replicate and be transported in several important model organisms, including zebrafish and chicks (Mundell et al., 2015).

The current use of transsynaptic viral vectors is limited to the capabilities of the vectors used. That is, we currently have only a limited understanding of how viruses transmit among neurons in the CNS. While RABV, VSV, and HSV/PRV have all displayed the potential to transsynaptically label neurons in multiple species, this could be expanded by, for example, expressing the appropriate viral receptors in the host cells, and/or enabling replication in otherwise non-permissive cells. For example, VSV does not appear to replicate in Drosophila neurons as a result of an innate immune response that triggers autophagy (Shelly et al., 2009). Developing a more nuanced understanding of the mechanisms of viral infection, replication, and transmission at the basic science level will permit a whole new generation of transsynaptic techniques that have the potential to refine and enhance the capabilities of these methods.

Closing Remarks

The considerations presented above remind us of the power, beauty and critical importance of research on the basic mechanisms of biology—even, or especially, of such seemingly exotic creatures as viruses. While some might believe that the main reason to study viruses is to create vaccines that limit their spread in human populations, it should be clear that we need to understand these remarkable entities in much more mechanistic detail so that we can engineer the next generation of neuroanatomical tools with which to solve the function of circuits within our brains and thus to tackle other devastating diseases—diseases of brain mis-wiring, such as autism (Minshew and Williams, 2007; Gepner and Féron, 2009) and schizophrenia (Rubinov and Bassett, 2011).

References

Ahmad, M., Polepalli, J. S., Goswami, D., Yang, X., Kaeser-Woo, Y. J., Südhof, T. C., et al. (2012). Postsynaptic complexin controls AMPA receptor exocytosis during LTP. *Neuron* 73, 260–267. doi: 10.1016/j.neuron.2011.11.020

Ahmed, M., and Lyles, D. S. (1997). Identification of a consensus mutation in M protein of vesicular stomatitis virus from persistently infected cells that affects inhibition of host-directed gene expression. *Virology* 237, 378–388. doi: 10.1006/viro.1997.8808

Akli, S., Caillaud, C., Vigne, E., Stratford-Perricaudet, L. D., Poenaru, L., Perricaudet, M., et al. (1993). Transfer of a foreign gene into the

brain using adenovirus vectors. *Nat. Genet.* 3, 224–228. doi: 10.1038/ng0393-224

Arenkiel, B. R., Peca, J., Davison, I. G., Feliciano, C., Deisseroth, K., Augustine, G. J. J., et al. (2007). *In Vivo* light-induced activation of neural circuitry in transgenic mice expressing channelrhodopsin-2. *Neuron* 54, 205–218. doi: 10.1016/j.neuron.2007.03.005

Aschauer, D. F., Kreuz, S., and Rumpel, S. (2013). Analysis of transduction efficiency, tropism and axonal transport of AAV serotypes 1, 2, 5, 6, 8 and 9 in the mouse brain. *PLoS One* 8:e76310. doi: 10.1371/journal.pone.0076310

Astic, L., Saucier, D., Coulon, P., Lafay, F., and Flamand, A. (1993). The CVS strain of rabies virus as transneuronal tracer in the olfactory system of mice. *Brain Res.* 619, 146–156. doi: 10.1016/0006-8993(93)91606-s

Atasoy, D., Aponte, Y., Su, H. H., and Sternson, S. M. (2008). A FLEX switch targets Channelrhodopsin-2 to multiple cell types for imaging and long-range circuit mapping. *J. Neurosci.* 28, 7025–7030. doi: 10.1523/jneurosci.1954-08.2008

Auricchio, A., Hildinger, M., O'Connor, E., Gao, G. P., and Wilson, J. M. (2001). Isolation of highly infectious and pure adeno-associated virus type 2 vectors with a single-step gravity-flow column. *Hum. Gene Ther.* 12, 71–76. doi: 10.1089/104303401450988

Baskerville, A., and Lloyd, G. (1977). Experimental infection of monkeys with Herpesvirus suis (Aujeszky's-disease virus). *J. Med. Microbiol.* 10, 139–144. doi: 10.1099/00222615-10-1-139

Bates, P., Young, J. A., and Varmus, H. E. (1993). A receptor for subgroup A Rous sarcoma virus is related to the low density lipoprotein receptor. *Cell* 74, 1043–1051. doi: 10.1016/0092-8674(93)90726-7

Beier, K. T., Saunders, A. B., Oldenburg, I. A., Sabatini, B. L., and Cepko, C. L. (2013a). Vesicular stomatitis virus with the rabies virus glycoprotein directs retrograde transsynaptic transport among neurons *in vivo*. *Front. Neural Circuits* 7:11. doi: 10.3389/fncir.2013.00011

Beier, K. T., Borghuis, B. G., El-Danaf, R. N., Huberman, A. D., Demb, J. B., and Cepko, C. L. (2013b). Transsynaptic tracing with vesicular stomatitis virus reveals novel retinal circuitry. *J. Neurosci.* 33, 35–51. doi: 10.1523/jneurosci.0245-12.2013

Beier, K. T., Samson, M. E., Matsuda, T., and Cepko, C. L. (2011a). Conditional expression of the TVA receptor allows clonal analysis of descendents from Cre-expressing progenitor cells. *Dev. Biol.* 353, 309–320. doi: 10.1016/j.ydbio.2011.03.004

Beier, K. T., Saunders, A., Oldenburg, I. A., Miyamichi, K., Akhtar, N., Luo, L., et al. (2011b). Anterograde or retrograde transsynaptic labeling of CNS neurons with vesicular stomatitis virus vectors. *Proc. Natl. Acad. Sci. U S A* 108, 15414–15419. doi: 10.1073/pnas.1110854108

Bentivoglio, M., Kuypers, H. G., Catsman-Berrevoets, C. E., Loewe, H., and Dann, O. (1980). Two new fluorescent retrograde neuronal tracers which are transported over long distances. *Neurosci. Lett.* 18, 25–30. doi: 10.1016/0304-3940(80)90208-6

Betley, J. N., Cao, Z. F. H., Ritola, K. D., and Sternson, S. M. (2013). Parallel, redundant circuit organization for homeostatic control of feeding behavior. *Cell* 155, 1337–1350. doi: 10.1016/j.cell.2013.11.002

Betley, J. N., and Sternson, S. M. (2011). Adeno-associated viral vectors for mapping, monitoring and manipulating neural circuits. *Hum. Gene Ther.* 22, 669–677. doi: 10.1089/hum.2010.204

Boldogkoi, Z., Balint, K., Awatramani, G. B., Balya, D., Busskamp, V., Viney, T. J., et al. (2009). Genetically timed, activity-sensor and rainbow transsynaptic viral tools. *Nat. Methods* 6, 127–130. doi: 10.1038/nmeth.1292

Boshart, M., Weber, F., Jahn, G., Dorsch-Häsler, K., Fleckenstein, B., and Schaffner, W. (1985). A very strong enhancer is located upstream of an immediate early gene of human cytomegalovirus. *Cell* 41, 521–530. doi: 10.1016/s0092-8674(85)80025-8

Bredenbeek, P. J., Frolov, I., Rice, C. M., and Schlesinger, S. (1993). Sindbis virus expression vectors: packaging of RNA replicons by using defective helper RNAs. *J. Virol.* 67, 6439–6446.

Büning, H., Perabo, L., Coutelle, O., Quadt-Humme, S., and Hallek, M. (2008). Recent developments in adeno-associated virus vector technology. *J. Gene Med.* 10, 717–733. doi: 10.1002/jgm.1205

Burger, C., Gorbatyuk, O. S., Velardo, M. J., Peden, C. S., Williams, P., Zolotukhin, S., et al. (2004). Recombinant AAV viral vectors pseudotyped with viral capsids from serotypes 1, 2 and 5 display differential efficiency and cell tropism after delivery to different regions of the central nervous system. *Mol. Ther.* 10, 302–317. doi: 10.1016/j.ymthe.2004.05.024

Carbone, K. M., Duchala, C. S., Griffin, J. W., Kincaid, A. L., and Narayan, O. (1987). Pathogenesis of Borna disease in rats: evidence that intra-axonal spread is the major route for virus dissemination and the determinant for disease incubation. *J. Virol.* 61, 3431–3440.

Card, J. P., and Enquist, L. W. (2014). Transneuronal circuit analysis with pseudorabies viruses. *Curr. Protoc. Neurosci.* 1.5.1–1.5.39 doi: 10.1002/0471142301.ns0105s68

Card, J. P., Rinaman, L., Schwaber, J. S., Miselis, R. R., Whealy, M. E., Robbins, A. K., et al. (1990). Neurotropic properties of pseudorabies virus: uptake and transneuronal passage in the rat central nervous system. *J. Neurosci.* 10, 1974–1994.

Card, J. P., Whealy, M. E., Robbins, A. K., and Enquist, L. W. (1992). Pseudorabies virus envelope glycoprotein gI influences both neurotropism and virulence during infection of the rat visual system. *J. Virol.* 66, 3032–3041.

Castle, M. J., Gershenson, Z. T., Giles, A. R., Holzbaur, E. L., and Wolfe, J. H. (2014). Adeno-associated virus serotypes 1, 8 and 9 share conserved mechanisms for anterograde and retrograde axonal transport. *Hum. Gene Ther.* 25, 705–720. doi: 10.1089/hum.2013.189

Cearley, C. N., and Wolfe, J. H. (2006). Transduction characteristics of adeno-associated virus vectors expressing cap serotypes 7, 8, 9 and Rh10 in the mouse brain. *Mol. Ther.* 13, 528–537. doi: 10.1016/j.ymthe.2005.11.015

Cetin, A. H., and Callaway, E. M. (2014). Optical control of retrogradely infected neurons using drug regulated "TLoop" lentiviral vectors. *J. Neurophysiol.* 111, 2150–2159. doi: 10.1152/jn.00495.2013

Charlton, K. M., and Casey, G. A. (1979). Experimental oral and nasal transmission of rabies virus in mice. *Can. J. Comp. Med.* 43, 10–15.

Chaudhury, D., Walsh, J. J., Friedman, A. K., Juarez, B., Ku, S. M., Koo, J. W., et al. (2013). Rapid regulation of depression-related behaviours by control of midbrain dopamine neurons. *Nature* 493, 532–536. doi: 10.1038/nature11713

Choi, G. B., Stettler, D. D., Kallman, B. R., Bhaskar, S. T., Fleischmann, A., and Axel, R. (2011). Driving opposing behaviors with ensembles of piriform neurons. *Cell* 146, 1004–1015. doi: 10.1016/j.cell.2011.07.041

Choi, J., Young, J. A. T., and Callaway, E. M. (2010). Selective viral vector transduction of ErbB4 expressing cortical interneurons *in vivo* with a viral receptor-ligand bridge protein. *Proc. Natl. Acad. Sci. U S A* 107, 16703–16708. doi: 10.1073/pnas.1006233107

Cowan, W. M., and Cuenod, M. (1975). *The Use of Axonal Transport for Studies of Neuronal Connectivity.* Amsterdam: Elsevier.

Cowan, W. M., Gottlieb, D. I., Hendrickson, A. E., Price, J. L., and Woolsey, T. A. (1972). The autoradiographic demonstration of axonal connections in the central nervous system. *Brain Res.* 37, 21–51. doi: 10.1016/0006-8993(72)90344-7

Cruikshank, S. J., Urabe, H., Nurmikko, A. V., and Connors, B. W. (2010). Pathway-specific feedforward circuits between thalamus and neocortex revealed by selective optical stimulation of axons. *Neuron* 65, 230–245. doi: 10.1016/j.neuron.2009.12.025

Dana, H., Chen, T.-W., Hu, A., Shields, B. C., Guo, C., Looger, L. L., et al. (2014). Thy1-GCaMP6 transgenic mice for neuronal population imaging *in vivo*. *PLoS One* 9:e108697. doi: 10.1371/journal.pone.0108697

Davison, A. J. (2010). Herpesvirus systematics. *Vet. Microbiol.* 143, 52–69. doi: 10.1016/j.vetmic.2010.02.014

de Hoop, M., Olkkonen, V., Ikonen, E., Williamson, E., von Roser, C., Meyn, L., et al. (1994). Semliki Forest virus as a tool for protein expression in cultured rat hippocampal neurons. *Gene Ther.* 1, S28–S31.

DeFalco, J., Tomishima, M., Liu, H., Zhao, C., Cai, X., Marth, J. D., et al. (2001). Virus-assisted mapping of neural inputs to a feeding center in the hypothalamus. *Science* 291, 2608–2613. doi: 10.1126/science.1056602

Desai, M., Kahn, I., Knoblich, U., Bernstein, J., Atallah, H., Yang, A., et al. (2011). Mapping brain networks in awake mice using combined optical neural control and fMRI. *J. Neurophysiol.* 105, 1393–1405. doi: 10.1152/jn.00828.2010

Desforges, M., Charron, J., Bérard, S., Beausoleil, S., Stojdl, D. F., Despars, G., et al. (2001). Different host-cell shutoff strategies related to the matrix protein lead to persistence of vesicular stomatitis virus mutants on fibroblast cells. *Virus Res.* 76, 87–102. doi: 10.1016/s0168-1702(01)00251-9

Deshpande, A., Bergami, M., Ghanem, A., Conzelmann, K.-K., Lepier, A., Götz, M., et al. (2013). Retrograde monosynaptic tracing reveals the temporal

evolution of inputs onto new neurons in the adult dentate gyrus and olfactory bulb. *Proc. Natl. Acad. Sci. U S A* 110, E1152–E1161. doi: 10.1073/pnas.1218991110

Dodding, M., and Way, M. (2011). Coupling viruses to dynein and kinesin-1. *EMBO J.* 30, 3527–3539. doi: 10.1038/emboj.2011.283

Doherty, F. C., Schaack, J. B., and Sladek, C. D. (2011). Comparison of the efficacy of four viral vectors for transducing hypothalamic magnocellular neurosecretory neurons in the rat supraoptic nucleus. *J. Neurosci. Methods* 197, 238–248. doi: 10.1016/j.jneumeth.2011.02.026

Donello, J. E., Loeb, J. E., and Hope, T. J. (1998). Woodchuck hepatitis virus contains a tripartite posttranscriptional regulatory element. *J. Virol.* 72, 5085–5092.

Dong, B., Nakai, H., and Xiao, W. (2010). Characterization of genome integrity for oversized recombinant AAV vector. *Mol. Ther.* 18, 87–92. doi: 10.1038/mt.2009.258

Douglas, R. J., and Martin, K. A. C. (2004). Neuronal circuits of the neocortex. *Annu. Rev. Neurosci.* 27, 419–451. doi: 10.1146/annurev.neuro.27.070203.144152

Dymecki, S. M., Ray, R. S., and Kim, J. C. (2010). Mapping cell fate and function using recombinase-based intersectional strategies. *Methods Enzymol.* 477, 183–213. doi: 10.1016/s0076-6879(10)77011-7

Ehrengruber, M. U., Lundstrom, K., Schweitzer, C., Heuss, C., Schlesinger, S., and Gähwiler, B. H. (1999). Recombinant Semliki Forest virus and Sindbis virus efficiently infect neurons in hippocampal slice cultures. *Proc. Natl. Acad. Sci. U S A* 96, 7041–7046. doi: 10.1073/pnas.96.12.7041

Ehrhardt, A., and Kay, M. A. (2005). Gutted adenovirus: a rising star on the horizon? *Gene Ther.* 12, 1540–1541. doi: 10.1038/sj.gt.3302597

Epstein, D. A., Herman, R. C., Chien, I., and Lazzarini, R. A. (1980). Defective interfering particle generated by internal deletion of the vesicular stomatitis virus genome. *J. Virol.* 33, 818–829.

Esposito, M. S., Capelli, P., and Arber, S. (2014). Brainstem nucleus MdV mediates skilled forelimb motor tasks. *Nature* 508, 351–356. doi: 10.1038/nature13023

Etessami, R., Conzelmann, K. K., Fadai-Ghotbi, B., Natelson, B., Tsiang, H., and Ceccaldi, P. E. (2000). Spread and pathogenic characteristics of a G-deficient rabies virus recombinant: an *in vitro* and *in vivo* study. *J. Gen. Virol.* 81, 2147–2153.

Farrell, M. S., and Roth, B. L. (2013). Pharmacosynthetics: reimagining the pharmacogenetic approach. *Brain Res.* 1511, 6–20. doi: 10.1016/j.brainres.2012.09.043

Fenno, L. E., Mattis, J., Ramakrishnan, C., Hyun, M., Lee, S. Y., He, M., et al. (2014). Targeting cells with single vectors using multiple-feature Boolean logic. *Nat. Methods* 11, 763–772. doi: 10.1038/nmeth.2996

Fenno, L., Yizhar, O., and Deisseroth, K. (2011). The development and application of optogenetics. *Annu. Rev. Neurosci.* 34, 389–412. doi: 10.1146/annurev-neuro-061010-113817

Fink, R. P., and Heimer, L. (1967). Two methods for selective silver impregnation of degenerating axons and their synaptic endings in the central nervous system. *Brain Res.* 4, 369–374. doi: 10.1016/0006-8993(67)90166-7

Fitzsimons, H. L., Bland, R. J., and During, M. J. (2002). Promoters and regulatory elements that improve adeno-associated virus transgene expression in the brain. *Methods* 28, 227–236. doi: 10.1016/s1046-2023(02)00227-x

Flint, S. J. (2000). *Principles of Virology: Molecular Biology, Pathogenesis and Control.* Washington, D.C.: ASM Press.

Flint, S. J. (2009). *Principles of Virology.* 3rd Edn. Washington, DC: ASM Press.

Frampton, A. R., Goins, W. F., Nakano, K., Burton, E. A., and Glorioso, J. C. (2005). HSV trafficking and development of gene therapy vectors with applications in the nervous system. *Gene Ther.* 12, 891–901. doi: 10.1038/sj.gt.3302545

Gao, G., Vandenberghe, L. H., Alvira, M. R., Lu, Y., Calcedo, R., Zhou, X., et al. (2004). Clades of Adeno-associated viruses are widely disseminated in human tissues. *J. Virol.* 78, 6381–6388. doi: 10.1128/jvi.78.12.6381-6388.2004

Gao, G., Vandenberghe, L. H., and Wilson, J. M. (2005). New recombinant serotypes of AAV vectors. *Curr. Gene Ther.* 5, 285–297. doi: 10.2174/1566523054065057

Gepner, B., and Féron, F. (2009). Autism: a world changing too fast for a mis-wired brain? *Neurosci. Biobehav. Rev.* 33, 1227–1242. doi: 10.1016/j.neubiorev.2009.06.006

Gerfen, C. R., and Sawchenko, P. E. (1984). An anterograde neuroanatomical tracing method that shows the detailed morphology of neurons, their axons and terminals: immunohistochemical localization of an axonally transported plant lectin, *Phaseolus vulgaris*-leucoagglutinin (PHA-L). *Brain Res.* 290, 219–238. doi: 10.1016/0006-8993(84)90940-5

Ghosh, S., Larson, S. D., Hefzi, H., Marnoy, Z., Cutforth, T., Dokka, K., et al. (2011). Sensory maps in the olfactory cortex defined by long-range viral tracing of single neurons. *Nature* 472, 217–220. doi: 10.1038/nature09945

Ginn, S. L., Fleming, J., Rowe, P. B., and Alexander, I. E. (2003). Promoter interference mediated by the U3 region in early-generation HIV-1-derived lentivirus vectors can influence detection of transgene expression in a cell-type and species-specific manner. *Hum. Gene Ther.* 14, 1127–1137. doi: 10.1089/104303403322167975

Glees, P. (1946). Terminal degeneration within the central nervous system as studied by a new silver method. *J. Neuropathol. Exp. Neurol.* 5, 54–59. doi: 10.1097/00005072-194601000-00005

Glickfeld, L. L., Andermann, M. L., Bonin, V., and Reid, R. C. (2013). Cortico-cortical projections in mouse visual cortex are functionally target specific. *Nat. Neurosci.* 16, 219–226. doi: 10.1038/nn.3300

Glover, J. C., Petursdottir, G., and Jansen, J. K. (1986). Fluorescent dextran-amines used as axonal tracers in the nervous system of the chicken embryo. *J. Neurosci. Methods* 18, 243–254. doi: 10.1016/0165-0270(86)90011-7

Gonatas, N. K., Harper, C., Mizutani, T., and Gonatas, J. O. (1979). Superior sensitivity of conjugates of horseradish peroxidase with wheat germ agglutinin for studies of retrograde axonal transport. *J. Histochem. Cytochem.* 27, 728–734. doi: 10.1177/27.3.90065

Gonçalves, M. A., and de Vries, A. A. (2006). Adenovirus: from foe to friend. *Rev. Med. Virol.* 16, 167–186. doi: 10.1002/rmv.494

Gonçalves, M. A., Janssen, J. M., Holkers, M., and de Vries, A. A. (2010). Rapid and sensitive lentivirus vector-based conditional gene expression assay to monitor and quantify cell fusion activity. *PLoS One* 5:e10954. doi: 10.1371/journal.pone.0010954

Goodpasture, E. W., and Teague, O. (1923). Transmission of the virus of herpes febrilis along nerves in experimentally infected Rabbits. *J. Med. Res.* 44, 139–184.7.

Gosztonyi, G., Dietzschold, B., Kao, M., Rupprecht, C., Ludwig, H., and Koprowski, H. (1993). Rabies and Borna disease: a comparative pathogenetic study of two neurovirulent agents. *Lab. Invest.* 68, 285–295.

Gradinaru, V., Mogri, M., Thompson, K. R., Henderson, J. M., and Deisseroth, K. (2009). Optical deconstruction of parkinsonian neural circuitry. *Science* 324, 354–359. doi: 10.1126/science.1167093

Gradinaru, V., Zhang, F., Ramakrishnan, C., Mattis, J., Prakash, R., Diester, I., et al. (2010). Molecular and cellular approaches for diversifying and extending optogenetics. *Cell* 141, 154–165. doi: 10.1016/j.cell.2010.02.037

Graham, R. C. Jr., and Karnovsky, M. J. (1965). The histochemical demonstration of monoamine oxidase activity by coupled peroxidatic oxidation. *J. Histochem. Cytochem.* 13, 604–605. doi: 10.1177/13.7.604

Granstedt, A. E., Kuhn, B., Wang, S. S.-H., and Enquist, L. W. (2010). Calcium imaging of neuronal circuits *in vivo* using a circuit-tracing pseudorabies virus. *Cold Spring Harb. Protoc.* 2010:pdb.prot5410. doi: 10.1101/pdb.prot5410

Gray, S. J., Foti, S. B., Schwartz, J. W., Bachaboina, L., Taylor-Blake, B., Coleman, J., et al. (2011). Optimizing promoters for recombinant adeno-associated virus-mediated gene expression in the peripheral and central nervous system using self-complementary vectors. *Hum. Gene Ther.* 22, 1143–1153. doi: 10.1089/hum.2010.245

Gwag, B. J., Kim, E. Y., Ryu, B. R., Won, S. J., Ko, H. W., Oh, Y. J., et al. (1998). A neuron-specific gene transfer by a recombinant defective Sindbis virus. *Brain Res. Mol. Brain Res.* 63, 53–61. doi: 10.1016/s0169-328x(98)00251-4

Hacein-Bey-Abina, S., Pai, S. Y., Gaspar, H. B., Armant, M., Berry, C. C., Blanche, S., et al. (2014). A modified gamma-retrovirus vector for X-linked severe combined immunodeficiency. *N. Engl. J. Med.* 371, 1407–1417. doi: 10.1056/NEJMoa1404588

Hacein-Bey-Abina, S., Von Kalle, C., Schmidt, M., McCormack, M. P., Wulffraat, N., Leboulch, P., et al. (2003). LMO2-associated clonal T cell proliferation in two patients after gene therapy for SCID-X1. *Science* 302, 415–419. doi: 10.1126/science.1088547

Hafler, B. P., Surzenko, N., Beier, K. T., Punzo, C., Trimarchi, J. M., Kong, J. H., et al. (2012). Transcription factor Olig2 defines subpopulations of retinal progenitor cells biased toward specific cell fates. *Proc. Natl. Acad. Sci. U S A* 109, 7882–7887. doi: 10.1073/pnas.1203138109

Harpavat, S., and Cepko, C. L. (2006). RCAS-RNAi: a loss-of-function method for the developing chick retina. *BMC Dev. Biol.* 6:2. doi: 10.1186/1471-213X-6-2

Haubensak, W., Kunwar, P. S., Cai, H., Ciocchi, S., Wall, N. R., Ponnusamy, R., et al. (2010). Genetic dissection of an amygdala microcircuit that gates conditioned fear. *Nature* 468, 270–276. doi: 10.1038/nature09553

Hendrickson, A. E. (1982). "The orthograde axoplamic transport autoradiographic tracing technique and its implications for additional neuroanatomical analysis of the striate cortex," in *Cytochemical Methods in Neuroanatomy*, eds V. Chan-Palay, S. L. Palay, and R. Alan (New York: Liss), 1–16.

Hendry, I. A., Stöckel, K., Thoenen, H., and Iversen, L. L. (1974). The retrograde axonal transport of nerve growth factor. *Brain Res.* 68, 103–121. doi: 10.1016/0006-8993(74)90536-8

Hirst, G. K., and Gotlieb, T. (1953). The experimental production of combination forms of virus. I. Occurrence of combination forms after simultaneous inoculation of the allantoic sac with two distinct strains of influenza virus. *J. Exp. Med.* 98, 41–52. doi: 10.1084/jem.98.1.41

Hnasko, T. S., Perez, F. A., Scouras, A. D., Stoll, E. A., Gale, S. D., Luquet, S., et al. (2006). Cre recombinase-mediated restoration of nigrostriatal dopamine in dopamine-deficient mice reverses hypophagia and bradykinesia. *Proc. Natl. Acad. Sci. U S A* 103, 8858–8863. doi: 10.1073/pnas.0603081103

Hoff, E. C. (1932). Central nerve terminals in the mammalian spinal cord and their examination by experimental degeneration. *Proc. R. Soc. B Biol. Sci.* 111, 175–188. doi: 10.1098/rspb.1932.0049

Holland, E. C., Hively, W. P., DePinho, R. A., and Varmus, H. E. (1998). A constitutively active epidermal growth factor receptor cooperates with disruption of G1 cell-cycle arrest pathways to induce glioma-like lesions in mice. *Genes Dev.* 12, 3675–3685. doi: 10.1101/gad.12.23.3675

Hollis, E. R. 2nd, Kadoya, K., Hirsch, M., Samulski, R. J., and Tuszynski, M. H. (2008). Efficient retrograde neuronal transduction utilizing self-complementary AAV1. *Mol. Ther.* 16, 296–301. doi: 10.1038/sj.mt.6300367

Honig, M. G., and Hume, R. I. (1986). Fluorescent carbocyanine dyes allow living neurons of identified origin to be studied in long-term cultures. *J. Cell Biol.* 103, 171–187. doi: 10.1083/jcb.103.1.171

Honig, M. G., and Hume, R. I. (1989). Dil and diO: versatile fluorescent dyes for neuronal labelling and pathway tracing. *Trends Neurosci.* 12, 333–335,340–341. doi: 10.1016/0166-2236(89)90040-4

Howard, D. B., Powers, K., Wang, Y., and Harvey, B. K. (2008). Tropism and toxicity of adeno-associated viral vector serotypes 1, 2, 5, 6, 7, 8 and 9 in rat neurons and glia *in vitro*. *Virology* 372, 24–34. doi: 10.1016/j.virol.2007.10.007

Hurst, E. W. (1933). Studies on Pseudorabies (Infectious Bulbar Paralysis, Mad Itch): I. Histology of the disease, with a note on the symptomatology. *J. Exp. Med.* 58, 415–433. doi: 10.1084/jem.58.4.415

Iwasaki, Y., Ohtani, S., and Clark, H. F. (1975). Maturation of rabies virus by budding from neuronal cell membrane in suckling mouse brain. *J. Virol.* 15, 1020–1023.

Jones, E. G. (1984). Laminar distribution of cortical efferent cells. *Cereb. cortex* 1, 521–553.

Junt, T., Moseman, E. A., Iannacone, M., Massberg, S., Lang, P. A., Boes, M., et al. (2007). Subcapsular sinus macrophages in lymph nodes clear lymph-borne viruses and present them to antiviral B cells. *Nature* 450, 110–114. doi: 10.1038/nature06287

Kaspar, B. K., Erickson, D., Schaffer, D., Hinh, L., Gage, F. H., and Peterson, D. A. (2002). Targeted retrograde gene delivery for neuronal protection. *Mol. Ther.* 5, 50–56. doi: 10.1006/mthe.2001.0520

Kato, S., Kobayashi, K. K., Inoue, K., Kuramochi, M., Okada, T., Yaginuma, H., et al. (2011). A lentiviral strategy for highly efficient retrograde gene transfer by pseudotyping with fusion envelope glycoprotein. *Hum. Gene Ther.* 22, 197–206. doi: 10.1089/hum.2009.179

Katz, L. C., Burkhalter, A., and Dreyer, W. J. (1984). Fluorescent latex microspheres as a retrograde neuronal marker for *in vivo* and *in vitro* studies of visual cortex. *Nature* 310, 498–500. doi: 10.1038/310498a0

Katz, L. C., and Iarovici, D. M. (1990). Green fluorescent latex microspheres: a new retrograde tracer. *Neuroscience* 34, 511–520. doi: 10.1016/0306-4522(90)90159-2

Keefer, D. A., Spatz, W. B., and Misgeld, U. (1976). Golgi-like staining of neocortical neurons using retrogradely transported horseradish peroxidase. *Neurosci. Lett.* 3, 233–237. doi: 10.1016/0304-3940(76)90048-3

Kelly, R. M., and Strick, P. L. (2000). Rabies as a transneuronal tracer of circuits in the central nervous system. *J. Neurosci. Methods* 103, 63–71. doi: 10.1016/s0165-0270(00)00296-x

King, M. A., Louis, P. M., Hunter, B. E., and Walker, D. W. (1989). Biocytin: a versatile anterograde neuroanatomical tract-tracing alternative. *Brain Res.* 497, 361–367. doi: 10.1016/0006-8993(89)90281-3

Kishi, N., Sato, K., Sasaki, E., and Okano, H. (2014). Common marmoset as a new model animal for neuroscience research and genome editing technology. *Dev. Growth Differ.* 56, 53–62. doi: 10.1111/dgd.12109

Kissa, K., Mordelet, E., Soudais, C., Kremer, E. J., Demeneix, B. A., Brûlet, P., et al. (2002). *In vivo* neuronal tracing with GFP-TTC gene delivery. *Mol. Cell. Neurosci.* 20, 627–637. doi: 10.1006/mcne.2002.1141

Knipe, D. M., and Howley, P. M. (2013). *Fields virology*. 6th Edn. Philadelphia, PA: Wolters Kluwer/Lippincott Williams and Wilkins Health.

Köbbert, C., Apps, R., Bechmann, I., Lanciego, J. L., Mey, J., and Thanos, S. (2000). Current concepts in neuroanatomical tracing. *Prog. Neurobiol.* 62, 327–351. doi: 10.1016/s0301-0082(00)00019-8

Kobiler, O., Lipman, Y., Therkelsen, K., Daubechies, I., and Enquist, L. W. (2010). Herpesviruses carrying a Brainbow cassette reveal replication and expression of limited numbers of incoming genomes. *Nat. Commun.* 1:146. doi: 10.1038/ncomms1145

Kopec, C. D., Real, E., Kessels, H. W., and Malinow, R. (2007). GluR1 links structural and functional plasticity at excitatory synapses. *J. Neurosci.* 27, 13706–13718. doi: 10.1523/jneurosci.3503-07.2007

Krashes, M. J., Shah, B. P., Madara, J. C., Olson, D. P., Strochlic, D. E., Garfield, A. S., et al. (2014). An excitatory paraventricular nucleus to AgRP neuron circuit that drives hunger. *Nature* 507, 238–242. doi: 10.1038/nature12956

Kratchmarov, R., Taylor, M. P., and Enquist, L. W. (2012). Making the case: married versus separate models of alphaherpes virus anterograde transport in axons. *Rev. Med. Virol.* 22, 378–391. doi: 10.1002/rmv.1724

Kremer, E. J., Boutin, S., Chillon, M., and Danos, O. (2000). Canine adenovirus vectors: an alternative for adenovirus-mediated gene transfer. *J. Virol.* 74, 505–512. doi: 10.1128/jvi.74.1.505-512.2000

Krisky, D. M., Wolfe, D., Goins, W. F., Marconi, P. C., Ramakrishnan, R., Mata, M., et al. (1998). Deletion of multiple immediate-early genes from herpes simplex virus reduces cytotoxicity and permits long-term gene expression in neurons. *Gene Ther.* 5, 1593–1603. doi: 10.1038/sj.gt.3300766

Kristensson, K. (1970). Transport of fluorescent protein tracer in peripheral nerves. *Acta Neuropathol.* 16, 293–300. doi: 10.1007/bf00686894

Kristensson, K., and Olsson, Y. (1971). Retrograde axonal transport of protein. *Brain Res.* 29, 363–365. doi: 10.1016/0006-8993(71)90044-8

Kumar, M., Keller, B., Makalou, N., and Sutton, R. E. (2001). Systematic determination of the packaging limit of lentiviral vectors. *Hum. Gene Ther.* 12, 1893–1905. doi: 10.1089/104303401753153947

Kuramoto, E., Ohno, S., Furuta, T., Unzai, T., Tanaka, Y. R., Hioki, H., et al. (2015). Ventral medial nucleus neurons send thalamocortical afferents more widely and more preferentially to layer 1 than neurons of the ventral anterior-ventral lateral nuclear complex in the rat. *Cereb. Cortex* 25, 221–235. doi: 10.1093/cercor/bht216

Kuypers, H. G., Bentivoglio, M., van der Kooy, D., and Catsman-Berrevoets, C. E. (1979). Retrograde transport of bisbenzimide and propidium iodide through axons to their parent cell bodies. *Neurosci. Lett.* 12, 1–7. doi: 10.1016/0304-3940(79)91471-x

Lafferty, W. E., Downey, L., Celum, C., and Wald, A. (2000). Herpes simplex virus type 1 as a cause of genital herpes: impact on surveillance and prevention. *J. Infect. Dis.* 181, 1454–1457. doi: 10.1086/315395

Lanciego, J. L., and Wouterlood, F. G. (2011). A half century of experimental neuroanatomical tracing. *J. Chem. Neuroanat.* 42, 157–183. doi: 10.1016/j.jchemneu.2011.07.001

Lasek, R., Joseph, B. S., and Whitlock, D. G. (1968). Evaluation of a radioautographic neuroanatomical tracing method. *Brain Res.* 8, 319–336. doi: 10.1016/0006-8993(68)90052-8

LaVail, J. H., and LaVail, M. M. (1972). Retrograde axonal transport in the central nervous system. *Science* 176, 1416–1417. doi: 10.1126/science.176.4042.1416

Lee, J. H., Durand, R., Gradinaru, V., Zhang, F., Goshen, I., Kim, D.-S., et al. (2010). Global and local fMRI signals driven by neurons defined optogenetically by type and wiring. *Nature* 465, 788–792. doi: 10.1038/nature09108

Levine, J. D., Zhao, X. S., and Miselis, R. R. (1994). Direct and indirect retinohypothalamic projections to the supraoptic nucleus in the female albino rat. *J. Comp. Neurol.* 341, 214–224. doi: 10.1002/cne.903410207

Lilley, C. E., Groutsi, F., Han, Z., Palmer, J. A., Anderson, P. N., Latchman, D. S., et al. (2001). Multiple immediate-early gene-deficient herpes simplex virus vectors allowing efficient gene delivery to neurons in culture and widespread gene delivery to the central nervous system *in vivo*. *J. Virol.* 75, 4343–4356. doi: 10.1128/jvi.75.9.4343-4356.2001

Lima, S. Q., Hromádka, T., Znamenskiy, P., and Zador, A. M. (2009). PINP: a new method of tagging neuronal populations for identification during *in vivo* electrophysiological recording. *PLoS One* 4:e6099. doi: 10.1371/journal.pone.0006099

Lo, L., and Anderson, D. J. (2011). A Cre-dependent, anterograde transsynaptic viral tracer for mapping output pathways of genetically marked neurons. *Neuron* 72, 938–950. doi: 10.1016/j.neuron.2011.12.002

Lomniczi, B., Watanabe, S., Ben-Porat, T., and Kaplan, A. S. (1987). Genome location and identification of functions defective in the Bartha vaccine strain of pseudorabies virus. *J. Virol.* 61, 796–801.

Looger, L. L., and Griesbeck, O. (2012). Genetically encoded neural activity indicators. *Curr. Opin. Neurobiol.* 22, 18–23. doi: 10.1016/j.conb.2011.10.024

Lundh, B. (1990). Spread of vesicular stomatitis virus along the visual pathways after retinal infection in the mouse. *Acta Neuropathol.* 79, 395–401. doi: 10.1007/bf00308715

Maday, S., Twelvetrees, A. E. E., Moughamian, A. J. J., and Holzbaur, E. L. F. L. (2014). Axonal transport: cargo-specific mechanisms of motility and regulation. *Neuron* 84, 292–309. doi: 10.1016/j.neuron.2014.10.019

Malinow, R., Hayashi, Y., Maletic-Savatic, M., Zaman, S. H., Poncer, J. C., Shi, S. H., et al. (2010). Introduction of green fluorescent protein (GFP) into hippocampal neurons through viral infection. *Cold Spring Harb. Protoc.* 2010:prot5406. doi: 10.1101/pdb.prot5406

Mansuy, I. M., and Bujard, H. (2000). Tetracycline-regulated gene expression in the brain. *Curr. Opin. Neurobiol.* 10, 593–596. doi: 10.1016/s0959-4388(00)00127-6

Marshel, J. H., Mori, T., Nielsen, K. J., and Callaway, E. M. (2010). Targeting single neuronal networks for gene expression and cell labeling *in vivo*. *Neuron* 67, 562–574. doi: 10.1016/j.neuron.2010.08.001

Masamizu, Y., Okada, T., Kawasaki, K., Ishibashi, H., Yuasa, S., Takeda, S., et al. (2011). Local and retrograde gene transfer into primate neuronal pathways via adeno-associated virus serotype 8 and 9. *Neuroscience* 193, 249–258. doi: 10.1016/j.neuroscience.2011.06.080

Mazarakis, N. D., Azzouz, M., Rohll, J. B., Ellard, F. M., Wilkes, F. J., Olsen, A. L., et al. (2001). Rabies virus glycoprotein pseudotyping of lentiviral vectors enables retrograde axonal transport and access to the nervous system after peripheral delivery. *Hum. Mol. Genet.* 10, 2109–2121. doi: 10.1093/hmg/10.19.2109

McCarty, D. M., Monahan, P. E., and Samulski, R. J. (2001). Self-complementary recombinant adeno-associated virus (scAAV) vectors promote efficient transduction independently of DNA synthesis. *Gene Ther.* 8, 1248–1254. doi: 10.1038/sj.gt.3301514

McCarthy, K. M., Tank, D. W., and Enquist, L. W. (2009). Pseudorabies virus infection alters neuronal activity and connectivity *in vitro*. *PLoS Pathog.* 5:e1000640. doi: 10.1371/journal.ppat.1000640

McCarty, D. M., Young, S. M. Jr., and Samulski, R. J. (2004). Integration of adeno-associated virus (AAV) and recombinant AAV vectors. *Annu. Rev. Genet.* 38, 819–845. doi: 10.1146/annurev.genet.37.110801.143717

McFarland, N. R., Lee, J. S., Hyman, B. T., and McLean, P. J. (2009). Comparison of transduction efficiency of recombinant AAV serotypes 1, 2, 5 and 8 in the rat nigrostriatal system. *J. Neurochem.* 109, 838–845. doi: 10.1111/j.1471-4159.2009.06010.x

McGettigan, J. P., Naper, K., Orenstein, J., Koser, M., McKenna, P. M., and Schnell, M. J. (2003). Functional human immunodeficiency virus type 1 (HIV-1) Gag-Pol or HIV-1 Gag-Pol and env expressed from a single rhabdovirus-based vaccine vector genome. *J. Virol.* 77, 10889–10899. doi: 10.1128/jvi.77.20.10889-10899.2003

McPhee, S. W., Janson, C. G., Li, C., Samulski, R. J., Camp, A. S., Francis, J., et al. (2006). Immune responses to AAV in a phase I study for Canavan disease. *J. Gene. Med.* 8, 577–588. doi: 10.1002/jgm.885

Mebatsion, T., Schnell, M. J., Cox, J. H., Finke, S., and Conzelmann, K. K. (1996). Highly stable expression of a foreign gene from rabies virus vectors. *Proc. Natl. Acad. Sci. U S A* 93, 7310–7314. doi: 10.1073/pnas.93.14.7310

Mesulam, M. M. (1982). "Principles of horseradish peroxidase neurohistochemistry and their applications for tracing neural pathways--Axonal transport, enzyme histochemistry and light microscopic analysis.," in *Tracing Neural Connections with Horseradish Peroxidase*, eds M. M. Mesulam (New York: John Wiley and Sons), 1–151.

Mingozzi, F., and High, K. A. (2013). Immune responses to AAV vectors: overcoming barriers to successful gene therapy. *Blood* 122, 23–36. doi: 10.1182/blood-2013-01-306647

Minshew, N. J., and Williams, D. L. (2007). The new neurobiology of autism: cortex, connectivity and neuronal organization. *Arch. Neurol.* 64, 945–950. doi: 10.1001/archneur.64.7.945

Miyamichi, K., Amat, F., Moussavi, F., Wang, C., Wickersham, I., Wall, N. R., et al. (2011). Cortical representations of olfactory input by trans-synaptic tracing. *Nature* 472, 191–196. doi: 10.1038/nature09714

Miyamichi, K., Shlomai-Fuchs, Y., Shu, M., Weissbourd, B. C., Luo, L., and Mizrahi, A. (2013). Dissecting local circuits: parvalbumin interneurons underlie broad feedback control of olfactory bulb output. *Neuron* 80, 1232–1245. doi: 10.1016/j.neuron.2013.08.027

Miyoshi, H., Blömer, U., Takahashi, M., Gage, F. H., and Verma, I. M. (1998). Development of a self-inactivating lentivirus vector. *J. Virol.* 72, 8150–8157.

Montiel-Equihua, C. A., Zhang, L., Knight, S., Saadeh, H., Scholz, S., Carmo, M., et al. (2012). The beta-globin locus control region in combination with the EF1alpha short promoter allows enhanced lentiviral vector-mediated erythroid gene expression with conserved multilineage activity. *Mol. Ther.* 20, 1400–1409. doi: 10.1038/mt.2012.50

Moore, R. Y., Speh, J. C., and Card, J. P. (1995). The retinohypothalamic tract originates from a distinct subset of retinal ganglion cells. *J. Comp. Neurol.* 352, 351–366. doi: 10.1002/cne.903520304

Morales, J. A., Herzog, S., Kompter, C., Frese, K., and Rott, R. (1988). Axonal transport of Borna disease virus along olfactory pathways in spontaneously and experimentally infected rats. *Med. Microbiol. Immunol.* 177, 51–68. doi: 10.1007/bf00189527

Mundell, N. A., Beier, K. T., Pan, Y. A., Lapan, S. W., Göz Aytürk, D., Berezovskii, V. K., et al. (2015). Vesicular stomatitis virus enables gene transfer and transsynaptic tracing in a wide range of organisms. *J. Comp. Neurol.* 523, 1639–1663. doi: 10.1002/cne.23761

Murlidharan, G., Samulski, R. J., and Asokan, A. (2014). Biology of adeno-associated viral vectors in the central nervous system. *Front. Mol. Neurosci.* 7:76. doi: 10.3389/fnmol.2014.00076

Nakai, H., Storm, T. A., and Kay, M. A. (2000). Recruitment of single-stranded recombinant adeno-associated virus vector genomes and intermolecular recombination are responsible for stable transduction of liver *in vivo*. *J. Virol.* 74, 9451–9463. doi: 10.1128/jvi.74.20.9451-9463.2000

Naldini, L., Blömer, U., Gallay, P., Ory, D., Mulligan, R., Gage, F. H., et al. (1996). *In vivo* gene delivery and stable transduction of nondividing cells by a lentiviral vector. *Science* 272, 263–267. doi: 10.1126/science.272.5259.263

Nance, D. M., and Burns, J. (1990). Fluorescent dextrans as sensitive anterograde neuroanatomical tracers: applications and pitfalls. *Brain Res. Bull.* 25, 139–145. doi: 10.1016/0361-9230(90)90264-z

Nassi, J. J., and Callaway, E. M. (2006). Multiple circuits relaying primate parallel visual pathways to the middle temporal area. *J. Neurosci.* 26, 12789–12798. doi: 10.1523/jneurosci.4044-06.2006

Nassi, J. J., and Callaway, E. M. (2007). Specialized circuits from primary visual cortex to V2 and area MT. *Neuron* 55, 799–808. doi: 10.1016/j.neuron.2007.07.037

Nassi, J. J., Lyon, D. C., and Callaway, E. M. (2006). The Parvocellular LGN provides a robust disynaptic input to the visual motion area MT. *Neuron* 50, 319–327. doi: 10.1016/j.neuron.2006.03.019

Nauta, W. J. H., and Gygax, P. A. (1951). Silver impregnation of degenerating axon terminals in the central nervous system. *Stain Technol.* 26, 5–11. doi: 10.3109/10520295109113170

Nguyen, T. D., Wirblich, C., Aizenman, E., Schnell, M. J., Strick, P. L., and Kandler, K. (2012). Targeted single-neuron infection with rabies virus for transneuronal multisynaptic tracing. *J. Neurosci. Methods* 209, 367–370. doi: 10.1016/j.jneumeth.2012.06.019

Ogawa, S. K., Cohen, J. Y., Hwang, D., Uchida, N., and Watabe-Uchida, M. (2014). Organization of monosynaptic inputs to the serotonin and dopamine neuromodulatory systems. *Cell Rep.* 8, 1105–1118. doi: 10.1016/j.celrep.2014.06.042

Osakada, F., Mori, T., Cetin, A. H., Marshel, J. H., Virgen, B., and Callaway, E. M. (2011). New rabies virus variants for monitoring and manipulating activity and gene expression in defined neural circuits. *Neuron* 71, 617–631. doi: 10.1016/j.neuron.2011.07.005

Osten, P., Dittgen, T., and Licznerski, P. (2006). Lentivirus-based genetic manipulations in neurons *in vivo*. *Front. Neurosci.* Chapter 13, 249–259. doi: 10.1201/9780203486283.ch13

Oyibo, H. K., Znamenskiy, P., Oviedo, H. V., Enquist, L. W., and Zador, A. M. (2014). Long-term Cre-mediated retrograde tagging of neurons using a novel recombinant pseudorabies virus. *Front. Neuroanat.* 8:86. doi: 10.3389/fnana.2014.00086

Paddison, P. J., Silva, J. M., Conklin, D. S., Schlabach, M., Li, M., Aruleba, S., et al. (2004). A resource for large-scale RNA-interference-based screens in mammals. *Nature* 428, 427–431. doi: 10.1038/nature02370

Palmer, D., and Ng, P. (2003). Improved system for helper-dependent adenoviral vector production. *Mol. Ther.* 8, 846–852. doi: 10.1016/j.ymthe.2003.08.014

Parks, R. J., Chen, L., Anton, M., Sankar, U., Rudnicki, M. A., and Graham, F. L. (1996). A helper-dependent adenovirus vector system: removal of helper virus by Cre-mediated excision of the viral packaging signal. *Proc. Natl. Acad. Sci. U S A* 93, 13565–13570. doi: 10.1073/pnas.93.24.13565

Peltékian, E., Garcia, L., and Danos, O. (2002). Neurotropism and retrograde axonal transport of a canine adenoviral vector: a tool for targeting key structures undergoing neurodegenerative processes. *Mol. Ther.* 5, 25–32. doi: 10.1006/mthe.2001.0517

Petreanu, L., Gutnisky, D. A., Huber, D., Xu, N., O'Connor, D. H., Tian, L., et al. (2012). Activity in motor-sensory projections reveals distributed coding in somatosensation. *Nature* 489, 299–303. doi: 10.1038/nature11321

Petreanu, L., Huber, D., Sobczyk, A., and Svoboda, K. (2007). Channelrhodopsin-2-assisted circuit mapping of long-range callosal projections. *Nat. Neurosci.* 10, 663–668. doi: 10.1038/nn1891

Pivetta, C., Esposito, M. S., Sigrist, M., and Arber, S. (2014). Motor-circuit communication matrix from spinal cord to brainstem neurons revealed by developmental origin. *Cell* 156, 537–548. doi: 10.1016/j.cell.2013.12.014

Plakhov, I. V., Arlund, E. E., Aoki, C., and Reiss, C. S. (1995). The earliest events in vesicular stomatitis virus infection of the murine olfactory neuroepithelium and entry of the central nervous system. *Virology* 209, 257–262. doi: 10.1006/viro.1995.1252

Pollak Dorocic, I., Fürth, D., Xuan, Y., Johansson, Y., Pozzi, L., Silberberg, G., et al. (2014). A whole-brain atlas of inputs to serotonergic neurons of the dorsal and median raphe nuclei. *Neuron* 83, 663–678. doi: 10.1016/j.neuron.2014.07.002

Ramón y Cajal, S. (1909). *Histologie du Systeme Nerveux de L'Homme et des Vertebres.* Facsimile. Paris: Maloine.

Rathelot, J.-A., and Strick, P. L. (2006). Muscle representation in the macaque motor cortex: an anatomical perspective. *Proc. Natl. Acad. Sci. U S A* 103, 8257–8262. doi: 10.1073/pnas.0602933103

Rathelot, J.-A., and Strick, P. L. (2009). Subdivisions of primary motor cortex based on cortico-motoneuronal cells. *Proc. Natl. Acad. Sci. U S A* 106, 918–923. doi: 10.1073/pnas.0808362106

Reiff, D. F., Plett, J., Mank, M., Griesbeck, O., and Borst, A. (2010). Visualizing retinotopic half-wave rectified input to the motion detection circuitry of Drosophila. *Nat. Neurosci.* 13, 973–978. doi: 10.1038/nn.2595

Roberts, A., Kretzschmar, E., Perkins, A. S., Forman, J., Price, R., Buonocore, L., et al. (1998). Vaccination with a recombinant vesicular stomatitis virus expressing an influenza virus hemagglutinin provides complete protection from influenza virus challenge. *J. Virol.* 72, 4704–4711.

Roth, A., and Breaker, R. R. (2009). The structural and functional diversity of metabolite-binding riboswitches. *Annu. Rev. Biochem.* 78, 305–334. doi: 10.1146/annurev.biochem.78.070507.135656

Rubinov, M., and Bassett, D. S. (2011). Emerging evidence of connectomic abnormalities in schizophrenia. *J. Neurosci.* 31, 6263–6265. doi: 10.1523/JNEUROSCI.0382-11.2011

Sabin, A. B., and Olitsky, P. K. (1937). Influence of host factors on neuroinvasiveness of vesicular stomatitis virus: I. Effect of age on the invasion of the brain by virus instilled in the nose. *J. Exp. Med.* 66, 15–34. doi: 10.1084/jem.66.1.15

Samaniego, L. A., Neiderhiser, L., and DeLuca, N. A. (1998). Persistence and expression of the herpes simplex virus genome in the absence of immediate-early proteins. *J. Virol.* 72, 3307–3320.

Saunders, A., Johnson, C. A., and Sabatini, B. L. (2012). Novel recombinant adeno-associated viruses for Cre activated and inactivated transgene expression in neurons. *Front. Neural Circuits* 6:47. doi: 10.3389/fncir.2012.00047

Schambach, A., Zychlinski, D., Ehrnstroem, B., and Baum, C. (2013). Biosafety features of lentiviral vectors. *Hum. Gene Ther.* 24, 132–142. doi: 10.1089/hum.2012.229

Schmued, L. C., and Fallon, J. H. (1986). Fluoro-Gold: a new fluorescent retrograde axonal tracer with numerous unique properties. *Brain Res.* 377, 147–154. doi: 10.1016/0006-8993(86)91199-6

Schnütgen, F., Doerflinger, N., Calléja, C., Wendling, O., Chambon, P., and Ghyselinck, N. B. (2003). A directional strategy for monitoring Cre-mediated recombination at the cellular level in the mouse. *Nat. Biotechnol.* 21, 562–565. doi: 10.1038/nbt811

Schwab, M. E., and Agid, I. (1979). Labelled wheat germ agglutinin and tetanus toxin as highly sensitive retrograde tracers in the CNS: the afferent fiber connections of the rat nucleus caudatus. *Int. J. Neurol.* 13, 117–126.

Schwab, M. E., Javoy-Agid, F., and Agid, Y. (1978). Labeled wheat germ agglutinin (WGA) as a new, highly sensitive retrograde tracer in the rat brain hippocampal system. *Brain Res.* 152, 145–150. doi: 10.1016/0006-8993(78)90140-3

Schwab, M. E., Suda, K., and Thoenen, H. (1979). Selective retrograde transsynaptic transfer of a protein, tetanus toxin, subsequent to its retrograde axonal transport. *J. Cell Biol.* 82, 798–810. doi: 10.1083/jcb.82.3.798

Seiler, M. P., Cerullo, V., and Lee, B. (2007). Immune response to helper dependent adenoviral mediated liver gene therapy: challenges and prospects. *Curr. Gene Ther.* 7, 297–305. doi: 10.2174/156652307782151452

Senn, V., Wolff, S. B. E., Herry, C., Grenier, F., Ehrlich, I., Gründemann, J., et al. (2014). Long-range connectivity defines behavioral specificity of amygdala neurons. *Neuron* 81, 428–437. doi: 10.1016/j.neuron.2013.11.006

Shelly, S., Lukinova, N., Bambina, S., Berman, A., and Cherry, S. (2009). Autophagy is an essential component of Drosophila immunity against vesicular stomatitis virus. *Immunity* 30, 588–598. doi: 10.1016/j.immuni.2009.02.009

Sommer, C. A., Sommer, A. G., Longmire, T. A., Christodoulou, C., Thomas, D. D., Gostissa, M., et al. (2010). Excision of reprogramming transgenes improves the differentiation potential of iPS cells generated with a single excisable vector. *Stem Cells* 28, 64–74. doi: 10.1002/stem.255

Sondhi, D., Johnson, L., Purpura, K., Monette, S., Souweidane, M. M., Kaplitt, M. G., et al. (2012). Long-term expression and safety of administration of AAVrh.10hCLN2 to the brain of rats and nonhuman primates for the treatment of late infantile neuronal ceroid lipofuscinosis. *Hum. Gene Ther. Methods* 23, 324–335. doi: 10.1089/hgtb.2012.120

Sosulski, D. L., Bloom, M. L., Cutforth, T., Axel, R., and Datta, S. R. (2011). Distinct representations of olfactory information in different cortical centres. *Nature* 472, 213–216. doi: 10.1038/nature09868

Soudais, C., Laplace-Builhe, C., Kissa, K., and Kremer, E. J. (2001). Preferential transduction of neurons by canine adenovirus vectors and their efficient retrograde transport *in vivo*. *FASEB J.* 15, 2283–2285. doi: 10.1096/fj.01-0321fje

Spaete, R. R., and Frenkel, N. (1982). The herpes simplex virus amplicon: a new eucaryotic defective-virus cloning-amplifying vector. *Cell* 30, 295–304. doi: 10.1016/0092-8674(82)90035-6

Stepien, A. E., Tripodi, M., and Arber, S. (2010). Monosynaptic rabies virus reveals premotor network organization and synaptic specificity of cholinergic partition cells. *Neuron* 68, 456–472. doi: 10.1016/j.neuron.2010.10.019

Stettler, D. D., and Axel, R. (2009). Representations of odor in the piriform cortex. *Neuron* 63, 854–864. doi: 10.1016/j.neuron.2009.09.005

Stoeckel, K., Schwab, M., and Thoenen, H. (1975). Comparison between the retrograde axonal transport of nerve growth factor and tetanus toxin in motor, sensory and adrenergic neurons. *Brain Res.* 99, 1–16. doi: 10.1016/0006-8993(75)90604-6

Stoeckel, K., Schwab, M., and Thoenen, H. (1977). Role of gangliosides in the uptake and retrograde axonal transport of cholera and tetanus toxin as compared to nerve growth factor and wheat germ agglutinin. *Brain Res.* 132, 273–285. doi: 10.1016/0006-8993(77)90421-8

Stoeckel, K., and Thoenen, H. (1975). Retrograde axonal transport of nerve growth factor: specificity and biological importance. *Brain Res.* 85, 337–341. doi: 10.1016/0006-8993(75)90092-x

Strack, A. M., and Loewy, A. D. (1990). Pseudorabies virus: a highly specific transneuronal cell body marker in the sympathetic nervous system. *J. Neurosci.* 10, 2139–2147.

Stuber, G. D., Sparta, D. R., Stamatakis, A. M., van Leeuwen, W. A., Hardjoprajitno, J. E., Cho, S., et al. (2011). Excitatory transmission from the amygdala to nucleus accumbens facilitates reward seeking. *Nature* 475, 377–380. doi: 10.1038/nature10194

Sun, N., Cassell, M. D., and Perlman, S. (1996). Anterograde, transneuronal transport of herpes simplex virus type 1 strain H129 in the murine visual system. *J. Virol.* 70, 5405–5413.

Sun, Y., Nguyen, A. Q., Nguyen, J. P., Le, L., Saur, D., Choi, J., et al. (2014). Cell-type-specific circuit connectivity of hippocampal CA1 revealed through cre-dependent rabies tracing. *Cell Rep.* 7, 269–280. doi: 10.1016/j.celrep.2014.02.030

Szpara, M. L., Kobiler, O., and Enquist, L. W. (2010). A common neuronal response to alphaherpesvirus infection. *J. Neuroimmune Pharmacol.* 5, 418–427. doi: 10.1007/s11481-010-9212-0

Takatoh, J., Nelson, A., Zhou, X., Bolton, M. M., Ehlers, M. D., Arenkiel, B. R., et al. (2013). New modules are added to vibrissal premotor circuitry with the emergence of exploratory whisking. *Neuron* 77, 346–360. doi: 10.1016/j.neuron.2012.11.010

Tang, J. C. Y., Rudolph, S., Dhande, O., Abraira, V. E., Choi, S., Lapan, S., et al. (in press). Cell Type-Specific Manipulation with GFP-Dependent Cre Recombinase. *Nat. Neurosci.*

Tang, J. C. Y., Szikra, T., Kozorovitskiy, G., Texeira, M., Sabatini, B. L., Roska, B., et al. (2013). A nanobody-based system using fluorescent proteins as scaffolds for cell-specific gene manipulation. *Cell* 154, 928–939. doi: 10.1016/j.cell.2013.07.021

Taylor, A. C., and Weiss, P. (1965). Demonstration of axonal flow by the movement of tritium-labeled protein in mature optic nerve fibers. *Proc. Natl. Acad. Sci. U S A* 54, 1521–1527. doi: 10.1073/pnas.54.6.1521

Taymans, J. M., Vandenberghe, L. H., Haute, C. V., Thiry, I., Deroose, C. M., Mortelmans, L., et al. (2007). Comparative analysis of adeno-associated viral vector serotypes 1, 2, 5, 7 and 8 in mouse brain. *Hum. Gene Ther.* 18, 195–206. doi: 10.1089/hum.2006.178

Timm, C., Akpinar, F., and Yin, J. (2014). Quantitative characterization of defective virus emergence by deep sequencing. *J. Virol.* 88, 2623–2632. doi: 10.1128/jvi.02675-13

Ting, J. T., and Feng, G. (2013). Development of transgenic animals for optogenetic manipulation of mammalian nervous system function: progress and prospects for behavioral neuroscience. *Behav. Brain Res.* 255, 3–18. doi: 10.1016/j.bbr.2013.02.037

Tomioka, R., and Rockland, K. S. (2006). Improved Golgi-like visualization in retrogradely projecting neurons after EGFP-adenovirus infection in adult rat and monkey. *J. Histochem. Cytochem.* 54, 539–548. doi: 10.1369/jhc.5a6838.2005

Towne, C., Schneider, B. L., Kieran, D., Redmond, D. E. Jr., and Aebischer, P. (2010). Efficient transduction of non-human primate motor neurons after intramuscular delivery of recombinant AAV serotype 6. *Gene Ther.* 17, 141–146. doi: 10.1038/gt.2009.119

Tripodi, M., Stepien, A. E., and Arber, S. (2011). Motor antagonism exposed by spatial segregation and timing of neurogenesis. *Nature* 479, 61–66. doi: 10.1038/nature10538

Trojanowski, J. Q., Gonatas, J. O., and Gonatas, N. K. (1981). Conjugates of horseradish peroxidase (HRP) with cholera toxin and wheat germ agglutinin are superior to free HRP as orthogradely transported markers. *Brain Res.* 223, 381–385. doi: 10.1016/0006-8993(81)91151-3

Trojanowski, J., Gonatas, J., and Gonatas, N. (1982). Horseradish peroxidase (HRP) conjugates of cholera toxin and lectins are more sensitive retrogradely transported markers than free HRP. *Brain Res.* 231, 33–50. doi: 10.1016/0006-8993(82)90005-1

Tsiang, H., Koulakoff, A., Bizzini, B., and Berwald-Netter, Y. (1983). Neurotropism of rabies virus: an *in vitro* study. *J. Neuropathol. Exp. Neurol.* 42, 439–452. doi: 10.1097/00005072-198307000-00006

Turner, D. L., and Cepko, C. L. (1987). A common progenitor for neurons and glia persists in rat retina late in development. *Nature* 328, 131–136. doi: 10.1038/328131a0

Ugolini, G. (1995). Specificity of rabies virus as a transneuronal tracer of motor networks: transfer from hypoglossal motoneurons to connected second-order and higher order central nervous system cell groups. *J. Comp. Neurol.* 356, 457–480. doi: 10.1002/cne.903560312

Ugolini, G., Kuypers, H. G., and Strick, P. L. (1989). Transneuronal transfer of herpes virus from peripheral nerves to cortex and brainstem. *Science* 243, 89–91. doi: 10.1126/science.2536188

van den Pol, A. N., Dalton, K. P., and Rose, J. K. (2002). Relative neurotropism of a recombinant rhabdovirus expressing a green fluorescent envelope glycoprotein. *J. Virol.* 76, 1309–1327. doi: 10.1128/jvi.76.3.1309-1327.2002

van den Pol, A. N., Ozduman, K., Wollmann, G., Ho, W. S., Simon, I., Yao, Y., et al. (2009). Viral strategies for studying the brain, including a replication-restricted self-amplifying delta-G vesicular stomatis virus that rapidly expresses transgenes in brain and can generate a multicolor golgi-like expression. *J. Comp. Neurol.* 516, 456–481. doi: 10.1002/cne.22131

Vandenberghe, L. H., Bell, P., Maguire, A. M., Xiao, R., Hopkins, T. B., Grant, R., et al. (2013). AAV9 targets cone photoreceptors in the nonhuman primate retina. *PLoS One* 8:e53463. doi: 10.1371/journal.pone.0053463

Veenman, C. L., Reiner, A., and Honig, M. G. (1992). Biotinylated dextran amine as an anterograde tracer for single- and double-labeling studies. *J. Neurosci. Methods* 41, 239–254. doi: 10.1016/0165-0270(92)90089-v

Viney, T. J., Balint, K., Hillier, D., Siegert, S., Boldogkoi, Z., Enquist, L. W., et al. (2007). Local retinal circuits of melanopsin-containing ganglion cells identified by transsynaptic viral tracing. *Curr. Biol.* 17, 981–988. doi: 10.1016/j.cub.2007.04.058

Vitreschak, A. G., Rodionov, D. A., Mironov, A. A., and Gelfand, M. S. (2004). Riboswitches: the oldest mechanism for the regulation of gene expression? *Trends Genet.* 20, 44–50. doi: 10.1016/j.tig.2003.11.008

Wall, N. R., Wickersham, I. R., Cetin, A., De La Parra, M., and Callaway, E. M. (2010). Monosynaptic circuit tracing *in vivo* through Cre-dependent targeting and complementation of modified rabies virus. *Proc. Natl. Acad. Sci. U S A* 107, 21848–21853. doi: 10.1073/pnas.1011756107

Wall, N., DeLaParra, M., Callaway, E., and Kreitzer, A. (2013). Differential innervation of direct- and indirect-pathway striatal projection neurons. *Neuron* 79, 347–360. doi: 10.1016/j.neuron.2013.05.014

Waller, A. (1850). Experiments on the section of the glossopharyngeal and hypoglossal nerves of the frog and observations of the alterations produced thereby in the structure of their primitive fibres. *Phil. Trans. R. Soc. Lond.* 140, 423–429. doi: 10.1098/rstl.1850.0021

Watabe-Uchida, M., Zhu, L., Ogawa, S. K., Vamanrao, A., and Uchida, N. (2012). Whole-brain mapping of direct inputs to midbrain dopamine neurons. *Neuron* 74, 858–873. doi: 10.3410/f.717597914.793052821

Weaver, W. (1958). The Rockefeller Foundation Annual Report, 1958. Available online at: http://www.rockefellerfoundation.org/app/uploads/Annual-Report-1958.pdf

Weiss, P., and Hiscoe, H. B. (1948). Experiments on the mechanism of nerve growth. *J. Exp. Zool.* 107, 315–395. doi: 10.1002/jez.1401070302

Weissbourd, B., Ren, J., DeLoach, K. E., Guenthner, C. J., Miyamichi, K., and Luo, L. (2014). Presynaptic partners of dorsal raphe serotonergic and GABAergic neurons. *Neuron* 83, 645–662. doi: 10.1016/j.neuron.2014.06.024

Whelan, S. P. J., Ball, L. A., Barr, J. N., and Wertz, G. T. W. (1995). Efficient recovery of infectious vesicular stomatitis virus entirely from cDNA clones. *Proc. Natl. Acad. Sci. U S A* 92, 8388–8392. doi: 10.1073/pnas.92.18.8388

Wickersham, I. R., Finke, S., Conzelmann, K.-K. K., and Callaway, E. M. (2007a). Retrograde neuronal tracing with a deletion-mutant rabies virus. *Nat. Methods* 4, 47–49. doi: 10.1038/nmeth999

Wickersham, I. R., Lyon, D. C., Barnard, R. J. O., Mori, T., Finke, S., Conzelmann, K. K., et al. (2007b). Monosynaptic restriction of transsynaptic tracing from single, genetically targeted neurons. *Neuron* 53, 639–647. doi: 10.1016/j.neuron.2007.01.033

Wickersham, I. R., Sullivan, H. A., and Seung, H. S. (2013). Axonal and subcellular labelling using modified rabies viral vectors. *Nat. Commun.* 4:2332. doi: 10.1038/ncomms3332

Wiznerowicz, M., and Trono, D. (2005). Harnessing HIV for therapy, basic research and biotechnology. *Trends Biotechnol.* 23, 42–47. doi: 10.1016/j.tibtech.2004.11.001

Wouterlood, F. G., Bloem, B., Mansvelder, H. D., Luchicchi, A., and Deisseroth, K. (2014). A fourth generation of neuroanatomical tracing techniques: exploiting the offspring of genetic engineering. *J. Neurosci. Methods* 235, 331–348. doi: 10.1016/j.jneumeth.2014.07.021

Wu, Z., Yang, H., and Colosi, P. (2010). Effect of genome size on AAV vector packaging. *Mol. Ther.* 18, 80–86. doi: 10.1038/mt.2009.255

Xiong, W., and Cepko, C. L. (2014). "Distinct expression patterns of AAV8 vectors with broadly active promoters from subretinal injections of neonatal mouse eyes at two different ages," in *Retinal Degeneration*, eds S. Westendorf M. LaVail, and R. Bowes (New York, New York: Springer Science+Business Media).

Xu, W., and Südhof, T. C. (2013). A neural circuit for memory specificity and generalization. *Science* 339, 1290–1295. doi: 10.1126/science.1229534

Yang, J., Zhou, W., Zhang, Y., Zidon, T., Ritchie, T., and Engelhardt, J. F. (1999). Concatamerization of adeno-associated virus circular genomes occurs through intermolecular recombination. *J. Virol.* 73, 9468–9477.

Yonehara, K., Balint, K., Noda, M., Nagel, G., Bamberg, E., and Roska, B. (2011). Spatially asymmetric reorganization of inhibition establishes a motion-sensitive circuit. *Nature* 469, 407–410. doi: 10.1038/nature09711

Zampieri, N., Jessell, T. M., and Murray, A. J. (2014). Mapping sensory circuits by anterograde transsynaptic transfer of recombinant rabies virus. *Neuron* 81, 766–778. doi: 10.1016/j.neuron.2013.12.033

Zemanick, M. C., Strick, P. L., and Dix, R. D. (1991). Direction of transneuronal transport of herpes simplex virus 1 in the primate motor system is strain-dependent. *Proc. Natl. Acad. Sci. U S A* 88, 8048–8051. doi: 10.1073/pnas.88.18.8048

Zhang, H., Yang, B., Mu, X., Ahmed, S. S., Su, Q., He, R., et al. (2011). Several rAAV vectors efficiently cross the blood-brain barrier and transduce neurons and astrocytes in the neonatal mouse central nervous system. *Mol. Ther.* 19, 1440–1448. doi: 10.1038/mt.2011.98

Zincarelli, C., Soltys, S., Rengo, G., and Rabinowitz, J. E. (2008). Analysis of AAV serotypes 1-9 mediated gene expression and tropism in mice after systemic injection. *Mol. Ther.* 16, 1073–1080. doi: 10.1038/mt.2008.76

Zuboff, A. (1981). "The Story of a Brain," in *The Mind's I*, eds D. R. Hofstadter and D. C. Dennett (New York, USA: Basic Books), 202–212.

Zufferey, R., Donello, J. E., Trono, D., and Hope, T. J. (1999). Woodchuck hepatitis virus posttranscriptional regulatory element enhances expression of transgenes delivered by retroviral vectors. *J. Virol.* 73, 2886–2892. doi: 10.1089/10430349950016942

Conflict of Interest Statement: The authors declare that the research was conducted in the absence of any commercial or financial relationships that could be construed as a potential conflict of interest.

frontiers in Neuroanatomy

ORIGINAL RESEARCH
published: 27 March 2015
doi: 10.3389/fnana.2015.00040

Whole-brain mapping of the direct inputs and axonal projections of POMC and AgRP neurons

Daqing Wang[1,2], Xiaobing He[3,4], Zhe Zhao[2], Qiru Feng[2], Rui Lin[2], Yue Sun[2], Ting Ding[3], Fuqiang Xu[3,4,5], Minmin Luo[1,2]* and Cheng Zhan[2]**

[1] School of Life Sciences, Tsinghua University, Beijing China, [2] National Institute of Biological Sciences, Beijing, China, [3] Key Laboratory of Magnetic Resonance in Biological Systems and State Key Laboratory of Magnetic Resonance and Atomic and Molecular Physics, Wuhan Institute of Physics and Mathematics, Chinese Academy of Sciences, Wuhan, China, [4] University of Chinese Academy of Sciences, Beijing, China, [5] Wuhan National Laboratory for Optoelectronics, Wuhan, China

OPEN ACCESS

Edited by:
Javier DeFelipe, Cajal Institute, Spain

Reviewed by:
Marina Bentivoglio, Université di Verona, Italy
Ursula H. Winzer-Serhan, Texas A&M Health Science Center, USA

***Correspondence:**
Fuqiang Xu, Key Laboratory of Magnetic Resonance in Biological Systems and State Key Laboratory of Magnetic Resonance and Atomic and Molecular Physics, Wuhan Institute of Physics and Mathematics, Chinese Academy of Sciences, West No. 30, Xiao Hong Shan, 430071 Wuhan, China
fuqiang.xu@wipm.ac.cn;
Minmin Luo, School of Life Sciences, Tsinghua University, 30 Shuang Qing Lu, Haidian, 100084 Beijing, China
luomm@mail.tsinghua.edu.cn;
Cheng Zhan, National Institute of Biological Sciences, 7# Science Park Road, Zhongguancun Life Science Park, 102206 Beijing, China
zhancheng@nibs.ac.cn

Received: 26 January 2015
Accepted: 12 March 2015
Published: 27 March 2015

Citation:
Wang D, He X, Zhao Z, Feng Q, Lin R, Sun Y, Ding T, Xu F, Luo M and Zhan C (2015) Whole-brain mapping of the direct inputs and axonal projections of POMC and AgRP neurons. Front. Neuroanat. 9:40. doi: 10.3389/fnana.2015.00040

Pro-opiomelanocortin (POMC) neurons in the arcuate nucleus (ARC) of the hypothalamus and nucleus tractus solitarius (NTS) of the brainstem play important roles in suppressing food intake and maintaining energy homeostasis. Previous tract-tracing studies have revealed the axonal connection patterns of these two brain areas, but the intermingling of POMC neurons with other neuron types has made it challenging to precisely identify the inputs and outputs of POMC neurons. In this study, we used the modified rabies virus to map the brain areas that provide direct inputs to the POMC neurons in the ARC and NTS as well as the inputs to the ARC AgRP neurons for comparison. ARC POMC neurons receive inputs from dozens of discrete structures throughout the forebrain and brainstem. The brain areas containing the presynaptic partners of ARC POMC neurons largely overlap with those of ARC AgRP neurons, although POMC neurons receive relatively broader, denser inputs. Furthermore, POMC neurons in the NTS receive direct inputs predominantly from the brainstem and show very different innervation patterns for POMC neurons in the ARC. By selectively expressing fluorescent markers in the ARC and NTS POMC neurons, we found that almost all of their major presynaptic partners are innervated by POMC neurons in the two areas, suggesting that there are strong reciprocal projections among the major POMC neural pathways. By comprehensively chartering the whole-brain connections of the central melanocortin system in a cell-type-specific manner, this study lays the foundation for dissecting the roles and underlying circuit mechanisms of specific neural pathways in regulating energy homeostasis.

Keywords: arcuate nucleus, POMC neurons, nucleus tractus solitarius, transsynaptic tracing, rabies virus, adeno-associated virus

Introduction

The central melanocortin system plays important roles in regulating energy homeostasis, cardiovascular function, and reproduction (Cone, 2005; Morton et al., 2006; Millington, 2007). This system includes three groups of projection neurons (Cone, 2005): POMC neurons in the arcuate nucleus (ARC) of the hypothalamus, POMC neurons in the nucleus tractus solitarius (NTS) of the medulla, and AgRP neurons in the ARC. Studies in previous decades have revealed apparently opposite functions for POMC neurons and AgRP neurons in regulating food intake. Stimulating POMC neurons

in the ARC and NTS suppresses feeding (Aponte et al., 2011; Zhan et al., 2013), whereas stimulating AgRP neurons rapidly elicits feeding behavior (Aponte et al., 2011; Krashes et al., 2011). By contrast, killing POMC neurons induces hyperphagia and obesity (Yaswen et al., 1999; Coll et al., 2004; Xu et al., 2005; Zhan et al., 2013), whereas ablating AgRP neurons in adult mice induces hypophagia and, ultimately, starvation (Gropp et al., 2005; Luquet et al., 2005).

Classic tract tracings have revealed that neurons in the ARC and NTS receive inputs from, and project to, broad brain areas (Makara and Hodacs, 1975; Ricardo and Koh, 1978; Schwaber et al., 1982; Chronwall, 1985; Gruber et al., 1987; Sim and Joseph, 1991; Magoul et al., 1993; Rinaman, 2010). Different cell types are intermingled in both brain areas, thus making it impossible to assign conventional tracing results to specific types of neurons among nuclei. The recent development of the rabies virus-based transynaptic tracing technique has enabled the precise mapping of direct inputs to various cell populations in a cell-type specific manner (Wickersham et al., 2007; Wall et al., 2010, 2013; Osakada et al., 2011; Arenkiel et al., 2012; Garcia et al., 2012; Watabe-Uchida et al., 2012; Ogawa et al., 2014; Pollak Dorocic et al., 2014; Stanek et al., 2014; Weissbourd et al., 2014). Using this strategy, Krashes and colleagues have unraveled the pattern of presynaptic inputs to AgRP neurons in the ARC (Krashes et al., 2014). However, the whole-brain inputs to POMC neurons have not yet been examined. In view of the outputs, the axon projection patterns of the AgRP neurons have been studied using the AAV-based anterograde tracing technique (Atasoy et al., 2008; Betley et al., 2013), but the outputs of POMC neurons in the ARC and NTS have not been systemically studied.

Here we used the modified rabies virus and the Cre/loxp gene expression system to map the whole-brain distribution patterns of the neurons that provide direct inputs to POMC neurons in the ARC and NTS. In addition, we studied the axon projection patterns of these two sets of POMC neurons by separately expressing fluorescent proteins of different colors. The input and output profiles of POMC neurons were compared to those of ARC AgRP neurons. Our results reveal distinct connectivity between POMC neurons in the ARC and NTS. Moreover, we show that POMC neurons and AgRP neurons form rich reciprocal connections with their respective upstream stations. The comprehensive mapping of connection patterns outlines the structural framework for future systematic studies of the neural circuits that underlie the behavioral and endocrinological functions of brain POMC neurons.

Abbreviations: Acb, accumbens nucleus; ADP, anterodorsal preoptic nucleus; AH, anterior hypothalamus; AHi, amygdalohippocampal area; AI, agranular insular cortex; AP, area postrema; ARC, arcuate nucleus; ATg, anterior tegmental nucleus; BST, bed nucleus of the stria terminalis; CeM, medial part of the central amygdaloid nucleus; Cg, cingulate cortex; Cu, cuneate nucleus; DB, diagonal band of Broca; DCN, deep nuclei of cerebellum; DM, dorsomedial hypothalamus; DP, dorsal peduncular cortex; DpG, deep gray layer of the superior Colliculus; DPGi, dorsal paragigantocellular nucleus; DpMe, deep mesencephalic nucleus; DRN, dorsal raphe nucleus; DS, dorsal subiculum; DTg, dorsal tegmental nucleus; DTT, dorsal tenia tecta; EW, Edinger-Westphal nucleus; Gi, gigantocellular reticular nucleus; GiA, alpha part of gigantocellular reticular nucleus; HDB, horizontal diagonal band of broca; IL, infralimbic cortex; InCo, intercollicular nucleus; INWH, intermediate white layer of the superior Colliculus; Int, interposed cerebellar nucleus; IRt, intermediate reticular nucleus; LA, lateroanterior hypothalamic nucleus; Lat, lateral cerebellar nucleus; LC, locus coeruleus; LDT, glaterodorsal tegmental nucleus; LH, lateral hypothalamus; LHb, lateral habenular nucleus; LPB, lateral parabrachial nucleus; LPGi, lateral paragigantocellular nucleus; LPO, lateral preoptic area; LRt, lateral reticular nucleus; LS, lateral septum; M1, primary motor cortex; M2, secondary motor cortex; MdD, dorsal parts of medullary reticular nucleus; MdV, ventral parts of medullary reticular nucleus; MEA, medial amygdaloid nucleus; Med, medial cerebellar nucleus; MM, medial mammillary nucleus; MnR, median raphe nucleus; MO, medial orbital cortex; MPA, medial preoptic area; MPO, medial preoptic nucleus; MS, medial septum; MTu, medial tuberal nucleus; MVe, medial vestibular nucleus; NI, nucleus incertus; NTS, nucleus tractus solitaries; P5, peritrigeminal zone; PAG, periaqueductal gray; PCRt, parvicellular reticular nucleus; PH, posterior hypothalamus; PM, premammillary nucleus; PMn, paramedian reticular nucleus; PnC, caudal parts of the pontine reticular nucleus; PnO, oral parts of the pontine reticular nucleus; PnV, ventral part of pontine reticular nucleus; Pr5, principal sensory trigeminal nucleus; PrL, prelimbic cortex; PSTh, parasubthalamic nucleus; PVN, paraventricular hypothalamic nucleus; PVT, paraventricular thalamic nucleus; Rch, retrochiasmatic area; RMg, raphe magnus nucleus; Rn, red nucleus; Rob, raphe obscurus nucleus; RS, retrosplenial cortex; RSG, retrosplenial granular cortex; Rt, reticular thalamic nucleus; RVL, rostroventrolateral reticular nucleus; S1, primary somatosensory cortex; S2, secondary somatosensory cortex; S, subiculum; SCN, suprachiasmatic nucleus; SLEA, sublenticular extended amygdala; SO, supraoptic nucleus; SP5C, spinal trigeminal nucleus; Su5, supratrigeminal nucleus; SubC, subcoeruleus nucleus; SuM, supramammillary nucleus; TC, tuber cinereum area; VMH, ventromedial hypothalamic nucleus; VP, ventral pallidum; VS, ventral subiculum; VTA, ventral tegmental area; VTg, ventral tegmental nucleus; ZI, zona incerta; 3V, third ventricle; 4V, fourth ventricle; cc, central canal; LV, lateral ventricle; AgRP, Agouti-related peptide; POMC, Pro-opiomelanocortin.

Materials and Methods

Mice

The animal care and use conformed to the institutional guidelines of National Institute of Biological Sciences, Beijing and the governmental regulations of China. Mice were housed under a controlled temperature (22–25°C) and 12 h light-dark cycle with standard mouse chow and water provided *ad libitum*. We used adult mice (2–4 month) of either sex. POMC-Cre [Jackson Laboratory strain name Tg(Pomc1-cre)16Lowl/J] (Balthasar et al., 2004) and AgRP-Cre [Jackson Laboratory strain Name Agrptm1(cre)Lowl/J] (Tong et al., 2008) mouse lines were backcrossed and maintained in a C57BL6 background. Littermate wildtype mice were used for control experiments.

Viral Vectors Production

The initial rabies viruses SAD-ΔG-mCherry (EnvA) and the cell lines for rabies propagation and titering were kindly sied by E.M. Callaway at Salt Institute. The rabies viruses were produced and concentrated as previously described (Osakada et al., 2011). The final titer of EnvA-RV-mCherry was 2×10^8 infecting unit per milliliter.

Cre-dependent adeno-associated virus (AAV) plasmids with a DIO sequence carrying rabies glycoprotein (RG) or TVA were generated as helper virus vectors for retrograde transsynaptic tracing. The AAV-DIO-EGFP-TVA plasmid was constructed by sub-cloning the CAG promoter from AAV-CAG-GFP-ires-CRE plasmid (Addgene plasmid 48201) and the coding region of GFP:2A:TVA from the AAV-EF1a-FLEX-GT plasmid (Addgene plasmid 26198) (Wall et al., 2010) into the DIO cassette of

the plasmid pAAV-EF1a-DIO-hChR2(H134R)-EYFP (Addgene plasmid 20298). The AAV-DIO-RG plasmid was constructed by sub-cloning the CAG promoter from the AAV-CAG-GFP-ires-CRE plasmid (Addgene plasmid 48201) and coding region of RG from AAV-EF1a-FLEX-GTB (Addgene plasmid 26197) (Haubensak et al., 2010) into the DIO cassette of the plasmid pAAV-EF1a-DIO-hChR2(H134R)-EYFP (Addgene plasmid 20298).

Another two Cre-dependent AAV plasmids were generated for tracing axonal projections. pAAV-EF1a-DIO-EmGFP and pAAV-EF1a-DIO-mtdTomato were constructed by replacing the coding region of hChR2(H134R)-EYFP with the coding sequence of the membrane-bound form of EGFP (EmGFP; Addgene plasmid 14757) (Matsuda and Cepko, 2007) or membrane-bound form of tdTomato in the AAV-EF1a-DIO-hChR2(H134R)-EYFP-WPRE-HGHpA plasmid (Addgene plasmid 20298). All AAV vectors were packaged into 2/9 serotypes with titers of approximately 2×10^{12} genome copies per milliliter.

Stereotaxic Virus Injection

To perform stereotaxic viral injections, mice were anesthetized with pentobarbital (i.p. 80 mg/kg) and then mounted in a stereotaxic holder. A small incision was made in the skin to expose the skull. After thoroughly cleaning the skull with 0.3% hydrogen peroxide solution, we drilled a small hole through the skull for virus injection. For cell-type-specific retrograde tracing, two Cre-dependent AAV-DIO-EGFP-TVA and AAV-DIO-RG were mixed with an equal volume prior to viral injections; then, 80–300 nl AAV mixtures filled in a pulled glass pipettes were stereotaxically injected into target areas (ARC coordinate AP/DV/ML: -1.7/-5.5/-0.2 mm; NTS coordinate AP/DV/ML: 8.4/3.3/0 mm) of POMC-Cre or AgRP-Cre mice using a microsyringe pump (Nanoliter 2000 Injector, WPI), which allowed EGFP-TVA and RG selectively expression in POMC or AgRP neurons. After 3 weeks of recovery and AAV expression, 300 nl SAD19ΔG-mCherry(EnvA) was injected into the same location in a biosafety level-2 environment. After 1 week of rabies virus infection and transsynaptic spread (Wall et al., 2010; Watabe-Uchida et al., 2012), the animals were sacrificed. To directly compare the axonal projections of POMC neurons in the ARC vs. the NTS, 300 nl anterograde tracer AAV-DIO-mtdTomato or AAV-DIO-EmGFP was injected into the ARC or NTS respectively. Similarly, 300 nl AAV-DIO-EmGFP was injected into the ARC of AgRP-Cre mice for anterograde tracing. To achieve strong labeling of the axons, animals were allowed to survive for 1 month post surgery (Gautron et al., 2010).

Histology and Immunostaining

Mice were anesthetized by i.p. injection of an overdose of pentobarbital, and then transcardially perfused with 0.9% saline followed by 4% paraformaldehyde (PFA) in PBS. After post fixation overnight, the brain was isolated and cryoprotected with 30% sucrose for 2 days. For further imaging and analysis, whole brains were coated with tissue freezing medium and coronal sections (40 μm thick) were prepared on a cryostat (Leica CM1900). Some mouse brains were cut sagittally to better visualize the axon projections. Brain sections mounted on chrome-gelatin subbed slides were washed with PBS four times every 6 min. For immunofluorescent staining, the sections were blocked with 3% BSA in PBS-0.3% Triton X-100 and subsequently incubated with primary antibodies rabbit anti-POMC (1:200, catalog# H-029-30, Phoenix Pharmaceuticals; overnight), goat anti-AgRP (15 μg/ml, catalog# GT15023, Neuromics; 72 h), or chicken anti-GFP (1:500, catalog#ab290, Abcam; overnight) at 4°C. Sections were then incubated with secondary antibodies, Alexa647 donkey anti-rabbit (1:500, Jackson ImmunoResearch), Alexa647 donkey anti-goat (1:500, Jackson ImmunoResearch) or Cy2 anti-rabbit (1:500, Jackson ImmunoResearch) for 4 h at room temperature. Finally, these brain sections were cover-slipped with 50% DAPI-glycerol mounting medium.

Imaging and Data Analysis

Whole brain sections were imaged with an automated slide scanner (VS120 Virtual Slide, Olympus) or a confocal microscope (DigitalEclipse A1, Nikon). The locations of the labeled neurons and outlines of the brain nuclei were manually defined in the commercial software Imaris (Bitplane, Zurich, Switzerland) according to the mouse brain atlas (Paxinos and Franklin, 2001). The cell number of each nucleus was counted automatically. Brightness, contrast and pseudocolor were adjusted, as needed, using ImageJ (NIH). For three-dimensional (3D) visualization, each imaged section was translated and rotated to align with its precursor image along the anteroposterior axis using AutoAligner (Bitplane). 3D visualizations of whole-brain inputs were generated with well-aligned image sequences using Imaris (Bitplane). For better visualization, each input neuron was represented as a red dot in the 3D models.

Results

Transynaptic Labeling of Direct Inputs to POMC and AgRP Neurons Using Rabies Virus and Cre-loxP Gene Expression

To achieve cell-type-specific retrograde transsynaptic tracing, we used the recently developed three-virus system in combination with the Cre/loxP gene-expression technique (**Figure 1A**) (Watabe-Uchida et al., 2012; Wall et al., 2013; Pollak Dorocic et al., 2014; Weissbourd et al., 2014). The modified rabies virus SAD-ΔG-mCherry(EnvA) was pseudotyped with the avian sarcoma leucosis virus envelope protein (EnvA), which allows the virus to selectively infect mammalian neurons that express TVA, the cognate receptor of EnvA. Additionally, the rabies glycoprotein (RG) gene required for transsynaptic spreading beyond initially infected neurons was replaced with the coding sequence of a red fluorescent protein, mCherry. Two Cre-dependent AAV recombinants, AAV-DIO-EGFP-TVA and AAV-DIO-RG, were stereotaxically infused into the unilateral ARC of POMC-Cre or AgRP-Cre mice (**Figures 1A,B**). After 3 weeks of the expression of EGFP-TVA and RG, the rabies virus SAD-ΔG-mCherry(EnvA) was injected into the same area. One week later, allowing for virus replication and transsynaptic spread, mouse brains were histologically prepared for examining the labeling patterns (**Figure 1B**).

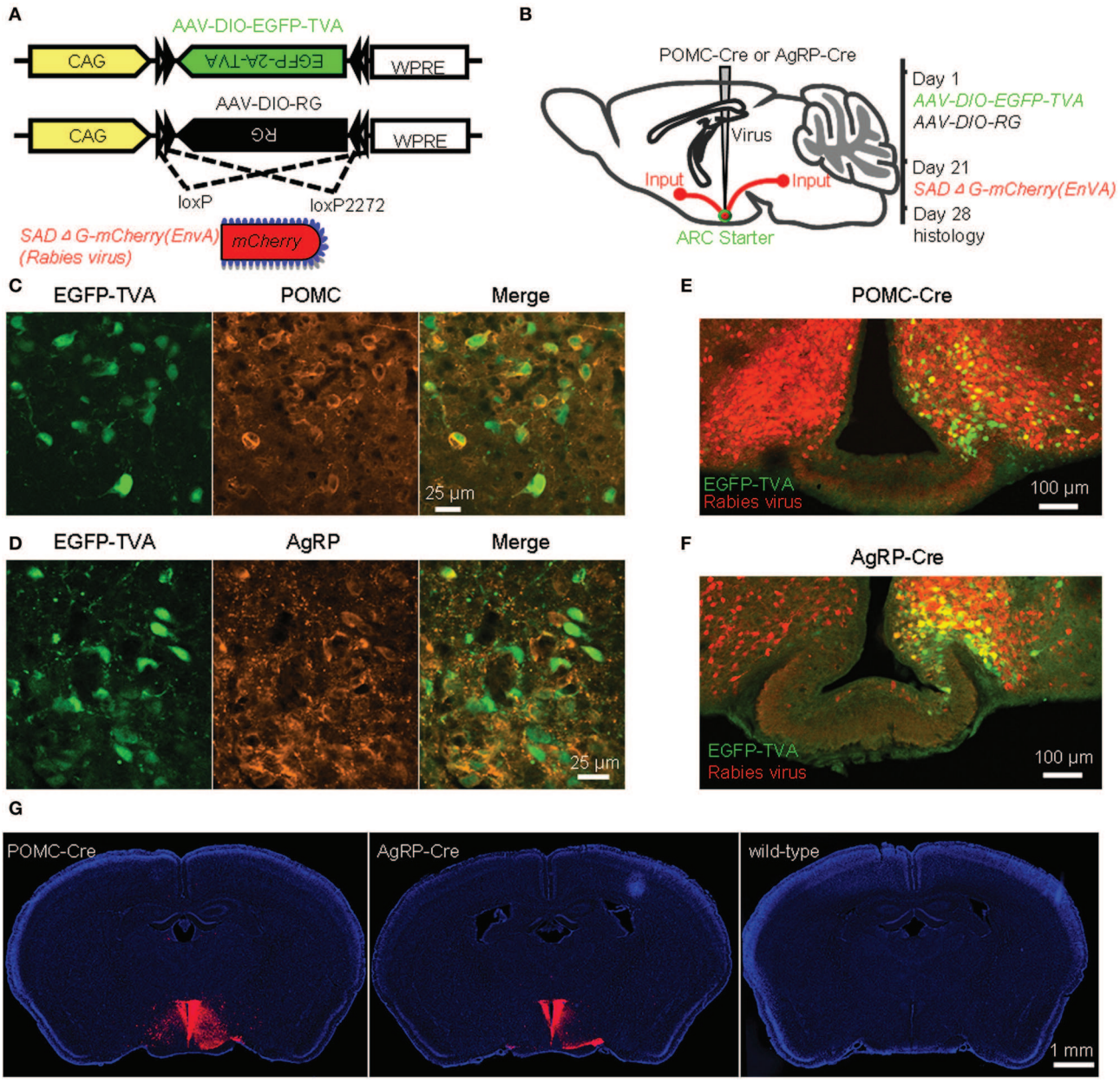

FIGURE 1 | Identification of direct inputs to POMC and AgRP neurons in the ARC using stereotaxic injection of the modified rabies virus into Cre-transgenic mice. (A) Design of recombinant AAV-DIO-EGFP-TVA, AAV-DIO-RG, and modified rabies virus. **(B)** Experimental design. **(C)** Selective expression of EGFP-TVA in POMC-expressing neurons following the unilateral injection of AAV-DIO-EGFP-TVA into the ARC of a POMC-Cre mouse. **(D)**, EGFP-TVA expression pattern in the ARC of an AgRP-Cre mouse. **(E,F)** Characterization of the distribution pattern of starter neurons (green) and retrogradely labeled neurons (red) in the ARC of POMC-Cre **(E)** and AgRP-Cre **(F)** mice. **(G)** Transsynaptic labeling (red) was observed in a Cre-transgenic mouse but not a wildtype control mouse. Blue indicates cell nuclear staining with DAPI.

EGFP-TVA signals were colocalized with POMC or AgRP immunoreactivity in the majority (~95%) of the neurons in the ARC (**Figures 1C,D**), confirming the accuracy of these two driver mouse lines (Balthasar et al., 2004; Tong et al., 2008). Starter neurons were characterized by the coexpression of RV-mCherry and EGFP-TVA, which was restricted within the ARC, unilateral to the injection site (**Figures 1E,F**). A substantial number of mCherry-positive neurons in the bilateral ARC did not express EGFP-TVA, suggesting the presence of local inputs (**Figures 1E,F**). We observed a large number of mCherry-expressing neurons outside of the ARC of POMC-Cre and AgRP-Cre mice (**Figure 1G** left and middle panels). In contrast, we did not detect any mCherry-positive neurons in wildtype littermates that were tested with the same procedures (**Figure 1G** right

panel). These results demonstrated that the mCherry signals outside the injection sites are produced by the spread of rabies virus from Cre-expressing starter neurons.

Input Patterns of the ARC POMC and AgRP Neurons

In POMC-Cre mice that were injected with the three viral vectors in the ARC, mCherry-labeled presynaptic neurons were located in dozens of discrete brain areas, including the lateral septum (LS), medial preoptic area and medial preoptic nucleus (MPA/MPO), anterior hypothalamus (AH), paraventricular hypothalamic nucleus (PVN), dorsomedial hypothalamus (DM), posterior hypothalamus (PH), amygdalohippocampal area (AHi), dorsal and ventral parts of subiculum (DS and VS), ventral tegmental nucleus (VTg), and nucleus incertus (NI) (**Figure 2A**). The presynaptic labeling was always bilateral, although it tended to be stronger in the hemisphere ipsilateral to the starter neurons. Despite the apparently opposite behavioral functions of POMC and AgRP neurons, the overall labeling pattern in POMC-Cre mice resembled that in AgRP-Cre mice at the level of brain nuclei (**Figure 2B**). 3D views of whole-brain inputs were constructed for better visualization (**Supplementary movie 1** for a POMC-Cre mouse and **Supplementary movie 2** for an AgRP-Cre mouse). Quantification of the number of labeled neurons in the individual coronal sections revealed a similar distribution along the anteroposterior axis, although ARC POMC neurons were innervated by more input neurons than ARC AgRP neurons (**Figure 2C**). On average, ARC POMC neurons received direct inputs from 43990 ± 8596 neurons (mean ± SEM) in the entire brain ($n = 4$ POMC-Cre mice). In contrast, ARC AgRP neurons received direct inputs from 17191 ± 4526 neurons ($n = 5$ AgRP-Cre mice). The numbers of starter cells in the ARC of these two mouse lines were similar (∼900 for the POMC-Cre line vs. ∼800 for the AgRP-Cre line), suggesting that the substantial difference in the number of input neurons reflects more inputs and a higher convergence ratio for POMC neurons (∼49 for POMC vs. ∼21 for AgRP).

We further measured the number of labeled neurons and the labeling density in individual brain areas. The locations of labeled neurons were determined using a standard mouse atlas (Paxinos and Franklin, 2001). To minimize bias, only brain areas with at least 10 labeled neurons in at least one mouse line were analyzed. To correct potential bias, the cell number in each nucleus was further normalized by the total inputs. A list of whole brain inputs was generated for the ARC POMC and AgRP neurons (**Figure 3**). Overall, the hypothalamic areas provided the majority of inputs to both POMC (∼60%) and AgRP (∼70%) neurons in the ARC. The hypothalamic input areas mainly included the AH, DM, lateroanterior hypothalamic nucleus (LA), PVN, lateral hypothalamus (LH), supraoptic nucleus (SO), ventromedial hypothalamic nucleus (VMH), PH, MPA/MPO, and lateral preoptic area (LPO). Although the DM provided the largest number of inputs for POMC neurons, the SO was the most densely labeled area. The major forebrain input areas outside the hypothalamus include the subiculum (S) in the hippocampus, LS in the septum, and bed nucleus of the stria terminalis (BST) in the pallidum (∼15% for POMC and ∼10% for AgRP). No substantial labeling was found in a majority of the cortical areas, thalamus, or striatum. Beyond the forebrain, a few discrete nuclei in the midbrain and pons contained the remaining inputs. These areas mainly include the medial mammillary nucleus (MM), median raphe, and pontine central gray. Although the NTS is the major brainstem area for regulating energy homeostasis (Cone, 2005; Zhang et al., 2010; Wu et al., 2012; Young, 2012), we did not find any labeled neurons in this area for either POMC-Cre mice or AgRP-Cre mice.

A total of 52 brain areas provide direct inputs to the ARC POMC neurons, while 35 of the 52 areas also project to AgRP neurons. Within the 35 brain areas, the cell density of POMC-targeting neurons was often significantly higher than that of AgRP-targeting neurons (**Figure 3**). **Figure 4A** shows several such examples, including the LS, MPO, AH, VTg, NI, and VS. One exception was the SO, which was the most densely labeled nucleus in AgRP mice and had more input neurons for AgRP neurons than for POMC neurons (**Figure 4B**). The 17 brain areas selectively targeting ARC POMC neurons constituted only a small proportion (∼7%) of the total inputs for POMC neurons. **Figure 4C** shows the labeling pattern of three such examples, including in the dorsal subiculum, horizontal diagonal band of broca (HDB), and dorsal raphe nucleus (DRN).

The major presynaptic partners of POMC neurons and AgRP neurons in the ARC are summarized in **Figure 5**. Overall, the hypothalamic areas and several other forebrain nuclei represent the major input sources for both POMC and AgRP neurons in the ARC, while some nuclei in the midbrain and pons prefer to connect to ARC POMC neurons.

Input Patterns of NTS POMC Neurons

In addition to the ARC, the NTS in the medulla also contains a substantial number of POMC-expressing neurons (Bronstein et al., 1992; Padilla et al., 2012). These NTS POMC neurons have been implicated in feeding behavior and energy metabolism (Rinaman et al., 1998; Fan et al., 2004; Zheng et al., 2005; Huo et al., 2006; Zhan et al., 2013). We asked whether the NTS POMC neurons receive direct inputs from the same sets of nuclei as those of the ARC POMC neurons.

We injected AAV-DIO-EGFP-TVA and AAV-DIO-G viral vectors and then the modified rabies virus into the NTS of POMC-Cre mice (**Figure 6A**). The entire mouse brain was sectioned coronally, and both EGFP-TVA and mCherry signals were imaged for all brain sections. The starter neurons were present only in the NTS (**Figure 6B**). We observed retrogradely labeled, mCherry-expressing neurons mainly in the BST, PVN, LH, medial part of the central amygdaloid nucleus (CeM), parasubthalamic nucleus (PSTh), red nucleus (Rn), oral and caudal parts of the pontine reticular nucleus (PnO and PnC), locus coeruleus (LC), intermediate reticular nucleus (IRt), gigantocellular reticular nucleus (Gi), raphe magnus nucleus (RMg), lateral and medial cerebellar nucleus (Lat and Med) (**Figures 6C,D**). The 3D reconstruction of whole-brain inputs to the NTS POMC neurons was shown in **Supplementary movie 3**. Overall, the starter neurons in the NTS (∼300) received direct inputs from 22,061 ± 5092 neurons ($n = 5$ POMC-Cre mice). Therefore, the

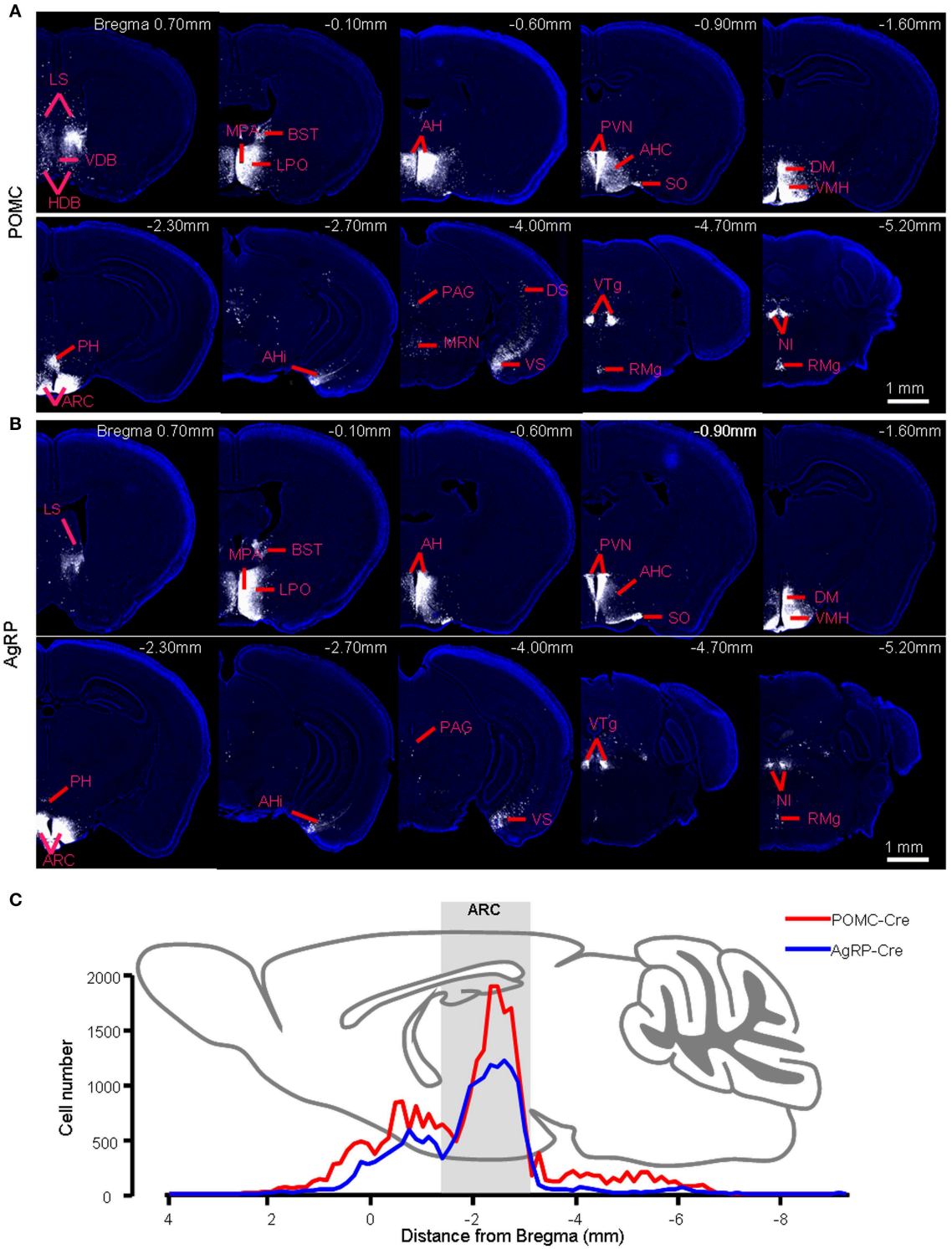

FIGURE 2 | Brain areas that provide presynaptic inputs to the ARC POMC and AgRP neurons. (A) Series of coronal sections show the pattern of retrograde labeling following rabies virus injection into the right hemisphere of a POMC-Cre mouse. Rabies virus labeling is pseudocolored for better contrast against the DAPI-counterstaining of cell nuclei (blue). **(B)** The retrograde labeling pattern of an AgRP-Cre mouse. **(C)** Distribution profiles of input neuron numbers in each brain section of a POMC-Cre mouse and an AgRP-Cre mouse along the anteroposterior axis.

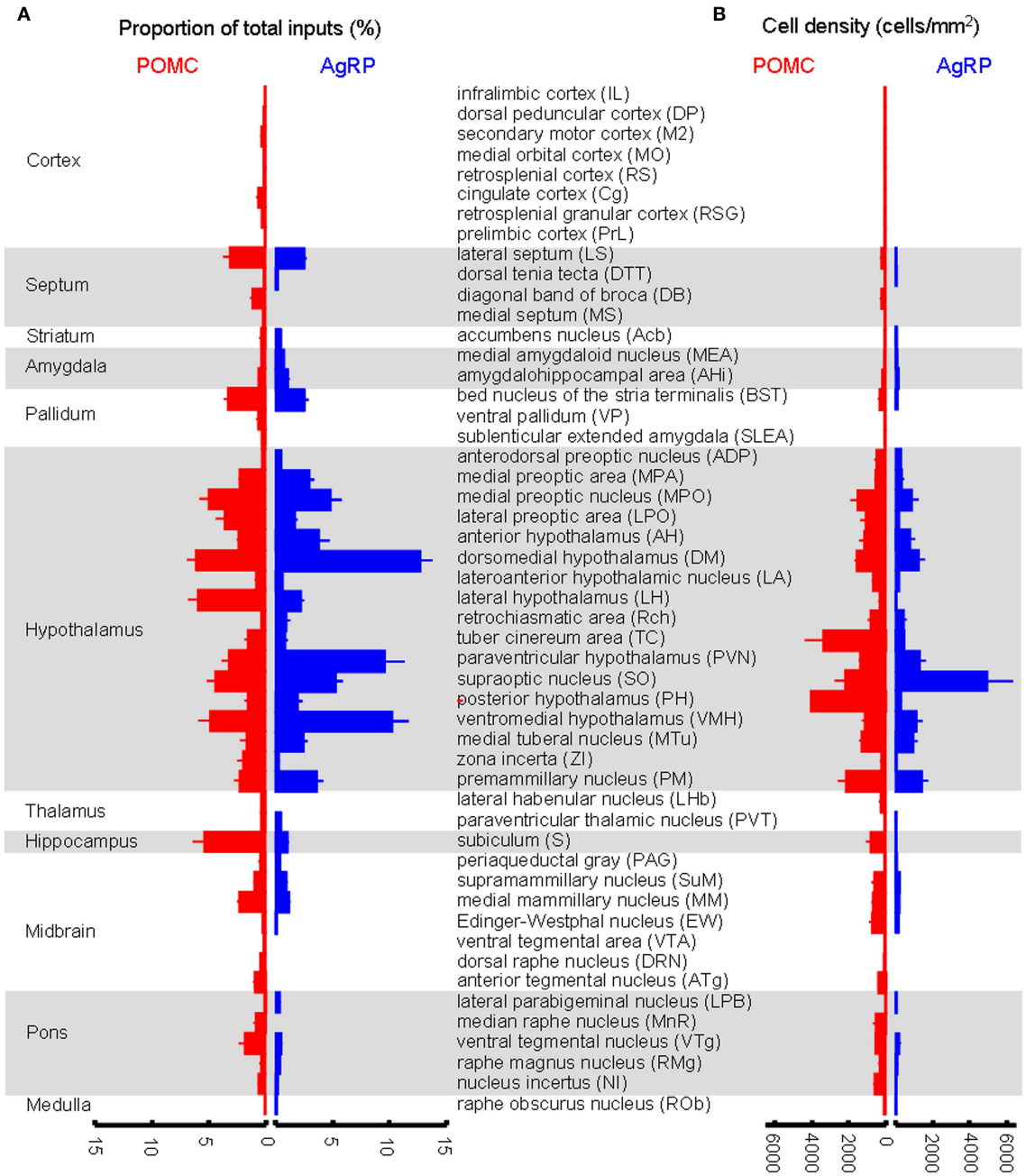

FIGURE 3 | Comparison of brain areas between POMC and AgRP neurons in the ARC. (A) Proportion of input neurons for ARC POMC neurons (red) and AgRP neurons (blue). The values are the normalized ratio of the cell number in each area against the total number of input neurons. Error bars represent the SEM in this and the following figures. $n = 4$ POMC-Cre mice and 5 AgRP-Cre mice. **(B)** Cell density of input neurons in each brain area.

convergence ratio for NTS POMC neurons is much higher than that for ARC POMC neurons (~74 vs. ~49).

Unlike POMC neurons in the ARC, POMC neurons in the NTS predominantly received their inputs from the pons and medulla (~80%) (**Figures 6E**, **7A**). There were also a substantial number of retrogradely labeled neurons in the cerebellum. Those hindbrain inputs were clustered in 29 nuclei, among which the supratrigeminal nucleus (Su5) and IRt were the two most densely labeled areas (**Figures 6D**, **7A**). In the forebrain, ~10% of the total inputs arose from the CeM, PVN, and PSTh (**Figures 6C,D, 7A**). Some labeling was also sparsely distributed in the ARC, suggesting a rather weak input from the ARC to NTS POMC neurons (**Figures 6C**, **7A**). In the cortex, we found some scattered labeling in the primary motor cortex and somatosensory cortex.

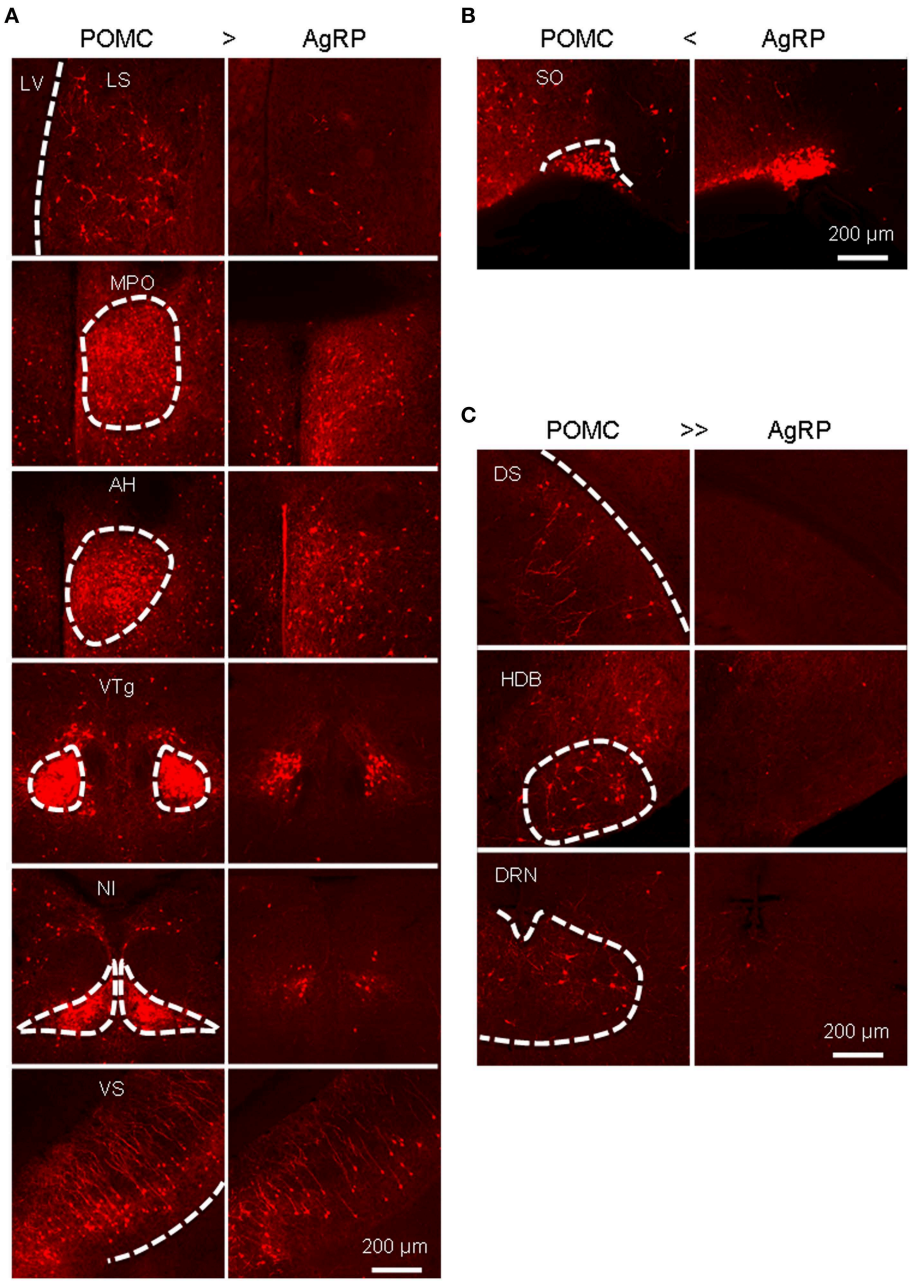

FIGURE 4 | Areas that provide different inputs to POMC and AgRP neurons in the ARC. (A) Representative brain areas that provide stronger inputs to POMC neurons than to AgRP neurons. **(B)** The supraoptic nucleus (SO) sends more inputs to AgRP neurons than to POMC neurons. **(C)** Representative brain areas that solely target POMC neurons but not AgRP neurons.

No labeling was detected in the vast majority of other cortical areas, hippocampus, striatum, or thalamus. The schematics in **Figure 7B** illustrate the major brain areas that target NTS POMC neurons.

Although the input patterns for POMC neurons in the ARC and NTS are very different, we did observe several brain areas that served as the common input sources for both groups of POMC neurons. With the exception of the PSTh, the hypothalamic areas that projected to POMC neurons in the NTS also provided direct inputs to POMC neurons in the ARC. Other overlapping areas included the secondary motor cortex (M2), BST, periaqueductal gray (PAG), Edinger-Westphal nucleus (EW), DRN, lateral parabrachial nucleus (LPB), RMg, and raphe obscurus nucleus (ROb). Among the presynaptic partners common to the two POMC neuron populations, BST, DM, LH, retrochiasmatic area (Rch), tuber cinereum area (TC), PVN, ARC, PAG, EW, LPB,

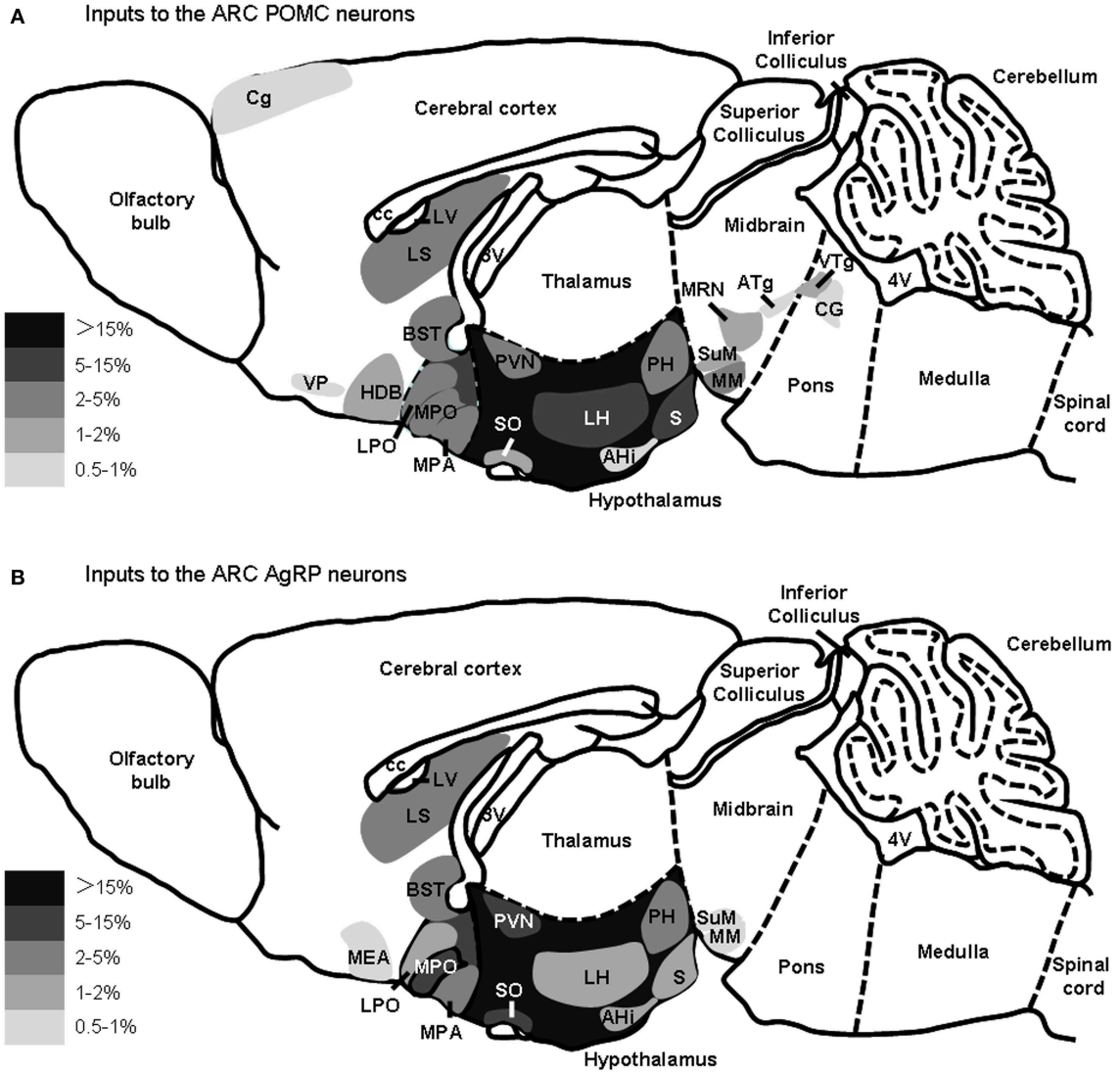

FIGURE 5 | Summary of the major presynaptic inputs to POMC neurons and AgRP neurons in the ARC. Brain areas that make up greater than 0.5% of total inputs to POMC neurons **(A)** or AgRP **(B)** neurons in the ARC are shown on a schematic sagittal section, respectively. Gray scale represents the percentage of total inputs. LV, lateral ventricle; 3V, third ventricle; 4V, fourth ventricle.

RMg, and ROb also provided direct inputs to the AgRP neurons in the ARC (**Figures 3**, **7**). These results suggested that the three groups of projection neurons in the central melanocortin system might be controlled or regulated by some common upstream nuclei.

Axonal Projection Patterns of POMC Neurons and AgRP Neurons

Previous anterograde tracing and immunocytochemistry labeling have revealed that POMC neurons project to the paraventricular thalamic nucleus (PVT) and several hypothalamic nuclei (Fodor et al., 1998; Bagnol et al., 1999; Cowley et al., 2001). In light of the transsynaptic retrograde tracing results that show projections from these areas to POMC neurons, we mapped the axonal projection patterns of the two populations of POMC neurons to test whether these neurons form reciprocal connections with their input nuclei.

We generated two Cre-dependent AAV reporter constructs, AAV-DIO-mtdTomato and AAV-DIO-EmGFP (**Figure 8A**). These two viral vectors were stereotaxically infused into the ARC and NTS of POMC-Cre mice, respectively (**Figure 8B**). Following the expression of the two membrane-tagged proteins of mtdTomato or EmGFP, ARC POMC neurons and their axonal fibers exhibited red fluorescence, whereas NTS POMC neurons were green. The green fluorescence of EmGFP was further enhanced using fluorescent immunohistochemistry.

Figure 8C shows a series of sagittal brain sections to illustrate the overall axon projections patterns of POMC neurons in the ARC and NTS. The heaviest projection of ARC POMC neurons was found in the hypothalamus, especially in the AH,

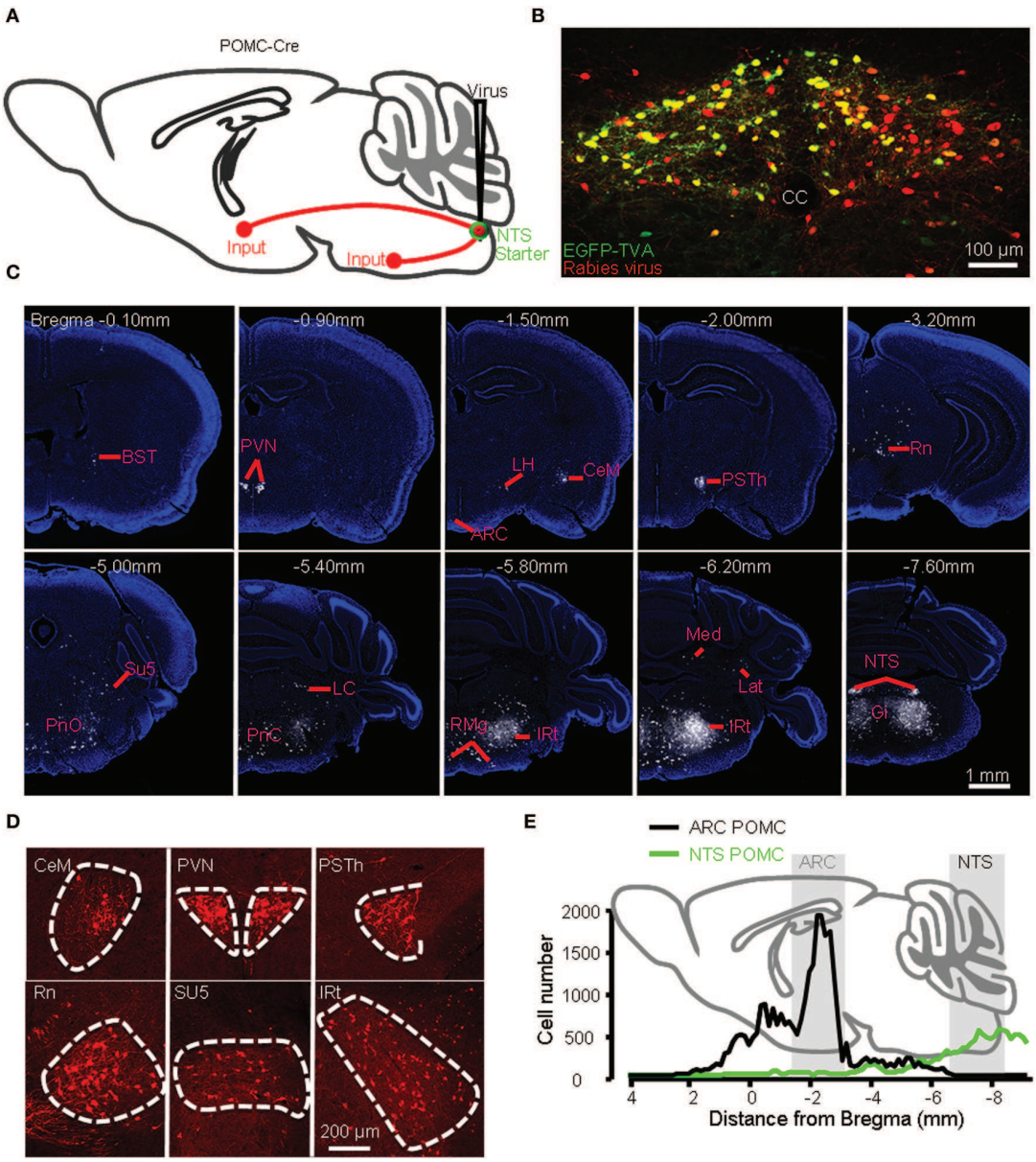

FIGURE 6 | Identification of presynaptic inputs to POMC neurons in the NTS. (A) Modified rabies virus was injected into the NTS of POMC-Cre mice. **(B)** Starter neurons (yellow) were restricted within the NTS. cc, central canal. Representative coronal sections **(C)** and several densely labeled nuclei **(D)**. **(E)** Numbers of input neurons to POMC neurons in the ARC (black line) vs. NTS (green line) from anterior to posterior.

MPA/MPO, LH, DM, VMH, PVN, PSTh, and PH (**Figure 8C** and **Table 1**). These axons form numerous branches and varicosities, suggesting that they are true axonal terminals rather than fibers-of-passage (**Figure 9A**). Elsewhere in the forebrain, dense axonal terminals were observed in the BST, LS, diagonal band of Broca (DB), and accumbens nucleus (Acb). In the midbrain, the PAG, deep gray layer of the superior colliculus (DpG), and deep mesencephalic nucleus (DpMe) received clear innervations from ARC POMC neurons.

NTS POMC neurons sent their axonal terminals rostrally to as far as the Acb (**Figure 8C** and **Table 1**). In the hypothalamus, moderate levels of axonal terminals were found in the PVN and PSTh. Most abundant fibers were found in discrete brainstem areas, including the parvicellular reticular nucleus (PCRt), dorsal and ventral parts of medullary reticular nucleus (MdD and MdV), subcoeruleus nucleus (SubC), Gi, PnO, IRT, Su5, and LPB (**Figures 8C**, **9A** and **Table 1**).

Reciprocal Projections between POMC/AgRP neurons and their Input Sources

To systemically analyze the mutual connections between POMC neurons and their presynaptic partners, we examined the axonal

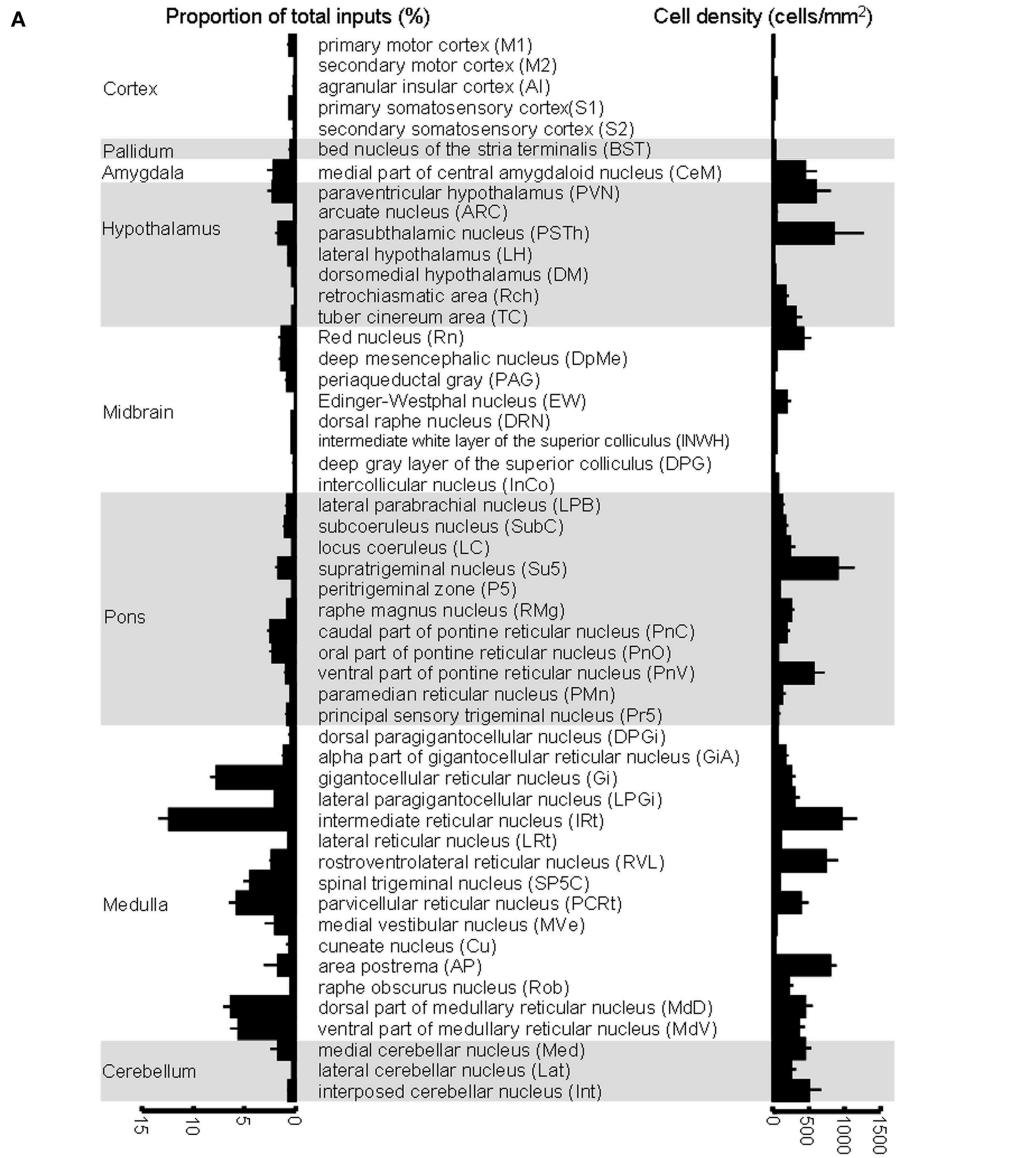

FIGURE 7 | Brain areas providing inputs to NTS POMC neurons. (A) Percentage of total input neurons (left) and the density of retrogradely labeled neurons (right) in different brain areas. **(B)** Schematic of major inputs to NTS POMC neurons. DCN, deep nuclei of cerebellum.

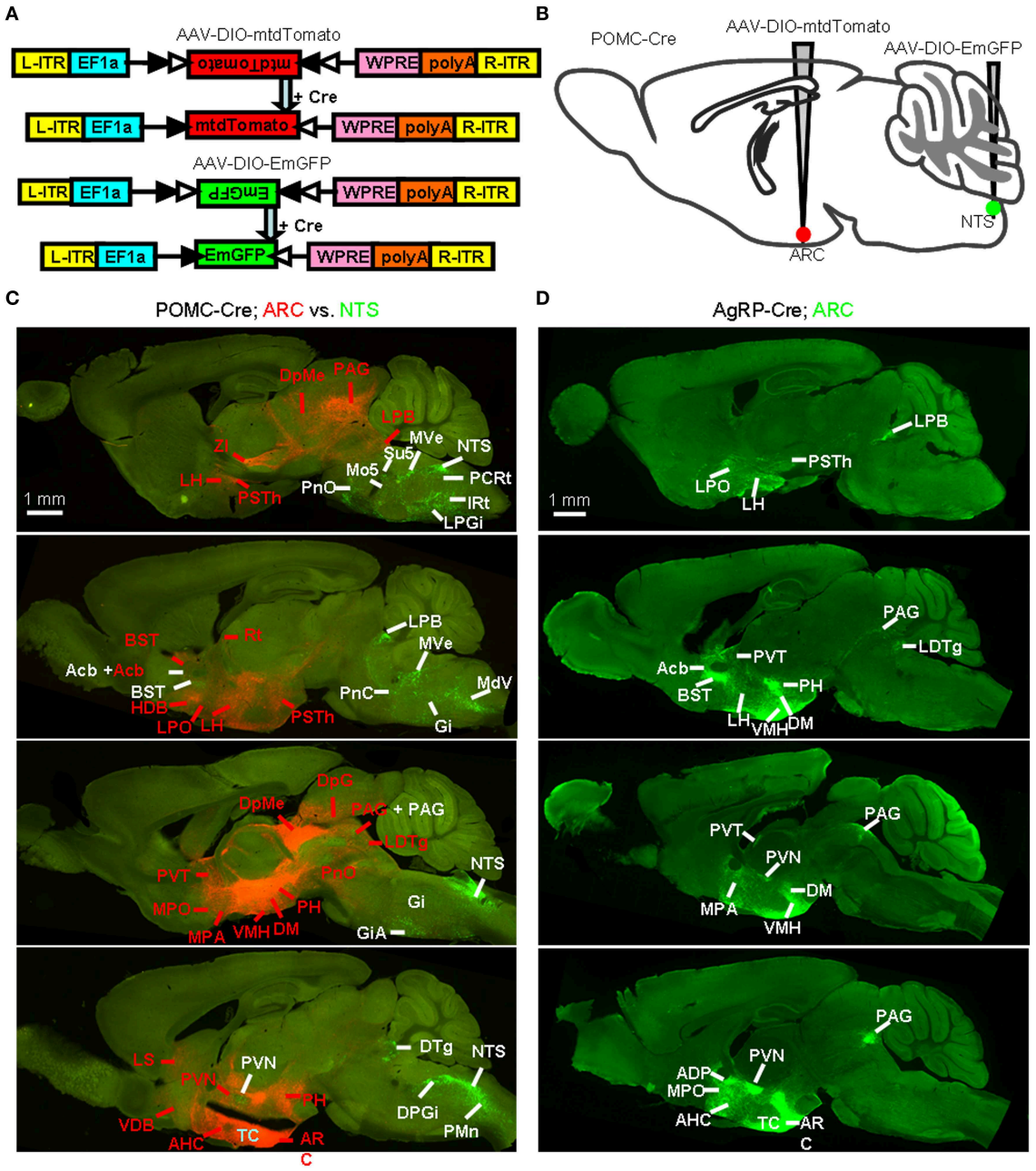

FIGURE 8 | Identification of whole-brain efferents of POMC neurons. **(A)** Design of recombinant AAV strains for Cre-dependent cell labeling. **(B)** AAV-DIO-mtdTomato and AAV-DIO-EmGFP were injected into the ARC and NTS of POMC-Cre mice respectively. **(C)** Direct comparison of the axon projections of the ARC and NTS POMC neurons. The dominant projections of the ARC (red, indicated with red words) and NTS (green, indicated with white words) were represented in a series of sagittal sections. DTg, dorsal tegmental nucleus; Rt, reticular thalamic nucleus. **(D)** Representative sagittal sections show the axon projections of AgRP neurons. LDTg, laterodorsal tegmental nucleus.

density in the brain areas that make up >1% of total inputs to POMC neurons. All presynaptic partners of POMC neurons received reciprocal projections from the POMC neurons (**Table 1**). For example, ARC POMC neurons projected heavily to all of their major input sources, including the LS, PVT, and MPO (**Figure 9A**). Similarly, NTS POMC neurons sent reciprocal projections axons to the IRT, LPB, and PVN (**Figure 9A**). We noted that ARC POMC neurons projected to the NTS, and NTS POMC neurons projected to the ARC (**Figure 9B**).

As a comparison, the axon projections of AgRP neurons were examined by injecting AAV-DIO-EmGFP into the ARC of AgRP-Cre mice. We observed rather similar projection patterns

TABLE 1 | Brain areas innervated by reciprocal projections from POMC and AgRP neurons.

Brain areas	ARC^{POMC}	ARC^{AgRP}	NTS^{POMC}
LS	****	*	–
BST	***	****	–
HDB	***	–	–
VDB	**	–	–
CeM	–	–	*
MPA	****	*	–
MPO	****	***	–
LPO	***	***	–
AH	***	**	–
PSTh	–	–	**
PVN	***	*****	**
LH	****	***	–
TC	***	–	–
SO	**	***	–
PH	****	***	–
VMH	***	***	–
MTu	***	***	–
ZI	****	–	–
PM	****	***	–
S	*	*	–
AHi	–	**	–
Rn	–	–	*
DPMe	–	–	**
SuM	**	–	–
MM	***	–	–
MnR	***	–	–
VTg	****	–	–
SubC	–	–	***
LPB	–	–	*****
Su5	–	–	****
PnO	–	–	***
PnV	–	–	**
GiA	–	–	**
Gi	–	–	**
LPGi	–	–	*
RVL	–	–	*
SP5C	–	–	*
PCRt	–	–	***
MdD	–	–	***
MdV	–	–	****
IRt	–	–	****
Med	–	–	*

*Only those make up greater than 1% of total inputs are listed. Mean fiber intensity (0 ~ 255): *1–30; **30–60; ***60–90; ****90–120; *****>120; –, null.*

between POMC and AgRP neurons in the ARC, although the axon projections from POMC neurons were distributed in broader brain areas (**Figures 8C,D**). In addition, ARC AgRP neurons projected their axonal terminals to all of their dominant input sources, including the LS, PVT, and MPO (**Figure 9A** and **Table 1**). Therefore, like ARC POMC neurons, ARC AgRP neurons form reciprocal connections with most of their upstream brain areas.

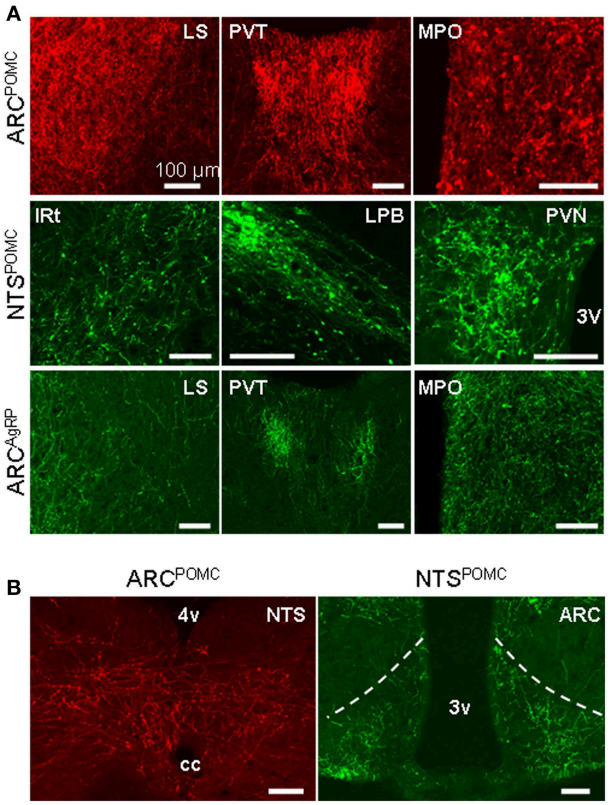

FIGURE 9 | Brain areas that form reciprocal neurons with POMC and AgRP neurons. (A) Axon projections from the ARC POMC (upper), NTS POMC (middle) and ARC AgRP (bottom) neurons to their respective input areas. **(B)** ARC POMC neurons project to the NTS (left), and NTS POMC neurons project to the ARC (right). Scale bar: 100 μm.

Discussion

In this study, we mapped the whole-brain direct inputs to POMC neurons in the ARC and NTS using cell-type specific infection and retrograde spread of modified rabies virus. We found that these two groups of POMC neurons have very different input patterns. POMC neurons in the ARC mainly receive inputs from the hypothalamus and other forebrain nuclei. POMC and AgRP neurons in the ARC share very similar inputs at the level of brain nuclei, although POMC neurons receive broader and denser inputs than AgRP neurons. Unlike ARC POMC neurons, NTS POMC neurons predominantly receive their inputs from the brainstem and cerebellum. Using cell-type specific expression of dual-color fluorescent proteins, we also characterized the axonal projection patterns of POMC neurons in the ARC and NTS. Similar to ARC AgRP neurons, ARC POMC neurons generally target forebrain centers. In contrast, NTS POMC neurons mainly send their axons in the brainstem. Moreover, POMC neurons in the ARC and NTS, as well as AgRP neurons in the ARC, often form

reciprocal connections with their respective input centers. These experiments reveal the structural basis underlying the brain regulation of the central melanocortin system and help outline further experiments to dissect the roles of various anatomical pathways in regulating energy homeostasis.

Comparison between Transsynaptic Tracing and Traditional Tracing

Hypothalamic POMC and AgRP neurons have been extensively investigated due to their important roles in feeding behavior and energy homeostasis. However, it had remained unclear whether POMC and AgRP neurons in the ARC are targeted by different brain areas. Previous tract tracing studies have consistently revealed a set of ARC-projecting brain centers, including the PVN, AH, PM, BST, LS, and PAG (Chronwall, 1985; Gruber et al., 1987; Magoul et al., 1993). Using the rabies virus-based approach of transsynaptic retrograde tracing, we found that many of these brain areas provide direct input to both types of ARC neurons. In addition, we detected retrograde labeling in several brain areas, such as the subiculum and zona incerta, that have not been previously identified. This likely reflected the higher sensitivity of the method of transsynaptic tracing using modified rabies virus. Traditional tract tracing studies tended to inject small amount of tracers into part of the ARC to avoid the potential confounding factors of tracer spill-over and tracer pickup by fibers-of-passage. Different research groups often reported variable labeling patterns, particularly for brain areas that provided moderate inputs to the ARC. Thus, both POMC and AgRP neurons in the ARC may integrate inputs from broader brain centers than those revealed using conventional tract tracing methods.

On the other hand, in spite of the increase in the labeling sensitivity, we did not observe any clear transsynaptic labeling in several structures that were identified in traditional tract tracing studies. For example, previous tracing studies reported that there is a projection from the suprachiasmatic nucleus to the ARC (Swanson and Cowan, 1975; Watts et al., 1987), but we did not observe any labeling in this nucleus following rabies virus infection of POMC neurons or AgRP neurons in the ARC. The NTS was reported to project to the ARC in a previous study using horseradish peroxidase (HRP) tracer (Ricardo and Koh, 1978). Consistent with this early finding, we observed the presence of axonal fibers projecting from the POMC neurons in the NTS to the ARC. However, the infection of POMC neurons or AgRP neurons in the ARC did not produce any transsynaptic labeling in the NTS. This difference could be explained by the possibility that neurons in the SCN or NTS target non-AgRP or non-POMC neurons in the ARC. Because of the close proximity between the ARC and SCN, it is also possible that the SCN was non-selectively labeled by the axonal fibers passing through the tracer injection sites in the traditional tracer studies.

Comparison between POMC Neurons and AgRP Neurons in the ARC

The overall similarity between the input patterns for POMC neurons and AgRP neurons in the ARC suggests that these two types of neurons integrate and compute signals from largely overlapping brain areas. It is interesting to note that recent transsynaptic tracing studies often have similar input patterns for non-overlapping cell types within the same brain structures, such as the D1- and D2- cells in the striatum (Wall et al., 2013) and serotonergic and GABAergic neurons in the dorsal raphe (Weissbourd et al., 2014). It remains to be tested whether POMC and AgRP neurons in the ARC receive inputs from separate or overlapping populations of input neurons within a given brain structure. Addressing this question requires the development of technique to transsynaptically label neurons with different colors for distinct starter cell populations within the same animal.

In spite of the overall similarity in input patterns, we found that the ARC POMC neurons receive more and broader afferents than AgRP neurons. Moreover, anterograde tracing revealed that ARC POMC neurons send denser and broader outputs than ARC AgRP neurons. In addition to releasing a fast neurotransmitter, such as GABA, POMC neurons may co-release over 10 different hormone products, including ACTH, beta-endorphin, and melanocyte-stimulating peptides (Millington, 2007). Therefore, POMC neurons integrate a wide array of brain inputs and modulate a broad set of downstream neurons using various signaling molecules.

Comparison between POMC Neurons in the ARC and the NTS

POMC neurons in the ARC and NTS respond to different signals from the brain and periphery and suppress feeding behaviors at different time scales (Cowley et al., 2001; Fan et al., 2004; Appleyard et al., 2005; Vong et al., 2011; Berglund et al., 2012; Zhan et al., 2013). Unlike their counterparts in the ARC, POMC neurons in the NTS mainly integrate inputs from the brainstem and provide outputs to brainstem structures. Many of these structures play essential roles in controlling and regulating consummatory ingestive behaviors. For example, IRt, PCRt, and Rn are implicated in chewing and swallowing (Chen et al., 2001; Satoh et al., 2008; Travers et al., 2010; Stanek et al., 2014). The difference in anatomical connections likely underlies the functional specialization for POMC neurons in the hypothalamus and brainstem. On the other hand, our tracings have identified 12 nuclei that provide direct inputs to the NTS POMC neurons, ARC POMC neurons, and ARC AgRP neurons. These structures include the PVN, the major center for regulating energy homeostasis (Leibowitz et al., 1981; Stanley and Leibowitz, 1985), and the RMg and Rob, two brainstem centers of serotonergic neurons (Bowker et al., 1981, 1983; Azmitia and Gannon, 1986). These common inputs may provide anatomical substrates for the concerted regulation of feeding behavior by targeting all three types of projection neurons in the melanocortin system.

Functional Implications

Our detailed mapping of the connectivity points to functional studies on the roles and circuit mechanisms of POMC neurons. Recent studies have deciphered the functions of several neural pathways to AgRP neurons (Krashes et al., 2014). Although numerous studies suggest the connections from the PVN to ARC POMC neurons and the importance of the PVN in the feeding behavior (Leibowitz et al., 1981; Stanley and Leibowitz, 1985;

Cowley et al., 1999; Balthasar et al., 2005; Atasoy et al., 2012), relatively little is known about the electrophysiological effects and functions of the projections from the PVN to POMC neurons in the ARC and NTS.

The lateral septum is another subcortical area that provides inputs to both POMC neurons and AgRP neurons in the ARC. Neuronal activity in the lateral septum is affected by gastric distension and ghrelin administration (Gong et al., 2013). Moreover, administering either opioid or noradrenaline into the septal nuclei increases food intake in rats (Majeed et al., 1986; Scopinho et al., 2008). It remains to be tested how the inputs from lateral septal neurons affect the physiology of ARC POMC and AgRP neurons as well as regulate feeding behavior.

In addition to the inputs from upstream stations to POMC and AgRP neurons, our anterograde tracing also reveals extensive projections from these neurons back to a majority of their input sources. The PVN, in particular, forms reciprocal connections with all three populations of melanocortin projection neurons. Optogenetic studies have demonstrated that the reciprocal projections between ARC AgRP neurons and PVN neurons promote feeding (Betley et al., 2013; Krashes et al., 2014). However, the functions of the vast majority of reciprocal projections have not yet been explored. Such functional studies will help elucidate the computational mechanisms underlying the regulation of energy homoeostasis.

ARC POMC neurons consist of a heterogeneous subpopulation of distinct neurotransmitter phenotypes (Hentges et al., 2004, 2009; Meister et al., 2006). Given this heterogeneity and the functional diversity of POMC neurons (Sohn and Williams, 2012), it is possible that different subsets of POMC neurons may be linked to specific subcircuits and mediate distinct physiological and behavioral functions. A recent study shows that distinct subpopulations of ARC AgRP neurons target different brain regions and not all of these neuronal subpopulations are sufficient to evoke feeding (Betley et al., 2013). It will be valuable to more precisely dissect neural circuits at the level of subpopulations of POMC and AgRP neurons.

Author Contributions

ML, FX and CZ designed the research; XH prepared the rabies virus; QF prepared the AAV; DW and ZZ performed the tracing experiments and analyzed data; YS performed the 3D reconstructions; ML and CZ wrote the paper.

Acknowledgments

We thank E. Callaway (Salk Institute) for providing us rabies virus and reagents for virus production, K. Deisseroth (Stanford University), D. Anderson (Caltech), and C. Cepko (Harvard University) for AAV vectors, Y. Wen and D. Qi (Olympus Corp.) for assistance with imaging, X. Nan and J. Wang (Bitplane Corp.) for assistance with imaging analysis. This work is supported by China MOST grants (2012CB837703, 2012CB837701, and 2012YQ03026005), NNSFC (91432114), and Beijing Municipal Government.

Supplementary Material

The Supplementary Material for this article can be found online at: http://www.frontiersin.org/journal/10.3389/fnana.2015.00040/abstract

Supplementary Image 1 | 3D visualization of whole-brain direct inputs to the ARC POMC neurons.

Supplementary Image 2 | 3D visualization of whole-brain direct inputs to the ARC AgRP neurons.

Supplementary Image 3 | 3D visualization of whole-brain direct inputs to the NTS POMC neurons.

References

Aponte, Y., Atasoy, D., and Sternson, S. M. (2011). AGRP neurons are sufficient to orchestrate feeding behavior rapidly and without training. *Nat. Neurosci.* 14, 351–355. doi: 10.1038/nn.2739

Appleyard, S. M., Bailey, T. W., Doyle, M. W., Jin, Y. H., Smart, J. L., Low, M. J., et al. (2005). Proopiomelanocortin neurons in nucleus tractus solitarius are activated by visceral afferents: regulation by cholecystokinin and opioids. *J. Neurosci.* 25, 3578–3585. doi: 10.1523/JNEUROSCI.4177-04.2005

Arenkiel, B. R., Hasegawa, H., Yi, J. J., Larsen, R. S., Wallace, M. L., Philpot, B. D., et al. (2012). Activity-induced remodeling of olfactory bulb microcircuits revealed by monosynaptic tracing. *PLoS ONE* 6:e29423. doi: 10.1371/journal.pone.0029423

Atasoy, D., Aponte, Y., Su, H. H., and Sternson, S. M. (2008). A FLEX switch targets Channelrhodopsin-2 to multiple cell types for imaging and long-range circuit mapping. *J. Neurosci.* 28, 7025–7030. doi: 10.1523/JNEUROSCI.1954-08.2008

Atasoy, D., Betley, J. N., Su, H. H., and Sternson, S. M. (2012). Deconstruction of a neural circuit for hunger. *Nature* 488, 172–177. doi: 10.1038/nature11270

Azmitia, E. C., and Gannon, P. J. (1986). The primate serotonergic system: a review of human and animal studies and a report on Macaca fascicularis. *Adv. Neurol.* 43, 407–468.

Bagnol, D., Lu, X. Y., Kaelin, C. B., Day, H. E., Ollmann, M., Gantz, I., et al. (1999). Anatomy of an endogenous antagonist: relationship between Agouti-related protein and proopiomelanocortin in brain. *J. Neurosci.* 19, RC26.

Balthasar, N., Coppari, R., McMinn, J., Liu, S. M., Lee, C. E., Tang, V., et al. (2004). Leptin receptor signaling in POMC neurons is required for normal body weight homeostasis. *Neuron* 42, 983–991. doi: 10.1016/j.neuron.2004.06.004

Balthasar, N., Dalgaard, L. T., Lee, C. E., Yu, J., Funahashi, H., Williams, T., et al. (2005). Divergence of melanocortin pathways in the control of food intake and energy expenditure. *Cell* 123, 493–505. doi: 10.1016/j.cell.2005.08.035

Berglund, E. D., Vianna, C. R., Donato, J. Jr., Kim, M. H., Chuang, J. C., Lee, C. E., et al. (2012). Direct leptin action on POMC neurons regulates glucose homeostasis and hepatic insulin sensitivity in mice. *J. Clin. Invest.* 122, 1000–1009. doi: 10.1172/JCI59816

Betley, J. N., Cao, Z. F., Ritola, K. D., and Sternson, S. M. (2013). Parallel, redundant circuit organization for homeostatic control of feeding behavior. *Cell* 155, 1337–1350. doi: 10.1016/j.cell.2013.11.002

Bowker, R. M., Westlund, K. N., and Coulter, J. D. (1981). Origins of serotonergic projections to the spinal cord in rat: an immunocytochemical-retrograde transport study. *Brain Res.* 226, 187–199. doi: 10.1016/0006-8993(81)91092-1

Bowker, R. M., Westlund, K. N., Sullivan, M. C., Wilber, J. F., and Coulter, J. D. (1983). Descending serotonergic, peptidergic and cholinergic pathways from the raphe nuclei: a multiple transmitter complex. *Brain Res.* 288, 33–48. doi: 10.1016/0006-8993(83)90079-3

Bronstein, D. M., Schafer, M. K., Watson, S. J., and Akil, H. (1992). Evidence that beta-endorphin is synthesized in cells in the nucleus tractus solitarius: detection of POMC mRNA. *Brain Res.* 587, 269–275. doi: 10.1016/0006-8993(92)91007-2

Chen, Z., Travers, S. P., and Travers, J. B. (2001). Muscimol infusions in the brain stem reticular formation reversibly block ingestion in the awake rat. *Am. J. Physiol. Regul. Integr. Comp. Physiol.* 280, R1085–R1094.

Chronwall, B. M. (1985). Anatomy and physiology of the neuroendocrine arcuate nucleus. *Peptides* 6(Suppl. 2), 1–11. doi: 10.1016/0196-9781(85)90128-7

Coll, A. P., Farooqi, I. S., Challis, B. G., Yeo, G. S., and O'rahilly, S. (2004). Proopiomelanocortin and energy balance: insights from human and murine genetics. *J. Clin. Endocrinol. Metab.* 89, 2557–2562. doi: 10.1210/jc.2004-0428

Cone, R. D. (2005). Anatomy and regulation of the central melanocortin system. *Nat. Neurosci.* 8, 571–578. doi: 10.1038/nn1455

Cowley, M. A., Pronchuk, N., Fan, W., Dinulescu, D. M., Colmers, W. F., and Cone, R. D. (1999). Integration of NPY, AGRP, and melanocortin signals in the hypothalamic paraventricular nucleus: evidence of a cellular basis for the adipostat. *Neuron* 24, 155–163. doi: 10.1016/S0896-6273(00)80829-6

Cowley, M. A., Smart, J. L., Rubinstein, M., Cerdan, M. G., Diano, S., Horvath, T. L., et al. (2001). Leptin activates anorexigenic POMC neurons through a neural network in the arcuate nucleus. *Nature* 411, 480–484. doi: 10.1038/35078085

Fan, W., Ellacott, K. L., Halatchev, I. G., Takahashi, K., Yu, P., and Cone, R. D. (2004). Cholecystokinin-mediated suppression of feeding involves the brainstem melanocortin system. *Nat. Neurosci.* 7, 335–336. doi: 10.1038/nn1214

Fodor, M., Csaba, Z., Epelbaum, J., Vaudry, H., and Jegou, S. (1998). Interrelations between hypothalamic somatostatin and proopiomelanocortin neurons. *J. Neuroendocrinol.* 10, 75–78. doi: 10.1046/j.1365-2826.1998.00629.x

Garcia, I., Huang, L., Ung, K., and Arenkiel, B. R. (2012). Tracing synaptic connectivity onto embryonic stem cell-derived neurons. *Stem Cells* 30, 2140–2151. doi: 10.1002/stem.1185

Gautron, L., Lazarus, M., Scott, M. M., Saper, C. B., and Elmquist, J. K. (2010). Identifying the efferent projections of leptin-responsive neurons in the dorsomedial hypothalamus using a novel conditional tracing approach. *J. Comp. Neurol.* 518, 2090–2108. doi: 10.1002/cne.22323

Gong, Y., Xu, L., Guo, F., Pang, M., Shi, Z., Gao, S., et al. (2013). Effects of ghrelin on gastric distension sensitive neurons and gastric motility in the lateral septum and arcuate nucleus regulation. *J. Gastroenterol.* 49, 219–230. doi: 10.1007/s00535-013-0789-y

Gropp, E., Shanabrough, M., Borok, E., Xu, A. W., Janoschek, R., Buch, T., et al. (2005). Agouti-related peptide-expressing neurons are mandatory for feeding. *Nat. Neurosci.* 8, 1289–1291. doi: 10.1038/nn1548

Gruber, K., McRae-Degueurce, A., Wilkin, L. D., Mitchell, L. D., and Johnson, A. K. (1987). Forebrain and brainstem afferents to the arcuate nucleus in the rat: potential pathways for the modulation of hypophyseal secretions. *Neurosci. Lett.* 75, 1–5. doi: 10.1016/0304-3940(87)90065-6

Haubensak, W., Kunwar, P. S., Cai, H., Ciocchi, S., Wall, N. R., Ponnusamy, R., et al. (2010). Genetic dissection of an amygdala microcircuit that gates conditioned fear. *Nature* 468, 270–276. doi: 10.1038/nature09553

Hentges, S. T., Nishiyama, M., Overstreet, L. S., Stenzel-Poore, M., Williams, J. T., and Low, M. J. (2004). GABA release from proopiomelanocortin neurons. *J. Neurosci.* 24, 1578–1583. doi: 10.1523/JNEUROSCI.3952-03.2004

Hentges, S. T., Otero-Corchon, V., Pennock, R. L., King, C. M., and Low, M. J. (2009). Proopiomelanocortin expression in both GABA and glutamate neurons. *J. Neurosci.* 29, 13684–13690. doi: 10.1523/JNEUROSCI.3770-09.2009

Huo, L., Grill, H. J., and Bjorbaek, C. (2006). Divergent regulation of proopiomelanocortin neurons by leptin in the nucleus of the solitary tract and in the arcuate hypothalamic nucleus. *Diabetes* 55, 567–573. doi: 10.2337/diabetes.55.03.06.db05-1143

Krashes, M. J., Koda, S., Ye, C., Rogan, S. C., Adams, A. C., Cusher, D. S., et al. (2011). Rapid, reversible activation of AgRP neurons drives feeding behavior in mice. *J. Clin. Invest.* 121, 1424–1428. doi: 10.1172/JCI46229

Krashes, M. J., Shah, B. P., Madara, J. C., Olson, D. P., Strochlic, D. E., Garfield, A. S., et al. (2014). An excitatory paraventricular nucleus to AgRP neuron circuit that drives hunger. *Nature* 507, 238–242. doi: 10.1038/nature12956

Leibowitz, S. F., Hammer, N. J., and Chang, K. (1981). Hypothalamic paraventricular nucleus lesions produce overeating and obesity in the rat. *Physiol. Behav.* 27, 1031–1040. doi: 10.1016/0031-9384(81)90366-8

Luquet, S., Perez, F. A., Hnasko, T. S., and Palmiter, R. D. (2005). NPY/AgRP neurons are essential for feeding in adult mice but can be ablated in neonates. *Science* 310, 683–685. doi: 10.1126/science.1115524

Magoul, R., Onteniente, B., Benjelloun, W., and Tramu, G. (1993). Tachykinergic afferents to the rat arcuate nucleus. A combined immunohistochemical and retrograde tracing study. *Peptides* 14, 275–286. doi: 10.1016/0196-9781(93)90042-F

Majeed, N. H., Przewlocka, B., Wedzony, K., and Przewlocki, R. (1986). Stimulation of food intake following opioid microinjection into the nucleus accumbens septi in rats. *Peptides* 7, 711–716. doi: 10.1016/0196-9781(86)90083-5

Makara, G. B., and Hodacs, L. (1975). Rostral projections from the hypothalamic arcuate nucleus. *Brain Res.* 84, 23–29. doi: 10.1016/0006-8993(75)90797-0

Matsuda, T., and Cepko, C. L. (2007). Controlled expression of transgenes introduced by *in vivo* electroporation. *Proc. Natl. Acad. Sci. U.S.A.* 104, 1027–1032. doi: 10.1073/pnas.0610155104

Meister, B., Gomuc, B., Suarez, E., Ishii, Y., Durr, K., and Gillberg, L. (2006). Hypothalamic proopiomelanocortin (POMC) neurons have a cholinergic phenotype. *Eur. J. Neurosci.* 24, 2731–2740. doi: 10.1111/j.1460-9568.2006.05157.x

Millington, G. W. (2007). The role of proopiomelanocortin (POMC) neurones in feeding behaviour. *Nutr. Metab. (Lond.)* 4:18. doi: 10.1186/1743-7075-4-18

Morton, G. J., Cummings, D. E., Baskin, D. G., Barsh, G. S., and Schwartz, M. W. (2006). Central nervous system control of food intake and body weight. *Nature* 443, 289–295. doi: 10.1038/nature05026

Ogawa, S. K., Cohen, J. Y., Hwang, D., Uchida, N., and Watabe-Uchida, M. (2014). Organization of monosynaptic inputs to the serotonin and dopamine neuromodulatory systems. *Cell Rep.* 8, 1105–1118. doi: 10.1016/j.celrep.2014.06.042

Osakada, F., Mori, T., Cetin, A. H., Marshel, J. H., Virgen, B., and Callaway, E. M. (2011). New rabies virus variants for monitoring and manipulating activity and gene expression in defined neural circuits. *Neuron* 71, 617–631. doi: 10.1016/j.neuron.2011.07.005

Padilla, S. L., Reef, D., and Zeltser, L. M. (2012). Defining POMC neurons using transgenic reagents: impact of transient Pomc expression in diverse immature neuronal populations. *Endocrinology* 153, 1219–1231. doi: 10.1210/en.2011-1665

Paxinos, G., and Franklin, K. B. (2001). *Mouse Brain in Stereotaxic Coordinates*. San Diego, CA: Academic Press.

Pollak Dorocic, I., Furth, D., Xuan, Y., Johansson, Y., Pozzi, L., Silberberg, G., et al. (2014). A whole-brain atlas of inputs to serotonergic neurons of the dorsal and median raphe nuclei. *Neuron* 83, 663–678. doi: 10.1016/j.neuron.2014.07.002

Ricardo, J. A., and Koh, E. T. (1978). Anatomical evidence of direct projections from the nucleus of the solitary tract to the hypothalamus, amygdala, and other forebrain structures in the rat. *Brain Res.* 153, 1–26. doi: 10.1016/0006-8993(78)91125-3

Rinaman, L. (2010). Ascending projections from the caudal visceral nucleus of the solitary tract to brain regions involved in food intake and energy expenditure. *Brain Res.* 1350, 18–34. doi: 10.1016/j.brainres.2010.03.059

Rinaman, L., Baker, E. A., Hoffman, G. E., Stricker, E. M., and Verbalis, J. G. (1998). Medullary c-Fos activation in rats after ingestion of a satiating meal. *Am. J. Physiol.* 275, R262–R268.

Satoh, Y., Ishizuka, K., and Murakami, T. (2008). Effects of lesions of the red nucleus on feeding and drinking in rats. *J. Oral Biosci.* 50, 200–206. doi: 10.1016/S1349-0079(08)80008-4

Schwaber, J. S., Kapp, B. S., Higgins, G. A., and Rapp, P. R. (1982). Amygdaloid and basal forebrain direct connections with the nucleus of the solitary tract and the dorsal motor nucleus. *J. Neurosci.* 2, 1424–1438.

Scopinho, A. A., Resstel, L. B., and Correa, F. M. (2008). alpha(1)-Adrenoceptors in the lateral septal area modulate food intake behaviour in rats. *Br. J. Pharmacol.* 155, 752–756. doi: 10.1038/bjp.2008.295

Sim, L. J., and Joseph, S. A. (1991). Arcuate nucleus projections to brainstem regions which modulate nociception. *J. Chem. Neuroanat.* 4, 97–109. doi: 10.1016/0891-0618(91)90034-A

Sohn, J. W., and Williams, K. W. (2012). Functional heterogeneity of arcuate nucleus pro-opiomelanocortin neurons: implications for diverging melanocortin pathways. *Mol. Neurobiol.* 45, 225–233. doi: 10.1007/s12035-012-8240-6

Stanek, E. T., Cheng, S., Takatoh, J., Han, B. X., and Wang, F. (2014). Monosynaptic premotor circuit tracing reveals neural substrates for oro-motor coordination. *Elife* 3:e02511. doi: 10.7554/eLife.02511

Stanley, B. G., and Leibowitz, S. F. (1985). Neuropeptide Y injected in the paraventricular hypothalamus: a powerful stimulant of feeding behavior. *Proc. Natl. Acad. Sci. U.S.A.* 82, 3940–3943. doi: 10.1073/pnas.82.11.3940

Swanson, L. W., and Cowan, W. M. (1975). The efferent connections of the suprachiasmatic nucleus of the hypothalamus. *J. Comp. Neurol.* 160, 1–12. doi: 10.1002/cne.901600102

Tong, Q., Ye, C. P., Jones, J. E., Elmquist, J. K., and Lowell, B. B. (2008). Synaptic release of GABA by AgRP neurons is required for normal regulation of energy balance. *Nat. Neurosci.* 11, 998–1000. doi: 10.1038/nn.2167

Travers, J. B., Herman, K., and Travers, S. P. (2010). Suppression of third ventricular NPY-elicited feeding following medullary reticular formation infusions of muscimol. *Behav. Neurosci.* 124, 225–233. doi: 10.1037/a0018928

Vong, L., Ye, C., Yang, Z., Choi, B., Chua, S. Jr., and Lowell, B. B. (2011). Leptin action on GABAergic neurons prevents obesity and reduces inhibitory tone to POMC neurons. *Neuron* 71, 142–154. doi: 10.1016/j.neuron.2011.05.028

Wall, N. R., De La Parra, M., Callaway, E. M., and Kreitzer, A. C. (2013). Differential innervation of direct- and indirect-pathway striatal projection neurons. *Neuron* 79, 347–360. doi: 10.1016/j.neuron.2013.05.014

Wall, N. R., Wickersham, I. R., Cetin, A., De La Parra, M., and Callaway, E. M. (2010). Monosynaptic circuit tracing *in vivo* through Cre-dependent targeting and complementation of modified rabies virus. *Proc. Natl. Acad. Sci. U.S.A.* 107, 21848–21853. doi: 10.1073/pnas.1011756107

Watabe-Uchida, M., Zhu, L., Ogawa, S. K., Vamanrao, A., and Uchida, N. (2012). Whole-brain mapping of direct inputs to midbrain dopamine neurons. *Neuron* 74, 858–873. doi: 10.1016/j.neuron.2012.03.017

Watts, A. G., Swanson, L. W., and Sanchez-Watts, G. (1987). Efferent projections of the suprachiasmatic nucleus: I. Studies using anterograde transport of *Phaseolus vulgaris* leucoagglutinin in the rat. *J. Comp. Neurol.* 258, 204–229. doi: 10.1002/cne.902580204

Weissbourd, B., Ren, J., Deloach, K. E., Guenthner, C. J., Miyamichi, K., and Luo, L. (2014). Presynaptic partners of dorsal raphe serotonergic and GABAergic neurons. *Neuron* 83, 645–662. doi: 10.1016/j.neuron.2014.06.024

Wickersham, I. R., Lyon, D. C., Barnard, R. J., Mori, T., Finke, S., Conzelmann, K. K., et al. (2007). Monosynaptic restriction of transsynaptic tracing from single, genetically targeted neurons. *Neuron* 53, 639–647. doi: 10.1016/j.neuron.2007.01.033

Wu, Q., Clark, M. S., and Palmiter, R. D. (2012). Deciphering a neuronal circuit that mediates appetite. *Nature* 483, 594–597. doi: 10.1038/nature10899

Xu, A. W., Kaelin, C. B., Morton, G. J., Ogimoto, K., Stanhope, K., Graham, J., et al. (2005). Effects of hypothalamic neurodegeneration on energy balance. *PLoS Biol.* 3:e415. doi: 10.1371/journal.pbio.0030415

Yaswen, L., Diehl, N., Brennan, M. B., and Hochgeschwender, U. (1999). Obesity in the mouse model of pro-opiomelanocortin deficiency responds to peripheral melanocortin. *Nat.Med.* 5, 1066–1070. doi: 10.1038/12506

Young, A. A. (2012). Brainstem sensing of meal-related signals in energy homeostasis. *Neuropharmacology* 63, 31–45. doi: 10.1016/j.neuropharm.2012.03.019

Zhan, C., Zhou, J., Feng, Q., Zhang, J. E., Lin, S., Bao, J., et al. (2013). Acute and long-term suppression of feeding behavior by POMC neurons in the brainstem and hypothalamus, respectively. *J. Neurosci.* 33, 3624–3632. doi: 10.1523/JNEUROSCI.2742-12.2013

Zhang, Y., Rodrigues, E., Gao, Y. X., King, M., Cheng, K. Y., Erdos, B., et al. (2010). Pro-opiomelanocortin gene transfer to the nucleus of the solitary track but not arcuate nucleus ameliorates chronic diet-induced obesity. *Neuroscience* 169, 1662–1671. doi: 10.1016/j.neuroscience.2010.06.001

Zheng, H., Patterson, L. M., Phifer, C. B., and Berthoud, H. R. (2005). Brain stem melanocortinergic modulation of meal size and identification of hypothalamic POMC projections. *Am. J. Physiol. Regul. Integr. Comp. Physiol.* 289, R247–R258. doi: 10.1152/ajpregu.00869.2004

Conflict of Interest Statement: The authors declare that the research was conducted in the absence of any commercial or financial relationships that could be construed as a potential conflict of interest.

frontiers in Neuroanatomy

REVIEW
published: 16 November 2015
doi: 10.3389/fnana.2015.00135

In Vivo Mapping of Cortical Columnar Networks in the Monkey with Focal Electrical and Optical Stimulation

Anna Wang Roe[1], Mykyta M. Chernov[2], Robert M. Friedman[2] and Gang Chen[1]*

[1] *Interdisciplinary Institute of Neuroscience and Technology, Zhejiang University, Hangzhou, China,* [2] *Department of Psychology, Vanderbilt University, Nashville, TN, USA*

There are currently largescale efforts to understand the brain as a connection machine. However, there has been little emphasis on understanding connection patterns between functionally specific cortical columns. Here, we review development and application of focal electrical and optical stimulation methods combined with optical imaging and fMRI mapping in the non-human primate. These new approaches, when applied systematically on a large scale, will elucidate functionally specific intra-areal and inter-areal network connection patterns. Such functionally specific network data can provide accurate views of brain network topology.

Keywords: cortical column, optogenetics, microstimulation, fMRI, monkey, optical imaging, optical stimulation, infrared neural stimulation

OPEN ACCESS

Edited by:
Kathleen S. Rockland, Boston University School of Medicine, USA

Reviewed by:
Zoltan F. Kisvarday, University of Debrecen, Hungary
Wim Vanduffel, Harvard Medical School, USA

****Correspondence:***
Anna Wang Roe
annawang@zju.edu.cn

Received: *19 June 2015*
Accepted: *12 October 2015*
Published: *16 November 2015*

Citation:
Roe AW, Chernov MM, Friedman RM and Chen G (2015) In Vivo Mapping of Cortical Columnar Networks in the Monkey with Focal Electrical and Optical Stimulation. Front. Neuroanat. 9:135. doi: 10.3389/fnana.2015.00135

A VIEW OF THE PRIMATE BRAIN

In primates (both human and non-human), much of brain volume (up to 80%) is occupied by connections between different parts of the cerebral cortex. Specificity of these connections forms information processing networks that are critical to normal sensory, motor, and cognitive function. Interruption of these connections (e.g., by trauma, stroke) leads to loss or alteration of function. In this sense, the brain can be viewed as a connection machine. There are now largescale projects (termed connectome projects) underway worldwide to study this connection machine (e.g., www.humanconnectomeproject.org, www.brainnetome.org, www.mouseconnectome.org). However, one aspect of these connectome studies that has largely been neglected is the fact that in humans and in primates, cerebral cortex is composed of basic functional columnar units. These units are on the order of a few hundred microns in size and have specific functions (e.g., in visual cortex: processing visual color, shape, depth, or motion information) and are connected in networks with other cortical columns of similar or related functionality (**Figure 1**). Such columnar networks form a basic feature of primate brain architecture. Thus, inherent in understanding the connection machine in primates is developing the ability to systematically map connection patterns between sets of cortical columns.

Current human connectomes (based on fMRI study) lack the spatial resolution for examining connection patterns at the columnar scale and therefore lack functional specificity inherent in columnar organization. Individual voxels in these studies represent averages of multiple functional columns (**Figure 2**, yellow box represents 3 mm voxel, white box represents 1 mm voxel); networks of voxels (**Figure 2**, yellow and white bidirectional arrows) therefore represent connections between averages of multiple functional networks. Due to the differential connectivity patterns of individual columns (e.g., color blobs to thin stripes vs. orientation columns to pale/thick

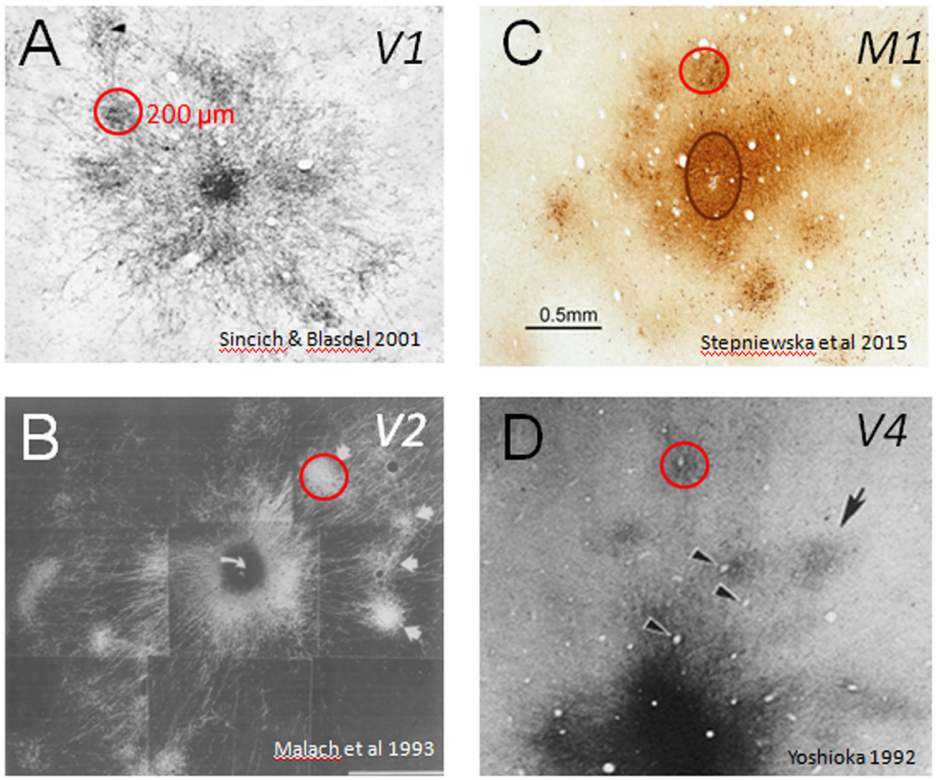

FIGURE 1 | Cortical modules are connected in specific networks. Examples of connected columns in **(A)** V1 (Sincich and Blasdel, 2001), **(B)** V2 (Malach et al., 1993), **(C)** M1 (Stepniewska et al., 2015), and **(D)** V4 (Yoshioka et al., 1992). Red circles indicate that column sizes, roughly 200 µm in size, are common to many cortical areas. Scale bar: 0.5 mm applies to all.

stripes, Livingstone and Hubel, 1984; Roe and Ts'o, 1999, 2015; Sincich et al., 2010; Federer et al., 2013), such averages can lead to inaccurate and misleading conclusions about cortical networks.

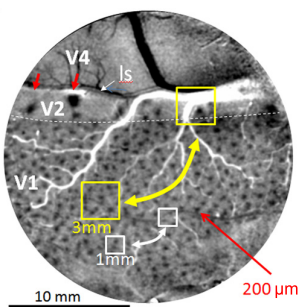

FIGURE 2 | Optical image of color response seen through an implanted cranial window over macaque monkey visual cortex (areas V1, V2, and V4). Image obtained by subtracting response to red-green isoluminant grating minus achromatic grating. Arrays of blobs in V1 and thin stripes in V2 (red arrows) reveal size of columnar networks (200 µm). Sizes of voxels used in human fMRI (yellow 3 mm and white 1 mm boxes) include many functional columns; functional resting state connections between these columns (bidirectional arrows) are therefore based on averaged signals and not functionally specific. Small red arrows: two visible thin (color) stripes in V2. ls: lunate sulcus. Dotted white line: V1/V2 border. Scale bar: 10 mm. (Image adapted from Lu and Roe, 2008).

Note on 'Column' Terminology

Cortical functional units have been described in many areas of visual cortex (V1, V2, V3, V4, MT, inferotemporal cortex) as well as other sensory, parietal, and prefrontal areas and have been termed columns, puffs, blobs, clusters, modules, and domains. Although each term is based on slightly different functional and/or anatomical criteria, they all capture the concept of modularity. For purposes of this review, we will use the term 'column,' as it is a generally familiar term and portrays the concepts of: 'small' (200–300 µm in size), 'repeated' (general architectural unit of the cortex), and 'functional' (composed of cluster of neurons which share similar function). This review proposes ways to examine the 'columnar connectome.'

Note that the concept of a column has of late been controversial, partly because there is not a single accepted definition and because by some criteria cortex is not clearly columnar (e.g., see Rockland, 2010). We use the term 'column' less as a physical construct (as its precise nature still needs further study) and more as a term to refer to a modular unit. Our concept of the 'column' is that it is a unique site of integration in cerebral cortex, one which is defined by a unique set of (often patchy) inputs and outputs. It is these inputs and outputs that result in a population response that is shared among a cluster of neurons. Although there is controversy regarding what exactly defines the column, the ability to visualize modules of

functionally distinct preference is a strong statement that there is modular organization.

A COLUMNAR MONKEY CONNECTOME: A PROPOSAL

We propose to pursue a *columnar connectome in the monkey*; such a connectome would provide a functionally specific understanding of brain networks. While attaining the spatial resolution needed to see columns in humans may be on the horizon (Cheng et al., 2001; Yacoub et al., 2008; Sun et al., 2013), the ability to do so in monkeys is already at hand. Functional imaging at high magnetic fields coupled with use of surface coils has enabled submillimeter resolution in anesthetized squirrel monkeys (Chen et al., 2007), and in awake macaque monkeys can sufficiently distinguish supra-, middle-, and infra-granular laminar specificity and fingerprint V1, V2, and V4 laminar profiles (Chen et al., 2012a,b, 2013; Goense et al., 2012; see also, Olman et al., 2012; Shih et al., 2013; Baek et al., 2015). Moreover, monkeys are excellent animal models for human behavior and disease. They share many commonalities with man including common behavioral repertoires and similar brain structures including the columnar nature of cortical organization (**Table 1**). Furthermore, monkeys can undergo experimental manipulations to answer questions in ways that are not possible in humans. Note that while mouse connectomes have decided advantages (e.g., genetic manipulability), mouse cerebral cortex (except for barrel cortex) is not columnar in the same way as primate cortex. For example, visual orientation selective neurons are not organized in columnar fashion (Metin et al., 1988; Schuett et al., 2002). These differences make certain comparisons less valid for understanding human brain structure, function, and behavior (**Table 1**). A columnar based understanding, we predict, would provide a fundamental component for developing a connectional theory of brain function, one that is not diluted by inaccurate averaged information.

NEED FOR LARGESCALE, FOCAL TRACING METHODS

Anatomical connections can be conducted at columnar scale and have provided some breathtaking views of cortical connection patterns. Perhaps some of the best examples come from monkey V1 where intra-areal patterns of connections have been well documented (e.g., Ts'o et al., 1986; Bosking et al., 1997). There are also a small number of studies on inter-areal columnar connectivity (Livingstone and Hubel, 1984; Roe and Ts'o, 1999; Shmuel et al., 2005; Federer et al., 2013). However, anatomical studies require sacrifice of the animal, and time consuming histological processing and tracer label reconstruction. Within a single animal, connection patterns from only a handful (about five, cf. Zingg et al., 2014) of distinct sites can be examined without compromising the certainty of label identification, placing a limit on the number of different networks one can study in a single brain.

Other methods for studying connections have yet to achieve columnar resolution. *In vivo* diffusion imaging is limited in spatial resolution and therefore accuracy. While it has been useful for some tracts (e.g., Jbabdi et al., 2013), a complete mapping of fiber connections at columnar resolution is unlikely (Thomas et al., 2014). Challenges such as identifying correct fiber courses at points of fiber intersection are still being addressed. Functional and anatomical tract tracing methods in humans using electrical stimulation and imaging (e.g., Lujan et al., 2013) or TMS and imaging (Ruff et al., 2009; Driver et al., 2010; Krieg et al., 2013; Johnen et al., 2015) have been informative, but are also low in spatial resolution. Resting state connectivity in humans (for review, Raichle, 2015), a method based on covariation of hemodynamic response between brain sites, also lacks the spatial resolution for revealing columnar connectivity. While high spatial resolution (mm-scale) resting state connectivity in monkeys can be achieved at high fields (Wang et al., 2013), columnar resolution has yet to be achieved.

Given the constraints of current methods, we have therefore sought to develop new methods to elucidate brain networks systematically, at high spatial resolution, and in a high-throughput manner. In the past few years, we have focused on developing *in vivo* functional tract tracing methods comprised of focal columnar stimulation coupled with optical or fMRI imaging, a method we view as a shortcut toward examining anatomical connectivity. A distinct advantage is that *in vivo* functional tract tracing does not require histological processing and therefore can be conducted repeatedly *in vivo* in the same animal. This enables the study of networks, both at the local and the global scale,

TABLE 1 | Comparison of behavioral repertoires and cerebral cortical organization in mouse, monkey, and man.

	Mouse	Monkey	Man
Vision			
Fovea, high acuity	No	Yes	Yes
Color vision	No	Yes	Yes
Face perception	No	Yes	Yes
Eye movements	No	Yes	Yes
Visual attention	No	Yes	Yes
Manual behavior			
Manual and digit behavior	No	Yes	Yes
Texture on skin	No	Yes	Yes
Limb kinematics	No	Yes	Yes
Shape perception via grasp	No	Yes	Yes
Visuomotor directed grasp	No	Yes	Yes
Social behavior			
Language/response alternation	No	Yes	Yes
Social complexity	No	Yes	Yes
Brain organization			
Orientation columns	No	Yes	Yes
Large cortex	No	Yes	Yes

from multiple stimulation sites, enabling systematic and large scale collection of connectivity data from a single animal. It is hoped that study of multiple connection networks within single animals can more easily provide data useful for graph theoretical analysis and characterization of network topologies (cf. Sporns, 2010). Note that functional tract tracing is not meant to replace anatomical studies of brain connections, but rather to complement and extend our understanding of the anatomical gold standard.

THREE FUNCTIONAL TRACT TRACING METHODS

In the following sections, we will describe three functional tract tracing methods that could be used in a high-throughput manner: electrical, optogenetic, and near infrared laser stimulation. Each has its strengths and weaknesses and may be chosen depending on the questions at hand.

Focal Electrical Stimulation

Electrical stimulation has been a long-standing tool for functional mapping of the brain (Rasmussen and Penfield, 1947). Its uses have spanned mapping cortical organization, distinguishing functional relationships between cortical areas, and applications in brain–machine interfaces (Tolias et al., 2005; Moeller et al., 2008; Stepniewska et al., 2009, 2011; Chase et al., 2012). Importantly, electrical stimulation has been shown to generate or alter normal percepts and behaviors in many species, including human and non-human primates (Salzman et al., 1990; Romo et al., 2000; Godde et al., 2002; Graziano et al., 2002; Murphey and Maunsell, 2007; Tehovnik and Slocum, 2009). However, the relationship between circuits and behaviors activated by electrical stimulation remains poorly understood. This is partially due to a lack of a good understanding of the intra-areal and inter-areal networks activated or modulated via intracortical microstimulation (Bullmore and Sporns, 2009). The power of combining electrical stimulation with functional imaging in a behavioral context has been pioneered in monkeys by Ekstrom et al. (2008, 2009). By conducting fMRI concurrently with stimulation of FEF in the macaque, they demonstrated a contrast-dependent enhancement of visual cortical processing, thereby linking visual behavioral effects with underlying anatomical networks. Developing this approach at columnar resolution would further our understanding of both local and global circuits underlying behavior.

Toward this goal, we have developed methods to map intra-areal and inter-areal circuits using optical imaging combined with focal microstimulation. The underlying viewpoint is that stimulation of a single functional column will lead to activation of other connected columns, both intra-areal and inter-areal. Although electrical stimulation is accompanied by current spread, when delivered at appropriate levels, the effect can remain relatively local. In a two photon study of local neuronal activation in response to well-controlled, low current (5–10 μA) electrical microstimulation, Histed et al. (2009) demonstrated that electrically activated neurons comprised a subset of the neurons within the local vicinity (300 μm) and that movement of the stimulating electrode by 10′s of microns resulted in activation of different subsets of neurons within the same local vicinity. This suggested that, with the right stimulation parameters and precise localization of stimulation location, microstimulation can have quite selective and focal effects.

This finding by Histed et al. (2009) suggested the feasibility of using electrical microstimulation to map local columnar networks. Encouraged by this study, we attempted functional mapping with electrical microstimulation in monkey somatosensory cortex. As electrical stimulation can produce either excitatory or suppressive effects depending on the stimulation intensity, it was vitally important to characterize stimulus amplitudes by systematically characterizing the stimulation parameter space (e.g., intensity, duration, laminar location, cf. Tehovnik et al., 2004, 2006, 2009). Using trains of biphasic pulses (typically 200 Hz, 0.4 ms pulse duration), and varying intensity by testing different current amplitudes (10–300 μA) and pulse numbers (1, 13, 26, 63 pulses, resulting in total train durations of 0.4, 50, 100, 250 ms), we examined the effect of stimulation intensity on neuronal firing and hemodynamic signal as measured with intrinsic signal optical imaging. With chosen electrical stimulation parameters (25 μA, 250 Hz, 100 ms), the imaged hemodynamic response to electrical stimulation mimicked that of tactile stimulation (**Figure 3C**);

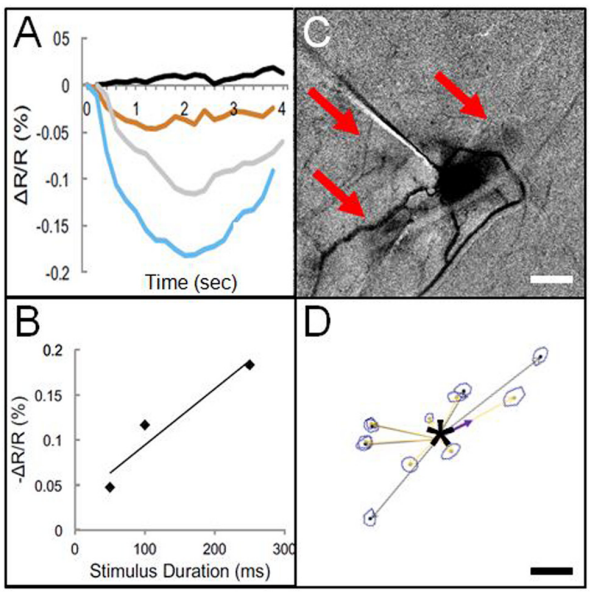

FIGURE 3 | Optical imaging of focal electrical stimulation in squirrel monkey somatosensory cortex. (A) Stimulation at 0 s (black), 50 ms (orange), 100 ms (gray), and 250 ms (blue) at 150 μA. *Y* axis: reflectance change dR/R. **(B)** Optical reflectance change increases with stimulus duration (measured at site of stimulation). **(C)** Optical image of local functional connectivity (from Brock et al., 2013) appears similar to **(D)** patches of anatomical label following focal (250 μm sized) injection (asterisk) of BDA tracer (adapted from Negyessy et al., 2013). **(C,D)** are from different animals. Scale bar for **(C,D)**: 1 mm.

both revealed a focal 1 mm activation site consistent with a single digit representation. Increasing intensity of stimulation [either current amplitude (**Figure 3A**) or number of pulses, (**Figure 3B**)] led to increasing magnitudes of imaged reflectance change. Importantly, stimulation (e.g., 200 μA for 250 ms) elicited not only a focal activation at the site of stimulation but other focal activations within 1–2 mm of the stimulated site (**Figure 3C**). This activation pattern is very similar in appearance to typical *intra-areal columnar networks* revealed by anatomical tracer studies (**Figures 1** and **3D**). Direct confirmation of this anatomical correspondence is currently in progress.

There is also potential for this approach to be used for mapping *inter-areal columnar connections*. Such an approach has been used to examine connections between motor and parietal areas in the prosimian primate the Galago (Stepniewska et al., 2011). Previous studies have shown that stimulation of parietal cortex at selected sites produces classes of complex behaviors (such as defensive postures, feeding, grooming; Cooke et al., 2003; Stepniewska et al., 2009). To understand the anatomical networks underlying these motor behaviors, optical imaging was used to map motor cortex during stimulation of behaviorally characterized parietal sites. Activations in motor cortex following parietal stimulation were intensity-dependent (**Figure 4A**) and revealed site-dependent differential topography (**Figures 4B,C**). In another study, Arsenault et al. (2014) mapped the functional consequences of stimulating ventral tegmental area with fMRI as well evaluating its behavioral effects and found that free choice behavior could be dramatically altered via widespread activation of the dopaminergic reward system. These studies suggest the possibility of simultaneously evoking or modulating a behavioral effect and mapping the underlying inter-areal circuit.

Focal Optical Stimulation

Advantages

2015 has been designated by the United Nations as the International Year of Light. We owe this to pioneers such as Nobel Laureates in Physics 2009 Charles Kao, Willard Boyle, and George Smith who were innovators in the development of fiber optics and CCD chips. These technologies enabled many advances in optical engineering and in medicine, including technologies for brain stimulation. There are several advantages to replacing wires with light. The most important advantage of this method over electrical stimulation is that it is not encumbered by current spread, making its effect focal. The volume of affected neural tissue is determined by the light wavelength and size of the delivery fiber optic. By selecting optical fibers with illumination spot sizes of 100 μm to 1 mm in diameter, activation of single to several cortical columns can be achieved (Cayce et al., 2011, 2013). Fiber optics can also be selected for stimulation at the brain surface without direct contact to neural tissue and can be easily targeted to specific cortical locations. Deep tissue stimulation via insertion of fiber optics into deep structures is also possible (e.g., Gerits et al., 2012). Another advantage of using light is that it is not accompanied by electrical stimulation artifact, making it readily compatible with electrical recordings. Also, light is easily applied within magnetic fields, making it useful for functional tracing in the MRI.

Stimulation through Optical Windows

Optical stimulation techniques can now be introduced via optical windows on the brain. In monkeys, both in anesthetized and awake behaving states, such windows offer the opportunity to probe the brain with multiple techniques. These windows permit multiscale study in individual animals, using methods such as behavioral study, fMRI, optical imaging, electrophysiology, focal stimulation (electrical, optogenetic near infrared laser stimulation), and the study of anatomical connectivity via targeted tracer injections through the window.

Infrared Neural Stimulation (INS)

The use of infrared wavelength light to evoke neural response was developed by Duco Jansen and colleagues at Vanderbilt University (Wells et al., 2005a,b, 2007a,b). First developed for stimulation of peripheral nerve, this effect is mediated via heat transient induced changes (absorption of infrared light by water) in membrane capacitance and protein conformation (Wells et al., 2007a; Shapiro et al., 2012). The transfer of energy is related to native resonance of water molecules: the better the match between stimulation wavelength and resonant frequency of water, the greater the energy transfer, and therefore, the greater the resulting heat transient; as a corollary, the greater the transfer, the less tissue penetration. Thus, Jansen and colleagues identified a stimulation wavelength (1.875 μm) that resulted in reasonable energy transfer and reasonable tissue penetration of 200–300 μms. When this near infrared wavelength light is presented in brief (0.25 ms) pulses, the transients lead to membrane depolarization and resulting action potentials (see Chernov and Roe, 2014a for review). In contrast to optogenetic approaches, this method is not dependent on viral infection and is thus more amenable to human application; however, unlike optogenetics, this method does not target specific cell types.

Infrared Neural Stimulation Intensity Predicts Magnitude of Cortical Response

Focal INS stimulation induces neural response as assessed with electrophysiology, optical imaging, and BOLD fMRI imaging. Magnitude of this response is related to the intensity of stimulation (**Figures 5A–C**). This focal stimulation can elicit functionally specific effects related to columnar organization. In visual cortex, application of focal stimulation to single ocular dominance columns in V1 can, in combination with visual stimulation, enhance response of shared eye ocular dominance columns (**Figures 5D,E**), suggesting a selective modulation of functionally specific intra-areal networks in V1. Similar modulatory results, by electrical stimulation, have been obtained by Ohayon et al. (2013).

Note that, similar to inhibitory effects of electrical stimulation, optical stimulation can also lead to relative suppression of cortical response. We have observed this using fiber optics of different diameters aimed at cortical columns. We find a U-shaped response where small fibers (100 μm) evoke a response weaker

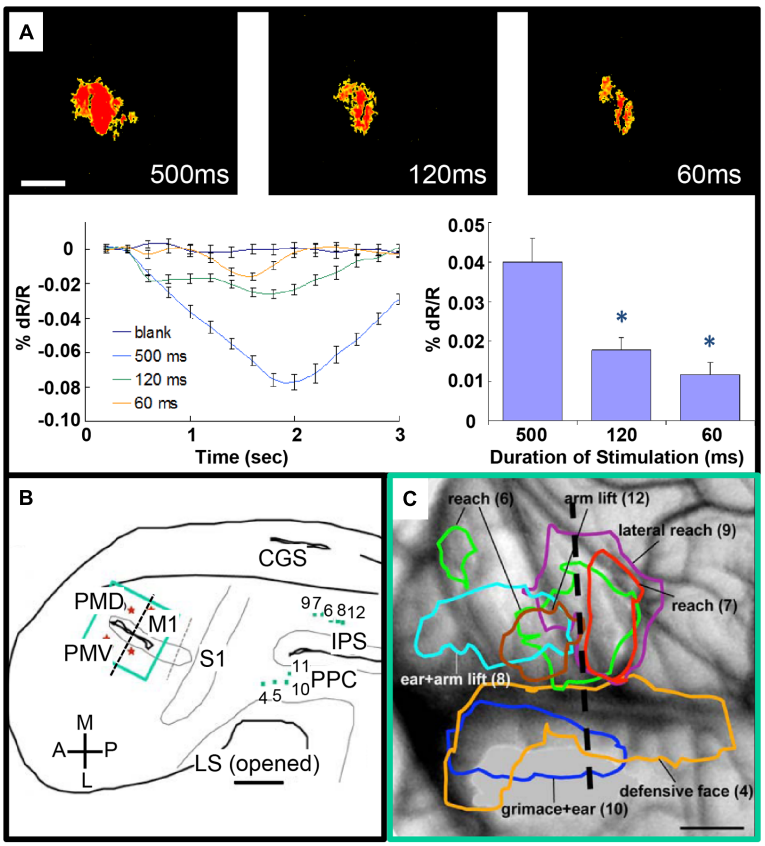

FIGURE 4 | Intrinsic motor cortex activity to different durations of electrical stimulation of PPC. (A) Top: three optical images (only significant pixels shown in red, *t*-test $*p < 0.01$) in response to electrical stimulation (400 μA, 0.1 ms biphasic, 300 Hz) of the dorsal PPC that evoked a lateral reaching movement (left: 500 ms, middle: 120 ms, right: 60 ms stimulation duration). Below: intrinsic signal time courses (left) and peak magnitudes (right). **(B)** Reconstruction of hemisphere. Green dots: stimulation sites in PPC. Green rectangle: imaging field of view centered over motor and premotor cortex. **(C)** Areas of activation in M1, PVD and PMV elicited by electrical stimulation of PPC. Colored outlines: areas activated during face movements (lateral) and forelimb movements (medial). Scale bars: 1 mm. (From Stepniewska et al., 2011).

than 200 μm fibers and 400 μm or 1 mm diameter fibers lead to relatively suppressed effects (**Figure 5F**). We interpret this as the larger fibers recruiting additional inhibitory circuits in the surround which change the balance of ongoing intra-areal networks and result in relative suppression.

Functional Tract Tracing with INS

Having characterized the effects of INS stimulation, we next examined whether it could be used as a tool for functional tract tracing. To further motivate the use of this approach, we examined the compatibility of INS with fMRI (Chen et al., 2012c). With fMRI, similar to hemodynamic signals measured with optical imaging, the relationship of INS intensity is proportional to hemodynamic BOLD response (**Figure 6A**). Preliminary studies in squirrel monkeys implanted with optical chambers over somatosensory cortex (imaged with surface coil in a 9.4T Varian magnet) have shown that targeted stimulation of single digit locations (e.g., D2 tip) via apposition of the stimulating fiber optic to the cortical surface at one somatosensory cortical location (**Figure 6B**) leads to significant BOLD response in topographically appropriate locations in nearby areas (**Figure 6C**). When imaged in coronal slices, activations appear localized to superficial or middle layers of cortical laminae, suggesting that this resolution is sufficient for superficial, middle, or deep laminar localization (**Figure 6C**). INS combined with fMRI thus provides the opportunity to examine intra- and inter-areal connection patterns of a stimulated site, as well as identify resulting laminar profiles, that will be useful for interpretation of feedforward or feedback connection patterns.

Behavioral Effects with INS

There is a long history of focal electrical stimulation producing highly specific behavioral effects (e.g., for motion direction percepts, Salzman et al., 1990; for tactile frequency percepts, Romo et al., 2000). Can INS also be used for similar applications? As a first attempt to examine this possibility, we tested whether focal INS stimulation in visual cortex of macaque monkeys could induce percepts of light spots (phosphenes). In awake fixating monkeys implanted with optical chambers over visual cortex (V1, V2, V4), we used intrinsic signal optical imaging to map the visuotopic representation within the optical chamber (Tanigawa et al., 2010). We then applied

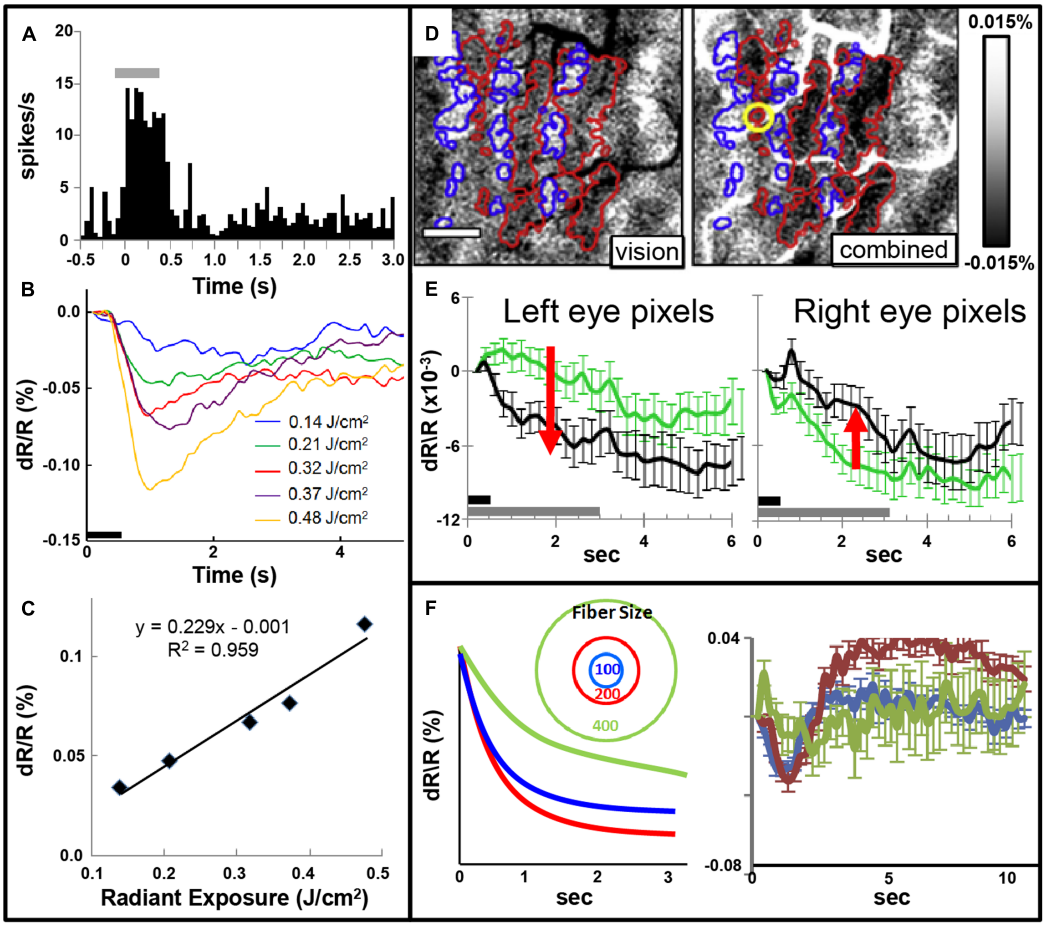

FIGURE 5 | (A) Post-stimulus time histogram of neural response evoked by INS stimulation (gray bar). **(B,C)** Increased INS radiant exposure leads to an increase in intrinsic signal magnitude. **(B)** Time course of signal for different radiant exposures. **(C)** Radiant exposure vs. peak amplitude of the intrinsic signal. Relationship fit with a linear equation. (Laser parameters: $\lambda = 1.875$ μm, 250 μs pulses at 200 Hz for 500 ms, 400 μm fiber; **D,E**) INS potentiates response to visual stimulation. **(D)** Red and blue outlines demarcate left and right: ocular dominance columns, respectively. Left: OD map generated by subtraction of left minus right eye. Right: INS applied to left eye column during visual stimulation leads to relative enhancement of left eye columns (darkening in red outlined areas) and relative suppression of right eye columns (lightening in blue outlined areas). Scale bar: 1 mm. **(E)** This is observed by examining averaged time courses from pixels in left eye (left panel, red arrow indicates increase in optical signal reflectance) and right eye (right panel, red arrow indicates decline in optical signal reflectance) columns. Dark gray bar: INS stimulation period. Light gray bar: visual stimulation period. Error bars: SEM. (INS parameters: $\lambda = 1.875$ μm, 1.3 J/cm^2, 250 μs pulses at 200 Hz for 500 ms, 100 μm fiber). *Y* axis: dR/R. **(F)** Effect of fiber size. Left: Schematic displaying 100, 200, and 400 μm diameter fibers. Predicted intrinsic signal responses: 200 μm fiber (red) produces larger enhancement than 100 μm fiber (blue). However, 400 μm fiber impinges on domains of other eye and leads to relative suppression (green). Right: actual data is consistent with prediction. (**A–C** from Cayce et al., 2011, **D–F** from Cayce et al., 2013).

INS stimulation to selected sites. As predicted, the induced percept of a light spot led to reliable eye saccades to the predicted site with the appropriate 300 ms latency for eye movements (Roe et al., 2013). This simple baseline test suggests that INS can be used to modulate behavioral outcome in ways similar to previous electrical stimulation studies. We predict that targeting stimulation to specific columnar locations will enable more selective behavioral effects than larger, multi-columnar activations.

Optogenetic Stimulation

The widespread use of optogenetics in neuroscience owes its thanks to the pioneering work of Karl Diesseroth, Edward Boyden, and their colleagues at Stanford and MIT. The key advantage of optogenetics is the ability to selectively target specific cell types. Neuronal response to optical stimulation is achieved by incorporation of light-sensitive rhodopsin molecules via molecular genetic techniques. They can be triggered with millisecond precision (Han and Boyden, 2007) and can lead to either excitatory (Boyden et al., 2005) or suppressive neuronal effects (Chow et al., 2010). Channelrhodopsin-2 (ChR2) is a light sensitive cation channel that leads to depolarization of neurons. Hyperpolarization can be achieved using halorhodopsin (a light-activated chloride pump) or archaerhodopsin (Arch; a light-activated proton pump; Boyden et al., 2005; Han and Boyden, 2007). In mice, this has been a boon to circuit dissection underlying behavior and disease (for review see Bernstein and Boyden, 2011).

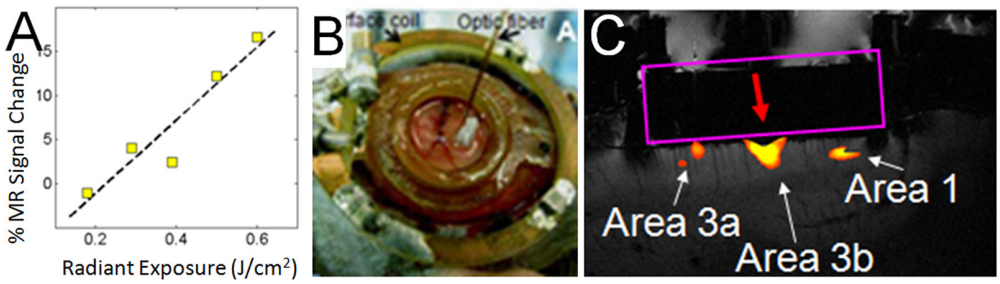

FIGURE 6 | Functional tract tracing with INS stimulation and fMRI. (A) Increasing INS stimulation intensity produces increasing BOLD response. **(B)** View of 400 μm fiber optic applied to optical window at D2 location (as determined by optical imaging in different session) in area 3b of somatosensory cortex in a squirrel monkey. The monkey was imaged at 9.4T (Varian Inova Magnet) with a 3 cm surface coil surrounding the optical window. **(C)** Red arrow indicates the location of apposed optical fiber. INS stimulation (0.4 J/cm^2, pulsed trains applied in blocks of 30 s ON, 30 s OFF) at this site produces strong BOLD response at fiber tip as well as at corresponding topographic locations in area 3a and area 1. Coronal slice: voxel 625 μm × 625 μm × 1000 μm.

In monkeys, however, progress has been slower. Initial studies in primates demonstrated feasibility of expression and behavioral effect (Han et al., 2009, 2011; Diester et al., 2011; Cavanaugh et al., 2012; Galvan et al., 2012; Jazayeri et al., 2012). Surprisingly, unlike electrical stimulation, optogenetic stimulation appears to have more subtle effects. Rather than eliciting robust motor responses, optogenetic activation appears to modulate activity, either ongoing neural activity or to activity induced by electrical stimulation. Examples include optogenetic inactivation of monkey superior colliculus which leads to saccadic eye movement deficits (Cavanaugh et al., 2012), optogenetic activation in FEF which has subthreshold eye movement effects when paired with electrical stimulation (Ohayon et al., 2013), and optogenetic activation in parietal cortex which lead to modulation of salience maps (Dai et al., 2014). There may be multiple reasons for the apparent 'weaker' effect of optogenetic stimulation, such as differences in the mechanism of activation, differences in neural populations being activated, or the small number of cells effectively transfected.

Yet another potential cause relates to limitations in methodology. These limitations include inconsistencies in viral delivery, robustness of viral infection and expression, accuracy of light delivery, and reliability of *in vivo* assessments of neural or behavioral effectiveness. One approach for improving optogenetic technology in monkeys is the use of optical windows. In the primate, the presence of heavy dura mater has necessitated use of large bore injectrodes, electrodes, and optrodes (e.g., Diester et al., 2011) which can damage cortex; the opacity of dura mater also leads to uncertainty about injected location, targeting accuracy of optrodes, and inability to assess the degree of genetic expression. To alleviate some of these problems, the use of optical windows has permitted clear visualization and targeting of functionally characterized sites, use of fine injection pipettes which do not damage cortical tissue, and repeated optical monitoring of expression. These benefits of optical windows apply for optogenetics studies in both anesthetized and awake animals (Ruiz et al., 2013). Using optical windows, Nassi et al. (2015) have demonstrated that optogenetic stimulation in awake monkey visual cortex can 'substitute' for normal visual stimulation in a manner following the divisive normalization model of visual neuronal response and that neuronal response can be parametrically modulated in a controlled fashion. This important advance improves the reliability and accuracy of optogenetics methodology in primates and further secures its role as a focal stimulation modality in non-human primate studies.

Functional Tract Tracing with Optogenetic Stimulation

One of the most exciting applications of optogenetics is its use as a behavioral modulation tool and for functional tract tracing. In monkeys, this approach has been used to reveal frontal circuits underlying eye movement behavior. By stimulating ChR2 sites in FEF (the anterior and posterior arcuate sulcus) during performance of target selected eye saccades, Vanduffel and colleagues demonstrated that saccades in trials with stimulation occurred with significantly shorter latency than in those without (Gerits et al., 2012). The shortened saccade latencies suggested that optogenetic stimulation either produced greater neuronal firing rates or recruited a greater number of neurons. The success of this stimulation paradigm was attributed to a few factors: the use of a cell type non-specific CAG promoter, targeted injections in saccade related domains identified with FMRI, and stronger stimulation via the use of dual light guides. Importantly, the assessment of effect was not the induction of eye movement *per se* but rather the facilitation of eye movement latency. Thus, in contrast to early negative results, more finely tuned assessments of behavioral effect can reveal clear, robust effects of optogenetic stimulation. A further and important benefit of this optogenetic approach is its compatibility with the MRI environment. Stimulation of the anterior arcuate in the MR activated loci in V1, V4, MSTd, and MSTv, leading to identification of circuits underlying the speeded eye movement behavior.

At a local scale, optogenetic stimulation has also been used to probe the effect of stimulating single or multiple orientation domains in V1 of the tree shrew (Huang et al., 2014). Rather than use optrodes or fiber optics, this study used a spatial light modulator to produce a pre-specified pattern of blue light to activate specific ChR2 infected orientation columns in the

cortex. Surprisingly, they did not find activation of nearby orientation domains of similar selectivity, but rather the effects appeared to fall off with distance from the stimulated domain. This result is not consistent with other results that demonstrate functionally selective effects of optogenetic stimulation via fiber optic delivery in Macaque monkey V1 (Chernov and Roe, 2014b). Stimulation of ocular dominance columns at single sites enhanced (increased reflectance change detected by optical imaging) the stimulated ocular dominance columns (similar to results obtained with INS, **Figures 5D–F**), and stimulation of single orientation domains led to relative enhancement of other orientation domains of similar selectivity. The differences between these studies may relate to intensity or effective depth of stimulation. Further studies are needed to evaluate these effects.

CONCLUSION

We have explored three different functional tract tracing methods that can be presented at the columnar scale in a targeted, functionally specific fashion. These methods do not require animal sacrifice and lengthy anatomical reconstruction, and potentially permit the study of connections from a greater number of sites within an individual animal. The similarities and differences between these methods and traditional anatomical tract tracing methods (e.g., in sensitivity to less robust connections) need to be further characterized and understood. While these methods cannot replace the gold standard of anatomical tract tracing, the advantages of *in vivo* functional tract tracing will make studying column-specific brain connections on a large scale more feasible.

The three methods presented each have their strengths and weaknesses. Electrical microstimulation is complicated by current spread but, at least within certain parameters and at a population level, appears to bias the activated circuits in a way that permits visualization of connections via functional imaging methods. Given that there is a wealth of studies demonstrating behavioral modulation using electrical stimulation, the use of electrical stimulation to map connections in the brain provides a direct link to these studies and could be conducted via methods that are already readily accessible. INS stimulation is a new method that is being developed for superficial and deep tissue stimulation. Applied via fiber optics, INS permits focal stimulation. INS does not require the use of viruses, giving it greater potential for human use. However, at this point in time, INS requires the delivery of specific infrared light wavelengths that are not yet commercially available. Optogenetics is a cell specific stimulation method that has revolutionized neuroscience. It requires the introduction of viruses that express light-sensitive rhodopsin molecules. Optogenetics has been enormously useful in studies in mice; its use in monkeys now also looks promising. Given the need for viral transfection, it is less amenable to use in humans.

The promise of conducting *in vivo* functional tract tracing studies calls for new future studies. We propose: (1) targeted, systematic, and large scale evaluation of columnar networks in different functional brain systems in monkeys (e.g., visual system, hand use system, working memory system), (2) cell type specific columnar mapping, (3) direct correlation of behavioral effects and mapped columnar networks, and (4) designing brain-machine interfaces based on targeting of columnar networks.

ACKNOWLEDGMENTS

We thank Duco Jansen and Anita Mahadevan-Jansen for their collaboration in the INS projects and the use of the INS laser (Capella Infrared Neuro-Stimulator, Lockheed Martin Aculight, Bothell WA). We thank John Gore and the Vanderbilt University Institute of Imaging Sciences for fMRI imaging support. We thank NIH for funding support: NS044375 (NINDS), MH095009 (NIMH), EY022853 (NEI), NS079471 (NINDS), as well as support from Vanderbilt Vision Research Center and the Center for Integrative and Cognitive Neuroscience at Vanderbilt. We also thank Zhejiang University for their support during the writing of this manuscript.

REFERENCES

Arsenault, J. T., Rima, S., Stemmann, H., and Vanduffel, W. (2014). Role of the primate ventral tegmental area in reinforcement and motivation. *Curr. Biol.* 24, 1347–1353. doi: 10.1016/j.cub.2014.04.044

Baek, K., Shim, W. H., Jeong, J., Radhakrishnan, H., Rosen, B. R., Boas, D., et al. (2015). Layer-specific interhemispheric functional connectivity in the somatosensory cortex of rats: resting state electrophysiology and fMRI studies. *Brain Struct. Funct.* [Epub ahead of print].

Bernstein, J. G., and Boyden, E. S. (2011). Optogenetic tools for analyzing the neural circuits of behavior. *Trends Cogn. Sci.* 15, 592–600. doi: 10.1016/j.tics.2011.10.003

Bosking, W. H., Zhang, Y., Schofield, B., and Fitzpatrick, D. (1997). Orientation selectivity and the arrangement of horizontal connections in tree shrew striate cortex. *J. Neurosci.* 17, 2112–2127.

Boyden, E. S., Zhang, F., Bamberg, E., Nagel, G., and Deisseroth, K. (2005). Millisecond-timescale, genetically targeted optical control of neural activity. *Nat. Neurosci.* 8, 1263–1268. doi: 10.1038/nn1525

Brock, A. A., Friedman, R. M., Fan, R. H., and Roe, A. W. (2013). Optical imaging of cortical networks via intracortical microstimulation. *J. Neurophysiol.* 110, 2670–2678. doi: 10.1152/jn.00879.2012

Bullmore, E., and Sporns, O. (2009). Complex brain networks: graph theoretical analysis of structural and functional systems. *Nat. Rev. Neurosci.* 10, 186–198. doi: 10.1038/nrn2575

Cavanaugh, J., Monosov, I. E., McAlonan, K., Berman, R., Smith, M. K., Cao, V., et al. (2012). Optogenetic inactivation modifies monkey visuomotor behavior. *Neuron* 76, 901–907. doi: 10.1016/j.neuron.2012.10.016

Cayce, J., Friedman, R. M., Jansen, D., Mahavaden-Jansen, A., and Roe, A. W. (2011). Pulsed infrared light alters neural activity in rat somatosensory cortex in vivo. *Neuroimage* 57, 155–166. doi: 10.1016/j.neuroimage.2011.03.084

Cayce, J., Friedman, R. M., Jansen, D., Mahadevan-Jansen, A., and Roe, A. W. (2013). Infrared neural stimulation of primary visual cortex in non-human primates. *Neuroimage* 84, 181–190. doi: 10.1016/j.neuroimage.2013.08.040

Chase, S. M., Kass, R. E., and Schwartz, A. B. (2012). Behavioral and neural correlates of visuomotor adaptation observed through a brain-computer interface in primary motor cortex. *J. Neurophysiol.* 108, 624–644. doi: 10.1152/jn.00371.2011

Chen, G., Wang, F., Dillenburger, C. D., Friedman, R. M., Chen, L. M., Gore, J. C., et al. (2012a). Functional magnetic resonance imaging of awake monkeys: some approaches for improving imaging quality. *Magn. Reson. Imaging* 30, 36–47. doi: 10.1016/j.mri.2011.09.010

Chen, G., Wang, F., Gore, J. C., and Roe, A. W. (2012b). Identification of cortical lamination in awake monkeys by high resolution magnetic resonance imaging. *Neuroimage* 59, 3441–3449. doi: 10.1016/j.neuroimage.2011.10.079

Chen, G., Cayce, J. M., Friedman, R. M., Wang, F., Tang, C., Jansen, D. E., et al. (2012c). Functional tract tracing in non-human primates using pulsed infrared lasers in conjunction with optical imaging and fMRI. *Paper Presented at the Society for Neuroscience Meeting*, New Orleans, LA.

Chen, G. C., Wang, F., Gore, J. C., and Roe, A. W. (2013). Layer-specific BOLD activation in awake monkey V1 revealed by ultra-high spatial resolution functional magnetic resonance imaging. *Neuroimage* 64, 147–155. doi: 10.1016/j.neuroimage.2012.08.060

Chen, L. M., Turner, G., Friedman, R. M., Gore, J. C., Roe, A. W., and Avison, M. J. (2007). High resolution maps of real and illusory tactile activation in SI: intra-individual correlation with fMRI, optical imaging and electrophysiology. *J. Neurosci.* 27, 9181–9191. doi: 10.1523/JNEUROSCI.1588-07.2007

Cheng, K., Waggoner, R. A., and Tanaka, K. (2001). Human ocular dominance columns as revealed by high-field functional magnetic resonance imaging. *Neuron* 32, 359–374. doi: 10.1016/S0896-6273(01)00477-9

Chernov, M., and Roe, A. W. (2014a). Infrared neural stimulation: a new stimulation tool for CNS applications. *Neurophotonics* 1:011011 doi: 10.1117/1.NPh.1.1.011011

Chernov, M., and Roe, A. W. (2014b). Optogenetic stimulation of monkey primary visual cortex. *Paper Presented at the Society for Neuroscience Meeting*, Washington, DC.

Chow, B. Y., Han, X., Dobry, A. S., Qian, X., Chuong, A. S., Li, M., et al. (2010). High-performance genetically targetable optical neural silencing by light-driven proton pumps. *Nature* 463, 98–102. doi: 10.1038/nature08652

Cooke, D. F., Taylor, C. S., Moore, T., and Graziano, M. S. (2003). Complex movements evoked by microstimulation of the ventral intraparietal area. *Proc. Natl. Acad. Sci. U.S.A.* 100, 6163–6168. doi: 10.1073/pnas.1031751100

Dai, J., Brooks, D. I., and Sheinberg, D. L. (2014). Optogenetic and electrical microstimulation systematically bias visuospatial choice in primates. *Curr. Biol.* 24, 63–69. doi: 10.1016/j.cub.2013.11.011

Diester, I., Kaufman, M. T., Mogri, M., Pashaie, R., Goo, W., Yizhar, O., et al. (2011). Anoptogenetic toolbox designed for primates. *Nat. Neurosci.* 14, 387–397. doi: 10.1038/nn.2749

Driver, J., Blankenburg, F., Bestmann, S., and Ruff, C. C. (2010). New approaches to the study of human brain networks underlying spatial attention and related processes. *Exp. Brain Res.* 206, 153–162. doi: 10.1007/s00221-010-2205-7

Ekstrom, L. B., Roelfsema, P. R., Arsenault, J. T., Bonmassar, G., and Vanduffel, W. (2008). Bottom-up dependent gating of frontal signals in early visual cortex. *Science* 321, 414–417. doi: 10.1126/science.1153276

Ekstrom, L. B., Roelfsema, P. R., Arsenault, J. T., Kolster, H., and Vanduffel, W. (2009). Modulation of the contrast response function by electrical microstimulation of the macaque frontal eye field. *J. Neurosci.* 29, 10683–10694. doi: 10.1523/JNEUROSCI.0673-09.2009

Federer, F., Williams, D., Ichida, J. M., Merlin, S., and Angelucci, A. (2013). Two projection streams from macaque V1 to the pale cytochrome oxidase stripes of V2. *J. Neurosci.* 33, 11530–11539. doi: 10.1523/JNEUROSCI.5053-12.2013

Galvan, A., Hu, X., Smith, Y., and Wichmann, T. (2012). In vivo optogenetic control of striatal and thalamic neurons in non-human primates. *PLoS ONE* 7:e50808. doi: 10.1371/journal.pone.0050808

Gerits, A., Farivar, R., Rosen, B. R., Wald, L. L., Boyden, E. S., and Vanduffel, W. (2012). Optogenetically induced behavioral and functional network changes in primates. *Curr. Biol.* 22, 1722–1726. doi: 10.1016/j.cub.2012.07.023

Godde, B., Leonhardt, R., Cords, S. M., and DInse, H. R. (2002). Plasticity of orientation preference maps in the visual cortex of adult cats. *Proc. Natl. Acad. Sci. U.S.A.* 99, 6352–6357.

Goense, J., Merkle, H., and Logothetis, N. K. (2012). High-resolution fMRI reveals laminar differences in neurovascular coupling between positive and negative BOLD responses. *Neuron* 76, 629–639. doi: 10.1016/j.neuron.2012.09.019

Graziano, M. S., Taylor, C. S., and Moore, T. (2002). Complex movements evoked by microstimulation of precentral cortex. *Neuron* 34, 841–851. doi: 10.1016/S0896-6273(02)00698-0

Han, X., and Boyden, E. S. (2007). Multiple-color optical activation, silencing, and desynchronization of neural activity, with single-spike temporal resolution. *PLoS ONE* 2:e299. doi: 10.1371/journal.pone.0000299

Han, X., Chow, B. Y., Zhou, H., Klapoetke, N. C., Chuong, A., Rajimehr, R., et al. (2011). A high-light sensitivity optical neural silencer: development and application to optogenetic control of non-human primate cortex. *Front. Syst. Neurosci.* 5:18. doi: 10.3389/fnsys.2011.00018

Han, X., Qian, X., Bernstein, J. G., Zhou, H. H., Franzesi, G. T., Stern, P., et al. (2009). Millisecond-timescale optical control of neural dynamics in the nonhuman primate brain. *Neuron* 62, 191–198. doi: 10.1016/j.neuron.2009.03.011

Histed, M. H., Bonin, V., and Reid, R. C. (2009). Direct activation of sparse, distributed population of cortical neurons by electrical microstimulation. *Neuron* 63, 508–522. doi: 10.1016/j.neuron.2009.07.016

Huang, X., Elyada, Y. M., Bosking, W. H., Walker, T., and Fitzpatrick, D. (2014). Optogenetic assessment of horizontal interactions in primary visual cortex. *J. Neurosci.* 34, 4976–4990. doi: 10.1523/JNEUROSCI.4116-13.2014

Jazayeri, M., Lindbloom-Brown, Z., and Horwitz, G. D. (2012). Saccadic eye movements evoked by optogenetic activation of primate V1. *Nat. Neurosci.* 15, 1368–1370. doi: 10.1038/nn.3210

Jbabdi, S., Lehman, J. F., Haber, S. N., and Behrens, T. E. (2013). Human and monkey ventral prefrontal fibers use the same organizational principles to reach their targets: tracing versus tractography. *J. Neurosci.* 33, 3190–3201. doi: 10.1523/JNEUROSCI.2457-12.2013

Johnen, V. M., Neubert, F. X., Buch, E. R., Verhagen, L., O'Reilly, J. X., Mars, R. B., et al. (2015). Causal manipulation of functional connectivity in a specific neural pathway during behaviour and at rest. *Elife* 9:4. doi: 10.7554/eLife.04585

Krieg, T. D., Salinas, F. S., Narayana, S., Fox, P. T., and Mogul, D. J. (2013). PET-based confirmation of orientation sensitivity of TMS-induced cortical activation in humans. *Brain Stimul.* 6, 898–904. doi: 10.1016/j.brs.2013.05.007

Livingstone, M. S., and Hubel, D. H. (1984). Anatomy and physiology of a color system in the primate visual cortex. *J. Neurosci.* 4, 309–356.

Lu, H. D., and Roe, A. W. (2008). Functional organization of color domains in V1 and V2 of Macaque monkey revealed by optical imaging. *Cereb. Cortex* 18, 516–533. doi: 10.1093/cercor/bhm081

Lujan, J. L., Chaturvedi, A., Choi, K. S., Holtzheimer, P. E., Gross, R. E., Mayberg, H. S., et al. (2013). Tractography-activation models applied to subcallosal cingulate deep brain stimulation. *Brain Stimul.* 6, 737–739. doi: 10.1016/j.brs.2013.03.008

Malach, R., Amir, Y., Harel, M., and Grinvald, A. (1993). Relationship between intrinsic connections and functional architecture revealed by optical imaging and in vivo targeted biocytin injections in primate striate cortex. *Proc. Natl. Acad. Sci. U.S.A.* 90, 10469–10473. doi: 10.1073/pnas.90.22.10469

Metin, C., Godement, P., and Imbert, M. (1988). The primary visual cortex in the mouse: receptive field properties and functional organization. *Exp. Brain Res.* 69, 594–612. doi: 10.1007/BF00247312

Moeller, S., Freiwald, W. A., and Tsao, D. Y. (2008). Patches with links: a unified system for processing faces in the macaque temporal lobe. *Science* 320, 1355–1359. doi: 10.1126/science.1157436

Murphey, D. K., and Maunsell, J. H. R. (2007). Behavioral detection of electrical microstimulation in different cortical visual areas. *Curr. Biol.* 17, 862–867. doi: 10.1016/j.cub.2007.03.066

Nassi, J. J., Avery, M. C., Cetin, A. H., Roe, A. W., and Reynolds, J. H. (2015). Normalization through local excitation and inhibition in primate visual cortex. *Neuron* 86, 1504–1517. doi: 10.1016/j.neuron.2015.05.040

Negyessy, L., Palfi, E., Ashaber, M., Palmer, C., Balazs, J., Friedman, R. M., et al. (2013). Intrinsic horizontal connections process global haptic features in the primary somatosensory cortex: neuroanatomical evidence. *J. Comp. Neurol.* 521, 2798–2817. doi: 10.1002/cne.23317

Ohayon, S., Grimaldi, P., Schweers, N., and Tsao, D. Y. (2013). Saccade modulation by optical and electrical stimulation in the macaque frontal eye field. *J. Neurosci.* 33, 16684–16697. doi: 10.1523/JNEUROSCI.2675-13.2013

Olman, C. A., Harel, N., Feinberg, D. A., He, S., Zhang, P., Ugurbil, K., et al. (2012). Layer-specific fMRI reflects different neuronal computations at different depths in human V1. *PLoS ONE* 7:e32536. doi: 10.1371/journal.pone.0032536

Raichle, M. E. (2015). The restless brain: how intrinsic activity organizes brain function. *Philos. Trans. R. Soc. Lond. B Biol. Sci.* 370. doi: 10.1098/rstb.2014.0172

Rasmussen, T., and Penfield, W. (1947). The human sensorimotor cortex as studied by electrical stimulation. *Fed. Proc.* 6(1Pt. 2), 184.

Rockland, K. S. (2010). Five points on columns. *Front. Neuroanat.* 4:22. doi: 10.3389/fnana.2010.00022

Roe, A. W., Chen, G., Cayce, J. M., Ye, X., Jansen, E. D., and Mahadevan-Jansen, A. (2013). Infrared neural stimulation of visual cortex induces visual perception in awake non-human primates. *Paper Presented at the Society for Neuroscience Meeting*, San Diego, CA.

Roe, A. W., and Ts'o, D. Y. (1999). Specificity of color connectivity between primate V1 and V2. *J. Neurophysiol.* 82, 2719–2731.

Roe, A. W., and Ts'o, D. Y. (2015). Specificity of V1-V2 orientation networks in the primate visual cortex. *Cortex* doi: 10.1016/j.cortex.2015.07.007 [Epub ahead of print].

Romo, R., Hernandez, A., Zainos, A., Brody, C. D., and Lemus, L. (2000). Sensing without touching: psychophysical performance based on cortical microstimulation. *Neuron* 26, 273–278. doi: 10.1016/S0896-6273(00)81156-3

Ruff, C. C., Driver, J., and Bestmann, S. (2009). Combining TMS and fMRI: from 'virtual lesions' to functional-network accounts of cognition. *Cortex* 45, 1043–1049. doi: 10.1016/j.cortex.2008.10.012

Ruiz, O., Lustig, B., Nassi, J. J., Reynolds, J., Callaway, E., Albright, T., et al. (2013). Optogenetics through windows on the brain in the nonhuman primate. *J. Neurophysiol.* 110, 1455–1467. doi: 10.1152/jn.00153.2013

Salzman, C. D., Britten, K. H., and Newsome, W. T. (1990). Cortical microstimulation influences perceptual judgements of motion direction. *Nature* 346, 174–177. doi: 10.1038/346174a0

Schuett, S., Bonhoeffer, T., and Hübener, M. (2002). Mapping retinotopic structure in mouse visual cortex with optical imaging. *J. Neurosci.* 22, 6549–6559.

Shapiro, M. G., Homma, K., Villarreal, S., Richter, C.-P., and Bezanilla, F. (2012). Infrared light excites cells by changing their electrical capacitance. *Nat. Commun.* 3, 736. doi: 10.1038/ncomms1742

Shih, Y. Y., Chen, Y. Y., Lai, H. Y., Kao, Y. C., Shyu, B. C., and Duong, T. Q. (2013). Ultra high-resolution fMRI and electrophysiology of the rat primary somatosensory cortex. *Neuroimage* 73, 113–120. doi: 10.1016/j.neuroimage.2013.01.062

Shmuel, A., Korman, M., Sterkin, A., Harel, M., Ullman, S., Malach, R., et al. (2005). Retinotopic axis specificity and selective clustering of feedback projections from V2 to V1 in the owl monkey. *J. Neurosci.* 25, 2117–2131. doi: 10.1523/JNEUROSCI.4137-04.2005

Sincich, L. C., and Blasdel, G. G. (2001). Oriented axon projections in primary visual cortex of the monkey. *J. Neurosci.* 21, 4416–4426.

Sincich, L. C., Jocson, C. M., and Horton, J. C. (2010). V1 interpatch projections to V2 thick stripes and pale stripes. *J. Neurosci.* 30, 6963–6974. doi: 10.1523/JNEUROSCI.5506-09.2010

Sporns, O. (2010). *Networks of the Brain*. Cambridge, MA: MIT Press.

Stepniewska, I., Cerkevich, C. M., and Kaas, J. H. (2015). Cortical connections of the caudal portion of posterior parietal cortex in prosimian Galagos. *Cereb. Cortex* doi: 10.1093/cercor/bhv132 [Epub ahead of print].

Stepniewska, I., Fang, P. Y., and Kaas, J. H. (2009). Organization of the posterior parietal cortex in galagos: functional zones identified by microstimulation. *J. Comp. Neurol.* 517, 765–782. doi: 10.1002/cne.22181

Stepniewska, I., Friedman, R. M., Gharbawie, O. A., Cerkevich, C. M., Roe, A. W., and Kaas, J. H. (2011). Optical imaging in galagos reveals parietal-frontal circuits underlying motor behavior. *Proc. Natl. Acad. Sci. U.S.A.* 108, E725–E732. doi: 10.1073/pnas.1109925108

Sun, P., Gardner, J. L., Costagli, M., Ueno, K., Waggoner, R. A., Tanaka, K., et al. (2013). Demonstration of tuning to stimulus orientation in the human visual cortex: a high-resolution fMRI study with a novel continuous and periodic stimulation paradigm. *Cereb. Cortex* 23, 1618–1629. doi: 10.1093/cercor/bhs149

Tanigawa, H., Lu, H. D., and Roe, A. W. (2010). Functional organization for color and orientation in macaque V4. *Nat. Neurosci.* 13, 1542–1548. doi: 10.1038/nn.2676

Tehovnik, E. J., and Slocum, W. M. (2009). Background luminance affects the detection of microampere currents delivered to macaque striate cortex. *Eur. J. Neurosci.* 30, 263–271. doi: 10.1111/j.1460-9568.2009.06810.x

Tehovnik, E. J., Slocum, W. M., and Schiller, P. H. (2004). Microstimulation of V1 delays the execution of visually guided saccades. *Eur. J. Neurosci.* 20, 264–272. doi: 10.1111/j.1460-9568.2004.03480.x

Tehovnik, E. J., Slocum, W. M., Smirnakis, S. M., and Tolias, A. S. (2009). Microstimulation of visual cortex to restore vision. *Prog. Brain Res.* 175, 347–375. doi: 10.1016/S0079-6123(09)17524-6

Tehovnik, E. J., Tolias, A. S., Sultan, F., Slocum, W. M., and Logothetis, N. K. (2006). Direct and indirect activation of cortical neurons by electrical microstimulation. *J. Neurophysiol.* 96, 512–521. doi: 10.1152/jn.00126.2006

Thomas, C., Ye, F. Q., Irfanoglu, M. O., Modi, P., Saleem, K. S., Leopold, D. A., et al. (2014). Anatomical accuracy of brain connections derived from diffusion MRI tractography is inherently limited. *Proc. Natl. Acad. Sci. U.S.A.* 111, 16574–16579. doi: 10.1073/pnas.1405672111

Tolias, A. S., Sultan, F., Augath, M., Oeltermann, A., Tehovnik, E. J., Schiller, P. H., et al. (2005). Mapping cortical activity elicited with electrical microstimulation using fMRI in the macaque. *Neuron* 48, 901–911. doi: 10.1016/j.neuron.2005.11.034

Ts'o, D. Y., Gilbert, C. D., and Wiesel, T. N. (1986). Relationships between horizontal interactions and functional architecture in cat striate cortex as revealed by cross-correlation analysis. *J. Neurosci.* 6, 1160–1170.

Wang, Z., Negyessy, L., Chen, L. M., Friedman, R. M., John G., and Roe, A. W. (2013). The relationship of anatomical and functional connectivity to resting state connectivity in primate somatosensory cortex. *Neuron* 78, 1116–1126. doi: 10.1016/j.neuron.2013.04.023

Wells, J., Kao, C., Jansen, E. D., Konrad, P., and Mahadevan-Jansen, A. (2005a). Application of infrared light for in vivo neural stimulation. *J. Biomed. Opt.* 10. doi: 10.1117/1.2121772

Wells, J., Kao, C., Mariappan, K., Albea, J., Jansen, Konrad, P., et al. (2005b). Optical stimulation of neural tissue in vivo. *Opt. Lett.* 30, 504–506. doi: 10.1364/OL.30.000504

Wells, J., Kao, C., Konrad, P., Milner, T., Kim, J., Mahadevan-Jansen, A., et al. (2007a). Biophysical mechanisms of transient optical stimulation of peripheral nerve. *Biophys. J.* 93, 2567–2580.

Wells, J., Konrad, P., Kao, C., Jansen, and Mahadevan-Jansen, A. (2007b). Pulsed laser versus electrical energy for peripheral nerve stimulation. *J. Neurosci. Methods* 163, 326–337. doi: 10.1016/j.jneumeth.2007.03.016

Yacoub, E., Harel, N., and Ugurbil, K. (2008). High-field fMRI unveils orientation columns in humans. *Proc. Natl. Acad. Sci. U.S.A.* 105, 10607–10612. doi: 10.1073/pnas.0804110105

Yoshioka, T., Levitt, J. B., and Lund, J. S. (1992). Intrinsic lattice connections of macaque monkey visual cortical area V4. *J. Neurosci.* 12, 2785–2802.

Zingg, B., Hintiryan, H., Gou, L., Song, M. Y., Bay, M., Bienkowski, M. S., et al. (2014). Neural networks of the mouse neocortex. *Cell* 156, 1096–1111. doi: 10.1016/j.cell.2014.02.023

Conflict of Interest Statement: The authors declare that the research was conducted in the absence of any commercial or financial relationships that could be construed as a potential conflict of interest.

frontiers in Neuroanatomy

ORIGINAL RESEARCH
published: 13 May 2015
doi: 10.3389/fnana.2015.00054

Cytoarchitectonic mapping of the human brain cerebellar nuclei in stereotaxic space and delineation of their co-activation patterns

Stefanie Tellmann[1,2], Sebastian Bludau[2], Simon Eickhoff[2,3], Hartmut Mohlberg[2], Martina Minnerop[2] and Katrin Amunts[2,4]**

[1] Department of Psychiatry, Psychotherapy and Psychosomatics, RWTH Aachen University and JARA-Brain, Aachen, Germany, [2] Institute of Neuroscience and Medicine (INM-1), Structural and Functional Organization of the Human Brain, Research Centre Jülich, Jülich, Germany, [3] Institute for Clinical Neuroscience and Medical Psychology, Heinrich Heine University, Düsseldorf, Germany, [4] Cécile and Oskar Vogt Institute of Brain Research, Heinrich Heine University, Düsseldorf, Germany

OPEN ACCESS

Edited by:
Kathleen S. Rockland, Boston University School of Medicine, USA

Reviewed by:
Antonio Di Ieva, Macquarie University Hospital, Australia
Andreas Wree, University of Rostock, Germany

***Correspondence:**
Katrin Amunts and Stefanie Tellmann, Institute of Neuroscience and Medicine (INM-1), Structural and Functional Organization of the Human Brain, Research Centre Jülich, Leo-Brandt-Straße, D-52428 Jülich, Germany
k.amunts@fz-juelich.de; s.tellmann@fz-juelich.de

Received: 12 March 2015
Accepted: 19 April 2015
Published: 13 May 2015

Citation:
Tellmann S, Bludau S, Eickhoff S, Mohlberg H, Minnerop M and Amunts K (2015) Cytoarchitectonic mapping of the human brain cerebellar nuclei in stereotaxic space and delineation of their co-activation patterns. Front. Neuroanat. 9:54. doi: 10.3389/fnana.2015.00054

The cerebellar nuclei are involved in several brain functions, including the modulation of motor and cognitive performance. To differentiate their participation in these functions, and to analyze their changes in neurodegenerative and other diseases as revealed by neuroimaging, stereotaxic maps are necessary. These maps reflect the complex spatial structure of cerebellar nuclei with adequate spatial resolution and detail. Here we report on the cytoarchitecture of the dentate, interposed (emboliform and globose) and fastigial nuclei, and introduce 3D probability maps in stereotaxic MNI-Colin27 space as a prerequisite for subsequent meta-analysis of their functional involvement. Histological sections of 10 human *post mortem* brains were therefore examined. Differences in cell density were measured and used to distinguish a dorsal from a ventral part of the dentate nucleus. Probabilistic maps were calculated, which indicate the position and extent of the nuclei in 3D-space, while considering their intersubject variability. The maps of the interposed and the dentate nuclei differed with respect to their interaction patterns and functions based on meta-analytic connectivity modeling and quantitative functional decoding, respectively. For the dentate nucleus, significant ($p < 0.05$) co-activations were observed with thalamus, supplementary motor area (SMA), putamen, BA 44 of Broca's region, areas of superior and inferior parietal cortex, and the superior frontal gyrus (SFG). In contrast, the interposed nucleus showed more limited co-activations with SMA, area 44, putamen, and SFG. Thus, the new stereotaxic maps contribute to analyze structure and function of the cerebellum. These maps can be used for anatomically reliable and precise identification of degenerative alteration in MRI-data of patients who suffer from various cerebellar diseases.

Keywords: cytoarchitecture, cerebellar nuclei, brain mapping, human brain atlas, SPM Anatomy Toolbox

Introduction

The cerebellar nuclei show a complex morphology and their full extent is partly invisible in routine Magnetic Resonance Imaging (MRI). Recently, a MRI-based atlas (SUIT) of the

three parted cerebellar nuclei (dentate, interposed, and fastigial), which is based on 7T MR images of 23 subjects, has been introduced (Diedrichsen et al., 2011). Its spatial resolution is 0.5 mm. This resolution, however, does not enable to identify cellular details as obtained in histological mapping in cell-body stained sections. Such detailed maps could be beneficial for an anatomical reliable and precise identification of activation foci obtained in neuroimaging experiment, or degenerative alteration in MRI-data of patients who suffer from various cerebellar diseases.

Impairment of the cerebellum and its output pathways can lead to several clinical syndromes, e.g., cerebellar ataxia (Manto, 2002). Neurodegeneration, targeting within the cerebellum especially the dentate nucleus, occurs, e.g., in an autosomal dominant inherited disorder, called Spinocerebellar Ataxia Type 3 (SCA3; Rub et al., 2008, 2013; Scherzed et al., 2012). However, these neuropathologically observed changes of the dentate nuclei in SCA3 have yet not been demonstrated by imaging techniques *in vivo*, most probably due to the spatial resolution.

The four cerebellar nuclei, i.e., the dentate (DN), emboliform (EN), globose (GN), and fastigial nucleus (FN), are located in the depth of the cerebellar hemispheres in close vicinity to the fourth ventricle. The most laterally located dentate nucleus appears as a convoluted band containing rounded large multipolar neurons. It is the largest nucleus and well visible in routine MR images. A partition of the human dentate nucleus into a dorsal micro- and a ventral macrogyric part has been mentioned in an early description of the cerebellar nuclei (Stilling, 1864). Since then, this subdivision has been repeatedly replicated both in early (Winkler, 1926; Vogt and Vogt, 1942; Hassler, 1950; Fix and Treff, 1970) and more recent (Arras, 1987; Voogd, 2003; Deoni and Catani, 2007) studies. It was also reported that the ventral part contains more iron than the dorsal one (Gans, 1924), which may indicate an increased vulnerability for degenerative disorders (e.g., Schulz and Pandolfo, 2013). A similar dorsal–ventral subdivision of the dentate nucleus was also shown in primates by using invasive tracing (Dum and Strick, 2003).

In contrast to the dentate nucleus, the interposed nucleus – the wedge-shaped emboliform nucleus and the more rounded globose nucleus – are found within the paravermal region, next to the medial border of the dentate nucleus, and close to the dentate hilus. The fastigial nucleus, also known as tegmental nucleus, is the most medially located cerebellar nucleus and builds the roof of the fourth ventricle (e.g., Kozlova, 1984; Nieuwenhuys et al., 2008). Each nucleus receives inhibitory afferents from distinct parts of the ipsilateral cerebellar cortex. Large parts of the cerebellar cortex project to the dentate nuclei of both hemispheres. The interposed nuclei receive information from the paravermal zone, and the fastigial nucleus from the vermal cerebellar cortex as well as from the flocculus (Manto, 2002).

All cerebellar nuclei are interconnected with the rest of the brain through the cerebellar peduncles. The middle cerebellar peduncle relays information from the cerebral cortex via the pontine nuclei to cerebellar structures. Efferent fibers of the dentate and interposed nuclei reach, via the superior peduncle, thalamic nuclei, and sensorimotor areas (Carpenter, 1991; Manto, 2002; Dum and Strick, 2003). Further efferents from the dentate nucleus project to the red nucleus and subsequently to the inferior olives; the latter in turn project back to the dentate nucleus, forming the *Guillain-Mollaret-Triangle* (Lavezzi et al., 2009). The fastigial nucleus sends projections through the inferior peduncle to the vestibular nuclei and the reticular formation. A few fibers depart from the cerebellar uncinate fascicle and ascend to thalamic subnuclei VLc and VPLo (Carpenter, 1991).

The vascular network forms another aspect of cerebellar organization. The cerebellar nuclei are supplied by the rhomboidal artery, a branch of the superior cerebellar artery (Icardo et al., 1982). It runs in parallel to the superior cerebellar peduncle. When the hilum of the dentate nucleus is reached, the rhomboidal artery divides into a network of smaller vessels, the arcuate arterioles, showing a precise vascular pattern, and building anastomoses with cortical branches from the posterior inferior cerebellar artery (Icardo et al., 1982). The veins of the dentate nucleus are composed of several veins draining its external surface (into the venous star and the cortex-perforating veins) and one single vein draining its internal surface, emerging from the hilum of the dentate nucleus, and running along the superior cerebellar peduncle to the precentral cerebellar vein (Tschabitscher and Perneczky, 1976; Tschabitscher, 1979; Di Ieva et al., 2011).

The role of mammalian cerebellar nuclei in motor functions has been described in detail (Jansen and Brodal, 1942; Chambers and Sprague, 1955; Jansen et al., 1958), but in accordance to more recent studies the cerebellar nuclei – especially the dentate nucleus – are not only involved in modulation of movements but also in cognition (Dum and Strick, 2003; Schmahmann and Caplan, 2006; Schmahmann, 2010; Kuper et al., 2011a, 2012; Timmann, 2012). The dorsal part of the dentate nucleus is supposed to be responsible for motor performance whereas a ventral part was identified as cognitive or non-motor part. Assuming a functional subdivision of the cerebellar nuclei (Manto, 2002; Timmann et al., 2003), it was postulated that certain nuclei or subdivisions of a nucleus are involved in a specific task of cognition and even emotion (see also Gerwig et al., 2003; Maschke et al., 2003; McNaughton et al., 2004; Kuper et al., 2013). For example it has been shown that the fastigial and interposed nuclei take part in conditioning (Timmann, 2012). The dentate nucleus, regarded as the phylogenetic highest developed cerebellar nucleus in humans (e.g., Mihajlovic and Zecevic, 1986; O'Rahilly and Müller, 2006), seems to be involved in speech or cognitive–associative learning (Thurling et al., 2011).

Several studies reported data regarding volumes, cell densities, and cell sizes of the cerebellar nuclei in humans (cf. Kölliker, 1889; Lugaro, 1895; Cajal and Santiago, 1953; Braak and Braak, 1983; Kozlova, 1984; Mihajlovic and Zecevic, 1986; Arras, 1987; Yamaguchi et al., 1989; Carpenter, 1991; Voogd, 2003; O'Rahilly and Müller, 2006; Manto, 2010; Ristanovic et al., 2010). Most of these studies were confined to the dentate nucleus and did not provide the nowadays required resolution and histologic preparation standards (e.g., shrinkage correction). The most accurate histological post mortem data are based on 100 human cerebella (age range 22–72 years) with a histological sections thickness of 0.5 mm (Kozlova, 1984). Albeit only maxima of the x, y, z extension had been reported this data allowed to roughly estimate the volume of each cerebellar nucleus. Diedrichsen et al. (2011) provided MR-based volume data of the cerebellar nuclei

and additionally computed the mean of the *x*, *y*, and *z* maxima, allowing an indirect comparison with Kozlova's (1984) data. The aim of the present study was to map the cerebellar nuclei in histological sections of 10 *post mortem* brains to create cytoarchitectonic 3D probability maps in a standard reference space and to evaluate anatomical and functional partition of the cerebellar nuclei. Therefore we integrated the computed maps in the SPM Anatomy Toolbox (Eickhoff et al., 2005), and then used the respective representations for meta-analytic connectivity modeling as well as functional decoding (Eickhoff et al., 2012). Consequently we achieved a cytoarchitectonically based representation of the cerebellar nuclei in 3D space, and assigned its corresponding function by meta-analytic connectivity modeling.

Materials and Methods

Histological Techniques

We investigated 10 human *post mortem* brains (male/female: 5/5, age 58.7 ± 17.3 years, range 30–85 years; cf. **Table 1**) collected through the body donor program of the University of Düsseldorf (Germany) in accordance to local legal and ethical requirements. Subjects had no known history of neurological or psychiatric diseases. Details of the histological processing have been previously described in detail (e.g., Amunts et al., 1999). In short, brains were fixed for several months in 4% formalin or Bodian fixative. During fixation, the brains were suspended on the basilar artery to avoid compression or distortions. T1-weighted MRI scans [1.5T Siemens Magnetom SP scanner, 3D fast low angle shot (3D FLASH) pulse sequence, flip angle = 40°, TR = 40 ms, TE = 5 ms, voxel size = 1 mm × 1 mm × 1.17 mm] were obtained to get a shape reference for further 3D-reconstruction of the histological sections. Artifacts (e.g., shrinkage of the brain, embedding in paraffin, and distortion of the sections due to cutting) could be eliminated in the reconstructed volume by matching it with the MR volume of the same brain using linear and non-linear correction procedures (cf. Homke et al., 2009). Following dehydration and embedding in paraffin, the brains were sectioned (20 μm). Nine coronal and one horizontal series of sections were analyzed. The sections were mounted on gelatin-coated glass slides, and stained for cell bodies with a modified silver method (Merker, 1983). On digital images of every 60th section the region of interest was marked and captured using a light microscope (Zeiss). The contours of the nuclei were drawn in serial section of both hemispheres, using high-resolution images (20 μm) of histological sections. Therefore, every 15th section was scanned with a flatbed scanner. The identification of the nuclei was done in accordance to criteria described in previous studies (e.g., Stilling, 1864; Weidenreich, 1899; Jakob, 1928; Carpenter, 1991; Nieuwenhuys et al., 2008).

TABLE 1 | Sample of *post mortem* brains used for cytoarchitectonic analysis.

ID	Age	Sex	Shrinkage factor	Brain weight (*g*)	Cause of death
5	59	Female	2.15	1142	Cardio-respiratory insufficiency
6	54	Male	2.50	1757	Myocardial infarct
7	37	Male	2.25	1437	Heart failure
8	72	Female	1.90	1216	Renal failure
9	79	Female	1.51	1110	Heart failure
10	85	Female	1.72	1046	Mesenteric artery infarction
11	74	Male	2.20	1381	Cardiac infarction
12	43	Female	2.14	1198	Cardio-respiratory insufficiency
15	54	Male	1.60	1260	Accident
21	30	Male	1.84	1409	Morbus Hodgkin

Volumetric Analysis of the Cerebellar Nuclei

The volumes of the nuclei were measured as previously described (Amunts et al., 2007). They were normalized and expressed as the fraction of the individual total brain volume in order to account for individual differences in total brain volume. The volumes were tested for sex and interhemispheric differences, as well as their interaction using pairwise permutation tests ($p < 0.05$; false discovery rate (FDR) corrected for multiple comparisons).

Analysis of the Subdivision of the Dentate Nucleus

Cell densities of the dorsal and ventral parts of the dentate nucleus were measured in order to analyze differences between both parts. Therefore, the marked regions of interest on images of histological sections were obtained using a CCD-Camera (Axiocam MRm, ZEISS, Germany), which was connected to a light microscope (Axioplan 2 imaging, ZEISS, Germany) and operated by the Zeiss image analysis software Axiovision (4.8.0). Three sections per structure, hemisphere and brain were analyzed. Cell densities where measured using parts of the Grey Level Index (GLI) calculation pipeline to estimate the volume fraction of cell bodies (Wree et al., 1982; Schleicher and Zilles, 1990; Schleicher et al., 1999).

Therefore we delineated the dentate nucleus into a ventral and a dorsal partition using ImageJ[1]. In a next step, the density of cells of each part was measured using in-house software based on MATLAB 8.1[2]. Both parts differed in the distribution, pattern, and morphology of neurons (see Results), resulting in a clear-cut border. Cell bodies were segmented in order to calculate binary-images (Schleicher and Zilles, 1990; Schleicher et al., 1999), and to measure the density of cells of each part using in-house software based on MATLAB 8.1[2]. Subsequently we calculated a quotient from the area of the segmented cells and the area of the whole structure [cell area (μm^3)]/[structure area (μm^3)] and compared the mean values between the two parts and hemispheres. Differences in cell density between the dorsal and ventral dentate nucleus were assessed using the non-parametric Wilcoxon-Sign-Rank test ($p < 0.05$, Bonferroni-corrected for multiple comparisons).

In addition, a Folding Index (FI) was estimated to quantify putative differences between a micro- and macrogyric aspect,

[1]http://imagej.nih.gov/ij/

[2]http://mathworks.com

which has previously been described (cf. Winkler, 1926; Voogd, 2003). These studies suggested that the dorsal part matches with the description of a microgyric part, while the ventral represents a macrogyric part. The FI is comparable to the Gyrification Index (Zilles et al., 1988, 2013), but estimates the gyrification of nuclei instead of the whole brain. In a first step, the contour of the dentate nucleus was labeled in images of 10 histological sections per hemisphere. In a second step, a convex hull representing the outer border of the dentate nucleus was drawn. The FI was then calculated as the ratio of these two measurements, i.e., FI = [Length (whole contour)]/[Length (hull contour)].

Analysis of the Subdivision Generation of Probability Maps and 3D Reconstruction

The delineated nuclei were 3D-reconstructed in each *post mortem* brain, and then normalized to the single subject reference template of the Montreal Neurological Institute to a resolution of 1 mm × 1 mm × 1 mm (stereotaxic MNI-Colin27; Collins et al., 1994; Holmes et al., 1998; Evans et al., 2012). In addition, a manual segmentation of the cerebellum was performed using the ITK Snap software (Yushkevich et al., 2006) to improve the registration of the cerebellum. Superimposing the individual maps of each nucleus across brains then, yielded a probabilistic map, indicating how likely each nucleus was found at each voxel of the stereotaxic MNI-Colin27 template space.

Mapping Function and Connectivity of the Delineated Nuclei

Functional interactions during task performance, in the context of neuroimaging experiments, i.e., co-activations, of the cerebellar nuclei were identified by meta-analytic connectivity modeling (Eickhoff et al., 2012) using the BrainMap database[3] (Fox and Lancaster, 2002; Laird et al., 2009, 2011). From this database, only mapping experiments in healthy subjects were considered, which yielded approximately 7.500 experiments at the time of analysis. Among these, all experiments with at least one peak activation coordinate within cytoarchitectonically defined seed regions were identified. The number of contributing studies was marginal for the ventral dentate nucleus (VDN) and dorsal dentate nucleus (DDN) separately or the emboliform and globose nuclei. Accordingly only minor effects occurred for probing these subregions. Therefore, the maximum probability map representations of the cytoarchitectonically defined entire dentate nucleus and interposed nucleus in stereotaxic MNI-Colin27 space were used as seed regions (Eickhoff et al., 2006). Across these, an Activation Likelihood Estimation meta-analysis (Eickhoff et al., 2012; Turkeltaub et al., 2012) was conducted in order to identify areas of converging activity across these experiments. Evidently, the highest convergence between studies occurs within the seed (as all included experiments were selected based upon co-activity with the seed region). In comparison, significant ($p < 0.05$) convergence in areas beyond the seed is indicative of consistent co-activation (i.e., functional connectivity) with the seed region. The resulting statistically thresholded co-activation map ($p < 0.05$, cluster-level family wise error (FWE) corrected for multiple comparisons) thus provided the results of the meta-analytic connectivity modeling analysis.

The functional characterization of the cerebellar nuclei was based on the meta-data available for each neuroimaging experiment included in the BrainMap database. Functional profiles were determined by identifying taxonomic labels, for which the probability of finding activation in the respective region was significantly ($p < 0.05$) higher than by chance. Significance was established using a binomial test ($p < 0.05$, corrected for multiple comparisons; Cieslik et al., 2013; Clos et al., 2013).

[3]www.brainmap.org

Results

Cytoarchitecture of the Cerebellar Nuclei

An overview of the cytoarchitectonic features of the four cerebellar nuclei including the subdivision of the dentate nucleus is provided in **Figure 1**. **Figure 2** shows a 3D representation of the cerebellar nuclei to illustrate the intern-relationship between the delineated structures.

The dentate nucleus is the largest and most lateral cerebellar nucleus. It consisted of densely packed rounded multipolar neurons. Although there was a mixture of cell sizes within the dentate nucleus, large cells were predominant. The dentate nucleus appeared as a convoluted band with its hilus located medially. Based on local differences in cell density and size, the dentate nucleus could be microscopically subdivided in a dorsal and ventral part by a clear-cut border, whereby the dorsal part had a significantly higher cell density than the ventral one. The mean Grey Level Index values, estimating cell density observer-independently (Wree et al., 1982; Schleicher and Zilles, 1990; Schleicher et al., 1999), and the corresponding SDs were as follows: left dorsal: 4.09 ± 0.78; right dorsal 4.09 ± 0.74; left ventral: 3.36 ± 0.62; right ventral: 3.45 ± 0.65 (cf. **Figure 3**). Differences between dorsal and ventral parts were significant ($p < 0.05$), whereas left–right differences did not reach significance ($p > 0.05$).

In contrast, no differences were observed with respect to the FI, which was nearly identical between both parts (FI dorsal average of left and right = 1.69 ± 0.57; ventral average of left and right = 1.69 ± 0.62; cf. **Figure 4**).

The emboliform nucleus was positioned close to the vermis, and next to the dentate hilus in all 10 brains. In comparison to the dentate nucleus, it was formed by less densely packed large neurons (**Figure 1**).

The globose nucleus was also located close to the vermis, between the emboliform and the fastigial nucleus. It was the smallest of the four cerebellar nuclei. In all investigated brains, its neurons were small and more densely packed as compared to those in the emboliform nucleus (**Figure 1**). As previously described (e.g., Kozlova, 1984), its shape did not follow the name "globose," as it often appeared variably elongated.

The fastigial nucleus was the most medially located cerebellar nucleus, located in close vicinity of the fourth ventricle. Starting at its lateral border, tentacle-like bands of more spikey cells were visible that spread to the lateral border of the vestibular nucleus.

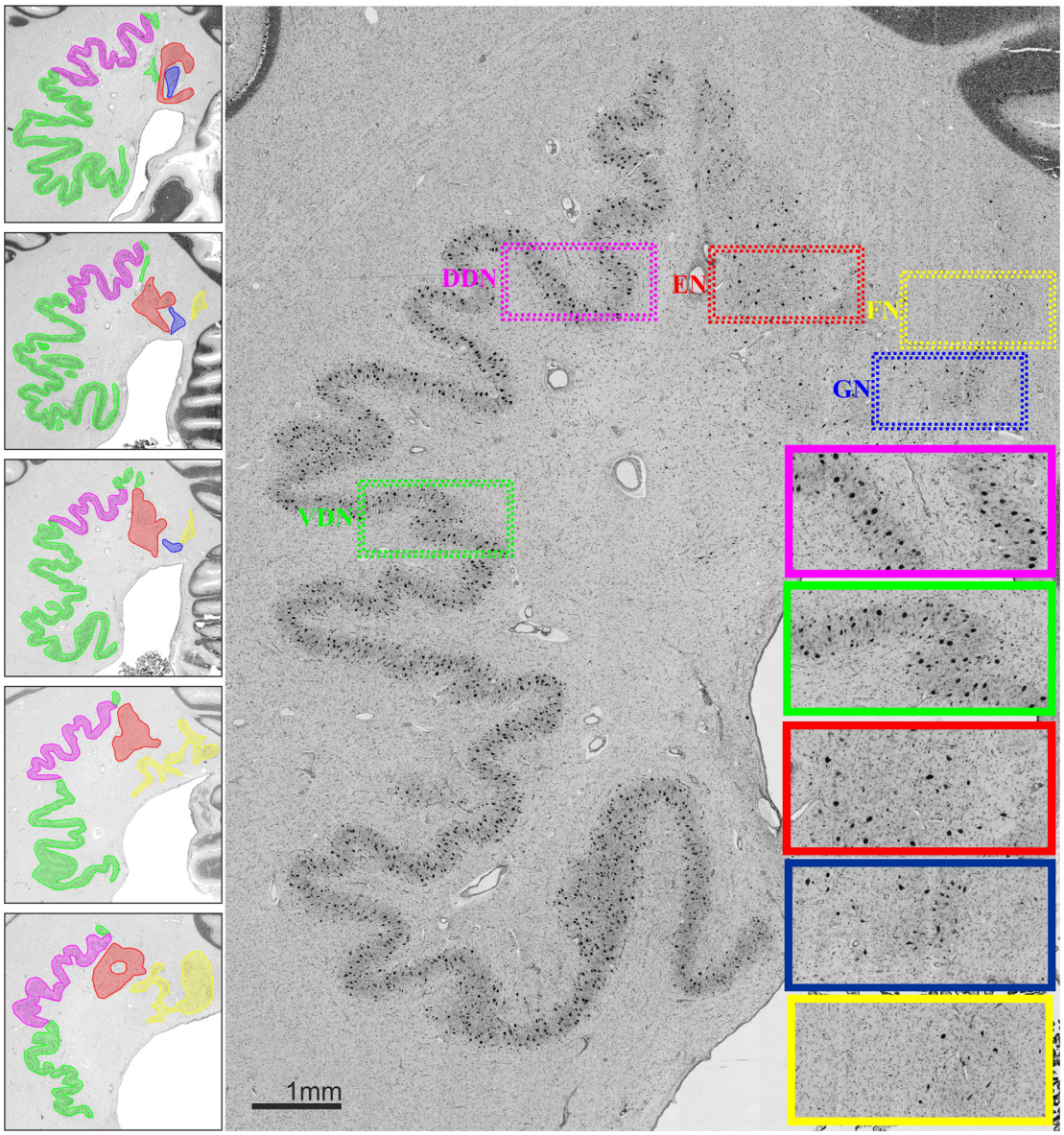

FIGURE 1 | (Left) Localization and extent of cerebellar nuclei in a rostro-caudal sequence of histological sections of a post mortem brain; distance between sections 60 μm. **(Right)** Cytoarchitecture of each cerebellar nucleus and the two parts of the dentate nucleus. Magenta: dorsal dentate nucleus (DDN); green: ventral dentate nucleus (VDN); red: emboliform nucleus (EN); blue: globose nucleus (GN); yellow: fastigial nucleus (FN).

Volumetric Analysis of the Cerebellar Nuclei

There were no statistically significant effects ($p < 0.05$) of sexes or hemisphere on the volumes of any of the delineated nuclei (**Table 2**). Bilateral mean values for each cerebellar nucleus and their SD are shown in **Table 2**. The dentate nucleus was the largest cerebellar nucleus, with its dorsal part being about three times smaller than the ventral one. Nevertheless, this (smaller) dorsal part of the dentate nucleus was still about two times larger than the emboliform and the fastigial nuclei. The globose nucleus as the smallest cerebellar nucleus comprised only approximately a fifth part of the volume of the emboliform nucleus.

Probabilistic Maps of the Cerebellar Nuclei

All delineated structures were spatially normalized to the stereotaxic MNI-Colin27 single subject template and then combined across subjects to calculate probabilistic maps of cerebellar nuclei in stereotaxic space. In correspondence to the localization of the nuclei in each individual brain, all nuclei were located in the depth of the cerebellar white matter and showed the expected relative position (laterally: dentate nucleus; paravermal: first emboliform, then globose nucleus; medial: fastigial nucleus). The interindividual variability of the nuclei was low (**Figure 5**). There was only a relatively moderate overlap between the probabilistic maps of neighboring nuclei. The

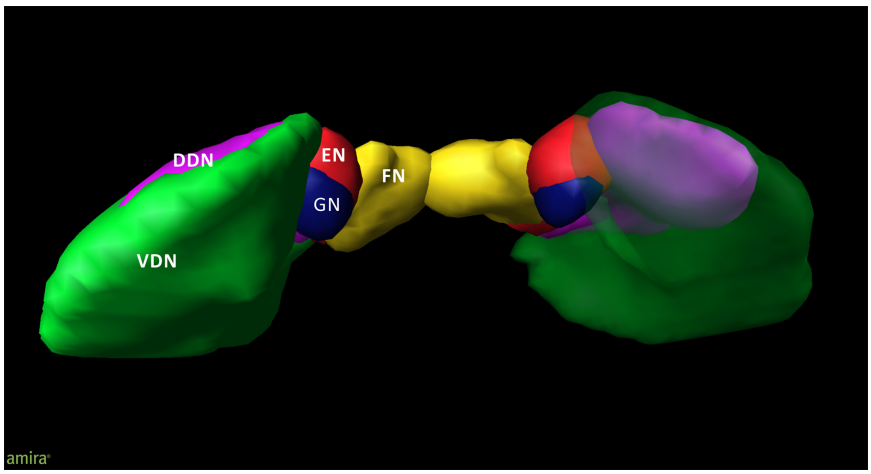

FIGURE 2 | 3D model of the deep cerebellar nuclei (posterior to anterior view) of an individual brain (post mortem brain10); visualization by Amira 5.6.0 (www.amira.com). Dorsal dentate nucleus (DDN; magenta); ventral dentate nucleus (VDN; green); emboliform nucleus (EN; red); globose nucleus (GN; blue); fastigial nucleus (FN; yellow). Due to the smoothing, the dentate appears less denticulated than it is. The transparency of the right ventral dentate nucleus clarifies the partly covered extend of the DDN.

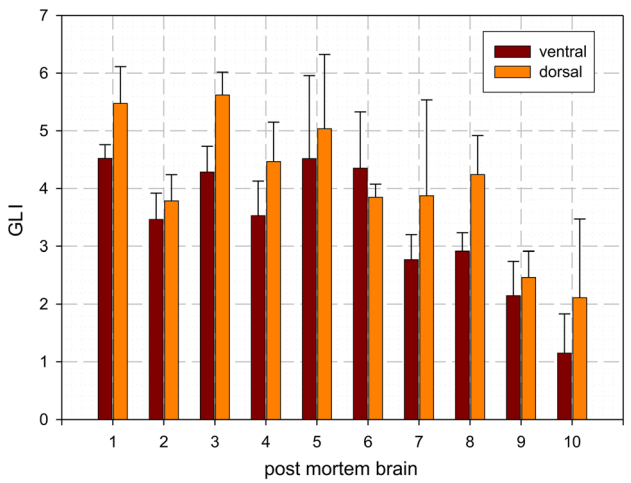

FIGURE 3 | Mean values and SD of cell density distribution of the ventral and dorsal dentate nucleus as estimated by the Grey Level Index (GLI): [cell area (μm^2)]/[structure area (μm^2)].

probabilistic maps were used to analyze co-activation patterns in order to characterize their involvement into different cognitive functions.

Whole-Brain Co-activation Patterns of the Cerebellar Nuclei

Co-activation mapping and functional decoding for the combined dentate (ventral and dorsal) and interposed (emboliform and globose) nuclei were performed. For these analyses, the regions of interest were defined by the maximum probability map representations of the respective histologically defined nuclei in stereotaxic MNI-Colin27 space (Eickhoff et al., 2006). For the dentate nucleus, we found significant ($p < 0.05$, corrected for multiple comparisons) co-activations with thalamus, supplementary motor area (SMA) and putamen as well as within area 44 (Amunts et al., 1999), superior parietal area 7PC (Scheperjans et al., 2008a), inferior parietal area PFt (Caspers et al., 2006), and the superior frontal gyrus (SFG). The interposed nucleus likewise showed, though more limited, co-activation with the putamen, SMA, area 44 and the SFG (cf. **Table 3**). Directly compared with the dentate nucleus (cf. **Figure 6**), the interposed nucleus showed a significantly ($p < 0.05$) higher connectivity with the left insular lobe [stereotaxic MNI-Colin27: (−40, 0, 2), cluster size: 104 mm^3] and the left thalamus [stereotaxic MNI-Colin27: (−10, −18, 8); cluster size: 90 mm^3]. In turn, the dentate nucleus showed higher connectivity with left area 6 [SMA; stereotaxic MNI-Colin27: (−4, −14, 54); cluster size: 215 mm^3], the left inferior parietal lobe [Pft; stereotaxic MNI-Colin27: (−46, −40, 56); cluster size: 138 mm^3], and the inferior frontal gyrus [area 44, stereotaxic MNI-Colin27: (−58, 8, 18); cluster size: 56 mm^3].

The behavioral domains and paradigm classes significantly ($p < 0.05$) associated with the dentate and interposed nuclei are illustrated in **Figure 6**. Both structures were found to be activated by pain. In addition, the interposed nucleus (green) was significantly ($p < 0.05$) associated with music comprehension and visual perception. In turn, the behavioral domains and paradigm classes of the dentate nucleus (red) comprised cognitive, speech, and in particular motor related functions.

Discussion

Cerebellar nuclei have a strategic position by representing the almost unique source of output within the cerebellar circuitry (Manto and Oulad Ben Taib, 2010). This study presents cytoarchitectonically based 3D probability maps of the human

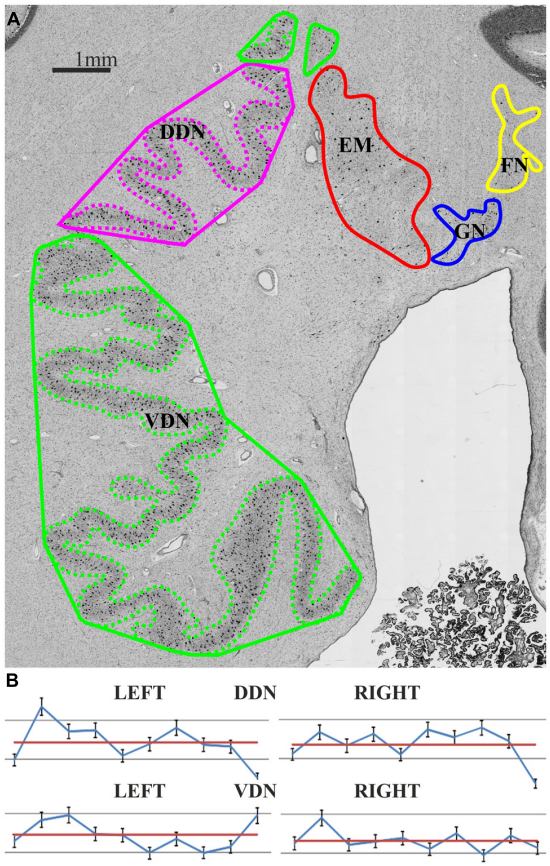

FIGURE 4 | (A) The Folding Index (FI) provides information about the gyrification and was estimated as the quotient of Length (whole contour: dashed line) per Length (hull contour: solid line). Magenta: dorsal dentate nucleus (DDN); green: ventral dentate nucleus (VDN); red: emboliform nucleus (EN); blue: globose nucleus (GN); yellow: fastigial nucleus (FN); **(B)** Individual FI values of each partition and hemisphere of 10 post mortem brains (blue: FI; red: mean FI).

cerebellar nuclei including their application to study their function and functional connectivity. Besides providing information on the cytoarchitectonic characteristics and precise anatomical localization of each nucleus, the current study also subdivided the dentate nucleus into a ventral and a dorsal part based on cytoarchitectonic criteria. These maps of the cerebellar nuclei in the stereotaxic MNI-Colin27 reference space are available to the scientific community[4], and may facilitate interpretation of *in vivo* structural and functional imaging data with respect to the microstructural correlates. We here employed these maps to investigate task-based functional connectivity of the cerebellar nuclei using meta-analytic co-activation mapping and to perform a quantitative functional characterization.

Mapping Results

In this study, the borders of the cerebellar nuclei, were delineated in 10 *post mortem* brains based on cytoarchitectonic differences, and stereotaxic maps were calculated (**Table 2** for comparison of the *post mortem* and recent MRI data: Diedrichsen et al., 2011). The current volume of the dentate nucleus is nearly identical to that reported based on MRI measurements. Small differences between both estimates may be caused by partial volume effects, which are more relevant in lower resolution MR images. Three other previous MRI studies provided substantially larger volumes (840 mm^3: Dimitrova et al., 2002, 2006; 900 mm^3: Deoni and Catani, 2007). They may overestimate the true volume, caused by the complex shape of the dentate with its large surface area. Finally, an older histological estimate yielded a much lower volume of the dentate nucleus, but no shrinkage correction was applied (155 mm^3: Höpker, 1951). Still, the volume would be considerably smaller than that of the present study. The volume of the interposed nucleus of the present study was slightly larger than previously estimated by MRI (Diedrichsen et al., 2011). The volume of the fastigial nucleus in the Diedrichsen et al. (2011) MRI atlas finally seemed to be underestimated relative to the current *post mortem* results, but also in comparison to earlier histological data (Dejerine and Dejerine-Klumpke, 1901; Jakob, 1928; Jansen et al., 1958).

To the best of our knowledge, no previous volumetric data has been presented for the ventral and dorsal subdivisions of the dentate nucleus and the subdivided interposed (globose and emboliform) nucleus. While the small size of these structures is still a major challenge for MRI based delineation *in vivo*, ultra-high field MRI with high resolution may allow an even better delineation in future (Forstmann et al., 2012). In summary, the estimated volumes for all cerebellar nuclei differ to some degree between studies of *in vivo* and *post mortem* approaches.

Although a comparison of volume data for the subdivision of dentate nucleus is currently not available, we will here contrast the current *post mortem* data with some other methods and studies. A significantly different cell density distribution between the ventral and dorsal part of the dentate nucleus, with the latter featuring a higher cell density and bigger cells, is in accordance with previous reports (Arras, 1987; Dum et al., 2002; Voogd, 2003; Timmann, 2012). Albeit transitional areas were reported (Arras, 1987), the present observation revealed a clear-cut border between the ventral and the dentate nucleus. Interestingly, the reported volume differences between these two parts of the dentate nucleus, with the ventral part being about three times larger, may relate to evolutionary development.

The larger size of the human ventral dentate nucleus may reflect the general evolutionary trend of "neocorticalization" and the marked development of higher motor functions and ultimately cognition in the primate lineage (Fix and Treff, 1970). Accordingly, the (larger) ventral part of the dentate nucleus has been termed "neo-dentate" (cf. Weidenreich, 1899). Moreover, the embryogenetic differentiation of the ventral dentate nucleus developed to the same time as the cerebellar hemispheres, while development of the dorsal part coincided with that of the vermal parts and the anterior lobe of the cerebellum (Murofushi, 1974). From a different angle, it has been shown that in case of neocerebellar atrophy the dorsal dentate nucleus remains untapped (Brun, 1917). Moreover, the number of interneurons is higher in

[4]www.fz-juelich.de/inm/inm-1/EN

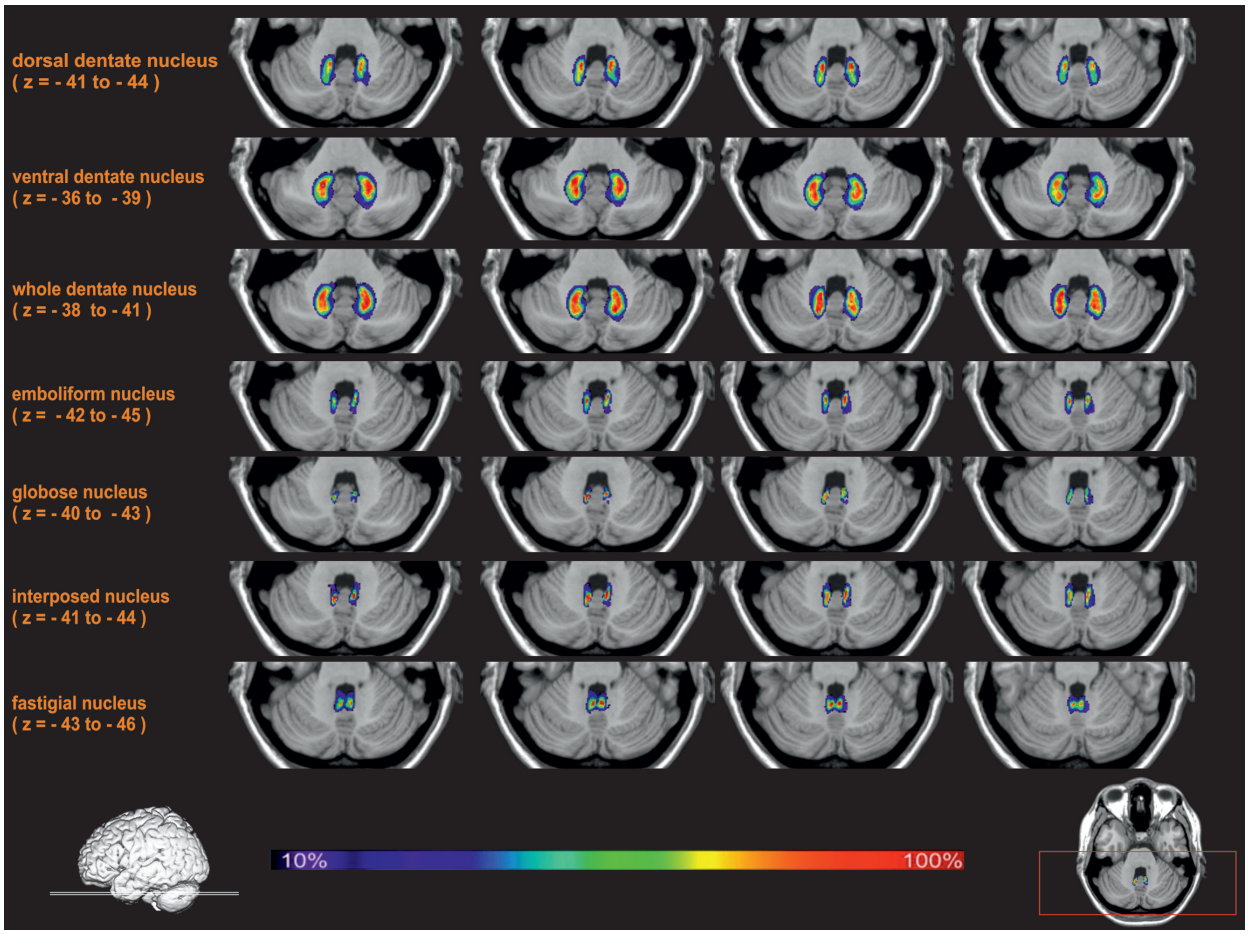

FIGURE 5 | Exemplary transversal sections through the stereotaxic MNI-Colin27 reference brain with probability maps of the cerebellar nuclei. The maximal overlap in each nucleus was 100% (shown in red). Regions with lower probabilities correspond to a higher intersubject variability and are shown in blue and green colors.

TABLE 2 | Mean volumes (mm^3) and SDs (in brackets) of each cerebellar nucleus of grouped hemispheres and sexes were calculated from the shrinkage corrected volumes of 10 post mortem brains. Male/female volumes represent the mean volumes of left and right hemisphere volumes. [(pair wise permutation tests; no differences with $p < 0.05$); DN: dentate nucleus; DDN: dorsal dentate nucleus; VDN: ventral dentate nucleus; IN: interposed nucleus; EN: emboliform nucleus; GN: globose nucleus; FN: fastigial nucleus] supplemented by MRI volume data [1] Diedrichsen et al. (2011).

	Post mortem					MRI[1]	
	Right	Left	Male	Female	Bilateral	Right	Left
DN	394.5 (94.5)	390.2 (99.3)	433.2 (104.9)	351.5 (75.6)	784.7 (192.7)	366.1 (85.2)	362.8 (89.2)
DDN	93.5 (46.2)	88.7 (42.1)	94.9 (49.6)	87.2 (43.2)	182.1 (88.1)	–	–
VDN	301.0 (61.3)	301.5 (67.9)	338.3 (57.8)	264.3 (48.6)	602.5 (127.3)	–	–
IN	59.8 (12.2)	59.0 (11.9)	61.2 (9.1)	57.6 (14.8)	118.7 (23.5)	36.1 (11.4)	35.9 (14.2)
EN	50.2 (12.4)	49.5 (12.2)	50.4 (12.3)	49.3 (13.1)	99.7 (24.0)	–	–
GN	9.5 (4.0)	9.5 (4.7)	10.8 (5.3)	8.3 (3.1)	19.0 (8.5)	–	–
FN	45.0 (8.5)	46.4 (13.4)	50.8 (11.6)	40.5 (5.8)	91.4 (20.4)	8.2 (5.2)	9.2 (5.2)

the parvocellular – ventral – part of the dentate nucleus (Arras, 1987), which has been interpreted as a developmental adaptation, described similarly for the isocortex (Schlegelberger and Braak, 1982). In summary, there is thus converging evidence for a dorsal–ventral distinction of the human dentate nucleus in which the larger ventral part has co-evolved with the cerebral cortex (cf. "neocorticalization" Fix and Treff, 1970) and is related to higher cognitive-motor functions. Morphological differences have long been discussed as another aspect of such differentiation (Jansen et al., 1958; Fix and Treff, 1970; Arras, 1987). Summarized, the

TABLE 3 | Co-activation clusters for the cerebellar nuclei.

	Cluster Size	Z	Stereotaxic MNI-Colin27			Anatomic Localization (probabilistic anatomical location)
			x	*y*	*z*	
Dentate nucleus*	2163	6.94	−34	+22	+4	Left anterior Insula Lobe
		6.26	−26	+18	−4	Left Medial Putamen
		6.09	−52	+6	+38	Left Precentral Gyrus (BA 44[1])
		5.84	−46	+4	+8	Left Rolandic Operculum
		5.78	−48	+6	+6	Left Inferior Frontal Gyrus
		5.49	−54	+8	+22	Left Inferior Frontal Gyrus (BA 44[1])
	1701	8.32	−2	+2	+54	Left SMA
		4.55	+6	+18	+46	Right SMA
		4.29	+20	+0	+58	Right Superior Frontal Gyrus
	646	8.31	+38	+20	−2	Right Anterior Insula Lobe
		5.01	+36	−4	+2	Right Putamen
		4.34	+28	+10	−4	Right Putamen
		4.18	+24	−2	+2	Right Pallidum
	538	8.32	−12	+20	+4	Left Thalamus
		8.31	−14	+14	+6	Left Thalamus
		4.18	−20	−16	+0	Left Thalamus
	516	5.86	+58	+10	+24	Right Inferior Frontal Gyrus (BA 44[1])
		5.50	+58	+8	+10	Right Rolandic Operculum (BA 44[1])
	420	5.72	−42	−48	+50	Left Inferior Parietal Lobe (7PC[2]) Left Inferior Parietal Lobule (PFt[3])
		5.54	−30	−50	+50	Left Inferior Parietal Lobule (7PC[2])
		5.50	+58	+8	+10	Right Rolandic Operculum (BA 44[1])
Interposed nucleus*	640	5.49	+20	+0	+58	Right Superior Frontal Gyrus
		5.41	+0	+10	+5	Left SMA
		4.56	−4	+22	+44	Left SMA
		4.44	+8	+4	+60	Left SMA
		3.81	+12	+14	+40	Right SMA
		3.28	−4	+2	+60	Left SMA (BA 6[4])
	307	7.99	−14	−14	+10	Left Thalamus
	238	5.53	+28	+10	−4	Right Putamen
		4.10	+40	+18	−4	Right Anterior Insula Lobe
		3.99	+38	+16	−6	Right Anterior Insula Lobe
	266	4.65	−48	+8	+2	Left Rolandic Operculum (BA 44[1])
		4.51	−44	+14	−4	Left Anterior Insula Lobe
		3.78	−44	+0	+2	Left Insula Lobe
		3.45	−44	+24	−4	Left Inferior Frontal Gyrus
	243	5.01	−32	+16	+8	Left Insula Lobe
		4.65	−22	+6	+2	Left Putamen

*Macroanatomic localization with respect to gyri, sulci, and major subcortical nuclei; localization with respect to cytoarchitectonic probabilistic maps if available. *$p_{FDR} < 0.05$. [1]Amunts et al. (1999), [2]Scheperjans et al. (2008b), [3]Caspers et al. (2008), [4]Geyer (2004).*

magnocellular dorsal part has been described as microgyric and the parvocellular ventral part as macrogyric (e.g., Voogd, 2003). In contrast to previous reports on a macro- and microgyric part within the dentate nucleus (Winkler, 1926; Voogd, 2003) no differences were found with respect to the FI as a measure of "gyrification." This finding, in turn, is in accordance with another more recent study, where a gyrification difference within the dentate was only found in macaques but not in human brains (Sultan et al., 2010). Finally it should be mentioned, that the literature provides evidence for a more subtle and somatotopic distinction of the cerebellar cortex (Hampson et al., 1946; Snider and Eldred, 1952; Grodd et al., 2001). It can therefore be hypothesized that this may also apply to the cerebellar nuclei, which are interconnected with the different parts of the cerebellar cortex. Arras (1987) reported a transitional area between the ventral and dorsal dentate nucleus. Results of the present observation did not support this assumption, and no differences in cytoarchitecture have been observed in-between the dorsal and the ventral parts. Other studies point toward a somatotopic organization of the dentate nucleus in human (*in vivo*) and monkeys (tracer studies; Dum et al., 2002; Dum and Strick, 2003; Kuper et al., 2013). Dum et al. (2002) used tracer injections into the primary motor cortex

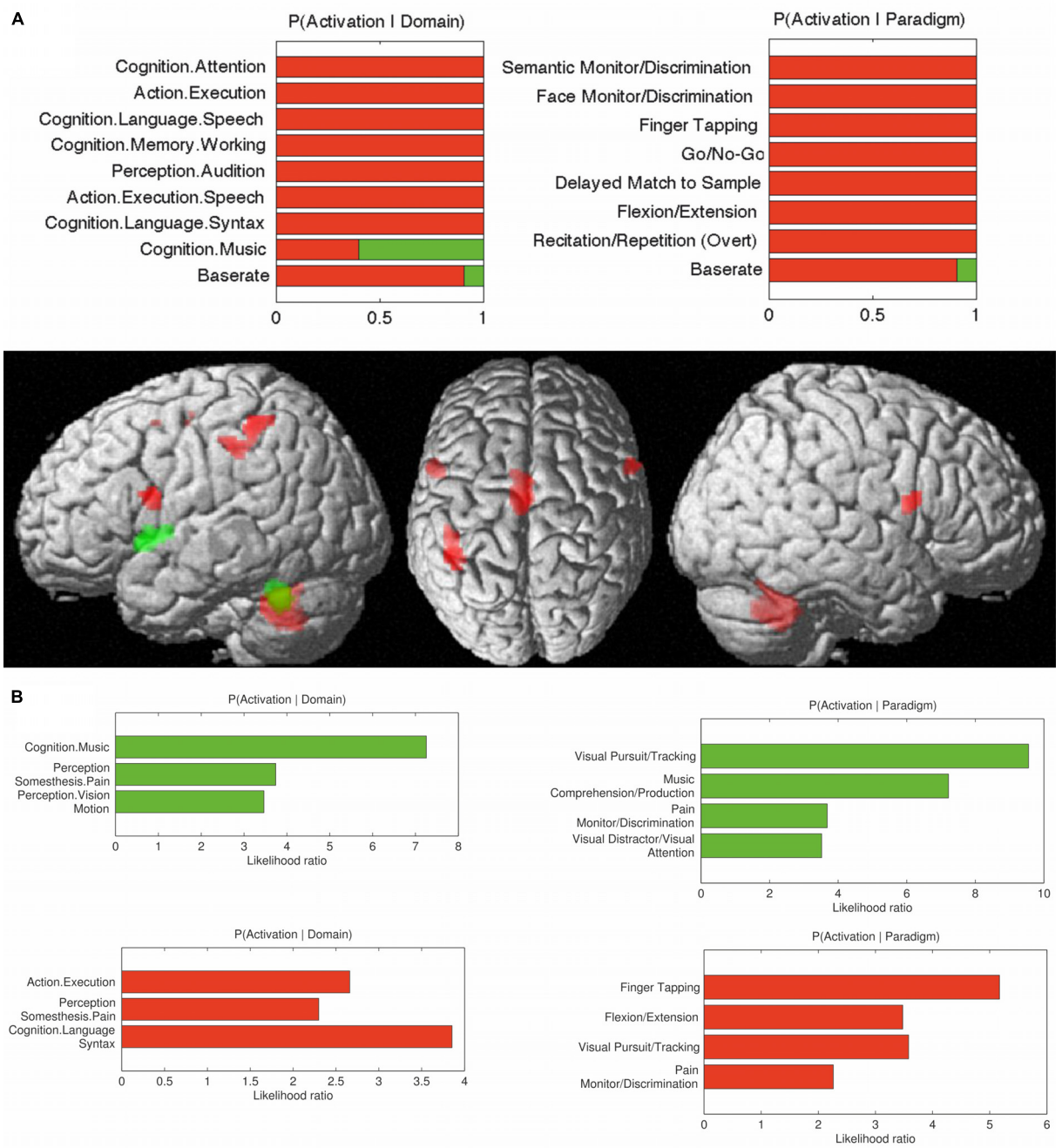

FIGURE 6 | (A) Contrasts in behavioral domains between cerebellar interposed (green) and the dentate (red) nuclei (pFDR < 0.05); **(B)** Behavioral domain information for the cerebellar interposed (green) and the dentate (red) nuclei (pFDR < 0.05).

to provide evidence for somatotopically organized connectivity patterns in the dorsal dentate nucleus (from rostral to caudal: arm, leg, and face), and somatotopic connectivity with the premotor cortex and in the middle third of the caudate. A third somatotopically organized pattern of connections to prefrontal areas 46, 9, and 7 was observed in the ventral dentate nucleus. In the present study we did not find consistent cytoarchitectonic evidence for further subdivisions of the dentate nucleus. This, however, does not rule out potential distinctions that may emerge from, e.g., myeloarchitecture or multi-receptor mapping.

Co-activation Patterns of the Cerebellar Nuclei

Recent studies showed that the cortex of the cerebellar hemispheres, in particular Crus I and Crus II (lobolus VIIA; cf. Schmahmann et al., 1999) is strongly involved in cognitive

functioning (Kelly and Strick, 2003; Balsters et al., 2013; see also Tomlinson et al., 2013 for an overview). These structures, in turn, are linked to the ventral dentate nuclei as described above (Voogd, 1964; Rossum, 1969). In line with this model and non-human approaches (e.g., Strick et al., 2009), the present study showed the dentate nucleus to be engaged in motor-related and cognitive processes. While single Tracer studies (Dum et al., 2002) distinguished a ventral and a dorsal part of the dentate nucleus, the meta-analysis shown here represents the functional associations and connections of the entire dentate nucleus, due to the limited number of contributing studies when analyzing subdivisions. Nevertheless, we found the dentate nucleus involved in basal executive as well as in higher order motor and cognitive functions. The results of our analysis on the entire dentate nucleus are in line with this focused investigation and primate data. In addition, the functional decoding not only showed an involvement of the dentate nucleus in cognitive and motor tasks, but also with respect to pain processing. Cerebellar involvement in pain-perception has been described earlier (Glickstein, 2007; Timmann and Daum, 2007; Strick et al., 2009). In general, the delineated functional connectivity of the dentate nucleus matches well with reports from invasive approaches dealing with structural connectivity mapping in non-human primates (see a review by Dum et al., 2002), even though no interactions with the primary motor cortex was observed in our findings. We did, however, observe significant ($p < 0.05$) co-activation between the dentate nucleus and the SMA. This finding matches with previous descriptions, which show that neurons from the dorsal "motor" domain of the dentate nucleus in monkey brains project to the SMA (Akkal et al., 2007). The co-activations of the dentate nucleus with the inferior and anterior parietal cortex are in line with tracing data revealing a connection between the parietal cortex and the (ventral) dentate nucleus (Dum et al., 2002). While there is no primate data to this end, the link between the dentate nucleus and speech as well as its co-activation with left BA 44 is in good agreement with a previous fMRI study (Thurling et al., 2012). Finally, it has been argued, that a particular function of the cerebellar hemisphere, which remits its output throughout the dentate nucleus, is rhythm perception and memory (Jerde et al., 2011; Pecenka et al., 2013). The current finding of an association between the dentate nucleus and music comprehension supports this view.

Only a small number of previous studies have reported on anatomy, function and connectivity of the interposed nuclei, most likely due to difficulties in the precise localization of these small structures. It has been reported that the paravermal interposed nuclei may be related to associative motor learning, i.e., eye blink reflex (Gerwig et al., 2003; Parker et al., 2009). The present study found that the interposed nuclei are associated with visual perception and attention as well as visuomotor tasks, which would be in line with these previous findings. Likewise, the association to somesthetic domain resonates well with older accounts which postulated a role for the interposed nuclei in (disturbed) sensory perception and cerebellar tremor (Vilis and Hore, 1977). Like the dentate nucleus, also the interposed nucleus features co-activations with the SMA. The SMA represents a key structure for bimanual movement coordination and reach-to-grasp functions (Wilson et al., 2014) and there is also strong evidence from human and monkey studies that the interposed nucleus plays an important role for reaching-to-grasp movements (van Kan et al., 1994; Monzee and Smith, 2004; Kuper et al., 2011b). Given that, we would thus argue, that these interactions may play a particular role in the cortico-cerebellar tuning of complex, coordinated arm, and hand movements.

Conclusion

We here reported on the first probabilistic atlas of the human cerebellar nuclei based on a cytoarchitectonic histological examination in 10 *post mortem* brains. The probabilistic maps in the stereotaxic MNI-Colin27 space provide new opportunities to relate structure, function, and dysfunction of the cerebellar nuclei as obtained in the living human brain to microscopically defined nuclei. To foster their use, the proposed maps will be integrated into the JuBrain atlas and freely distributed as part of the SPM Anatomy Toolbox[5].

Author Contributions

ST performed the cytoarchitectonic mapping, interpretation of data and wrote the first draft of the manuscript.
SB contributed to the development of methods for parcellation and analysis and revised the manuscript.
SE contributed to the meta-analytic connectivity modeling analysis and revised the manuscript.
HM contributed to the 3D reconstruction of the postmortem brains, their transformation into the stereotaxic MNI-Colin27 space and the computation of the probabilistic maps.
MM contributed to interpretation of data for the work and revised the manuscript.
KA contributed to the design of the study, the development of methods for parcellation and analysis, the interpretation of results and writing the manuscript.

All authors have approved the final version of the work to be published and agree to be accountable for all aspects of the work in ensuring that questions related to the accuracy or integrity of any part of the work are appropriately investigated and resolved.

Acknowledgments

This study was supported by the Deutsche Forschungsgemeinschaft (DFG, EI 816/4-1, LA 3071/3-1; EI 816/6-1.), the National Institute of Mental Health (R01-MH074457), and the European Union Seventh Framework Programme (FP7/2007-2013) under grant agreement no. 604102 (Human Brain Project). The authors thank Peter Pieperhoff, David Gräßel, and Karl Zilles for helpful discussions.

[5]http://www.fz-juelich.de/SharedDocs/Downloads/INM/INM-1/DE/Toolbox

References

Akkal, D., Dum, R. P., and Strick, P. L. (2007). Supplementary motor area and presupplementary motor area: targets of basal ganglia and cerebellar output. *J. Neurosci.* 27, 10659–10673. doi: 10.1523/JNEUROSCI.3134-07.2007

Amunts, K., Schleicher, A., Bürgel, U., Mohlberg, H., Uylings, H. B., Zilles, K., et al. (1999). Broca's region revisited: cytoarchitecture and intersubject variability. *J. Comp. Neurol.* 412, 319–341. doi: 10.1002/(SICI)1096-9861(19990920)412:2<319::AID-CNE10>3.0.CO;2-7

Amunts, K., Schleicher, A., and Zilles, K. (2007). Cytoarchitecture of the cerebral cortex-more than localization. *Neuroimage* 37, 1061–1068. doi: 10.1016/j.neuroimage.2007.02.037

Arras, C. (1987). *Architektonische Gliederung des Nucleus dentatus im Gehirn des Menschen*. Dissertation, University of Cologne, Cologne.

Balsters, J. H., Whelan, C. D., Robertson, I. H., and Ramnani, N. (2013). Cerebellum and cognition: evidence for the encoding of higher order rules. *Cereb. Cortex* 23, 1433–1443. doi: 10.1093/cercor/bhs127

Braak, H., and Braak, E. (1983). Morphological studies of local circuit neurons in the cerebellar dentate nucleus of man. *Hum. Neurobiol.* 2, 49–57. doi: 10.1016/j.jtbi.2015.01.024ů2.30

Brun, R. (1917). Zur Kenntnis der Bildungsfehler des Kleinhirns. *Schweiz. Arch. Neurol. Psychiatr.* 1, 61–123. doi: 10.1007/BF01814443

Cajal, R. Y., and Santiago. (1953). *Histologie du Systeĭme Nerveux de L'homme and des Verteìbreis*. Madrid: Consejo Superior de Investigaciones Cientiìficas, Instituto Ramoìn y Cajal.

Carpenter, M. B. (1991). *Core Text of Neuroanatomy*. Baltimore, MD: Williams & Wilkins. doi: 10.1007/s00429-008-0195-z

Caspers, S., Eickhoff, S. B., Geyer, S., Scheperjans, F., Mohlberg, H., Zilles, K., et al. (2008). The human inferior parietal lobule in stereotaxic space. *Brain Struct. Funct.* 212, 481–495. doi: 10.1016/j.neuroimage.2006.06.054

Caspers, S., Geyer, S., Schleicher, A., Mohlberg, H., Amunts, K., Zilles, K., et al. (2006). The human inferior parietal cortex: cytoarchitectonic parcellation and interindividual variability. *Neuroimage* 33, 430–448. doi: 10.1001/archneurpsyc.1955.02330180071008

Chambers, W. W., and Sprague, J. M. (1955). Functional localization in the cerebellum. II. Somatotopic organization in cortex and nuclei. *AMA Arch. Neurol. Psychiatry* 74, 653–680. doi: 10.1093/cercor/bhs256

Cieslik, E. C., Zilles, K., Caspers, S., Roski, C., Kellermann, T. S., Jakobs, O., et al. (2013). Is there "one" DLPFC in cognitive action control? Evidence for heterogeneity from co-activation-based parcellation. *Cereb. Cortex* 23, 2677–2689. doi: 10.1093/cercor/bhs256

Clos, M., Amunts, K., Laird, A. R., Fox, P. T., and Eickhoff, S. B. (2013). Tackling the multifunctional nature of Broca's region meta-analytically: co-activation-based parcellation of area 44. *Neuroimage* 83, 174–188. doi: 10.1016/j.neuroimage.2013.06.041

Collins, D. L., Neelin, P., Peters, T. M., and Evans, A. C. (1994). Automatic 3D intersubject registration of MR volumetric data in standardized Talairach space. *J. Comput. Assist. Tomogr.* 18, 192–205. doi: 10.1097/00004728-199403000-00005

Dejerine, J., and Dejerine-Klumpke, A. (1901). *Anatomie des Centres Nerveux*. Paris: Rueff.

Deoni, S. C., and Catani, M. (2007). Visualization of the deep cerebellar nuclei using quantitative T1 and rho magnetic resonance imaging at 3 Tesla. *Neuroimage* 37, 1260–1266. doi: 10.1016/j.neuroimage.2007.06.036

Diedrichsen, J., Maderwald, S., Küper, M., Thürling, M., Rabe, K., Gizewski, E. R., et al. (2011). Imaging the deep cerebellar nuclei: a probabilistic atlas and normalization procedure. *Neuroimage* 54, 1786–1794. doi: 10.1016/j.neuroimage.2010.10.035

Di Ieva, A., Tschabitscher, M., Galzio, R. J., Grabner, G., Kronnerwetter, C., Widhalm, G., et al. (2011). The veins of the nucleus dentatus: anatomical and radiological findings. *Neuroimage* 54, 74–79. doi: 10.1016/j.neuroimage.2010.07.045

Dimitrova, A., Weber, J., Redies, C., Kindsvater, K., Maschke, M., Kolb, F. P., et al. (2002). MRI atlas of the human cerebellar nuclei. *Neuroimage* 17, 240–255. doi: 10.1006/nimg.2002.1124

Dimitrova, A., Zeljko, D., Schwarze, F., Maschke, M., Gerwig, M., Frings, M., et al. (2006). Probabilistic 3D MRI atlas of the human cerebellar dentate/interposed nuclei. *Neuroimage* 30, 12–25. doi: 10.1016/j.neuroimage.2005.09.020

Dum, R. P., Li, C., and Strick, P. L. (2002). Motor and nonmotor domains in the monkey dentate. *Ann. N. Y. Acad. Sci.* 978, 289–301. doi: 10.1111/j.1749-6632.2002.tb07575.x

Dum, R. P., and Strick, P. L. (2003). An unfolded map of the cerebellar dentate nucleus and its projections to the cerebral cortex. *J. Neurophysiol.* 89, 634–639. doi: 10.1152/jn.00626.2002

Eickhoff, S. B., Bzdok, D., Laird, A. R., Kurth, F., and Fox, P. T. (2012). Activation likelihood estimation meta-analysis revisited. *Neuroimage* 59, 2349–2361. doi: 10.1016/j.neuroimage.2011.09.017

Eickhoff, S. B., Schleicher, A., Zilles, K., and Amunts, K. (2006). The human parietal operculum. I. Cytoarchitectonic mapping of subdivisions. *Cereb. Cortex* 16, 254–267. doi: 10.1093/cercor/bhi105

Eickhoff, S. B., Stephan, K. E., Mohlberg, H., Grefkes, C., Fink, G. R., Amunts, K., et al. (2005). A new SPM toolbox for combining probabilistic cytoarchitectonic maps and functional imaging data. *Neuroimage* 25, 1325–1335. doi: 10.1016/j.neuroimage.2004.12.034

Evans, A. C., Janke, A. L., Collins, D. L., and Baillet, S. (2012). Brain templates and atlases. *Neuroimage* 62, 911–922. doi: 10.1016/j.neuroimage.2012.01.024

Fix, J. D., and Treff, W. M. (1970). Structural principles of the phylogenetic development of the cerebellar nuclei in primates. *Acta Anat. (Basel)* 76, 337–351. doi: 10.1159/000143501

Forstmann, B. U., Keuken, M. C., Jahfari, S., Bazin, P. L., Neumann, J., Schäfer, A., et al. (2012). Cortico-subthalamic white matter tract strength predicts interindividual efficacy in stopping a motor response. *Neuroimage* 60, 370–375. doi: 10.1016/j.neuroimage.2011.12.044

Fox, P. T., and Lancaster, J. L. (2002). Opinion: mapping context and content: the BrainMap model. *Nat. Rev. Neurosci.* 3, 319–321. doi: 10.1038/nrn789

Gans, A. (1924). Beitrag zur kenntnis des aufbaus des nucleus dentatus aus zwei teilen, namentlich auf grund von untersuchungen mit der eisenreaktion. *Z. Gesamte Neurol. Psychiatr.* 93, 750–755. doi: 10.1007/BF02900080

Gerwig, M., Dimitrova, A., Kolb, F. P., Maschke, M., Brol, B., Kunnel, A., et al. (2003). Comparison of eyeblink conditioning in patients with superior and posterior inferior cerebellar lesions. *Brain* 126, 71–94. doi: 10.1093/brain/awg011

Geyer, S. (2004). The microstructural border between the motor and the cognitive domain in the human cerebral cortex. *Adv. Anat. Embryol. Cell Biol.* 174:I–VIII, 1–89. doi: 10.1007/978-3-642-18910-4_1

Glickstein, M. (2007). What does the cerebellum really do? *Curr. Biol.* 17, R824–R827. doi: 10.1016/j.cub.2007.08.009

Grodd, W., Hulsmann, E., Lotze, M., Wildgruber, D., and Erb, M. (2001). Sensorimotor mapping of the human cerebellum: fMRI evidence of somatotopic organization. *Hum. Brain Mapp.* 13, 55–73. doi: 10.1002/hbm.1025

Hampson, J. L., Harrison, C. R., and Woolsey, C. N. (1946). Somatotopic localization in the cerebellum. *Fed. Proc.* 5, 41.

Hassler, R. (1950). Cerebellar projections to the midbrain and thalamus in man. *Dtsch. Z. Nervenheilkd.* 163, 629–671. doi: 10.1007/BF00213160

Holmes, C. J., Hoge, R., Collins, L., Woods, R., Toga, A. W, Evans, A. C., et al. (1998). Enhancement of MR images using registration for signal averaging. *J. Comput. Assist. Tomogr.* 22, 324–333. doi: 10.1097/00004728-199803000-00032

Homke, L., Amunts, K., Bönig, L., Fretz, C., Binkofski, F., Zilles, K., et al. (2009). Analysis of lesions in patients with unilateral tactile agnosia using cytoarchitectonic probabilistic maps. *Hum. Brain Mapp.* 30, 1444–1456. doi: 10.1002/hbm.20617

Höpker, W. (1951). Das Altern des nucleus dentatus. *Z. Altersforsch.* 5, 256–277.

Icardo, J. M., Ojeda, J. L., Garcia-Porrero, J. A., and Hurle, J. M. (1982). The cerebellar arteries: cortical patterns and vascularization of the cerebellar nuclei. *Acta Anat. (Basel)* 113, 108–116. doi: 10.1159/000145545

Jakob, A. (1928). "Das Kleinhirn," in *Möllendorfs Handbuch der Mikroskopischen Anatomie des Menschen*, ed. W. V. Möllendorff (Berlin: Springer), 674–916. doi: 10.1007/978-3-642-66443-4_12

Jansen, J., and Brodal, A. (1942). *Experimental Studies on the Intrinsic Fibers of the Cerebellum: The Cortico-Nuclear Projection in the Rabbit and the Monkey*. Oslo: Dybwad.

Jansen, J., Brodal, A., Möllendorff, W. V., and Bargmann, W. (1958). *Das Kleinhirn*. Berlin: Springer. doi: 10.1007/978-3-662-21749-8

Jerde, T. A., Childs, S. K., Handy, S. T., Nagode, J. C., and Pardo, J. V. (2011). Dissociable systems of working memory for rhythm and melody. *Neuroimage* 57, 1572–1579. doi: 10.1016/j.neuroimage.2011.05.061

Kelly, R. M., and Strick, P. L. (2003). Cerebellar loops with motor cortex and prefrontal cortex of a nonhuman primate. *J. Neurosci.* 23, 8432–8444. doi: 10.3791/52302

Kölliker, A. V. (1889). *Handbuch der Gewebelehre des Menschen*. Leipzig: Engelmann.

Kozlova, G. P. (1984). Individual anatomical variations in cerebellar nuclei. *Neurosci. Behav. Physiol.* 14, 63–67. doi: 10.1007/BF01148733

Kuper, M., Dimitrova, A., Thürling, M., Maderwald, S., Roths, J., Elles, H. G., et al. (2011a). Evidence for a motor and a non-motor domain in the human dentate nucleus-an fMRI study. *Neuroimage* 54, 2612–2622. doi: 10.1016/j.neuroimage.2010.11.028

Kuper, M., Hermsdörfer, J., Brandauer, B., Thürling, M., Schoch, B., Theysohn, N., et al. (2011b). Lesions of the dentate and interposed nuclei are associated with impaired prehension in cerebellar patients. *Neurosci. Lett.* 499, 132–136. doi: 10.1016/j.neulet.2011.05.055

Kuper, M., Thurling, M., Maderwald, S., Ladd, M. E., and Timmann, D. (2012). Structural and functional magnetic resonance imaging of the human cerebellar nuclei. *Cerebellum* 11, 314–324. doi: 10.1007/s12311-010-0194-5

Kuper, M., Wünnemann, M. J., Thürling, M., Stefanescu, R. M., Maderwald, S., Elles, H. G., et al. (2013). Activation of the cerebellar cortex and the dentate nucleus in a prism adaptation fMRI study. *Hum. Brain Mapp.* 35, 1574–1586. doi: 10.1002/hbm.22274

Laird, A. R., Eickhoff, S. B., Kurth, F., Fox, P. M., Uecker, A. M., Turner, J. A., et al. (2009). ALE meta-analysis workflows via the brainmap database: progress towards a probabilistic functional brain atlas. *Front. Neuroinformatics* 3:23. doi: 10.3389/neuro.3311.3023.2009

Laird, A. R., Eickhoff, S. B., Mickle Fox, P., Uecker, A. M., Ray, K. L., Saenz, J. J. Jr., et al. (2011). The BrainMap strategy for standardization, sharing, and meta-analysis of neuroimaging data. *BMC Res. Notes* 4:349. doi: 10.1186/1756-0500-4-349

Lavezzi, A. M., Corna, M., Matturri, L., and Santoro, F. (2009). Neuropathology of the Guillain-Mollaret triangle (dentato-rubro-olivary network) in sudden unexplained perinatal death and SIDS. *Open Neurol. J.* 3, 48–53. doi: 10.2174/1874205X00903010048

Lugaro, E. (1895). Sulla strutura del nucleo dentate del cerveletto nell' uomo. *Monit. Zoologico Ital.* 6, 5–12.

Manto, M.-U. (2002). *The Cerebellum and its Disorders*. Cambridge; New York, NY: Cambridge University Press.

Manto, M. U. (2010). *Cerebellar Disorders A Practical Approach to Diagnosis and Management*. Cambridge: Cambridge University Press. doi: 10.1017/CBO9780511750557

Manto, M., and Oulad Ben Taib, N. (2010). Cerebellar nuclei: key roles for strategically located structures. *Cerebellum* 9, 17–21. doi: 10.1007/s12311-010-0159-8

Maschke, M., Erichsen, M., Drepper, J., Jentzen, W., Müller, S. P., Kolb, F. P., et al. (2003). Cerebellar representation of the eyeblink response as revealed by PET. *Neuroreport* 14, 1371–1374. doi: 10.1097/00001756-200307180-00018

McNaughton, S., Timmann, D., Watts, S., and Hore, J. (2004). Overarm throwing speed in cerebellar subjects: effect of timing of ball release. *Exp. Brain Res.* 154, 470–478. doi: 10.1007/s00221-003-1677-0

Merker, B. (1983). Silver staining of cell bodies by means of physical development. *J. Neurosci. Methods* 9, 235–241. doi: 10.1016/0165-0270(83)90086-9

Mihajlovic, P., and Zecevic, N. (1986). Development of the human dentate nucleus. *Hum. Neurobiol.* 5, 189–197.

Monzee, J., and Smith, A. M. (2004). Responses of cerebellar interpositus neurons to predictable perturbations applied to an object held in a precision grip. *J. Neurophysiol.* 91, 1230–1239. doi: 10.1152/jn.01120.2002

Murofushi, K. (1974). Normal development and dysgenesias of the dentate nucleus and inferior olive. *Acta Neuropathol.* 27, 317–328. doi: 10.1007/BF00690696

Nieuwenhuys, R., Huijzen, C., and Voogd, J. (2008). *The Human Central Nervous System*. Berlin: Springer. doi: 10.1007/978-3-540-34686-9

O'Rahilly, R., and Müller, F. (2006). *The Embryonic Human Brain : An Atlas of Developmental Stages*. Hoboken, NJ: Wiley-Interscience. doi: 10.1002/0471973084

Parker, K. L., Zbarska, S., Carrel, A. J., and Bracha, V. (2009). Blocking GABAA neurotransmission in the interposed nuclei: effects on conditioned and unconditioned eyeblinks. *Brain Res.* 1292, 25–37. doi: 10.1016/j.brainres.2009.07.053

Pecenka, N., Engel, A., and Keller, P. E. (2013). Neural correlates of auditory temporal predictions during sensorimotor synchronization. *Front. Hum. Neurosci.* 7:380. doi: 10.3389/fnhum.2013.00380

Ristanovic, D., Milosevic, N. T., Stefanovic, B. D., Maric, D. L., and Rajkovic, K. (2010). Morphology and classification of large neurons in the adult human dentate nucleus: a qualitative and quantitative analysis of 2D images. *Neurosci. Res.* 67, 1–7. doi: 10.1016/j.neures.2010.01.002

Rossum, J. V. (1969). *Corticonuclear and Corticovestibular Projections of the Cerebellum : An Experimentel Investigation of the Anterior Lobe, the Simple Lobule and the Caudal Vermis in the Rabbit*. Assen: Van Gorcum.

Rub, U., Brunt, E. R., and Deller, T. (2008). New insights into the pathoanatomy of spinocerebellar ataxia type 3 (Machado-Joseph disease). *Curr. Opin. Neurol.* 21, 111–116. doi: 10.1097/WCO.0b013e3282f7673d

Rub, U., Schöls, L., Paulsonet, H. L., Auburger, G., Kermer, P., Jen, J. C., et al. (2013). Clinical features, neurogenetics and neuropathology of the polyglutamine spinocerebellar ataxias type 1, 2, 3, 6 and 7. *Prog. Neurobiol.* 104, 38–66. doi: 10.1016/j.pneurobio.2013.01.001

Scheperjans, F., Eickhoff, S. B., Hömke, L., Mohlberg, H., Hermann, K., Amunts, K., et al. (2008a). Probabilistic maps, morphometry, and variability of cytoarchitectonic areas in the human superior parietal cortex. *Cereb. Cortex* 18, 2141–2157. doi: 10.1093/cercor/bhm241

Scheperjans, F., Hermann, K., Eickhoff, S. B., Amunts, K., Schleicher, A., Zilles, K., et al. (2008b). Observer-independent cytoarchitectonic mapping of the human superior parietal cortex. *Cereb. Cortex* 18, 846–867. doi: 10.1093/cercor/bhm116

Scherzed, W., Brunt, E. R., Heinsen, H., de Vos, R. A., Seidel, K., Bürk, K., et al. (2012). Pathoanatomy of cerebellar degeneration in spinocerebellar ataxia type 2 (SCA2) and type 3 (SCA3). *Cerebellum* 11, 749–760. doi: 10.1007/s12311-011-0340-8

Schlegelberger, T., and Braak, H. (1982). The packing density of supragranular pigment-laden stellate cells in phylogenetically older and newer portions of the human telencephalic cortex. *J. Hirnforsch.* 23, 49–53.

Schleicher, A., Amunts, K., Geyer, S., Morosan, P., and Zilles, K. (1999). Observer-independent method for microstructural parcellation of cerebral cortex: a quantitative approach to cytoarchitectonics. *Neuroimage* 9, 165–177. doi: 10.1006/nimg.1998.0385

Schleicher, A., and Zilles, K. (1990). A quantitative approach to cytoarchitectonics: analysis of structural inhomogeneities in nervous tissue using an image analyser. *J. Microsc.* 157, 367–381. doi: 10.1111/j.1365-2818.1990.tb02971.x

Schmahmann, J. D. (2010). The role of the cerebellum in cognition and emotion: personal reflections since 1982 on the dysmetria of thought hypothesis, and its historical evolution from theory to therapy. *Neuropsychol. Rev.* 20, 236–260. doi: 10.1007/s11065-010-9142-x

Schmahmann, J. D., and Caplan, D. (2006). Cognition, emotion and the cerebellum. *Brain* 129, 290–292. doi: 10.1093/brain/awh729

Schmahmann, J. D., Doyon, J., McDonald, D., Holmes, C., Lavoie, K., Hurwitz, A. S., et al. (1999). Three-dimensional MRI atlas of the human cerebellum in proportional stereotaxic space. *Neuroimage* 10, 233–260. doi: 10.1006/nimg.1999.0459

Schulz, J. B., and Pandolfo, M. (2013). 150 years of Friedreich ataxia: from its discovery to therapy. *J. Neurochem.* 126(Suppl. 1), 1–3. doi: 10.1111/jnc.12327

Snider, R. S., and Eldred, E. (1952). Cerebrocerebellar relationships in the monkey. *J. Neurophysiol.* 15, 27–40.

Stilling, B. (1864). *Untersuchungen über den Bau des Kleinen Gehirns des Menschen*. Cassel: Kay.

Strick, P. L., Dum, R. P., and Fiez, J. A. (2009). Cerebellum and nonmotor function. *Annu. Rev. Neurosci.* 32, 413–434. doi: 10.1146/annurev.neuro.31.060407.125606

Sultan, F., Hamodeh, S., and Baizer, J. S. (2010). The human dentate nucleus: a complex shape untangled. *Neuroscience* 167, 965–968. doi: 10.1016/j.neuroscience.2010.03.007

Thurling, M., Hautzel, H., Küper, M., Stefanescu, M. R., Maderwald, S., Ladd, M. E., et al. (2012). Involvement of the cerebellar cortex and nuclei in verbal and visuospatial working memory: a 7 T fMRI study. *Neuroimage* 62, 1537–1550. doi: 10.1016/j.neuroimage.2012.05.037

Thurling, M., Küper, M., Stefanescu, R., Maderwald, S., Gizewski, E. R., Ladd, M. E., et al. (2011). Activation of the dentate nucleus in a verb generation task: a 7T MRI study. *Neuroimage* 57, 1184–1191. doi: 10.1016/j.neuroimage.2011.05.045

Timmann, D. (2012). Contribution of the cerebellum to cognition. *Fortschr. Neurol. Psychiatr.* 80, 44–52. doi: 10.1055/s-0031-1282022

Timmann, D., and Daum, I. (2007). Cerebellar contributions to cognitive functions: a progress report after two decades of research. *Cerebellum* 6, 159–162. doi: 10.1080/14734220701496448

Timmann, D., Dimitrova, A., Hein-Kropp, C., Wilhelm, H., and Dorfler, A. (2003). Cerebellar agenesis: clinical, neuropsychological and MR findings. *Neurocase* 9, 402–413. doi: 10.1076/neur.9.5.402.16555

Tomlinson, S. P., Davis, N. J., and Bracewell, R. M. (2013). Brain stimulation studies of non-motor cerebellar function: a systematic review. *Neurosci. Biobehav. Rev.* 37, 766–789. doi: 10.1016/j.neubiorev.2013.03.001

Tschabitscher, M. (1979). [Veins of the human cerebellum]. *Acta Anat. (Basel)* 105, 344–366. doi: 10.1159/000145139

Tschabitscher, M., and Perneczky, A. (1976). [Vascularization of cerebellar dentate nucleus]. *Verh. Anat. Ges.* 70, 393–400.

Turkeltaub, P. E., Eickhoff, S. B., Laird, A. R., Fox, M., Wiener, M., Fox, P., et al. (2012). Minimizing within-experiment and within-group effects in activation likelihood estimation meta-analyses. *Hum. Brain Mapp.* 33, 1–13. doi: 10.1002/hbm.21186

van Kan, P. L., Horn, K. M., and Gibson, A. R. (1994). The importance of hand use to discharge of interpositus neurones of the monkey. *J. Physiol.* 480, 171–190. doi: 10.1113/jphysiol.1994.sp020351

Vilis, T., and Hore, J. (1977). Effects of changes in mechanical state of limb on cerebellar intention tremor. *J. Neurophysiol.* 40, 1214–1224. doi: 10.1136/jnnp.2004.044305

Vogt, C., and Vogt, O. (1942). *Morphologische Gestaltungen unter Normalen und Pathogenen Bedingungen : Ein Hirnanatomischer Beitrag zu ihrer Kenntnis*. Leipzig: Barth.

Voogd, J. (1964). *The Cerebellum of the Cat: Structure and Fibre Connexions*. Assen: Van Gorcum.

Voogd, J. (2003). The human cerebellum. *J. Chem. Neuroanat.* 26, 243–252. doi: 10.1016/j.jchemneu.2003.07.005

Weidenreich, F. (1899). *Zur Anatomie der Centralen Kleinhirnkerne der Säuger*. Stuttgart: Nägele.

Wilson, T. W., Kurz, M. J., and Arpin, D. J. (2014). Functional specialization within the supplementary motor area: a fNIRS study of bimanual coordination. *Neuroimage* 85(Pt 1), 445–450. doi: 10.1016/j.neuroimage.2013.04.112

Winkler, C. (1926). *Handboek der Neurologie*. Haarlem: Bohn.

Wree, A., Schleicher, A., and Zilles, K. (1982). Estimation of volume fractions in nervous tissue with an image analyzer. *J. Neurosci. Methods* 6, 29–43. doi: 10.1016/0165-0270(82)90014-0

Yamaguchi, K., Goto, N., and Yamamoto, T. Y. (1989). Development of human cerebellar nuclei. Morphometric study. *Acta Anat. (Basel)* 136, 61–68. doi: 10.1159/000146799

Yushkevich, P. A., Piven, J., Hazlett, H. C., Smith, R. G., Ho, S., Gee, J. C., et al. (2006). User-guided 3D active contour segmentation of anatomical structures: significantly improved efficiency and reliability. *Neuroimage* 31, 1116–1128. doi: 10.1016/j.neuroimage.2006.01.015

Zilles, K., Armstrong, E., Schleicher, A., and Kretschmann, H. J. (1988). The human pattern of gyrification in the cerebral cortex. *Anat. Embryol. (Berl.)* 179, 173–179. doi: 10.1007/BF00304699

Zilles, K., Palomero-Gallagher, N., and Amunts, K. (2013). Development of cortical folding during evolution and ontogeny. *Trends Neurosci.* 36, 275–284. doi: 10.1016/j.tins.2013.01.006

Conflict of Interest Statement: The authors declare that the research was conducted in the absence of any commercial or financial relationships that could be construed as a potential conflict of interest.

frontiers in Neuroanatomy

ORIGINAL RESEARCH
published: 03 September 2015
doi: 10.3389/fnana.2015.00118

A multiscale approach for the reconstruction of the fiber architecture of the human brain based on 3D-PLI

Julia Reckfort[1], Hendrik Wiese[1]*, Uwe Pietrzyk[2,3], Karl Zilles[1,4], Katrin Amunts[1,5] and Markus Axer[1]*

[1] Institute of Neuroscience and Medicine (INM-1), Structural and Functional Organization of the Human Brain, Research Centre Jülich, Jülich, Germany, [2] Institute of Neuroscience and Medicine (INM-4), Medical Imaging Physics, Research Centre Jülich, Jülich, Germany, [3] Department of Mathematics and Natural Sciences, University of Wuppertal, Wuppertal, Germany, [4] Department of Psychiatry, Psychotherapy and Psychosomatics, University Hospital, RWTH Aachen University and JARA Translational Brain Medicine, Aachen, Germany, [5] Cécile and Oskar Vogt Institute for Brain Research, Heinrich-Heine University Düsseldorf, Düsseldorf, Germany

Structural connectivity of the brain can be conceptionalized as a multiscale organization. The present study is built on 3D-Polarized Light Imaging (3D-PLI), a neuroimaging technique targeting the reconstruction of nerve fiber orientations and therefore contributing to the analysis of brain connectivity. Spatial orientations of the fibers are derived from birefringence measurements of unstained histological sections that are interpreted by means of a voxel-based analysis. This implies that a single fiber orientation vector is obtained for each voxel, which reflects the net effect of all comprised fibers. We have utilized two polarimetric setups providing an object space resolution of 1.3 μm/px (microscopic setup) and 64 μm/px (macroscopic setup) to carry out 3D-PLI and retrieve fiber orientations of the same tissue samples, but at complementary voxel sizes (i.e., scales). The present study identifies the main sources which cause a discrepancy of the measured fiber orientations observed when measuring the same sample with the two polarimetric systems. As such sources the differing optical resolutions and diverging retardances of the implemented waveplates were identified. A methodology was implemented that enables the compensation of measured different systems' responses to the same birefringent sample. This opens up new ways to conduct multiscale analysis in brains by means of 3D-PLI and to provide a reliable basis for the transition between different scales of the nerve fiber architecture.

Keywords: polarized light imaging, brain, fiber orientation, multiscale approach, connectome

OPEN ACCESS

Edited by:
Kathleen S. Rockland, Boston University School Medicine, USA

Reviewed by:
Jose L. Lanciego, University of Navarra, Spain
Van Jay Wedeen, Harvard Medical School - Massachusetts General Hospital, USA

****Correspondence:***
Julia Reckfort and Hendrik Wiese, Institute of Neuroscience and Medicine (INM-1), Fiber Architecture, Structural and Functional Organization of the Human Brain, Research Centre Jülich, Leo-Brandt-Strasse, 52428 Jülich, Germany
j.reckfort@fz-juelich.de; h.wiese@fz-juelich.de

Received: *27 May 2015*
Accepted: *19 August 2015*
Published: *03 September 2015*

Citation:
Reckfort J, Wiese H, Pietrzyk U, Zilles K, Amunts K and Axer M (2015) A multiscale approach for the reconstruction of the fiber architecture of the human brain based on 3D-PLI. Front. Neuroanat. 9:118. doi: 10.3389/fnana.2015.00118

1. Introduction

Decoding the human brain is one of the major targets for neuroscientists and researchers around the world. To understand the function of the brain and clinical symptoms in patients with neuropsychiatric disorders, it is indispensable to study its underlying structure, i.e., the organization of neurons and their intricate connections. The mapping of the nerve fiber architecture of the brain is a multiscale challenge as the size of the structures range from a few nanometers for the diameter of microfilaments to several centimeters for long distance inter-hemispheric fibers.

Over the past century several imaging techniques were developed to address the brain's fiber architecture, ranging from macroscopic techniques (e.g., dissection, Klingler, 1935; Tüere et al., 2000; diffusion tensor imaging, Basser et al., 1994; Pierpaoli and Basser, 1996; Conturo et al., 1999; Beaulieu, 2002; Mori and Zhang, 2006; Schmahmann et al., 2007; Johansen-Berg and Rushworth, 2009; high angular resolution imaging methods, Tuch et al., 2002; Jansons and Alexander, 2003; Tournier et al., 2004, 2007; Behrens et al., 2007; Dell'Acqua et al., 2007; Descoteaux et al., 2007) to microscopic techniques (classical myelin staining, Bürgel et al., 1997, 2006; polarization-sensitive optical coherence tomography, de Boer et al., 1997; Wang et al., 2011; knife-edge scanning microscopy, Li et al., 2010; or light-sheet fluorescence microscopy, Silvestri et al., 2012).

So far, it is difficult or even impossible to integrate most of the multimodal imaging data sets. This is caused by the lack of tools to bridge different scales and types of structural descriptions, thus, preventing the investigation of the organization of the brain at different levels of detail. A solution of such a problem is to realize a "multiscale approach" with imaging setups that provide complementary resolutions, and rely on the same imaging technique.

3D-Polarized Light Imaging (3D-PLI, Axer et al., 2011a) allows to investigate fiber tracts micro- and macroscopically, depending on the optical setup. Using 3D-PLI, it is possible to derive unit vectors that describe the orientation of fiber tracts and single nerve fibers in histological sections of postmortem brains. The potential to investigate nerve fibers by means of polarimetry is known for more than a century (Brodmann, 1903; Goethlin, 1913; Schmidt, 1923; Schmitt and Bear, 1937; Wolman, 1975), but only the recent advances in digital image acquisition, 3D reconstruction, and big data processing has enabled the systematic investigation of the 3D orientation of nerve fibers (Axer et al., 2011b; Amunts et al., 2013b). Utilization of high performance computing tools and techniques paved the way toward whole brain analyses (Amunts et al., 2013a). As a result, 3D-PLI enables unique whole brain studies in rodents, monkeys, and even humans with reasonable efforts in laboratory work and infrastructure within affordable time frames. Nonetheless, the complexity of the entire human brain is still a challenge and mapping its fiber architecture will benefit significantly from the multiscale approach presented here as it provides a rational and accessible merger of context and detail.

In the present study, two custom-made polarimeters with different optical resolutions and sensitivities optimized for 3D-PLI measurements were employed to establish a multiscale approach, the polarizing microscope (PM) and the large-area polarimeter (LAP). Each system offers unique features (Axer et al., 2011b): The PM enables mosaic-like scanning of sections at microscopical resolution, thus, even enabling the detection of single fibers within the different layers of the cerebral cortex. A large single human brain section which is scanned in up to 4880 tiles requires about 21 h scanning time, resulting in a data volume of 703 GB. The LAP allows to image a whole human brain section within a single shot. The imaging procedure consists of the imaging of the section from five different view angles which takes about 15 min of scanning time and generates a data amount of 3 GB per section. The fast acquisition time is a prerequisite to map long-distance white matter tracts of complete human brains. A strategy to circumvent parts of the methodical challenges of the PM is to combine the information gained with both systems. Moreover, such combination of the two systems with different optical resolutions closes the gap between different spatial scales. This requires that the fiber orientations measured with both systems are comparable. Previous studies revealed that the systems differ in their properties resulting in different system responses to the same sample (Reckfort et al., 2013). Therefore, the purpose of this study was to develop a methodology to compensate these differences by means of corrections applicable to image analysis and signal interpretation for PM and LAP.

2. Materials and Methods

2.1. Principles of 3D-Polarized Light Imaging

3D-Polarized Light Imaging (Axer et al., 2011a,b) utilizes the optical birefringence of nerve fibers that is attributed to the highly ordered molecular organization of the lipids and proteins building the myelin sheaths surrounding axons (Martenson, 1992). In 3D-PLI, a polarimetric setup enables the detection of birefringent structures and the determination of their spatial orientation within a given sample. For this purpose, the brain tissue has to be cut into 70 μm thin unstained histological sections (cf. Section 2.4) to achieve transmissive imaging in the visible spectrum.

Both polarimetric setups employed in this study are composed of three optical filters (two crossed linear polarizers and one quarter waveplate with its fast axis adjusted at an angle of 45° with respect to the transmission axes of the first linear polarizer) to control the polarization state of the incident light and to analyze its changes after interacting with the nerve fibers of the tissue section (**Figure 1A**).

By rotating at least one of the linear polarizers in equidistant angles (i.e., $\Delta\rho = 10°$) within the range of $\rho = 0°$ and 170° a stack of 18 images is acquired. The measured intensity profile for an individual pixel across the stack of images describes a sinusoidal curve that depends on the orientation of fibers within this pixel (**Figure 1B**). The physical description of the light intensity profile is derived by the Jones matrix calculus (Larsen et al., 2007), as the system is composed of linear optical elements and the light is considered fully polarized:

$$I_T(\rho) = \frac{I_{T0}}{2}\left[1 + \sin(2\rho - 2\varphi)r\right] \tag{1}$$

with

$$r = \left|\sin\left(2\pi\,\frac{t\Delta n}{\lambda}\cos^2\alpha\right)\right|, \tag{2}$$

where $I_T(\rho)$ describes the measured light intensity for the filters rotated by an angle of ρ and I_{T0} reflects the attenuated light intensity. The retardation r indicates the strength of birefringence and is quantified by the amplitude of the measured signal normalized by I_{T0}. The retardation r depends on the wavelength λ of the light source, the birefringence of the tissue Δn, the

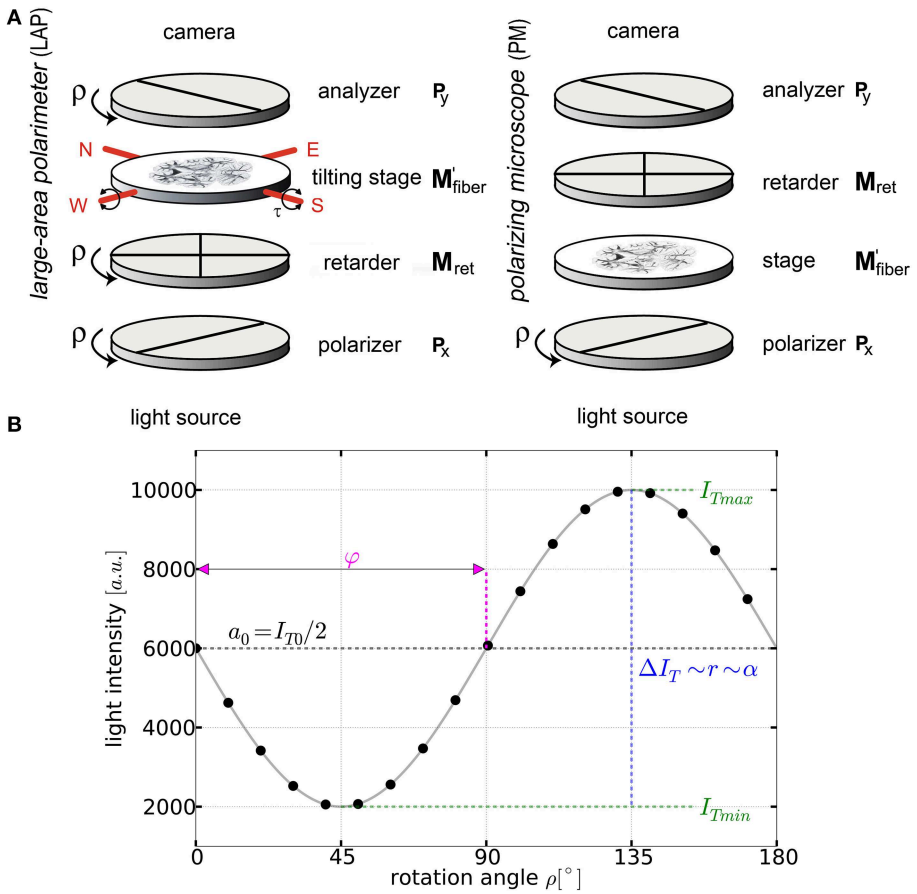

FIGURE 1 | Basic principles of 3D-PLI. (A) Schemes of the large-area rotating polarimeter with a tilting stage and of the polarizing microscope (PM) from Taorad GmbH (Germany). **(B)** The signal intensity profile depending on the rotation angle ρ of the filters for a single pixel measured with a polarimeter. To obtain the fiber orientation, the measured light intensities are studied pixel-wise as a function of discrete rotation angles. The derived physical model provides (continuous black line) and relates the sine phase to the direction φ and the amplitude to the inclination angle α.

section thickness t, and the inclination angle α describing the fiber elevation with respect to the sectioning plane.

Equation (1) can be parameterized by means of discrete harmonic Fourier analysis (Glazer et al., 1996; Axer et al., 2011b) as follows:

$$I_T(\rho) = a_0 + a_1 \sin(2\rho) + b_1 \cos(2\rho), \tag{3}$$

with

$$a_0 = \frac{I_{T0}}{2},\ a_1 = \frac{I_{T0}}{2} r \cos(2\varphi),\ b_1 = -\frac{I_{T0}}{2} r \sin(2\varphi). \tag{4}$$

These coefficients are computed from the measured intensity profile $I_T(\rho_i)$ in each individual pixel by

$$a_0 = \frac{1}{N}\sum_{i=1}^{N} I_T(\rho_i),\ a_1 = \frac{2}{N}\sum_{i=1}^{N} I_T(\rho_i)\sin(2\rho_i),$$
$$b_1 = \frac{2}{N}\sum_{i=1}^{N} I_T(\rho_i)\cos(2\rho_i), \tag{5}$$

where ρ_i denotes the filter rotation angle and $N(=18)$ the total number of sampled data points.

Combining the Fourier coefficients, it is possible to retrieve light retardation, light transmittance and to quantify the fiber orientation (α,φ) for each image pixel:

$$\textbf{Transmittance}: \quad I_{T0} = 2a_0, \tag{6}$$

$$\textbf{Retardation}: \quad r = (a_1^2 + b_1^2)^{\frac{1}{2}}/a_0, \tag{7}$$

$$\textbf{Direction}: \quad \varphi = \frac{1}{2}\arctan2(b_1, -a_1) + \frac{\pi}{2} = \frac{1}{2} arg(a_1 + ib_1) \tag{8}$$

The fiber inclination angle α can be extracted from Equation (2), though it has to be noted that it is not possible to determine the sign of the inclination angle with a single planar measurement. To resolve the ambiguity of the sign of the inclination angle the specimen stage has to be tilted. For more detail please refer to (Kleiner et al., 2012; Wiese et al., 2014). Furthermore, to determine the fiber inclination angle the

wavelength, the tissue birefringence and the section thickness have to be known precisely. As it is difficult to determine these parameters individually, they have been merged to a single parameter referred to as relative thickness t_{rel} as introduced by Axer et al. (2011a). The relative thickness is defined as the ratio of the actual section thickness t and the section thickness at which a fiber that runs parallel to the sectioning plane (i.e., $\alpha \approx 0^\circ$) acts as an ideal quarter waveplate. This approach leads to

$$r = \left| \sin\left(\frac{\pi}{2} t_{\mathrm{rel}} \cos^2 \alpha\right) \right|. \tag{9}$$

Equation (9) enables the determination of t_{rel} by means of reference measurements in brain sections with fiber bundles that have been cut along their principal paths (i.e., $\alpha \approx 0^\circ$). Both direction angle φ and inclination angle α constitute a unit vector that describes the local spatial fiber orientation. The image of all derived fiber orientations covering an entire brain section represents the fiber orientation map (FOM, Axer et al., 2011a).

2.2. Polarimetric Equipment

In order to realize the multiscale approach, two polarimeters (cf. **Figure 1A**) were used in the present study: the polarization microscope (PM) and the large-area polarimeter (LAP, Axer et al., 2011b). In the LAP, the brain section is illuminated with circularly polarized light. In this setup, all optical filters are rotated simultaneously during the measurement. In contrast, the light path through the filters is reversed in the PM and only the polarizer is rotated. The light intensity profiles obtained with both setups, however, can be described by the same equation (Equation 1) which enables the employment of the same strategy for data analysis.

2.2.1. LAP

The LAP is equipped with a quarter waveplate optimized for $\lambda_{\mathrm{ret}} = 560\,\mathrm{nm}$ and an LED light source emitting at $\lambda_{\mathrm{ill}} = (525 \pm 25)\,\mathrm{nm}$. It has specifically been designed to digitize large histological sections ($\sim 200\,\mathrm{cm}^2$, i.e., whole human brain sections) in single shot acquisitions. Moreover, the LAP has a tilting specimen stage providing tilt angles of $|\tau| \leq 8^\circ$. This feature has been introduced to compensate for intrinsic limitations of planar projection imaging technologies, such as the inclination sign ambiguity (Kleiner et al., 2012; Wiese et al., 2014). By assigning a definite preference to the inclination angle, the tracking of fiber bundles across neighboring brain sections becomes feasible. The optical resolution limit according to the Rayleigh criterion was determined to be 159 μm and the object space resolution to be 64 μm/px (Reckfort et al., 2013). Based on repeated measurements of the same tissue sample, the variances of the measured retardation and direction values were extracted to be $\sigma(r_{\mathrm{LAP}}) = 0.008$ and $\sigma(\varphi_{\mathrm{LAP}}) = 0.36^\circ$, respectively.

2.2.2. PM

In the PM, a quarter waveplate with an optimal working wavelength of $\lambda_{\mathrm{ret}} = 545\,\mathrm{nm}$ and an LED light source with $\lambda_{\mathrm{ill}} = (543.5 \pm 10)\,\mathrm{nm}$ as central peak wavelength, are implemented. The determined optical resolution limit is 3.9 μm and the object space resolution is 1.33 μm/px (Reckfort et al., 2013). The PM has a limited field of view of $(2.7 \times 2.7)\,\mathrm{mm}^2$ and the brain sections are scanned stepwise with an overlapping field of view of 30% to enable robust stitching of the neighboring images to create a consistent image of the whole section. In total, a whole brain section is build of up to 4880 single tiles and takes about 21 h scanning time. The PM's imaging procedure is limited to planar measurements, i.e., no tilting of the specimen stage is possible. Hence, the current PM setup does not provide an unambiguous sign for the fiber inclination angle. The variances of the measured retardation and direction values were extracted from repeated measurements of the same object to be $\sigma(r_{\mathrm{PM}}) = 0.007$ and $\sigma(\varphi_{\mathrm{PM}}) = 0.29^\circ$, respectively.

2.3. Influence of the Wavelength Discrepancy

A previous study by Reckfort et al. (2013) indicated that the discrepancy of the illumination peak wavelength and the design wavelength of the quarter-waveplate used in the LAP influences the response of the system to birefringent samples. The current analysis (cf. Equations 1–8) assumes that the light is retarded by a quarter-wavelength by the used waveplate. As for the LAP setup the retardance (i.e., phase retardation) induced by the waveplate for the wavelength of the employed illumination source has not been specified by the manufacturer, the data analysis described in Section 2.1 had to be adapted. For this purpose, the derivation of the transmitted light intensity by means of the Jones calculus was generalized in such a way that the retardance γ induced by the waveplate is arbitrary.

To describe the optical setup the Jones matrices P_x and P_y denote the implemented linear polarizers and the matrix $M_{\mathrm{ret}}(\gamma)$ the waveplate inducing an arbitrary retardance. Further the brain tissue is represented by a Jones matrix for a quarter-wave retarder with an arbitrary rotation angle and retardance.

$$\vec{E_T}'(\delta, \beta, \gamma) = P_y \cdot M'_{\mathrm{fiber}}(\delta, \beta) \cdot M_{\mathrm{ret}}(\gamma) \cdot P_x \cdot \vec{E}. \tag{10}$$

When an arbitrary retardance induced by the waveplate is assumed, the intensity profile of the current setup is described, similarly to Equation (3), by a Fourier series with the coefficients a_0, a_1, b_1, a_2, and b_2[1]. This enables a precise description of the measured intensity profile.

$$I'_T(\rho) = a'_0 + a'_1 \sin(2\rho) + b'_1 \cos(2\rho) + a'_2 \sin(4\rho) + b'_2 \cos(4\rho), \tag{11}$$

with the Fourier coefficients:

$$\begin{aligned}
a'_0 &= \frac{I'_{T0}}{2} \sin^2(\delta/2) + I'_{T0} \sin^2(\gamma/2) \cos^2(\delta/2), \\
a'_1 &= \frac{I'_{T0}}{2} \sin(\gamma) \sin(\delta) \cos(2\varphi), \\
b'_1 &= -\frac{I'_{T0}}{2} \sin(\gamma) \sin(\delta) \sin(2\varphi), \\
a'_2 &= -\frac{I'_{T0}}{2} \cos(\gamma) \sin^2(\delta/2) \cos(4\varphi), \\
b'_2 &= -\frac{I'_{T0}}{2} \cos(\gamma) \sin^2(\delta/2) \sin(4\varphi).
\end{aligned}$$

[1] A more detailed derivation is given in the Supplementary Material.

The new determined Fourier coefficients differ from the ones determined for the ideal case of a phase retardance of $\gamma = \pi/2$ (cf. Equation 4). If the light retardance differs from the ideal case, additional coefficients a_2' and b_2' have to be considered. The fiber direction angle (phase of sinus) can be calculated as before by (cf. Equation 4):

$$\varphi' = \frac{1}{2}\arctan 2(b_1', -a_1') + \frac{\pi}{2}. \tag{12}$$

In contrast, the retardation and transmittance differ as compared to the original description which considers a retardance induced by a quarter waveplate. It is possible to derive the retardation r' and transmittance I_{T0}' by employing all five of the new Fourier coefficients:

$$r' = \sqrt{a_1'^2 + b_1'^2} \cdot \frac{2\sin^2(\gamma/2)}{|\sin(\gamma)|} \left(a_0' - \frac{\sqrt{a_2'^2 + b_2'^2}}{|\cos(\gamma)|} \left(1 - 2\sin^2(\gamma/2)\right) \right)^{-1}, \tag{13}$$

$$I_{T0}' = \frac{1}{\sin^2(\gamma/2)} \left(a_0' - \frac{\sqrt{a_2'^2 + b_2'^2}}{|\cos(\gamma)|}\left(1 - 2\sin^2(\gamma/2)\right) \right) \tag{14}$$

The dependency of r' and I_{T0}' on the Fourier components are more complex as compared to the ideal quarter-wave retardance. Therefore, it is no longer possible to assign the measured relative amplitude to the retardation and the average intensity across all 18 measurements to the transmittance.

2.4. Tissue Preparation

The influence of the different system properties on tissue measurements was investigated in coronal sections of a postmortem vervet/African green monkey brain (*Chlorocebus aethiops sabaeus)* (**Figures 2A,B**). The brain was retrieved through the NIH program *1R01MH092311-01A1* in accordance with legal and ethical requirements. The vervet monkey was a member of the Vervet Research Colony (VRC) at Wake Forest University. The Wake Forest University complies with the Principles for Use of Animals, the Guide for the Care and Use of Laboratory Animals, and all provisions of the Animal Welfare Act. The project was approved by the UCLA Chancellor's Animal Research Committee (ARC) ARC #2011-135 and by the Wake Forest Institutional Animal Care and Use Committee IACUC #A11-219.

The vervet monkey brain was perfusion fixed in 4% buffered paraformaldehyde, cryo-protected with a 20% glycerin solution and deep frozen at −70°C. The brain was serially sectioned in the coronal plane (section thickness: 70 μm) employing a cryostat microtome (Polycut CM 3500, Leica, Germany), embedded with a glycerin solution and coverslipped. Afterwards, the sections were immediately measured with the LAP and the PM.

2.5. Correlation between LAP and PM Measurements

To evaluate the consistency of the fiber orientations obtained with the PM and the LAP, one exemplary coronal section of the vervet monkey brain has been selected and processed here.

For a pixel-wise comparison, the stitched PM image (44, 517 × 34, 024 px) was downsampled to match the image resolution and dimension of the LAP data set (937 × 716 px). This was done by means of a circular Gaussian filter. The standard deviation $\sigma = 20\,\text{px} \sim 159/3.9\,\mu\text{m}$ was chosen to replicate the lower optical resolution of the LAP. Furthermore, the filtered images were scaled by a factor of $0.0208 = 1.33/64$, which corresponds to the ratio of the object space resolutions of both systems and reproduces the spatial sampling of the CCD camera implemented in the LAP. As a result, one downsampled pixel value corresponds to the average value of approximately 48 × 48 px of the Gaussian filtered PM image. These two steps of downsampling were performed with the open source image processing software *Fiji* (Schindelin et al., 2012).

The downsampling was applied directly to the maps of the Fourier coefficients [a_0, a_1, and b_1 (cf. Equation 3)]. This approach reproduces the averaging process of the sinusoidal signals during the imaging process. Based on the downsampled Fourier coefficient maps, the downsampled direction and retardation maps were calculated according to Equation (4). The direction values determined with the PM were corrected by adding a value of 20.63° as the x-axis of the first linear polarizer is rotated by this value.

The LAP image was non-linearly registered to the PM image to ensure pixel-precise comparison. This is necessary as a cryo-section embedded in glycerin and coverslipped can still undergo slight deformations or movements. However, the changes are very slow compared to the duration of a single measurement. Still, to ensure the best possible comparison a non-linear registration was performed to align both images. The images were subdivided into four regions of interest (ROI) to minimize the influence of local rectifications. The images were pre-registered using a rigid and affine transformation. The registration was further improved by applying a b-spline transformation (Yoo et al., 2002). All registration steps were based on the toolbox elastix (Klein et al., 2010).

The retrieved fiber direction angle and retardation maps measured with the LAP and the downsampled PM were evaluated pixel-wise by means of difference images and scatter plots. For a correct interpretation of the difference map based on the measured direction, the represented data needs to be filtered to account for the periodicity of the parameter space of the direction angle. When analyzing the discrepancy between the direction of two fiber orientations, it has to be ensured that always the angle smaller than 90° is retrieved. This is realized by subtracting 180° from all values larger than $\Delta\varphi = 90°$ and to add 180° to all values lower than $\Delta\varphi = 90°$ in the differential map. The analysis was based on the evaluation of the white matter and basal ganglia (see red rimmed area in **Figure 2**). In total 206,788 px single pixels in the white matter were evaluated. The scatterplots were fitted based on a simple linear regression.

To investigate the consequences of the newly proposed evaluation analysis of the measured signals, the data obtained with the LAP was evaluated employing a retardance of $\gamma_1 = 0.25\pi$ and $\gamma_2 = 0.259\pi$. The determined retardation values were further compared to measurements of the PM.

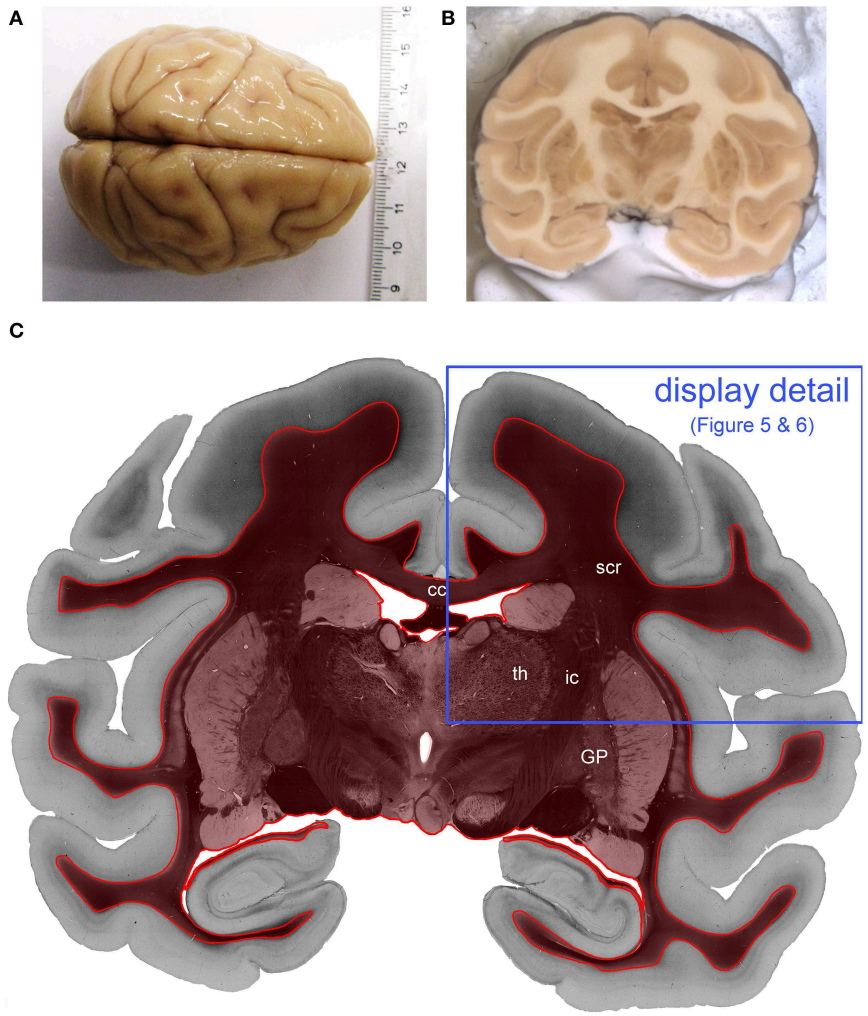

FIGURE 2 | Processed vervet monkey brain. (A) Shows the whole vervet monkey brain before sectioning and **(B)** shows the a blockface image which is captured during the cutting procedure and **(C)** is the transmittance image of the evaluated coronal, vervet monkey brain section. The red label indicates the evaluated region of interest. The blue frame indicates the detail of the section which is displayed in **Figures 4**, **5**. (cc, corpus callosum; GP, globus pallidus; ic, internal capsule; scr, superior corona radiata; th, thalamus.)

2.6. Influence of the Lateral Partial Volume Effect

In order to realize a multiscale approach for connectivity studies the influence of the different optical resolutions of the employed polarimetric systems is considered. These different resolutions affect particularly measurements of heterogeneous tissue (e.g., regions which contain crossing fibers).

If a single volume element (voxel) contains only a single fiber, the measured intensity profile within the corresponding pixel will encode the spatial fiber orientation. For a coarser optical resolution the signals of multiple pixels (in the image-plane) are averaged and cause the "lateral partial volume effect." Depending on the arrangement of fibers, which are measured in the same pixel, it is difficult to decode the information about multiple fiber orientations from a single sinusoidal signal. The more dispersed the fiber orientations are, the more pronounced is the partial volume effect. The lateral partial volume effect in 3D-PLI depends on the inhomogeneity of biological tissue and the employed spatial resolution with which these structures are imaged. Knowing the magnitude of the local lateral partial volume effect improves the interpretation of 3D-PLI measurements. A suitable measure for this magnitude can be derived by analyzing the averaging of the signals in the downsampling procedure. To understand this process, the averaging of the sinusoidal signals of two individual pixels (cf. Equation 1)

$$I_{T1}(\rho) = \frac{I_{T0}}{2}(1 + r_1 \sin(2\rho - 2\varphi_1)),$$
$$I_{T2}(\rho) = \frac{I_{T0}}{2}(1 + r_2 \sin(2\rho - 2\varphi_2)),$$

is examined. The arithmetic mean of two sinusoidal curves results in a new sinusoidal curve with an amplitude $\tilde{r}$ and a phase $\tilde{\varphi}$:

$$\frac{I_{T1}(\rho)+I_{T2}(\rho)}{2}=\frac{I_{T0}}{2}(1+\tilde{r}\sin(2\rho-2\tilde{\varphi})), \tag{15}$$

with

$$\tilde{r}=\frac{I_{T0}}{2}\sqrt{r_1^2+r_2^2+2r_1r_2\cos(2\varphi_1-2\varphi_2)}\leq\frac{r_1+r_2}{2} \tag{16}$$

and

$$\tilde{\varphi}=\frac{1}{2}\arctan\left(\frac{r_1\sin(2\varphi_1)-r_2\sin(\varphi_2)}{r_1\cos(2\varphi_1)+r_2\cos(\varphi_2)}\right). \tag{17}$$

The difference between the averaged amplitude ($\bar{r}=(r_1+r_2)/2$) and the amplitude of the averaged sinusoidal curves ($\tilde{r}$) increases when the difference of the in-plane direction (correlated to the phase difference) of the two fibers increases. Hence, $\bar{r}-\tilde{r}$ can be used to quantify the heterogeneity of the tissue. For example, for parallel fibers, the averaging of the amplitudes of each pixel gives the same results as when the sinusoidal curves are averaged. As soon as the alignment of the fibers is heterogeneous, the averaged amplitude value is higher than the amplitude value of the averaged sinusoidal signals.

In order to test the hypothesis that the difference between the averaged amplitude value and the amplitude of the averaged sinus curves is a suited measure for the quantification of the lateral partial volume effect, the downsampled PM data was compared to LAP data. For this purpose, the PM data was downsampled by applying a Gaussian filter and scaling factor ($\sigma_{\text{gauss}}=20, f_{\text{sc}}=1/48$) to the retardation map based on the original PM measurements. This represents an averaging of the amplitudes, while the LAP measurement represents the averaging of the sinusoidal signals. Then the two retardation maps were subtracted from each other.

3. Results

3.1. Correlation between LAP and PM Measurements

The fiber direction angles and retardation values measured with the PM and the LAP were compared in scatterplots (cf. **Figures 3B**, **4B,C**). The scatterplot in **Figure 3B** shows the correlation between the value of the in-plane fiber direction measured with the LAP (x-axis) and the PM (y-axis). For the values along the line that bisects the x- and y-axis (magenta line) exactly the same values are measured with the PM and the LAP. The linear fit through the scatterplot (dotted cyan line) is identical to the line that bisects the x- and y-axis within the margin of error. The determined fiber directions are consistent between both systems as the Pearson coefficient is 0.9885. The retardation values show a deviation of $< 6.72^\circ$ from the linear fit within the first confidence interval of the standard deviation (68%). These small deviations are also visible in the differential map (cf. **Figure 3A**), particularly in brain regions of homogeneous fiber courses, such as the corpus callosum. Larger deviations occurred only in brain regions that contained heterogeneous fiber courses, such as the thalamus and Globus pallidus.

The comparison of the retardation values derived from measurements and evaluated according to Equation (13) with $\gamma = 0.25\pi$, shows significant differences between PM and LAP (cf. **Figure 4**). Most retardation values derived from the LAP measurement are lower than the ones based on PM measurements, indicated by the fact that most dots are above the line that bisects the x- and y-axis. With increasing retardation values, the absolute difference between the values measured with the LAP and the PM increases as indicated by the higher slope of the fit function in **Figure 4B** (cyan line). Still, the data is highly correlated which is indicated by a Pearson coefficient of 0.9867. By employing the new analysis method [cf. Equation (13) with $\gamma = 0.259\pi$] to interpret the LAP measurements, higher retardation values are derived. As a result, the fit function through the data points (cyan line) coincides with the line that bisects the x- and y-axis.

Within the first confidence interval of the standard deviation the retardation value based on LAP measurements differs from the downsampled value of the PM by 0.050. Differences in the retardation values are observed particularly in the thalamus, internal capsule and superior corona radiata (**Figure 4A**).

Figure 5 shows resulting fiber orientation maps opposing PM and corrected LAP data sets visualized in a HSV color coding scheme (i.e., colors are assigned to distinct fiber orientations). This example demonstrates the general similarity of both measurements (**Figures 5B/C,E/F**). Large fiber structures, such as fiber bundles in the internal capsule (**Figures 5E,F**), are contrasted with PM and LAP equally. The PM detects even single fibers in the cerebral cortex and within nuclei (**Figures 5C,E**), while the LAP FOMs show the orientation in the corresponding brain regions.

3.2. Influence of the Lateral Partial Volume Effect

The comparison of the retardation values measured with the LAP (r'_{LAP}) and the mean retardation value of the corresponding 48×48 PM pixels ($\hat{r}_{\text{PM}}$) revealed that in most cases the averaged PM-value is higher than the LAP-value (cf. **Figure 6A**). For brain regions with predominantly parallel fibers, the downsampled and the averaged retardation values are similar (e.g., corpus callosum). In contrast, in heterogeneous regions (where fiber populations with different orientations are present), the downsampled retardation values are much lower than average values. Such regions (e.g., thalamus and the superior part of the Corona radiata) appear highlighted in the differential map. In these regions the mixing of different fiber bundles is indicated by a decrease in the signal strength in the retardation map (cf. **Figure 6B**).

4. Discussion

The main purpose of this study was to develop a strategy to combine polarized light imaging (3D-PLI) measurements which were captured at different optical resolutions obtained with different setups. This is an indispensable prerequisite to realize a multiscale approach over two orders of magnitude (in-plane). We accomplished this aim for the in-house developed large-area polarimeter and the polarizing microscope provided by Taorad

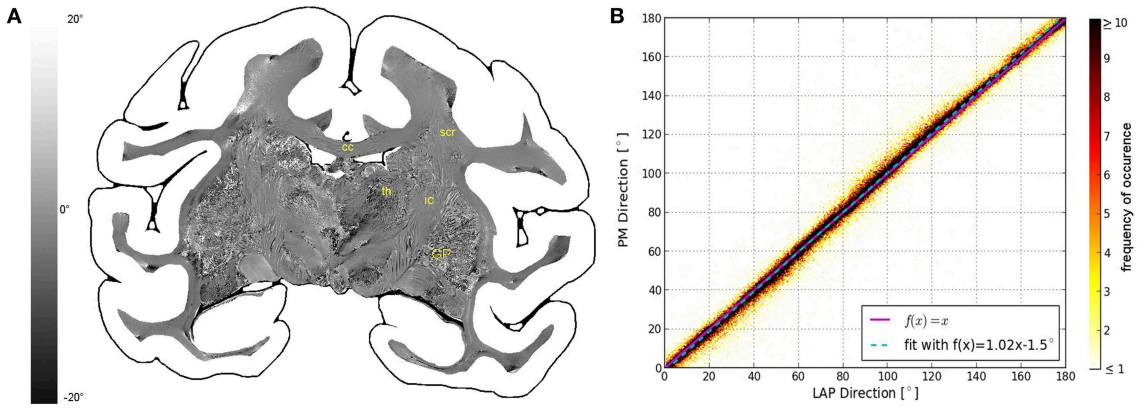

FIGURE 3 | Consistency of the measured fiber direction angle. (A) Displays a differential map of the fiber direction maps obtained with the PM and LAP. It highlights in which areas the largest differences of the measured fiber directions occur. **(B)** Shows a scatterplot displaying a direct comparison of the measured fiber direction angles. The color code indicates the number of occurrences.

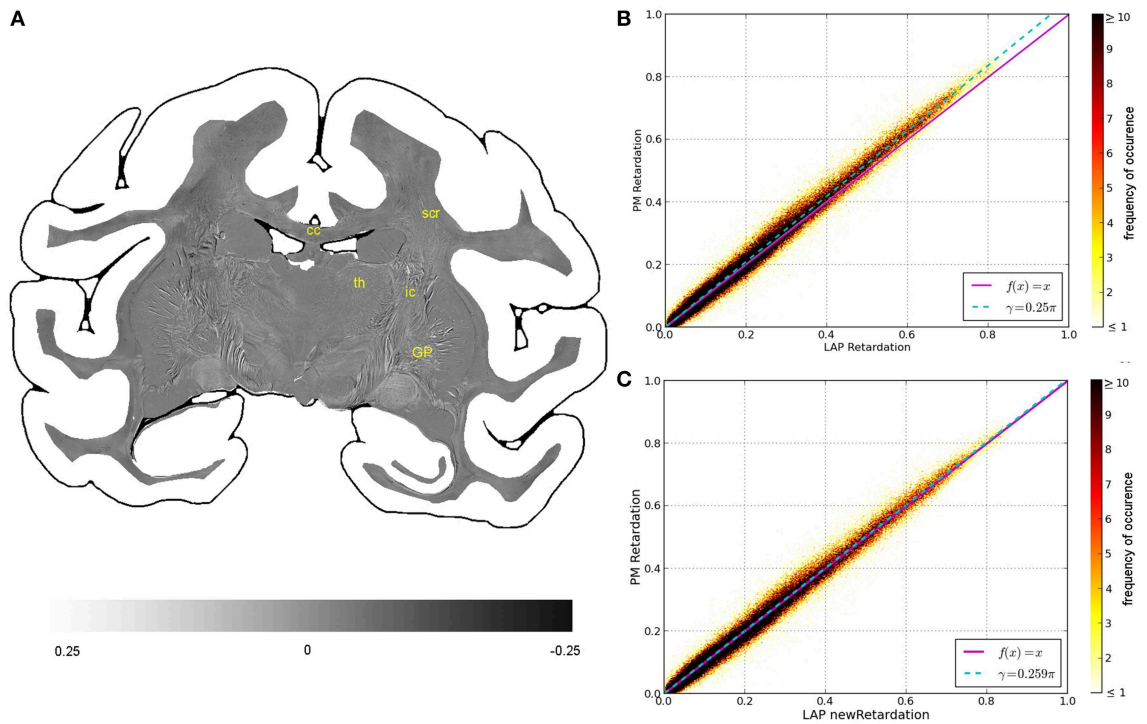

FIGURE 4 | Consistency of the measured retardation value. (A) Shows a differential map obtained from subtracting the retardation map measured with the LAP from the downsampled PM retardation map. Bright pixels highlight in which areas the largest differences between the two maps occur. **(B,C)** Are scatterplots which show a direct comparison of the measured retardation values. For both scatterplots the same PM data were used while the analysis of the LAP measurements differ. For **(B)** the LAP retardation values are derived employing a retardance of $\gamma = 0.25\pi$ and for **(C)** a retardance of $\gamma = 0.259\pi$ was used. The color code indicates the number of occurrences.

GmbH, Germany (Axer et al., 2011a). The extracted direction and retardation maps turned out to be well suited to identify sources of differences in the PM and LAP measurements.

This study corroborated that the discrepancy of the peak wavelength of the illumination source and the design wavelength of the used quarter-waveplate has significant impact on the determined retardation signal and consequently on the estimated fiber orientation. Such a discrepancy exists for the LAP, but not for the PM. However, by generalizing the mathematical description of the retardance γ induced by the waveplate and using $\gamma = 0.259\pi$ for the LAP setup (instead of $\gamma = 0.25\pi$) we achieved similar retardation values for the LAP and

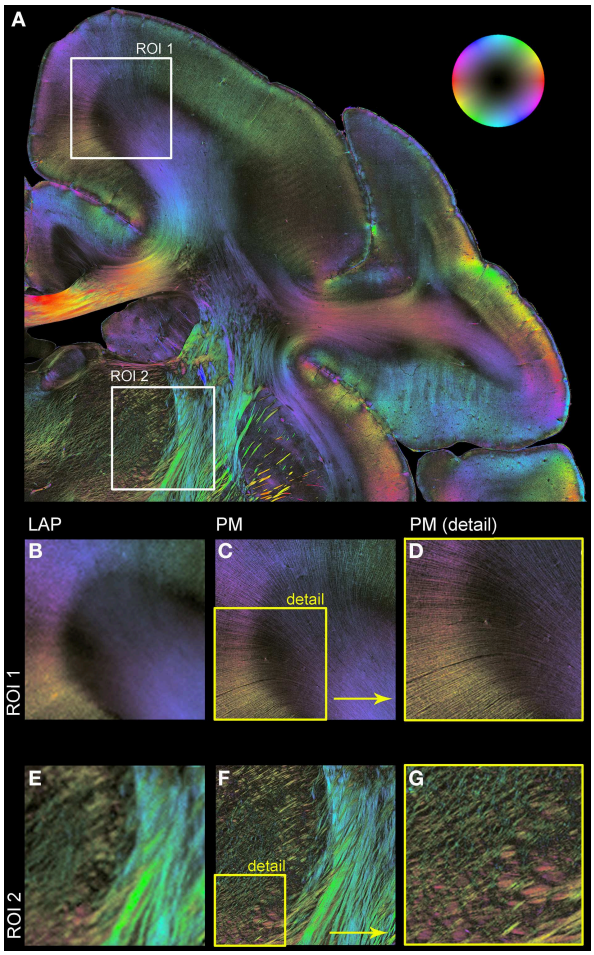

FIGURE 5 | Comparison of LAP and PM based on FOMs. Orientation of nerve fibers is color coded according to the color scheme indicated by the bubble in **(A)**. **(A)** Displays a region of interest of a vervet monkey section measured with the PM. For further illustration of the differences and similarities of the LAP **(B,E)** and the PM **(C,D,F,G)** two regions of interest (ROI 1 and ROI 2) are enlarged. **(D,G)** represent an enlargement of **(C,F)** to highlight the high-resolution capabilities of the PM.

PM measurements by the Fourier-based downsampling. The PM measurements were chosen here as a reference, since (i) previous studies confirmed the optimal matching of illumination wavelength and design wavelength for this setup (Reckfort et al., 2013) and (ii) the optical resolution of the PM is in the same order of magnitude as the targeted axonal diameters (cf. Aboitiz et al., 1992). This approach is superior to the methodology described by Reckfort et al. (2013), where an empirical correction factor was proposed to compensate for the differences between PM and LAP measurements, without considering the extensive effects on fiber orientation estimations (especially in brain regions of complex fiber architecture).

A second key element toward a reliable comparison of PM and LAP data is the downsampling methodology which models the lateral partial volume effects that are very specific to 3D-PLI measurements. Since the measurements provide sinusoidal intensity curves per pixel, combining a neighborhood of pixels into an averaged signal requires the superposition of the individual sinusoidal curves rather than averaging scalar values (i.e., retardation values and direction angles). Consequently, the downsampling procedure was applied to the individual Fourier coefficients to preserve the sinusoidal characteristic of the measurements. Theoretically it is possible to interpolate the LAP images and compare them with the original PM images, however in order to significantly contribute to the neuroanatomical interpretation a sophisticated interpolation such as used in super resolution imaging is necessary. Such a comparison might be interesting and could be considered for a future study.

In addition, it was demonstrated that a simple averaging of the retardation values does not correctly describe the lateral partial volume effects observed in 3D-PLI. Averaging PM retardation values in regions of 48 × 48 pixels led to higher values than measured with the LAP in the corresponding pixel. This is attributed to the fact that the superposition of sinusoidal signals cannot be described adequately in the scalar retardation/direction space (cf. Section 2.6). Nonetheless, the comparison of downsampled PM and measured LAP retardation maps indicated that a differential map of the averaged retardation and the retardation of the averaged sinusoidal curves is a good

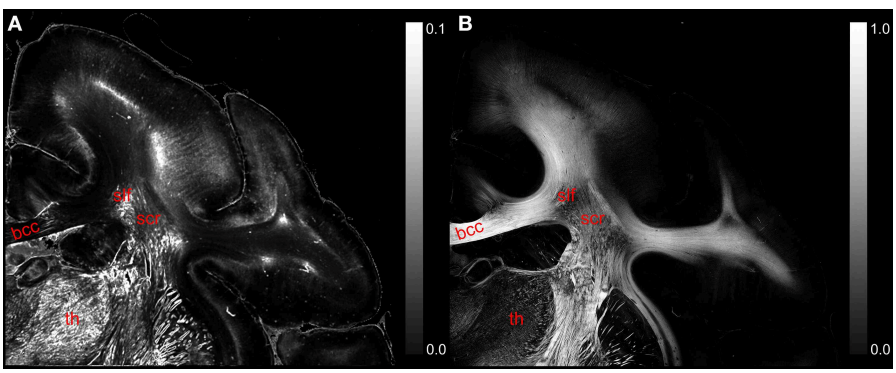

FIGURE 6 | (A) Displays a differential map of the downsampled averaged retardation values based on PM measurements and the retardation map determined with the LAP with $\gamma = 0.259\pi$. **(B)** Shows in comparison the retardation map obtained with the PM. (bcc, body of corpus callosum; scr, superior corona radiata; slf, superior longitudinal fasciculus; th, thalamus.)

measure for the magnitude of the lateral partial volume effect expected in LAP measurements. By this means, brain regions of heterogeneous and homogeneous fiber distributions can be classified, which adds valuable information to the estimated fiber orientations. Recent 3D-PLI simulations demonstrated that the extracted fiber orientations of heterogeneous areas are significantly influenced by the relative mixture of fibers Dohmen et al. (2015). The study showed that this is relevant particularly for non-orthogonally crossing fibers where not the predominant fiber direction is estimated, but rather the intermediate fiber direction. Thus, the experimental identification of reliable estimates of fiber orientations will significantly improve the data interpretation. Fiber tractography algorithms running on LAP data sets, for example, will benefit from this information, as they can be guided differently and more reliably through brain regions of known different fiber constellations.

To conclude, the employed polarimetric setups were optimized for investigating nerve fibers at different scales and independently from the optical system properties. We could demonstrate both the mutual and complementary contributions of the two polarimeters. Thus, it is now possible to retrieve comparable results with the large-area polarimeter and the polarization microscope, enabling the investigation of short-range axonal projections and long-distance fiber connections at the sub-millimeter scale. The 3D-PLI data serves as a multiscale description of the human fiber architecture. This consolidates 3D-PLI as a key technology to understand the organization of the human fiber architecture.

Author Contributions

JR substantially contributed to the conception and design of the work as well as to the acquisition, analysis, and interpretation of data for the work. HW substantially contributed to the theoretical derivations of the new approach in this study and the analysis of the measured data. JR and HW drafted co-jointly the manuscript, revised it and both approved the final version to be published. UP substantially contributed to the development of methods, the interpretation of results and revising the manuscript. KZ substantially contributed to the method of tissue preparation and processing, and to the anatomical content of this paper. He further contributed to revision of the manuscript. KA substantially contributed to the anatomical content of this paper, the interpretation of the results and revised the manuscript. MA substantially contributed to the design of the study, the development of methods, the interpretation of results and revising the manuscript. All authors gave their final approval to the submitted version and agreed to be accountable for all aspects of the work.

Funding

This study was partially supported by the National Institutes of Health under grant agreement no. *R01MH 092311*, by the Helmholtz Association through the Helmholtz Portfolio Theme "Supercomputing and Modeling for the Human Brain," and by the European Union Seventh Framework Programme (FP7/2007-2013) under grant agreement no. *604102* (Human Brain Project).

Acknowledgments

We would like to thank Markus Cremer, Patrick Nysten, Lutz Pohlen (Research Centre Jülich, Germany) and Roger Woods (University of California, Los Angeles, USA) for excellent technical assistance and preparation of the histological sections.

Supplementary Material

The Supplementary Material for this article can be found online at: http://journal.frontiersin.org/article/10.3389/fnana.2015.00118

References

Aboitiz, F., Scheibel, A. B., Fisher, R. S., and Zaidel, E. (1992). Fiber composition of the human corpus callosum. *Brain Res.* 598, 143–153. doi: 10.1016/0006-8993(92)90178-C

Amunts, K., Bücker, O., and Axer, M. (2013a). "Towards a multiscale, high-resolution model of the human brain," in *Brain-Inspired Computing*, eds L. Grandinetti, T. Lippert, and N. Petkov (Cetraro: Springer), 3–14. doi: 10.1007/978-3-319-12084-3_1

Amunts, K., Lepage, C., Borgeat, L., Mohlberg, H., Dickscheid, T., Rousseau, M.-E., et al. (2013b). Bigbrain: an ultrahigh-resolution 3D human brain model. *Science* 340, 1472–1475. doi: 10.1126/science.1235381

Axer, M., Amunts, K., Gräßel, D., Palm, C., Dammers, J., Axer, H., et al. (2011a). A novel approach to the human connectome: ultra-high resolution mapping of fiber tracts in the brain. *NeuroImage* 54, 1091–1101. doi: 10.1016/j.neuroimage.2010.08.075

Axer, M., Gräßel, D., Kleiner, M., Dammers, J., Dickscheid, T., Reckfort, J., et al. (2011b). High-resolution fiber tract reconstruction in the human brain by means of three-dimensional polarized light imaging. *Front. Neuroinform.* 5:34. doi: 10.3389/fninf.2011.00034

Basser, P. J., Mattiello, J., and Lebihan, D. (1994). Estimation of the effective self-diffusion tensor from the NMR spin echo. *J. Magn. Reson. B* 103, 247–254. doi: 10.1006/jmrb.1994.1037

Beaulieu, C. (2002). The basis of anisotropic water diffusion in the nervous system - a technical review. *NMR Biomed.* 15, 435–455. doi: 10.1002/nbm.782

Behrens, T. E. J., Berg, H. J., Jbabdi, S., Rushworth, M. F. S., and Woolrich, M. W. (2007). Probabilistic diffusion tractography with multiple fibre orientations: what can we gain? *NeuroImage* 34, 144–155. doi: 10.1016/j.neuroimage.2006.09.018

Brodmann, K. (1903). Bemerkungen zur untersuchung des nervensystems im polarisierten licht. *J. Psychol. Neurol.* 2, 211–213.

Bürgel, U., Amunts, K., Hoemke, L., Mohlberg, H., Gilsbach, J., and Zilles, K. (2006). White matter fiber tracts of the human brain: three-dimensional mapping at microscopic resolution topography and intersubject variability. *Neuroimage* 29, 1092–1105. doi: 10.1016/j.neuroimage.2005.08.040

Bürgel, U., Mecklenburg, I., Blohm, U., and Zilles, K. (1997). Histological visualization of long fiber tracts in the white matter of adult human brains. *J. Brain Res.* 38, 397–404.

Conturo, T. E., Lori, N. F., Cull, T. S., Akbudak, E., Snyder, A. Z., Shimony, J. S., et al. (1999). Tracking neuronal fiber pathways in the living human

brain. *Proc. Natl. Acad. Sci. U.S.A.* 96, 10422–10427. doi: 10.1073/pnas.96.18.10422

de Boer, J. F., Milner, T. E., van Gemert, M. J. C., and Nelson, J. S. (1997). Two-dimensional birefringence imaging in biological tissue by polarization-sensitive optical coherence tomography. *Opt. Lett.* 22, 934–936. doi: 10.1364/OL.22.000934

Dell'Acqua, F., Rizzo, G., Scifo, P., Clarke, R. A., Scotti, G., and Fazio, F. (2007). A model-based deconvolution approach to solve fiber crossing in diffusion-weighted MR imaging. *IEEE Trans. Biomed. Eng.* 54, 462–472. doi: 10.1109/TBME.2006.888830

Descoteaux, M., Angelino, E., Fitzgibbons, S., and Deriche, R. (2007). Regularized, fast, and robust analytical Q-ball imaging. *Magn. Reson. Med.* 58, 497–510. doi: 10.1002/mrm.21277

Dohmen, M., Menzel, M., Wiese, H., Reckfort, J., Hanke, F., Pietrzyk, U., et al. (2015). Understanding fiber mixture by simulation in 3D polarized light imaging. *NeuroImage* 111, 464–475. doi: 10.1016/j.neuroimage.2015.02.020

Glazer, A., Lewis, J., and Kaminsky, W. (1996). An automatic optical imaging system for birefringent media. *Proc. R. Soc. A Math. Phys. Eng. Sci.* 452, 2751–2765. doi: 10.1098/rspa.1996.0145

Goethlin, G. (1913). Die doppelbrechenden eigenschaften des nervengewebes - ihre ursachen und ihre biologischen konsequenzen. *Kungl. Svenska Vetenskapsakad. Handl.* 51, 1–92.

Jansons, K. M., and Alexander, D. C. (2003). Persistent angular structure: new insights from diffusion magnetic resonance imaging data. *Inverse Probl.* 19, 1031–1046. doi: 10.1088/0266-5611/19/5/303

Johansen-Berg, H., and Rushworth, M. F. S. (2009). Using diffusion imaging to study human connectional anatomy. *Annu. Rev. Neurosci.* 32, 75–94. doi: 10.1146/annurev.neuro.051508.135735

Klein, S., Staring, M., Murphy, K., Viergever, M., and Pluim, J. (2010). Elastix: a toolbox for intensity based medical image registration. *IEEE Trans. Med. Imaging* 29, 196–205. doi: 10.1109/TMI.2009.2035616

Kleiner, M., Axer, M., Gräßel, D., Reckfort, J., Pietrzyk, U., Amunts, K., et al. (2012). "Classification of ambiguous nerve fiber orientations in 3D polarized light imaging," in *Proceeding MICCAI*, eds N. Ayache, H. Delingette, P. Golland, and K. Mori (Heidelberg: Springer), 206–213. doi: 10.1007/978-3-642-33415-3

Klingler, J. (1935). Erleichterung der makroskopischen praeparation des gehirns durch den gefrierprozess. *Schweiz. Arch. Neurol. Psychiatr.* 36, 247–256.

Larsen, L., Griffin, L. D., Gräßel, D., Witte, O. W., and Axer, H. (2007). Polarized light imaging of white matter architecture. *Microsc. Res. Tech.* 70, 851–863. doi: 10.1002/jemt.20488

Li, A., Gong, H., Zhang, B., Wang, Q., Yan, C., Wu, J., et al. (2010). Micro-optical sectioning tomography to obtain a high-resolution atlas of the mouse brain. *Science* 330, 1404–1408. doi: 10.1126/science.1191776

Martenson, R. (1992). *Myelin: Biology and Chemistry.* Boca Raton, FL: CRC Press.

Mori, S., and Zhang, J. (2006). Principles of diffusion tensor imaging and its applications to basic neuroscience research. *Neuron* 51, 527–539. doi: 10.1016/j.neuron.2006.08.012

Pierpaoli, C., and Basser, P. J. (1996). Toward a quantitative assessment of diffusion anisotropy. *Magn. Reson. Med.* 36, 893–906. doi: 10.1002/mrm.1910360612

Reckfort, J., Wiese, H., Dohmen, M., Gräßel, D., Pietrzyk, U., Zilles, K., et al. (2013). "Extracting the inclination angle of nerve fibers within the human brain with 3D-PLI independent of system properties, Vol. 8873," in *Proceeding SPIE - International Society of Optical Engineering* (San Diego, CA). doi: 10.1117/12.2023198

Schindelin, J., Arganda-Carreras, I., Frise, E., Kaynig, V., Longari, M. Pietzsch, T., et al. (2012). Fiji: an open-source platform for biological-image analysis. *Nat. Methods* 9, 676–682. doi: 10.1038/NMETH.2019

Schmahmann, J. D., Pandya, D. N., Wang, R., Dai, G., D'Arceuil, H. E., De Crespigny, A. J., et al. (2007). Association fibre pathways of the brain: parallel observations from diffusion spectrum imaging and autoradiography. *Brain* 130, 630–653. doi: 10.1093/brain/awl359

Schmidt, W. (1923). Zur doppelbrechung des nervenmarks. *Z. Wiss. Mikrosk.* 41, 29–38.

Schmitt, F., and Bear, R. (1937). The optical properties of vertebrate nerve axons as related to fiber size. *J. Cell. Comp. Physiol.* 9, 261–273. doi: 10.1002/jcp.1030090209

Silvestri, L., Bria, A., Sacconi, L., Iannello, G., and Pavone, F. S. (2012). Confocal light sheet microscopy: micron-scale neuroanatomy of the entire mouse brain. *Opt. Express* 20, 20582–20598. doi: 10.1364/OE.20.020582

Tournier, J., Calamante, F., and Connelly, A. (2007). Robust determination of the fiber orientation distribution in diffusion MRI: non-negativity constrained super-resolved spherical deconvolution. *NeuroImage* 35, 1459–1472. doi: 10.1016/j.neuroimage.2007.02.016

Tournier, J., Calamante, F., Gadian, D., and Connelly, A. (2004). Direct estimation of the fiber orientation density function from diffusion-weighted mri data using spherical deconvolution. *NeuroImage* 23, 1176–1185. doi: 10.1016/j.neuroimage.2004.07.037

Tuch, D. S., Reese, T. G., Wiegell, M. R., Makris, N., Belliveau, J. W., and van Wedeen, J. (2002). High angular resolution diffusion imaging reveals intravoxel white matter fiber heterogeneity. *Magn. Reson. Med.* 48, 577–582. doi: 10.1002/mrm.10268

Tüere, U., Yasargil, M. G., Friedmann, A. H., and Al-Mefty, O. (2000). Fiber dissection technique: lateral aspect of the brain. *Neurosurgery* 47, 417–427. doi: 10.1097/00006123-200008000-00028

Wang, H., Black, A. J., Zhu, J., Stigen, T. W., Al-Qaisi, M. K., Netoff, T. I., et al. (2011). Reconstructing micrometer-scale fiber pathways in the brain: multi-contrast optical coherence tomography based tractography. *NeuroImage* 58, 984–992. doi: 10.1016/j.neuroimage.2011.07.005

Wiese, H., Gräßel, D., Pietrzyk, U., Amunts, K., and Axer, M. (2014). "Polarized Light Imaging of the Human Brain: A New Approach to the Data Analysis of Tilted Sections," in *Proceedings of SPIE-International Professional Society Optics and Photonics Technology*, ed D. B. Chenault and D. H. Goldstein (Baltimore: International Society of Optical Engineering).

Wolman, M. (1975). Polarized-light microscopy as a tool of diagnostic pathology - review. *J. Histochem. Cytochem.* 23, 21–50. doi: 10.1177/23.1.1090645

Yoo, T., Ackerman, M., Lorensen, W., Schroeder, W., Chalana, V., Aylward, S., et al. (2002). Engineering and algorithm design for an image processing API: a technical report on ITK-the insight toolkit. *Stud. Health Technol. Inform.* 85, 586–592. doi: 10.1.1.2.1280

Conflict of Interest Statement: The authors declare that the research was conducted in the absence of any commercial or financial relationships that could be construed as a potential conflict of interest.

frontiers in Neuroanatomy

MINI REVIEW
published: 20 May 2015
doi: 10.3389/fnana.2015.00061

About connections

Kathleen S. Rockland[1,2]*

[1] Department of Anatomy and Neurobiology, Boston University School of Medicine, Boston, MA, USA, [2] Cold Spring Harbor Laboratory, Cold Spring Harbor, NY, USA

Despite the attention attracted by "connectomics", one can lose sight of the very real questions concerning "What are connections?" In the neuroimaging community, "structural" connectivity is ground truth and underlying constraint on "functional" or "effective" connectivity. It is referenced to underlying anatomy; but, as increasingly remarked, there is a large gap between the wealth of human brain mapping and the relatively scant data on actual anatomical connectivity. Moreover, connections have typically been discussed as "pairwise", point *x* projecting to point *y* (or: to points *y* and *z*), or more recently, in graph theoretical terms, as "nodes" or regions and the interconnecting "edges". This is a convenient shorthand, but tends not to capture the richness and nuance of basic anatomical properties as identified in the classic tradition of tracer studies. The present short review accordingly revisits connectional weights, heterogeneity, reciprocity, topography, and hierarchical organization, drawing on concrete examples. The emphasis is on presynaptic long-distance connections, motivated by the intention to probe current assumptions and promote discussions about further progress and synthesis.

Keywords: cerebral cortex, connectome, hierarchy, network, projections, reciprocal, topography

OPEN ACCESS

Edited by:
Menno P. Witter, Norwegian University of Science and Technology, Norway

Reviewed by:
Pierre Lavenex, University of Lausanne, Switzerland
Guy Elston, Centre for Cognitive Neuroscience, Australia

***Correspondence:**
Kathleen S. Rockland, Department of Anatomy and Neurobiology, Boston University School of Medicine, 72 East Concord St. L-1004, Boston, MA, 02118, USA
krock@bu.edu

Received: *07 March 2015*
Accepted: *02 May 2015*
Published: *20 May 2015*

Citation:
Rockland KS (2015) About connections. Front. Neuroanat. 9:61. doi: 10.3389/fnana.2015.00061

Introduction

This mini-Review is a thumbnail treatment of some basic properties associated with long-distance cortical connections, mainly from the presynaptic perspective. This falls within the emerging "mesoscale" light microscopic framework, and largely leaves aside more detailed pre- and postsynaptic microcircuitry. I hope by discussion and specific examples to raise questions that might help in thinking about connections and in critically navigating the anatomical literature. Species and area differences, and interneuron distribution and pyramidal cell features (e.g., Elston et al., 2011), are largely neglected, owing to space constraints.

The early modern period of connectivity studies is often dated from the 1970's, when tracer techniques using physiological axonal transport became routinely available (Köbbert et al., 2000; Lanciego and Wouterlood, 2011). Despite impressive progress in mapping the general connectivity of the brain over the intervening 45 years or so, there are still woefully few hard data, especially for the human cerebral cortex. Moreover, the relation between structure and function is often difficult to ascertain.

Experimental investigations of anatomical connections, in animal models, routinely begin with *in vivo* injection of tracer which is transported from the injected site, anterogradely to visualize all recipient (target) structures or retrogradely to visualize all input (source) structures. This unfortunately gives rise to a "source and target", input/output convention, and is really shorthand for a much more complex reality. Axons of single neurons branch divergently to hundreds or thousands of postsynaptic neurons, and postsynaptic neurons

can receive thousands of presynaptic inputs, converging from multiple different structures. Connectional divergence can be investigated by intracellular or very small extracellular injections of anterograde tracers, that produce stunning detail of an individual neuron, its axon branches and trajectory, and the distal terminations (**Figure 1**). This technique, despite the advantages of being high resolution, has suffered from the technical challenge of collecting strict serial histology sections and reconstructing intricate axonal branches in 3-dimensional brain space. In this regard, rapid developments in global imaging, as in the various "CLARITY" protocols, potentially offer a useful complementary approach (for applications and limitations, see, among others, Chung and Deisseroth, 2013; Osten and Margrie, 2013; Silvestri et al., 2013; Renier et al., 2014).

"Connections" or connectivity, as used here, refers to both distal pre-synaptic arborization and network organization, and is synonymous with "projections" (but not "projectome", as sometimes used narrowly in reference to white matter). Connectivity summaries often show connections as lines between two intercommunicating structures. This is a convenient convention, but tends to cloud important issues of connectional strength, heterogeneity, reciprocity, topography, and hierarchy, issues that are briefly discussed in this mini-review. Longer reviews have treated the promise and pitfalls of newer mapping techniques (Yook et al., 2013), and further discussed the need for closing the gap between current "connectome" maps and the "real underlying anatomy" (Budd and Kisvárday, 2012; Mesulam, 2012; Catani et al., 2013).

Connectional Strength

Connectional "strength" is hard to establish. Anatomical approaches rely on density of retrogradely labeled neurons or density of anterogradely labeled synaptic terminations. This is a reasonable first approximation, but one that must be used with caution. One major issue is that retrogradely labeled neurons and anterogradely labeled terminations are usually not homogeneous. Aside from anatomical heterogeneity, substantial evidence points to time-varying correlated activity (Calhoun et al., 2014; Kopell et al., 2014; Roland et al., 2014). A second issue is individual variability between brains, as influenced by maturational and other factors (cf. Markov et al., 2014). This can be mitigated by replicating results in multiple brains, but, in primate and even rodent brains, is likely to remain a factor. A third issue, as summarized elsewhere (Glickfeld et al., 2014), is that synaptic efficacy depends on multiple factors, such as the specific inhibitory or excitatory postsynaptic targets, synaptic location on the postsynaptic dendrite, and distribution of ionotrophic or metabotrophic receptors.

Equating "dense" projections with strength or efficacy can easily lead to erroneous conclusions. A long-standing puzzle, for example, has been that thalamocortical projections to the primary sensory areas comprise only a small proportion of the synaptic input to layer 4 neurons, but nevertheless strongly excite their postsynaptic targets (Peters and Payne, 1993; Latawiec et al., 2000; da Costa and Martin, 2011). Size of postsynaptic density or number of synaptic vesicles could be one factor, but the median size of the thalamic synapse is only slightly larger than that of other synapses (in cat: da Costa and Martin, 2011). One recent *in vivo* study reports, for rat somatosensory cortex at least, direct measurements of synaptic strength showing that thalamocortical and corticocortical synapses are both weak. Thalamic synapses are sufficiently convergent (~90 thalamic neurons: 1 postsynaptic cortical neuron) and coincidentally active to exert an "outsized influence" (Schoonover et al., 2014).

A second example of how numbers can mislead is from corticothalamic projections (Lee and Sherman, 2011; Sherman and Guillery, 2013). These can be subdivided into two broad

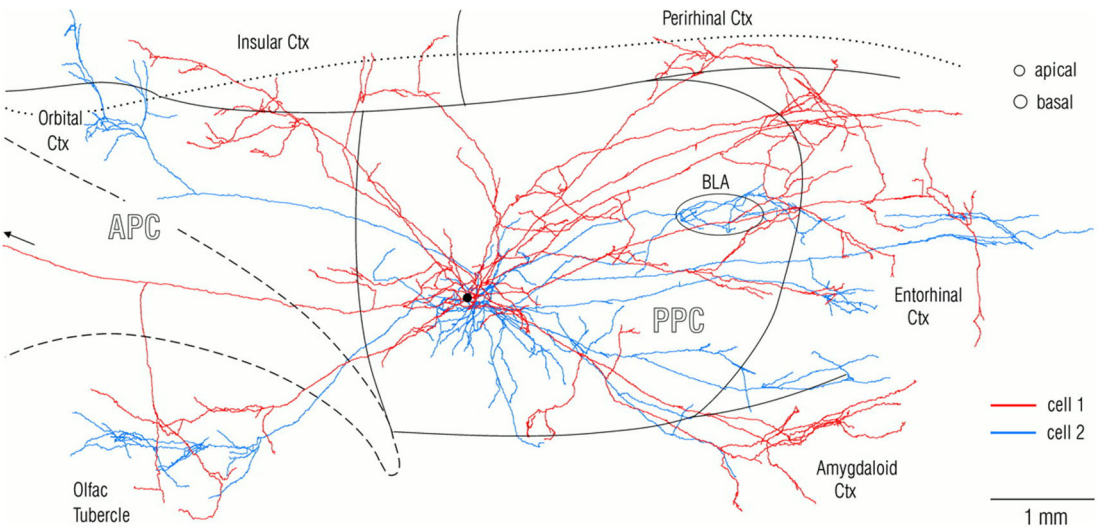

FIGURE 1 | Visualization at single-axon resolution, after intercellular fills, of two adjacent neurons (red and blue) in rat posterior piriform cortex. Note widespread, but non-identical divergence of the two axons. Reproduced with permission from Johnson et al. (2000) Figure 2.

types, distinguished in part by having large or small synapses. Type 2, with large synapses, are considered "driving", but they originate from a much smaller neuronal population of neurons (in layer 5) than the population (in layer 6) giving rise to the "modulatory" type 1 projections (estimated as 1:50 in monkey temporal areas, Rockland, 1996; and see revised terminology in Lee and Sherman, 2011). In this case, the difference in efficacy has been attributed both to synapse size and more proximal postsynaptic location of the type 2 projections. In somatosensory thalamus of rodents, the effect of cortical "driver" input appears to be influenced by other, near coincident "driving" brainstem activity, converging on the same thalamocortical neuron (Groh et al., 2014).

In summary, the number of labeled neurons in retrograde tracer experiments or density of anterogradely labeled terminations is a useful estimate of connectional "strength," but strictly speaking is a density measurement. It cannot and should not be equated with efficacy.

Connectional Heterogeneity and Subtypes

There are connectional subtypes. The major cortical connectional systems (corticothalamic, corticocortical, corticostriatal, corticocollicular, and others) are conveniently classified to a first approximation by features of the parent cell in the source structure (laminar location and dendritic morphology), and the terminations and arborization in the target structure. There has been less consideration of finer subtypes, largely due to paucity of criteria, but it is worth considering that the degree of heterogeneity within any connection might actually be high.

One criterion for finer subdivisions is the classification of pyramidal cells, the neurons giving rise to connections. A recent study in rat frontal cortex identified "more than 10" different pyramidal subtypes on the basis of dendritic morphology and firing properties (van Aerde and Feldmeyer, 2014). This relatively small number (10) is likely to become much larger when factoring in criteria from gene expression levels and distribution of ion channels and receptors.

Subdivisions can be established from the basic characteristics of the pyramidal cell extrinsic axon. In what also appears to be a high degree of diversity, these vary morphologically in spatial divergence, axon diameter, and number of terminal arbors and specializations. A survey focusing on axon diameters alone, from projection neurons in monkey parietal area, found that each cortical and subcortical projection consists of axons with different diameters (Innocenti et al., 2014, their Table 2). The authors suggest this implies an "extraordinary complexity of axonal pathways operating at different conduction speed and generating different conduction delays between brain sites."

Connectional subtypes have too often been seen as anatomical dualities. This carries an assumption of a functional dichotomy, even though anatomical evidence actually points to greater diversification. Corticothalamic projections, as already noted, have been classified into two broad categories on the basis of multiple criteria, but these have been further differentiated into two classes of type 1 axons and four classes of type 2 axons, based on morphological features of axon diameter, axon branching, and density of terminal specializations (Kultas-Ilinsky et al., 2003). The implication is that there are "multiple modes" of corticothalamic communication "feeding into a variety of functionally different neuronal networks, with each processing specific information."

Cortical "feedback" and "feedforward" connections are another striking example, where pronounced structural differences (in laminar origin and termination, and spatial divergence of the terminal axon arbors) have been construed as evidence for two subtypes (discussion in Rockland, 1997; Markov and Kennedy, 2013; Markov et al., 2014). For feedback connections, however, there are at least four criteria for further subdivisions. (1) There is typically a bistratified distribution of cells of origin, in the supra- and infragranular layers (respectively, layers 2, 3A and 6); (2) Investigations of the ventral visual pathway report that a subpopulation of feedback-projecting neurons in layer 6, but not those in layer 2 or 3, uses synaptic zinc, an activity-related neuromodulator (Ichinohe et al., 2010); (3) The supra- and infragranular projecting populations differ in dendritic morphology, synaptic inputs, and local axon collateralization; and (4) There are substantial differences in the terminal axon portions, with Anderson and Martin (2009) distinguishing three subtypes of feedback axons from area V2 to V1 on the basis of axon caliber and density of terminal specializations. Similarly, a study in the auditory cortex notes that both feedforward and feedback projections include multiple "strands" within the main bundle, that target neurons in different layers (Hackett et al., 2014).

Evidence for finer subtypes of feedforward cortical connections is more indirect, but still suggestive. Parent cells, located through the thickness of layer 3, are likely to be heterogeneous; and even projections from area V1 to area V2 originate from neurons in layer 5 as well as layer 3 (Kennedy and Bullier, 1985; Sincich et al., 2010). Axon diameters are not uniform. EM data for cortical connections from both V1 and V2 to MT/V5 show a diameter distribution from less than 1.0 μm to 3.5 μm, with the majority of profiles being about 1.5 μm (Anderson and Martin, 2002).

Pyramidal cell axons have intrinsic collaterals (i.e., near the parent soma and within the same cortical area). The pattern of intrinsic collaterals in relation to extrinsic targets is another criteria for subtypes. From analysis of local axon collaterals, correlated with differences in dendritic trees, Wiser and Callaway (1996) distinguished two broad classes of layer 6 neurons in area V1 of macaques, each with further subdivisions. Also, corticothalamic neurons in layer 5 have widespread collaterals in the deeper layers, while the local collaterals of corticothalamic neurons in layer 6 project to layer 4 and are less divergent (Ojima et al., 1992). A safe assumption is that this heterogeneity is widely typical of various connectional systems, and that it is indicative of functional heterogeneity within connections.

The number, spatial extent, and laminar distribution of intrinsic collaterals has yet to be codified, but can be an important classification criterion of pyramidal cells. Importantly, a recent intracellular labeling investigation reports substantial within-layer heterogeneity for local collaterals of superficial pyramidal

neurons (Martin et al., 2014). For 33 pyramidal cells, the number of local collaterals ranged to about 9 (supple. materials in Martin et al.). Co-registration of bouton clusters with optically imaged orientation domains revealed that intrinsic collaterals of a single pyramidal cell targeted a variety of different orientation domains. From these two results, the authors conclude that "instead of treating the lateral connections as a single homogeneous network, the real clue to its structure and function may lie in its heterogeneity of connections. . . and it is this heterogeneity that needs to be explained."

In summary, there is abundant evidence for intra-class connectional heterogeneity. This can be assumed to support a variegated functional repertoire.

Connectional Reciprocity

At the source-to-target, area-to-area level, reciprocity is common but clearly not ubiquitous, and why only some connections are reciprocal has not been explained. A number of corticothalamic, corticoamygdala, and corticocortical connections are reciprocal at the area-to-area level, whereas corticostriatal, corticocollicular, and other cortico-subcortical connections are not. Even at the area level, there are intriguing differences. For example, the amygdala projects to cortical areas that extend throughout the ventral visual stream, including area V1; but there are no projections from area V1 back to the amygdala (macaque: Freese and Amaral, 2005). In the network of visual cortical connections, temporal areas project back to multiple areas, including V1, but do not receive projections from V1 (Rockland and Van Hoesen, 1994; Rockland et al., 1994). Hippocampal CA1 has reciprocal connections with entorhinal cortex, but there are only input (afferent) connections from parietal cortex (macaque: Rockland and Van Hoesen, 1999), and only output (efferent) connections to frontal cortex (macaque: Barbas and Blatt, 1995; Cavada et al., 2000; rat: Vertes, 2006). One interesting discussion about "reciprocity" is that this may be a secondary consequence of other factors. Reciprocity of corticothalamic projections, for example, has been discussed as a consequence of the branching patterns of different classes of prethalamic inputs ("rule of parity" proposed by Deschênes et al., 1998).

At the cell-to-cell level there are essentially no data *in vivo* about direct reciprocity. For long-distance cortical connections, a general rule has been that pyramidal cells target a mixed population of other pyramidal neurons and inhibitory neurons, in an approximate ratio of 80% to 20%. Cortical inhibitory neurons necessarily represent a non-reciprocal component. Moreover, continuing with the example of cortical connections, these typically have multiple spatially separated terminal arbors, each contacting dozens to hundreds of postsynaptic neurons. An unanswered question is whether the pyramidal neurons in all or only one of the postsynaptic foci send return projections to the parent cell and/or to its immediate neighbors.

In summary, reciprocity is potentially an important network property, but, despite the common invocation, has not been actually demonstrated at the cell-to-cell level, is under-investigated and likely over-assumed even at the inter-areal level.

Topographic and Non-Topographic Connections

Topographically organized maps are an important principle of cortical organization, especially for the primary and early sensory cortices, where the cortical areas have an ordered relationship to retinotopic, cochleatopic, or somatosensory peripheral space. Even for these sensory areas, however, there are many examples of seemingly non-topographic or "distributed" processing. Projections that target layer 1, in particular, are widely divergent; and feedback cortical and thalamocortical connections, visualized at the single axon level, clearly extend widely in layer 1, including over different cortical areas. In addition, local intrinsic collaterals of pyramidal cells are often widespread: collaterals of layer 2 neurons in the tree shrew (Rockland et al., 1982), of layer 2 neurons in rat retrosplenial cortex (Kurotani et al., 2013), of layer 3 pyramidal neurons (Gilbert and Wiesel, 1983; Martin et al., 2014), and of layer 6 corticoclaustral neurons (Katz, 1987). The spatial distances extend well beyond the parent neuron, likely to a different part of a topographic map (and see Haber and Calzavara, 2009 for cortico-basal ganglia networks).

A single axon can have multiple arbors, in what might be a mixed topographic and non-topographic pattern. In rat motor cortex, a single thalamocortical axon to the middle layers spans more than 5.0 mm (**Figure 2**; Kaneko, 2013). In the early visual association areas in macaque, connections from V1 to MT/V5 and from V2 to V4 have three or four spatially separate arbors, distributed over 2.0–3.0 mm (Rockland, 1989, 1992). How the individual arbors relate to retinotopic organization in the target area is not known. Possibly, one of the arbors ("principal"?) may terminate in a topographically equivalent locus, while the others do not.

In summary, there is both topographic and non-topographic connectivity. This can be in relation to different systems (layer 1- vs. layer 4-terminating), different areas (motor vs. sensory), or different arbors of one axon in one area.

Connections and Hierarchical Architecture

The identification of cortical areas has naturally led to a quest for how these are organized. A popular idea has favored a hierarchical organization, with primary sensory areas at the "lowest" level, initiating a serial connectivity (e.g., Felleman and Van Essen, 1991). There have, however, been extensive discussions about "reverse hierarchies" (i.e., connections directed *into* the sensory areas; Hochstein and Ahissar, 2002), and about "alternative hierarchies" based on properties such as reaction times (Petroni et al., 2001). Besides, the organization may be something quite different. One paper posits a mix of "partial gradients, fractures, swirls, regions that resemble separate areas in some ways but not others, and in not a lack of topographic maps but an excess of maps overlaid on each other, no one of which seems to be entirely correct" (Graziano and Aflalo, 2007). This evokes something like the "fractured

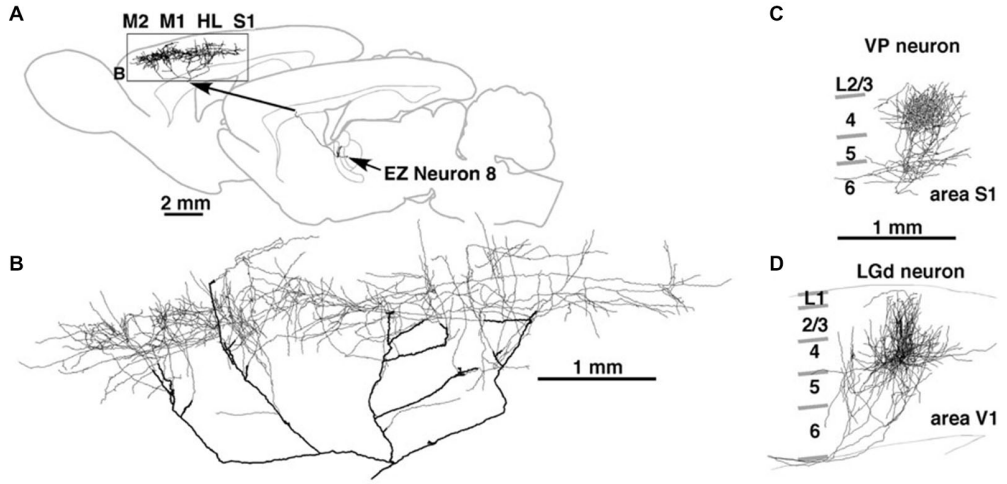

FIGURE 2 | Thalamocortical terminations at single axon resolution in rat motor cortex in (A) and, higher magnification, (B); in primary somatosensory cortex (C); and in primary visual cortex (D). Note high degree of divergence in motor cortex, and area-specific differences in tangential spread. Reproduced from Kaneko (2013) and, with permission, from figure 8 of Kuramoto et al. (2009). M1 = primary motor cortex; M2 = secondary motor cortex; HL = hindlimb representation; EZ = excitatory subcortical – input zone (of motor thalamus).

topography" recognized for cerebellar cortex (Leergaard et al., 2006).

More specifically, one of several arguments against a purely sensory-based cortical hierarchy is the fact that primary sensory cortices are directly interconnected with multisensory cortices and with other primary and/or secondary sensory cortices (Rockland and Van Hoesen, 1994; Borra and Rockland, 2011; Stehberg et al., 2014). Physiological results corroborate that under certain behavioral conditions, primary sensory areas can be activated by other modalities (Henschke et al., 2015). In this regard, they are not just the "origin" or start-point of a unimodal sensory progression.

Another consideration is the increasing evidence for iterative, non-serial interareal interactions: (1) Simultaneous recordings from V1 and extrastriate area V4 in awake monkeys show that visual information about global contours in a cluttered background emerges initially in V4, ∼40 ms sooner than in V1, and continues to develop in parallel in both areas (Chen et al., 2014). The anatomical interpretation is an incremental integration where feedback connections, in conjunction with local intrinsic connections, act to disambiguate signal from noise. (2) Re-examination of cortical processing streams in the visual cortex emphasizes an "expanded neural framework for processing object quality. . . containing neural representations of object quality both utilized and constrained by at least six distinct cortical and subcortical systems." This is contrasted with the earlier view of the ventral visual pathway "as a largely serial staged hierarchy that culminates in singular object representations" (Kravitz et al., 2013).

In summary, hierarchical organization does not convincingly capture the full complexity of anatomical connectivity. The notion of a hierarchy does not incorporate subcortical loops and neglects the temporal dimension or dynamics, both of which are critical aspects of anatomical and functional organization.

Concluding Remarks

What are connections? They are not arrows, not homogeneous, and, despite the popularity of graph theory (Bullmore and Sporns, 2009), are only partly approximated by "edges." Anatomically depicted connections—whether in images or tables—can look static; but the idea of fixed anatomical connectivity is deceptive and an accident of methodology, just as musical notes are only indicators of the actual music in performance. The static mode of representation makes it easy to forget that connections are heterogeneous in efficacy, in type, and in time, and operate through flexible roles and flexible routes in different behaviors.

Acknowledgments

I thank Drs. Gerald Schneider and R. Jarrett Rushmore for helpful discussions and critical comments on drafts of the manuscript.

References

Anderson, J. C., and Martin, K. A. C. (2002). Connection from cortical area V2 to MT in macaque monkey. *J. Comp. Neurol.* 443, 56–70. doi: 10.1002/cne.10100

Anderson, J., and Martin, K. A. (2009). The synaptic connections between cortical areas V1 and V2 in macaque monkey. *J. Neurosci.* 29, 11283–11293. doi: 10.1523/jneurosci.5757-08.2009

Barbas, H., and Blatt, G. J. (1995). Topographically specific hippocampal projections target functionally distinct prefrontal areas in the

rhesus monkey. *Hippocampus* 5, 511–533. doi: 10.1002/hipo.450050604

Borra, E., and Rockland, K. S. (2011). Projections to early visual areas V1 and V2 in the calcarine fissure from parietal association areas in the macaque. *Front. Neuroanat.* 5:35. doi: 10.3389/fnana.2011.00035

Budd, J. M., and Kisvárday, Z. F. (2012). Communication and wiring in the cortical connections. *Front. Neuroanat.* 6:42. doi: 10.3389/fnana.2012.00042

Bullmore, E., and Sporns, O. (2009). Complex brain networks: graph theoretical analysis of structural and functional systems. *Nat. Rev. Neurosci.* 10, 186–198. doi: 10.1038/nrn2575

Calhoun, V. D., Miller, R., Pearlson, G., and Adali, T. (2014). The chronnectome: time-varying connectivity networks as the next frontier in fMRI data discovery. *Neuron* 84, 262–274. doi: 10.1016/j.neuron.2014.10.015

Catani, M., Thiebaut de Schotten, M., Slater, D., and Dell'Acqua, F. (2013). Connectomic approaches before the connectome. *Neuroimage* 80, 2–13. doi: 10.1016/j.neuroimage.2013.05.109

Cavada, C., Compañy, T., Tejedor, J., Cruz-Rizzolo, R. J., and Reinoso-Suárez, F. (2000). The anatomical connections of the macaque monkey orbitofrontal cortex. A review. *Cereb. Cortex* 10, 220–242. doi: 10.1093/cercor/10.3.220

Chen, M., Yan, Y., Gong, X., Gilbert, C. D., Liang, H., and Li, W. (2014). Incremental integration of global contours through interplay between visual cortical areas. *Neuron* 82, 682–694. doi: 10.1016/j.neuron.2014.03.023

Chung, K., and Deisseroth, K. (2013). CLARITY for mapping the nervous system. *Nat. Methods* 10, 508–513. doi: 10.1038/nmeth.2481

da Costa, N. M., and Martin, K. A. (2011). How thalamus connects to spiny stellate cells in the cat's visual cortex. *J. Neurosci.* 31, 2925–2937. doi: 10.1523/jneurosci.5961-10.2011

Deschênes, M., Veinante, P., and Zhang, Z.-W. (1998). The organization of corticothalamic projections: reciprocity versus parity. *Brain Res. Brain Res. Rev.* 28, 286–308. doi: 10.1016/s0165-0173(98)00017-4

Elston, G. N., Benavides-Piccione, R., Elston, A., Manger, P. R., and Defelipe, J. (2011). Pyramidal cells in fromtal cortex of primates: markes differences in neuronal structure among species. *Front. Neuroanat.* 5:2. doi: 10.3389/fnana.2011.00002

Felleman, D. J., and Van Essen, D. C. (1991). Distributed hierarchical processing in the primate cerebral cortex. *Cereb. Cortex* 1, 1–47. doi: 10.1093/cercor/1.1.1

Freese, J. L., and Amaral, D. G. (2005). Organisation of projections from the amygdala to visual cortical areas TE and V1 in the macaque monkey. *J. Comp. Neurol.* 486, 295–317. doi: 10.1002/cne.20520

Gilbert, C. D., and Wiesel, T. N. (1983). Clustered intrinsic connections in cat visual cortex. *J. Neurosci.* 3, 1116–1133.

Glickfeld, L. L., Reid, R. C., and Andemann, M. L. (2014). A mouse model of higher visual cortical function. *Curr. Opin. Neurobiol.* 24, 28–33. doi: 10.1016/j.conb.2013.08.009

Graziano, M. S., and Aflalo, T. N. (2007). Rethinking cortical organization: moving away from discrete areas arranged in hierarchies. *Neuroscientist* 13, 138–147. doi: 10.1177/1073858406295918

Groh, A., Bokor, H., Mease, R. A., Plattner, V. M., Hangya, B., Stroh, A., et al. (2014). Convergence of cortical and sensory driver inputs on single thalamocortical cells. *Cereb. Cortex* 24, 3167–3179. doi: 10.1093/cercor/bht173

Haber, S., and Calzavara, R. (2009). The cortico-basal ganglia integrative network: the role of the thalamus. *Brain Res. Bull.* 78, 69–74. doi: 10.1016/j.brainresbull.2008.09.013

Hackett, T. A., de la Mothe, L. A., Camalier, C. R., Falchier, A., Lakatos, P., Kajikawa, Y., et al. (2014). Feedforward and feedback projections of caudal belt and parabelt areas of auditory cortex: refining the hierarchical model. *Fron. Neurosci.* 8:72. doi: 10.3389/fnins.2014.00072

Henschke, J. U., Noesselt, T., Scheich, H., and Budinger, E. (2015). Possible anatomical pathways for short-latency multisensory integration processes in primary sensory cortices. *Brain. Struct. Funct.* 220, 955–977. doi: 10.1007/s00429-013-0694-4

Hochstein, S., and Ahissar, M. (2002). View from the top: hierarchies and reverse hierarchies in the visual system. *Neuron* 36, 791–804. doi: 10.1016/S0896-6273(02)01091-7

Ichinohe, N., Matsushita, A., Ohta, K., and Rockland, K. S. (2010). Pathway-specific utilization of synaptic zinc in the macaque ventral visual cortical areas. *Cereb. Cortex* 20, 2818–2831. doi: 10.1093/cercor/bhq028

Innocenti, G. M., Vercelli, A., and Caminiti, R. (2014). The diameter of cortical axons depends both on the area of origin and target. *Cereb. Cortex* 24, 2178–2188. doi: 10.1093/cercor/bht070

Johnson, D., Illig, M. G., Behan, K. R., and Haberly, L. B. (2000). New features of connectivity in piriform cortex visualized by intracellular injection of pyramidal cells suggest that "primary" olfactory cortex functions like "association" cortex in other sensory systems. *J. Neurosci.* 20, 6974–6982.

Kaneko, T. (2013). Local connections of excitatory neurons in motor-associated cortical areas of the rat. *Front. Neural Circuits* 7:75. doi: 10.3389/fncir.2013.00075

Katz, L. C. (1987). Local circuitry of identified projection neurons in cat visual cortex brain slices. *J. Neurosci.* 7, 1223–1249.

Kennedy, H., and Bullier, J. (1985). A double-labeling investigation of the afferent connectivity to cortical areas V1 and V2 of the macaque monkey. *J. Neurosci.* 5, 2815–2830.

Köbbert, C., Apps, R., Bechmann, I., Lanciego, J. L., Mey, J., and Thanos, S. (2000). Current concepts in neuroanatomical tracing. *Prog. Neurobiol.* 62, 327–351. doi: 10.1016/s0301-0082(00)00019-8

Kopell, N. J., Gritton, H. J., Whittington, M. A., and Kramer, M. A. (2014). Beyond the connectome: the dynome. *Neuron* 83, 1319–1328. doi: 10.1016/j.neuron.2014.08.016

Kravitz, D. J., Saleem, K. S., Baker, C. I., Ungerleider, L. G., and Mishkin, M. (2013). The ventral visual pathway: an expanded neural framework for the processing of object quality. *Trends Cogn. Sci.* 17, 26–49. doi: 10.1016/j.tics.2012.10.011

Kultas-Ilinsky, K., Sivan-Loukianova, E., and Ilinsky, I. A. (2003). Reevaluation of the primary motor cortex connections with the thalamus in primates. *J. Comp. Neurol.* 457, 133–158. doi: 10.1002/cne.10539

Kuramoto, E., Furuta, T., Nakamura, K. C., Unzai, T., Hioki, H., and Kaneko, T. (2009). Two types of thalamocortical projections from the motor thalamic nuclei of the rat: a single neuron-tracing study using viral vectors. *Cereb. Cortex* 19, 2065–2077. doi: 10.1093/cercor/bhn231

Kurotani, T., Miyashita, T., Wintzer, M., Konishi, T., Sakai, K., Ichinohe, N., et al. (2013). Pyramidal neurons in the superficial layers of the rat retosplenial cortex exhibit a late-spiking firing property. *Brain Struct. Funct.* 281, 239–254. doi: 10.1007/s00429-012-0398-1

Lanciego, J. L., and Wouterlood, F. G. (2011). A half century of experimental neuroanatomical tracing. *J. Chem. Neuroanat.* 42, 157–183. doi: 10.1016/j.jchemneu.2011.07.001

Latawiec, D., Martin, K. A., and Meskenaite, V. (2000). Terminations of the geniculocortical projection in the striate cortex of macaque monkey: a quantitative immunoelectron microscopic study. *J. Comp. Neurol.* 419, 306–319. doi: 10.1002/(sici)1096-9861(20000410)419:3<306::aid-cne4>3.0.co;2-2

Lee, C. C., and Sherman, S. M. (2011). On the classification of pathways in the auditory midbrain, thalamus and cortex. *Hear. Res.* 276, 79–87. doi: 10.1016/j.heares.2010.12.012

Leergaard, T. B., Lillehaug, S., De Schutter, E., Bower, J. M., and Bjaalie, J. G. (2006). Topographical organization of pathways from somatosensory cortex through the pontine nuclei to tactile regions of the rat cerebellar hemispheres. *Eur. J. Neurosci.* 24, 2801–2812. doi: 10.1111/j.1460-9568.2006.05150.x

Markov, N., and Kennedy, H. (2013). The importance of being hierarchical. *Curr. Opin. Neurobiol.* 23, 187–194. doi: 10.1016/j.conb.2012.12.008

Markov, N. T., Vezoli, J., Chameau, P., Falchier, A., Quilodran, R., Huissoud, C., et al. (2014). Anatomy of hierarchy: feedforward and feedback pathways in macaque visual cortex. *J. Comp. Neurol.* 522, 225–259. doi: 10.1002/cne.23458

Martin, K. A. C., Roth, S., and Rusch, E. S. (2014). Superficial layer pyramidal cells communicate heterogeneously between multiple functional domains of cat primary visual cortex. *Nat. Commun.* 5:5252. doi: 10.1038/ncomms6252

Mesulam, M. (2012). The evolving landscape of human cortical connectivity: facts and inferences. *Neuroimage* 62, 2182–2189. doi: 10.1016/j.neuroimage.2011.12.033

Ojima, H., Honda, C. N., and Jones, E. G. (1992). Characteristics of intracellularly injected infragranular pyramidal neurons in cat primary auditory cortex. *Cereb. Cortex* 2, 197–216. doi: 10.1093/cercor/2.3.197

Osten, P., and Margrie, T. W. (2013). Mapping brain circuitry with a light microscope. *Nat. methods* 10, 515–523. doi: 10.1038/nmeth.2477

Peters, A., and Payne, B. R. (1993). Numerical relationships between geniculocortical afferents and pyramidal cell modules in cat primary visual cortex. *Cereb. Cortex* 3, 69–78. doi: 10.1093/cercor/3.1.69

Petroni, F., Panzeri, S., Hilgetag, C. C., Kötter, K., and Young, M. P. (2001). Simultaneity of responses in a hierarchical visual network. *Neuroreport* 12, 2753–2759. doi: 10.1097/00001756-200108280-00032

Renier, N., Wu, Z., Simon, D. J., Yang, J., Ariel, P., and Tessier-Lavigne, M. (2014). iDisco: a simple, rapid method to immunolabel large tissue samples for volume imaging. *Cell* 159, 896–910. doi: 10.1016/j.cell.2014.10.010

Rockland, K. S. (1989). Bistratified distribution of terminal arbors of individual axons projecting from area V1 to middle temporal area (MT) in the macaque monkey. *Vis. Neurosci.* 3, 155–170. doi: 10.1017/s0952523800004466

Rockland, K. S. (1992). Configuration, in serial reconstruction, of indiviual axons projecting from area V2 to V4 in the macaque monkey. *Cereb. Cortex* 2, 353–374. doi: 10.1093/cercor/2.5.353

Rockland, K. S. (1996). Two types of corticopulvinar terminations: round (type 2) and elongate (type 1). *J. Comp. Neurol.* 368, 57–87. doi: 10.1002/(sici)1096-9861(19960422)368:1<57::aid-cne5>3.0.co;2-j

Rockland, K. S. (1997). "Elements of cortical architecture: hierarchy revisited," in *Extrastriate Cortex in Primates*, eds K. S. Rockland, J. H. Kaas and A. Peters (New York: Plenum Press), 243–293.

Rockland, K. S., Lund, J. S., and Humphrey, A. L. (1982). Anatomical banding of intrinsic connections in striate cortex of tree shrew (*Tupaia glis*). *J. Comp. Neurol.* 209, 41–58. doi: 10.1002/cne.902090105

Rockland, K. S., Saleem, K. S., and Tanaka, K. (1994). Divergent feedback connections from areas V4 and TEO in the macaque. *Vis. Neurosci.* 11, 579–600. doi: 10.1017/s0952523800002480

Rockland, K. S., and Van Hoesen, G. W. (1994). Direct temporal-occipital feedback connectons to striate cortex (V1) in the macaque monkey. *Cereb. Cortex* 4, 300–313. doi: 10.1093/cercor/4.3.300

Rockland, K. S., and Van Hoesen, G. W. (1999). Some temporal and parietal cortical connections converge in CA1 of the primate hippocampus. *Cereb. Cortex* 9, 232–237. doi: 10.1093/cercor/9.3.232

Roland, P. E., Hilgetag, C. C., and Deco, G. (2014). Cortico-cortical communication dynamics. *Front. Syst. Neurosci.* 8:19. doi: 10.3389/fnsys.2014.00019

Schoonover, C. E., Tapia, J. C., Schilling, V. C., Wimmer, V., Blazeski, R., Zhang, W., et al. (2014). Comparative strength and dendritic organization of thalamocortical and corticocortical synapses onto excitatory layer 4 neurons. *J. Neurosci.* 34, 6746–6758. doi: 10.1523/jneurosci.0305-14.2014

Sherman, S. M., and Guillery, R. W. (2013). *Functional Connections of Cortical Areas.* Cambridge, MA: MIT Press.

Silvestri, L., Sacconi, L., and Pavone, F. S. (2013). The connectomics challenge. *Funct. Neurol.* 28, 167–173. doi: 10.11138/FNeur/2013.28.3.167

Sincich, L. C., Jocson, C. M., and Horton, J. C. (2010). V1 interpatch projections to V2 thick stripes and pale stripes. *J. Neurosci.* 30, 6963–6974. doi: 10.1523/JNEUROSCI.5506-09.2010

Stehberg, J., Dang, P. T., and Frostig, R. D. (2014). Unimodal primary sensory cortices are directly connected by long-range horizontal projections in rat sensory cortex. *Fron. Neuroanat.* 8:93. doi: 10.3389/fnana.2014.00093

van Aerde, K. I., and Feldmeyer, D. (2014). Morphological and physiological characterization of pyramidal neurn subtypes in rat medial prefrontal cortex. *Cereb. Cortex* 25, 788–805. doi: 10.1093/cercor/bht278

Vertes, R. P. (2006). Interactions among the medial prefrontal cortex, hippocampus and midline thalamus in emotional and cognitive processing in the rat. *Neuroscience* 142, 1–20. doi: 10.1016/j.neuroscience.2006.06.027

Wiser, A. K., and Callaway, E. M. (1996). Contributions of individual layer 6 pyramidal neurons to local circuitry in macaque primary visual cortex. *J. Neurosci.* 16, 2724–2739.

Yook, C., Druckmann, S., and Kim, J. (2013). Mapping mammalian synaptic connectivity. *Cell. Mol. Life Sci.* 70, 4747–4757. doi: 10.1007/s00018-013-1417-y

Conflict of Interest Statement: The author declares that the research was conducted in the absence of any commercial or financial relationships that could be construed as a potential conflict of interest.

frontiers in Neuroanatomy

TECHNOLOGY REPORT
published: 27 May 2015
doi: 10.3389/fnana.2015.00066

Automatic target validation based on neuroscientific literature mining for tractography

Xavier Vasques[1,2,3†], *Renaud Richardet*[1†], *Sean L. Hill*[1], *David Slater*[4,5], *Jean-Cedric Chappelier*[6], *Etienne Pralong*[5], *Jocelyne Bloch*[5], *Bogdan Draganski*[4,5] *and Laura Cif*[4,5,7*]

[1] *Blue Brain Project, Brain Mind Institute, Ecole Polytechnique Fédérale de Lausanne, Lausanne, Switzerland,* [2] *IBM Systems, France,* [3] *Laboratoire de Recherche en Neurosciences Cliniques, France,* [4] *Laboratoire de Recherche Neuroimagerie, Université de Lausanne, Lausanne, Switzerland,* [5] *Département des Neurosciences Cliniques, Centre Hospitalier Universitaire Vaudois, Université de Lausanne, Lausanne, Switzerland,* [6] *School of Computer and Communication Sciences, Ecole Polytechnique Fédérale de Lausanne, Lausanne, Switzerland,* [7] *Département de Neurochirurgie, Hôpital Gui de Chauliac, Centre Hospitalier Régional Universitaire de Montpellier, Université Montpellier 1, Montpellier, France*

OPEN ACCESS

Edited by:
Javier DeFelipe, Cajal Institute, Spain

Reviewed by:
Leon French, Rotman Research Institute, Canada
Florian Leitner, Universidad Politécnica de Madrid, Spain

****Correspondence:***
Laura Cif, Laboratoire de Recherche en Neuroimagerie, Département des Neurosciences Cliniques, Centre Hospitalier Universitaire Vaudois, Université de Lausanne, Lausanne, Switzerland; Département de Neurochirurgie, Hôpital Gui de Chauliac, Centre Hospitalier Régional Universitaire de Montpellier, Université Montpellier 1, Montpellier, France
a-cif@chu-montpellier.fr; ana-laura.cif@chuv.ch

† These authors have contributed equally to this work.

Received: *27 January 2015*
Accepted: *09 May 2015*
Published: *27 May 2015*

Citation:
Vasques X, Richardet R, Hill SL, Slater D, Chappelier J-C, Pralong E, Bloch J, Draganski B and Cif L (2015) Automatic target validation based on neuroscientific literature mining for tractography. Front. Neuroanat. 9:66. doi: 10.3389/fnana.2015.00066

Target identification for tractography studies requires solid anatomical knowledge validated by an extensive literature review across species for each seed structure to be studied. Manual literature review to identify targets for a given seed region is tedious and potentially subjective. Therefore, complementary approaches would be useful. We propose to use text-mining models to automatically suggest potential targets from the neuroscientific literature, full-text articles and abstracts, so that they can be used for anatomical connection studies and more specifically for tractography. We applied text-mining models to three structures: two well-studied structures, since validated deep brain stimulation targets, the internal globus pallidus and the subthalamic nucleus and, the nucleus accumbens, an exploratory target for treating psychiatric disorders. We performed a systematic review of the literature to document the projections of the three selected structures and compared it with the targets proposed by text-mining models, both in rat and primate (including human). We ran probabilistic tractography on the nucleus accumbens and compared the output with the results of the text-mining models and literature review. Overall, text-mining the literature could find three times as many targets as two man-weeks of curation could. The overall efficiency of the text-mining against literature review in our study was 98% recall (at 36% precision), meaning that over all the targets for the three selected seeds, only one target has been missed by text-mining. We demonstrate that connectivity for a structure of interest can be extracted from a very large amount of publications and abstracts. We believe this tool will be useful in helping the neuroscience community to facilitate connectivity studies of particular brain regions. The text mining tools used for the study are part of the HBP Neuroinformatics Platform, publicly available at http://connectivity-brainer.rhcloud.com/.

Keywords: tractography, text mining, globus pallidus internus, subthalamic nucleus, nucleus accumbens, information extraction, natural language processing

Introduction

Determining the wiring diagram of the human brain is one of the greatest challenges in neurosciences (Sporns, 2011). In initiatives such as the Human Connectome Project (HCP) (www.humanconnectome.org), tractography occupies a key place in establishing the structural basis of the human connectome. Diffusion tensor imaging (DTI) has been introduced to document and measure *in vivo* anatomical connectivity between regions (Jbabdi and Johansen-Berg, 2011). DTI offers an overall view of brain anatomy, including the pattern and degree of connectivity between different regions, raising immediate hypothesis for brain function and for clinical applications such as deep brain stimulation (DBS) (Coenen et al., 2011, 2012a,b). DBS is a therapeutical approach for movement (Pouratian et al., 2011; Rozanski et al., 2014; Sweet et al., 2014a,b) and psychiatric disorders (Lujan et al., 2008; Lakhan and Callaway, 2010; Lehman et al., 2011), targeting different basal ganglia structures and delivering chronic stimulation to them (Barkhoudarian et al., 2010; Sedrak et al., 2010; Traynor et al., 2010; Taljan et al., 2011; Lambert et al., 2012; Chowdhury et al., 2013). In combination with other technologies, DTI represents a powerful tool providing further insight on the networks influenced by neuromodulation (Barkhoudarian et al., 2010; Chaturvedi et al., 2010; McIntyre and Foutz, 2013; Howell et al., 2014) and consequently a better understanding of the mechanism of action and effects of DBS.

One of the major limitations of tractography is related to its outputs because of, potential underestimates of the fiber tracts when compared to other methods (Ciccarelli et al., 2003a,b; Kinoshita et al., 2005) such as fiber pathways that are reported in dissection and tracer studies that are absent in diffusion tensor tractography studies (Behrens et al., 2007). Therefore, responsible use of tractography requires careful consideration of the scope and limitations of the different techniques (Johansen-Berg and Behrens, 2006), knowing that observations are only fraction of the reality. Probabilistic tractography approach, as opposed to deterministic approach, depicts more fibers, thus leading to a more limited underestimation, since it assumes a distribution of orientation, as opposed to a single orientation at each voxel. Local tractography fits pathways step by step and is suitable for exploratory studies of connections compared with global tractography, and is more suitable for reconstruction of known white matter pathways. It is essential to have a thorough previous knowledge of the connections between the regions under investigation in order to validate the relevant fibers depicted via tractography, to pinpoint misses and for the choice of the method to be used. Mainly two approaches are used in probabilistic tracking (Catani et al., 2002; Wakana et al., 2007). In the first approach, all fiber tracts are obtained through a single seed region of interest (ROI) such that only fibers passing through the seed are included in the reconstructed tract. In the second one, the knowledge-based multiple-ROI approach, all fiber tracts are obtained through a seed to target ROIs, with logical and concatenation of two ROIs, such that only fibers passing through both ROIs are included in the reconstructed tract. Obviously spurious fibers are removed from the fiber tract by using an additional avoidance ROI (logical NOT operation) (Wakana et al., 2007). In the first approach, we only have to create a mask of the ROI (automatically or manually), in order to generate a connectivity distribution from the specified region of interest. Probabilistic tractography is performed from every voxel with a value greater than 0 in this mask. The output file is a single image in the space of the specified seed mask. All brain voxels have a value (though many of these may be zero) representing the number of samples that pass through that voxel from the seed mask. Target identification is a further crucial step for guided tractography from a seed region, to estimate the probability of their interconnection. Target identification requires solid anatomical knowledge documented by an extensive literature review across species for each seed structure to be studied. Existing literature in human is often conflicting and limited. Furthermore, experiments studying connectivity between individual brain regions are not reported in a normalized, structured and centralized repository, but published in plain text, scattered among individual scientific publications (Richardet et al., 2015). Consequently, manual literature review (LIT) to identify targets for a given seed region is tedious and potentially subjective. Therefore, complementary approaches would be very useful for the neuroscience community.

In this article, we propose to use text-mining (TM) models to automatically generate potential targets from the neuroscientific literature, so that they can be used for anatomical connection studies and more specifically for tractography studies. These TM models aggregate brain region connectivity from a very large amount of published neuroscience full-text articles and PubMed abstracts. To illustrate and evaluate the methodology, we applied TM models to three structures: two well-studied structures, since validated DBS targets for movement disorders, the internal globus pallidus (GPi) and the subthalamic nucleus (STN) and, the nucleus accumbens (NAcc), exploratory target for treating psychiatric disorders. We performed a systematic review of the literature to document the projections of the three selected structures and compared it with the structures proposed by TM models, both in rat and primate (including human). To assess the results of the TM models, a comparison has been made between the two methods for the well-described GPi and STN. Finally, we ran probabilistic tractography on the NAcc and compared the output with the results of the TM models and literature review. The objective of this paper is to document/support the validity of the TM models approach in helping to identify the targets to be explored for a given seed structure in (probabilistic) tractography projects.

Materials and Methods

Search Strategy for Identification of the Three Seed Structures and Their Connections in Rat and Primates, Including Humans

Relevant publications were obtained using the PubMed database and references from the consulted articles. The PubMed database was manually searched for articles describing connections of the three nuclei, globus pallidus internus, subthalamic nucleus,

and nucleus accumbens. MeSH headings used were "globus pallidus," "entopeduncular nucleus" (corresponding to the medial segment of the globus pallidus in rats), "subthalamic nucleus," and "nucleus accumbens." We further searched for the following terms: "globus pallidus internus," "pallidum internum," "internal globus pallidus," "globus pallidus pars interna," and "medial globus pallidus." We combined them with the following MeSH headings for the studied species: "rats," "primates," and "human" and with the following key words: "connections," "projections," "afferents," and "efferents." Only articles written in English were reviewed. We used Terminologia Anatomica as reference for official nomenclature of the studied regions and structures.

Automatic Information Extraction from the Neuroscientific Literature

To accelerate manual literature search, we used TM methods that distill very large amount of scientific articles in order to extract brain regions that are potentially connected. The TM process consist of three phases: first, identifying mentions of brain regions in text; second, determining which of these brain regions are connected, and third, aggregating and reporting on potential connections in a database easily searchable by neuroscientists. For the identification of brain regions, two complementary named entity recognizers (NER) were developed. The first NER uses a lexicon of all 1197 brain regions from the Allen Mouse Brain Atlas (ABA) (http://www.brain-map.org) that is automatically augmented with corresponding synonyms found in several lexica (Richardet et al., 2015) of rodent brain region: the Brain Architecture Management System (BAMS) (Bota and Swanson, 2008), Neuronames (Bowden and Martin, 1995; Bowden and Dubach, 2003), Paxinos and Watson (Paxinos and Watson, 2007), Swanson (Puelles Lopez, 2000).

The second NER (BrainNER) relies on a machine-learning model (linear chain conditional random field) trained on WhiteText, a manually annotated corpus of 18,242 brain region mentions (French, 2009; French et al., 2012). The advantage of this statistical approach is that the model will match complex brain region names, even if they are not present in a lexicon, for example "contralateral prepositus hypoglossal nucleus" or "distal parts of the inferior anterior cerebellar cortex."

Once brain regions were identified, the second step was to determine whether two brain regions mentioned in a sentence were anatomically connected or not. To this end, three different models were combined: (1) FILTER considers all possible brain region co-occurrences, and subsequently applies filters to remove unlikely ones; (2) KERNEL relies on a supervised machine-learning classifier; (3) RULES consist of 9 manually crafted rules of the kind "*projection from the region A to the region C and the region D*." The resulting database shows, by selecting a region of interest, all other connected regions extracted from the literature and the possibility to drill down to the individual sentences for detailed analysis. The complete methodology can be found in Richardet et al. (2015).

The database is publicly accessible through a simple and intuitive web application. This application provides a matrix of brain regions co-occurences displaying the top N regions for which the most connection mentions was found (see **Supplementary Figure 1**). All matrix values are linked to the corresponding detailed list of sentences from neuroscientific articles. For example, **Supplementary Figure 3** displays the extracted sentences between the Allen Brain Atlas regions "Periaqueductal gray" and "Nucleus accumbens." Each sentence is itself linked to PubMed so that the user can go back to the original article. Additionally, the user has the ability to provide feedback by either validating the sentence or rejecting it. Finally, it is possible to search for one particular brain regions of interest, and then list all the other brain regions potentially connected to it (for which connectivity events have been found in the literature), see **Supplementary Figure 2**. The web application also exposes a REST API to interact with the extracted connectivity programmatically.

Guided Probabilistic Tractography of Nucleus Accumbens

High-resolution multi-parameter quantitative MRI (MPM) and high angular resolution diffusion imaging (HARDI) were acquired on a 3T whole-body MRI system (Magnetom Prisma, Siemens Medical System, Germany). The quantitative MPM acquisitions consisted of three multi-echo 3D fast low angle shot (FLASH) with proton density (PD), magnetization transfer (MT) and T1 weighted contrast as described elsewhere (Helms et al., 2008), whole brain coverage, 1 mm^3 resolution, FOV: (240, 176, 256) mm along A-P, L-R, H-F directions. Since previous research demonstrated that MT saturation maps provide better contrast in subcortical structures compared to T1w images (Helms et al., 2008), MT saturation maps were used for delineation of the NAcc. For the diffusion weighted acquisition we used a HARDI protocol with 60 gradient directions at b-value = 2000 $s.mm^{-2}$ and 13 interleaved b0 images. The following acquisition parameters were set: TE/TR = 69/7400 ms; 2 × 2 × 2 mm isotropic resolution with 70 axial slices; FoV read = 192 mm, FoV phase = 212 mm; matrix size 96 × 106; and GRAPPA factor 2. The study collecting imaging data in healthy subjects and disease conditions was approved by the Commission cantonale (VD) d'éthique de la recherche sur l'être humain, Switzerland (Protocole 207/10). Informed consent was obtained from all subjects.

HARDI preprocessing included motion correction, eddy current and correction of the vectors using the Artifact correction in diffusion MRI (ACID) toolbox (Mohammadi et al., 2010) into the batch system of Statistical Parametric Mapping 8 (SPM8). We used FSL and FMRIB's Diffusion Toolbox (FDT) (www.fmrib.ox.ac.uk/fsl) to perform segregation of brain tissue from non-brain tissue using the Brain Extraction Tool, local fitting of diffusion tensors and construction of individual FA maps using DTIFIT, and tensor estimation with BEDPOSTX routine with the following options: Fibers (3), Weight (1), Burn In (1000). A segregation of brain tissue from non-brain tissue using the Brain Extraction Tool (BET) was performed on the structural images. The left and right NAcc were segmented using FIRST from FSL on structural images. After the segmentation, we applied boundaries correction using first_boundary_corr

that is used for the classification of the boundary voxels in the volumetric output for a single structure. We applied *fast* boundary correction method that used FSL's FAST-based tissue classification for correcting boundary voxels. The results were visualized and checked using Freesurfer (Freeview) image analysis suite (Version 5.1.0) (http://surfer.nmr.mgh.harvard.edu/). The same method has been applied to extract subcortical target masks. The other target masks were extracted with Individual Brain Atlases using SPM (IBMASPM) (Aleman-Gomez et al., 2006). The masks have been extracted using ITK-SNAP (http://www.itksnap.org). All the masks have been binarized. Masks have been taken by manually drawing the region of interest, when automatic extraction results did not reach quality expectations or when region masks were not available within the previously mentioned tools. This was the case for subthalamic nucleus, substantia nigra, ventral tegmental area, hypothalamus, habenula and subcalosal cingulate (Chowdhury et al., 2013). Registration from structural to diffusion space was performed using FMRIB's Linear Image Registration Tool (FLIRT) in FSL. We performed a 3D-to-3D registration between diffusion and structural image with the affine model, 12° of Freedom and the use of the Tri-linear final interpolation method. The resulting structural to diffusion registration was manually checked to ensure satisfactory alignment, with particular attention paid to the regional borders of the BG in general and NAcc, in particular. We run tractography analysis with probabilistic tracking (probtrackx) in FSL using the segmented left and right NAcc seeds, the target masks and the output matrix from the registration (structural to diffusion). We used the following parameters: curvature threshold of 0.2 corresponding to a minimum angle of approximately 80°, number of samples 5000 and, loopcheck option. We developed a Matlab script in order to extract from the probabilistic tractography outputs the number of tracts that leave a voxel from NAcc to reach a given target. A Python script has been developed to calculate the number of voxels within the NAcc that have a probability greater than 1% to be connected to a specific target. Voxels with a connection probability of at least 0.01 were included as voxels containing anatomically valid pathway. The 1% threshold is a typical threshold used in probabilistic tractography (Lambert et al., 2012; Li et al., 2013). Threshold was set to 1% (out of the 5000 generated from each seed voxel) to reject voxels with low probability. This means that at least 1% of the identified fibers intersect the voxels in the valid pathway. This gave us a matrix of "strengths" of interconnection on a scale of 0–100%.

We built up the NAcc connectivity maps, with the associative map corresponding to the NAcc putative core [the prefrontal cortex including frontal superior, frontal middle and frontal inferior opercular and triangular gyri as well as the lateral orbitofrontal (l-OFC) cortex] and the limbic map corresponding, to the NAcc putative shell (distribution to medial OFC, frontal inferior orbital, frontal superior orbital, anterior cingulate cortex, subcalosal cingulate cortex, amygdala, hippocampus, habenula, hypothalamus, and ventral tegmental area) (Kopell and Greenberg, 2008; Baliki et al., 2013).

Results

Manual Literature Review (LIT)

The literature review has been performed by two of the authors (LC and JB) and took approximately 5 working days for the three regions. Below follows a detailed description of the three seed structures and their connections in rat and primates, including humans, based on a systematic review of the literature. The summary of the systematic review is presented in **Table 1**.

Internal Globus Pallidus

The globus pallidus is composed by two segments, a lateral, larger segment, the external globus pallidus (GPe) and a smaller, medial segment, the GPi. Furthermore, according to its vertical orientation, the subcomissural part of the globus pallidus is known as the ventral pallidum. In rat, the internal segment is called the entopedoncularis nucleus, the globus pallidus referring

TABLE 1 | Summary of the manual literature review.

Afferents	Efferents
GLOBUS PALLIDUS INTERNUS	
Subthalamic nucleus	Thalamus
Substantia nigra pars compacta	Lateral habenula
Ventral tegmental area	Substantia nigra
Neostriatum	Pedunculopontine nucleus
	Cerebral cortex (rat)
	Neostriatum
SUBTHALAMIC NUCLEUS	
Primary motor cortex	Globus Pallidus internus
Supplementary motor area	Globus Pallidus externus
Frontal eye field	Substantia nigra pars compacta
Somatosensory cortex	Substantia nigra pars reticulata
Anterior cingulate	Ventral thalamic nuclei ipsilaterally
Globus Pallidus externus	Parafascicularis thalamic nucleus contralaterally (rat)
Substantia nigra pars compacta	Substantia innominata
Ventral tegmental area	Ventral pallidum
Dorsal raphe nucleus	Pedunculopontine nucleus
Pedunculopontine nucleus	Ipsilateral cortex (rat)
Centro-median/parafascicularis complex	Neostriatum (rat)
	Spinal cord (rat)
NUCLEUS ACCUMBENS	
Orbitofrontal cortex	Ventral pallidum
Anterior cingulate	Substantia nigra pars compacta
Subgenual cortex	Substantia nigra pars reticulate
Pregenual cortex	Ventral tegmental area
Hippocampus	Hippocampus
Parahippocampal cortex	Caudate
Amygdala	Putamen
Substantia nigra pars compacta	Medio-dorsal thalamus
Ventral tegmental area	Cingulate gyrus
	Substantia innominata (rat)
	Lateral preoptic area (rat)
	Lateral hypothalamic area (rat)

only to the external globus pallidus. In human, the two segments are separated by the medial medullary lamina. The GPi is further subdivided into a medial (GPi-m) and a lateral segment (GPi-l) by the accessory medullary lamina. Since the GPi is the DBS target for treating movement disorders, we will further focus only on the GPi.

In rat, the two major afferents of the entopeduncular nucleus are the neostriatum and the STN, which have opposing physiological effects on entopeduncular neurons. The striato-fugal fibers project to the entopeduncular nucleus as well as to substantia nigra, although the majority of the fibers terminate in the globus pallidus (Wu et al., 2000). Topographical and synaptic organization of the so-called direct (neostriatum to entopeduncular nucleus) and indirect pathways (involving the STN and the globus pallidus) is capable of mediating the inhibition and excitation of output neurons in the entopeduncular nucleus (Bevan and Bolam, 1995). Reciprocal connections between internal and external segments have been identified (Kincaid et al., 1991a,b) and between the pallidal complex and the STN (Smith and Bolam, 1991). A projection from the NAcc to the entopeduncular nucleus terminates in its antero-ventral (subcomissural) part (Mogenson and Nielsen, 1983; Mogenson et al., 1983). The ventral pallidum receives substantial input from the ventral tegmental area (VTA) (Napier and Maslowski-Cobuzzi, 1994). Other afferent projections to the globus pallidus and entopeduncular nucleus as well as to the ventral pallidum have been described, from the cortex (Naito and Kita, 1994), thalamus (parafascicular nucleus), dorsal raphe nucleus (Kincaid et al., 1991a,b). The entopeduncular nucleus projects mainly to the thalamus, the ventrolateral (VL), ventromedial (VM), medial dorsal, and centromedian-parafascicular complex, but also to the lateral habenula, the pedunculopontine nucleus, and the frontal cortex (Kha et al., 2000).

In non-human primate and human, afferents to the GPi are constituted by the projections of the striatal medium spiny neurons (representing the direct pathway) (Haber et al., 1990a,b) that will converge toward the GPi and by the neurons of the subthalamic nucleus. Both, caudate and putamen project to the GPi. The ventral striatum that includes NAcc projects to the ventral or limbic pallidum, including the rostral to the anterior capsule region of the globus pallidus. The projections from the neostriatum including NAcc use gamma-amminobutyric acid (GABA) as neurotransmitter and are supposed to be inhibitory. The subthalamo-pallidal projection is excitatory and glutaminergic (Smith and Parent, 1988). Dopaminergic projections from the substantia nigra (SN) and ventral tegmental area (VTA) have been demonstrated and these fibers pass to both, GPi and GPe. The major output arising exclusively from the GPi is to the thalamus (Hazrati and Parent, 1991) and the pedunculopontine nucleus (PPN) (Parent and Cicchetti, 1998). It has been suggested that the GPi has two distinct sites of origin of efferent fibers: a central "motor" zone sending axons to the thalamus, mainly the ventro-lateralis anterior nucleus following nomenclature of Jones (Jones, 1990), to the supplementary motor cortices and, the PPN. The second zone, the "peripheral" limbic zone, projects to the lateral hypothalamus and habenula (Parent, 1979), the STN and SN (Parent and De Bellefeuille, 1983; Parent et al., 1984) and to the prefrontal cortex via the dorsomedial nucleus of thalamus. In humans, when functional neurosurgery is proposed for movement disorders, the sensorimotor GPi is targeted at the posteroventral and lateral aspect of the nucleus (Laitinen et al., 1992; Coubes et al., 2004). The centro-median/parafascicular (CM/Pf) complex receives a substantial innervation from the GPi (Baron et al., 2001; Sidibe et al., 2002). Pallidal neurones project to a lesser degree, to the nucleus ventralis anterior. The associative and limbic areas of the GPi also project to the PPN (Shink and Smith, 1995). The majority of this information is derived from primate studies. The pallido-thalamic projection is mainly inhibitory and GABA-ergic.

Subthalamic Nucleus

The STN is located within the caudal part of the diencephalon, between the ventral part of the zona incerta and the dorsal portion of the cerebral peduncles, ventral to the thalamus and lateral to the hypothalamus, parallel to the internal capsule, placed medially to the apex of globus pallidus. STN receives direct glutaminergic cortical projections as well as from the intralaminary thalamic nuclei (mainly ipsilateral but also contralateral). The main afferents to the STN are the cortico-subthalamic projections and the pallido-subthalamic pathways.

In rat, the STN receives massive cortical projections from the primary motor, prefrontal, anterior cingulate, primary somatosensory cortices (Kitai and Deniau, 1981). Pallido-subthalamic fibers arise from the globus pallidus (Smith and Bolam, 1990a,b; Kita and Kitai, 1994). The nigro-subthalamic pathway arises from SN and retrorubal and ventral tegmental areas (Hassani et al., 1997), providing dopaminergic innervation. Thalamo-subthalamic projections arise from the CM/Pf complex passing through zona incerta to reach the ipsilateral rostral STN. This pathway is demonstrated in rat (Sugimoto and Hattori, 1983; Sugimoto et al., 1983) but its role in humans remains uncertain. Other projections originate within the dorsal raphe nucleus and PPN (Canteras et al., 1990; Bevan et al., 1994a,b, 1995a,b; Bevan and Bolam, 1995). STN efferent projections are directed toward the basal ganglia nuclei. In rat, STN efferents are directed toward the GP and the SN pars reticulata but also pars compacta. Furthermore, STN projects to the thalamic ventral motor nuclei ipsilaterally and to the parafascicularis nucleus contralaterally. Further projections of the STN have been described to substantia innominata, ventral pallidum, PPN, neostriatum, ipsilateral cerebral cortex (Degos et al., 2008) and the spinal cord.

In non-human primate and human, a monosynaptic cortical connection has been described as the hyperdirect pathway originating within the primary motor cortex, the supplementary motor area and the frontal eye field and conveying the information from cortex to the GPi more rapidly than via the cortico-striato-pallidal route (Nambu et al., 2000). The GPe projects to the subthalamic neurons using GABAergic transmission. This projection is supposed to be inhibitory and belongs to the indirect pathway. The nigro-subthalamic pathway arises from SN pars compacta (Lanciego et al., 2012) retrorubal area and VTA providing dopaminergic innervation which in

humans may be by the way of the dopamine D1 receptors (Augood et al., 2000). Most STN efferent neurons send axons that simultaneously innervate the GPi, GPe, and SN pars reticulata (Nauta and Cole, 1978; Rico et al., 2010). In addition to STN projections to the GPi, GPe, and SN pars reticulata, efferent STN neurons also innervate thalamic targets, ipsilateral ventral thalamic motor nuclei (Nauta and Cole, 1978; Rico et al., 2010) and contralateral parafascicular nucleus. Furthermore, dual retrograde tract-tracing studies have shown that subthalamic projections reaching the GPi and ventral thalamic nuclei arise from different subpopulations of STN neurons (Rico et al., 2010).

Nucleus Accumbens

NAcc together with the ventral part of the caudate and of the putamen constitute the ventral striatum. The anatomical continuity between NAcc and the structures of the extended amygdala, the ventral pallidum and nucleus basalis of Meynert illustrate the strong relationship between the ventral subcomissural part of the basal ganglia (BG) and the subcortical limbic system, rendering precise delimitation of them challenging. A topographic subdivision of the NAcc into shell and core region has been described (Voorn et al., 1989; Heimer et al., 1997; Zahm, 1999), sharply marked in rodents (Meredith et al., 1996) but more challenging to identify and delineate in primates and human, in whom several different histochemical markers must be associated (Meredith et al., 1996; Brauer et al., 2000). The shell represents the ventral and medial part and the core the dorsal and central part of the nucleus. Nevertheless, significant differences exist between location and connections in rat and primates and more specifically in human. As for the striosome/matrix subdivision for the striatum, the core/shell subdivision is relevant for the information processing within the BG since each of the compartments have at least partially distinct cortical afferents. Overall, afferents to NAcc originate in the hippocampus, and prefrontal areas such as the orbitofrontal cortex and anterior cingulate. Other projections originate in subcortical structures, including amygdala.

In rat, the core receives projections from the dorsal part of the medial prefrontal cortex (corresponding to the dorsal prelimbic and anterior cingulate cortex) and from the parahippocampal cortex, while the shell receives projections mostly from the ventral parts of the medial prefrontal cortex (corresponding to the infralimbic and ventral prelimbic cortices) (Berendse et al., 1992a,b). The major part of the amygdalar projections to the BG is to the NAcc (McDonald, 1991), different for the core/shell subdivisions, respectively. The core receives projections from the anterior part of the basolateral amygdala via the ventral amygdalo-fugal pathway while the shell receives afferences from its posterior aspect and from the central nucleus of amygdala via the sublenticular and supracapsular parts of the extended amygdala (Alheid et al., 1998). The shell also receives afferences from the hippocampus (Kelley and Domesick, 1982). The core projects mainly to the dorsal subcomisural part of the ventral pallidum. The shell project to the ventral and medial part of the ventral pallidum, to the hypothalamus and the the mesencephalic dopaminergic neurons (VTA and SNc) (Berendse et al., 1992a; Heimer et al., 1997). Fibers from NAcc also pass to subpallidal structures including the substantia innominata (Berendse et al., 1992a), lateral preoptic and lateral hypothalamic area (Mogenson et al., 1983).

In primate and human, the literature reporting on NAcc connections is poorer and subjective, since it is based mainly on data from rodents and non-primate mammalians. The equivalent of the shell would receive predominant afferences from the subgenual cortices in comparison to the orbitofrontal cortex, while the core would receive similar projections from these different regions (Haber et al., 2000). NAcc, especially the putative shell region, receives a strong dopaminergic input from the VTA and from the dorsal tier of the substantia nigra (mainly the putative core) (Haber et al., 2000; Haber, 2003). Based on rodent studies, one can hypothesize that NAcc afferents are provided by the baso-lateral amygdala and most probably also the central and medial amygdalar nuclei. NAcc main efferents innervate the pallidum, striatum, mediodorsal thalamus, prefrontal, including cingulate cortex and the mesolimbic dopaminergic areas (Baliki et al., 2013). The putative core projects mainly to the dorsal subcomisural part of the ventral pallidum. The core also projects to the ventromedial SN pars compacta but also to more lateral aspects of the substantia nigra. The shell would project to the ventral and medial part of the ventral pallidum, to the hypothalamus and the VTA, as well as to the SN pars reticulata.

Text-Mining (TM)

TM models were evaluated at different levels. First, the two NERs and three extractors are evaluated against a manually annotated corpus. Second, the complete system is evaluated against *in-vivo* connectivity from ABA. The TM models were then applied on two large corpora, and the extracted brain regions and connections are discussed. Last, we compared and analyzed the results between TM and LIT for the three structures.

The precision of both NERs was estimated on the WhiteText annotation corpus and is 84.6% (BraiNER), meaning that 85 out of 100 brain regions are correctly identified. The performance of all three extractors was evaluated on 3097 manually annotated connectivity relations, reaching a precision of 45, 60, and 72%, respectively. The resulting database contains over 4 million (lexical) and 4.5 million (machine learning) brain region mentions, and over 100,000 (lexical) and 460,000 (machine-learning) potential brain region connections. The complete system was evaluated against *in vivo* connectivity data from ABA with an estimated precision of 78% for the brain region connections that were found in the literature (recall could not be evaluated). This means that almost 8 out of 10 connections predicted by the TM system have also been experimentally measured *in vivo*. **Table 2** provides the statistics of the corpora used, extracted brain regions and connections (Richardet et al., 2015).

Table 3 lists potential targets for the GPi and STN, as provided by the TM models. The potential targets are ranked by their decreasing score, the score representing the rounded number of connection mentions, normalized by the confidence[1] that each

[1]Confidence (precision) has been evaluated for each extractor.

TABLE 2 | Statistics about corpus, extracted brain regions and connections (reproduced from Richardet et al., 2015).

Corpus	Documents (words)	Brain regions mentions		Connections mentions	
		Lexical	Machine-learning	Lexical	Machine-learning
All PubMed abstracts	13,293,649 (2.1×10^9)	1,705,549	1,992,747	41,965	188,994
Full text neuroscience articles	630,216 (6.1×10^9)	2,327,586	2,751,952	62,095	279,100

TABLE 3 | Brain regions for which connections have been found in the literature for the globus pallidus, internal segment and the subthalamic nucleus using text-mining models.

Globus pallidus internus		Subthalamic nucleus	
Region	Score	Region	Score
Caudoputamen	143	Globus pallidus, external segment	105
Globus pallidus, external segment	117	Caudoputamen	74
Pallidum	23	Cerebral cortex	43
Substantia nigra, reticular part	21	Pallidum	34
Subthalamic nucleus	20	Pedunculopontine nucleus	16
Lateral habenula	12	Thalamus	16
Thalamus	10	Globus pallidus, internal segment	15
internal capsule	7	Primary motor area	11
Cerebral cortex	4	Somatomotor areas	9
Hypothalamus	3	Substantia nigra, reticular part	9
Substantia nigra, compact part	3	Parafascicular nucleus	7
Pedunculopontine nucleus	2	Zona incerta	5
Cerebellar nuclei	2	Substantia nigra, compact part	5
Midbrain	2	Ventral tegmental area	3
Parafascicular nucleus	2	Midbrain	2
Lateral preoptic area	2	Lateral hypothalamic area	2
Cerebellum	1	Hypothalamus	2
Reticular nucleus of the thalamus	1	Brain stem	2
internal medullary lamina of the thalamus	1	Pons	1
Striatum-like amygdalar nuclei	1	internal medullary lamina of the thalamus	1
Zona incerta	1	Red nucleus	1
stria medullaris	1	striatonigral pathway	1
Fields of Forel	1	Isocortex	1
Magnocellular nucleus	1	Dentate nucleus	1
Central lateral nucleus of the thalamus	1	Substantia innominata	1
Claustrum	1	Bed nuclei of the stria terminalis	1
Substantia innominata	1	Islands of Calleja	1
Brain stem	1	Dorsal nucleus raphe	1
nigrostriatal tract	1	Cerebral nuclei	1
Interbrain	1	Olfactory tubercle	1
optic tract	1	Auditory areas	1
Ammon's horn	1		

connection has been extracted correctly. Therefore, a high score means that many articles have been found. We stress the fact that the frequency of a brain region connection reported in the scientific literature does not necessarily reflect the physiological intensity of a connection; the former reflecting the interest for the region.

All the results including suggested articles, nucleus and scores can be found in http://connectivity-brainer.rhcloud.com.

For the "Globus pallidus, internal segment," all LIT targets have been correctly suggested by the TM algorithm using ABA lexicon, except for one, ventral tegmental area, VTA. However, VTA is correctly proposed while searching using

ABA or BraiNER for "Pallidum" or "Pallidum, ventral region" instead of globus pallidus, internal segment. The result can be checked in http://connectivity-brainer.rhcloud.com/static/br/search.html.

TM proposes more targets for the GPi than the manual literature review, including connections with hypothalamus (3 publications), cerebellar nuclei (2), midbrain (2), parafascicular nucleus (2), and lateral preoptic area (2). The majority of the suggested targets includes or belongs to targets resulted from the manual literature review: midbrain includes SN; parafascicular nucleus relates to thalamus. However some of the targets proposed by TM were not found by LIT. Analyzing one such abstract suggested by TM, globus pallidus connection to the hypothalamus, the parafascicular nucleus and the lateral preoptic area are explicitely reported. TM found confirmatory sentences for the previously mentioned connections: ≪ *On the other hand, the dense substance P-positive wooly-fiber plexus filling the internal pallidal segment (entopeduncular nucleus) expands medialward into the lateral hypothalamic region.* ≫ or ≪ The **entopeduncular nucleus** invades the **hypothalamus** also with a loose plexus of enkephalin-positive wooly fibers ≫ (Haber and Nauta, 1983). For connections with the cerebellar nuclei, TM suggests papers that were not found by LIT, but these papers do not contain evidence of a connection. For illustration, we found three sentences that do not contain evidence of a connection with the cerebellar nuclei and all of them concern the cat. One example is ≪ Seventy *seven thalamic neurons in the VA-VL nuclear complex of the cat which projected to the anterior sigmoid gyrus (ASG) were studied extracellularly, and their responses to stimulation of both the* ***cerebellar nuclei*** *(CN) and the* ***entopeduncular nucleus*** *(ENT) were examined.* ≫ (Jinnai et al., 1987). This sentence is an example of a coordinating conjunction (e.g., ≪ Region A *and* Region B were examined. ≫). It was suggested by the simplest TM model that is not capable of filtering out coordinating conjunctions (even though they very rarely represent a connection).

For the STN, all the LIT targets have been found by TM, except for specific subdivisions of a given, such as ipsilateral ventral thalamic nuclei, ventral pallidum or the anterior cingulate. However, less specific regions (thalamus, pallidum) are correctly proposed. In addition, when using the machine learning named entity recognizer, the connection between STN and the ventral pallidum, anterior cingulate and ventral lateral thalamus are found as shown in: http://connectivity-brainer.rhcloud.com/static/br/region.html?db=20140522_brainer&br=1922.

For NAcc, **Table 4** (left) lists brain regions for which connections have been found in the literature based on the ABAlex named entity recognizer. Additionally, **Table 4** (right) also includes results from BraiNER (machine learning named entity recognizer). As discussed in Section Text-Mining, BraiNER is not constrained on a list of brain regions (like ABAlex) and is able to identify complex brain region names, even if they are not present in a lexicon. However, the regions returned by BraiNER have to be manually identified and curated as provided by the following link http://connectivity-brainer.rhcloud.com/static/br/region.html?br=912&db=20140522_brainer.

All the LIT targets, except the subgenual and pregenual cortex, have been found by the TM with the exact terminology. The two exceptions are explained by the fact that they are subdivisions of the anterior cingulate that figures as target.

Overall, TM has a precision of 36%, meaning that it proposed three times as many targets as could be identified with LIT. Such a low precision is acceptable for the task at hand, since the priority is to suggest all targets (high recall), even if that requires manual curation of search results (since precision is only 36%) The overall recall of TM against LIT in our study was 98%, meaning that over all the targets for the three selected seeds, only one target have been missed by TM (Frontal eye field for the STN) (**Table 5**).

Species Differentiation

Table 6 lists the number of publications found by text mining, ordered by species. Species were identified using Linnaeus, a machine-learning model to identify species in biomedical text and resolve it to the NCBI taxonomy (Gerner et al., 2010). One interesting observation is the difference between the number of studies on NAcc in rat and in primates, demonstrating the little available information on NAcc connectivity coming from studies in primates including human

Probabilistic Tractography

The targets for NAcc found during LIT and TM were used to perform tractography.

We selected one subject to illustrate the results of the DTI in the current manuscript.

Figure 1 shows the strength of connectivity of NAcc to its targets by depicting the number of voxels within the NAcc that has a probability superior to 1% to be connected to a specific target.

Cortical targets such as the anterior and subcalosal cingulate, medial and lateral orbitofrontal cortex, ventrolateral prefrontal cortex, insula, gyrus rectus, olfactory cortex all exhibited connection to NAcc. Conversely, hippocampus and amygdala exhibited a lower probability of connection to NAcc than expected. Hypothalamus and thalamus and basal ganglia including caudate, putamen and pallidum well as STN exhibited a strong probability of connection. In agreement with previous knowledge, midbrain dopaminergic structures, SN and VTA exhibited high probability of connections with NAcc.

Figure 2 shows the probabilistic tractography output from FSL for the nucleus accumbens, based on the pattern of connectivity. We built up the NAcc connectivity maps with the **associative map** corresponding to the **NAcc putative core** (probabilistic connectivity to the prefrontal cortex, including frontal superior, frontal middle and frontal inferior-pars opercularis, -pars triangularis) and, the lateral orbitofrontal (l-OFC) cortex) and the **limbic map** corresponding to the **NAcc putative shell** (with distribution to medial-orbitofrontal cortex (m-OFC), anterior cingulate cortex, subcalosal area (Brodman area 25), amygdala, hippocampus, habenula, hypothalamus and ventral tegmental area (Baliki et al., 2013).

TABLE 4 | The 25 brain regions with highest scores for which connections have been found in the literature for the nucleus accumbens based on ABA and braiNER lexicons.

Nucleus accumbens			
ABA		Brainer	
Region	Score	Region	Score
Ventral tegmental area	454	ventral tegmental area	238
Caudoputamen	412	Striatum	95
Cerebral cortex	295	prefrontal cortex	68
Striatum-like amygdalar nuclei	175	Amygdala	54
Hippocampal region	122	medial prefrontal cortex	52
Ammon's horn	93	Hippocampus	47
Hippocampal formation	70	Hippocampal	41
Pallidum	61	basolateral amygdala	40
Midbrain	53	caudate-putamen	39
Subiculum	38	Cortical	35
Thalamus	28	Mesolimbic	31
Hypothalamus	28	hippocampal formation	29
Periaqueductal gray	23	ventral pallidum	26
Olfactory tubercle	22	ventral striatum	20
Basolateral amygdalar nucleus	19	caudate putamen	16
Fimbria	18	Thalamus	14
Nucleus raphe pontis	18	Neostriatum	13
Entorhinal area	18	Septum	13
Dorsal nucleus raphe	13	caudate nucleus	13
Globus pallidus, external segment	12	Mesencephalic	13
medial forebrain bundle	11	Amygdaloid	12
Paraventricular nucleus of the thalamus	11	Limbic	12
Lateral preoptic area	9	dorsal raphe nucleus	11
Nucleus of the solitary tract	8	paraventricular of the thalamus	11
stria terminalis	8	corpus striatum	11

The complete results can be found in http://connectivity-brainer.rhcloud.com.

TABLE 5 | Overall performance of TM against LIT.

	Found by LIT	Proposed by TM	Missed by TM	Precision	Recall
GPi	10	32	0	0.31	1.00
STN	23	31	1	0.76	0.96
Nucleus Accumbens	21	85	0	0.24	1.00
Overall	54	148	1	0.36	0.98

Discussion

An exponentially growing amount of data is being produced and published in neuroscience, propelled by improvements in existing and new measurement recording technologies (Brown, 2007; Schierwagen, 2008). This staggering growth represents a major challenge to identify useful information and do not lack valuable information (Balan et al., 2014). Much legacy information about neural connections is inaccurate or is misleading because it is vastly oversimplified and must be evaluated critically since brain circuitry has been examined with a succession of increasingly reliable methods Already available BAMS (Bota et al., 2003) have been designed and implemented for storing and manipulating structural data about the nervous system in text- and table-based format allowing searching by region name, species and references (author, source, year) (Bota and Arbib, 2004).

In this article, we proposed to assess text-mining (TM) models to automatically suggest targets from the neuroscientific literature for tractography studies. Many publications deal with DTI limitations (Hilgetag et al., 2000; Lin et al., 2001; Mori and van Zijl, 2002; Parker et al., 2002; Ciccarelli et al., 2003a,b; Kinoshita et al., 2005; Johansen-Berg and Behrens, 2006; Behrens et al., 2007; Jbabdi and Johansen-Berg, 2011; Campbell and Pike, 2014; Thomas et al., 2014). One of them is related to DTI outputs that are not yet fully validated, inaccurate (Thomas et al., 2014) and difficult to quantify with a potential underestimate of the fiber tracts, as mentioned previously, when compared to electrophysiological tests (Lin et al., 2001; Parker et al., 2002; Ciccarelli et al., 2003a,b; Kinoshita et al., 2005). Other limitations of tractography are related to resolution, termination criteria,

TABLE 6 | Number of publications and percentage for which connections have been found for the 3 nuclei by species using text-mining.

	NAcc		STN		GPi	
Species	**Number of publications**	**Percentage**	**Number of publications**	**Percentage**	**Number of publications**	**Percentage**
Rattus	1572	45.1	198	29.7	260	41.9
Mus	133	3.8	14	2.1	10	1.6
Homo Sapiens	83	2.4	34	5.1	13	2.1
Simiiformes	23	0.7	12	1.8	2	0.3
Chordata	72	2.1	12	1.8	15	2.4
Felidae	36	1.0	21	3.2	54	8.7
Canis	17	05	3	0.5	20	3.2
No species found	1550	44.5	372	55.9	247	39.8

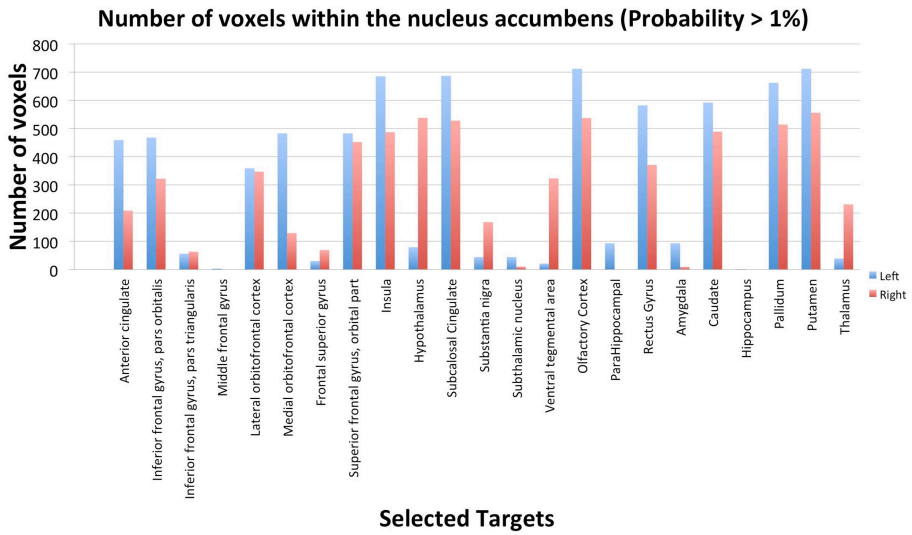

FIGURE 1 | Number of voxels within the nucleus accumbens that have a probability of more than 1% to be connected to a specific target in one subject (healthy control, right handed male, age 42). Left nucleus accumbens (in blue) has a total of 712 voxels and the right nucleus accumbens (in red) has a total of 559 voxels.

the effect of noise on the accuracy of the tracking and partial volume effects (Mori and van Zijl, 2002). The termination criteria correspond to the inability from tractography to determine the precise origin/termination of connections in the cortex (Jbabdi and Johansen-Berg, 2011) and to detect synapses. Accuracy quantification and error detection are also limitations of tractography, unable to provide any confidence scores on the output results even if efforts are being made to improve imaging techniques and algorithms (Hilgetag et al., 2000; Behrens et al., 2007). Tractography is unable to tell whether an axon is afferent or efferent (Jbabdi and Johansen-Berg, 2011). However, although current tractography methods have limitations, the ability to localize fiber bundles is of great help to understand connections and structural organization of the human brain. Anatomical knowledge can be used to impose constraint in the tract reconstruction, thereby effectively reducing the likelihood of the occurrence of erroneous results. Even if this approach is applied to anatomically well-documented tracts (Mori and van Zijl, 2002), it is essential to validate probabilistic results and in particular in DBS, to explore a specific seed by studying patterns of connectivity, sub-parcellation and confirmation of functional zones (Parker et al., 2002; Ciccarelli et al., 2003b; Kinoshita et al., 2005; Johansen-Berg and Behrens, 2006; Barkhoudarian et al., 2010; Lakhan and Callaway, 2010; Sedrak et al., 2010; Traynor et al., 2010; Coenen et al., 2011, 2012a; Pouratian et al., 2011; Taljan et al., 2011; Lambert et al., 2012; Chowdhury et al., 2013; Rozanski et al., 2014; Sweet et al., 2014a). Brain structures as nucleus accumbens, are less documented in human. We believe that TM approaches can help neuroscientist to use the provided information to identify targets for tractography and document them in human. Two well-established DBS targets for movement disorders have been studied (GPi and STN) and, NAcc, an exploratory DBS target for psychiatric disorders. The output of the TM method was compared with the output of a manual, systematic review of the literature and the output of the probabilistic tractography using NAcc as seed structure. The concordance with data from manual search is significant and robust. The overall performance of the TM algorithm

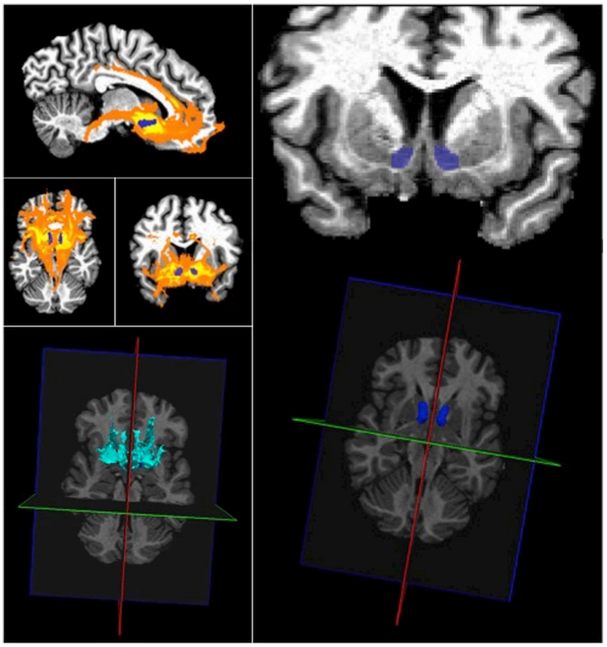

FIGURE 2 | At the top left, the probabilistic tractography output of FSL with the left and right accumbens (in blue) on sagittal, axial and frontal slices (healthy control, right handed male, age 42). Tracking the fibers passing through the nucleus accumbens with multi-fiber (3) tractography. A sagittal, axial and coronal maximum intensity projection is shown (yellow-orange). Bottom left: 3D view of the probabilistic tractography output. A 3D maximum intensity projection is shown in cyan with an axial MRI. On the right side, at the top, the identification of the left and right accumbens (blue) on coronal slice and at the bottom, the identification of the left and right accumbens in 3D (blue).

against manual literature review (LIT) in our study was 98% recall, meaning that almost all regions found with LIT were also proposed by TM. In particular, when compared with the systematic search of the literature, for the "Globus pallidus, internal segment," all LIT targets but one (VTA) have been correctly suggested when using the restricted ABA lexicon. This missing target could be recovered when using the machine learning named entity recognizer (BraiNER). For the STN, all the targets identified by manual literature review have been found with TM, except for subsequent divisions of a given target, identified (again) when using BraiNER. For NAcc, all the targets, except for the subdivisions of the anterior cingulate cortex have been identified. Overall and as expected, TM returns and proposes more targets than manual literature review, but also provides indication for the plausibility of a given connection between two regions. As an example, the connection between GPi and the Caudoputamen has a score of 143, making the connection highly probable. In contrast, only one single article has been found for the connection between GPi and Ammon's horn (Hippocampus).

The key advantage of TM is the ability to screen millions of documents and billion of words in a matter of hours. This way, the *complete* available biomedical literature can be processed and analyzed. Another advantage is the possibility to search within results, and order them according to relevance. It is also possible to provide feedback to the models and subsequently retrain them with that additional data in order to improve results. However, TM has several shortcomings and manual post-processing of results is mandatory. For example, complex sentences are tedious to analyze and often yield incorrect or empty results. In fact, one has to keep in mind that the estimated precision of the proposed target regions by TM is 36%. TM is not yet able to extract the directionality of the connection, nor metadata like neurotransmitter type or if the connection is inhibitory or excitatory. Additionally, TM lacks the ability to clearly differentiate between facts and hypothesis and is not yet able to trace the source of a connectivity statement (e.g., when an articles cites another reference).

When compared to the TM models, the manual, systematic search of the literature has the major advantage to select and interpret data in the light of the known anatomy, resulting in a deep and thorough analysis of the available literature. Researchers are able to filter, synthetize and aggregate very disparate and complex information into a consistent knowledge base. They are capable of interpreting every connectivity statement, of replacing it in its specific context (including experimental setting, field of expertize of the authors), and therefore of judging the exact pertinence of a connectivity statement. This detailed manual analysis comes at the cost of scaling, meaning that only a fraction of the published data will be considered.

Obviously, both approaches have compelling advantages. However, we found that the winning strategy is to *combine* and leverage the strength of *both* approaches. Indeed: TM can be deployed as a first step to screen and aggregate the scientific literature, capable of ingesting millions of documents. Thereafter comes the time for a manual and meticulous analysis and verification of the suggested connectivity statements, with the possibility to drill down to the original source (published article). The manual effort can be directed on intelligent tasks like validating and searching proposed connectivity statement, instead of their painstakingly identification from within millions of publications. Using this dual strategy (TM prior to manual review), it took less than 2 h to have proposed a set of 25 potential targets for NAcc. In comparison, it took approximately a week for a user trained in neuroanatomy to conduct the isolated literature review of NAcc as presented in Section Manual Literature Review. Therefore, the connectivity database significantly accelerates the manual search of metascale brain region connectivity, by providing a centralized repository of connectivity data for neuroscientists. Another advantage of this dual approach is the possibility for neuroscientist to collectively curate a knowledge base and therefore improve it.

Regarding the distinction of connectivity statements from different species: as demonstrated by the review for the NAcc, the majority of the available data comes from rodent studies (Berendse et al., 1992a; Zahm, 1999; Van Kuyck et al., 2007). There is a striking need to disentangle human data from non-human primate data (Brauer et al., 2000). Frequently, information reported in humans is inferred from animal studies without further notice (Meredith et al., 1996). As provided by the results section, there is no sharp correspondence for the nomina

between species for a given structure (e.g., globus pallidus, internal segment) rendering inferences from specie to another highly risky.

Furthermore, the pattern of connectivity for a given structure may differ between species (Ramnani et al., 2006; Bohland et al., 2009). Whether significant connections are reported between NAcc, hippocampus and amygdala through the available literature as identified via manual search and suggested by TM, the strength of connections between the aforementioned structures as output of the probabilistic tractography in healthy controls is not confirmatory of this result. A similar observation was reported for the subthalamic nucleus by Accolla et al. (2014). However, there are many examples of fiber pathways that are reported in dissection and tracer studies that are lacking in diffusion tensor tractography studies (Behrens et al., 2007), highlighting the importance of the selected tractography technique, its limitations and the potential role of the TM in validating connectivity information and support further investigations.

The design of an integrated platform where neuroscientist can access and curate proposed connectivity statements and share knowledge, using a standardized approach will provide significant new insights to neuroscience research. Early understanding on how to shape the TM can inform the design of future tools for neuroscience. The mining of large volumes of data and existing publications to identify patterns of and relationships between data from different levels of biological organization could help to predict parameters for experimental data to test and calibrate model implementations. Data curation and standardization is critically important to answer to brain modeling efforts as targeted by the Human Brain Project (Markram, 2012). One of the HBP objectives is to make it easier for neuroscientists to organize and access the massive volumes of heterogeneous data, knowledge and tools produced by the international neuroscience community. There is a need to bring together data from the literature, and from on-going research, and to provide a single source of annotated, high quality data.

Neuroscience is an incredibly diverse field with researcher coming from many disciplines. The cognitive psychologist might refer to Brodmann area 4, while the behavioral neuroscientist might refer to the primary motor cortex (Buitelaar et al., 2005). A researcher would not be disturbed by the different terminologies but a computer is. Furthermore, a researcher needs to have an overview of the existing difficulties posed by text before deciding on how to deal with. This is why curation process and standardization is crucial to fine-tune the TM outputs.

Which ontologies are used is also of major importance to ensure semantic heterogeneity when extracting information from various text sources. As we have seen, different instances of a region name can be used in publications which make the processing more complicated (Buitelaar et al., 2005; Ambert and Cohen, 2012). Several initiatives are trying to standardize neurosciences such as the International Neuroinformatics Coordinating Facility (INCF; http://www.incf.org/) with a global approach and more specifically Neuronames (Bowden and Martin, 1995; Bowden and Dubach, 2003) or the Neuroscience Information Framework (http://www.neuinfo.org) to fulfilling the need for standardized terminologies in neurosciences.

These techniques will provide predictions of fundamental importance for brain modeling in the operational phase of the project (Markram, 2012).

In the current study, we focused on the target identification using TM for tractography studies. TM improvements are also needed for the specificity of tractography applications, to visualize and explore projections extracted from the literature on a 3D atlas, to better evaluate topology, and speed up evaluation of results.

We believe that the TM approach could be useful for neuroscientists exploring specific DBS targets. DBS is one application but we also think that the text mining approach should be useful in helping the neuroscience community to facilitate global connectivity studies and in particular brain regions (Jbabdi and Johansen-Berg, 2011; Sporns, 2011). The applications of TM can be numerous in computational anatomy studies and in functional imaging in healthy and diseased brain. TM has also wide variety of applications in neuroscience (Tirupattur et al., 2011). The identification of biological entities such as protein and genes names as well as chemical compounds and drugs in free text, the association of gene clusters by microarray experiments with the biological context provided by the literature, automatic extraction of protein interactions and associations of proteins to functional concepts.

In conclusion, we demonstrate that connectivity for a structure of interest can be extracted from a very large amount of publications and abstracts. We believe this kind of approach will be useful in helping neuroscience community to facilitate connectivity studies of particular brain regions. The text mining tools used for the present study are indeed part of the HBP Neuroinformatics Platform and are freely available for the neuroscience community.

Acknowledgments

We acknowledge our colleagues, Antoine Lutti, Sara Lorio, Anne Ruef and Lester Melie-Garcia for the validation and implementation of the structural imaging protocols at LREN. The research leading to these results has received funding from the European Union Seventh Framework Program (FP7/2007-2013) under grant agreement n° 604102 (Human Brain Project).

Supplementary Material

The Supplementary Material for this article can be found online at: http://journal.frontiersin.org/article/10.3389/fnana.2015.00066/abstract

Supplementary Figure 1 | Brain regions co-occurrences matrix displaying the top 20 regions for which the most connection mentions was found. Matrix values represent the number of connectivity events, normalized by the confidence that each event has been extracted correctly (precision). All matrix values are linked to the corresponding detailed list of article sentences (see **Supplementary Figure 3**). The corresponding url for that figure is http://connectivity-brainer.rhcloud.com/static/br/matrix.html?db=20140226_aba&size=20.

Supplementary Figure 2 | Listing of brain regions potentially connected to Nucleus accumbens, for which connectivity events have been found in the literature. The score represents the number of connectivity events, normalized by the confidence that each event has been extracted correctly (precision). All regions are linked to the corresponding detailed list of article sentences (see **Supplementary Figure 3**). The corresponding url for that figure is http://connectivity-brainer.rhcloud.com/static/br/region.html?br=56&db=20140226_aba.

Supplementary Figure 3 | Detailed list of sentences from neuroscientific articles, in this case between "Periaqueductal gray" and "Nucleus accumbens" (list truncated for readability). Each sentence is linked to the original article on PubMed. Additionaly, the user has the ability to provide feedback: clicking on the red icon (thumbs down) will remove that sentence, and log it into the database. Similarly, clicking on the green icon (thumbs up) will confirm that sentence and log it in the database. The corresponding url for that figure is http://connectivity-brainer.rhcloud.com/static/br/details.html?br1=795&br2=56&db=20140226_aba/.

References

Accolla, E. A., Dukart, J., Helms, G., Weiskopf, N., Kherif, F., Lutti, A., et al. (2014). Brain tissue properties differentiate between motor and limbic basal ganglia circuits: brain tissue properties in Basal Ganglia. *Hum. Brain Mapp.* 35, 5083–5092. doi: 10.1002/hbm.22533

Aleman-Gomez, Y., Melie-Garcia, L., and Valdes-Hernandez, P. (2006). "IBASPM: toolbox for automatic parcellation of brain structures," in *Presented at the 12th Annual Meeting of the Organization for Human Brain Mapping June 11-15 2006*, Vol. 27 (Florence).

Alheid, G. F., Beltramino, C. A., De Olmos, J. S., Forbes, M. S., Swanson, D. J., and Heimer, L. (1998). The neuronal organization of the supracapsular part of the stria terminalis in the rat: the dorsal component of the extended amygdala. *Neuroscience* 84, 967–996. doi: 10.1016/S0306-4522(97)00560-5

Ambert, K. H., and Cohen, A. M. (2012). "Text-mining and neuroscience," in *International Review of Neurobiology* (Elsevier), 109–132. Available online at: http://linkinghub.elsevier.com/retrieve/pii/B978012388408400006X (Accessed: October 23, 2014).

Augood, S. J., Hollingsworth, Z. R., Standaert, D. G., Emson, P. C., and Penney, J. B. Jr. (2000). Localization of dopaminergic markers in the human subthalamic nucleus. *J. Comp. Neurol.* 421, 247–255. doi: 10.1002/(SICI)1096-9861(20000529)421:2<247::AID-CNE9>3.0.CO;2-F

Balan, P. F., Gerits, A., and Vanduffel, W. (2014). A practical application of text mining to literature on cognitive rehabilitation and enhancement through neurostimulation. *Front. Syst. Neurosci.* 8:182. doi: 10.3389/fnsys.2014.00182

Baliki, M. N., Mansour, A., Baria, A. T., Huang, L., Berger, S. E., Fields, H. L., et al. (2013). Parceling human accumbens into putative core and shell dissociates encoding of values for reward and pain. *J. Neurosci.* 33, 16383–16393. doi: 10.1523/JNEUROSCI.1731-13.2013

Barkhoudarian, G., Klochkov, T., Sedrak, M., Frew, A., Gorgulho, A., Behnke, E., et al. (2010). A role of diffusion tensor imaging in movement disorder surgery. *Acta Neurochir. (Wien.)* 152, 2089–2095. doi: 10.1007/s00701-010-0742-2

Baron, M. S., Sidibe, M., DeLong, M. R., and Smith, Y. (2001). Course of motor and associative pallidothalamic projections in monkeys. *J. Comp. Neurol.* 429, 490–501. doi: 10.1002/1096-9861(20010115)429:3<490::AID-CNE9>3.0.CO;2-K

Behrens, T. E. J., Berg, H. J., Jbabdi, S., Rushworth, M. F. S., and Woolrich, M. W. (2007). Probabilistic diffusion tractography with multiple fibre orientations: what can we gain? *Neuroimage* 34, 144–155. doi: 10.1016/j.neuroimage.2006.09.018

Berendse, H. W., Galis-de Graaf, Y., and Groenewegen, H. J. (1992a). Topographical organization and relationship with ventral striatal compartments of prefrontal corticostriatal projections in the rat. *J. Comp. Neurol.* 316, 314–347. doi: 10.1002/cne.903160305

Berendse, H. W., Groenewegen, H. J., and Lohman, A. H. (1992b). Compartmental distribution of ventral striatal neurons projecting to the mesencephalon in the rat. *J. Neurosci.* 12, 2079–2103.

Bevan, M. D., and Bolam, J. P. (1995). Cholinergic, GABAergic, and glutamate-enriched inputs from the mesopontine tegmentum to the subthalamic nucleus in the rat. *J. Neurosci.* 15, 7105–7120.

Bevan, M. D., Bolam, J. P., and Crossman, A. R. (1994a). Convergent synaptic input from the neostriatum and the subthalamus onto identified nigrothalamic neurons in the rat. *Eur. J. Neurosci.* 6, 320–334. doi: 10.1111/j.1460-9568.1994.tb00275.x

Bevan, M. D., Crossman, A. R., and Bolam, J. P. (1994b). Neurons projecting from the entopeduncular nucleus to the thalamus receive convergent synaptic inputs from the subthalamic nucleus and the neostriatum in the rat. *Brain Res.* 659, 99–109. doi: 10.1016/0006-8993(94)90868-0

Bevan, M. D., Francis, C. M., and Bolam, J. P. (1995a). The glutamate-enriched cortical and thalamic input to neurons in the subthalamic nucleus of the rat: convergence with GABA-positive terminals. *J. Comp. Neurol.* 361, 491–511. doi: 10.1002/cne.903610312

Bevan, M. D., Francis, C. M., and Bolam, J. P. (1995b). The glutamate-enriched cortical and thalamic input to neurons in the subthalamic nucleus of the rat: convergence with GABA-positive terminals. *J. Comp. Neurol.* 361, 491–511. doi: 10.1002/cne.903610312

Bohland, J. W., Wu, C., Barbas, H., Bokil, H., Bota, M., Breiter, H. C., et al. (2009). A proposal for a coordinated effort for the determination of brainwide neuroanatomical connectivity in model organisms at a mesoscopic scale. *PLoS Comput. Biol.* 5:e1000334. doi: 10.1371/journal.pcbi.1000334

Bota, M., and Arbib, M. A. (2004). Integrating databases and expert systems for the analysis of brain structures: connections, similarities, and homologies. *Neuroinformatics* 2, 19–58. doi: 10.1385/NI:2:1:019

Bota, M., Dong, H.-W., and Swanson, L. W. (2003). From gene networks to brain networks. *Nat. Neurosci.* 6, 795–799. doi: 10.1038/nn1096

Bota, M., and Swanson, L. W. (2008). BAMS Neuroanatomical ontology: design and implementation. *Front. Neuroinform.* 2:2. doi: 10.3389/neuro.11.002.2008

Bowden, D. M., and Dubach, M. F. (2003). NeuroNames 2002. *Neuroinformatics* 1, 43–59. doi: 10.1385/NI:1:1:043

Bowden, D. M., and Martin, R. F. (1995). NeuroNames brain hierarchy. *Neuroimage* 2, 63–83. doi: 10.1006/nimg.1995.1009

Brauer, K., Hausser, M., Hartig, W., and Arendt, T. (2000). The core-shell dichotomy of nucleus accumbens in the rhesus monkey as revealed by double-immunofluorescence and morphology of cholinergic interneurons. *Brain Res.* 858, 151–162. doi: 10.1016/S0006-8993(00)01938-7

Brown, E. N. (2007). *Signal Processing and Statistical Challenges in Neuroscience Data Analysis*. Vol. 40, From SIAM News.

Buitelaar, P., Cimiano, P., and Magnini, B. (Eds.). (2005). *Ontology Learning from Text: Methods, Evaluation and Applications*. Amsterdam; Washington: IOS Press.

Campbell, J. S. W., and Pike, G. B. (2014). Potential and limitations of diffusion MRI tractography for the study of language. *Brain Lang.* 131, 65–73. doi: 10.1016/j.bandl.2013.06.007

Canteras, N. S., Shammah-Lagnado, S. J., Silva, B. A., and Ricardo, J. A. (1990). Afferent connections of the subthalamic nucleus: a combined retrograde and anterograde horseradish peroxidase study in the rat. *Brain Res.* 513, 43–59. doi: 10.1016/0006-8993(90)91087-W

Catani, M., Howard, R. J., Pajevic, S., and Jones, D. K. (2002). Virtual *in vivo* interactive dissection of white matter fasciculi in the human brain. *Neuroimage* 17, 77–94. doi: 10.1006/nimg.2002.1136

Chaturvedi, A., Butson, C. R., Lempka, S. F., Cooper, S. E., and McIntyre, C. C. (2010). Patient-specific models of deep brain stimulation: influence of field model complexity on neural activation predictions. *Brain Stimulat.* 3, 65–67. doi: 10.1016/j.brs.2010.01.003

Chowdhury, R., Lambert, C., Dolan, R. J., and Düzel, E. (2013). Parcellation of the human substantia nigra based on anatomical connectivity to the striatum. *Neuroimage* 81, 191–198. doi: 10.1016/j.neuroimage.2013.05.043

Ciccarelli, O., Parker, G. J., Toosy, A. T., Wheeler-Kingshott, C. A., Barker, G. J., Boulby, P. A., et al. (2003a). From diffusion tractography to quantitative white matter tract measures: a reproducibility study. *Neuroimage* 18, 348–359. doi: 10.1016/S1053-8119(02)00042-3

Ciccarelli, O., Toosy, A. T., Parker, G. J. M., Wheeler-Kingshott, C. A. M., Barker, G. J., Miller, D. H., et al. (2003b). Diffusion tractography based group mapping of major white-matter pathways in the human brain. *Neuroimage* 19, 1545–1555. doi: 10.1016/S1053-8119(03)00190-3

Coenen, V. A., Allert, N., and Mädler, B. (2011). A role of diffusion tensor imaging fiber tracking in deep brain stimulation surgery: DBS of the dentato-rubro-thalamic tract (drt) for the treatment of therapy-refractory tremor. *Acta Neurochir. (Wien.)* 153, 1579–1585. doi: 10.1007/s00701-011-1036-z

Coenen, V. A., Schlaepfer, T. E., Allert, N., and Mädler, B. (2012a). "Diffusion tensor imaging and neuromodulation," in *International Review of Neurobiology* (Elsevier), 207–234. Available online at: http://linkinghub.elsevier.com/retrieve/pii/B9780124047068000115 (Accessed April 16, 2014).

Coenen, V. A., Schlaepfer, T. E., Allert, N., and Madler, B. (2012b). Diffusion tensor imaging and neuromodulation: DTI as key technology for deep brain stimulation. *Int. Rev. Neurobiol.* 107, 207–234. doi: 10.1016/B978-0-12-404706-8.00011-5

Coubes, P., Cif, L., El Fertit, H., Hemm, S., Vayssiere, N., Serrat, S., et al. (2004). Electrical stimulation of the globus pallidus internus in patients with primary generalized dystonia: long-term results. *J. Neurosurg.* 101, 189–194. doi: 10.3171/jns.2004.101.2.0189

Degos, B., Deniau, J. M., Le Cam, J., Mailly, P., and Maurice, N. (2008). Evidence for a direct subthalamo-cortical loop circuit in the rat. *Eur. J. Neurosci.* 27, 2599–2610. doi: 10.1111/j.1460-9568.2008.06229.x

French, L. (2009). Automated recognition of brain region mentions in neuroscience literature. *Front. Neuroinformatics* 3:29. doi: 10.3389/neuro.11.029.2009

French, L., Lane, S., Xu, L., Siu, C., Kwok, C., Chen, Y., et al. (2012). Application and evaluation of automated methods to extract neuroanatomical connectivity statements from free text. *Bioinformatics* 28, 2963–2970. doi: 10.1093/bioinformatics/bts542

Gerner, M., Nenadic, G., and Bergman, C. M. (2010). LINNAEUS: a species name identification system for biomedical literature. *BMC Bioinformatics* 11:85. doi: 10.1186/1471-2105-11-85

Haber, S. N. (2003). The primate basal ganglia: parallel and integrative networks. *J. Chem. Neuroanat.* 26, 317–330. doi: 10.1016/j.jchemneu.2003.10.003

Haber, S. N., Fudge, J. L., and McFarland, N. R. (2000). Striatonigrostriatal pathways in primates form an ascending spiral from the shell to the dorsolateral striatum. *J. Neurosci.* 20, 2369–2382.

Haber, S. N., Lynd, E., Klein, C., and Groenewegen, H. J. (1990a). Topographic organization of the ventral striatal efferent projections in the rhesus monkey: an anterograde tracing study. *J. Comp. Neurol.* 293, 282–298. doi: 10.1002/cne.902930210

Haber, S. N., and Nauta, W. J. (1983). Ramifications of the globus pallidus in the rat as indicated by patterns of immunohistochemistry. *Neuroscience* 9, 245–260. doi: 10.1016/0306-4522(83)90291-9

Haber, S. N., Wolfe, D. P., and Groenewegen, H. J. (1990b). The relationship between ventral striatal efferent fibers and the distribution of peptide-positive woolly fibers in the forebrain of the rhesus monkey. *Neuroscience* 39, 323–338. doi: 10.1016/0306-4522(90)90271-5

Hassani, O. K., Francois, C., Yelnik, J., and Feger, J. (1997). Evidence for a dopaminergic innervation of the subthalamic nucleus in the rat. *Brain Res.* 749, 88–94. doi: 10.1016/S0006-8993(96)01167-5

Hazrati, L. N., and Parent, A. (1991). Contralateral pallidothalamic and pallidotegmental projections in primates: an anterograde and retrograde labeling study. *Brain Res.* 567, 212–223. doi: 10.1016/0006-8993(91)90798-Z

Heimer, L., Alheid, G. F., de Olmos, J. S., Groenewegen, H. J., Haber, S. N., Harlan, R. E., et al. (1997). The accumbens: beyond the core-shell dichotomy. *J. Neuropsychiatry Clin. Neurosci.* 9, 354–381. doi: 10.1176/jnp.9.3.354

Helms, G., Dathe, H., Kallenberg, K., and Dechent, P. (2008). High-resolution maps of magnetization transfer with inherent correction for RF inhomogeneity and T1 relaxation obtained from 3D FLASH MRI. *Magn. Reson. Med.* 60, 1396–1407. doi: 10.1002/mrm.21732

Hilgetag, C. C., O'Neill, M. A., and Young, M. P. (2000). Hierarchical organization of macaque and cat cortical sensory systems explored with a novel network processor. *Philos. Trans. R. Soc. Lond. B Biol. Sci.* 355, 71–89. doi: 10.1098/rstb.2000.0550

Howell, B., Naik, S., and Grill, W. M. (2014). Influences of interpolation error, electrode geometry, and the electrode-tissue interface on models of electric fields produced by deep brain stimulation. *IEEE Trans. Biomed. Eng.* 61, 297–307. doi: 10.1109/TBME.2013.2292025

Jbabdi, S., and Johansen-Berg, H. (2011). Tractography: where do we go from here? *Brain Connect.* 1, 169–183. doi: 10.1089/brain.2011.0033

Jinnai, K., Nambu, A., and Yoshida, S. (1987). Thalamic afferents to layer I of anterior sigmoid cortex originating from the VA-VL neurons with entopeduncular input. *Exp. Brain Res.* 69, 67–76. doi: 10.1007/BF00247030

Johansen-Berg, H., and Behrens, T. E. (2006). Just pretty pictures? What diffusion tractography can add in clinical neuroscience. *Curr. Opin. Neurol.* 19, 379–385. doi: 10.1097/01.wco.0000236618.82086.01

Jones, E. G. (1990). Correlation and revised nomenclature of ventral nuclei in the thalamus of human and monkey. *Stereotact. Funct. Neurosurg.* 54-55, 1–20. doi: 10.1159/000100184

Kelley, A. E., and Domesick, V. B. (1982). The distribution of the projection from the hippocampal formation to the nucleus accumbens in the rat: an anterograde- and retrograde-horseradish peroxidase study. *Neuroscience* 7, 2321–2335. doi: 10.1016/0306-4522(82)90198-1

Kha, H. T., Finkelstein, D. I., Pow, D. V., Lawrence, A. J., and Horne, M. K. (2000). Study of projections from the entopeduncular nucleus to the thalamus of the rat. *J. Comp. Neurol.* 426, 366–377. doi: 10.1002/1096-9861(20001023)426:3<366::AID-CNE2>3.0.CO;2-B

Kincaid, A. E., Penney, J. B. Jr., Young, A. B., and Newman, S. W. (1991a). Evidence for a projection from the globus pallidus to the entopeduncular nucleus in the rat. *Neurosci. Lett.* 128, 121–125. doi: 10.1016/0304-3940(91)90774-N

Kincaid, A. E., Penney, J. B. Jr., Young, A. B., and Newman, S. W. (1991b). The globus pallidus receives a projection from the parafascicular nucleus in the rat. *Brain Res.* 553, 18–26. doi: 10.1016/0006-8993(91)90224-J

Kinoshita, M., Yamada, K., Hashimoto, N., Kato, A., Izumoto, S., Baba, T., et al. (2005). Fiber-tracking does not accurately estimate size of fiber bundle in pathological condition: initial neurosurgical experience using neuronavigation and subcortical white matter stimulation. *Neuroimage* 25, 424–429. doi: 10.1016/j.neuroimage.2004.07.076

Kita, H., and Kitai, S. T. (1994). The morphology of globus pallidus projection neurons in the rat: an intracellular staining study. *Brain Res.* 636, 308–319. doi: 10.1016/0006-8993(94)91030-8

Kitai, S. T., and Deniau, J. M. (1981). Cortical inputs to the subthalamus: intracellular analysis. *Brain Res.* 214, 411–415. doi: 10.1016/0006-8993(81)91204-X

Kopell, B. H., and Greenberg, B. D. (2008). Anatomy and physiology of the basal ganglia: implications for DBS in psychiatry. *Neurosci. Biobehav. Rev.* 32, 408–422. doi: 10.1016/j.neubiorev.2007.07.004

Laitinen, L. V., Bergenheim, A. T., and Hariz, M. I. (1992). Ventroposterolateral pallidotomy can abolish all parkinsonian symptoms. *Stereotact. Funct. Neurosurg.* 58, 14–21. doi: 10.1159/000098965

Lakhan, S. E., and Callaway, E. (2010). Deep brain stimulation for obsessive-compulsive disorder and treatment-resistant depression: systematic review. *BMC Res. Notes* 3:60. doi: 10.1186/1756-0500-3-60

Lambert, C., Zrinzo, L., Nagy, Z., Lutti, A., Hariz, M., Foltynie, T., et al. (2012). Confirmation of functional zones within the human subthalamic nucleus: patterns of connectivity and sub-parcellation using diffusion weighted imaging. *Neuroimage* 60, 83–94. doi: 10.1016/j.neuroimage.2011.11.082

Lanciego, J. L., Luquin, N., and Obeso, J. A. (2012). Functional neuroanatomy of the basal ganglia. *Cold Spring Harb. Perspect. Med.* 2:a009621. doi: 10.1101/cshperspect.a009621

Lehman, J. F., Greenberg, B. D., McIntyre, C. C., Rasmussen, S. A., and Haber, S. N. (2011). Rules ventral prefrontal cortical axons use to reach their targets: implications for diffusion tensor imaging tractography and deep brain stimulation for psychiatric illness. *J. Neurosci.* 31, 10392–10402. doi: 10.1523/JNEUROSCI.0595-11.2011

Lin, C. P., Tseng, W. Y., Cheng, H. C., and Chen, J. H. (2001). Validation of diffusion tensor magnetic resonance axonal fiber imaging with registered manganese-enhanced optic tracts. *Neuroimage* 14, 1035–1047. doi: 10.1006/nimg.2001.0882

Li, Y., Wang, Y., Hu, Y., Liang, Y., and Chen, F. (2013). Structural changes in left fusiform areas and associated fiber connections in children with abacus training: evidence from morphometry and tractography. *Front. Hum. Neurosci.* 7:335. doi: 10.3389/fnhum.2013.00335

Lujan, J. L., Chaturvedi, A., and McIntyre, C. C. (2008). Tracking the mechanisms of deep brain stimulation for neuropsychiatric disorders. *Front. Biosci. J. Virtual Libr.* 13, 5892–5904. doi: 10.2741/3124

Markram, H. (2012). The human brain project. *Sci. Am.* 306, 50–55. doi: 10.1038/scientificamerican0612-50

McDonald, A. J. (1991). Topographical organization of amygdaloid projections to the caudatoputamen, nucleus accumbens, and related striatal-like areas of the rat brain. *Neuroscience* 44, 15–33. doi: 10.1016/0306-4522(91)90248-M

McIntyre, C. C., and Foutz, T. J. (2013). Computational modeling of deep brain stimulation. *Handb Clin. Neurol.* 116, 55–61. doi: 10.1016/B978-0-444-53497-2.00005-X

Meredith, G. E., Pattiselanno, A., Groenewegen, H. J., and Haber, S. N. (1996). Shell and core in monkey and human nucleus accumbens identified with antibodies to calbindin-D28k. *J. Comp. Neurol.* 365, 628–639.

Mogenson, G. J., and Nielsen, M. A. (1983). Evidence that an accumbens to subpallidal GABAergic projection contributes to locomotor activity. *Brain Res. Bull.* 11, 309–314. doi: 10.1016/0361-9230(83)90166-1

Mogenson, G. J., Swanson, L. W., and Wu, M. (1983). Neural projections from nucleus accumbens to globus pallidus, substantia innominata, and lateral preoptic-lateral hypothalamic area: an anatomical and electrophysiological investigation in the rat. *J. Neurosci.* 3, 189–202.

Mohammadi, S., Möller, H. E., Kugel, H., Müller, D. K., and Deppe, M. (2010). Correcting eddy current and motion effects by affine whole-brain registrations: evaluation of three-dimensional distortions and comparison with slicewise correction. *Magn. Reson. Med.* 64, 1047–1056. doi: 10.1002/mrm.22501

Mori, S., and van Zijl, P. C. M. (2002). Fiber tracking: principles and strategies - a technical review. *NMR Biomed.* 15, 468–480. doi: 10.1002/nbm.781

Naito, A., and Kita, H. (1994). The cortico-nigral projection in the rat: an anterograde tracing study with biotinylated dextran amine. *Brain Res.* 637, 317–322. doi: 10.1016/0006-8993(94)91252-1

Nambu, A., Tokuno, H., Hamada, I., Kita, H., Imanishi, M., Akazawa, T., et al. (2000). Excitatory cortical inputs to pallidal neurons via the subthalamic nucleus in the monkey. *J. Neurophysiol.* 84, 289–300.

Napier, T. C., and Maslowski-Cobuzzi, R. J. (1994). Electrophysiological verification of the presence of D1 and D2 dopamine receptors within the ventral pallidum. *Synapse* 17, 160–166. doi: 10.1002/syn.890170304

Nauta, H. J., and Cole, M. (1978). Efferent projections of the subthalamic nucleus: an autoradiographic study in monkey and cat. *J. Comp. Neurol.* 180, 1–16. doi: 10.1002/cne.901800102

Parent, A. (1979). Identification of the pallidal and peripallidal cells projecting to the habenula in monkey. *Neurosci. Lett.* 15, 159–164. doi: 10.1016/0304-3940(79)96106-8

Parent, A., and De Bellefeuille, L. (1983). The pallidointralaminar and pallidonigral projections in primate as studied by retrograde double-labeling method. *Brain Res.* 278, 11–27. doi: 10.1016/0006-8993(83)90222-6

Parent, A., Bouchard, C., and Smith, Y. (1984). The striatopallidal and striatonigral projections: two distinct fiber systems in primate. *Brain Res.* 303, 385–390. doi: 10.1016/0006-8993(84)91224-1

Parent, A., and Cicchetti, F. (1998). The current model of basal ganglia organization under scrutiny. *Mov. Disord.* 13, 199–202. doi: 10.1002/mds.870130202

Parker, G. J. M., Stephan, K. E., Barker, G. J., Rowe, J. B., MacManus, D. G., Wheeler-Kingshott, C. A. M., et al. (2002). Initial demonstration of *in vivo* tracing of axonal projections in the macaque brain and comparison with the human brain using diffusion tensor imaging and fast marching tractography. *Neuroimage* 15, 797–809. doi: 10.1006/nimg.2001.0994

Paxinos, G., and Watson, C. (2007). *The Rat Brain in Stereotaxic Coordinates*. Amsterdam; Boston: Elsevier.

Pouratian, N., Zheng, Z., Bari, A. A., Behnke, E., Elias, W. J., and DeSalles, A. A. F. (2011). Multi-institutional evaluation of deep brain stimulation targeting using probabilistic connectivity-based thalamic segmentation: clinical article. *J. Neurosurg.* 115, 995–1004. doi: 10.3171/2011.7.JNS11250

Puelles Lopez, L. (2000). Brain maps: structure of the rat brain (2nd edn) by L.W. Swanson. *Trends Neurosci.* 23, 88–89. doi: 10.1016/S0166-2236(99)01519-2

Ramnani, N., Behrens, T. E. J., Johansen-Berg, H., Richter, M. C., Pinsk, M. A., Andersson, J. L. R., et al. (2006). The evolution of prefrontal inputs to the cortico-pontine system: diffusion imaging evidence from Macaque monkeys and humans. *Cereb. Cortex* 16, 811–818. doi: 10.1093/cercor/bhj024

Richardet, R., Chappelier, J.-C., Telefont, M., and Hill, S. (2015). Large-scale extraction of brain connectivity from the neuroscientific literature. *Bioinforma. Oxf. Engl.* 31, 1640–1647. doi: 10.1093/bioinformatics/btv025

Rico, A. J., Barroso-Chinea, P., Conte-Perales, L., Roda, E., Gomez-Bautista, V., Gendive, M., et al. (2010). A direct projection from the subthalamic nucleus to the ventral thalamus in monkeys. *Neurobiol. Dis.* 39, 381–392. doi: 10.1016/j.nbd.2010.05.004

Rozanski, V. E., Vollmar, C., Cunha, J. P., Tafula, S. M. N., Ahmadi, S.-A., Patzig, M., et al. (2014). Connectivity patterns of pallidal DBS electrodes in focal dystonia: a diffusion tensor tractography study. *Neuroimage* 84, 435–442. doi: 10.1016/j.neuroimage.2013.09.009

Schierwagen, A. (2008). Neuronal morphology: shape characteristics and models. *Neurophysiology* 40, 366–372. doi: 10.1007/s11062-009-9054-7

Sedrak, M., Gorgulho, A., Bari, A., Behnke, E., Frew, A., Gevorkyan, I., et al. (2010). Diffusion tensor imaging (DTI) and colored fractional anisotropy (FA) mapping of the subthalamic nucleus (STN) and the globus pallidus interna (GPi). *Acta Neurochir. (Wien.)* 152, 2079–2084. doi: 10.1007/s00701-010-0813-4

Shink, E., and Smith, Y. (1995). Differential synaptic innervation of neurons in the internal and external segments of the globus pallidus by the GABA- and glutamate-containing terminals in the squirrel monkey. *J. Comp. Neurol.* 358, 119–141. doi: 10.1002/cne.903580108

Sidibe, M., Pare, J. F., and Smith, Y. (2002). Nigral and pallidal inputs to functionally segregated thalamostriatal neurons in the centromedian/parafascicular intralaminar nuclear complex in monkey. *J. Comp. Neurol.* 447, 286–299. doi: 10.1002/cne.10247

Smith, A. D., and Bolam, J. P. (1990a). The neural network of the basal ganglia as revealed by the study of synaptic connections of identified neurones. *Trends Neurosci.* 13, 259–265. doi: 10.1016/0166-2236(90)90106-K

Smith, Y., and Bolam, J. P. (1991). Convergence of synaptic inputs from the striatum and the globus pallidus onto identified nigrocollicular cells in the rat: a double anterograde labelling study. *Neuroscience* 44, 45–73. doi: 10.1016/0306-4522(91)90250-R

Smith, Y., and Bolam, J. P. (1990b). The output neurones and the dopaminergic neurones of the substantia nigra receive a GABA-containing input from the globus pallidus in the rat. *J. Comp. Neurol.* 296, 47–64. doi: 10.1002/cne.902960105

Smith, Y., and Parent, A. (1988). Neurons of the subthalamic nucleus in primates display glutamate but not GABA immunoreactivity. *Brain Res.* 453, 353–356. doi: 10.1016/0006-8993(88)90177-1

Sporns, O. (2011). The human connectome: a complex network: the human connectome. *Ann. N.Y. Acad. Sci.* 1224, 109–125. doi: 10.1111/j.1749-6632.2010.05888.x

Sugimoto, T., and Hattori, T. (1983). Confirmation of thalamosubthalamic projections by electron microscopic autoradiography. *Brain Res.* 267, 335–339. doi: 10.1016/0006-8993(83)90885-5

Sugimoto, T., Hattori, T., Mizuno, N., Itoh, K., and Sato, M. (1983). Direct projections from the centre median-parafascicular complex to the subthalamic nucleus in the cat and rat. *J. Comp. Neurol.* 214, 209–216. doi: 10.1002/cne.902140208

Sweet, J. A., Walter, B. L., Gunalan, K., Chaturvedi, A., McIntyre, C. C., and Miller, J. P. (2014a). Fiber tractography of the axonal pathways linking the basal ganglia and cerebellum in Parkinson disease: implications for targeting in deep brain stimulation: Clinical article. *J. Neurosurg.* 120, 988–996. doi: 10.3171/2013.12.JNS131537

Sweet, J. A., Walter, B. L., Munyon, C., and Miller, J. P. (2014b). Multitract orthogonal microelectrode localization of the subthalamic nucleus: description of a novel technique. *Neurosurgery* 10(Suppl. 2), 240–245; discussion: 245. doi: 10.1227/NEU.0000000000000295

Taljan, K., McIntyre, C., and Sakaie, K. (2011). Anatomical connectivity between subcortical structures. *Brain Connect.* 1, 111–118. doi: 10.1089/brain.2011.0011

Thomas, C., Ye, F. Q., Irfanoglu, M. O., Modi, P., Saleem, K. S., Leopold, D. A., et al. (2014). Anatomical accuracy of brain connections derived from diffusion MRI tractography is inherently limited. *Proc. Natl. Acad. Sci. U.S.A.* 111, 16574–16579. doi: 10.1073/pnas.1405672111

Tirupattur, N., Lapish, C. C., Mukhopadhyay, S., Pham, T. D., Zhou, X., Tanaka, H., et al. (2011). 2011 International symposium on computational models for life sciences (CMLS-11). *AIP Conf. Proc.* 1371, 118–127.

Traynor, C., Heckemann, R. A., Hammers, A., O'Muircheartaigh, J., Crum, W. R., Barker, G. J., et al. (2010). Reproducibility of thalamic segmentation based on probabilistic tractography. *Neuroimage* 52, 69–85. doi: 10.1016/j.neuroimage.2010.04.024

Van Kuyck, K., Gabriels, L., Cosyns, P., Arckens, L., Sturm, V., Rasmussen, S., et al. (2007). Behavioural and physiological effects of electrical stimulation in the nucleus accumbens: a review. *Acta Neurochir. Suppl.* 97, 375–391. doi: 10.1007/978-3-211-33081-4_43

Voorn, P., Gerfen, C. R., and Groenewegen, H. J. (1989). Compartmental organization of the ventral striatum of the rat: immunohistochemical distribution of enkephalin, substance P, dopamine, and calcium-binding protein. *J. Comp. Neurol.* 289, 189–201. doi: 10.1002/cne.902890202

Wakana, S., Caprihan, A., Panzenboeck, M. M., Fallon, J. H., Perry, M., Gollub, R. L., et al. (2007). Reproducibility of quantitative tractography methods applied to cerebral white matter. *Neuroimage* 36, 630–644. doi: 10.1016/j.neuroimage.2007.02.049

Wu, Y., Richard, S., and Parent, A. (2000). The organization of the striatal output system: a single-cell juxtacellular labeling study in the rat. *Neurosci. Res.* 38, 49–62. doi: 10.1016/S0168-0102(00)00140-1

Zahm, D. S. (1999). Functional-anatomical implications of the nucleus accumbens core and shell subterritories. *Ann. N.Y. Acad. Sci.* 877, 113–128. doi: 10.1111/j.1749-6632.1999.tb09264.x

Conflict of Interest Statement: The authors declare that the research was conducted in the absence of any commercial or financial relationships that could be construed as a potential conflict of interest.

Advantages of publishing in Frontiers

OPEN ACCESS
Articles are free to read, for greatest visibility

COLLABORATIVE PEER-REVIEW
Designed to be rigorous – yet also collaborative, fair and constructive

FAST PUBLICATION
Average 85 days from submission to publication (across all journals)

COPYRIGHT TO AUTHORS
No limit to article distribution and re-use

TRANSPARENT
Editors and reviewers acknowledged by name on published articles

SUPPORT
By our Swiss-based editorial team

IMPACT METRICS
Advanced metrics track your article's impact

GLOBAL SPREAD
5'100'000+ monthly article views and downloads

LOOP RESEARCH NETWORK
Our network increases readership for your article

Frontiers
EPFL Innovation Park, Building I • 1015 Lausanne • Switzerland
Tel +41 21 510 17 00 • Fax +41 21 510 17 01 • info@frontiersin.org
www.frontiersin.org

Find us on